



L U V O I R

FINAL REPORT APPENDICES



CONTENTS

Appendix A.	Further LUVOIR science cases.....	A-1
A.1	Observations of Venus with LUVOIR	A-2
A.2	Geology and surface processes in the solar system	A-6
A.3	Imaging the unseen northern hemispheres of the large moons of Uranus and Triton	A-8
A.4	Ocean worlds science with LUVOIR	A-10
A.5	Small bodies of the inner solar system	A-14
A.6	Comets and minor planets: the importance of the small things	A-17
A.7	Exo-cartography for terrestrial planets	A-22
A.8	Prospects for mapping terrestrial exoplanets with LUVOIR	A-25
A.9	Detecting liquid surface water on exoplanets	A-28
A.10	The detection of terrestrial planets in the habitable zones of A-stars.....	A-33
A.11	Transit spectroscopy of Earth-sized planets around M-dwarfs.....	A-36
A.12	A statistical search for global habitability and biospheres beyond Earth	A-39
A.13	A statistical test of the habitable zone	A-43
A.14	Observation of oxygen and hydrogen exospheres of Earth-like exoplanets.....	A-47
A.15	Detecting methane biosignatures on transiting exoplanets	A-49
A.16	Leveraging planetary seasonality to recognize habitability and to detect the pulse of a biosphere.....	A-52
A.17	Technosignature observations with LUVOIR	A-56
A.18	Exoplanet diversity in the LUVOIR era.....	A-61
A.19	Detecting exomoons with LUVOIR.....	A-64
A.20	The transmission spectra of rock atmospheres on magma worlds.....	A-69
A.21	Spatially resolved maps of star-forming gas with LUVOIR.....	A-72
A.22	Protostellar outflows/jets.....	A-74
A.23	The quiescent UV spectra of cool dwarf stars.....	A-77
A.24	UV characterization of exoplanet host stars: keys to atmospheric photochemistry and evolution	A-80
A.25	Resolved photometry of young super star clusters.....	A-83
A.26	LUVOIR for stars, stellar evolution, and the local universe.....	A-86
A.27	The rise of the periodic table	A-92
A.28	Extragalactic massive stars	A-97
A.29	White dwarfs as probes of fundamental astrophysics	A-100
A.30	Characterizing the nuclear outflow at the galactic core	A-104
A.31	Ultraviolet haloes around edge-on galaxies	A-107
A.32	The attenuation relation in overlapping galaxies	A-110
A.33	Quest for the first quasars	A-113
A.34	Exploring the high energy processes in microquasars as an exemplar case for high time resolution astrophysics.....	A-116
A.35	Uncovering the transition between the cosmic dark age and the cosmic dawn	A-119

Appendix B.	Design reference missions.....	B-1
B.1	The LUVUOIR science simulation tools.....	B-1
B.2	Signature Science Case #1: Finding habitable exoplanet candidates.....	B-9
B.3	Signature Science Case #2: Searching for biosignatures and confirming habitability	B-22
B.4	Signature Science Case #3: The search for habitable worlds in the solar system.....	B-31
B.5	Signature Science Case #4: Comparative atmospheres.....	B-37
B.6	Signature Science Case #5: The formation of planetary systems	B-48
B.7	Signature Science Case #6: Small bodies in the solar system	B-59
B.8	Signature Science Case #7: Connecting the smallest scales across cosmic time.....	B-63
B.9	Signature Science Case #8: Constraining dark matter using high precision astrometry	B-67
B.10	Signature Science Case #9: Tracing ionizing light over cosmic time.....	B-74
B.11	Signature Science Case #10: The cycles of galactic matter	B-80
B.12	Signature Science Case #11: The multiscale assembly of galaxies	B-88
B.13	Signature Science Case #12: Stars as the engines of galactic feedback.....	B-93
Appendix C.	Complete science traceability matrices.....	C-1
Appendix D.	Completed technical trades.....	D-1
D.1	Aperture geometry.....	D-1
D.2	Telescope optical design.....	D-5
D.3	Secondary mirror deployment	D-6
D.4	Primary mirror baffle	D-8
D.5	Attitude control systems and gimbal architectures	D-8
Appendix E.	Detailed technical budgets.....	E-1
E.1	Mass.....	E-1
E.2	Power	E-5
E.3	Wavefront error	E-5
E.4	Optical telescope assembly (OTA) and spacecraft thermal assumptions and budgets.....	E-5
E.5	Structural analysis.....	E-13
E.6	Propulsion	E-18
Appendix F.	Heritage	F-1
Appendix G.	Detailed schedule	G-1
Appendix H.	Further POLLUX details	H-1
H.1	POLLUX consortium.....	H-1
H.2	Cost of POLLUX	H-6
H.3	UV polarimeters	H-7
H.4	Budgets	H-17
H.5	Calibration unit	H-23

H.6	Performances.....	H-31
H.7	A simulator for POLLUX.....	H-40
H.8	Echelle gratings	H-43
H.9	Detectors for POLLUX.....	H-48
H.10	DRMs.....	H-53
Appendix I.	Additional LUVOIR instrument concepts.....	I-1
I.1	Starshades for LUVOIR	I-1
I.2	Extension of LUVOIR’s capabilities to 5 μm or beyond	I-6
I.3	JAXA transit spectrometer for LUVOIR.....	I-13
Appendix J.	Astro2020 pre-Decadal cost estimation of LUVOIR.....	J-1
J.1	Introduction.....	J-1
J.2	LUVOIR cost input assumptions	J-4
J.3	NASA GSFC’s LUVOIR costing methodologies	J-6
J.4	NASA’s GSFC cost estimates for LUVOIR-A and LUVOIR-B	J-10
J.5	LUVOIR Work Breakdown Structure (WBS)	J-12
J.6	Summary and conclusion	J-12
References	Ref-1

APPENDIX A. FURTHER LUVOIR SCIENCE CASES

To better capture the full range of LUVOIR’s capabilities, this appendix includes short additional LUVOIR science programs contributed by the community and LUVOIR team members. The topics range from remote sensing of solar system bodies, to exoplanet observations, to a wide range of general astrophysics studies. In some instances, the authors have chosen to provide further details—or put their own perspective—on a case that is mentioned in the main science chapters. These cases of varying lengths show how LUVOIR can provide powerful science capabilities for a broad range of planetary scientists, astrobiologists, and astrophysicists.

A.1 Observations of Venus with LUVVOIR

Giada Arney (NASA GSFC), Valeria Cottini (NASA GSFC), Shawn Domagal-Goldman (NASA GSFC), Lori Glaze (NASA GSFC), Eric Lopez (NASA GSFC), Victoria Meadows (UW), Ravi Kopparapu (NASA GSFC), Roser Juanola Parramon (NASA GSFC)

A.1.1 Introduction

At its closest approach, Venus is the nearest planet to Earth, yet much still remains unknown about Earth's twisted sister. Many important Venus science questions can be addressed with sys-Earth telescopic observations. A sufficiently small solar elongation viewing angle for LUVVOIR ($\leq 45^\circ$) enables such observations of Venus. This, together with a darkening neutral density filter, opens the door to exciting and much needed data on the Venusian atmosphere. Three interesting case studies that could be investigated with LUVVOIR are described briefly below as examples of the types of Venus science LUVVOIR can make possible.

1. Observations from the JAXA Akatsuki orbiter have revealed an unusual stationary bow-shaped wave at the Venus cloud tops (65 km) observable at multiple wavelengths from the UV at 283 nm (corresponding to a SO_2 absorption band) to the longwave infrared at 8–12 microns (Fukuhara et al. 2017). Normal wind speeds at these high altitudes whip across the planet at roughly 100 m/s, but this UV-bright, bow-shaped feature remains stationary relative to the surface far below. The center of the bow-shaped feature (**Figure A-1**) is located above the western slope of equatorial highland region Aphrodite Terra, and is interpreted to be a stationary atmospheric gravity wave associated with lower atmosphere wind flows over the terrain. However, the propagation of such waves to the cloud tops is difficult to reconcile with current understanding of convection in the Venus atmosphere (Seiff et al. 1985). Thus, the dynamics of the Venus atmosphere may be more complex than previously thought. Monitoring the temporal evolution of features such as this could provide new insights into the physics of Venus atmosphere circulation.

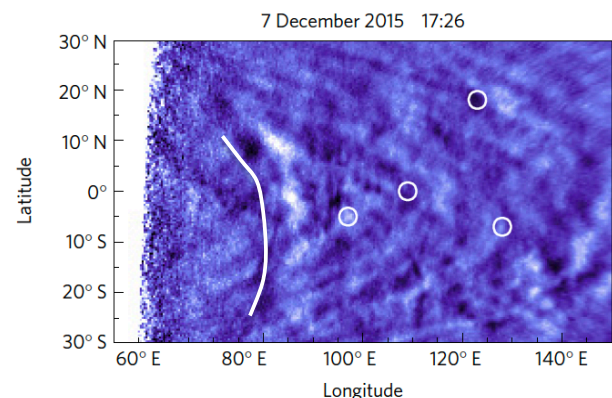


Figure A-1. A bow-shaped UV bright wave in the Venus upper atmosphere (highlighted with solid white line) seen with Akatsuki above the highland region Aphrodite Terra could be observed with LUVVOIR and shed light on Venus atmospheric dynamics. Circles indicate displaced air parcels. Credit: Fukuhara et al. 2017

2. Long temporal baseline (1970s–2012) monitoring of Venus across multiple Venus missions at $\lambda = 215$ and 283 nm has revealed quasi-periodic variations in high altitude (70 km) SO_2 abundance (Marcq et al. 2012) with reported variations from ~ 400 ppbv to less than 100 ppbv. This variability may be related to poorly understood oscillations in atmospheric circulation, and/or volcanic injections of SO_2 into the upper atmosphere. The amount of SO_2 currently in the atmosphere has been estimated to be in excess of equilibrated conditions by a factor of 100, implying a source (i.e. volcanism) within the past 20 million years (Bullock & Grinspoon 2001). Monitoring of SO_2 variations may therefore shed light on multiple processes related to atmospheric dynamics and/or

volcanic processes. Such a monitoring campaign demands a UV-enabled space-based platform that can observe Venus over years or decades.

3. Besides SO_2 , several other trace gases can be observed in the Venus spectrum, providing insights into chemical, dynamical, and photochemical processes that occur on Venus. For example, significant and surprising variability has been observed in the abundances and distributions of trace gases in the Venusian sub-cloud atmosphere (Arney et al. 2014). These variations hint at poorly understood chemical and physical mechanisms operating in the lower atmosphere. They also suggest the presence of H_2SO_4 virga events (rain that evaporates before reaching the surface). Between $1\text{--}2.5\ \mu\text{m}$, one can observe upwelling thermal radiation from the sub-cloud (0–45 km) atmosphere on the Venus nightside. This enables deep-atmosphere observations of HDO, H_2O , SO_2 , HCl, CO, and OCS, which have been observed to vary both spatially and temporally on poorly constrained timescales.

Because exo-Venus planets may be one of the most common types of exoplanets (Kane et al. 2014), better understanding the planet next door will enable us to better interpret observations of exo-Venus worlds.

A.1.2 The role of LUVOIR

Currently, there is no planned NASA mission to Venus. Periodic monitoring of Venus over long time baselines can reveal important information about variations in atmospheric species that may constrain theories of dynamical, chemical, and geophysical processes occurring on Venus. LUVOIR-A can point to a minimum solar elongation angle of 33° , which is small enough to enable observations of Venus at even less than its maximum elongation. Observations towards crescent phase will enable observations of nightside thermal radiation upwelling from below the cloud deck. Certain UV observations (e.g., of high altitude SO_2 variations and of the “bow” shaped feature) require a space-based observatory, as they cannot be performed from the ground.

LUVOIR could achieve extremely good spatial resolution on Venus. **Figure A-2** shows a view of Venus from the Akatsuki orbiter at $\sim 2\ \mu\text{m}$ showing variations in opacity of the lower



Figure A-2. A view of Venus from JAXA's Akatsuki. LUVOIR-A would obtain comparable spatial resolution. Credit: R. Juanola Parramon (NASA GSFC)/Damia Bouic/JAXA Akatsuki

Program at a Glance

Science goal: Obtain high spatial and high spectral resolution data of Venus at UV-VIS-NIR wavelengths to monitor for atmospheric variability possibly related to atmospheric dynamics, chemistry, and/or volcanic activity.

Program details: Venus will have an angular diameter $\sim 30''$ at maximum solar elongation, and its day-side magnitudes are: $U = -2.79$, $V = -3.68$, $B = -4.38$, $R = -4.95$, $I = -5.08$, $R_c = -4.73$, $I_c = -5.04$.

Instrument(s) + configuration(s): ECLIPS and LUMOS could be used to obtain medium to very high-resolution spectra. LUMOS can fit Venus in its FOV; ECLIPS would require mosaicing. HDI can obtain extremely high spatial resolution images from the UV to NIR.

Key observation requirements: Observations of Venus will require neutral density filters and the ability to observe at a sufficiently small solar elongation angle ($< 45^\circ$). This is compatible with the design of the notional LUVVOIR-A.

cloud deck on the planet's nightside. LUVVOIR-A (B) could achieve a spatial resolution of 30 (56) km/resolution element at this wavelength when the planet is at quadrature, and 7 (15) km/resolution element at 550 nm. The Venus Monitoring Camera aboard ESA's Venus Express orbiter could obtain 0.2–45 km/pixel depending on how far the spacecraft was from the planet (Markiewicz et al. 2007). LUVVOIR allows for orbiter-quality monitoring of Venus.

A.1.3 The science program

Venus is significantly brighter than other sources LUVVOIR will observe ($m_v = -4.4$ on the dayside), necessitating neutral density filters to view this interesting target. To underscore this point, the brightest source the online LUMOS ETC includes has an AB magnitude of 15, and the brightest source included for HDI is magnitude 20. Venus is an extremely bright target for LUVVOIR. However, LUVVOIR is also considering observations of Jupiter, which has $m_v = -2.7$, so Venus is comparable to other bright solar system targets under consideration.

The angular diameter of Venus is $\sim 30''$ when the planet is close to maximum elongation. The LUVVOIR-A LUMOS spectrometer currently has a wavelength range 100–400 nm, and it may be extended to 1000 nm. LUMOS has several available resolutions ($R = 500, 16000, 63200, 100000$), enabling moderate and very high-resolution spectroscopy. For comparison, previous observations probing isotopes in the Venus atmosphere have used $R = 10^5$ (Krasnopolsky et al 2010), while measurement of gas species in the nightside thermal windows can be accomplished with $R = 2000$ (Arney et al 2014), so the range of resolutions used by LUVVOIR are useful for a variety of science. The LUMOS field-of-view (FOV) is $2' \times 2'$, so Venus fits comfortably within it. LUVVOIR-A HDI has a FOV of $2' \times 3'$, which also allows for full views of Venus in a single frame.

References

- Arney, G., Meadows, V., Crisp, D., et al. 2014, *J Geophys Res Planets*, 119, 1860
 Bullock, M., & Grinspoon, D. 2001, *Icarus*, 150, 19

Fukuhara, T., Futaguchi, M., Hashimoto, G. L., et al. 2017, *Nat Geosci*, 10, 85
Kane, S. R., Kopparapu, R. K., & Domagal-Goldman, S. D. 2014, *Astrophys J*, 794, L5
Marcq, E., Bertaux, J., Montmessin, F., & Belyaev, D. 2012, *Nat Geosci*, 6, 1
Markiewicz, W. J., Titov, D. V., Fiethe, B., et al. 2007, *ESA Spec Publ*, 1
Seiff, A., Schofield, J. T., Kliore, A. J., et al. 1985, *Adv Sp Res*, 5, 3

A.2 Geology and surface processes in the solar system

Noah Petro (NASA Goddard Space Flight Center)

A.2.1 Introduction

All solid objects in the Solar System undergo regular variations due to internal and external forces. However, we know now that these variations can cause measureable changes to the surface and exosphere of small, airless, bodies. The large moons of Jupiter and Saturn, for example, experience tidal heating that can trigger geysers or possibly volcanic eruptions. However, in order to measure these events requires nearly constant monitoring of an object over multiple hours or even days, so that the full range of variation in surface properties (surface temperature changes, albedo and/or compositional changes) can be measured. Spectral measurements of the erupted material (either volcanic or via geyser, see **Figure A-3**) and comparison to the surface will provide important constraints on compositional variations of the source regions of these moons. Additionally, watching an entire eruption and being able to characterize any compositional changes that occur will provide insights into the mechanism by which these eruptions occur.

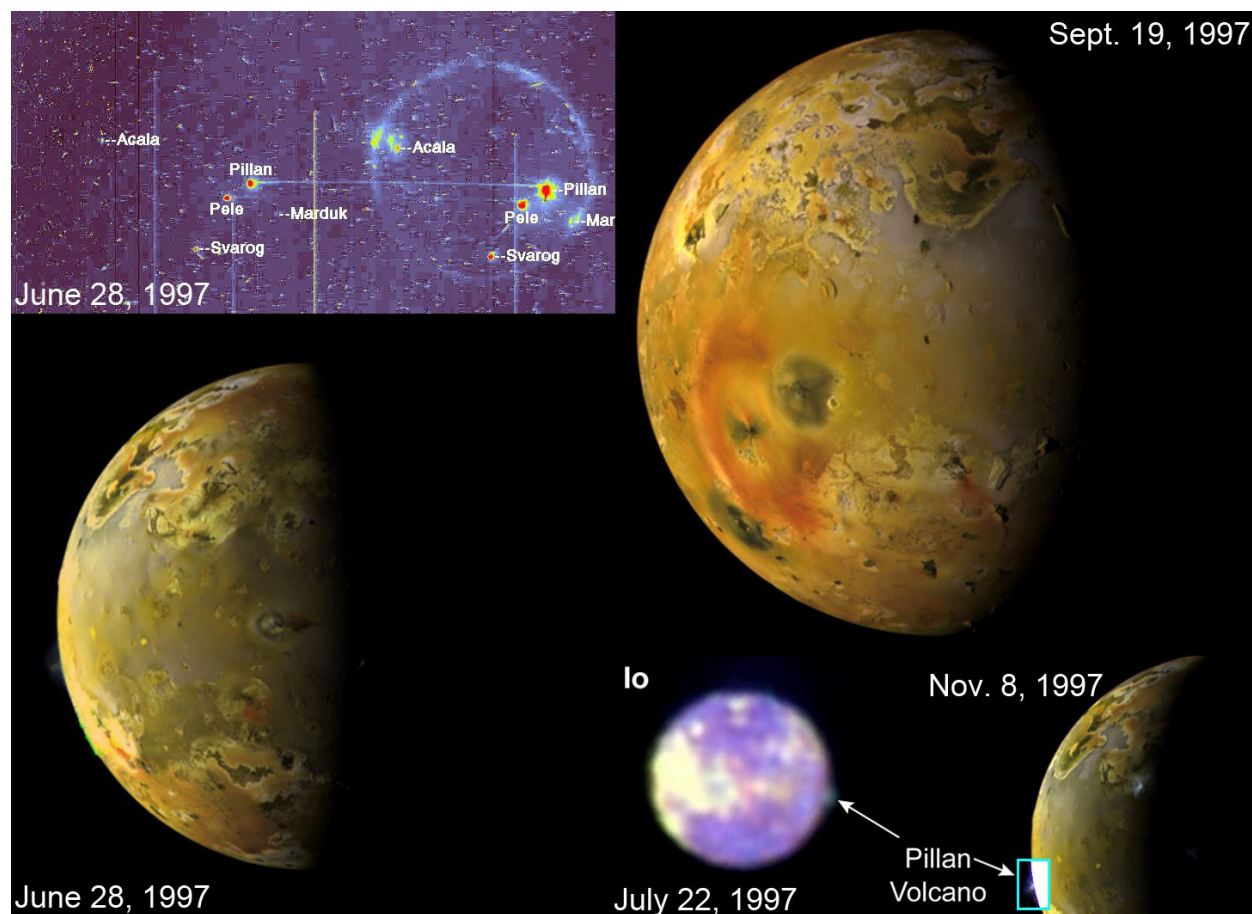


Figure A-3. *Galileo* (June/28/1997: daylight and eclipse, Nov/8/1997, Sep/19/1997) and *HST* (July/22/1997) observations of the eruptions on *Io*. Montage by Jason Perry

Program at a Glance

Science goal: Planetary observations to identify surface and environmental changes on the moons of Jupiter and Saturn.

Program details: Observing silicate and icy bodies extensively (over days and possibly weeks) allows for the identification of changes, for example, volcanic or eruptive activity on outer Solar System moons. Measurements into thermal bands will support observations of Io's volcanic activity.

Instrument(s) + configuration(s): HDI

Key observation requirements: Imaging at 0.5–3.5 μm ; several meter-km spatial resolution. Observations of the moons of Jupiter and Saturn require tracking and high-precision pointing.

A.2.2 The role of LUVVOIR

A highly capable observatory in space provides an excellent opportunity to make high-resolution (spatial, spectral, and temporal) observations of planetary bodies. Any of the observations listed above could be the focus of one or more dedicated missions to those bodies. LUVVOIR could fulfill, complement, or supplement any mission objectives for a mission to those bodies.

A.2.3 The science program

Observations of the moons of Saturn and Jupiter would require planning for optimal viewing of their transits about their planet. Imaging with HDI would be useful for characterizing the composition of these moons and to identify activity there. Ideally, wavelengths should go beyond 3 μm for water observations (longer for thermal observations).

A.3 Imaging the unseen northern hemispheres of the large moons of Uranus and Triton

Richard Cartwright (SETI Institute)

A.3.1 Introduction

The satellite systems of Uranus and Neptune are relatively unexplored compared to the moons of Jupiter and Saturn, which have been visited by orbiting spacecrafts and multiple spacecraft flybys. Consequently, the processes modifying the surface compositions of the Uranian and Neptunian moons are still poorly understood. The spatially-resolved data collected by Voyager 2 of the five large moons of Uranus and the large Neptunian moon Triton almost exclusively sampled their southern latitudes. Furthermore, the instrument suite onboard Voyager 2 did not include a near-infrared (NIR) spectrometer, and no spatially-resolved NIR spectra of these moons exists. Very few ultraviolet (UV) observations have been made of these moons (none of which were spatially-resolved), limiting our ability to investigate the importance of UV and charged particle irradiation of their surfaces. Thus, the limited spatial extent and limited wavelength coverage of previous observations greatly diminishes our ability to constrain the processes modifying the surfaces of these satellites.

A.3.2 The role of LUVUOIR

Observations made using the HDI instrument ($\sim 0.2\text{--}2.5\ \mu\text{m}$) onboard LUVUOIR would dramatically improve our understanding of these satellite systems, providing spatially-resolved data over a wide wavelength range (with either the A or B architectures).

A.3.3 The science program

We propose to observe the leading and trailing hemispheres of the tidally-locked Uranian satellites Miranda, Ariel, Umbriel, Titania, and Oberon, and the Neptunian moons Proteus and Triton with HDI (we also propose to collect two observations of the non-tidally-locked Neptunian satellite Nereid). Properties of these worlds are provided in **Table A-1**. Based on the available online tools, HDI (UVIS and IR channels) can easily achieve signal-to-noise (SNR) > 100 for these eight moons ($V_{\text{mag}} \sim 13.5\text{--}20$) in ~ 10 s or less of integration time per filter, per target. The proposed grism for HDI might require ~ 30 to 600 s of integration time per target, depending on the wavelength range covered by the grism. We provide a conservative estimate of **8 hours of total observing time** to observe the leading and trailing hemispheres of all seven tidally-locked moons (and two observations of Nereid) with HDI (12 m aperture). The proposed field of view for HDI ($2' \times 3'$) is wide enough to allow multiple moons to be imaged at the same time. With savvy scheduling, all five Uranian moons can fit in the FOV of HDI and be imaged simultaneously, and at Neptune, both Triton and Proteus can be imaged in the same frame by HDI. Thus, depending on the final design of HDI (grism settings and the number of narrow filters spanning ~ 0.2 to $2.5\ \mu\text{m}$), and the scheduling constraints of these proposed observations, the total amount of observing time required for this project could decrease substantially.

These observations are accomplishable in 16 pointings to image each moon twice using the HDI UVIS and IR detectors. Sufficient data can be obtained in a set of 10 exposures per pointing, collected in a dithering pattern, with exposure lengths of ~ 5 to 30 s in length

Table A-1. *Observation requirements for detecting key atmospheric features that constrain the presence of liquid surface water on rocky exoplanets.*

Planetary System	Satellite	Vmag	Mean Orbital Radius (km)	*Max. Elongtion (arcsec.)	Angular Diameter (arcsec.)
Uranus	Miranda	16.5	130,000	9.0	0.03
	Ariel	14.4	191,000	14.0	0.08
	Umbriel	15.1	266,000	16.5	0.08
	Titania	14.0	436,000	32.0	0.11
	Oberon	14.2	584,000	42.0	0.11
Neptune	Proteus	19.8	118,000	5.5	0.02
	Triton	13.5	355,000	17.0	0.13
	Nereid	19.2	5,514,000	457.0	0.02

*Max elongation values are for a ground-based facility observing these moons in 2018.

Program at a Glance

Science goal: To study surfaces of satellites of Uranus and Neptune.

Program details: Imaging of icy moon surfaces, with time separated imaging to study the leading and trailing hemispheres. Exposures are 5–30 s in length.

Instrument(s) + configuration(s): HDI imaging (+ grism spectroscopy). HDI FOV (2' x 3') wide enough to enable observations of multiple moons at once.

Key observation requirements: 0.2–2.5 μm ; SNR > 100s.

per exposure (approximately up to 10x longer if using the grism mode), depending on the brightness of the target. Repeated observations (two total) will allow us to image both the leading and training hemispheres of these moons, which may have different compositions. The length of time separation between these observations will vary depending on the target's orbital period.

A.4 Ocean worlds science with LUV0IR

Marc Neveu (NASA GSFC/U of MD College Park)

A.4.1 Introduction

Ocean worlds in the solar system, defined as bodies with a current local or global liquid ocean (Hendrix, Hurford et al. 2019) may harbor life beyond Earth. There is strong evidence for subsurface oceans and/or related surface activity on Jupiter’s moons Europa, Ganymede, and Callisto (Khurana et al. 1998; Kivelson et al. 2000, 2002), Saturn’s moons Enceladus (e.g. Porco et al. 2006) and Titan (Iess et al. 2012), and Neptune’s moon Triton (Smith et al. 1989). Enceladus’ plume is sourced from a global ocean (Thomas et al. 2016) at conditions compatible with life (Sekine et al. 2015), providing energy and bioessential element sources (Waite et al. 2017; Postberg et al. 2018). Europa too may be intermittently erupting water to space (Roth et al. 2014; Sparks et al. 2016, 2017; Jia et al., 2018). Titan is a world of two oceans: surface light hydrocarbons and subsurface water. Indirect evidence indicates that Pluto and Saturn’s moon Dione too may have a deep ocean (Nimmo et al. 2016; Beuthe et al. 2016), and that the last pockets of briny water may be freezing on Ceres (Neveu and Desch 2015). There may be many more in the solar system, yet to be investigated.

The solar system community has developed a NASA Roadmap to Ocean Worlds (Hendrix, Hurford et al. 2019) that outlines milestones in assessing the potential for ocean worlds to host life (**Figure A-4**). Ideally, these goals would be addressed by robotic exploration at each

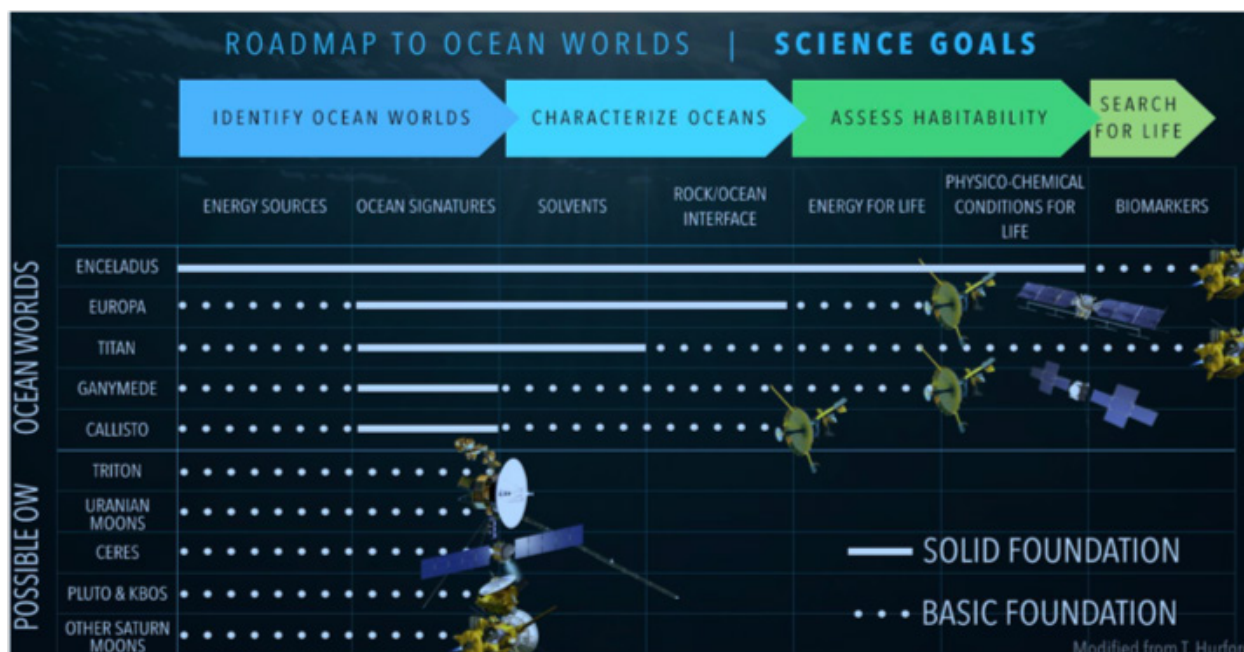


Figure A-4. Science goals for ocean world exploration. White lines across milestones depict the state of knowledge from past exploration by the Cassini, Galileo, Voyager, Dawn, and New Horizons spacecrafts (from top to bottom). The upcoming missions Europa Clipper (NASA) to Europa and JUICE (ESA) to Ganymede will make further progress, but there is a need for a higher cadence of observations of many more worlds that requires complementary telescopic observations. Modified from Hendrix, Hurford et al. (2019).

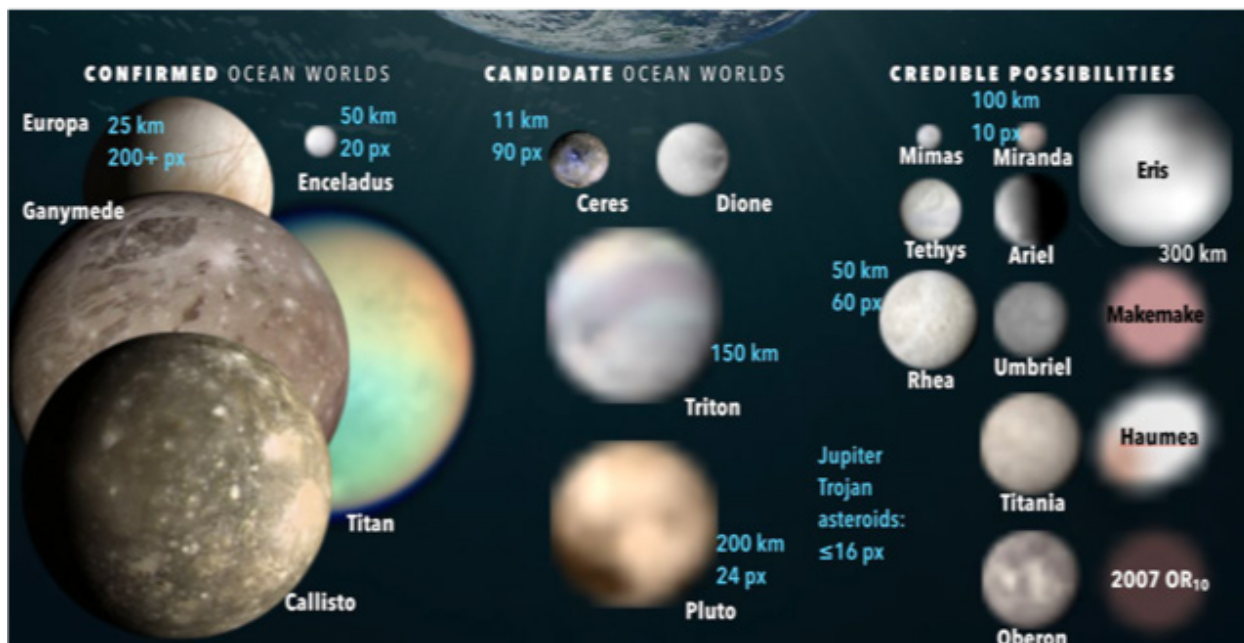


Figure A-5. “Confirmed” ocean worlds, “candidates,” and “credible possibilities” (Hendrix, Hurford et al. 2019), with Earth limb at top for scale. For each, a spacecraft image (or for KBOs, a disk of approximate albedo/color) has been downgraded to the spatial resolution of 15-m LUVOIR-A at 500 nm, assuming 2 pixels per resolution element.

world. However, the sheer number of targets (**Figure A-5**) and need for monitoring at practical timescales of days to decades makes complementary telescopic observations essential. Two Roadmap questions could be addressed in unique ways by LUVOIR:

1. Is there a sufficient energy source to support a persistent ocean? The Roadmap’s first goal, to identify the ocean worlds of the solar system, requires targeting many dwarf planets and moons. This question pertains to the tidal energy available to moons, which depends on the moons’ orbital properties that, in turn, change depending in part on the interior properties of the host planet. Measuring these changes constrains the past and current tidal energy able to support an ocean.
2. Are signatures of ongoing geological activity (or current liquids) detected? Such signatures have been instrumental in observing Enceladus’ plume and Titan’s surface seas, shaping exploration strategies for Europa’s potential plumes, and putting Triton, Pluto, and Ceres on the ocean worlds roadmap.

A.4.2 The role of LUVOIR

LUVOIR would be uniquely capable of observing: (1) a **wide number of solar system targets** (unlike missions to these targets), (2) in **spectral windows masked** by atmospheric absorption on the ground, and (3) for **arbitrary periods of time** from the Earth-Sun L2 point, uninterrupted by orbital constraints, targets below horizon, or weather. LUVOIR would provide spatial resolution comparable to a not-too-distant flyby at Ceres, Jupiter, and Saturn, and revealing large-scale surface geology on many Kuiper belt worlds (**Figure A-5**).

Program at a Glance

Science goal: Monitor surfaces and atmospheres/exospheres of ocean worlds. Measure their orbital evolution due to tidal interactions with the host planet, both directly and by constraining host planet interiors with methods derived from asteroseismology.

Program details: Imaging of ocean worlds and the giant planets ($m_v = -2.7$ to 7). UV spectroscopy of ocean worlds ($m_v = 5.2$ to 21).

Instrument(s) + configuration(s): HDI imaging at highest spatial resolution from UV to near-IR, LUMOS for medium to very high spatial and spectral resolution UV spectra.

Key observation requirements: Neutral density filter for moon (host planet in HDI 2' x 3' field of view) and host planet observations.

A.4.3 The science program

Doppler imaging of the host planet using HDI and techniques derived from asteroseismology (Gaulme et al. 2015) can reveal the structure of its interior (Ice Giants SDT, 2017). In turn, this informs how internal tidal dissipation takes place and therefore its influence on the moons' orbits and changing tidal energy supply (e.g. Fuller et al. 2016; Lainey et al. 2017). This can require continuous or repeated observations on daily timescales over long time baselines.

Astrometry of the moons' orbits (semi-major axis, eccentricity, inclination through time) constrains the present and past levels of tidal energy that can be dissipated in the moons given their changing orbital configuration. This requires intermittent measurements at high spatial resolution on timescales as long as possible (Lainey et al. 2017), using HDI.

Plume and atmospheric/exospheric activity can be monitored at high spatial resolution, without the interference of Earth's atmosphere, over a variety of timescales. Enceladus has been continuously erupting for more than a decade, but Europa's potential plumes are intermittent or vary enough as to evade most detection attempts. UV emission features (Roth et al. 2014) offer the best spatial resolution and can constrain to first order the plume composition. Absorption of the continuum of a transited host planet could work too (Sparks et al. 2016, 2017), although at high spatial resolution the background may be highly variable. Both observations would use LUMOS. Vibrational (IR) features too may be observed with HDI, but at comparatively lower spatial resolution. Plumes on Triton and Kuiper belt worlds would be unresolved, but global atmospheric changes can be monitored by observing punctual, short stellar occultations (e.g. Elliot et al. 1998).

Surface feature tracking with HDI can constrain the interior of moons from their rotational (non-synchronous rotation, polar wander) or libration properties (Thomas et al. 2016). For distant Kuiper belt objects, it can complement light curves in determining rotation periods and spin poles to constrain e.g. the moments of inertia (degree of interior differentiation), key inputs to geophysical evolution models (e.g. Castillo-Rogez & McCord, 2010). Feature tracking requires high spatial resolution and pointing over daily timescales.

Source brightnesses range from $m_v \geq -2.7$ (Jupiter) to ≈ 7 (Neptune) for host planets. For ocean worlds, they range from $m_v \geq 5.2$ (Europa) to ≈ 21 (dark KBOs). Even for the faintest targets with LUMOS, exposure times would take minutes.

References

- Beuthe, M., Rivoldini, A., & Trinh, A. 2016, *Geophys Res Lett*, 43, 10088.
- Castillo-Rogez, J. C. & McCord, T. B. 2010, *Icarus*, 205, 443.
- Elliot, J.L., Hammel, H. B., Wasserman, L. H., et al. 1998, *Nature*, 393, 765.
- Fuller, J., Luan, J. & Quataert, E. 2016, *MNRAS*, 458, 3867.
- Gaulme, P., Mosser, B., Schmider, F.X., et al. 2015. In *Extraterrestrial Seismology*, Cambridge Univ Press.
- Hendrix, A. R., Hurford, T. A., Barge, L. M., et al. 2019, *Astrobiology*, 19, 1.
- Ice Giants Science Definition Team, 2017, https://www.lpi.usra.edu/icegiants/mission_study/Full-Report.pdf
- Iess, L., Jacobson, R. A., Ducci, M., et al. 2012, *Science*, 337, 457.
- Jia, X., Kivelson, M. G., Khurana, K. K., et al. 2018, *Nat Astron*, 2, 459.
- Khurana, K. K., Kivelson, M. G., Stevenson, D. J., et al. 1998, *Nature*, 395, 777.
- Kivelson, M. G., Khurana, K. K., Russell, C. T., et al. 2000, *Science*, 289, 1340.
- Kivelson, M. G., Khurana, K. K., & Volwerk, M. 2002, *Icarus*, 157, 507.
- Lainey, V., Jacobson, R. A., Tajeddine, R., et al. 2017, *Icarus*, 281, 286.
- Neveu, M. & Desch, S.J. 2015, *Geophys Res Lett*, 42, 10197.
- Nimmo, F., Hamilton, D. P., McKinnon, W. B., et al. 2016, *Nature*, 540, 94.
- Porco, C. C., Helfenstein, P., Thomas, P. C., et al. 2006, *Science*, 311, 1393.
- Postberg, F., Khawaja, N., Abel, B., et al. 2018, *Nature*, 558, 564. 4
- Roth, L., Saur, J., Retherford, K.D., et al. 2014. *Science*, 343, 171.
- Sekine, Y., Shibuya, T., Postberg, F., et al. 2015, *Nat Comm*, 6, 8604.
- Smith, B. A., Soderblom, L. A., Banfield, D., et al. 1989, *Science*, 246, 1422. 1422
- Sparks, W. B., Hand, K. P., McGrath, M. A., et al. 2016, *ApJ*, 829, 121. 121
- Sparks, W. B., Schmidt, B. E., McGrath, M. A., et al. 2017. *ApJL*, 839, L18.
- Thomas, P. C., Tajeddine, R., Tiscareno, M. S., et al. 2016, *Icarus*, 264, 37. 037
- Waite, J. H., Glein, C. R., Perryman, R. S., et al. 2017, *Science*, 356, 155.

A.5 Small bodies of the inner solar system

Andrew S. Rivkin (Johns Hopkins University Applied Physics Laboratory), Geronimo L. Villanueva (NASA Goddard Space Flight Center)

A.5.1 Introduction

The term “asteroid” covers a wide range of compositions from metal to rock to primordial mixtures of ice, organics, and silicates, and sizes ranging from planetary embryos to objects that can fit comfortably inside a grad student office. The range of research addressing the asteroids is similarly broad, and LUVUOIR particularly promises to allow major advances due to its high spatial resolution, high-contrast imaging, and sensitivity.

1. Dawn’s visits to Ceres and Vesta demonstrate that regional and local variations occur on large asteroids. There are over 200 asteroids with diameters >100 km, and roughly 30 with diameters >200 km. We want to understand the homogeneity/heterogeneity of large asteroid surfaces.
2. Ongoing activity on Ceres is a matter of ongoing debate. Main belt comets are known, but we have no data sensitive enough to detect ice/water/sublimation.
3. Binary systems are commonly found on NEOs with radar, but they are difficult to characterize. The Ida/Dactyl system was discovered by Galileo flyby, but unobservable from current Earth-based systems (or JWST). Study of these systems is important to understand collisional evolution.
4. Positional measurements of very high precision are of potential use for certain objects like hazardous NEOs, or small asteroids that are going to make close passes to large asteroids (so mass can be determined).

A.5.2 The role of LUVUOIR

LUVUOIR will permit orders of magnitude greater characterization of asteroids than what is currently done, with the detection capability up to 50 meters bodies (millions of asteroids, see **Figure A-6**). Specifically, LUVUOIR can go ~ 4 times deeper in $\sim 10\%$ of the time that HST requires, and it will be much more sensitive than any of the ELTs for this kind of observation (mainly due to reduce background).

A.5.3 The science program

Imaging

- **FOV:** Primarily useful for recovery of lost objects or discovery surveys, neither of which is likely to be a driver for LUVUOIR observations. Observations of impact ejecta or active asteroid comae/tails likely to need similar or smaller field-of-view as cometary observations.
- **Filters/Wavelength coverage:** Filters used during the Eight Color Asteroid Survey (ECAS) of the 1980s covered wavelengths from 300-1100 nm and are still in use

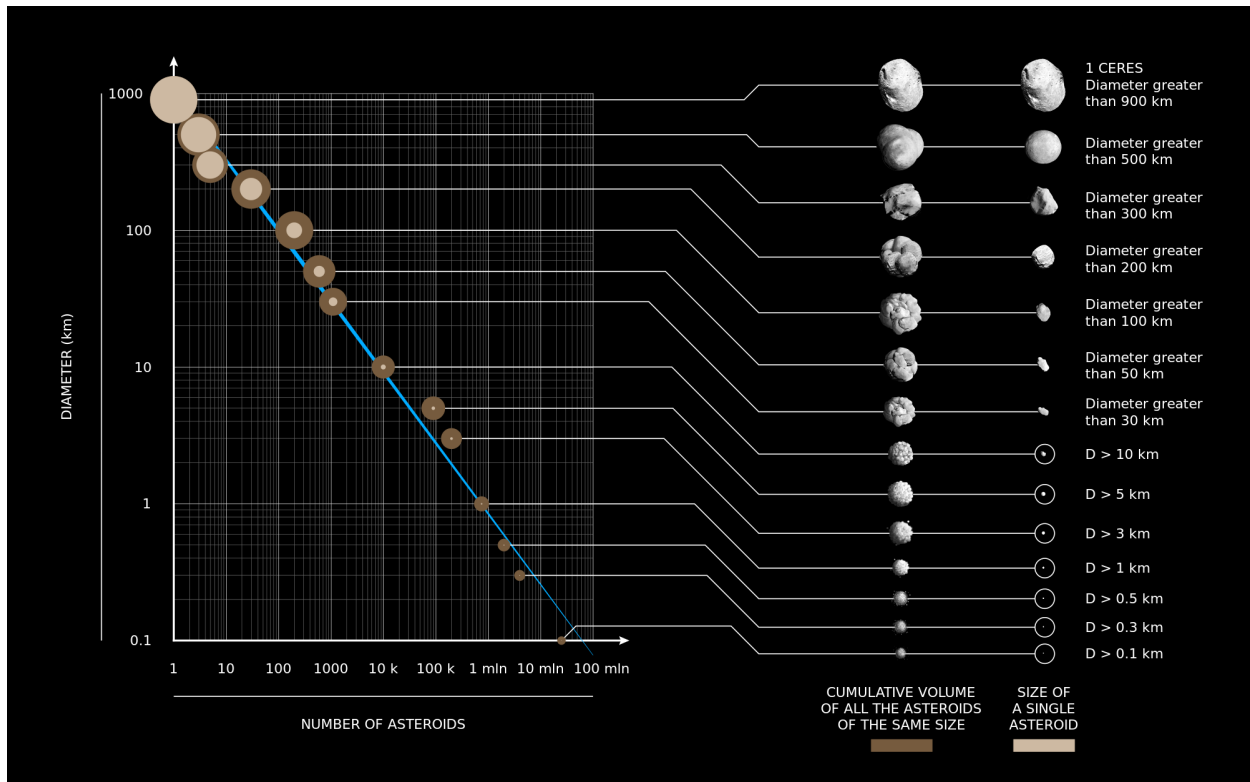


Figure A-6. The asteroids of the Solar System, categorized by size and number. Credit: M. Colombo (DensityDesign Research Lab).

on some spacecraft today. Nevertheless, their exact placement could be revisited. Longer wavelength regions include important absorptions due to silicates (~ 2000 nm) and clays (~ 2200 – 2300 nm). In addition, the ability to use a neutral density filter could be useful—several targets of interest have been unobservable by earlier space observatories because they are too bright. Objects of potential interest range can be as bright as $V \sim 7.5$. The faint limit for discovered and cataloged objects is currently at $V \sim 21$ – 22 , but may be pushed fainter with new surveys.

- **Spatial Resolution:** A spatial resolution of $0.01''$ would allow ~ 10 km resolution in the middle of the asteroid belt and ~ 15 km resolution at its far edge. This resolution would resolve the largest 200 asteroids to have ~ 100 pixels or more, and allow the satellites of Mars and the very largest Trojan asteroids to be similarly resolved. For binary system studies, Ida/Dactyl can be used as an example: They are separated by roughly 70 milliarcseconds, and have a magnitude difference of 6.7 magnitudes.
- **Depth:** Albedo variations on objects are typically a few percent. Detection of sublimation from active asteroids will have requirements similar to comets at a similar solar distance.
- **Comments:** Irregular satellites may also be lumped in with asteroids. The giant planets have dozens of irregular satellites that are thought to be captured asteroids, for many of them no physical properties are available.

Program at a Glance

Science goal: Characterization of the smallest bodies in the asteroid belt (> 50 m), ensuring the early detection of potentially hazardous objects (planetary defense) and opening a new window into the evolution of our planet and the inner solar system.

Program details: Observations of asteroids may include targeted imaging of large objects to study surface features, targeted spectroscopy of objects to obtain measurements not obtainable from Earth due to wavelength or SNR requirements, targeted astrometric measurements of near-Earth objects, or parallel observations of objects in the field during measurements of astrophysical targets.

Instrument(s) + configuration(s): HDI and LUMOS appear likely to be the instruments of main utility for asteroid studies, although the multi-object capability of LUMOS is not likely to be used for asteroids.

Key observation requirements: Absorption bands on asteroids typically are 10% or less in band depth in the wavelengths in question. Objects of possible interest range from $V < 10$ to $V > 20$, potentially reaching arbitrary faintness (for instance, a small NEO observed near aphelion). Tracking rates of objects of interest will range from near-sidereal to > 100 arcsec per hour.

Spectroscopy

- **Wavelength coverage:** Major asteroid types typically have absorptions near 1 and 2 μm or else a shallow absorption centered near 700 nm when considering wavelengths shortward of 2.5 μm . Very little asteroid data exists shortward of 400 nm or so, but HST and spacecraft observations of Ceres and Lutetia show evidence of features at wavelengths as short as 110–120 nm.
- **Resolution:** Spectral resolutions are typically low for asteroid observations, as absorptions are typically very broad. A low spectral resolution mode ($R \sim 200$ to 250?) will be of use.
- **Multiplexing/IFU:** possible, but difficult to co-locate several dynamical objects in a single FOV.
- **Depth:** Band depths in the 1–2 μm region are typically a few percent.

A.6 Comets and minor planets: the importance of the small things

Noemi Pinilla-Alonso (Florida Space Institute, University of Central Florida, Orlando, USA),
Alvaro Alvarez-Candal (Observatorio Nacional, Rio de Janeiro, Brazil)

A.6.1 Introduction

Minor planets and comets are rocky and/or icy objects, usually ranging in size from a few meters to a few hundreds of kilometers. They comprise near-Earth and main belt asteroids, Trojans (of Jupiter and other giant planets), trans-Neptunian objects, Centaurs, comets, and a recently discovered category called the transitional objects (de Leon et al. 2018).

The study of minor planets over the last decades has led to dramatic changes in our understanding of the process of planet formation and evolution, and the relationship between our Solar System and other planetary systems. Small bodies also serve as large populations of “test particles” recording the dynamical history of the giant planets, revealing the nature of the Solar System impactor population over time, and illustrating the size distributions of planetesimals, which were the building blocks of planets. The number of discoveries regarding exoplanets and debris disks is continuously increasing, and therefore it is crucial to first understand our own solar system’s provenance and evolution in order to better interpret what is going on in newly discovered planetary systems.

Telescope observations from the ground or in Earth orbit telescopes have increased in the last decade and form the basis for understanding these small bodies. Also, detailed information from some particular targets is available through missions such as Rosetta, Dawn and New Horizons Missions. However, when compared with the number of small bodies estimated to be part of the Solar System, or even with the ones already detected (~700,000 asteroids, ~ 3,000 trans-Neptunian objects, ~7,000 Jupiter Trojans, and ~5,500 comets), actual knowledge of the small bodies population is sparse.

A key program for a space telescope such as LUVOIR dedicated to observations of comets and minor planets, from the ultra-violet to the infrared wavelengths, would revolutionize the actual knowledge of the Solar System in a lot of different areas. Below I detail some of them.

A.6.2 The role of LUVOIR

Size/Shape/Ring detection and characterization: In the last years rings have been detected around three minor bodies (**Figure A-7**) (Braga-Ribas et al. 2014, Ortiz et al. 2015, Ortiz et al. 2017). The viewing geometry of these rings change secularly due to the movement of these bodies around the Sun. High angular and spatial resolution would allow direct confirmation of its presence and possibly detection of other rings or small moons. Spectroscopy of the systems under different viewing circumstances would allow compositional studies of these rings (Duffard et al. 2014).

Direct spatial resolution would also enable studies of the shape of minor planets. The most effective tool in that regard is radar imaging, but this only works for targets that pass very close to the Earth. Very recently, a survey using Adaptive Optics for the ~100 brightest asteroids is aiming to determine the shapes of these bodies, VLT/SHEPRE (Garufi et al. 2017). For the rest of the populations, most asteroids, Trojans, Centaur and TNOs, only inversion techniques applied to lightcurves provide an approach to the shape of these bodies.

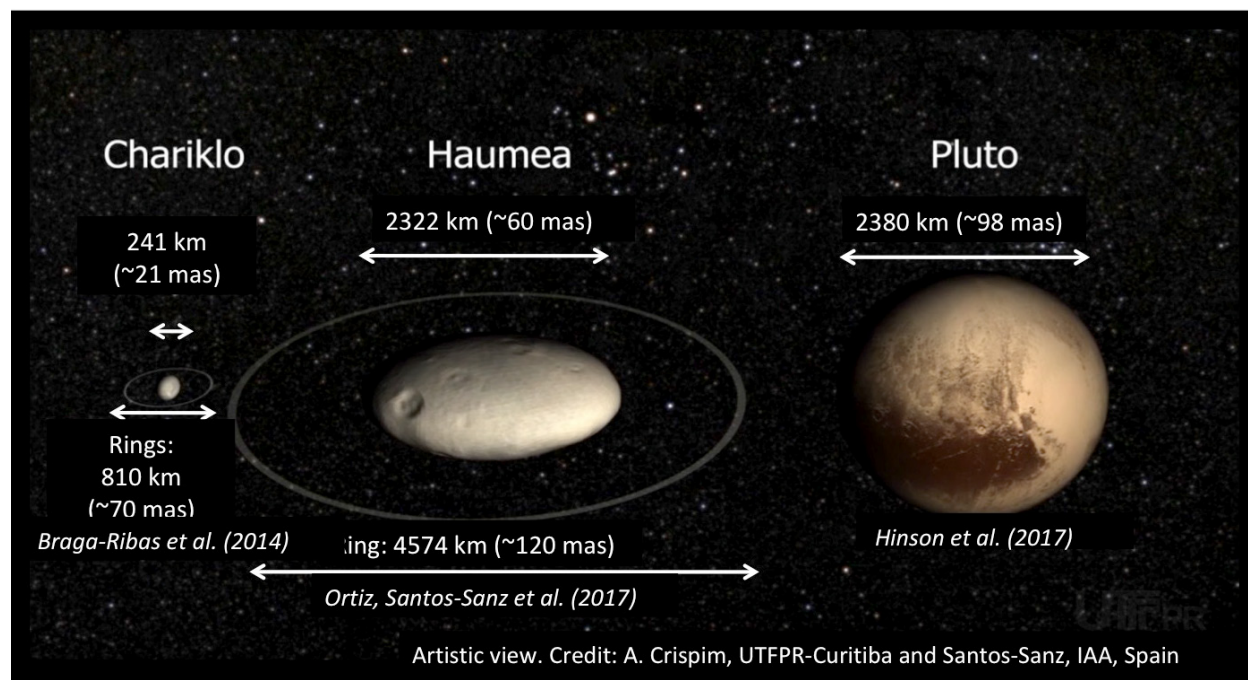


Figure A-7. The Chariklo and Haumea rings systems, to scale, detected by occultations. Pluto is shown for comparison.

Surface Composition: Some solid ices (e.g. Cruz-Diaz et al. 2014a,b), and mineral spectral features (Cloutis et al. 2008) occur at wavelengths accessible with LUV OIR but not from the ground (see **Figure A-8** and **Figure A-9**). The ultraviolet end of the spectrum is particularly interesting. Wavelengths below 400 nm have been largely unexplored. These wavelengths are particularly sensitive to water (either in the form of water ice or in the form of hydrated materials), ammonia compounds, CO₂, complex organic materials and Fe-rich materials, which result as a product of space weathering. They are also more sensitive to hydrated minerals than the NIR-wavelengths (~3 μm). In particular, the study of small bodies at the UV wavelengths with LUV OIR would provide new insights in tracing the water ice and organics, the seeds of life on Earth, in the Solar System. Also it would be key in studying the nature of ices at different penetration depths than VNIR spectroscopy.

Binary detections and characterization: The number of detected and well-characterized binary systems among the TNO population is as low as some tens. The great LUV OIR improvement in angular resolution would open a new field that is dormant now because of the lack of adequate technology. The determination of the density of minor bodies is a key question in the determination of density and mass that are crucial to better understand the structure of the interior of these bodies and on the physical characteristics of the superficial materials (rubble-pile vs. monolithic, porosity etc.).

At wavelengths below 2 μm JWST will not provide any power in excess of HST in terms of ability to resolve tightly bound binary TNO systems and even at 2 μm it will be similar to WFC3 UVIS (Benecchi et al. 2009). At mid-IR wavelengths, JWST's spatial resolution (as low as ~1" at the longest wavelengths) is insufficient to resolve all but the rare, wide binary TNO systems (Parker et al. 2016).

Additionally, one key distinguishing feature of TNO binary systems is the common optical colors of the components that would give indication of formation of the system (Benecchi

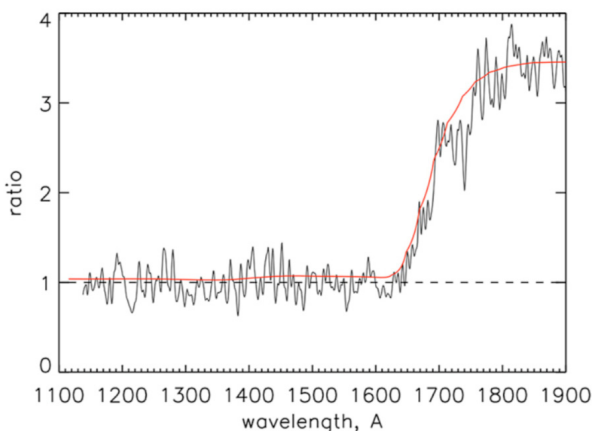


Figure A-8. Spectral ratio of bright terrain to average dark terrain on Iapetus. The ratio is very similar to pure water ice suggesting that the major difference between two terrains is the amount of water ice present (Hendrix et al. 2010)

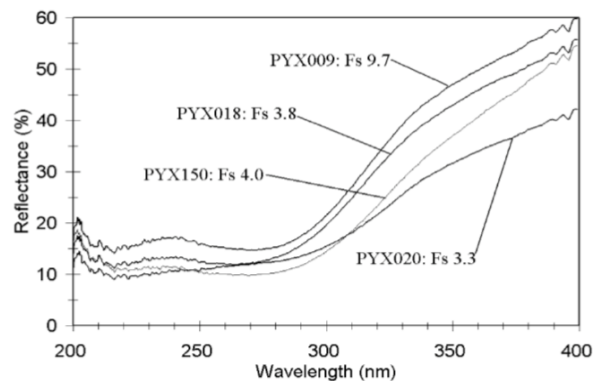


Figure A-9. Reflectance spectra of three different sets of high-calcium pyroxenes with different ratios of F_2+ to Fe_3+ (Cloutis et al. 2008).

et al. 2009), in this regards multicolor imaging of binary systems coupled with better angular resolution would enable us to explore this subject.

Activity (comets and active asteroids): The traditional separation between the rocky inactive asteroids and the icy active comets has disappeared during the last two decades due to the discovery of several objects with the dynamics of asteroids displaying activity as comets (the active asteroids, AAs Jewitt et al 2015). These asteroids display activity in the form of particle loss at rates ranging from 10^{-2} to 4 kg/s (Jewitt, et al. 2015). For the currently known active asteroids, several driver processes have been identified, including solar radiation sweeping of particles, electrostatic effects, ice sublimation, and thermal disintegration of surface regolith. Understanding the mechanisms that lead to the activity on these bodies will have implications on both our understanding of the origins of the Solar System and the future of space exploration, and in particular planetary defense and mitigation..

The activity of these targets can last from weeks to months. In some cases it has lead to the disappearance of the target after a complete break-up, while in others the activity has been observed recurrently (see **Figure A-10**). For the cases of a total break up, observation of the fragments is crucial and has to happen soon after the discovery. Using HST limits to the size of fragments has been placed to $H_v \sim 23.5$ and a size of ~ 35 m (Moreno et al. 2017).

A.6.3 The science program

Size/Shape/Ring detection and characterization: his program requires high spatial and angular resolution for direct observations of rings and an observing mode allowing multiple visits or a chain of observations in order to cover a whole rotation for the shape studies (HDI). The superb angular resolution provided by LUVOIR in the UVIS mode (where happens the best balance between collected light and spatial resolution) of 2.73 mas per pixel will allow detection of the ring system of Chariklo with a spread of 25 pixels (its major projected axis). See **Figure A-7** for the size of the ring systems in comparison with dwarf-planet Pluto.

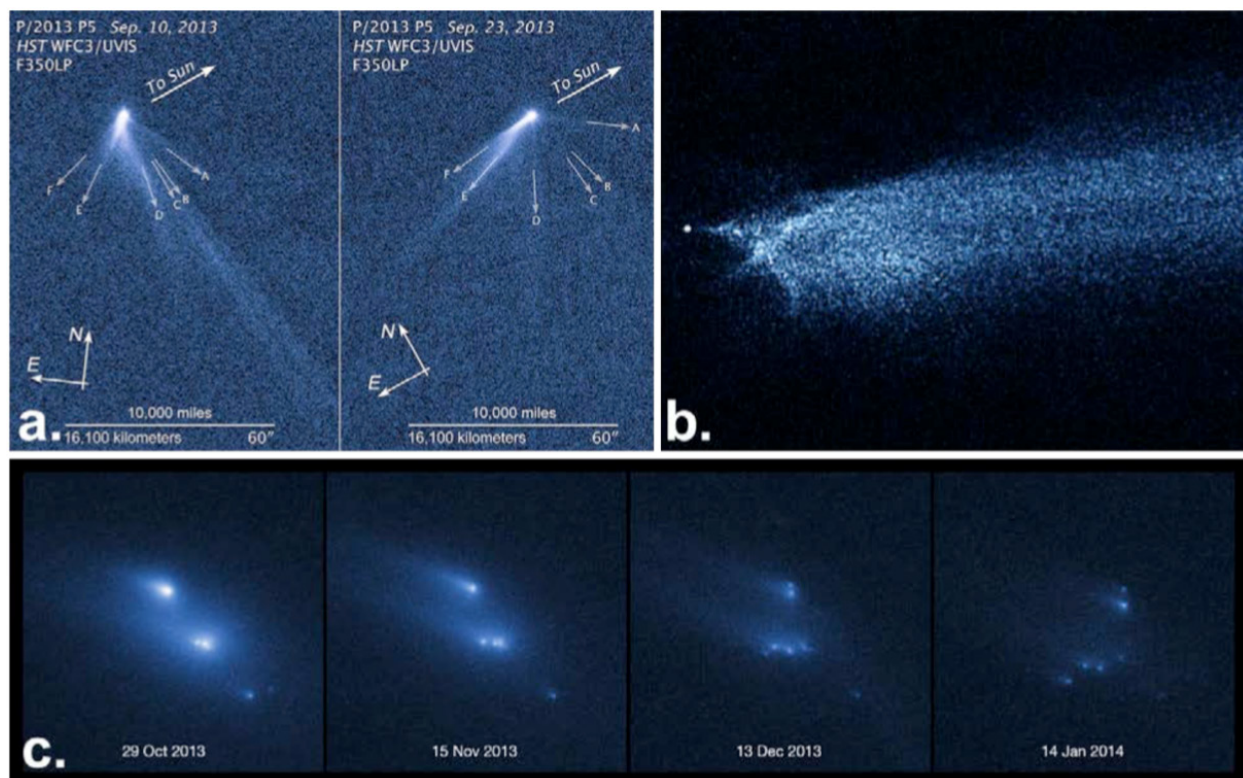


Figure A-10. Images of active asteroids a) *P/2013 P5* multiple tails; b) *P/2010 A2* (LINEAR) tail and nucleus; c) *P/2013 R3* (Catalina-PANSTARRS) breaking up (Jewitt et al. 2015).

Surface Composition: For this purpose of compositional studies we could use LUMOS and HDI. We would need low and medium spectroscopy (<30000) of small bodies. According to the LUMOS-ETC provided by STSCI we can obtain $\text{SNR} > 10$ in 1 h for all targets with $\text{AB mag} < 22$. Regular detailed observations on some targets are desirable, this may mean rotational coverage i.e. multiple visits with time constrain.

Using the HDI we could characterize almost all known Centaurs and trans-Neptunian objects, which are typically fainter and more difficult to characterize (as listed in the Minor Planets Center). Using HDI ETC we get that we could get spectrophotometry with high S/N in about 1 hr. of exposure per filter. Survey mode will be highly desirable.

Solar System science would extraordinarily benefit from Large Programs (to systematically collect VNIR data from targets in particular populations not reachable with other telescopes) and Fillers (to increase the knowledge on a population without any special requirement in the number of targets observed) in VNIR but also in the UV, where no data exist up to date and even a small number of targets would provide groundbreaking information.

Binary detections and characterization: This program requires HDI spectro-photometry. The minimum angular distance in TNO binaries observed in Benecchi et al. 2009 is comparable to the angular size of Chariklo's ring system (which we have showed if would have an excellent coverage by LUVUOIR). Using the UVIS mode, we could easily observe binary systems with half that angular size and study the properties of tight binary systems. Observations should be carried out as large programs, with multiple visits to determine orbits.

Program at a Glance

Science goal: Detection and characterization of minor bodies, their rings, and their binarity. Measurements of water ice and organics in Centaurs and TNOs. Activity in comets and asteroids.

Program details: High spatial and angular resolution imaging. Low and medium spectroscopy (<30000). Multi-object spectroscopy.

Instrument(s) + configuration(s): HDI (UVIS mode), LUMOS.

Key observation requirements: SNR > 10 in 1 h for all targets with AB mag < 22. Telescope tracking the source.

Activity (comets and active asteroids): Exceptional imaging capabilities that would allow detection of the tiniest fragments. Multi-object spectroscopy would be desirable to be able to study the different fragments as well as the coma. A target-of-opportunity program would be desirable, with the possibility of activating it in the first 24 hours after the discovery of the activity, and subsequent follow-up that could be concentrated in one week or over several months.

LAST BUT NOT LEAST, most of these observations have to be done with the telescope tracking the source, so this capability is extremely important.

References

- Benecchi et al. 2009, *Icarus*, 200, 292
 Braga-Ribas et al. 2014, *Nature*, 508, 72
 Cloutis et al. 2008, *Icarus*, 197, 321
 Cruz-Diaz et al. 2014a, *A&A*, 562, 119
 Cruz-Diaz et al. 2014b, *A&A*, 562, 120
 De Leon et al. 2017, *Handbook of Exoplanets*, Ed. by Hans J. Deeg and Juan Antonio Belmonte, Springer Living Reference Work, ISBN: 978-3-319-30648-3, 2017, id.55, 55
 Garufi et al. 2017, *The Messenger*, 169, 32
 Jewitt et al. 2015, *Asteroids IV*, 221
 Ortiz et al. 2017, *Nature*, 550, 219
 Duffard et al. 2014, *A&A*, 576, 18
 Moreno et al. 2017, *AJ*, 154, 248
 Ortiz et al. 2015, *A&A*, 576, 18
 Parker et al. 2016, *PASP*, 128, 8010

A.7 Exo-cartography for terrestrial planets

Claire Marie Guimond (McGill University), Nicolas B. Cowan (McGill University)

A.7.1 Introduction

LUVUOIR and its predecessors will have yielded us alien pale blue dots; the next step is to study their habitability. There are undoubtedly cases where understanding a planet requires understanding the diversity of its regions, especially since oceans and continents imply long-term habitability. Planets without a mix of water and land may not have a significant silicate weathering feedback, which regulates the CO₂ greenhouse on Earth and keeps her climate temperate (Cowan 2015).

With exo-cartography, we can infer the number, reflectance spectra, and longitudinal locations of major surface types (Fujii et al. 2017; Cowan and Strait 2013; Kawahara and Fujii 2011). This works because directly imaged planets show diurnal brightness variations as different surface and cloud features rotate into view (see Cowan and Fujii 2017). The light-curve collected from the planet is the disk-integrated reflectance per exposure (**Figure A-11**). In theory, we can invert lightcurves to piece out latitude-longitude albedo maps (Kawahara and Fujii 2010; **Figure A-12**).

A.7.2 The role of LUVUOIR

The very large aperture of LUVUOIR will enable reflected light surface mapping and spin determination for terrestrial planets (Pallé et al. 2008; Oakley and Cash 2009; Cowan et al. 2009, 2011; Kawahara and Fujii 2010, 2011; Fujii and Kawahara 2012). Previous mapping papers have adopted the optimistic 1% photometric uncertainty (S/N of 100) for 1-hr integrations. For a 15-m telescope, this will only be possible for a super-Earth at 1 pc. However, Cowan et al. (2009) claimed they could do essentially the same science with 3% photometry in 1-hr integrations (24 data per rotation, each of S/N = 33).

As **Figure A-13** shows, for an Earth twin at 10 pc, we can only expect an S/N of ~10 with one rotation, but for more slowly rotating planets and/or larger radii, this value can double or triple. Further, decreasing the time resolution (i.e., longitudinal sample rate) by a factor

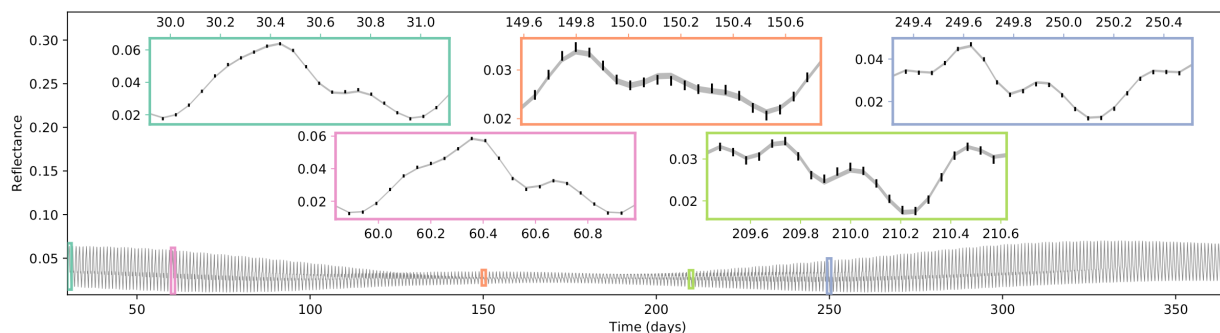


Figure A-11. Simulated light curve and resulting fit from an Earth analog with 0 degree (face-on) inclination and 90 degree obliquity. The simulated data and measurement errors are shown in the five insets, representing five epochs, each lasting one rotation, collected over the course of a year with a one hour cadence. The shaded region in each inset shows the central 90% posterior credible interval for the constructed light curve. From Farr et al. (2018, in prep.).

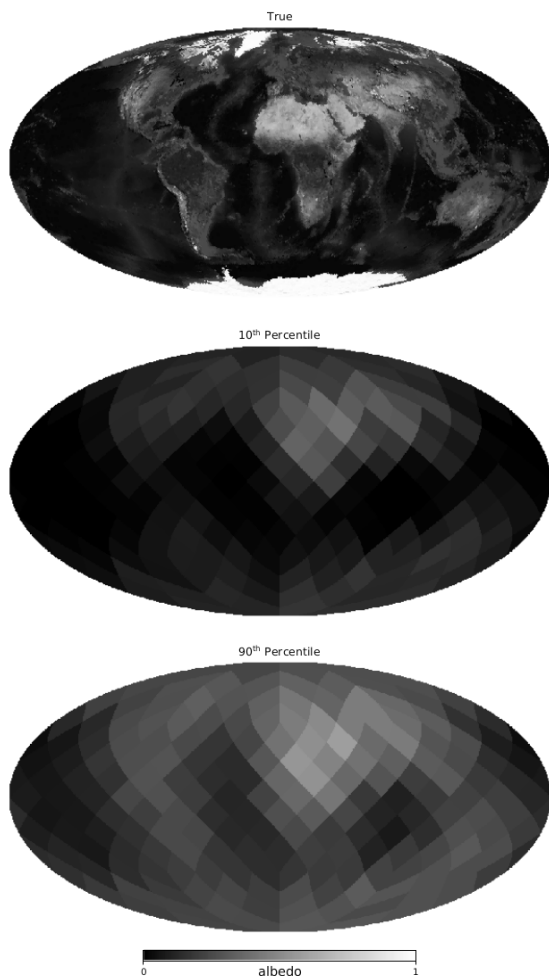


Figure A-12. Demonstration of albedo map retrieval using a simulated lightcurve of the Earth (top), with 10th percentile (middle) and 90th percentile (bottom) of the marginal posterior distributions for the albedo of each pixel. The 10th percentile map clearly shows a reflecting region (the Sahara Desert) while the 90th percentile clearly shows dark regions corresponding to the Pacific, Atlantic, and Indian Oceans. These maps therefore establish the presence of continents and oceans on the planet. Adapted from Farr et al. (2018, in prep.)

of 16 increases the per-integration S/N by a factor of 4—this would set the number of pixels in the final map. Stacking multiple epochs of observations can be problematic, as clouds strongly influence reflected light fluxes, and these atmospheric features are prone to change between epochs (Oakley and Cash 2009).

Thus only with a 15-m class space telescope such as LUVOIR can we start to map super-Earth exoplanets. For the smallest targets, only spin orientation and low-resolution longitudinal maps will be retrievable.

A.7.3 The science program

This program will target the Earth-twin planets we expect to have been detected (Stark et al. 2014) in the habitable zone of G stars ($M_V \sim 4.8$). We limit observations to one rotation period, to better avoid confounding with diurnal cloud variation. Hence rotation period sets total

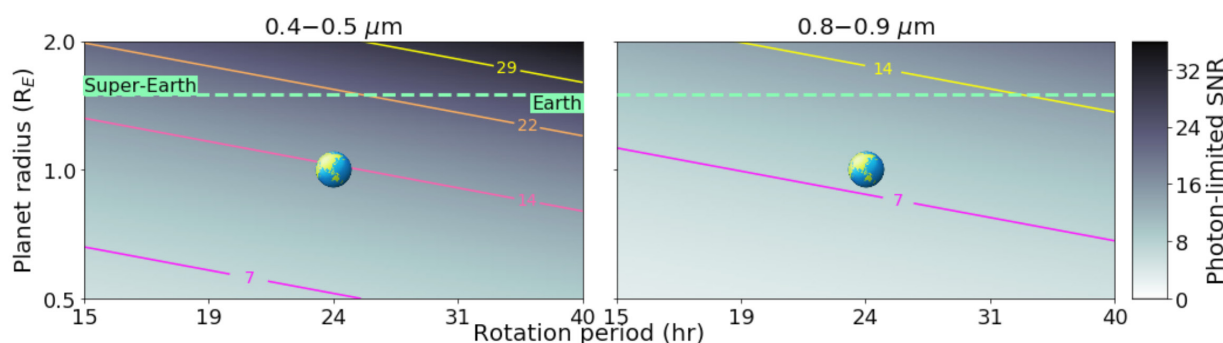


Figure A-13. Signal-to-noise ratio at the poisson limit for two bandpasses as a function of rotation period and planet radius, for a planet at 10 pc with semi-major axis of 1 AU, geometric albedo of 0.3, nominal telescope diameter of 15 m, and coronagraph throughput of 15%

Program at a Glance

Science goal: Construct rough longitudinal maps of Earth twins using rotational mapping techniques.

Program details: Observe brightness variations over one rotation period, using point source multi-band photometry, for the nearest handful of $< 2 R_E$ planets in the habitable zones of G stars.

Instrument(s) + configuration(s): Differential HDI photometry with ECLIPS.

Key observation requirements: Two imaging bands of 400–500 nm and 800–900 nm with signal-to-noise $\gtrsim 10$, and planet-star contrast $\gtrsim 10^{-10}$.

integration time. We assume a sampling rate of four exposures per rotation—e.g., 6 hours of exposure for a 24-hour rotation—as the bare minimum to detect rotational variation.

We adopt the wavelength ranges 400–500 nm (UVIS channel) and 800–900 nm (UVIS/NIR channels). The inverted reflectivity difference across these bands has been shown to suppress the cloud signal and roughly recover the continental distribution (Kawahara and Fujii 2011).

The observations use LUVUOIR’s Extreme Coronagraph for Living Planetary Systems to suppress light from the host star, in conjunction with the High Definition Imager. The maximum angular separation between an Earth-twin on a 1-AU circular orbit 10 pc away is 100 mas, which would be within the outer working angle of the coronagraph. For the highest signal, planets will be imaged at the projected separation corresponding to the coronagraph’s inner working angle. We will pursue targets with planet-star flux contrast $\geq 10^{-10}$, due to expected instrument limitations.

References

- Cowan, N. B. 2015, ArXiv e-prints, arXiv:1511.04444
- Cowan, N. B., & Fujii, Y. 2017, ArXiv e-prints, arXiv:1704.07832
- Cowan, N. B., & Strait, T. E. 2013, *ApJ*, 765, L17
- Cowan, N. B., Agol, E., Meadows, V. S., et al. 2009, *ApJ*, 700, 915
- Cowan, N. B., Robinson, T., Livengood, T. A., et al. 2011, *ApJ*, 731, 76
- Farr, B., Farr, W. M., Cowan, N. B., Haggard, H. M., Robinson, T. D. 2018, in prep.
- Fujii, Y., Lustig-Yaeger, J., & Cowan, N. B. 2017, *AJ*, 154, 189
- Fujii, Y., & Kawahara, H. 2012, *ApJ*, 755, 101
- Kawahara, H., & Fujii, Y. 2010, *ApJ*, 720, 1333
- . 2011, *ApJ*, 739, L62
- Oakley, P. H. H., & Cash, W. 2009, *ApJ*, 700, 1428
- Pallé, E., Ford, E. B., Seager, S., Montañés-Rodríguez, P., & Vazquez, M. 2008, *ApJ*, 676, 1319
- Stark, C. C., Roberge, A., Mandell, A., & Robinson, T. D. 2014, *ApJ*, 795, 2

A.8 Prospects for mapping terrestrial exoplanets with LUVOIR

Jacob Lustig-Yaeger (University of Washington), Victoria S. Meadows (University of Washington), Guadalupe Tovar (University of Washington), Edward Schwieterman (University of California, Riverside), Yuka Fujii (Tokyo Institute of Technology)

A.8.1 Introduction

Future direct imaging missions offer a means to characterize the surface habitability of terrestrial exoplanets, probing deeper atmospheric regions not accessible to transmission spectroscopy. Nulling the star with a coronagraph enables directly-imaged photometry and spectroscopy to capture disk-integrated light emitted and reflected from an exoplanet along an ensemble of relatively short atmospheric paths, compared to transmission spectroscopy which probes the upper regions of atmospheres along longer slanted paths (Fortney 2005). Photons on more direct paths through the atmosphere encounter lower optical depths, and therefore possess a greater sensitivity to the lower atmosphere and surface. Geometric arguments alone make direct imaging well suited for future habitability and biosignature assessments of terrestrial exoplanets.

To complement coronagraph spectroscopy of the disk-averaged surface and atmosphere, time-series observations offer a unique window into the two-dimensional surface heterogeneity of terrestrial exoplanets. Rotating planets that are spatially heterogeneous induce photometric variability in their observable light curves (Ford et al. 2001; Palle et al. 2008; Oakley et al. 2009). Numerous studies have explored time-series observations for exoplanet surface identification and mapping (for a recent review, see Cowan and Fujii 2017). Multi-wavelength, time-series observations of Earth have been used to construct longitudinal maps of land, ocean, and clouds (Cowan et al. 2009; Fujii et al. 2010, 2011). Further generalizing these observations and modeling methods have shown promise for uncovering the reflectance spectrum and longitudinal distribution of individual surfaces on exoplanets (Cowan et al. 2013), including the possibility of detecting extrasolar oceans (Fujii et al. 2017). Longitudinal mapping using multi-wavelength, time-series observations of terrestrial exoplanets offers a path towards identifying oceans and assessing habitability.

A.8.2 The role of LUVOIR

LUVOIR is critical for performing surface habitability studies of terrestrial exoplanets because it is a large aperture, space-based, coronagraph-equipped telescope. A space-based observatory is necessary for (a) achieving the coronagraph contrast ratio required to observe Earth-like exoplanets ($\sim 10^{-10}$), (b) escaping the diurnal cycle of Earth for continuous observations that may span multiple days, and (c) accessing wavelengths that are optically thick to space from the ground due to atmospheric opacity. In particular, the near-UV (~ 300 nm) is sensitive to the cloud variability of Earth-like planets. The large aperture considered for LUVOIR (~ 12 – 15 m) will also allow both shorter cadence time-series (~ 1 hour)—providing higher surface resolution to the inferred maps—and access to solar-analog systems out to a greater distance, which increases the yield for such investigations.

Program at a Glance

Science goal: Study the rotation rate, surface colors, geography, and habitability of directly imaged terrestrial exoplanets.

Program details: Construct time-series observations of habitable terrestrial exoplanets using the single spectrum exposures that will be required to build-up much longer integration times for spectroscopy.

Instrument(s) + configuration(s): ECLIPS coronagraph spectroscopy

Key observation requirements: Single coronagraph bandpass (0.7–0.8 μm), $R = 100\text{--}200$, $S/N \geq 0.5$ per spectral element per exposure ($S/N \geq 2.5$ per bandpass per exposure), coronagraph design contrast 10^{-10}

A.8.3 The science program

We propose a science program that enhances the science return from spectroscopic observations that motivate the design of the LUVUOIR coronagraph. Approximately 100 hours will be required to detect the presence of O_2 in the atmosphere of an Earth-like exoplanet at 10 pc with the 15-m LUVUOIR concept. Our program will leverage these long integrations to “mine” for rotationally induced exoplanet time variability using individual ~ 1 hour exposures from a longer composite spectrum. If these observations include data within the 0.7–0.8 μm LUVUOIR bandpass (which contains the 0.76 μm O_2 A band), we can bin the spectrum into a single photometric point and construct a lightcurve of a terrestrial exoplanet over the total spectrum exposure time. Our simulations suggest that this dataset can be used to infer the rotation rate of Earth to within $\sim 5\%$ (Lustig-Yaeger et al. 2017). Binning the time-dependent spectra into two or more photometric points is an effective means of constructing simultaneous multi-wavelength lightcurves, which could potentially infer the crude longitudinal distribution and color of oceans on an Earth analog (Lustig-Yaeger et al. 2017). Other wavelengths can be used either instead of or in concert with the 0.7–0.8 μm LUVUOIR bandpass, such as the 0.4–0.45 μm bandpass, where Rayleigh scattering masks surface features and enhances sensitivity to heterogeneous cloud coverage. However, the 0.7–0.8 μm bandpass is still preferred for the initial assessment because of its sensitivity to both atmospheric oxygen and the planetary surface.

This science program would allow a long spectral exposure, to yield two unique studies along both the spectral and temporal dimensions. Co-adding in time will give a long integration spectrum at the native instrument spectral resolution that can be used to study the atmospheric composition of the targeted exoplanet. Co-adding in wavelength will give a long baseline lightcurve with little to no spectral resolution that can be used to study the targeted exoplanet’s rotation rate and surface map. Since the time-resolution of a lightcurve depends on the individual exposure times that comprise the time-series data, low noise or noiseless detectors that can support shorter exposure times will greatly improve the feasibility and scientific return of this program.

References

- Cowan, N. B., Agol, E., Meadows, V. S., et al. 2009, *ApJ*, 700, 915
- Cowan, N. B., & Strait, T. E. 2013, *ApJL*, 765, L17
- Cowan, N. B., & Fujii, Y. 2017, ArXiv e-prints, arXiv:1704.07832
- Ford, E. B., Seager, S., & Turner, E. L. 2001, *Nature*, 412, 885
- Fortney, J. J. 2005, *MNRAS*, 364, 649
- Fujii, Y., Kawahara, H., Suto, Y., et al. 2010, *ApJ*, 715, 866
- Fujii, Y., Kawahara, H., Suto, Y., et al. 2011, *ApJ*, 738, 184
- Fujii, Y., Lustig-Yaeger, J., & Cowan, N. B. 2017, *AJ*, 154, 189
- Lustig-Yaeger, J., Tovar, G., Schwieterman, E. W., Fujii, Y., & Meadows, V. S. 2017, LPI Contributions, 2042, 4110
- Oakley, P. H. H., & Cash, W. 2009, *ApJ*, 700, 1428
- Pallé, E., Ford, E. B., Seager, S., Montañés-Rodríguez, P., & Vazquez, M. 2008, *ApJ*, 676, 1319

A.9 Detecting liquid surface water on exoplanets

Tyler D. Robinson (Northern Arizona University & Virtual Planetary Laboratory) and Mark S. Marley (NASA Ames Research Center)

A.9.1 Introduction

Planetary habitability requires liquid water stability at the surface of a terrestrial planet (e.g., Kasting et al. 1993). The remote characterization of habitability for planets detected in reflected light will require either (1) information about the near-surface atmospheric state for a confirmed terrestrial world, or (2) the direct detection of surface liquid water via ocean glint and/or polarization measurements. This brief report explores what telescope and instrument requirements would be required to make either of these two observations.

Surface liquid water stability depends on both temperature and pressure from the overlying atmosphere. Unfortunately, we know of no studies that investigate how well atmospheric pressure and temperature can be constrained from visible and near-infrared spectral observations of terrestrial planets—more work here is clearly required. A Rayleigh scattering slope, or detection of dimer or pressure-induced absorption features (Misra et al. 2014b), could indicate pressure. Detection of Rayleigh scattering requires observations at blue-visible wavelengths, and would not place strict requirements on spectral resolution. Misra et al.

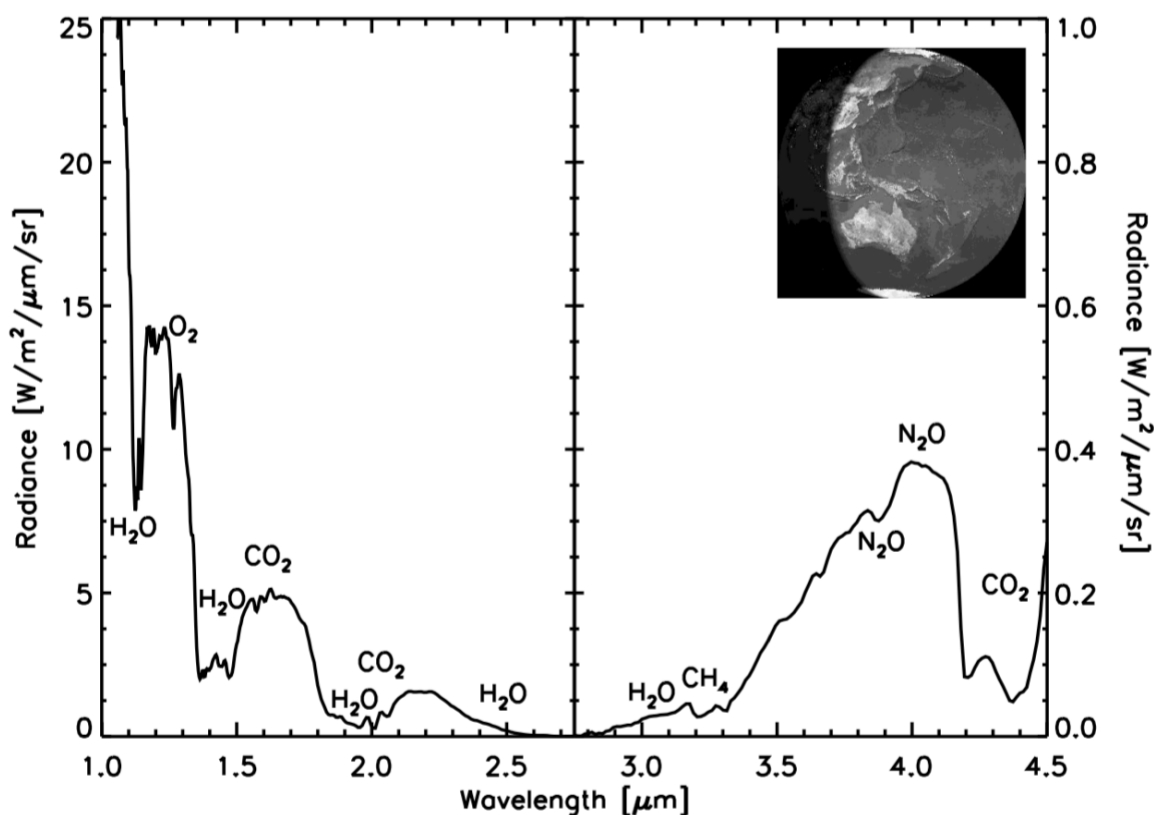


Figure A-14. A moderate resolution, near-infrared spectrum of Earth, from the validated models of Robinson et al. (2011). Key features are labeled. Note the separate y-axis for wavelengths beyond 2.75 μm , which helps show the rise in thermal emission beyond this wavelength.

(2014b) emphasize dimer detection at $1.06\ \mu\text{m}$ at a resolution ($\lambda/\Delta\lambda$) of 100.

Temperatures will be difficult to constrain in the absence of a detection of planetary thermal radiation. However, it may be possible to constrain temperature, and also habitability, by detecting a water vapor profile consistent with condensation (i.e., a condensation curve). Detection of clouds and weather (e.g., from variability) would also indicate condensation, but not necessarily at/near the surface. **Figure A-15** pressure at the $\tau=1$ level for a clearsky Earth atmosphere, and this roughly indicates the pressure levels sensed by a spectrum. Comparison of high- ($\lambda/\Delta\lambda=1,000$) and moderate- ($\lambda/\Delta\lambda=100$)

resolution spectra shows that, for water vapor, not much vertical resolution is gained by pushing beyond a spectral resolution of roughly 100. Notably, while the $0.94\ \mu\text{m}$ water band probes the near-surface environment, pushing to the $1.4\ \mu\text{m}$ and $1.9\ \mu\text{m}$ water bands is necessary for probing Earth's middle and upper troposphere. Thus, these bands may be essential to constraining water vapor profiles for potentially habitable exoplanets.

Direct detection of surface liquid water may prove a challenging endeavor, but would be complimentary to any atmospheric spectral retrieval analysis (like that outlined above). The near-infrared is best suited to polarization or glint detection, owing to the lack of Rayleigh scattering here (Robinson et al. 2010; Zugger et al. 2011), and detection could be accomplished with photometric observations at continuum wavelengths (i.e., between strong atmospheric absorption bands). Performing observations in the near-infrared would also minimize glint false positive signatures from polar ices (Cowan et al. 2012), whose reflectivity is diminished at these wavelengths. For an Earth-twin, clouds and hazes would likely obscure any polarization signature from surface oceans (Zugger et al. 2011). Thus, glint is the best option for the direct detection of surface liquid water, and, at least for Earth, is most pronounced near a star-planet-observer (phase) angle of 150° , where a glinting planet would be nearly twice as bright as a non-glinting planet. The ability to measure planetary phase functions to such close planet-star separations will depend on the inner-working angle (IWA) of the high-contrast field-of-view, and cannot be achieved for planetary systems with inclinations below about 60 degrees. For an Earth-Sun twin system at 10 parsecs, the required IWA would be $1.8\ \lambda/D$ (at the $1.33\ \mu\text{m}$ continuum and for a 10-meter diameter aperture). As another example, taking an Earth-like planet near the inner edge of the habitable zone for a mid-K dwarf, the requirement shrinks to $0.9\ \lambda/D$ at 10 parsecs. Thus, an IWA of $2\ \lambda/D$ could allow glint detection out to almost 10 pc for habitable planets around G dwarfs, and almost 5 pc for K dwarfs. These distances decrease to 6 pc and 3 pc, respectively, for a $3\ \lambda/D$ IWA.

We briefly note that the James Webb Space Telescope (JWST) will not be capable of probing the near-surface environment of habitable zone planets orbiting stellar types earlier than M (Misra et al. 2014a). Depending on systematics, JWST may be able to characterize potentially habitable worlds around nearby M dwarf stars, but these worlds possess their own

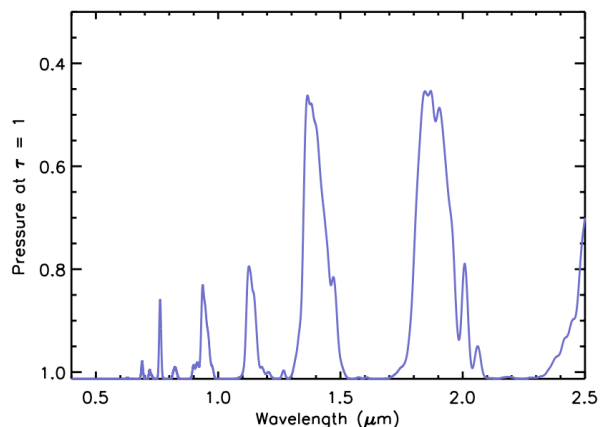


Figure A-15. The pressure of the $\tau=1$ level for a clearsky Earth atmosphere at $\lambda/\Delta\lambda=100$. Note the strong water vapor bands at 0.94 , 1.1 , 1.4 , and $1.9\ \mu\text{m}$.

unique challenges to habitability (e.g. Luger & Barnes 2015). Finally, while not discussed at length here, the capability of measuring profiles of atmospheric water vapor through an atmosphere will also be useful for studies of gaseous worlds interior to and throughout the habitable zone, as water should be a key radiatively active species (and greenhouse gas) for these planets (Cahoy et al. 2010)

In summary, $R=70$ (or greater) spectra of Earth-like planets would be suitable for constraining water vapor abundance profiles. Future work is necessary to determine the minimum signal-to-noise ratios required for such an analysis. Broadband detection of glint in the phase function of a habitable zone exoplanet is possible in the near-infrared with a $2/\lambda/D$ IWA and becomes restricted for a $3/\lambda/D$ IWA. The tables below contain additional information on requirements for detecting water vapor and carbon dioxide features (for climate modeling constraints).

Note on near-infrared CO₂ features: Carbon dioxide is a key greenhouse gas for Earth, whose greenhouse forcing is essential to maintaining Earth's habitability (Hansen et al. 2013). Thus, inferring atmospheric CO₂ concentrations from near-infrared spectra of Earth-like planets would be essential to running predictive/forward climate models for these worlds (thereby helping to inform our understanding of the potential habitability of these planets). The strongest CO₂ features in Earth's near-infrared, reflected-light spectrum are a pair of double features at 1.59 μm and 2.03 μm . Both would require a spectral resolution of $\lambda/\Delta\lambda=100$ to place a single spectral resolution element across the bands, and double this resolution could enable better detections. The features at the shorter wavelength are shallower, requiring a SNR of order 40 to distinguish. The longer wavelength features are deeper, requiring an SNR only of order 10, but may be more difficult to detect due to the overall decrease in stellar brightness at these longer wavelengths. These details are represented in **Table A-2**.

A.9.2 The role of LUVVOIR

While the above observations are enabled by a direct imaging mission, they are difficult and require either long observations to increase the signal-to-noise on a spectral feature, or multiple visits to a target to observe it at multiple phases. Additionally, some of these phases will be at small inner working angles. All of these problems benefit from an observatory with

Program at a Glance

Science goal: Definitively show the presence of liquid water on the surface of rocky exoplanets.

Program details: Coronagraphic imaging at phase angles as close to 150° as possible to maximize glint signal. More generally, glint can be observed between gibbous and crescent phase. Direct spectroscopy to measure atmospheric water vapor concentrations. Direct spectroscopy to measure NIR CO₂ features and constrain greenhouse effect.

Instrument(s) + configuration(s): ECLIPS imaging and IFS

Key observation requirements: Contrast $< 10^{-10}$; Multiple visits; Water vapor features at 0.94, 1.1, 1.4, and 1.9 μm , $R \sim 100$; CO₂ feature at 1.59 μm , $R > 100$.

Table A-2. Observation requirements for detecting key atmospheric features that constrain the presence of liquid surface water on rocky exoplanets.

Optical/Near-IR Direct Spectroscopy of CO₂ Features

Observation Requirement	Major Progress	Substantial Progress	Incremental Progress
Wavelengths	0.4-2.2 μm	0.4-1.7 μm	n/a
Spatial resolution			
Spectral resolution	200	100	n/a
Field-of-view			
Contrast	10^{-10}	10^{-10}	n/a
Telescope aperture	12	8	n/a
SNR	50	50	n/a

Optical/Near-IR Direct Spectroscopy of H₂O Features

Observation Requirement	Major Progress	Substantial Progress	Incremental Progress
Wavelengths	0.4-1.6 μm	0.4-1.6 μm	0.4-1.0 μm
Spatial resolution			
Spectral resolution	70	70	70
Field-of-view			
Contrast	10^{-10}	10^{-10}	10^{-10}
Telescope aperture	12	8	4
SNR	50	20	10

a larger aperture, which increases the signal from the planet, decreases the amount of time for an observation (which in turn enables multiple visits), and decreases the inner working angle of the observatory. Finally, the wavelength range of LUVOIR encompasses multiple water vapor features, from 0.94–1.9 μm , will allow crude determination of the water vapor profile of an exoplanet's troposphere.

A.9.3 The science program

Detection of glint from liquid surface water on rocky exoplanets will require multiple visits of ECLIPS coronagraphic imaging to the same target. These multiple visits will conduct

phase-dependent imaging in polarized light, and (if time allows) direct spectroscopy to measure H₂O vapor concentrations.

References

- Cahoy, K. L., Marley, M. S., and Fortney, J. J. 2010, *ApJ*, 724, 189.
- Cowan, N. B., Abbot, D. S., and Voigt, A. 2012, *ApJL*, 752, L3.
- Hansen, J. M., Sato, M., Russell, G., and Kharecha, P. 2013, *Phil. Trans. Roy. Soc. A*, 371, 20120294.
- Kasting, J. F., Whitmire, D. P., and Reynolds, R. T. 1993, *Icarus*, 101, 108-128.
- Luger, R., and Barnes, R. 2015, *Astrobiology*, 15, 119-143.
- Misra, A., Meadows, V., and Crisp, D. 2014a, *ApJ*, 792, 61.
- Misra, A., Meadows, V., Claire, M., and Crisp, D. 2014b, *Astrobiology*, 14, 67-86.
- Robinson, T. D., Meadows, V. S., and Crisp, D. 2010, *ApJL*, 721, L67.
- Zugger, M. E., Kasting, J. F., Williams, D. M., Kane, T. J., and Philbrick, C. R. 2011, *ApJ*, 739, 12.

A.10 The detection of terrestrial planets in the habitable zones of A-stars

Ramses Ramirez (Earth-Life Science Institute, Tokyo Institute of Technology), Aki Roberge (NASA GSFC)

A.10.1 Introduction

Most habitable zone (HZ) studies focus on terrestrial planets orbiting F–M main-sequence stars. This is largely because an arbitrarily long timescale of 1 Gyr, corresponding to the minimum thought for life to arise, is also as long as the entire main-sequence lifetime of an early F-star. However, life on Earth had already appeared by ~3.8 Gyr ago, if not sooner. Indeed, life may have evolved even earlier had our planet not been beset by ongoing impacts during the late heavy bombardment. Evidence from zircons also suggests habitable conditions on Earth by 4.3 Gyr ago, only ~300 Myr after formation of the planet. Thus, in order to explore the range of conditions under which life can arise, we should include A-stars in the search for habitable planets.

A-star systems for which exoplanets have already been directly imaged include: Fomalhaut (7.7 parsecs), Beta Pictoris (19.4 pc), HR 8799 (39 pc), HD 95086 (90 pc), and HD 15082 (118 pc). Direct imaging is currently the best way to discover exoplanets around A-stars, as indirect methods like radial velocity and transits have proven ineffective. The known A-star planets are massive (e.g., Jovian or larger) and located far beyond their host stars' respective HZs. Previous A-stars surveys have not found smaller terrestrial planets, since the required ultra-high contrast is not yet available. Should terrestrial planets exist within the HZs of these stars, however, we may be able to detect them using the ECLIPS coronagraph to block out extraneous starlight.

A.10.2 The role of LUVOIR

The extreme high contrast needed to directly observe Earth-like planets around Sun-like stars ($\sim 1 \times 10^{-10}$) is only possible with a space-based telescope and ultra-high performance starlight suppression instrument (like LUVOIR). The situation is harder for terrestrial planets around early-type stars, as the planet-to-star flux ratio is even smaller (see below).

A.10.3 The science program

The effective stellar flux of a planet near the conservative inner and outer edges of the classical HZ of Fomalhaut (A4V; $T_{\text{eff}} = 8600\text{K}$; $L = \sim 16.63 L_{\text{sun}}$) is ~1.25 and 0.5 times that received by the Earth, respectively (**Figure A-16**), which corresponds to orbital distances of ~ 3.65 and 5.8 AU. The inner working angle (IWA) of ECLIPS is $3.5 \lambda/D = 48$ milliarcsec at 1 micron. So HZ inner edge is exterior to the IWA for A4V stars out to 76 parsecs, at wavelengths shorter than 1 micron. This shows how the large separation of the HZ for A-type stars is advantageous for high-contrast imaging and spectroscopy.

However, the planet-to-star flux ratio is smaller than it is for the Earth around the Sun. A planet at the equivalent insolation distance has about the same absolute bolometric magnitude, no matter the star. Equation 15 in Turnbull et al. (2012) gives the approximate planet-to-star flux ratio for an Earth-twin planet at the inner edge of the HZ. Adapting that equation for a $1.4 R_{\text{Earth}}$ super-Earth exoplanet gives

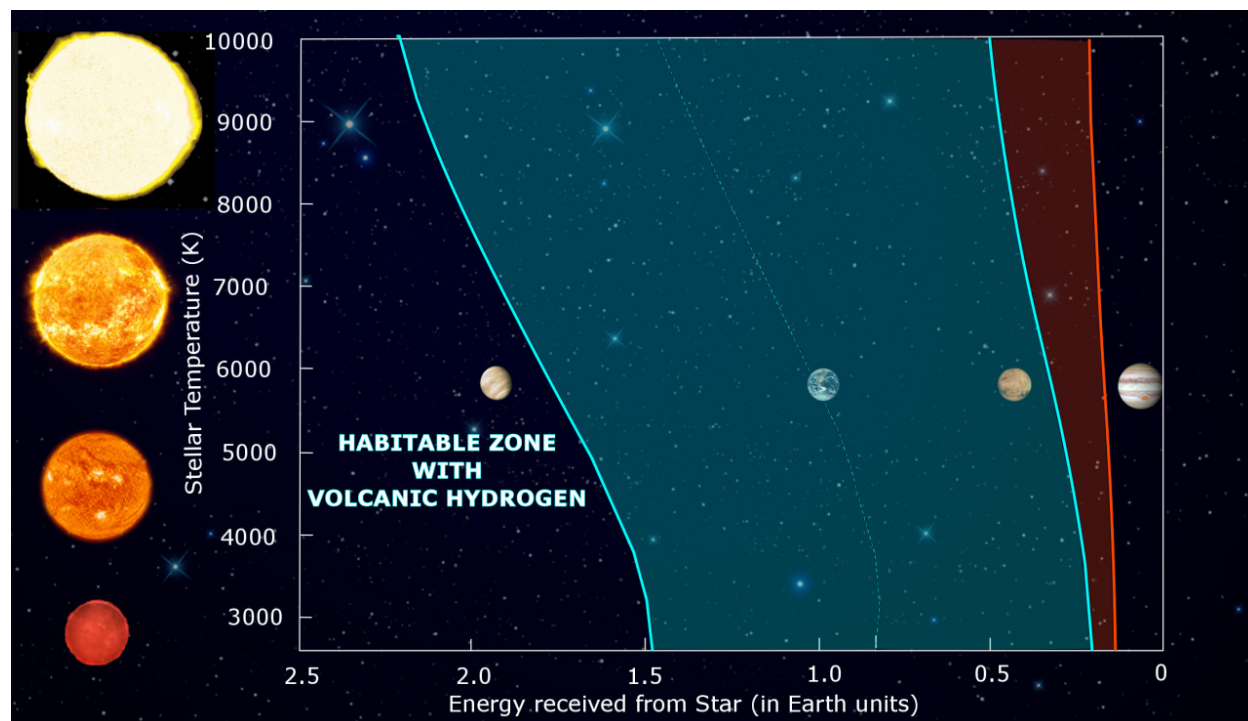


Figure A-16. The classical $\text{CO}_2\text{-H}_2\text{O}$ habitable zone (blue) with volcanic hydrogen extension (red). Adapted from Ramirez and Kaltenegger (2017).

$$\frac{F_{\text{super-Earth}}}{F_{\text{star}}} \sim (1.4^2) * 2 \times 10^{-10} / L_{\text{star}}$$

Setting the planet-to-star flux ratio to the ECLIPS contrast limit of $\sim 3 \times 10^{-11}$, we can estimate the most luminous star for which an Earth-like super-Earth at the inner edge of the HZ can be detected. The limiting stellar luminosity is $< 13.1 L_{\text{Sun}}$. Therefore, such exoplanets can be detected around stars with spectral types of $\sim \text{A7V}$ and later, albeit with very long exposure times. We will calculate the required exposure times at a later date.

Program at a Glance

Science goal: Discover terrestrial exoplanets in the habitable zones of A-type stars and probe their atmospheres to investigate their habitability.

Program details: Direct imaging and low-resolution Vis/NIR spectroscopy of super-Earth exoplanets in the habitable zones of early-type stars with spectral types $\sim \text{A7V}$ and later, out to ~ 76 parsec.

Instrument(s) + configuration(s): ECLIPS imaging and IFS spectroscopy

Key observation requirements: Contrast floor $< 3 \times 10^{-11}$, IWA $< 3.5 \lambda/D$

References

Ramirez, R., & Kaltenegger, L. 2017, *ApJ*, 837, L4

Turnbull, M. C., Glassman, T., Roberge, A., et al. 2012, *PASP*, 124, 418

A.11 Transit spectroscopy of Earth-sized planets around M-dwarfs

Avi Mandell (NASA GSFC) and Eric Lopez (NASA GSFC)

A.11.1 Introduction

Studying transiting planets is highly complementary to studies of directly imaged planets : (1) we can readily measure the mass and radius of transiting planets, linking atmospheric properties to bulk composition and formation, (2) many transiting planets are strongly irradiated resulting in novel atmospheric physics, and (3) the most common temperate terrestrial planets orbit close to red dwarf stars (M-dwarfs) and are difficult to image directly, but comparatively likely to transit at high signal to noise. The Transiting Exoplanet Survey Satellite (TESS) will discover transiting planets orbiting the brightest stars and should discover a small number of temperate terrestrial planets transiting nearby early-to-mid M-dwarfs. Furthermore, ground-based surveys of very-late M-dwarfs and sub-stellar primaries may yield additional targets—in fact, one of the best Earth-sized HZ targets to date is TRAPPIST-1e (Gillon et al. 2017). Follow-up of these discoveries should provide the first opportunity to place constraints on the atmospheres and habitability of temperate terrestrial planets.

JWST will be a fantastic platform for examining larger and brighter planets, resulting in a revolution in our understanding of hot planets orbiting close to their parent star. However, characterizing the smaller, cooler worlds will be incredibly time-intensive: JWST will need months of integration time to provide tantalizing constraints on the presence of an atmosphere. The amplitude of spectral features for a temperate terrestrial planet transiting in front of a nearby M-dwarf is comparable to the single-transit photon-counting precision with JWST; therefore, in the absence of a systematic noise floor, 100 transits of such a planet could yield a 10- σ detections of greenhouse gases—and this neglects the effects of cloud opacity in damping the signal of spectral absorption (Cowan et al. 2014). Spending a total of one month of JWST time to characterize the atmosphere of a potentially habitable world is compelling, but the observations would have to be spread out over nearly a decade for a planet in a month-long orbit (this scheduling problem is somewhat alleviated for planets in the habitable zones of later M-dwarfs and sub-stellar companions, which have shorter orbital periods).

A.11.2 The role of LUVUOIR

JWST will most likely make important inroads into the exploration of temperate Earth-sized planets around M-dwarfs, but it is entirely possible that little will be known about the atmospheres of these planets by the time JWST ends its mission—and further (and deeper) study will be left for a future flagship mission with equal or greater photon-gathering power.

LUVUOIR will be a capable successor to JWST in this regard. LUVUOIR Architecture A will have a collecting area 178 m², a factor of 7x larger than JWST, and observations will reach the same SNR with 2.7x less integration time. The primary instrument for transit spectroscopy with LUVUOIR will be the High Definition Imager (HDI), due to the broad simultaneous wavelength coverage (200 nm - 2.5 μ m) and the ability to spatially scan the spectra of bright stars across the large focal plane detectors. HDI will have sets of grisms and will operate

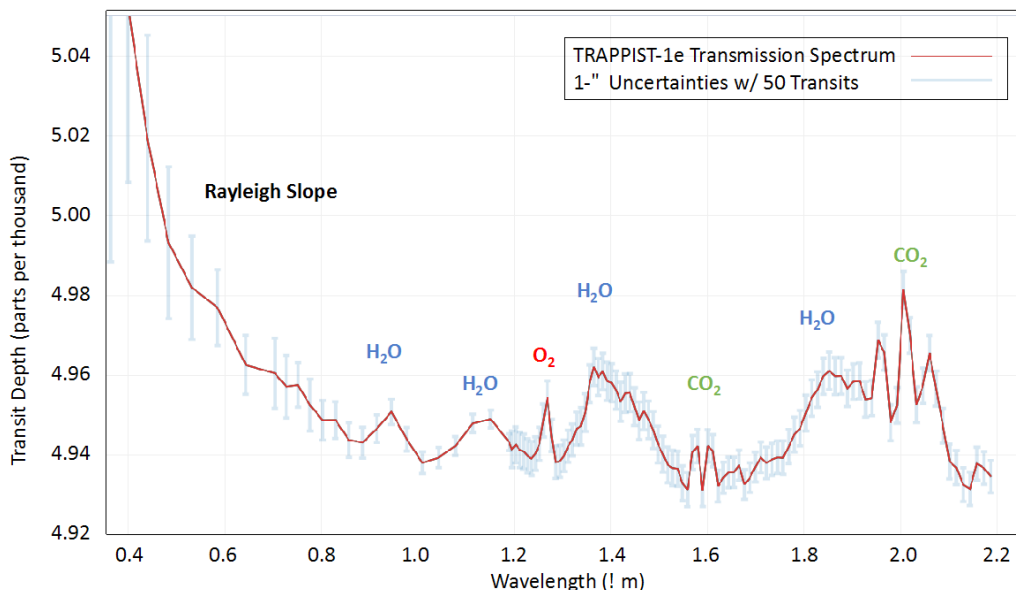


Figure A-17. Simulated transit spectrum of TRAPPIST-1e with LUVOIR-A (15-m), assuming 50 transits combined. The effective resolution of the spectrum is $R=150$ at $\lambda > 1.2 \mu\text{m}$, $R = 30$ at $700 \text{ nm} < \lambda < 1.2 \mu\text{m}$, and $R = 10$ at $\lambda < 700 \text{ nm}$. Spectral bands of multiple key atmospheric species are visible by eye, enabling constraints on habitability. Credit: [Planetary Spectrum Generator Tool](#)

similarly to the Wide Field Camera 3 (WFC3) instrument currently on HST. It will have the capability of full-throughput observations in either short (200–900 nm) or long (800 nm–2.5 μm) wavelength channels, or simultaneous observations with both bands but at half the throughput. Spectral resolution will be $R \sim 500$, enabling full characterization of spectral bands of molecular as well as atomic species.

LUVOIR will improve on JWST measurements between 0.8 and 2.5 μm , a band which covers molecular features of H_2O and CH_4 and therefore provides constraints on the water vapor content and oxidation state of the atmosphere. At shorter wavelengths (0.2–0.8 μm), LUVOIR’s capabilities will be unique. In particular, measurements of Rayleigh scattering and possibly O_3 at 200–300 nm will be the first searches for these key biomarkers of photosynthetic life.

A.11.3 The science program

The TRAPPIST-1 system will be a high priority for any future transit spectroscopy science program. **Figure A-17** illustrates what could be accomplished with 50 transits on the potentially habitable Earth-sized planet TRAPPIST-1e. A number of molecules are visible even by eye, and it is clear that strong constraints on the atmospheric chemistry and even on biomarker species such as O_2 will be possible.

Sullivan et al. (2015) modeled the yield of planets discovered by the TESS mission, determining that the mission would discover between 2 and 7 temperate Earth-sized planets orbiting M-dwarfs with $K < 9$. These stellar hosts will be larger than TRAPPIST-1, but will also

Program at a Glance

Science goal: Characterizing the atmospheres of potentially habitable planets to constrain the chemical compositions and search for signs of life.

Program details: Transit spectroscopy of Earth-sized planets in the habitable zones of nearby M-dwarf and brown dwarf primaries.

Instrument(s) + configuration(s): HDI grism spectroscopy

Key observation requirements: 0.4 nm–2.5 μm ; $R \sim 150$; ultra-high precision spectroscopy of bright sources (photometric uncertainty < 3 ppm).

be brighter, and may therefore provide a similar SNR with the same amount of observing time.

References

Cowan, N., et al. 2015, *PASP*, 127, 311

Gillon, M., et al. 2017, *Nature*, 542, 456

A.12 A statistical search for global habitability and biospheres beyond Earth

Shawn Domagal-Goldman (NASA GSFC), Jacob Bean (University of Chicago), Eliza Kempton (Grinnell College, University of Maryland), Sara Walker (Arizona State University)

A.12.1 Introduction

Here, we propose a statistical search for habitability and life. Such a search would provide tests for our understanding of the top-level factors controlling planetary habitability and raise the overall confidence that we are not alone. This search would be conducted by searching for signs of habitability and of life on multiple planets, both in and beyond the habitable zone.

The statistical search for habitability would turn the concept of the habitable zone into a testable hypothesis. According to the habitable zone hypothesis, there is a region around the star for which feedback processes in the climate system work to stabilize surface temperatures to allow for sustained, global reservoirs of liquid surface water. Beyond this zone, the climate would stabilize in water-poor regimes, with vastly different surface temperatures. Because of all the feedbacks in the climate system, multiple aspects of a planet's spectral signatures should also change beyond the habitable zone: CO₂ concentrations (and their features) should increase on either side of the habitable zone (due to lack of a CO₂ weathering feedback); water-soluble gases and aerosols should increase in concentration; and water vapor and water cloud features themselves should disappear. For a more thorough discussion of this concept, and how it can begin with near-term observations, see Bean, Abbot, & Kempton (2017).

A statistical search for life should raise the overall confidence in our detection of life beyond Earth compared to what is achievable by the search for life on a single exoplanet (Walker et al., 2018). For example, consider an exoplanet for which LUVOIR detects the presence of water (H₂O), molecular oxygen (O₂) and ozone (O₃), but not methane (CH₄). This is a plausible scenario, given the long integration times required to detect CH₄ in LUVOIR's wavelength range. The combination of these measurements, as well as constraints on UV fluxes from observations of the host star, would produce a scenario for which the most likely explanation is life on that planet. However, the lack of CH₄ on that planet may be enough to prevent a conclusion as bold as "We are not alone." As an alternative, consider a scenario where LUVOIR detects this same set of features multiple times on worlds in different planetary systems. This would suggest that either our understanding of photochemical processes is woefully incomplete and under-predicting some O₂-producing mechanism, or that life is present on at least some subset of these worlds.

This example would also apply to other biosignatures. An organic haze in the presence of a CO₂-rich atmosphere has been recently proposed as a biosignature (Arney et al., 2018). While consideration to false positives has been given, a haze-biosignature has not undergone the same amount of thorough scrutiny as O₂/O₃. Thus, one might place a lower amount of confidence in this biosignature than the detection of O₂/O₃. To quantify this example, if we are to assume that ~50% of CO₂-rich, haze-bearing habitable zone worlds have life, the detection of multiple such planets would increase the likelihood that *at least one* of these planets has a biosphere (whereas a search focused on a single target would not be able to draw such a strong conclusion).

This search does not necessarily need to focus on the same signature being present on multiple worlds. It would also apply to any combination of potential biosignature across multiple planets, and thereby allow the mission to conduct both a broad survey for easy-to-detect biosignatures on multiple planets and a detailed assessment of the biosignatures on LUVUOIR's best targets. The approach could therefore be optimized so that detailed assessments (such as the measurement of longitudinal-dependent colors/spectra) are only conducted on relatively close targets, for which such assessments are capable of being conducted with reasonable investments of telescope time.

A statistical search will also be useful in the case of no (or very poor) signs of life being detected by LUVUOIR. Instead of just a full null result, the process of quantifying the likelihood on each planet, with a statistical combination of those likelihoods, will yield an overall confidence level that sets an upper-bound on the frequency of life. Such a conclusion is not really possible, unless we conduct a statistical survey of multiple worlds than a deep dive on a single planet. Further, the more planets we assess, the stronger our conclusions will be. Detecting no biosignatures on 55 habitable-zone planets would give a 2- σ upper limit on the frequency of life of 6%. Thus, our uncertainty on " η_{life} " would decrease by an order of magnitude, from a range of 0–1.0 to a range of 0–0.06.

Again, it is useful to consider an example: if LUVUOIR finds multiple Earth-sized worlds in the habitable zone of other stars and determines that many of them have "anti-biosignatures" (such as high atmospheric concentrations of H_2 and either CO or CO_2), the confidence level that life is rare might be high.

There are two requirements to such an approach to the search for life:

1. The science community must be able to ascribe a quantitative estimate a given data set resulted from a biosphere on any particular planet; and
2. We must be able to collect spectroscopic data on many worlds.

The former requirement demands development in the research tools utilized by the astrobiology and exoplanet communities. Options for quantifying our assessment that a given planet has a biosphere are discussed and reviewed by Walker et al. (2018, in press), and leverage similar efforts to quantify signs of life in our own Solar System. The latter requirement inevitably leads to a LUVUOIR-sized telescope.

A.12.2 The role of LUVUOIR

A statistical approach to habitability and the habitable zone does not require LUVUOIR, as it could begin with ground- and space-based surveys for H_2O and CO_2 features via transit spectroscopy (Bean et al., 2017). LUVUOIR would extend this statistical approach to new targets, with new observational techniques. Specifically, LUVUOIR would expand the search to planets around Sun-like (F, G, K) stars. It would also provide new information on clouds and aerosols on planets around Sun-like and M-type stars, via a wavelength range that is complementary to currently-planned transit spectroscopy observatories.

While other missions might attempt to search for signs of life, and perhaps detect them on one world, a statistical approach requires that this search be conducted on a large number of worlds. This, in turn, demands a large-aperture telescope, to drive up the yield of planets that the mission can discover and characterize. LUVUOIR will be able to detect over 50 such planets. This is a large enough sample size to conduct a statistical search for signs of life on

Program at a Glance

Science goal: To find signs of life—or conclusively rule out life in our Sun’s local neighborhood.

Program details: This requires an optimized search for biosignatures

Instrument(s) + configuration(s): This would require all of the bandpasses and spectroscopy modes of ECLIPS.

Key observation requirements: The main requirement here is a broad wavelength range for ECLIPS, running from $\sim 0.2 \mu\text{m}$ to $\sim 2 \mu\text{m}$, so that different signatures with different integration times can be detected. This also requires a large-aperture telescope, in order to detect and characterize dozens of potentially habitable exoplanets.

exoplanets. If detectable biospheres exist on at least 10% of potentially habitable worlds, LUVOIR will find at least one such biosphere. But if life is relatively common, LUVOIR has the potential to find signs of life on many worlds. If it is rare, we will be able to set upper bounds on the frequency of life.

A.12.3 The science program

A statistical search for habitability and life would be consistent with the main exoplanet observing program outlined in **Chapter 3**. It would be conducted almost exclusively via ECLIPS observations of exoplanets in the habitable zones of their host stars, and LUMOS observations would obtain the UV spectral energy distribution of those host stars. It would use different bands within the ECLIPS wavelength range, depending on the distance to the target and the spectral feature in question, and likely would run ECLIPS to the point where integration on individual bands becomes time-limited. Details of this approach are below.

The main difference of the approach outlined here to the main exoplanet characterization program is in how optimized the biosignature search becomes, and how the data from that search are processed. This approach would likely *require* an optimized search for biosignatures, spending as little time as possible confirming/rejecting biosignatures on each planet. This search would likely focus on planets with atmospheric H_2O , which would be found during LUVOIR’s planet detection phase. In addition to weeding out dry planets, this initial phase would also include a search for H_2O beyond the habitable zone. This would help test the habitable zone concept by mapping the presence of H_2O water vapor as a function of stellar irradiation (Bean et al. 2017).

Then, the search would turn towards easy-to-detect, but low-confidence biosignatures, such as O_3 and atmospheric organic haze, both of which can be detected in the UV channel of ECLIPS. This initial biosignature search would include some planets near—but not in—the habitable zone. This would provide a basis for comparison of presumed “dead” planets, which could lead to more robust conclusions about the detection of life and help inform the science community if something about our understanding of photochemical and geological processes is dramatically incomplete.

For planets with O_3 or an organic haze, LUVOIR would proceed to the detection of O_2 (for O_3 -bearing worlds) and CO_2 (for haze-bearing worlds). However, it would only do so if

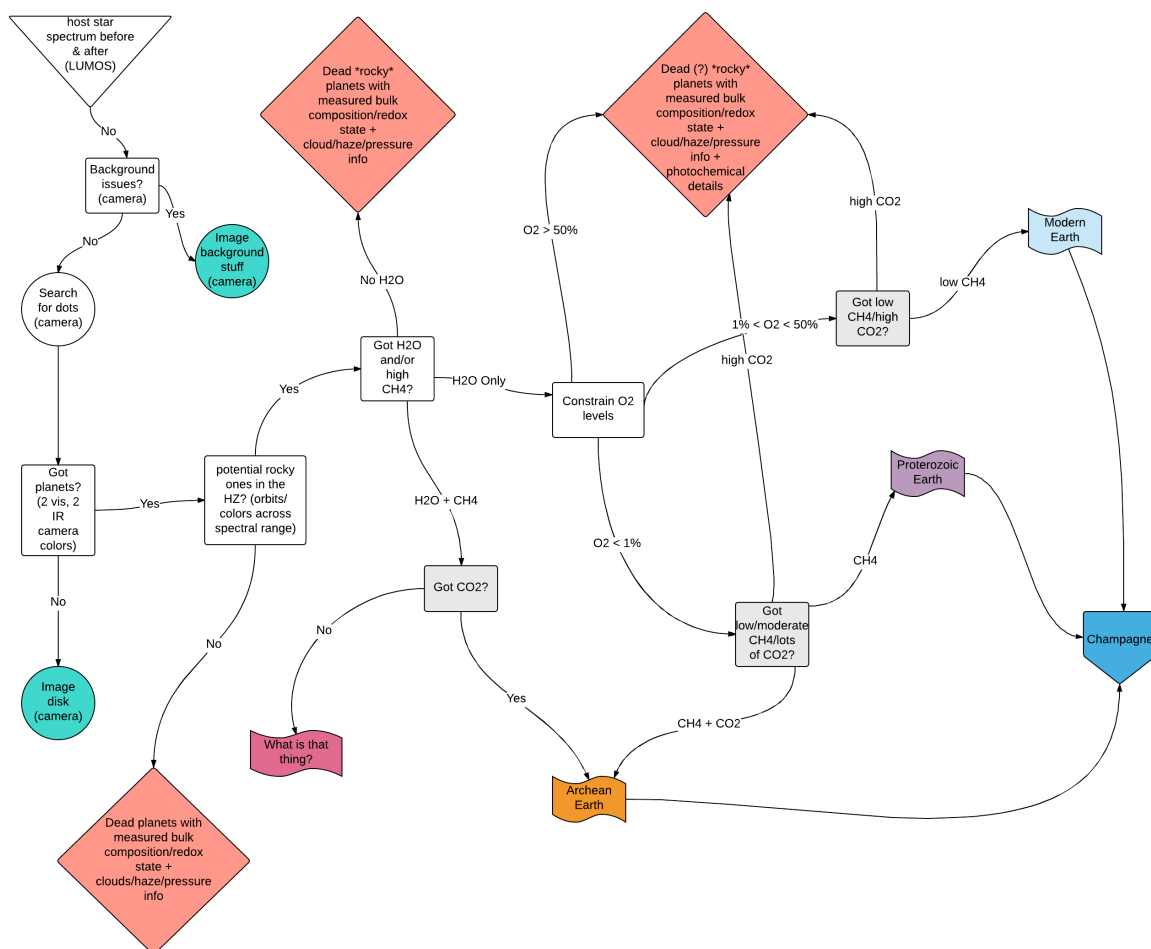


Figure A-18. An example of the observing strategy for a statistical approach to the search for life on biosignatures. Credit: S. Domagal-Goldman (NASA GSFC)

the detection of this second feature was permissible in a reasonable integration time. (The definition of “reasonable” would be up to a future time allocation committee, but history suggests $\lesssim 100$ hours.) If O_2 or CO_2 is detected, LUVUOIR would then proceed to further spectral measurements to rule out false positives, search for secondary biosignature gases (such as CH_4) or attempt to characterize the surface. Again, this would be limited on a target-by-target bases based on required integration time. A full decision tree for such a search is shown in **Figure A-18**.

The totality of these observations, at varying degrees of detail depending on the target, would maximize LUVUOIR’s ability to test our ideas of planetary habitability and search for life across the set of exoplanets it characterizes.

References

- Arney, G. A. et al. 2018, *AsBio*, 18,4
 Bean, J., Abbot, D., & Kempton, E. 2017, *ApJ*, 841, L24

A.13 A statistical test of the habitable zone

Jade Checlair (University of Chicago), Dorian S. Abbot (University of Chicago), Robert J. Webber (New York University), Y. Katherina Feng (UC Santa Cruz), Jacob L. Bean (University of Chicago), Christopher C. Stark (STScI), Tyler D. Robinson (Northern Arizona University), Eliza Kempton (University of Maryland)

A.13.1 Introduction

Until now, we have had to base many interpretations of observations on habitability hypotheses that have remained untested. To test these theories observationally, we propose a statistical approach to questions of planetary habitability. The key objective of this approach will be to make quick and cheap measurements of critical planetary characteristics on a large sample of exoplanets, exploiting statistical marginalization to answer broad habitability questions.

The habitable zone concept is an important tool used to characterize potentially habitable exoplanets. Despite this, the habitable zone and its theoretical limits have not been tested observationally. A statistical approach will present us with the opportunity to test this concept, and further our understanding of the processes that govern habitability.

Testing climate regulation within the habitable zone: Traditional habitable zone theory (Kasting et al. 1993) predicts that the surface temperature of habitable planets is regulated inside the habitable zone, which allows for surface liquid water. This theory assumes that the silicate-weathering feedback (Walker et al. 1981) regulates the atmospheric CO_2 of planets within the habitable zone through a stabilizing negative feedback. As a planet's surface temperature decreases, the weathering rate (intake of CO_2 by the crust) slows, which allows CO_2 to accumulate in the atmosphere—resulting in an increase in surface temperature. This feedback significantly extends the outer edge of the habitable zone, from 1.01 AU (Hart 1979) to 1.67 AU (Kasting et al. 1993), where outer planets build dense CO_2 atmospheres to maintain habitable surface conditions. It is also believed to be responsible for allowing Earth to escape Snowball events. There is some non-definitive evidence that this feedback has functioned throughout Earth's history (Stolper et al. 2016, e.g.), but it is untested in an exoplanet context. If the silicate-weathering feedback functions, we should observe a decrease in the CO_2 mixing ratio as a function of stellar irradiation for planets in the habitable zone.

Testing the limits of the habitable zone: The main assumption of traditional habitable zone theory (Kasting et al. 1993) is that terrestrial planets are able to maintain surface liquid water within the two defined boundaries of the habitable zone. If this assumption is correct, two testable predictions can be made. First, the abundance of water vapor should be greater inside than it is outside the habitable zone. Terrestrial planets inside the inner edge of the habitable zone are expected to have lost all of their water vapor as a result of runaway greenhouse processes, while those outside the outer edge are expected to have all of their water vapor condensed out of the atmosphere and frozen on the surface. Second, terrestrial planets inside the habitable zone should tend to have a lower albedo than frozen planets outside the outer edge. If these predictions are correct, we should be able to detect threshold orbital radii where the albedo and water vapor concentration increase and/or decrease using a large sample of planets.

Planetary color has been previously proposed as a method for discriminating Earth-like worlds from other planetary objects (Crow et al. 2011; Traub 2003) and optimized photometric bands for identifying exo-Earths in future space-based surveys have been calculated (Krissansen-Totton et al. 2016). The carbonate-silicate cycle predicts that CO_2 concentrations will rise with increasing distance from the host star until very high CO_2 levels are reached at the maximum greenhouse limit, which defines the outer edge of the habitable zone (Kasting et al. 1993; Kopparapu et al. 2013). Habitable planets near the outer edge will be both brighter than planets near the inner edge and bluer due to enhanced Rayleigh scattering from a larger atmospheric mass. If this is correct, we should observe an increase in planetary “blueness” as a function of decreasing irradiation from the inner to the outer boundary. Frozen, ice-covered planets outside the outer boundary should be substantially less blue than planets just inside it due to atmospheric collapse of CO_2 , reducing Rayleigh scattering (residual N_2 may remain, as N_2 has a significantly lower condensation temperature). Dry and barren planets like Mars should also be distinguishable using planetary color as most oxidized minerals have blue-absorption coupled with increasing spectral albedos into the red and infrared (Baldrige et al. 2009; Clark et al. 2007).

A.13.2 The role of LUVUOIR

Statistically testing habitability hypotheses such as the concept of the habitable zone will require a large-aperture telescope. The large aperture of LUVUOIR (8–15m) will allow us to observe a large enough number of exo-Earths to statistically test the concept of the habitable zone. Its smallest design (8-m aperture, segmented on-axis) will yield ~30 exo-Earths, while its largest design (15-m aperture, segmented on-axis) will yield ~50 exo-Earths (Stark et al. 2019). Our preliminary work indicates that we would need to observe ~20 exo-Earths to test the silicate-weathering feedback on exoplanets in the habitable zone. Testing the limits of the habitable zone may similarly require dozens of exo-Earths observations. A 4- or 6-m class mission will comparatively yield ~10 exo-Earths, which is likely insufficient to conduct statistical studies and test habitability hypotheses.

A.13.3 The science program

Statistically testing habitability hypotheses will require us to measure each individual planetary property (e.g. CO_2 mixing ratio) on as many targets as possible. An advantage of this approach is that these measurements will be done relatively quickly, maximizing scientific return from minimal telescope time.

Testing the silicate-weathering feedback will require estimating the CO_2 mixing ratio of a large number of planets at different orbital separations from their stars. An idealized example of this from Bean et al. (2017) is shown in **Figure A-19**. The salient point from this plot is that the mean CO_2 mixing ratio of planets decreases as the stellar irradiation they receive increases in order to maintain a roughly constant surface temperature. This trend could be observable if enough planets are measured to marginalize over variation in planetary properties. The CO_2 signatures will be detectable at 1.21 and 1.6 μm .

Similarly, testing for changes in the abundance of water vapor at the edges of the habitable zone will require detecting H_2O at any of 0.65, 0.72, 0.82, 0.94, 1.12, 1.4, 1.85 μm on a large number of planets at different orbital separations from their stars.

Program at a Glance

Science goal: To test the concept and limits of the canonical habitable zone.

Program details: Measure CO₂ and H₂O signatures on a large number of planets at different orbital separations. Measure planetary albedo on a large number of planets inside the habitable zone inside and outside the habitable zone and outside its outer edge.

Instrument(s) + configuration(s): Broadband spectroscopy and photometry with ECLIPS.

Key observation requirements: This requires a large-aperture telescope that will yield dozens of exo-Earths and can detect signatures at wavelengths from ~0.2 to ~2.0 μm .

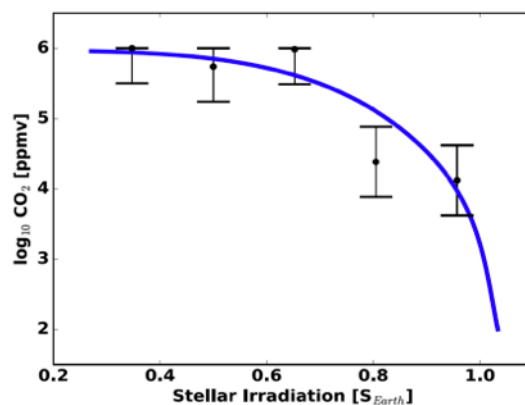


Figure A-19. This plot shows how the silicate-weathering feedback hypothesis, which assumes a decrease in atmospheric CO₂ as stellar irradiation increases, could be tested on exoplanets. The blue curve shows the predicted CO₂ needed to maintain a surface temperature of 290 K.

To estimate the albedo of terrestrial exoplanets, we will need to measure their reflected starlight, orbital distance, and the luminosity of the star they orbit. We will need to do this for a large number of planets at orbital separations both inside and outside the habitable zone.

Planetary color is likely less expensive to secure than spectra with a space-based imaging survey and it may be possible to design optimized band passes for identifying the inner and outer edge transitions. Although the specific band passes are still to be defined, we will need to obtain broadband re averages of bandpasses between ~0.4 and ~0.9 μm .

References

- Baldrige, A. S. et al. 2009, Remote Sensing of Environment, 113, 4.
- Bean, J. et al. 2017. *ApJ*, 841, 2.
- Clark, R. N., et al. 2007. US geological survey, digital data series, 231.
- Crow, C. A. 2011. *ApJ*. 729, 2.
- Hart, M. H. 1979. *Icarus*, 37, 1.
- Kasting, J. F. et al. 1993. *Icarus*, 101, 1.
- Kopparapu, R. K, et al. 2013. *ApJ*, 765, 2.
- Krissansen-Totton et al. 2016. *ApJ*, 817, 1.

Stark, C. C. et al. 2019. *Journal of Astronomical Telescopes Instruments and Systems*, 5, 2.
Stolper, D. 2016. *Science*, 353, 6306.
Traub, W. 2003, *Scientific Frontiers in Research on Extrasolar Planets*, 294.
Walker, J. C. et al. 1981. *JGR*, 86, NC10.

A.14 Observation of oxygen and hydrogen exospheres of Earth-like exoplanets

Shingo Kameda (Rikkyo University), N. Osada (Rikkyo University), Tadayuki Kodama (Subaru Telescope), Gen Murakami (Institute of Space and Astronautical Science), Masahiro Ikoma (University of Tokyo), Norio Narita (National Astronomical Observatory of Japan), Keigo Enya (Japan Aerospace Exploration Agency), N. Terada (Subaru Telescope), Hideaki Fujiwara (Subaru Telescope), Takahiro Sumi (Osaka)

A.14.1 Introduction

The PROCYON (Proximate Object Close flyby with Optical Navigation) satellite's Lyman Alpha Imaging CAmera has observed Earth's upper-atmospheric corona (**Figure A-20**) (Kameda et al., 2017). The corona, formed from exospheric atoms, was observed extended to more than 240,000 km, about 38 Earth radii. The hydrogen density is estimated about 20 atoms/cm³ at a distance of ~60,000 km in the Earth's exosphere. The same amount of density is expected to be observed at a distance 10,000-20,000 km in Venus and 30,000-35,000 km in Mars. This is caused by the difference of mixing ratio of CO₂ in the upper atmosphere. Venus and Mars have CO₂-rich atmospheres with a lower exospheric temperature. On Earth, CO₂ was removed from its atmosphere by a carbon cycle with its ocean and tectonics. Translating these arguments to exoplanets in a habitable zone presents a possible marker to distinguish an Earth-like planet from a Mar-like or Venus-like planet (Tavrov et al., 2018). The expanded exospheres can be observed in UV, during the exoplanet transit event in a primary eclipse. It reduces the stellar flux, when an exoplanet orbiting in front of the host star.

A.14.2 The role of LUVOIR

Theoretical exospheric models have considered what might be possible for an oxygen exosphere. There are three oxygen emission lines that may be observed (O I triplet), at wavelengths of 130.2 nm, 130.5 nm, and 130.6 nm. Though the observation at low earth orbit is affected by Earth's oxygen emission lines, this interference would not occur using LUVOIR at L2, far away from the Earth's oxygen exosphere. The 130.2-nm line emission is caused by resonance scattering from oxygen at the ground state and is absorbed by interstellar atomic oxygen. Thus, we cannot use this line to observe exoplanets. On the other hand, the other two lines are not affected by inter stellar atomic oxygen.

If we assume that Proxima Centauri b, at which the EUV irradiation is much higher than at Earth, is either the Earth-like, Mars-like or Venus-like, the temperature of upper atmosphere for the Earth-like is estimated to be ~10,000 K. By contrast, Mars-like and

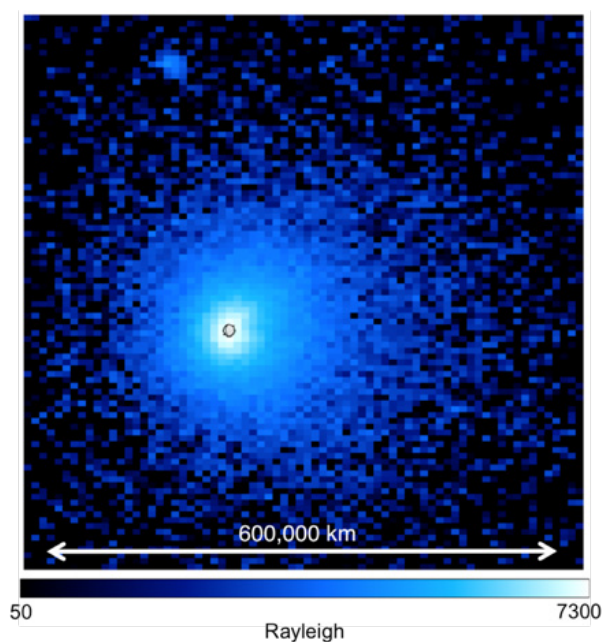


Figure A-20. The extended hydrogen exosphere of Earth

Program at a Glance

Science goal: Observe oxygen and hydrogen exospheres of Earth-like exoplanets.

Program details: UV spectroscopy of O I triplet lines.

Instrument(s) + configuration(s): LUMOS spectroscopy of atomic oxygen (130 nm) and hydrogen (122 nm).

Key observation requirements: Observations at 130 and 122 nm. SNR ~ 10 for a transit depth of 75% at the O I line center.

Venus-like are estimated to be ~300 K and ~600 K, respectively. Therefore, the transit depth at the line center for each case is 76%, 0.7%, or 3.8%, respectively. Due to the large difference in the transit depth, the Earth-like case can potentially be distinguished from the Venus-like and the Mars-like cases.

A.14.3 The science program

For an Earth-twin exoplanet orbiting a star identical to Proxima Centauri, **Figure A-21** illustrates how far such planet's exosphere could be observed as a function of the diameter of the telescope, assuming a total observing time of 2 hours (~1 transit). If the diameter is 15 m, detectable range is ~ 50 pc. According to the RECONS (Research Consortium on Nearby Stars) catalog, at least in the range of < 50 pc, there are ~3700 M dwarfs and 1% of them would have Earth-size planets in the habitable zone, observable by transit spectroscopy. The number of Earth-like exoplanets will be updated after TESS and PLATO projects.

Note that even if we detect oxygen O I in transit, this is not a direct evidence for biogenic activity. We must consider the diversity of processes that could produce such an atmosphere..

VIS-NIR observations of these planets at the same or close time will be complementary. The target of the UV spectrograph is the upper atmosphere and that of VIS-NIR observation is the lower atmosphere.

References

Kameda, S. et al. 2017, JGR Letters, 44, 23
Tarov, A. et al, 2018, J Astron Telesc Inst, 4, 4

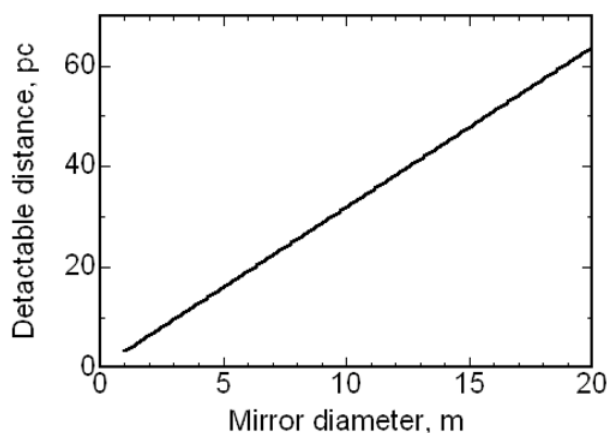


Figure A-21. The distance that Earth-like exospheres orbiting a low temperature star can be observed as a function of telescope mirror diameter.

A.15 Detecting methane biosignatures on transiting exoplanets

Joshua Krissansen-Totton (University of Washington), David Catling (University of Washington), Ryan Garland (University of Oxford), Patrick Irwin (University of Oxford)

A.15.1 Introduction

Waste gases produced by life may alter the composition of planetary atmospheres in ways that are remotely detectable. Oxygen is a promising biosignature gas because abiotic processes cannot easily sustain O_2 -rich atmospheres (Meadows et al. 2018). However, O_2 biosignatures may be uncommon because (i) oxygenic photosynthesis is a complex metabolism that only evolved once (Knoll 2008), and (ii) even if oxygenic photosynthesis is common, it may take billions of years for detectable O_2 levels to accumulate (Lyons et al. 2014). Technology that enables the search for alternative biosignatures is therefore desirable. One possible alternative biosignature for anoxic atmospheres is the coexistence of carbon dioxide (CO_2) and abundant methane (CH_4). CH_4 has a relatively short lifetime in anoxic terrestrial planet atmospheres, and so cannot persist without replenishment. Analyses of the Archean Earth's (4.0–2.5 billion years ago) atmosphere show that CH_4 and CO_2 were in chemical disequilibrium due to microbial CH_4 (Krissansen-Totton et al. 2018b).

For habitable exoplanets, the coexistence of CH_4 and CO_2 is a promising biosignature due to the lack of plausible abiotic CH_4 sources. Biogenicity would be especially compelling if CH_4 was abundant ($>0.1\%$) because abiotic water-rock reactions—the most plausible “false positive” for methane-producing life—are unlikely to yield abundant CH_4 (Figure A-22). Further, the absence of carbon monoxide (CO) would strengthen the case for life. This is because abiotic processes such as volcanic outgassing are unlikely to produce carbon in

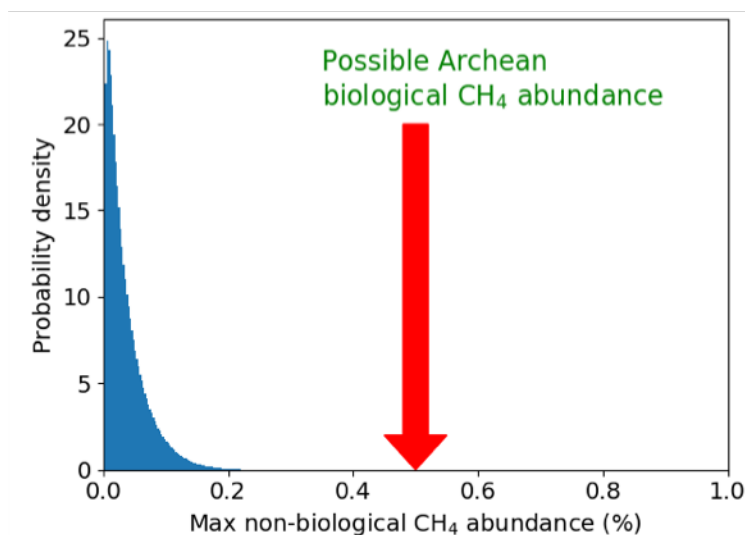


Figure A-22. Probability distribution for the maximum CH_4 abundance from non-biological water-rock reactions. This is calculated assuming surface CH_4 fluxes are balanced by photodissociation and diffusion-limited H escape to space in a temperate, anoxic atmosphere. The red arrow shows a data-driven estimate for the CH_4 abundance on the Archean Earth at 3.5 Ga (Zahnle et al. 2019).

Key point: CH_4 abundances exceeding $\sim 0.1\%$ (in the presence of CO_2) are difficult to explain without biological methane production. Adapted from Krissansen-Totton et al. (2018b).

Program at a Glance

Science goal: Search for methane biosignatures on Earth-like planets with anoxic atmospheres.

Program details: Transit spectroscopy of potentially habitable exoplanets around nearby M-dwarfs such as TRAPPIST-1 and TESS objects.

Instrument(s) + configuration(s): HDI grism spectroscopy

Key observation requirements: The main requirement is $\sim 0.2\text{--}2.5\ \mu\text{m}$ low resolution ($R\sim 100$) spectroscopy. Extending upper wavelength limits to $\sim 5\ \mu\text{m}$ using alternative instruments (no cryogenic cooling required) and using a 15 m aperture would allow abiotic scenarios to be ruled out with higher confidence.

its most oxidized form (CO_2) and its least oxidized form (CH_4) without producing carbon with intermediate oxidation (CO) (Krissansen-Totton et al. 2018b). **In summary, the coexistence of CO_2 with $>0.1\%$ CH_4 (plus low or absent CO) in habitable exoplanet atmospheres is a promising disequilibrium biosignature with no known false positives.**

This CH_4+CO_2 biosignature is potentially more common than oxygen biosignatures because, in contrast to the complexity of oxygenic photosynthesis, methanogenesis is primitive and ancient (Wolfe & Fournier 2018). Life detection via direct imaging using LUVUOIR is discussed elsewhere. Here, we show that LUVUOIR would enable the detection of CH_4+CO_2 biosignatures via transit spectroscopy.

A.15.2 The role of LUVUOIR

Krissansen-Totton et al. (2018a) computed simulated James Webb Space Telescope (JWST) transit retrievals of TRAPPIST-1e (Gillon et al. 2017), the most likely habitable planet in the TRAPPIST-1 system (Turbet et al. 2018). TRAPPIST-1e was assumed to be an Archean Earth-like analog with abundant CH_4 in combination with CO_2 , and negligible CO. It was found that ~ 10 coadded transits may be sufficient to detect the CH_4+CO_2 biosignature on TRAPPIST-1e (Krissansen-Totton et al. 2018a). However, such detections would be tentative because gas abundances cannot be tightly constrained with JWST, potentially allowing for abiotic explanations. Follow-up observations with future instruments will be necessary to confirm the presence of life and to extend the search to more targets. Transiting observation in the thermal infrared are not well suited to confirming CH_4+CO_2 biosignatures because they cannot easily constrain CH_4 and CO_2 gas abundances (Krissansen-Totton et al. 2019). Instead, as demonstrated below, NIR transit observations with a large aperture space telescope such as LUVUOIR are required.

A.15.3 The science program

Figure A-23 shows abundance constraints from a simulated transmission spectrum retrieval of 10 transits of an Archean Earth-like TRAPPIST-1e with both a 15m and 8m LUVUOIR telescope.

Retrievals for both $0.2\text{--}2.5\ \mu\text{m}$ (nominal wavelength range for HDI instrument) and $0.2\text{--}5\ \mu\text{m}$ wavelength ranges are shown (alternative instrument, no cryogenic cooling). The third

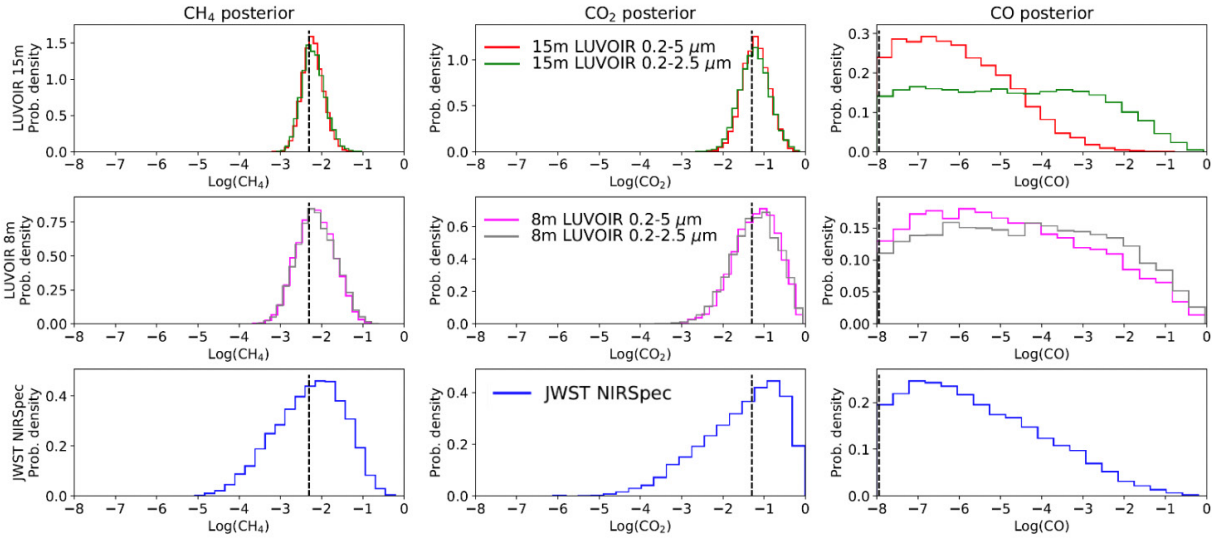


Figure A-23. CH_4+CO_2 biosignatures are detectable with LUVOIR. Gas abundance posteriors for 10 transits of an Archean Earth-like TRAPPIST-1e. Columns show CH_4 , CO_2 , and CO mixing ratio posteriors. Vertical dashed black lines are “true” values. Row 1 shows 15m LUVOIR retrievals for the nominal 0.2–2.5 μm HDI wavelength range (green), and a 0.2–5 μm instrument (red). Row 2 shows 8m LUVOIR retrievals for both the nominal 0.2–2.5 μm HDI instrument (grey) and 0.2–5 μm instrument (fuchsia). Row 3 shows a JWST NIRSpec prism simulated retrieval (blue). Archean Earth-like CH_4+CO_2 biosignature detection is straightforward with LUVOIR, although either a 5 μm long wavelength limit or complementary JWST observations are required to constrain CO (ruling out abiotic scenarios). LUVOIR noise estimated using Goddard’s Planetary Spectrum Generator.

row shows a comparison to simulated JWST observations of the same object using NIRSpec prism. Unless otherwise stated, the methodology used to generate these synthetic retrievals is described in Krissansen-Totton et al. (2018a) where the NEMESIS radiative transfer code was used (Irwin et al. 2008). **Both 15m and 8m versions of LUVOIR could constrain CH_4+CO_2 abundances sufficiently precisely to allow biosignature detection on transiting, Archean Earth-like exoplanets such as TRAPPIST-1e.** A 15m LUVOIR with an upper wavelength limit of a 5 μm would be necessary to constrain CO abundances, thereby ruling out non-biological CH_4 production scenarios (or alternatively this could be done with complementary JWST observations).

References

- Gillon, M., Triaud, A. H., Demory, B.-O., et al. 2017, *Natur*, 542, 456
 Irwin, P., Teanby, N., De Kok, R., et al. 2008, *JQSRT*, 109, 1136
 Knoll, A. H. 2008, *The Cyanobacteria: Molecular Biology, Genomics, and Evolution*, 484
 Krissansen-Totton, J., Arney, G., Catling, D., et al. 2019, in *Astro2020 Science White Paper*
 Krissansen-Totton, J., Garland, R., Irwin, P. G., & Catling, D. 2018a, *AJ*, 156
 Krissansen-Totton, J., Olson, S., & Catling, D. C. 2018b, *Science advances*, 4, eaao5747
 Lyons, T. W., Reinhard, C. T., & Planavsky, N. J. 2014, *Natur*, 506, 307
 Meadows, V. S., Reinhard, C. T., Arney, G. N., et al. 2018, *AsBio*, 18, 1
 Turbet, M., Bolmont, E., Leconte, J., et al. 2018, *A&A*
 Wolfe, J. M., & Fournier, G. P. 2018, *Nature ecology & evolution*, 2, 897
 Zahnle, K. J., Gacesa, M., & Catling, D. C. 2019, *Geochim Cosmochim Acta*, 244, 56

A.16 Leveraging planetary seasonality to recognize habitability and to detect the pulse of a biosphere

Stephanie L. Olson (University of Chicago), Edward W. Schwieterman (UC Riverside)

A.16.1 Introduction

Earth experiences seasons in response to obliquity-driven changes in insolation. These changes have far-reaching impacts on Earth's hydrologic cycle and biosphere that manifest as seasonality in the spectral appearance of our planet. For example, seasonality in ice extent, cloud cover, and cloud structure impart seasonality to planetary albedo. Changes in the H₂O content of our atmosphere also drive seasonality in OH radical production via H₂O photolysis and the abundance of trace gases like CH₄. Meanwhile, seasonal shifts in the balance of photosynthesis:



And aerobic respiration:



result in striking antithetic oscillations of CO₂ and O₂ (Keeling et al., 1976; Keeling & Shertz, 1992). Seasonality is thus a promising habitability indicator and biosignature (Meadows, 2008; Olson et al., 2018).

As a biosignature, seasonality has several potential advantages compared to conventional static biosignatures. If life elsewhere is carbon based, and if CO₂-dependent weathering feedbacks are essential for long-term habitability, it is reasonable to expect that seasonality in the biosphere may manifest as seasonality in atmospheric CO₂ on other inhabited planets— independent of the details of biochemistry on those worlds. Moreover, seasonality may allow us to recognize life using time-variability in the abundance of gases that are not uniquely biological products (e.g., CO₂, CH₄). The greatest appeal, however, is that these signals may sometimes be the strongest hint of life on inhabited exoplanets. Mid-Proterozoic Earth, ~1.8–0.8 billion years ago, provides an example of such a scenario.

Despite an early origin for oxygenic photosynthesis on Earth, O₂ did not achieve high levels in our atmosphere until relatively recently (Lyons et al., 2014). Low levels of O₂ throughout the Proterozoic nonetheless had dramatic consequences for Earth's biosphere, including the buildup of sulfate in our ocean, that severely limited the abundance of CH₄ in the atmosphere (Olson et al., 2016). Thus, viewing mid-Proterozoic Earth as an exoplanet, it is not obvious that either O₂ or CH₄ would be remotely detectable (Reinhard et al., 2017). In the worst case, a remote observer might mistakenly believe our planet was sterile—but seasonality provides a path forward.

Ozone is not a biological product, but the abundance of O₃ in planetary atmospheres reflects biogenic O₂ levels. Weakly oxygenated planets, such as mid-Proterozoic Earth, are likely to have unsaturated O₃ spectral features in the UV. These features may thus experience seasonality in response to O₂ oscillations. **Figure A-24** illustrates this point. Each spectrum in

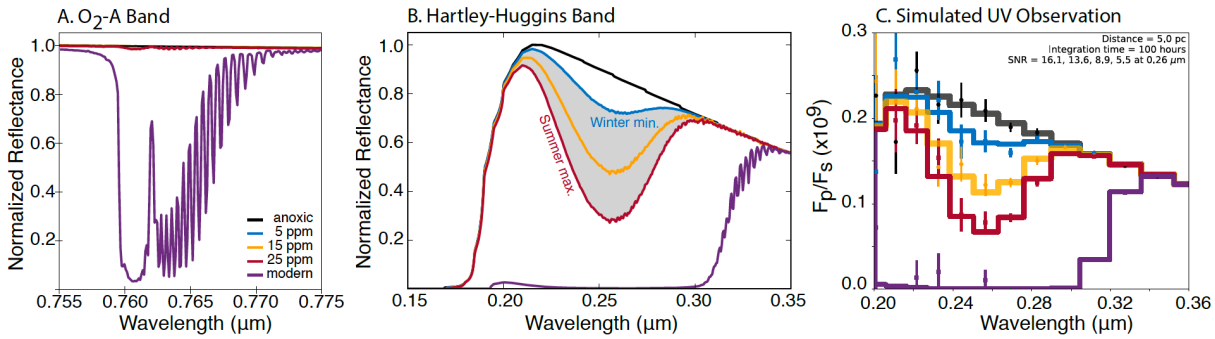


Figure A-24. A Proterozoic O_2/O_3 seasonality scenario. Shown here are synthetic spectra centered on the O_2 -A band at $0.76 \mu\text{m}$ (left) and the Hartley-Huggins O_3 feature in the UV (middle) from Olson et al. (2018). Ozone oscillations in response to biogenic O_2 seasonality are remotely characterizable with a LUVOIR-type telescope (right), but O_2 is not itself detectable at mid-Proterozoic-like levels.

Figure A-24 corresponds to O_2 scenarios that differ only slightly and collectively represent a potentially detectable seasonality scenario. Although O_2 itself is never abundant enough to be spectrally observable for the mid-Proterozoic, the seasonal O_2 maxima and minima manifest in distinctly different absorption signals for O_3 in the UV Hartley-Huggins bands (Olson et al., 2018). At a distance of 5 parsecs, these oscillations may be characterizable with a LUVOIR-like architecture within 100 hours exposure time at each of several orbital phases. Thus, O_3 seasonality may fingerprint O_2 seasonality and provide compelling evidence for life in the absence of detectable O_2 .

A.16.2 The role of LUVOIR

Characterizing planetary seasonality is a major observational challenge. There are three primary considerations:

1. Detecting seasonal biosignatures with transmission spectroscopy is not viable because transiting exoplanets reveal the same seasonal view with each transit. These signals thus specifically require a direct imaging mission.
2. Seasonal biosignatures may require broad wavelength coverage, inclusive of the UV.
3. Achievement of sufficient SNR to recognize ppmv-level gas oscillations—without requiring long exposure times with respect to the timescale of atmospheric variability—necessitates a large aperture telescope.

LUVOIR meets all of these criteria. For these reasons, LUVOIR may uniquely enable studies of exoplanet seasonality to inform habitability and support life detection. If recent suggestions that O_3 seasonality represents the most compelling biosignature for mid-Proterozoic biospheres are correct (Olson et al., 2018), it follows that a LUVOIR-like mission may be essential to recognizing life on some terrestrial planets that would otherwise yield false negatives from more conventional biosignatures.

Program at a Glance

Science goal: Use LUVUOIR to identify seasonality in the composition of exoplanet atmospheres. Seasonality may arise from an active hydrologic cycle and/or a biosphere, and it may thus be leveraged to recognize habitability and/or life.

Program details: Characterizing seasonality requires direct imaging of a given target planet at several orbital phases.

Instrument(s) + configuration(s): Seasonality studies will make use of the ECLIPS instrument, inclusive of all three wavelength channels.

Key observation requirements: The search for seasonality requires broad wavelength coverage from the UV (O_3) to the visible and NIR for identification of conventional biosignatures (e.g. O_2 , CH_4). Compared to static biosignature analysis, characterizing seasonality will likely require high signal-to-noise, but the total slew + integration time must be short compared to the timescale of atmospheric variability on the target planet.

A.16.3 The science program

Characterizing seasonal cycles on exoplanets using LUVUOIR will require deep (100+ hr), multi-epoch integrations of Habitable Zone target planets. These observations should leverage all three ECLIPS wavelength channels, from the UV to the NIR. UV observations will facilitate recognition of O_3 seasonality, as in the example above. Observations of H_2O , O_2 , CO_2 , and CH_4 features will provide additional constraints on planetary habitability and inhabitation status. For example, an active hydrologic cycle underlies our understanding of habitability—and seasonality in H_2O is likely inevitable on such worlds assuming non-zero obliquity or eccentricity. Likewise, CO_2 seasonality may be common to all planets hosting C-based life on their surfaces if CO_2 weathering feedbacks are responsible for long-term climate stability.

LUVUOIR's primary exoplanet mission will begin with a broadband survey of nearby stars with a primary goal of detecting planets and determining their orbits rather than characterizing these worlds and evaluating their habitability/inhabitation. Among Habitable Zone planets detected during this initial phase, there are two distinct motivations for follow up observations to constrain seasonality:

Deep integration of exoplanets with tentative biosignature detection. Should they exist, these targets are a high priority for follow up. As an alternative to stacking the results of many hours of integration spanning visits at various orbital phases, our observing program will emphasize deep integrations at 3–4 points in the orbit, roughly a quarter phase apart (half phase increments are insufficient because we could potentially observe an equinox-to-equinox shift). In addition to enabling the search for seasonal biosignatures, pursuing several deep, multi-epoch observations will also facilitate photometric rotation mapping and support determination of continentality, a key habitability consideration.

False negative mitigation in the face of apparent habitability. It is also important to follow up on rocky Habitable Zone planets that do not display obvious biosignatures on initial observation given the potential for biosignature false negatives discussed above. Our

observing program will prioritize planets with H₂O detections (apparent habitability) and low-inclination, phase-on orbits, which will be most conducive to detectable seasonality. For each target, we need deep integrations one-quarter phase and one-half phase apart to identify biosignatures that might only be detectable seasonally (or rule out their presence).

This program requires a substantial commitment of observing time, but in either case, the risks in implementing these detailed observations are negligible because the target planets will already be of high interest given their presence in the Habitable Zone and the detection of H₂O. Independent of the life-detection outcomes of our program, these observations will inform the distribution of habitable and inhabited planets in the Universe.

References

- Keeling C.D., et al. 1976. *Tellus*, 28, 538
Keeling R.F., Shertz S.R. 1992. *Nature*, 358, 723
Lyons T.W., Reinhard C.T., Planavsky N.J. 2014. *Nature*, 506, 307
Meadows V. S. 2008 *Exoplanets* ed J. W. Mason (Berlin: Springer) 259
Olson S.L., Reinhard C.T., Lyons T.W. 2016. *PNAS*, 113, 11447
Olson S.L. et al. 2018. *ApJL*, 858, L14
Reinhard, C.T. et al. 2017. *AsBio*, 17, 287

A.17 Technosignature observations with LUVUOIR

Ravi Kopparapu, (NASA GSFC), Thomas G. Beatty (U. Arizona), Svetlana Berdyugina (Leibniz Institute), Jacob Haqq-Misra (BMSIS), Emilio Enriquez (U. C. Berkeley)

A.17.1 Introduction

A primary goal of LUVUOIR's search for life beyond the solar system is to identify biosignatures on inhabited planets around other stars. The search for technosignatures, by analogy with biosignatures, refers to any sign of technological life that modifies its environment in ways that are detectable including communicative transmissions and other technologies that are passive (Tarter 2007, Haqq-Misra & Kopparapu 2012, Wright et al. 2016, Enriquez et al. (2017)). Technosignatures logically share a continuum with the search for biosignatures, and just like them, likely span a broad range of possibilities. However, we can define systematic strategies to search for technosignatures based on our current level and understanding of what constitutes a technological civilization. Here we identify some technosignature science cases that may be possible with LUVUOIR.

Similar to biosignatures, large telescopes with high-contrast imaging capabilities, such as LUVUOIR/ECLIPS, will be able to detect two types of TS (Berdyugina et al. 2018):

- atmospheric TS, i.e., gaseous and particle compounds of technological origin in exoplanetary atmospheres,
- structural TS, i.e., spatially resolved structures on exoplanetary surfaces or in the near-planetary space, which arise due to clustering of organisms or localized activity.

One example of atmospheric TS is chlorofluorocarbons (CFCs) that do not occur naturally but result from anthropogenic activity. They are also proposed as artificial super-greenhouse gases for warming up (terraforming) cooler exoclimates (e.g., on Mars, Marinova et al. 2005). Models were computed for CF_4 and CCl_3F in the mid IR for Earth-size planets transiting white dwarf stars: if the concentration of these pollutants was ~ 10 times the current terrestrial values, they could be detected by JWST (Lin et al. 2014). Detection requires days of JWST observing time, but LUVUOIR-A could detect such signatures with high confidence within about a day of observing time.

Examples of structural TS include artificial megastructures (AMS), geoengineering projects, as well as waste heat and light pollution due to civilization clustering and activity. Detecting structural TS will be crucial for identifying sources of suspected technogenic activities. Both LUVUOIR-A and LUVUOIR-B will be able to indirectly map exoplanet surfaces and resolve large-scale artificial structures and structures (see below).

By scaling up human civilization activities on the Earth, one can envision several structural TS on exoplanets with advanced civilizations. For example, they may construct artificial megastructures (AMS) either on the surface or in the near-space of an exoplanet (circumplanetary space). AMS could be of some regular shape and/or homogeneous albedo. In the circumplanetary space, AMS could be "geostationary," e.g., for communications or for harvesting stellar energy. Low-albedo installations similar to our photovoltaic systems can be employed on the planets' surface and in space. High-albedo installations can redirect the incident stellar light, e.g., for heat mitigation by reflecting the light back into space. Such

AMS may efficiently absorb/reflect only a particular part of the spectrum, similar to photosynthetic organisms having specific spectral edges (Berdyugina et al. 2016; Lingam & Loeb 2017). Other examples of structural TS include clustered waste heat (Kuhn & Berdyugina 2015) and artificial illumination (Loeb & Turner 2012) due to civilization urban-like activity as well as geoengineering projects such as Palm islands in Dubai, United Arab Emirates.

A.17.2 The role of LUVOIR

One of the distinct signatures of human civilization on Earth is the presence of nightside city lights. Though the total energy emitted into space from city lights is relatively low, the sodium-vapor lamps commonly used on Earth show narrow spectral features near 660 nm that are significantly brighter and distinguishable from the background thermal emission of the planetary nightside. Observations of the Earth from the Soumi-NPP satellite give a maximum disk-integrated intensity of $0.5 \text{ erg/s/cm}^2/\text{\AA}$ from city lights, compared to background nightside emission of $0.1 \text{ erg/s/cm}^2/\text{\AA}$.

The large aperture of LUVOIR will allow for the potential signal from nightside city lights to be detected on Earth-sized exoplanets around nearby stars (**Figure A-25**). If we assume that the lights used in these cities are an equal mix of the high- and low-pressure sodium street lighting used on Earth, then for present-day urbanization levels the emission from these lights will show a distinct spectroscopic signature in the planetary nightside emission.

Both LUVOIR-A and LUVOIR-B will have large enough aperture to resolve nearby Earth-like exoplanets from their host stars. Considering that the ECLIPS instrument will provide a very high contrast (10^{-10}) at IWA larger than $3.5 \lambda/D$ in the UV band and $4 \lambda/D$ in the visual and NIR bands, the light reflected from the exoplanetary surface can be collected with a high efficiency and SNR. For example, for an Earth-size planet with an average geometrical albedo 0.2 in the habitable zone of Alpha Cen A, LUVOIR-B/ECLIPS would be able to achieve SNR of 10 to 40 in the Johnson UBVRI bands during 1 hour exposure time. Similarly, LUVOIR-A/ECLIPS will achieve SNR of 30 to 100 (**Figure A-27**). When such measurements are done over the course of the planet's rotational and orbital periods, the

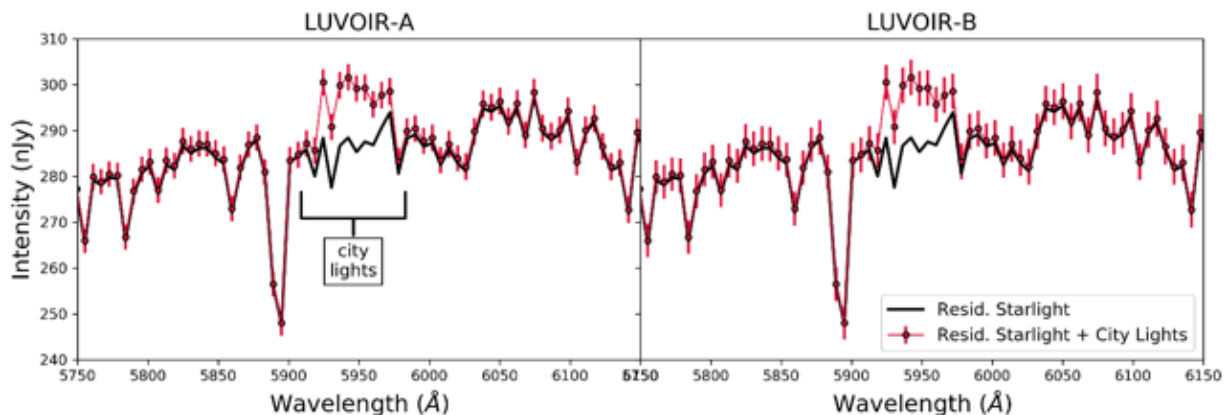


Figure A-25. Both LUVOIR-A/ECLIPS and LUVOIR-B/ECLIPS would be able to strongly detect the nightside city lights from present-day Earth on an Earth-like planet orbiting Alpha Cen A. This assumes a mixture of high- and low-pressure sodium lights similar to what is used on Earth. LUVOIR-A would detect these lights at 8-sigma, while LUVOIR-B/ECLIPS would detect the lights at 6-sigma. (Beatty, in prep.)

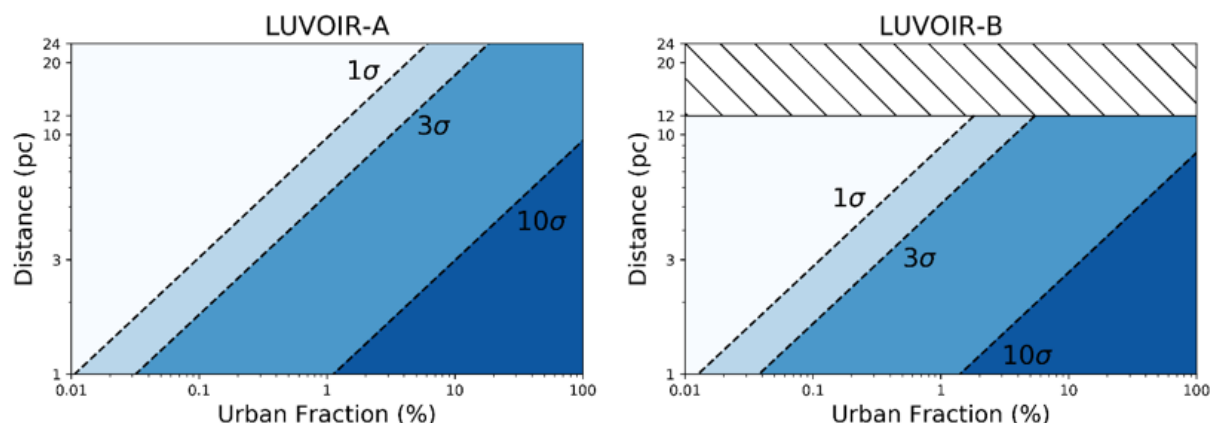


Figure A-26. LUVOIR-A would be able to detect Earth-like urban fractions out to a distance of 3 pc, while LUVOIR-B would be able to detect Earth-like urbanization out to 2 pc. For both architectures the limiting distance is set by the inner working angle of ECLIPS near 600 nm, which limits LUVOIR-A to approximately 24 pc and LUVOIR-B to 12 pc. The hatched region in the right panel shows this inaccessible range for LUVOIR-B. Note that an ecumenopolis (a city-wide planet) would be strongly detectable by both architectures (Beatty, in prep).

obtained time-dependent light-curve can be inverted into a 2D albedo map of the exoplanet. Recently a new powerful inversion technique ExoPlanet Surface Imaging (EPSI) has been developed and demonstrated for resolving both biosignatures and technosignatures on Earth-like exoplanets (Berdyugina & Kuhn 2019). By inverting light-curves measured in near-UV, visual and NIR bands simultaneously, one can obtain “true-color” albedo maps of exoplanet structures and identify their nature through broad-band spectrophotometry.

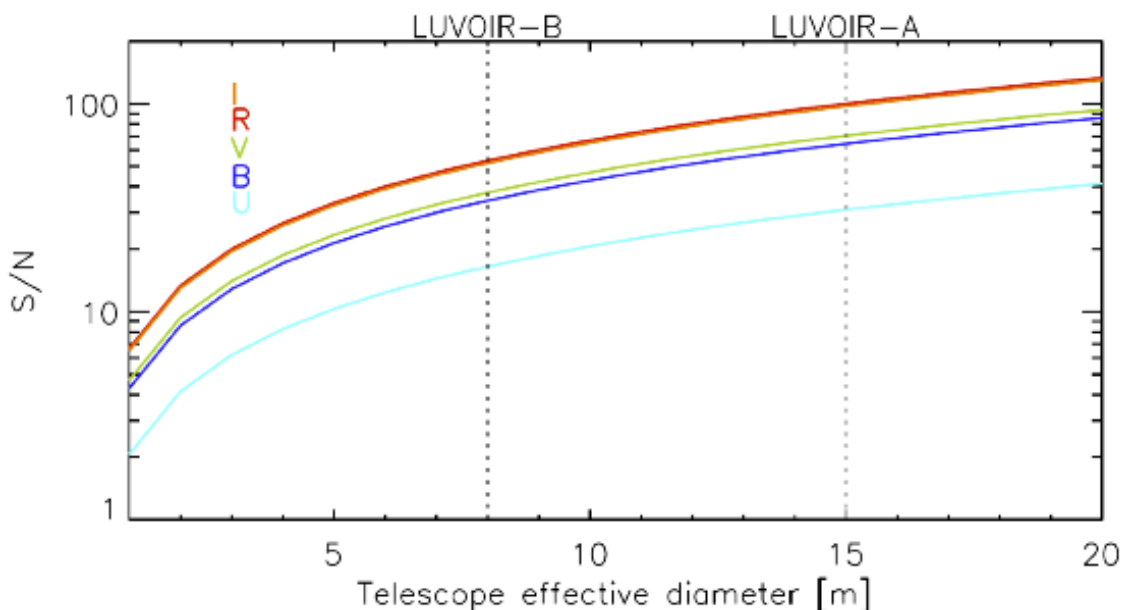


Figure A-27. LUVOIR-A/ECLIPS would be able to achieve sufficient SNR in all UBVR bands for mapping technosignatures on an Earth-size planet with an average geometrical albedo 0.2 in the habitable zone of Alpha Cen A and several other nearby exoplanets. LUVOIR-B/ECLIPS would achieve a similar performance in visual and NIR bands but not in the near-UV.

Program at a Glance

Science goal: Obtain high spectral resolution at VIS wavelengths to identify spectral features of sodium vapor lamps, artificial structures, nightside illumination and constrain the percentage of urbanization level based on the SNR and distance to the target planet.

Program details: IFS optical and near-IR spectra of a) all planets in the field during long integrations on stars with habitable zone planet candidates and b) a selected set of known planets around other stars.

Instrument(s) + Configuration: ECLIPS high-contrast, point-source spectroscopy

Key observation requirements: Spectral bandpass from 200 nm to 2000 nm, $R \sim 100$, Continuum SNR > 10

Examples of AMS and other artificial structures that can be detected by LUVOIR in reflected light using the EPSI inversion technique are shown in **Figure A-28**.

A.17.3 The science program

The nightside signal from present-day city lights on an Earth-sized exoplanet would be detectable using both LUVOIR-A/ECLIPS and LUVOIR-B/ECLIPS. The cities of a present-day Earth in a 1 AU orbit about Alpha Cen A would be detected at 8-sigma using LUVOIR-A and at 6-sigma using LUVOIR-B. LUVOIR-A would actually be able to significantly detect (>3-sigma) present-day cities out to 3 pc, a volume which includes Alpha and Proxima Cen, Barnard's Star, Wolf 359, Lalande 21185, and Sirius.

Present-day Earth has about 0.25% of its surface covered by cities, and increased urbanization levels would be detectable at even greater distances. As shown in the left panel

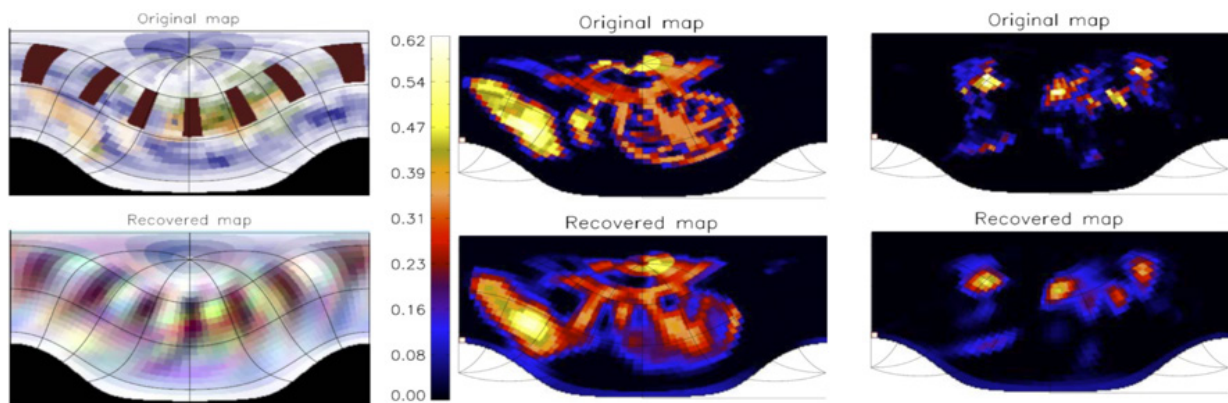


Figure A-28. Test inversions for Earth-size exoplanets with artificial structures. Left: Photovoltaic-like panels evenly distributed on an orbit around the planet above clouds, which resembles a partial “Dyson sphere” AMS. The panels harvest solar energy in the visible with high absorbing efficiency which can be identified through a low-resolution multi-band spectrophotometry. From Berdyugina & Kuhn (2019). Middle: A Palm island extrapolated to the planetary scale as a geoengineering project. The geometrical albedo scale is the same for both original and recovered images. Right: An Earth-like artificial illumination pattern on the night-side of the planet scaled by a factor of 20. From Berdyugina (in prep.).

of **Figure A-26**, LUVUOIR-A would be able to detect urbanization levels of 2.5% out to approximately 10 pc, and 10% out to approximately 24 pc using 100 hours of integration time. Beyond this distance the inner working angle of LUVUOIR-A/ECLIPS at 600 nm would prevent the separate detection of the target planets.

LUVUOIR-B would be able to detect the city lights from present-day Earth out to approximately 2 pc using 100 hours of integration time. The increased inner working angle of LUVUOIR-B/ECLIPS limits the maximum detection distance to about 12 pc, at which point the spacecraft would be able to significantly detect planets with a greater than 2% urban fraction (i.e., 16 times present-day Earth).

An example of a low-albedo installation in space (above clouds) is shown in **Figure A-28**, left (Berdyugina & Kuhn 2019). It may be considered as a partial Dyson sphere (“Dyson belt”) AMS, but on the planetary scale, which Type I civilizations similar to ours could build in order to harvest stellar energy arriving to the planet (Dyson 1960, Kardashev 1964).

An example of anthropogenic geoengineering projects is Palm islands in Dubai, United Arab Emirates. The island takes the form of a palm tree, topped by a crescent. When extrapolated to a planetary scale, such an artificial structure may be detected by LUVUOIR/ECLIPS in an exoplanet albedo map (**Figure A-28**, middle).

An example of an Earth-like artificial illumination pattern on the night-side of the planet is shown in **Figure A-28**, right. The pattern can be resolved and detected as shown, if scaled by a factor of 20 from the current highest light level of artificial illumination (0.5 klx), i.e., to the level of an indirect sunlight illuminance (10 klx).

References

- Berdyugina, S. V., & Kuhn, J. R. 2019, *ApJ*, in press (arXiv:1711.00185)
- Berdyugina, S. V., Harrington, D. M., Kuhn, J. R., Santl-Temkiv, T., Messersmith, E. J. 2016, *Int. J. Astrobiology*, 15, 45
- Berdyugina, S.V., Kuhn, J.R., Langlois, M., et al. 2018, *SPIE Proc.*, 10700, id. 107004I
- Dyson, F. 1960, *Science*, 131, 1667
- Enriquez, J. E. et al., *The Astrophysical Journal* 849 (2):104
- Haqq-Misra, J., Kopparapu, R. 2012, *Acta Astronautica*, 72, 15
- Kardashev, N. 1964, *Soviet Astronomy*, 8, 217
- Kuhn, J. R., & Berdyugina, S. V. 2015, *Int. J. Astrobiology*, 14, 401
- Lin, H. W., Gonzalez Abad, G., & Loeb, A. 2014, *ApJ Lett.*, 792, id. L7
- Lingam, M., & Loeb, A. 2017, *MNRAS Lett.*, 470, L82
- Loeb, A., & Turner, E. L. 2012, *Astrobiology*, 12, 290
- Marinova, M. M., McKay, C. P., & Hashimoto, H. 2005, *J. Geophys. Res.*, 110, id. E03002
- Tarter, J. C. 2007, *Highlights of Astronomy*, 14, 14
- Wright, J. T. et al., *The Astrophysical Journal* 816

A.18 Exoplanet diversity in the LUVOIR era

Ravi Kopparapu (UMD/NASA GSFC), Eric Hebrard (University of Exeter), Rus Belikov (NASA Ames), Natalie M. Batalha (NASA Ames), Gijs D. Mulders (LPL), Chris Stark (STScI), Dillon Teal (UMD), Shawn Domagal-Goldman (NASA GSFC), Avi Mandell (NASA GSFC), Aki Roberge (NASA GSFC)

A.18.1 Introduction

In the search for exoEarth candidates with LUVOIR, we will undoubtedly detect a multitude of brighter planets. According to Stark et al. (2014), for an 8-m size telescope, the number of exoEarth candidates detected is ~ 20 (see Figure 4 in Stark et al. 2014), although this is strongly dependent on the value of η_{Earth} . At the same time, the number of stars observed to detect these exo-Earth candidates is ~ 500 . If we assume that, on an average, every star has a planet of some size (Cassan et al. 2012; Suzuki et al. 2016), then there are ~ 500 exoplanets of all sizes that can be observed. Not considering the ~ 20 exoEarth candidates, the bulk of the exoplanets will fall into “non-Earth” classification, without any distinguishing features between them. This provides a motivation to devise a scheme based on planetary size and corresponding comparative atmospheric characteristics of exoplanets.

With some exceptions of Venus-type exoplanets (Kane et al. 2012), there has not been an overarching way to classify planets beyond the habitable zone (HZ). Classifying different size planets based on the transition/condensation of different species at different stellar fluxes (i.e. orbital distances) provides a physical motivation in estimating exoplanet mission yields, separate from exoEarth candidate yields (**Figure A-29**).

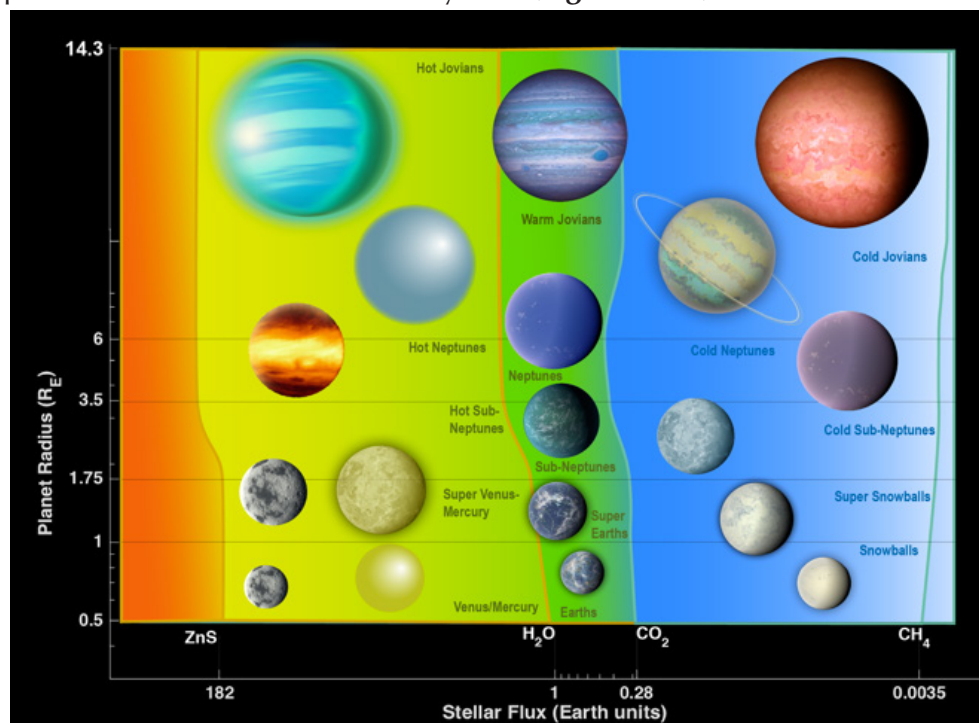


Figure A-29. The boundaries of the boxes represent where different chemical species are condensing in the atmosphere of a planet at a stellar flux, according to equilibrium chemistry calculations Credit: Kopparapu et al. (2018)

Program at a Glance

Science goal: Measure atmospheric composition for a wide range of exoplanets with different sizes, orbits, and host stars.

Program details: IFS optical and near-IR spectra of a) all planets in the field during long integrations on stars with habitable zone planet candidates and b) a selected set of known planets around other stars.

Instrument(s) + Configuration: ECLIPS high-contrast, point-source spectroscopy

Key observation requirements: Spectral bandpass from 200 nm to 2000 nm, $R \sim 100$, Continuum SNR > 10

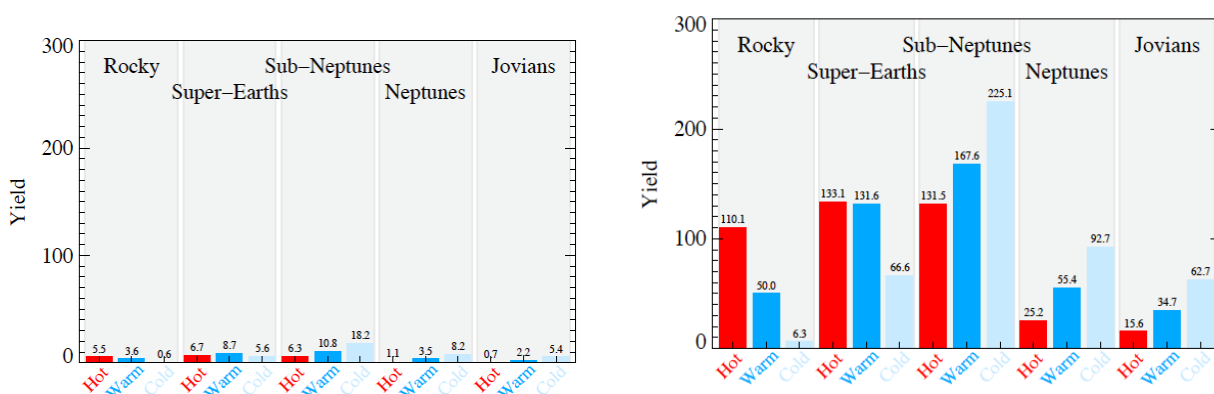


Figure A-30. Expected number of exoplanets observed for hot (red), warm (blue) and cold (ice-blue) incident stellar fluxes shown in **Figure A-11**. The left panel is for a telescope size of 4-m and the right is for 15-m.

A.18.2 The role of LUVUOIR

The histogram plot (**Figure A-30**) visualizes the total scientific impact of the habitable planet candidate survey, along with the several other classes of exoplanets, based on different telescope diameter. The y-axis gives the expected total numbers of exoplanets observed (yields), which are also given by the numbers above the bars. It is at the LUVUOIR-type telescope sizes (~9-m and 15-m size) that one can truly see the diversity in exoplanet yields, and further characterize different classes of planets. We note that in general, larger apertures are less sensitive to changes in mission parameters than smaller apertures.

A.18.3 The science program

With a 4-m class mission, observations that are designed to maximize the yield of potential Earths will also yield the detection and characterization of all of the planet types discussed here, with the exception of hot Jupiters. Hot Jupiters are not observed by a 4-m class mission because of the tight inner working angle, and because of the low abundances of hot Jupiters.

A 15-m telescope will bring the ability to not only observe planets, but to test the occurrence of different features within each of the planet types. It would observe dozens of each planet type, providing larger sample sizes which enables to study each planet type as a population.

References

- Kane, S. R., Kopparapu, R. K., Domagal-Goldman, S. 2014, *ApJ*, 794, L5
Kopparapu, R. K., Hebrard, E., Belikov, R., et al. (2018) *ApJ*, 856, 2
Stark, C. C., Roberge, A., Mandell, A., Robinson, T. D. et al. 2014, *ApJ*, 795, 122
Stark, C. C. et al. 2015, *ApJ*, 808, 149

A.19 Detecting exomoons with LUVVOIR

Eric Agol (University of Washington, NASA Astrobiology Virtual Planetary Laboratory), Tiffany Jansen (Columbia University), Brianna Lacy (Princeton University), Tyler D. Robinson (Northern Arizona University), Victoria Meadows (University of Washington, NASA Astrobiology Virtual Planetary Laboratory)

A.19.1 Introduction

The detection of exomoons has proven elusive, and is becoming an increasingly prominent goal of exoplanet studies. LUVVOIR can open the possibility of the detection of exomoons in the habitable zones of main sequence stars via spectroastrometry: the astrometric shift versus wavelength that occurs between wavelengths with flux dominated by the exoplanet vs. wavelengths dominated by the exomoon. The several requirements to reach this goal are: 1) a large telescope aperture; 2) astrometric calibration and stability; 3) ability to measure the centroid of the planet's light simultaneously over a broad range of wavelengths; 4) ability to revisit the planet many times; and 4) extension to near-IR wavelengths. In addition to enabling the detection of exomoons, this technique may allow for the characterization of the planet via the orbit of the exomoon.

The Moon has likely played a critical role in the evolution of planet Earth, from influencing the geological and chemical composition (Smith 1977; Canup 2012), to modifying the mass and angular momentum of the Earth/Moon system (Canup & Asphaug 2001), to possibly stabilizing the obliquity of the Earth (Laskar et al. 1993). Lunar tides may have played an outsized role in influencing the evolution of life on Earth (Balbus 2014). Speculation that habitable exomoons could orbit giant planets makes an intriguing alternate niche for life (Williams et al. 1997; Kaltenegger 2010). Caveats exist for each of these scenarios (Lissauer et al. 2012; Heller et al. 2014; Lammer et al. 2014), so a search for exomoons is necessary to ascertain the importance of moons on planetary physics and biology.

There are a range of proposed techniques for detection of exomoons, from transiting planet observations (Cabrera & Schneider 2007; Kipping 2009), to phase function measurements in direct imaging (Moskovitz et al. 2009; Robinson 2011). Each of these techniques has drawbacks: transiting exomoons may be swamped by stellar variability, while phase variations may be mimicked by variations in planetary atmospheres.

We recently proposed a new approach for the detection of exomoon surveys that could result in an instantaneous detection of an exomoon, and would allow for measurements of the exoplanet-moon system: spectroastrometry (Agol et al. 2015). This technique relies on the observation that a moon can outshine a planet at wavelengths where the planet is non-reflective, i.e. in strong molecular absorption bands (Williams & Knacke 2004; Moskovitz et al. 2009). The Earth is outshined by the Moon at $\approx 2.7\mu\text{m}$, and the Earth would outshine a companion Jovian planet in several methane bands between $0.9\text{--}2.7\mu\text{m}$ (**Figure A-31**). The technique is summarized in **Figure A-32**, which schematically shows how the centroid of the PSF may vary with between wavelengths dominated by the planet versus wavelengths dominated by the moon.

The detection technique proceeds by simultaneous measurement of the centroid as a function of wavelength. The wavelengths at which the planet is dim would have a stronger contribution from the moon, and thus cause a shift of the centroid towards the position of

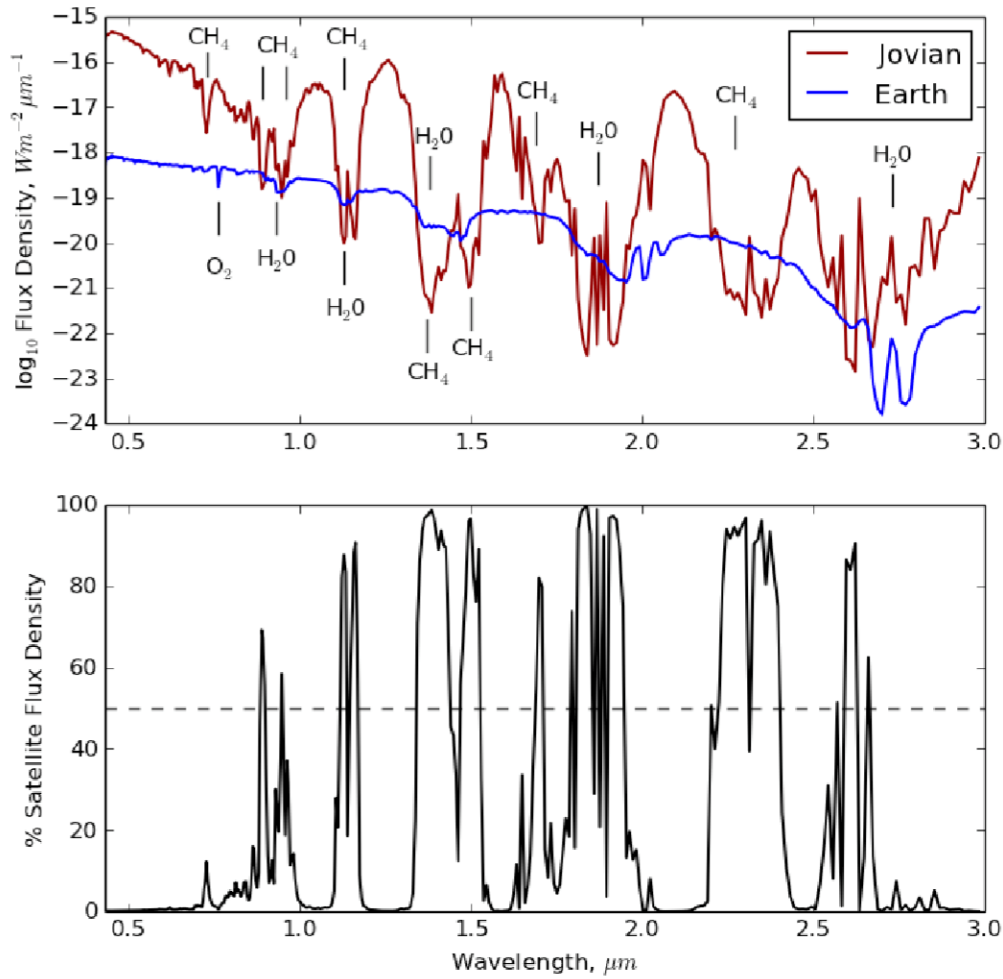


Figure A-31. The flux of the Earth-like moon and the warm Jupiter at quadrature phase angle as a function of wavelength in microns (top) and the contribution of flux due to the moon shown as a fraction of the total flux (bottom). The maximum fraction of the moon's flux for the Jovian-Earth system occurs at $\lambda = 1.83 \mu\text{m}$, contributing 99.1% to the total flux.

the moon. Thus, even if the moon and planet are not resolved, the moon may still be detected via the spectroastrometric signal.

The astrometric signal, which is proportional to the angular separation of the planet and moon, scales as r/d , where r is the separation of the moon and planet on the sky, and d is the distance to the system. The astrometric noise scales as $(\lambda/D)(d/D)$, as the PSF width scales as λ/D , while the precision of the measurement of the centroid scales as d/D , where D is the diameter of the telescope. Thus, the signal-to-noise scales as $r(D/d^2)/\lambda$, and so the ability to search a large volume V for exomoons within the nearby galaxy scales as $V \propto d^3 \propto D^3$. To increase the odds of a successful search, then, *requires the largest diameter telescope possible*.

This relation assumes that the Poisson-noise limit applies, and thus also requires: 1) high-contrast to avoid additional contribution to the noise from scattered light; 2) precise control of the PSF, the astrometric pointing, and the relative astrometric precision between wavelengths. Ideally, this approach will be made more efficient with simultaneous astrometric measurements at a range of wavelengths, which might be accomplished with an IFU or

Spectroastrometric detection of exomoons

(Agol, Jansen, Lacy, Robinson & Meadows 2015)

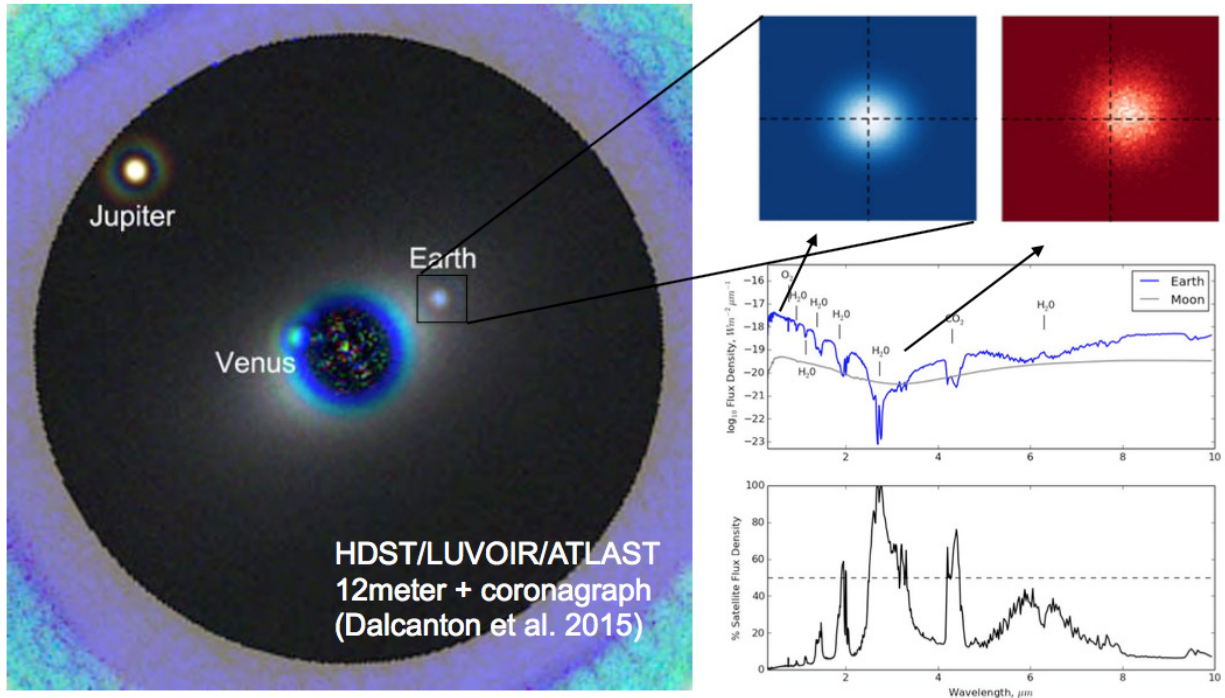


Figure A-32. Diagram indicating spectroastrometric signal.

an MKID device. One advantage of this technique is that only the *relative* position needs to be measured as a function of wavelength, not the absolute position. Another advantage is that the signal will vary with time as the moon orbits the planet, which makes it reproducible and difficult to confound with other systematic errors or sources of noise. This makes this technique more powerful than other proposed techniques for detecting exomoons, which may require observation at specific times or geometries (such as transit of the moon in front of the star, or transit of the moon in front of the planet), or may not have repeatability of the observation, such as microlensing (Han & Han 2002). Spectroastrometry may also allow for the measurement of the mass of the planet+moon with Kepler's law, as well as a disentangling of the moon/planet spectrum (Agol et al. 2015).

A.19.2 The role of LUV0IR

Spectroastrometry of habitable-zone (HZ) Earths will not be feasible from ground-based telescopes as these may only probe the HZ of late time M dwarf stars, for which the planets are close enough that they will likely not harbor stable exomoons. A space telescope is required to achieve high contrast (10^{-11} – 10^{-10}) to enable the detection of an exomoon, to avoid interference of the atmosphere with spectral features that show the sharpest variation in the spectroastrometric signal, to allow for repeated visits and long exposures, and to achieve stability of the PSF.

Table A-3. The moon and planetary parameters used in our model, where D_{tele} is the telescope diameter, d is the distance from the observer, t_{obs} is the duration of exposure, ϵ is the telescope efficiency factor.

System	Moon radius (m)	Planet radius (m)	Planet-moon separation (m)	Orbital period (d)	D_{tele} (m)	d (pc)	t_{obs}	ϵ	Semi-major axis (AU)
Earth-Moon	1.738×10^6	6.371×10^6	3.844×10^8	27.32	12	1.34	24	0.2	1.23
Jovian-Earth	6.371×10^6	6.991×10^7	3.064×10^9	34.60	12	10	24	0.2	1

A large telescope will be necessary due to the strong scaling of the astrometric signal-to-noise with telescope aperture ($\propto D^2$), which will allow the search for this signal for a larger number of stars. The larger aperture allows for a sharper PSF and a larger number of photons, both of which improve the astrometric precision and allow for resolving out surface brightness due to (exo-)zodi and speckles.

Relative astrometric precision between bands of ≈ 0.1 mas should be sufficient for the expected ≈ 1 mas shift for the two cases examined here. For the Earth-Moon at Alpha Centauri example, near-infrared coverage to > 1.5 micron will be required, while coverage to 2.7 micron would be preferred to obtain a strong Moon/Earth flux ratio. For the Earth-Jupiter case, coverage to 1 micron should allow for detection, while 2 micron will give a stronger Earth/Jupiter flux ratio. A broad range of wavelengths will need to be imaged simultaneously, which an IFU or MKID detector may allow for. The inner working angle and field of view may accommodate searches closer or further from stars, while for the two examples we explored we just examined the HZ, which is well covered by current LUVOIR specifications. A detailed technical and science case for spectroastrometry will require more realistic simulations.

A.19.3 The science program

It is impossible to forecast the properties of an ensemble of planet-moon systems, and so in lieu of this, here are two case-studies that could drive technical requirements of LUVOIR: 1) an Earth-Moon twin orbiting Alpha Centauri A (1.34 pc); 2) an Earth-Jovian pair orbiting a G2V star at 10 pc with a separation of 30% of the Hill sphere. **Table A-3** gives the properties

Program at a Glance

Science goal: Detection of moons orbiting exoplanets

Program details: Precisely measure the positions of directly imaged exoplanets at different wavelengths and times to look for photocenter shifts (spectroastrometry).

Instrument(s) + configuration(s): ECLIPS IFS spectral imaging

Key observation requirements: Contrast $> 10^{-9}$ for Jupiter orbited by Earth-like moon, Contrast $> 10^{-11}$ for Earth orbited by Moon; NIR wavelengths ($> 1.0 \mu\text{m}$ for Earth-Jupiter case, $> 1.5 \mu\text{m}$ for Earth-Moon case); Relative astrometric precision between wavelength bands of ≈ 0.1 mas.

of these two systems. One could imagine, of course, a broader range of possibilities with the Solar System as building blocks, e.g., a Mars-sized moon orbiting a Neptune-sized ice giant. However, our two case studies in some sense bracket a range of possibilities, although a true Jovian- satellite analog system would probably be challenging to detect with this technique. Spectroastrometry might also be used to search for rings of planets since Saturn is dark in methane bands, while its ring system is still reflective. The pattern of illumination of the rings will impart a centroid offset relative to the centroid of Saturn.

The Moon-Earth analog centroid offset is ≈ 0.4 mas at $1.4 \mu\text{m}$, 0.9 mas at $1.9 \mu\text{m}$, and 2 mas at $2.7 \mu\text{m}$. Thus, near-infrared capability is required to apply this technique to an Earth-Moon analog system. *Relative astrometric stability between wavebands at better than $80 \mu\text{as}$ would be required to make a detection exceeding $5\text{--}\sigma$.* The planet-star contrast at these wavelengths is $\approx 10^{-11}$, and so is going to be affected significantly by speckles if a contrast of 10^{-10} is achieved. *Thus, pushing towards a contrast of 10^{-11} may be necessary for detection of a Moon-like exomoon.*

The Earth-Jupiter analog (with Jupiter moved into 1 AU) has a centroid offset of 1.3 mas at $0.86 \mu\text{m}$. A 12- meter telescope with $R = 80$ could detect this offset at $S/N = 13$ with a 24-hour exposure, assuming the Poisson-noise limit. The planet/star contrast at this wavelength is $\approx 10^{-9}$, and so will not be as affected by speckles for a telescope design that approaches 10^{-10} contrast.

Our investigation has the drawback that we neglected exozodiacal light and speckles, as well as other sources of instrumental noise, so further work to create realistic simulations is needed to estimate the impact of these on the spectroastrometric signal.

References

- Agol, E., Jansen, T., Lacy, B., Robinson, T. D., & Meadows, V. 2015, *ApJ*, 812, 5
- Balbus, S. A. 2014, Proceedings of the Royal Society A: Mathematical, Physical and Engineering Sciences, 470, 20140263
- Cabrera, J., & Schneider, J. 2007, *Astronomy and Astrophysics*, 464, 1133
- Canup, R. M. 2012, *Science*, 338, 1052
- Canup, R. M., & Asphaug, E. 2001, *Nature*, 412, 708
- Han, C., & Han, W. 2002, *ApJ*, 580, 490
- Heller, R., Williams, D., Kipping, D., et al. 2014, *Astrobiology*, 14, 798
- Kaltenegger, L. 2010, *ApJ*, 712, L125
- Kipping, D. M. 2009, *Monthly Notices of the Royal Astronomical Society*, 392, 181
- Lammer, H., Schiefer, S.-C., Juvan, I., et al. 2014, *Origins of Life and Evolution of Biospheres*, 44, 239
- Laskar, J., Joutel, F., & Robutel, P. 1993, *Nature*, 361, 615
- Lissauer, J. J., Barnes, J. W., & Chambers, J. E. 2012, *Icarus*, 217, 77
- Moskovitz, N. A., Gaidos, E., & Williams, D. M. 2009, *Astrobiology*, 9, 269
- Robinson, T. D. 2011, *ApJ*, 741, 51
- Smith, J. V. 1977, in Lunar and Planetary Science Conference Proceedings, Vol. 8, Lunar and Planetary Science Conference Proceedings, ed. R. B. Merrill, 333–369
- Williams, D., & Knacke, R. 2004, *Astrobiology*, 4, 400
- Williams, D. M., Kasting, J. F., & Wade, R. A. 1997, *Nature*, 385, 234

A.20 The transmission spectra of rock atmospheres on magma worlds

Eric Lopez (NASA GSFC) and Avi Mandell (NASA GSFC)

A.20.1 Introduction

One of the most exciting revelations from planetary transit surveys has been the discovery of a new population of extremely irradiated rocky planets on ultra-short-period (USP) orbits (e.g., Charbonneau et al. 2009; Léger et al. 2009; Batalha et al. 2010; Sanchis-Ojeda et al. 2014). The irradiation on these planets is so intense, with dayside temperatures reaching over 2500 K, that they are expected to have dayside surfaces that are partially or completely molten (Kite et al. 2017). Although completely uninhabitable, these planets have the potential to teach us a great deal about geophysical processes under extreme conditions. Indeed, models predict that these planets should partially vaporize their rocky mantles and outgas significant but highly refractory atmospheres dominated by silicates and heavy metals, potentially allowing us to directly probe the bulk mantle compositions (Miguel et al. 2011). Moreover, models also predict that alkali metals in this outgassed material may be escaping at significant rates, producing highly extended metallic exospheres possibly reaching all the way to the Roche lobe (Kite et al. 2017). However, these exospheres would be highly time-variable driving the need to obtain higher S/N over a single transit. Indeed, recently there was a claimed detection of significant thermal variability in the dayside emission from the USP 55 Cancri e (Demory et al. 2016) along with the possible detection of highly extended exospheric Na and Ca⁺ absorption (Ridden-Harper et al. 2016).

Given their short periods and extremely high temperatures, JWST is extremely well suited to characterizing the overall thermal emission from these planets (Samuel et al. 2014) and to detect emission from SiO at 4 and 10 microns (Ito et al. 2015). However, due to its wavelength coverage JWST will be limited in its ability to characterize the atmospheric compositions of USP planets with transmission or emission spectroscopy since many of the primary lines for the relevant metal species aside from SiO are found in the optical and near UV between 300 and 800 nm (e.g., Na, K, Ca, Mg, Fe, TiO, VO), and therefore are inaccessible with JWST. At the same time, the intrinsic rarity of these USP planets means that even after the NASA's TESS mission concludes, most of the known USPs will be around relatively faint FGK stars (V-mag >11), making them difficult to characterize with HST due to its smaller aperture.

A.20.2 The role of LUVOIR

With its combination of large aperture and broad UV and optical wavelength coverage, LUVOIR using will be uniquely suited to probe the compositions of vaporized atmospheres on USP planets. Between 300 and 800 nm, a range covered by the UVIS

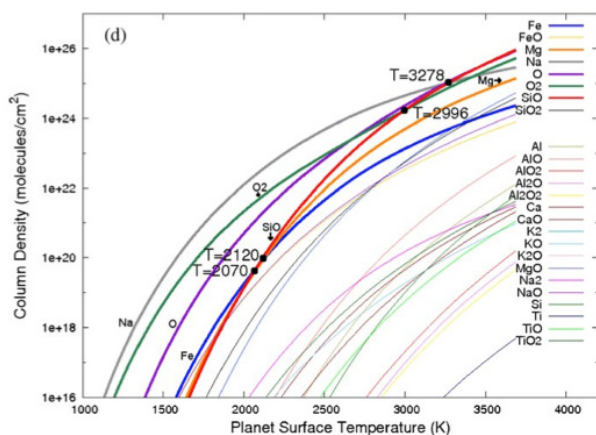


Figure A-33. Predicted compositions of out-gassed atmospheres for a Bulk Silicate Earth composition from Miguel et al. (2011), black points show transitions where the dominant species changes.

Program at a Glance

Science goal: Characterizing the compositions of vaporized silicate and metal atmospheres from extremely hot molten rocky planets.

Program details: ~250 hours for multi-wavelength and multi-epoch NUV and optical transmission and emission spectroscopy for the best ~5 ultra-short-period exoplanets.

Instrument(s) + configuration(s): HDI UVIS spectroscopy

Key observation requirements: 300–800 nm; $R=500$; ultra-high precision spectroscopy of bright sources (photometric uncertainty ~ 2–7 ppm)

channel on HDI, are a series major spectral features for the key metal species predicted by outgassing models. In particular, features like sodium D at 590 nm, calcium H & K at 390 nm, potassium at 770nm, and the TiO from 600 to 800 nm, should all be detectable in either transmission or emission spectroscopy along with a wide range of iron and magnesium lines between 300 and 600 nm. For example, modeling the emission spectra of several known USPs, Ito et al. (2015) predicted that both the 590 nm Na and 770 nm K features should be observable with moderate spectral resolution ($R\sim 500$) in emission at ~9 ppm for a 2500 K USP planet and ~36 ppm for a 3000 K planet.

Additionally, if these planets do intend possess extended exospheres then these should be detectable in transmission at S/N in single transit, which is important given the expected variability in both the planetary atmospheric escape rates and the stellar spectrum. The possible detection of exospheric Na & Ca+ on 55 Cancri e by Ridden-Harper et al. (2016) claimed a 7% transit in the 590 nm sodium line extending all the way to the planet's Roche lobe at ~5 Earth radii.

Given the extremely short orbital periods, typical transit durations are just 1.5–2 hours, however with the 15-m LUVUOIR Architecture A should be able to reach a precision of ~16 ppm at a $R\sim 500$ for a 12th magnitude G-star at ~150 pc in a single 1.5-hour integration. This will allow the detection of any exospheric metals at high S/N in single transit, while for planet with dayside temperature of 3000 K, sodium should be detectable in emission from the lower atmosphere at $\sim 5\sigma$ with just 5 transits or ~10 hours of integration.

A.20.3 The science program

Given the relatively short integration times needed, it should be possible to obtain multi-epoch observations for multiple spectral features on multiple exoplanets, especially in transmission. Currently there are already five well-studied USP planets (55 Cancri e, CoRoT-7b, Kepler-10b, Kepler-78b, and K2-141b), which would be well suited to these observations, with the likelihood that at least a few more will be found by upcoming surveys like TESS and PLATO. With just ~50 hours per planet it will be possible to obtain ~10 transits and 5–20 eclipses per planet, which will allow us to search for extended exospheres in multiple species, including all the common alkalis, characterize those species in emission close to the planet's surface, and study their time variability.

References

- Charbonneau, D., Berta, Z. K., Irwin, J., et al. 2009, *Nature*, 462, 891
- Léger, A., Rouan, D., Schneider, J., et al., 2009, *A&A*, 506, 287
- Batalha, N.M., Borucki, W.J., Bryson, S.T., et al. 2011, *ApJ*, 729, 27
- Miguel, Y., Kaltenegger, L., Fegley, B., & Scafer, L., 2011, *ApJ*, 742, 19
- Sanchis-Ojeda, R., Rappaport, S., Winn, J., N., et al., 2014, *ApJ*, 787, 47
- Samuel, B., Leconte, J., Rouan, D., et al. 2014, *A&A*, 563, 103
- Ito, Y., Ikoma, M., Kawahara, H., et al., 2015, *ApJ*, 801, 144
- Demory, B., Gillon, M., Madhusudhan, N., & Queloz, D., 2016, *MNRAS*, 455, 2018
- Kite, E. S., Fegley, B., Schaefer, L., & Gaidos, E., 2016, *ApJ*, 828, 80
- Ridden-Harper, A.R., Snellen, I.A.G., Keller, C.U., et al., 2016, *A&A*, 593, 129

A.21 Spatially resolved maps of star-forming gas with LUV0IR

John M. O'Meara (Saint Michael's College)

A.21.1 Introduction

Strong HI absorption, specifically the Damped Lyman alpha systems, have been used for decades to study the bulk of the neutral gas in the universe (Wolfe et al. 2005), and thus the reservoirs for star formation. Large samples of DLA now exist (e.g., Noterdaeme et al. 2012) and the metallicity for the DLA has been obtained for hundreds of systems (Rafelski et al. 2012). Despite their long history of study, the size of the DLA at high- z has gone largely unconstrained, as they are observed toward very small emitters on the sky (e.g., quasars or GRBs). If instead *spatially extended* objects such as galaxies are used as a background source, it would allow for a direct study of the spatial extent of any foreground intervening DLA gas, along with a map of its variation in metallicity. This methodology can be applied to higher HI column density Lyman limit systems as well, provided their Lyman alpha line alone is sufficient to determine $N(\text{HI})$.

Figure A-34 demonstrates this idea showing variable absorption towards a strong gravitationally lensed galaxy at $z \sim 2.8$ (O'Meara et al. 2018, in prep) with KCWI on Keck. Gravitationally lensed galaxies are unfortunately rare, limiting our ability to apply this technique en masse and to compare the results statistically to simulations. Furthermore, ground based observations of the DLA are limited to $z > 1.6$, excluding the majority of the history of the universe, and with it much of the transition of galaxies from star-forming to passive,

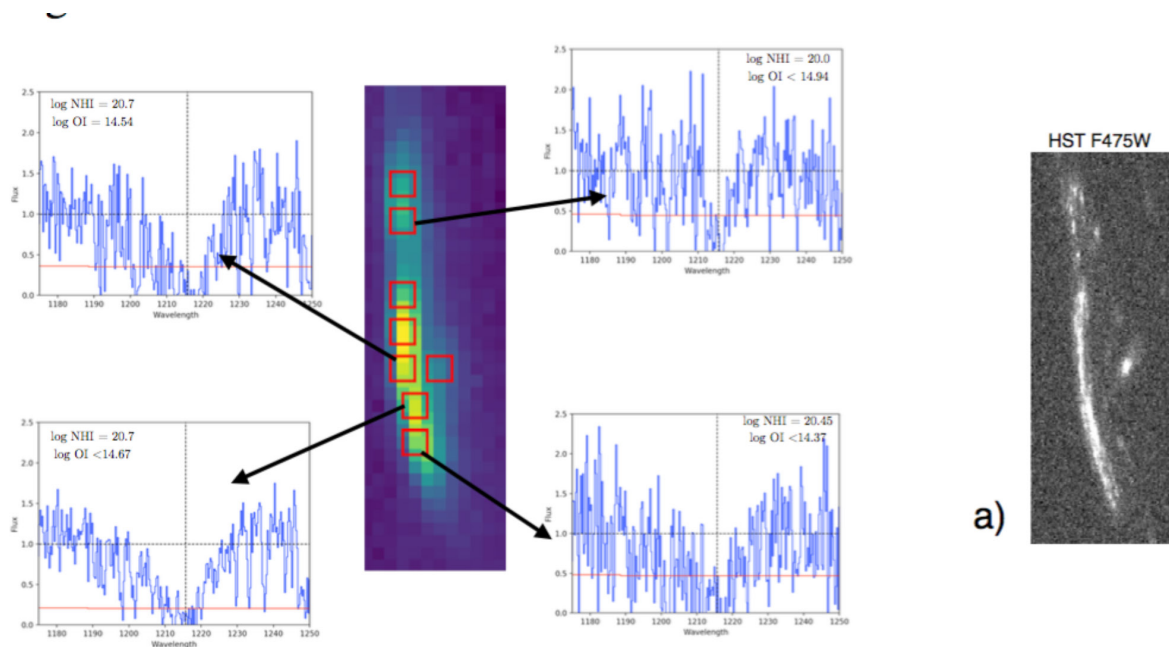


Figure A-34. Keck KCWI spectra of a $z \sim 2.8$ lensed galaxy. Spectra from multiple positions along the galaxy show variations in HI column density in an intervening $z \sim 2.5$ DLA. Metal lines are also observed for this system, allowing for constraints to be made on variations in gas metallicity on kpc scales, similar to scales in cosmological simulations.

Program at a Glance

Science goal: Spatially resolved maps of HI and metals in star-forming gas at $0 < z < 2$

Program details: LUMOS observations of $z < 2$ galaxies with intervening HI and metal absorption. Multiple LUMOS MOS shutters across each galaxy provide the spatial sampling.

Instrument(s) + configuration(s): LUMOS G120, G150, G180, G300M

Key observation requirements: S/N > 10 per spectrum. Wavelength coverage of HI Lyman-alpha and key metallicity tracers (OI, CII, SIII) all in the rest frame FUV.

an epoch where a detailed understanding of the “where and when” of star-forming gas is critical.

A.21.2 The role of LUVOIR

LUVOIR provides two essential opportunities: First, the UV capabilities of LUMOS allow for the technique to be applied for HI Lyman alpha anywhere from $0 < z < 2.2$, essentially the last 11 billion years of cosmic history. At lower redshifts, the extent on the sky of the background galaxy increases, facilitating finer and finer spatial sampling. Second, LUVOIR’s immense aperture allows for the technique to be applied to the more general population of galaxies. As a result, instead of relying on very rare gravitational lens scenarios, galaxies at FUV magnitudes of 20 (for LUMOS high resolution modes) or 23 (for low resolution modes still capable of detecting HI and metal absorption) are reachable in ~1 hr integration time.

A.21.3 The science program

LUMOS shutters will be placed across $z < 2$ galaxies (identified either through ground based spectra or photometry), ideally in the M modes for higher resolution (FUV mag 20.5 or brighter). Selection of G120M, G150M, G180M, G300M will depend on the redshift of the intervening absorption, and will be made to cover HI Ly-a, along with key metal line diagnostics such as OI, SIII, and CII. Sources can be as faint as FUV mag 23, if the G145LL mode is employed. Observations will reach S/N = 10 or greater, which is possible for all M gratings for sources FUV mag 20.5 or brighter.

Each LUMOS micro-shutter spectrum will be analyzed for intervening HI and metal line absorption, and a spatial map of HI and metallicity variations will be made for each absorber.

Follow-up observations with either LUMOS or HDI may be warranted to observe the galaxies associated with the HI gas.

References

- Wolfe, A. M. et al. 2005, *ARA&A*, 43, 861W
 Noterdaeme, P. et al. 2012, *A&A*, 547L
 Rafelski, M. et al. 2012, *ApJ*, 755, 89
 O’Meara, J. M. et al. 2018, in prep.

A.22 Protostellar outflows/jets

Christian Schneider (Hamburger Sternwarte) & Gregory Herczeg (Kavli Institute for Astronomy and Astrophysics)

A.22.1 Introduction

Stars grow by accreting matter from their surrounding protoplanetary disk, which requires the efficient redistribution of angular momentum—a process still highly uncertain. Simulations of disks with non-ideal magneto-hydrodynamics suggest a magnetically-driven disk wind may extract angular momentum from the disk, thereby leading to accretion (see Illustration below, review by Hartmann et al. 2016 and Bai & Stone 2013). The accretion onto the star is readily observed (e.g. Balmer jump, H-alpha emission), but observational constraints on the physics of mass transport, with implications for planet growth and migration as well as the dispersal of the natal envelope, need new instrumentation.

A.22.2 The role of LUV0IR

By the time of LUV0IR, sophisticated simulations of protoplanetary disks will exist, which will require observational tests of angular momentum transport from the mass loss rates and wind velocities in the inner au around the central star. Current observations of disk winds are limited to unresolved line emission or line-of-sight absorption, with large uncertainties (e.g., Edwards et al. 2006; Rigliaco et al. 2013). Similar observational challenges limit the interpretation of possible jet rotation signatures (Bacciotti et al. 2002, Coffey et al. 2012) and jet collimation shocks (Schneider et al. 2013). Currently, the major instrumental limitations are a lack of spatial resolution compared with insufficient sensitivity, e.g., the FUV emission

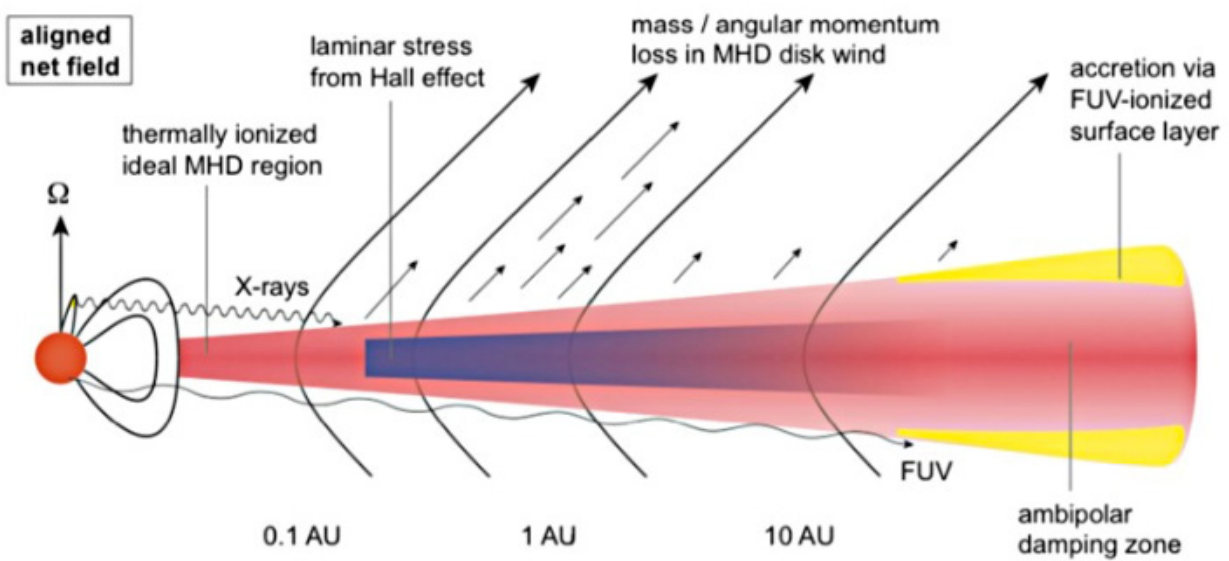


Figure A-35. Sketch of a protoplanetary disk and angular momentum transport mechanisms. Credit: Simon et al. 2015, MNRAS 454.

lines require several orbits with HST for a single long-slit spectrum and several slit positions are required to sufficiently sample the spatial structure of the jet. LUVOIR will overcome these issues and is needed even in the era of ALMA, JWST or 30-m telescopes as none of these is capable of imaging the primary disk wind tracers or accretion flows close to the star nor covers diagnostics of the relevant temperature regime. The primary disk wind diagnostics are at UV to optical wavelengths, where high spectral and spatial resolution (preferably with an IFU) are not feasible, even with AO systems. Further, disk images in FUV CO and H₂ emission will reveal accretion flows within the disk and onto the star or protoplanets in exquisite detail inaccessible by ground-based instruments.

A.22.3 The science program

Measure the launching and mass flux in disk winds. The launching of MHD winds from the disk may drive the accretion flow. Disk winds are thought to be launched from a range of radii resulting in streamlines with different velocities and temperatures. Therefore, a large repertoire of diagnostics is needed to sample the total mass flux. Measuring the mass flux and velocity for objects of different evolutionary stages and stellar masses will allow us to derive the angular momentum extracted by the disk wind. This mass loss combined with accurate accretion rates will provide rigorous tests of models for wind launching and to understand energy, mass, and angular momentum transport by jets and accretion.

Measure jet collimation and rotation properties. Jets are collimated by a magnetic field anchored in the protoplanetary disk. Depending on the anchor/launch point in the disk, different streamlines possess different collimation properties. Sampling collimation properties and jet rotation for different outflow components is needed to study jet launching, envelope dispersal, and the disk's magnetic field.

Measure the mass flows in the inner disk. ALMA and scattered light observations revealed that disks have large radial dust traps and azimuthal asymmetries likely induced by disk physics, chemistry, or planet-disk interactions. While the disk should be Keplerian, recent ALMA observations suggest that radial mass flows exist, too. At the highest spatial resolution, LUVOIR will be able to reveal any non-Keplerian flows in the inner au and onto protoplanets forming in the disk.

Description of Observations

To measure mass flux rates, we need to sample relevant temperature regimes. Important emission lines include H₂, [O I], [S II], [N II], [O III], Balmer, and C IV lines with fluxes in the range of 10^{-14} erg/s/cm⁻² or above for the nearby objects and contrast ratios of ~1:100 at 0.1 arcsec from the star. Typical outflow velocities range from a few 10 to several 100 km/s.

With LUMOS, one can efficiently measure the collimation and rotation signatures of the jet close to the launching region on scales of ~10 au (~100 mas, nearby star forming (SF) region) with high spectral resolution to trace different flow components using the micro-shutter array. Roughly speaking, the flow velocity close to the jet base relates to the launching radius. Sampling the collimation properties in several velocity channels in the range from <10 km/s up to several 100 km/s will be critical for this. With expected rotation signatures in the km/s range at scales of 0.1 arcsec (nearby SF region), LUMOS is ideally suited to perform high S/N, high spectral resolution ($R > 10,000$) observations. Also, the region of interest,

Program at a Glance

Science goal: Understand mass-flows around forming stars

Program details: Spatially and spectrally resolved observations of young stellar objects, forming planets, and protostellar jets

Instrument(s) + configuration(s): LUMOS high spectral-resolution spatially resolved spectroscopy, other instruments?

Key observation requirements: $R > 10,000$, spatial resolution better than 0.1 arcsec, contrast of 100:1 at 0.1 arcsec.

a few 100 au translating to an apparent size of a few arcsec for the nearby star formation regions, is ideally matched to the LUMOS FOV.

References

- Bacciotti et al. 2002, *ApJ*, 576, 222
Bai & Stone 2013, *ApJ*, 169, 76
Coffey et al. 2012, *ApJ*, 749, 139
Edwards et al. 2006, *ApJ*, 646, 319
Hartmann, Herczeg, & Calvet 2016, Annual Reviews, 54
Rigliaco et al. 2013, *ApJ*, 772, 60
Schneider et al. 2013, *A&A*, 550, 1

A.23 The quiescent UV spectra of cool dwarf stars

Allison Youngblood (NPP / NASA GSFC)

A.23.1 Introduction

The UV spectra of cool dwarf stars (F, G, K, & M) are dominated by emission lines originating from the magnetically heated upper layers of the stellar atmosphere (**Figure A-36**); <10% of their photospheric/blackbody continuum is emitted in the UV ($\lambda < 3000$ K). Chromospheric, transition region, and coronal emission lines from species like H I, Mg II, C IV, Si IV, and N V are ultimately powered by the star's magnetic dynamo, which also controls the rotational evolution of these stars via magnetized stellar winds (Skumanich 1972). UV emission line fluxes and widths can diagnose temperature, pressure, density, and kinematics throughout the stellar atmosphere, even indicating H₂ fluorescence from the star's own UV photons (e.g., Kruczek et al. 2017, Jaeggli et al. 2018). When obtained for a wide range of masses and ages, UV spectra can elucidate the evolutionary processes of cool stars (e.g., Guinan et al. 2003).

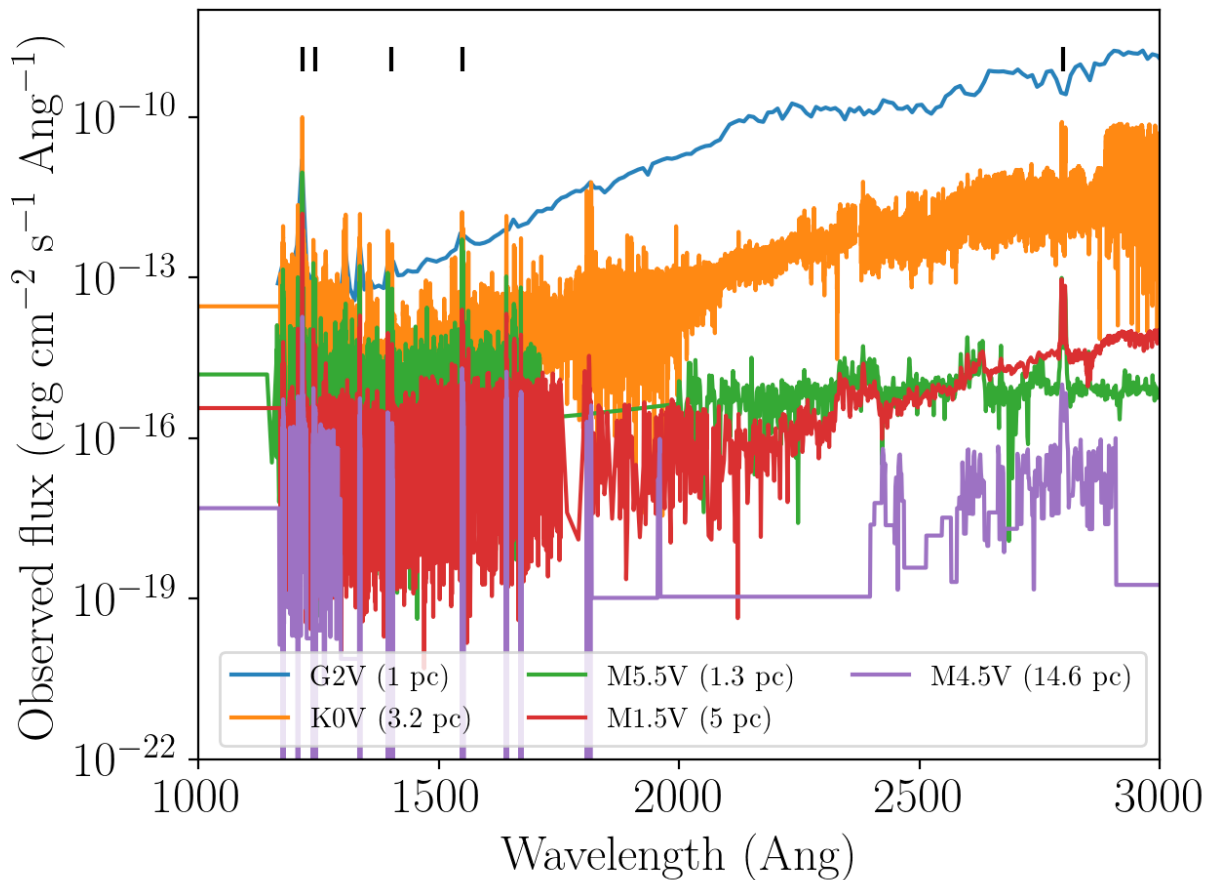


Figure A-36. The UV spectrum from 1000–3000 Å for a sample of cool dwarfs observed with Hubble and Solar Mesosphere Explorer. Lyman alpha, N V, Si IV, C IV, and Mg II are labeled with tick marks

Program at a Glance

Science goal: Characterizing the quiescent UV spectra of cool dwarf stars (F, G, K, and M dwarfs) to better understand the physical conditions in their atmospheres and how they evolve in time.

Program details: F, G, K, and M dwarfs covering a wide parameter space of mass and age should be targeted.

Instrument(s) + configuration(s): LUMOS spectroscopy.

Key observation requirements: 1000–3000 Å, $R=30,000$, $S/N > 10$.

Of special note is H I Lyman alpha (1215.67 Å), the brightest emission line in the FUV and NUV spectrum of a cool dwarf. A complete UV characterization of these stars cannot be obtained without it, but Lyman alpha observations are challenging. The Earth's extended atmosphere glows brightly in Lyman alpha, and interstellar H I attenuates the entire line core for even the closest stars. The core of the Lyman alpha line must be reconstructed from the observed line wings (e.g., Youngblood et al. 2016), which can prove difficult for faint targets.

A.23.2 The role of LUVUOIR

LUVUOIR's LUMOS instrument will have a sensitivity two orders of magnitude better than HST's STIS, enabling measurements of the chromospheric heating rate for even the most seemingly inactive cool stars (e.g., older M dwarfs; Guinan et al. 2016). LUMOS will provide access to more emission lines with a wider range of formation temperatures (probing from the lower chromosphere to the corona) not only because of its increased sensitivity but also its increased spectral range compared to STIS and COS (e.g., sensitive access to 1000–1200 Å). Its microshutter array can also create a long slit, which is essential for spatially separating the stellar Lyman alpha emission from the bright geocoronal Lyman alpha emission, and the sensitivity should be great enough to measure continuum emission.

A.23.3 The science program

To obtain a 1000 Å – 3000 Å spectrum of a cool dwarf, a combination of at least 2 gratings must be employed. Using the medium resolution gratings ($R \sim 30,000$) throughout will resolve line multiplets (e.g., C II, O IV) and the line widths themselves. Two lower resolution gratings ($R \sim 8,000$ and 500) are also suitable alternatives for fainter targets.

After 5 hours of integration (representative of the integration time for the K and M dwarfs of HST's MUSCLES Treasury Survey; France et al. 2016), $S/N = 10$ for the faintest emission lines of an early M dwarf's FUV spectrum will be achieved for stars down to $FUV_{GALEX} = 23$ mag (9-m LUVUOIR) or $FUV_{GALEX} = 25$ mag (15-m LUVUOIR). For reference, the M2 V star GJ 832 at $d = 5$ pc is $FUV_{GALEX} = 21$ mag. LUMOS's microchannel plate detectors enable time-tagging photons as they arrive, so any flares that occur during integration will be able to be distinguished from quiescent emission, warranting their own analysis.

References

- France, K., Loyd, R. O. P., Youngblood, A., et al. 2016, *ApJ*, 820, 89
- Guinan, E. F., Ribas, I., & Harper, G. M. 2003, *ApJ*, 594, 561
- Jaeggli, S. A., Judge, P. G., & Daw, A. N. 2018, arXiv:1802.03779
- Kruczek, N., France, K., Evonosky, W., et al. 2017, *ApJ*, 845, 3
- Skumanich, A. 1972, *ApJ*, 171, 565
- Youngblood, A., France, K., Loyd, R. O. P., et al. 2016, *ApJ*, 824, 101

A.24 UV characterization of exoplanet host stars: keys to atmospheric photochemistry and evolution

Kevin France (University of Colorado at Boulder)

A.24.1 Introduction

The planetary effective surface temperature alone is insufficient to accurately interpret biosignature gases when they are observed with LUV0IR, particularly for planets orbiting low-mass stars (K and M dwarfs). The UV stellar spectrum drives and regulates the upper atmospheric heating and chemistry on Earth-like planets, is critical to the definition and interpretation of oxygen species and other biosignature gases (e.g., Seager et al. 2013). As discussed in **Chapter 3**, the specifics of the stellar spectrum may produce false-positives in our search for biologic activity (Hu et al. 2012; Tian et al. 2014; Domagal-Goldman et al. 2014; Harman et al. 2015).

A.24.2 The role of LUV0IR

The chemistry of important potential biomarker molecules in the atmosphere of an Earth-like planet depends sensitively on the strength and shape of the host star's UV spectrum. H_2O , CH_4 , and CO_2 are sensitive to far-UV radiation (FUV; 100–175 nm), while the atmospheric oxygen chemistry is driven by a combination of FUV and near-UV (NUV; 175–320 nm) radiation (**Figure A-37**). Additionally, the temporal variability in UV emission lines can be an

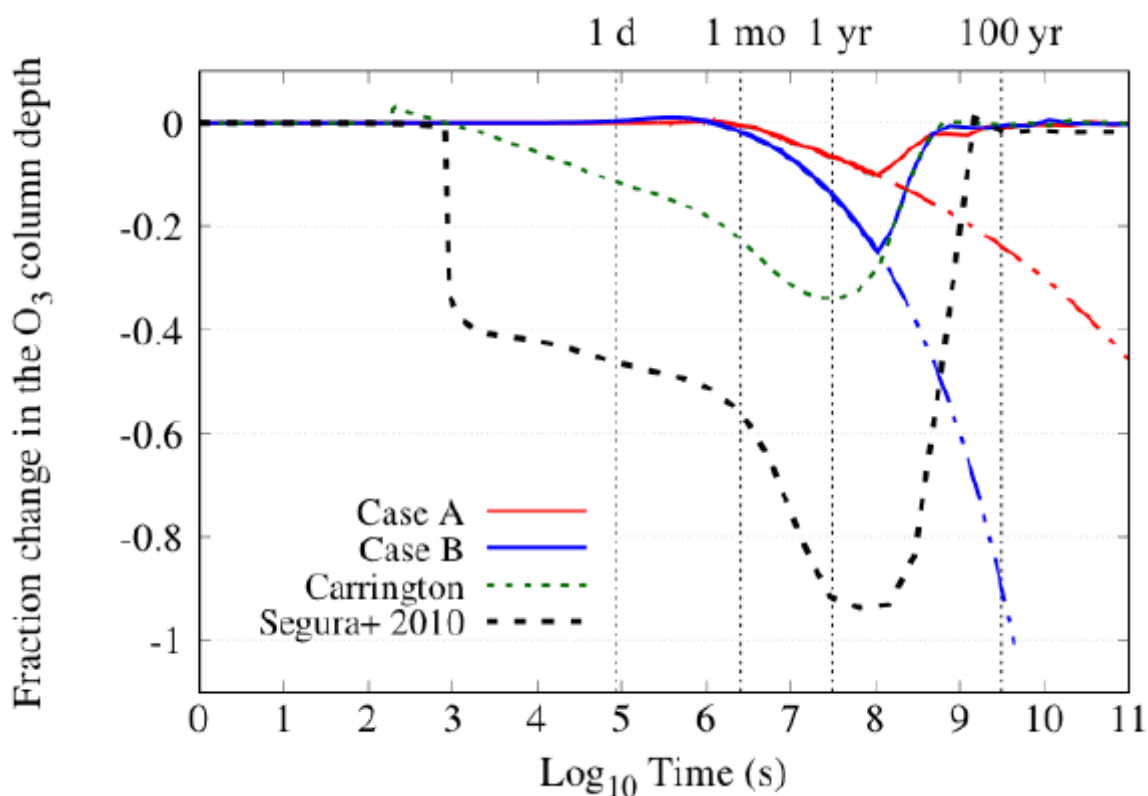


Figure A-37. Impact of FUV-derived particle impact on long-term ozone depletion (Youngblood et al. 2017, Tilley et al. 2018.) Red and blue curves are particle fluences constrained by the FUV data.

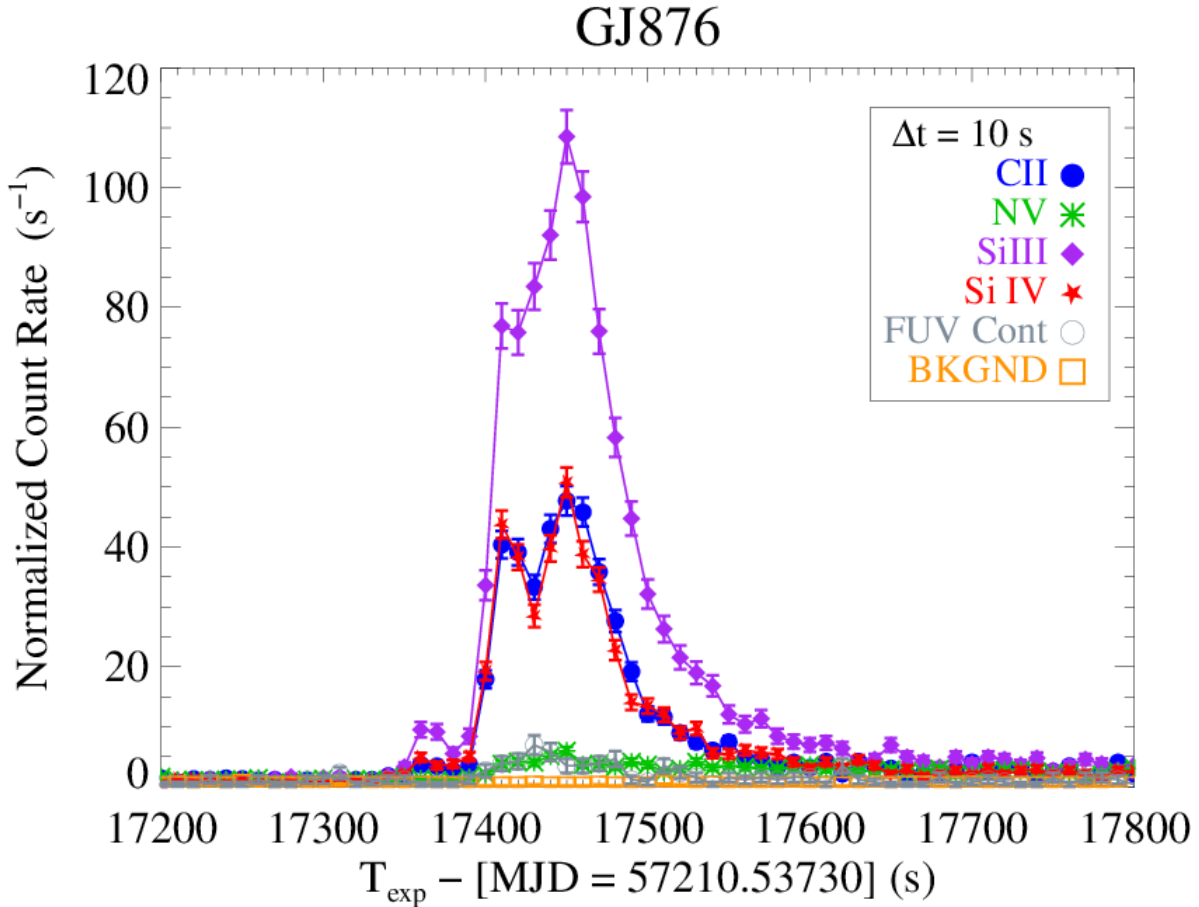


Figure A-38. FUV flare from the local M dwarf GJ 876 with an effective HZ strength equivalent of an X38-class solar flare (France et al. 2016; Youngblood et al. 2017).

indicator of strong charged particle release (e.g., Youngblood et al. 2017). Energetic particle deposition into the atmosphere of an Earth-like planet during a large M dwarf flare can lead to significant atmospheric O_3 depletions ($> 90\%$ for large flares; Segura et al. 2010). This alters the atmospheric chemistry and increases the penetration depth of UV photons that could potentially sterilize (or catalyze) surface life. Given that particle fluxes are not (typically) directly measured for stars other than the Sun, UV observations offer the best estimates of these important particle environments.

The high sensitivity and temporal resolution of the LUVOIR-LUMOS spectrograph will enable a thorough characterization of the UV host star spectrum for every potentially inhabited star observed by LUVOIR. At present, there are no other UV-capable facilities projected to be available to the astronomical community in the 2030s, making LUVOIR's contribution essential for this important host star characterization. Furthermore, the high sensitivity enabled by the large aperture and high efficiency of LUMOS (France et al. 2017) mean that regular monitoring of these systems will be possible during exoplanet characterization campaigns with a minimum of observatory impact to the primary exoplanet observation.

A.24.3 The science program

This study requires the acquisition of a UV spectrum for each LUVOIR target with a habitable zone planet showing atmospheric spectral signatures. The UV spectrum is then essential to

Program at a Glance

Science goal: Characterization of the exoplanet host star’s high-energy irradiance enabling detailed photochemical and atmospheric evolution modeling.

Program details: FUV and NUV time-resolved spectroscopy of the host star of every exoplanetary system targeted by LUVUOIR.

Instrument(s) + configuration(s): LUMOS medium-resolution ($R = 30,000$), single-object spectroscopy

Key observation requirements: S/N of 20 per spectral resolution element

accurately model and interpret those features. This is particularly true for M and K dwarf host stars, where stellar atmosphere models still require a comprehensive panchromatic data set to optimize the temperature-pressure profile of the star’s chromosphere, transition region, and corona (e.g., Fontenla et al. 2016). In practice, a comprehensive study of low-mass stars is required to understand the full parameter-space of age, mass, and metallicity of the system. This requires a sample of ~ 400 stars, including the LUVUOIR earth-like planet candidates, and a range of stellar ages that will likely require going beyond LUVUOIR’s direct imaging survey volume.

As most of these objects are well distributed on the sky, this will be primarily an object-by-object survey of F-M stars. We will require spectral coverage across the major UV and optical diagnostics for chromospheric ($\sim 10^4$ K), transition region ($\sim 10^5$ K), and coronal ($\sim 10^6$ K) gas. This includes lines of O VI (103.2 nm; **Figure A-37**), Fe XIX (111.9 nm), Lyman-alpha (121.6 nm), Fe XII (124.2 nm), NV (123.8 nm), O I (130.4 nm), C II (133.5 nm), Fe XXI (135.4 nm), Si IV & O IV] (140 nm), C IV (154.8 nm), He II (164.0 nm), C I (165.7 nm), Fe II (240 and 260 nm), Mg II (280 nm), Ca II (394 nm), and H-alpha (656.3 nm).

Time-resolution of 1 second is required because the characteristic time scale for strong stellar/solar flares is ~ 1 –5 minutes and 1 second allows us to resolve flare lightcurves—important for inferring properties of CMEs and to understand the duration of energy deposition into the orbiting planet’s atmosphere. This requires a photon-counting detector.

References

- Harman, C., et al. 2015, *ApJ*, 812, 137
 France, K., et al. 2017, *SPIE*, 10397, 13
 France, K., et al. 2016, *ApJ*, 820, 89
 Youngblood et al. 2016, *ApJ*, 824, 101
 Domagal-Goldman, S., et al. 2014, *ApJ*, 792, 90
 Hu, R. 2012, *ApJ*, 761, 166
 Segura, A., et al. 2010, *AsBio*, 10, 751
 Tian, F., et al. 2014, *E&PSL*, 385, 22
 Seager, S., et al. 2013, *ApJ*, 775, 104
 Tilley, M., et al. 2017, *ArXiv*
 Fontenla, J., et al. 2016, *ApJ*, 830, 154

A.25 Resolved photometry of young super star clusters

Søren S. Larsen (Department of Astrophysics/IMAPP, Radboud University, Nijmegen, The Netherlands)

A.25.1 Introduction

Star clusters were traditionally viewed as excellent examples of "simple stellar populations"—consisting of stars with a single age and a single chemical composition. While this still appears to hold true for low-mass open clusters, it is now clear that massive globular clusters that inhabit the Galactic halo are far more complex systems. Colour-magnitude diagrams (CMDs) from the Hubble Space Telescope show multiple populations that reveal themselves through parallel main sequences, split red giant branches, and other features not reproduced by standard models for stellar evolution (Gratton et al. 2012; Bastian & Lardo 2018).

Two key capabilities of HST have been crucial in uncovering the variety of this phenomenon in old GCs: 1) from space, it is possible to achieve exquisite photometric accuracy that is very hard to reach from the ground, especially in crowded environments, 2) space-based observations provide access to important spectral features in the UV (OH, CH, CN, and NH molecular bands) that are sensitive to the light-element abundance variations that trace the multiple populations.

The Magellanic Clouds provide the closest examples of young star clusters with masses approaching those of ancient GCs. HST imaging has revealed a surprising complexity of the CMDs in these clusters, too, with extended main sequence turn-offs, parallel young main sequences, and other puzzling features (Milone et al. 2016). It is unclear, however, to what extent these phenomena are related to the multiple populations observed in old GCs.

The stellar populations in ancient GCs tend to become increasingly complex with increasing mass, and the same may well be the case for their younger counterparts. However, small number statistics are a crucial limitation in young clusters, especially for post-main sequence stars, as even a $10^5 M_{\odot}$ cluster only contains 20–30 post-MS stars (Larsen et al. 2011). Young clusters with masses well above $10^5 M_{\odot}$, also known as *Super Star Clusters* (SSCs), are rare and tend to be located beyond the Local Group. HST has played a crucial role in finding these objects, but the next step—characterizing their stellar contents—will require a much larger space-based telescope. Nevertheless, it is already evident that the CMDs of some young SSCs are not well reproduced by standard models for stellar evolution (Larsen et al. 2011). A number of effects, including stellar rotation, binary evolution, age spreads, and chemical abundance anomalies may all play a role. Current work is already pushing HST to the limit of its capabilities, and it is clear that there is still a lot to learn.

A.25.2 The role of LUVOIR

Imaging with a 10 m class LUVOIR will make it possible to obtain exquisite photometry for individual stars in SSCs well beyond the Local Group. In evolved stars, the wavelength range 250–450 nm provides access to strong molecular features that are sensitive to light element abundances. For hot stars, observations at longer wavelengths (e.g., ground-based AO-assisted imaging) lack the temperature sensitivity necessary to properly characterise (sub-)populations within the SSCs.

HST ACS/WFC

6.5 m LUVVOIR / HDI

15 m LUVVOIR / HDI

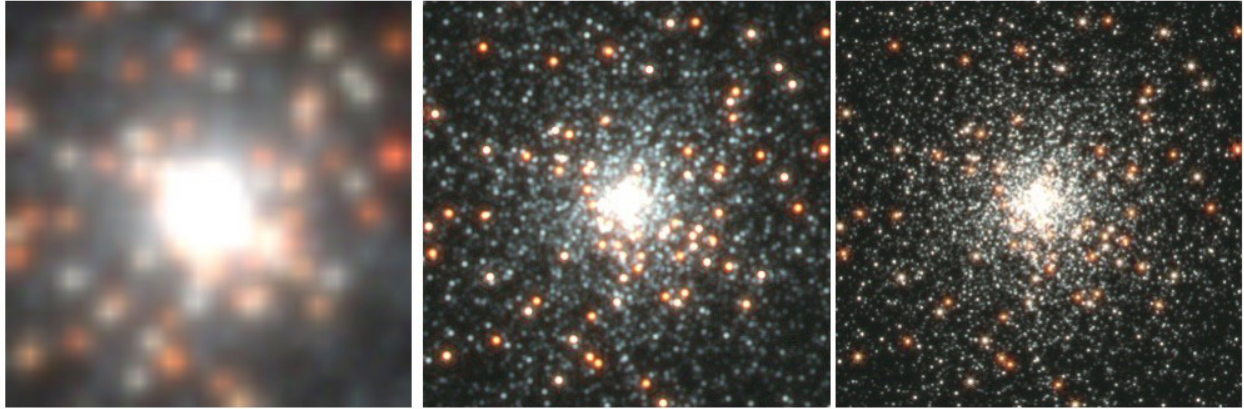


Figure A-39. Simulated 1800 s exposures ($2'' \times 2''$) of a 50 Myr old star cluster in the galaxy NGC 1313 (Larsen et al. 2011), at a distance of 4 Mpc. This cluster has a mass of about $200,000 M_{\odot}$.

The difference between the current state-of-the art and LUVVOIR is illustrated in **Figure A-39**, which shows simulated images of an actual cluster in the galaxy NGC1313, at a distance of 4 Mpc (Larsen et al. 2011). HST can only resolve the supergiants and the brightest main sequence stars in this 50 Myr old cluster and provide a crude CMD, while LUVVOIR can provide accurate photometry reaching far down the main sequence (**Figure A-40**). Blue/UV photometry with LUVVOIR would establish whether variations in light-element abundances (C, N) are present in this and other young clusters, and would also put tight constraints on any age spreads. In **Figure A-41**, the same cluster as in **Figure A-39** has been simulated for an age of 1 Gyr. Even the brightest stars are now barely detectable with HST, while LUVVOIR will be able to reach well below the main sequence turn-off in a few hours of exposure time per bandpass. The difference between a 6.5 m and 15 m aperture is also evident. If past experience is any guide, LUVVOIR CMDs of such clusters will likely reveal surprising new features not yet imagined.

A.25.3 The science program

We envision a LUVVOIR survey of SSCs in a sample of relatively nearby star-forming galaxies, out to distances of ~ 5 Mpc. The targets would cover a variety of galaxy types, metallicities,

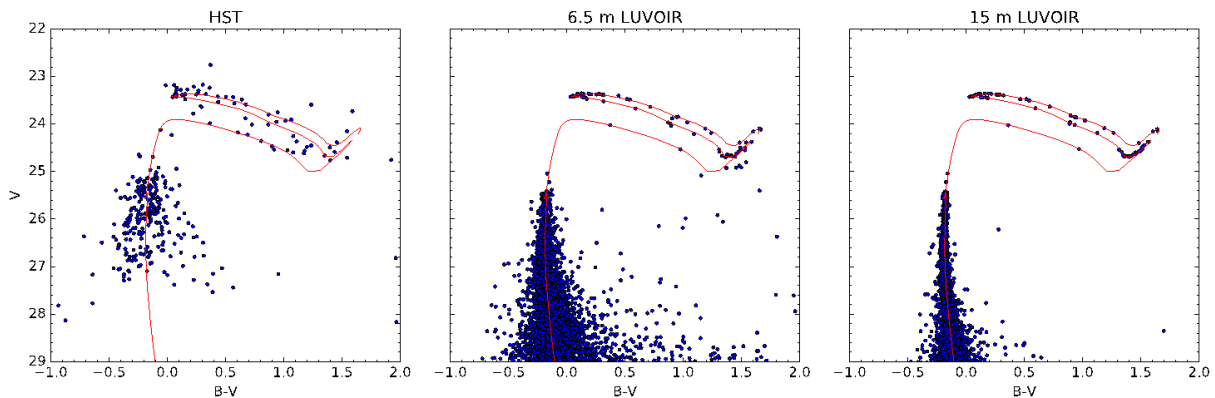


Figure A-40. Color-magnitude diagrams for the simulated images in **Figure A-39**.

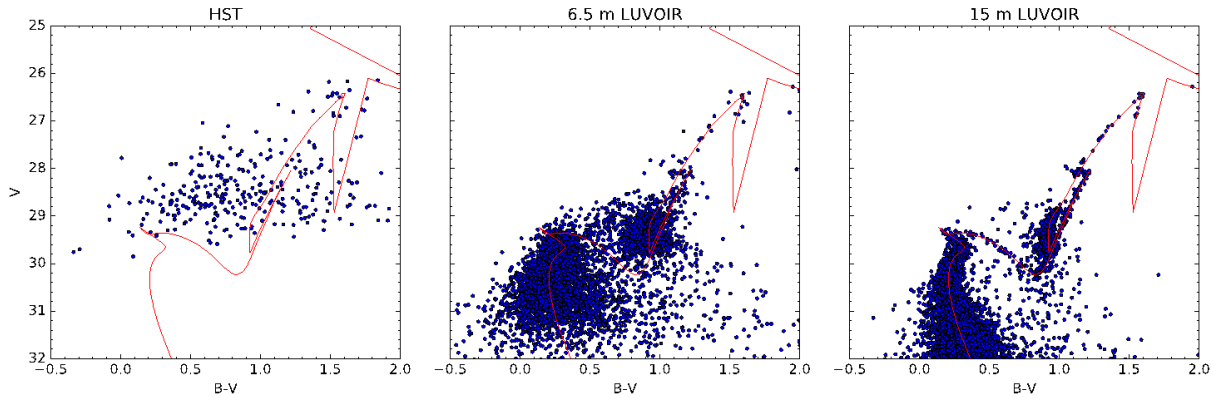


Figure A-41. Color-magnitude diagrams for the same cluster, but for an age of 1 Gyr and an exposure time of 5 hours per filter.

Program at a Glance

Science goal: Characterize the stellar contents of massive star clusters in nearby (~ 5 Mpc) galaxies via high quality color-magnitude diagrams.

Program details: Imaging in blue/UV filters (F275W/F336W/F343N/F439W equivalent), exposure times from ~ 30 min to several hours per filter.

Instrument(s) + configuration(s): HDI

Key observation requirements: SNR should be ~ 100 per filter (errors ~ 0.015 mag) to clearly detect C, N abundance variations in cool stars.

environments, etc., ranging from dwarf starburst galaxies to large spirals. The survey could also include nuclear star clusters. The global characteristics of the SSC populations in most nearby galaxies are already well known, and will be studied in more detail by missions such as Euclid and WFIRST prior to LUVOIR. Somewhat further away, the rich cluster population in the Antennae merger would offer interesting, but challenging targets.

References

- Bastian, N., & Lardo, C. 2017, *ARA&A*, arXiv:1712.01286
 Gratton, R., Carretta, E., & Bragaglia, A. 2012, *A&AR*, 20, 1
 Larsen, S. S., de Mink, S. E., Eldridge, J. J. et al. 2011, *A&A*, 532, A147
 Milone, A., Marino, A., D'Antona, F. et al. 2016, *MNRAS*, 458, 4368

A.26 LUVVOIR for stars, stellar evolution, and the local universe

Bruce Elmegreen (IBM T.J. Watson Research Center)

A.26.1 Introduction

LUVVOIR is a ~12-meter class UV-Vis-NIR space telescope for the 2030s and beyond. Because of the large aperture and short observing wavelength, it will have very high angular resolution, corresponding to an Airy disk of 5×10^{-8} radian for optical light (10 milliarcsec). It will also have broad wavelength coverage from 100 nm to 2.5 microns, allowing a wide range of science investigations. The field of view is proposed to be very wide, making it ideal for surveys: the High Definition Imager would have a field of view of $2' \times 3'$ with 2.73 mas/pix at UVIS and 8.2 mas/pix at NIR. This means the image sizes will be 2.9 Gpix and 0.32 Gpix, respectively, and the file sizes 1^{-10} GByte per image. It will also have a multi-object spectrograph from 100 nm–850 nm, as well as other instruments. With these specifications, taken from Dalcanton et al. (2015) and Elmegreen et al. (2017), LUVVOIR will revolutionize the study of stars, stellar evolution, and the local universe.

A.26.2 The role of LUVVOIR

The accelerating progress of our view of the sky over the last two millennia—the time since systematic Astronomical studies and star catalogs began—is shown schematically in **Figure A-42**, which plots the number of distinguishable pixels in the sky versus time. The first major jump from 1 arcmin resolution with the eye to 1 arcsec resolution with a telescope started in

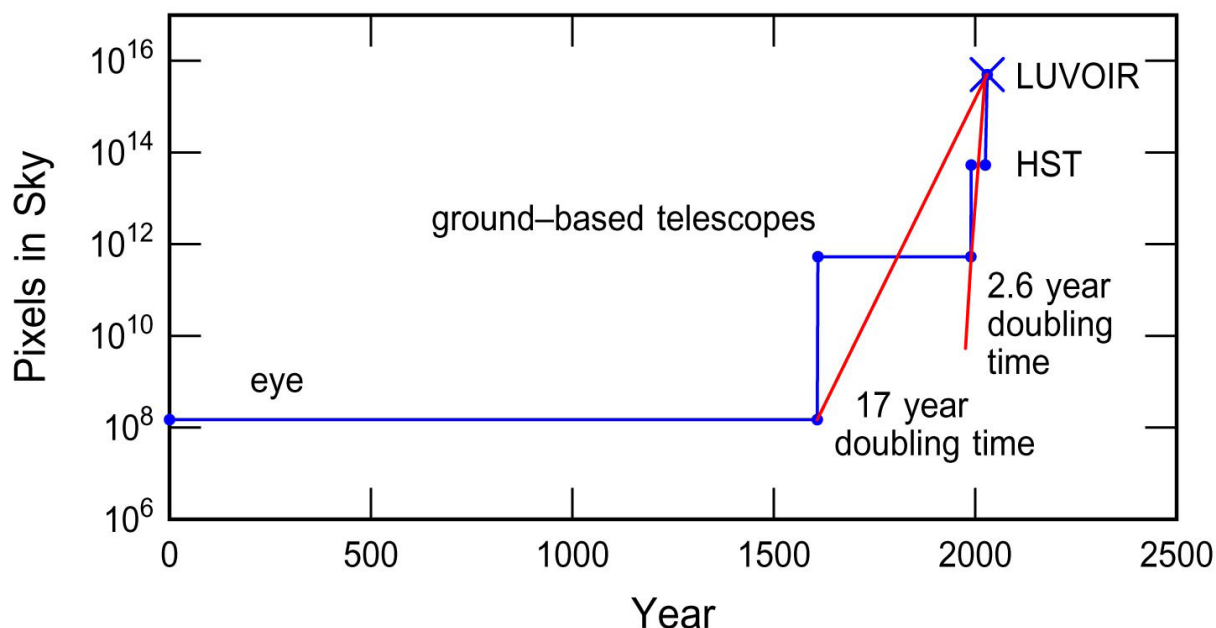


Figure A-42. The total number of pixels in the sky, calculated as the ratio of the sky solid angle to the angular resolution of the instrument, is plotted versus the year in history. Three major technology jumps have occurred, the invention of telescopes, the placement of telescopes in space, and the ability to have large telescopes in space. The first two each revolutionized astronomy, and the third is likely to as well.

early 1600 with a long gap before the Hubble Space Telescope improved the resolution further by factor of 10. The next jump to LUVOIR comes rather quickly on this scale, showing another factor of 10 gain with a 2.6-year doubling time in the most recent era. This pace is comparable to the advance in general technology, reflecting a combination of what is possible and what gains we can expect. From this long-term viewpoint, LUVOIR will improve our resolution of the sky by the same factor over HST as HST improved it over Galileo's first telescope. Some of the science gains from this improvement will be discussed in the next section.

A.26.3 The science program

Local star formation

Star formation in the solar neighborhood will be resolved at 1–10 AU scales, showing dusty accretion to protostars, planet-forming regions of young disks, central jets, and close binary stars in mutual formation. The Orion protoplanetary disks discovered with HST—the so-called Proplyds (O'dell et al. 1993)—will be observable at 5 AU resolution where their interaction with the hot radiation and winds from nearby massive stars will be visible. Interactions like these could have introduced radioisotopes from supernovae into the early Solar Nebula, giving our meteorites their Al-Mg anomalies (MacPherson & Boss 2011). The dusty structures of the Taurus filaments, which are regions of low-mass star formation, will be observed at 1.4 AU resolution, which is 10^{-4} times their size. This will easily resolve the transition from supersonic to subsonic turbulence and reveal for the first time the thermal, turbulent and gravitational processes that form low mass stars and their disks.

Imaging stellar surfaces

LUVOIR will be able to resolve and image some dozen nearby stars (Ochsenbein & Halbwachs 1982; van Belle et al. 1996) to look for star spots, limb darkening, rotation, flares and other possible features in optical and UV light. For example, Betelgeuse has been resolved with optical interferometry (Haubois 2010), Antares was resolved with the VLT1 interferometer (Ohnaka et al. 2013) and Mira was resolved with HST (Karovska 1997). The LUVOIR resolution of 10 mas corresponds to a solar radius at a distance of 0.45 pc. Larger stars like supergiants will be resolvable to proportionally larger distances.

Local group galaxies

The Local Group of galaxies, including M31, M33, the LMC, SMC and many smaller galaxies, will be resolved at 0.05 pc, allowing us to study hundreds of supernova remnants and planetary nebula in great detail. From the structures and line emission of these nebulae, we will learn about the final stages in stellar lives, nucleosynthetic element dispersal in the surrounding gas, and dust formation in dense remnant winds.

The high resolution of LUVOIR will allow us to distinguish between individual stars as well. According to the calculation of integration time versus point source absolute magnitude on page 49 of Dalcanton et al. (2015), in 1 hour we can see a solar type star at a distance of 2.8 Mpc using the F555W filter at an apparent AB magnitude of 32. Within 2.8 Mpc there are 9 large galaxies, i.e., with absolute magnitude less than -16 , and about 60 small galaxies. At the stellar surface density in the solar neighborhood, which is about 60

solar masses per pc^2 , there are 150 stars per pc^2 larger than 0.01 solar masses and 10 stars pc^{-2} larger than 1 solar mass (using the Kroupa 2001 initial stellar mass function). The mean projected separations between these stars are 6 mas and 24 mas at 2.8 Mpc. The second number is larger than the angular resolution of LUV OIR, so we will be able to separate solar mass stars in galaxy disks within 2.8 Mpc, i.e., for dozens of galaxies of various types and for the highly diverse conditions in these galaxies. By counting these stars and the more massive stars, which are separated by even larger distances, we can determine the field star mass function and approximate star formation history in all regions with fairly low extinction. Variations in this field star mass function for a given history would suggest comparable variations in the stellar initial mass function. This will be the first time that the stellar IMF can be directly compared to environmental conditions and star formation rates. Such comparisons should give us greater understanding of the origin of the IMF.

Nuclear regions of nearby galaxies

LUV OIR will resolve nearby nuclear star clusters, disks and black hole activity with 1 pc resolution or better out to 20 Mpc, which includes thousands of galaxies. NGC 300, for example, has a nuclear star cluster with a 3-pc radius (van der Marel et al. 2007) that corresponds to 300 mas—easily resolved by LUV OIR. In M31, the nuclear region has a 108 solar mass black hole with intriguing red and blue structures nearby, as observed by HST (Lauer et al. 2012). The active galactic nucleus in NGC 4261 has an optical disk 1.7 arcseconds across (Ferrarese et al. 1996), which is 170 resolution elements. The implications are enormous for studies of black hole accretion, nuclear disk storms, small-scale flaring activity, nuclear spirals and torques

Proper motions with sub-pixel accuracy

Proper motions with HST could reach 0.02 pixel accuracy (Anderson & King 2000, 2003) with simultaneous fitting of the average stellar point spread function and the stellar positions. 0.02 pixel for LUV OIR equals 10^{-9} radians or 0.21 mas. This means that with a 5-year baseline, the proper motion that can be measured, in km/s, equals 0.2 times the distance in kpc. With this we can observe a wide variety of interesting and important motions for the first time: the random motions of dust features in local star forming regions at the sonic speed, 0.1 km/s, the expansion of supernova remnants, planetary nebulae and “pillars of creation” at 1 km/s, the internal motions of Milky Way globular clusters to within 2 km/s, the rotation of the LMC and SMC to within 10 km/s, and the rotation of M31 within 140 km/s. For example, proper motions have already been measured in the LMC (Kallivayalil et al. 2013) although with less precision. This is a completely new capability to study the dynamics of nearby dust and emission line structures, and of stars and stellar systems, especially in regions where the Gaia satellite will not be able to distinguish individual stars.

Extensions to high redshifts

As noted in the LUV OIR technical summaries (Dalcanton et al. 2015), the angular resolution will be about 100 pc or better for all redshifts. This is equivalent to ground-based resolution (1 arcsec) for all galaxies within 20 Mpc, which is essentially the Hubble Atlas of Galaxies (Sandage 1984). Deep images at high redshift will cover the same co-moving volume as the Sloan Digital Sky Survey with the same or better resolution (Dalcanton et al. 2015). As a

result, we will be able to see for the first time at high redshift the substructure of star formation clumps in young galaxies, we will resolve young bars and bulges, see multiple nuclei from recent mergers, map spiral arms, and discover dwarf galaxy companions. The radial profiles will be resolved too, allowing some understanding of the origin of the exponential radial structure in disks. Decades of research on local galaxies observed from the ground will suddenly have a counterpart in the epoch of galaxy formation.

Multi-object spectroscopy

LUVOIR will observe spectral line emission from low-lying states of atoms, which are primarily in the UV and unobservable from the ground. Such observations were a primary driver of going into space in the first place as mentioned by Spitzer (1946) in his “Report to Project Rand: Astronomical Advantages of an Extra-Terrestrial Observatory.” Most atoms are in these ground states and both absorption and emission lines are in the UV or FUV. Dalcanton et al. (2015) have a diagram of the observable wavelength for many important lines as a function of lookback time in the Universe. Most low-level ion transitions cannot be observed from the ground after a lookback time of some 10 Gyr, which means these lines are invisible for most of the Universe unless they are observed from space.

With FUV emission lines, we can see interstellar and active galactic nuclei emission from 106 K gas at redshifts greater than 0.3 and compare it to the observable x-ray gas at the same temperature. We can observe circumgalactic (CGM) emission in Lyman alpha, OVI, and CIV faster than on the ground by factors of 10 to 100 because of the lower levels of background light in space (Dalcanton et al. 2015). An example of a Lyman alpha blob in space is shown in Cai et al. (2017).

LUVOIR will also observe absorption lines from ground states in the FUV. We expect 100 times as many background galaxies in a deep field at redshifts less than 1 to 2 for observations of foreground CGM absorption, and 100 times as many QSOs (Dalcanton et al. 2015). This will allow us to map the CGM around galaxies, trace element formation, outflows and inflows and see galaxies building up and quenching by outflows for the first time.

Extensive observations of the CGM in both emission and absorption will revolutionize our understanding of galaxy formation and evolution, just as most of the other new capabilities mentioned here will be revolutionary in their own fields. Not only will we see more and smaller galaxies at high redshift, but we will also start to fill in the space between the galaxies.

Figure A-43 shows the impact of this change on another plot with a historical perspective. This is the sky-covering fraction of known astronomical objects as a function of year. For all time before the invention of telescopes, humans could only see some 5000 stars at 1 arcmin resolution. The fraction of the sky covered by these light sources was very small, letting us think that most of the Universe was empty space. When the telescope was invented, the sky covering fraction got even smaller because, although many more stars could be seen, each was 60 times smaller at 1 arcsecond resolution, so more blank space could be seen as well. However, with larger telescopes to collect fainter light (in William Herschel’s era), and with photographic images that allowed collection of this faint light over long periods of time (thousands of times longer than the eye could integrate), the sky started to be seen as covered with faint galaxies and nebulae, filling in the blank space and increasing the covering fraction by a factor of 100. HST increased it by another factor of 100 by finding

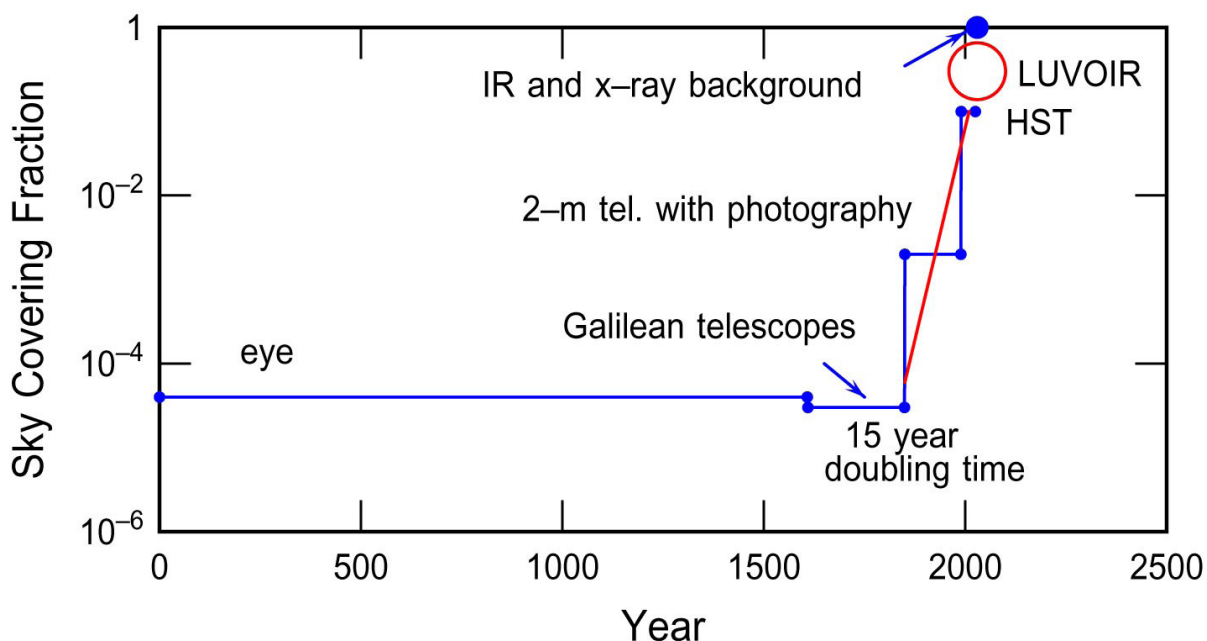


Figure A-43. The fraction of the sky covered with known astronomical objects is plotted versus the year in history. As telescopes reach fainter objects and deeper fields, more and more objects become known. LUVOIR will add to this progression by mapping the circumgalactic gas.

Program at a Glance

Science goal: Study local star formation, the stellar initial mass function, and nuclear regions in local galaxies, image stellar surfaces to explore activity, probe dynamics of nearby dust structures, determine properties of young galaxies, and map the circumgalactic medium.

Program details: High-resolution imaging and multi-object spectroscopy of local stars, dust and galaxies out to high redshift, young galaxies.

Instrument(s) + configuration(s): HDI imaging, multi-object spectroscopy

Key observation requirements: Resolution < 10 mas

faint galaxies at high redshift between all the nearby galaxies and stars, covering deep fields at nearly the 10% level. LUVOIR will make the next jump with its ability to see gas between the galaxies, and its possible first-time resolution of unknown objects that have appeared up to now to be only a smooth background. LUVOIR will literally fill the sky with discoveries!

My thanks to Aki Roberge, Daniela Calzetti, and Bradley Peterson for their invitation to speak on this topic at the AAS Winter Meeting 2018. Many of the numbers and ideas presented here are from the comprehensive summaries by Dalcanton et al. (2015) and Elmegreen et al. (2017).

References

- Anderson, J. & King, I.R. 2000, *PASP*, 112, 1360
- Anderson, J. & King, I.R. 2003, *PASP*, 115, 113
- Cai, Z. et al. 2017, *ApJ*, 837, 71
- Dalcanton, J. & Seager, S. 2015, AURA committee publication
- Elmegreen, D.M., van Dishoeck, E., Spergel, D., & Davies, R. 2017, Kavli Foundation Report for the IAU, arXiv:1709.06992
- Ferrarese, L., Ford, H.C., Jaffe, W. 1996, *ApJ*, 470, 444
- Haubois, X. 2010, APOD “The spotty surface of Betelgeuse”
- Kallivayalil, N., van der Marel, R.P., Besla, G., Anderson, J. & Alcock, C. 2013, *ApJ*, 764, 161
- Karovska, M. 1997, News release ID: STScI-1997-26
- Kroupa, P. 2001, *MNRAS*, 322, 231
- Lauer, T.R., Bender, R., Kormendy, J., Rosenfield, P. & Green, R.F. 2012, *ApJ*, 745, 121
- MacPherson, G.J. & Boss, A. 2011, PNAS, Vol. 108, No. 48, p 19152
- Ochsenbein, F. & Halbwachs, J. L. 1982, *A&AS*, 47, 523
- O'dell, C. R., Wen, Z., Hu, X. 1993, *ApJ*, 410, 696
- Ohnaka, K., Hofmann, K.-H., Schertl, D., Weigelt, G., Baffa, C., Chelli, A., Petrov, R., & Robbe-Dubois, S. 2013, *A&A*, 555, A24
- Sandage, A. 1984, The Hubble Atlas of Galaxies, Carnegie Inst of Washington
- Spitzer, L., Jr. 1946, Report to Project Rand: Astronomical Advantages of an Extra-Terrestrial Observatory
- van Belle, G. T., Dyck, H. M., Benson, J. A. & Lacasse, M. G. 1996, *AJ*, 112, 2147
- van der Marel, R.P., Rossa, J., Walcher, C.J., Boeker, T., Ho, L.C., Rix, H.-W., & Shields, J.C. 2007, IAU Symposium 241, Stellar Populations as Building Blocks of Galaxies, ed. A. Vazdekis & R. F. Peletier, Cambridge University Press: Cambridge, p. 475

A.27 The rise of the periodic table

John O’Meara (Keck Observatory), Ian Roderer (U of Michigan)

A.27.1 Introduction

The first stars and metals. The nucleosynthetic signatures of the first stars and supernovae are imprinted in the compositions of the most metal-poor stars found today. No first-generation (Population III, or Pop III) stars are known at present, but dozens of candidate second-generation stars are known. These stars have iron abundances less than $10^{-4.5}$ times the solar abundance (i.e., $[\text{Fe}/\text{H}] < -4.5$), or are iron-poor but highly enhanced in carbon. Hundreds more are expected to be found among ongoing and future surveys (e.g., LAMOST, LSST). When compared with predicted model yields, these abundance patterns reveal the nature of the elusive Pop III stars, providing the only direct tests of the evolution and end states of individual Pop III stars (e.g., Frebel & Norris 2015). Their locations and kinematics reveal the nature of the environments and the epochs when they formed and released the first metals into the Universe.

Only a few tens of absorption lines are commonly found in the optical spectra of these second-generation stars, so only ~ 5 – 10 elements are regularly detected. Many others (Be, B, Si, P, S, Sc, V, Cr, Mn, Co, Ni, and Zn) are expected to be present but are rarely detected, and the upper limits derived from their optical non-detections are often uninformative. The UV part of the spectrum is an unexplored window that would allow all of these elements to be detected if present in the most metal-poor stars known (**Figure A-44**). Key lines include those of boron (B; atomic number $Z=5$; BI lines at 2088, 2089 Å), phosphorus (P; $Z=15$; PI lines at 2135, 2136 Å), sulphur (S; $Z=16$; SI lines at 1807, 1820, 1826 Å), chromium (Cr; $Z=24$; CrII lines at 2055, 2061, 2065 Å), and zinc (Zn; $Z=30$; ZnII lines at 2025, 2062 Å) (e.g., Roederer et al. 2016).

Elements heavier than iron. The elements heavier than iron are formed by neutron-capture reactions. They have been detected in the ancient stars of the Galactic halo, in the ISM, dust grains, meteorites, and on Earth, are formed by neutron-capture reactions (e.g., Sneden, Cowan, & Gallino 2008). Relatively high neutron densities ($\sim 10^{22}$ – 10^{28} cm $^{-3}$) lead to heavy-element nucleosynthesis via the rapid neutron-capture process (r-process) in supernovae or neutron star mergers. Lower neutron densities ($\sim 10^7$ – 10^{10} cm $^{-3}$) lead to nucleosynthesis via the slow neutron-capture process (s-process) in AGB stars or the late evolutionary stages of massive stars. Neutron densities intermediate between these two extremes ($\sim 10_{15}$ cm $^{-3}$) lead to nucleosynthesis via the intermediate neutron-capture process (i-process), which may occur in a variety of sites including super-AGB stars, post-AGB stars, He-core and He-shell flashes in low-metallicity low-mass stars, and massive stars.

Optical spectra obtained from the ground can reveal the nature of the enrichment (e.g., the r-process), but key elements useful to discriminate between models have no absorption lines in the optical domain. High-resolution UV spectroscopy enables a 40% improvement, compared to optical/near-IR spectra, in the number of elements (~ 15 to 20) that can be detected in the atmospheres of late-type (FGK) stars that retain the chemical signatures of nucleosynthesis in earlier generations of stars. These include elements like germanium (Ge; atomic number $Z=32$; GeI line at 3039 Å), selenium (Se; $Z=34$; SeI line at 2074 Å), cadmium (Cd; $Z=48$; CdI line at 2288 Å), tellurium (Te; $Z=52$; TeI line at 2385 Å), platinum

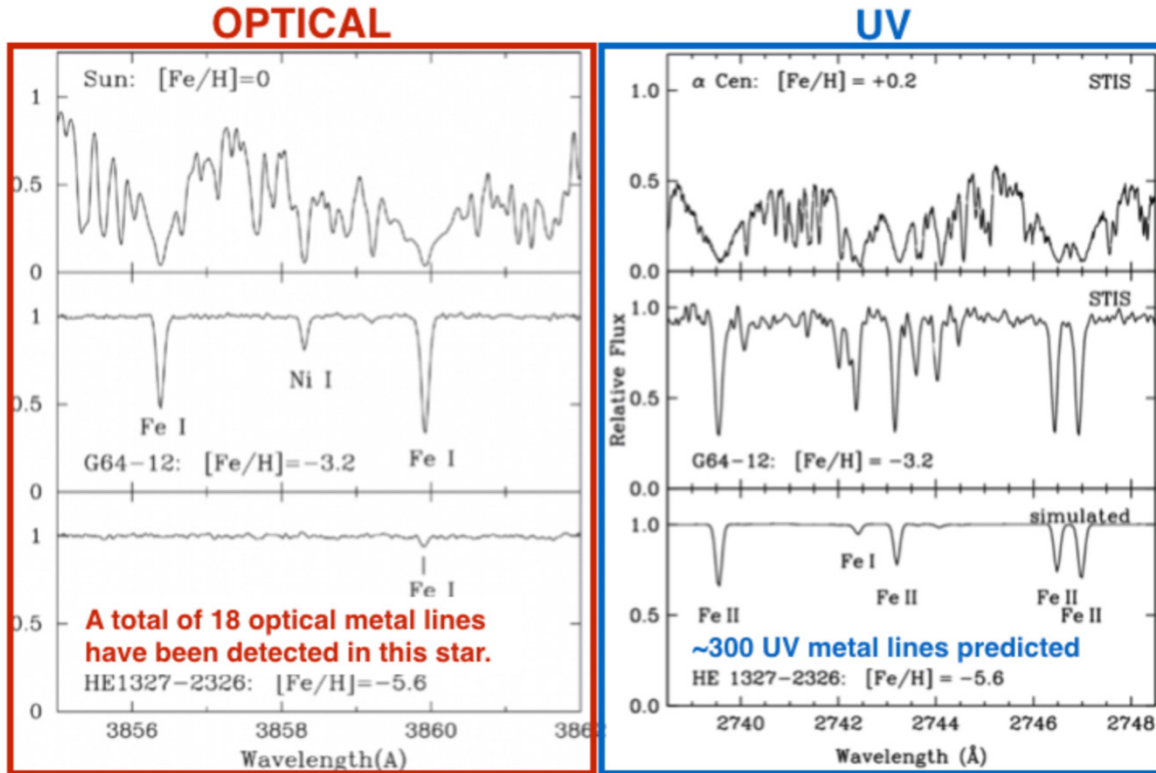


Figure A-44. Comparison of the optical and UV spectral domains of a normal G dwarf star at solar metallicity (top row), a typical metal poor G subgiant (middle row), and one of the candidate second generation stars (bottom row). The red panel is from Aoki et al. (2006). LUVOIR could observe the UV spectrum of every candidate second-generation star in the field, and many more in nearby dwarf galaxies, obtaining data similar to the lower right panel across a much wider spectral range.

(Pt; $Z=78$; Pt I line at 2659 Å), and mercury (Hg; $Z=80$; Hg II line at 1942 Å), among others (e.g. Roederer et al. 2012). These abundances provide new, critical constraints on stellar nucleosynthesis mechanisms like the r-, s-, and i-processes. High SNR, high resolution UV spectroscopy of elements like Ge, Se, Cd, Te, Pt, and Hg in solar-type stars (**Figure A-45**) will provide new, critical constraints on stellar nucleosynthesis process for elements heavier than iron.

A.27.2 The role of LUVOIR

A large-aperture telescope with a high-resolution UV spectrometer enables observations of these elements in all known second-generation stars in the halo field, and many more found in nearby dwarf galaxies. Presently, with COS on HST, only one or two of the brightest candidate second-generation stars can be observed, but even in these cases the data quality is insufficient to detect all elements that could in principle be detected. With LUVOIR, an observing program to obtain high-quality UV spectra ($R \sim 30,000$; $\text{SNR} \sim 25$; $200 \text{ nm} < \lambda < 400 \text{ nm}$) for 100 metal-poor F, G, K dwarfs in the Milky Way halo takes only 11 days with LUVOIR-A and 29 days with LUVOIR-B. This advance would enable us to increase the stellar sample sizes by about two orders of magnitude, revolutionizing our understanding of the first stars, the first supernovae, and the first metals in the universe. In other words,

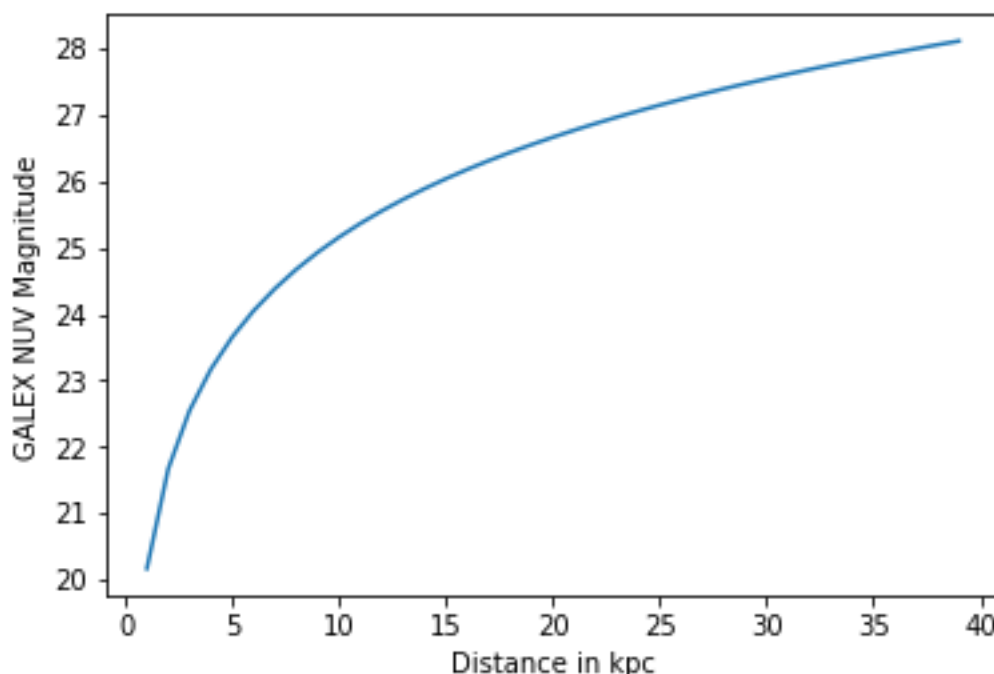


Figure A-45. GALEX NUV (effective wavelength $\sim 2200 \text{ \AA}$) AB magnitudes for a G2V star at various distances.

LUVUOIR+LUMOS would enable the acquisition of high-quality UV spectra of the vast majority of stars whose optical spectra can be observed today from the ground.

For elements heavier than iron, a large-aperture telescope with a high-resolution UV spectrometer would enable observations of these elements in samples of stars best suited to revealing the complex physics that drives the nucleosynthesis of the heaviest elements. Presently, with STIS or COS on Hubble, only the handful of brightest stars in the solar neighborhood can be observed, and these are sub-optimal representatives of stars reflecting dominant contributions from the r-, s-, or i-processes.

A.27.3 The science program

The first stars and metals. We will obtain complete point-source NUV spectra of solar-type stars with the LUMOS G300M grating.

Targets. 100 metal poor F, G, K stars in the Milky Way halo. We require a single pointing per star. The number of pointings would be reduced if multiple stars happen to fall in the LUMOS FOV.

Exposure times & overheads. Current and future surveys are actively looking for very metal poor stars from the ground. Since the exact target population is not yet known, we tabulate the science exposure times needed for 3 magnitudes (**Table A-4**). Times for LUVUOIR-A were calculated using the LUMOS exposure time calculator to provide SNR=25 at 2200 \AA using the LUMOS G300M grating. The times for LUVUOIR-B were scaled by the ratio of the collecting areas (155 m^2 for LUVUOIR-A and 43.8 m^2 for LUVUOIR-B). We simply assume a 50% overhead allocation for this program, to account for grating changes, wavelength calibration, and repointing maneuvers.

Table A-4. Science exposure times per star for complete LUMOS NUV spectra of very metal poor stars in the Milky Way halo

GALEX NUV mag	LUVOIR-A science exposure times (hours)	LUVOIR-B science exposure times (hours)
25	1.1	3.9
26	2.6	9.2
27	6.3	22.3

Table A-5. Science exposure times for complete LUMOS NUV spectra of a G2V star at different distances

Distance	LUVOIR-A science exposure times (hours)	LUVOIR-B science exposure times (hours)
1 kpc	0.11	0.39
2 kpc	0.57	2.02
5 kpc	3.42	12.10

Results. To calculate the total science exposure time for a representative sample of 100 very metal poor stars, we adopt the following proportions of stars with different magnitudes:

1. 70 stars with NUV mag = 25
2. 25 stars with NUV mag = 26
3. 5 stars with NUV mag = 27

This gives a total LUVOIR-A science exposure time of 174 hours and a total program time of 174 hours + 87 hours = 261 hours. With LUVOIR-B, the total science exposure time is 634 hours. The overheads should be the same for both programs; therefore, the total program time for LUVOIR-B is 615 hours + 87 hours = 702 hours.

Elements heavier than iron. We will obtain complete point-source NUV spectra of solar-type stars with the LUMOS G300M grating.

Targets. 100 F,G,K dwarf stars and a few giant stars to explore each of the 3 processes (r-, s-, i-). We require a single pointing per star. The number of pointings would be reduced if multiple stars happen to fall in the LUMOS FOV.

Exposure times & overheads. Since the exact target population is not yet known, we calculate the science exposure times needed for spectra of a G dwarf star at three distances (**Table A-5**). Times for LUVOIR-A were calculated using the LUMOS exposure time calculator to provide SNR=80 at 2200 Å using the LUMOS G300M grating. The times for LUVOIR-B were scaled by the ratio of the collecting areas (155 m² for LUVOIR-A and 43.8 m² for LUVOIR-B). The desired SNR constraints were provided by Ian Roderer. We simply assume a 50% overhead allocation for this program, to account for grating changes, wavelength calibration, and repointing maneuvers.

Results. To estimate the total science exposure time for a representative sample of solar-type dwarf stars, we adopt the following proportions of stars with different magnitudes:

1. 70 stars at 1 kpc distance
2. 25 stars at 2 kpc distance
3. 5 stars at 5 kpc distance

Program at a Glance

Science goal: Investigate the origins of elements heavier than helium by: 1) Determining elemental abundance in very metal poor stars to constrain nucleosynthesis in the first (population III) stars; 2) Determining the elemental abundances in late-type stars to constrain R-, S-, and I- process nucleosynthesis.

Program details: LUMOS point-source UV spectroscopy of 100 very metal poor stars in the Milky Way halo and the same for 100 F, G, and K dwarfs to constrain nucleosynthesis of heavy elements.

Instrument(s) + configuration(s): LUMOS point source spectroscopy between 200-400 nm.

Key observation requirements: Access to UV wavelengths. $R > 30,000$. SNR ~ 25 for metal-poor stars, SNR ~ 80 for elements heavier than iron.

This gives a total LUVUOIR-A science exposure time of 39 hours and a total program time of 39 hours + 20 hours = 59 hours. With LUVUOIR-B, the total science exposure time is 138 hours. The overheads should be the same for both programs; therefore, the total program time for LUVUOIR-B is 138 hours + 20 hours = 158 hours. The true sample of stars will contain multiple types (F,G,K dwarfs and some giants), so these times are only representative.

References

- Aoki, W., et al. (2006). *The Astrophysical Journal*, 639(2), 897.
- Frebel, A., & Norris, J. E. (2015). *Annual Review of Astronomy and Astrophysics*, 53, 631-688.
- Roederer, I. U., et al. (2012). *The Astrophysical Journal Letters*, 747(1), L8.
- Roederer, I. U., Placco, V. M., & Beers, T. C. (2016). *The Astrophysical Journal Letters*, 824(2), L19.
- Snedden, C., Cowan, J. J., & Gallino, R. (2008). *Annu. Rev. Astron. Astrophys.*, 46, 241-288.

A.28 Extragalactic massive stars

Miriam Garcia (CAB, CSIC-INTA), Chris Evans (UKATC, STFC)

A.28.1 Introduction

Massive stars are cosmic engines and make valuable probes of the Universe. They are mighty sources of ionizing radiation and mechanical energy, giving rise to striking bubbles, giant HII regions, and galactic-scale outflows during their lives. In death they are the progenitors of supernovae and long-duration γ -ray bursts, with the latter so bright they can be detected in galaxies up to $z = 9$ (Robertson & Ellis, 2012). These dramatic explosions release chemical elements that are essential to life (e.g., oxygen) into the interstellar medium, and their remnants (neutron stars, pulsars, black holes) are the sites of extreme physics and sources of gravitational waves (Abbott et al. 2016).

A critical area of research in the field is characterizing the role of metallicity (abundance of elements heavier than H and He) on the lifecycle of massive stars. The Universe has become increasingly enriched in metals since the Big Bang so, to correctly interpret observations of distant galaxies, we need models of stellar physics and evolution that match their metal content. The ultimate goal is to investigate the paradigm of the first generation of (effectively metal-free) massive stars in the Universe (so-called Population III), a suggested source of reionisation at $z > 6$ (Haiman & Loeb, 1997).

A key observable of massive stars are their radiatively-driven stellar winds, via which solar masses of material can be lost throughout their lives, directly influencing their evolutionary sequence, feedback to the local medium, and pre-explosion core mass. The wind momentum depends strongly on metallicity (Kudritzki & Puls, 2000), implying a strong metallicity dependence to evolution and feedback. Only UV spectroscopy from space can provide the data required to assess the properties of such winds (e.g., Fullerton et al. 2006; Sundqvist et al. 2014). IUE, FUSE and HST-STIS/COS have made unprecedented and long-lasting contributions.

Studies in nearby galaxies such as the SMC (60kpc), IC1613 (750kpc), WLM, Sextans A and NGC3109 (~1.2Mpc) have enabled studies of the properties of massive stars with metallicities of 10-20% solar (e.g., Venn et al. 2003; Bresolin et al. 2007; Evans et al. 2007; Camacho et al. 2016) providing valuable empirical templates (e.g., Leitherer et al. 2001) and important tests of theory (e.g., Mokiem et al. 2007). However, significant uncertainties remain over their wind behavior at low metallicity, even when UV data are available (Tramper et al. 2011; Herrero et al. 2012; Garcia et al. 2014; Bouret et al. 2015) because of the sensitivity limits of current facilities. Moreover, we need to go at least an order-of-magnitude lower in metallicity to match conditions in distant absorption-line systems (e.g., Prochaska et al. 2003) and to move toward robust models of Pop III stars, but these are simply out of reach of current facilities (HST, 8-10m ground-based telescopes).

A.28.2 The role of LUVOIR

The ambitious goal in this topic is studies of individual massive stars in I Zw 18, a star-forming galaxy at 18 Mpc (see **Figure A-46**) with a metallicity of 2-3% solar (Vilchez & Iglesias-Paramo). The task will require outstanding spatial resolution and sensitivity. Optical/NIR spectroscopy, needed to determine some key physical properties (temperatures, luminosities)

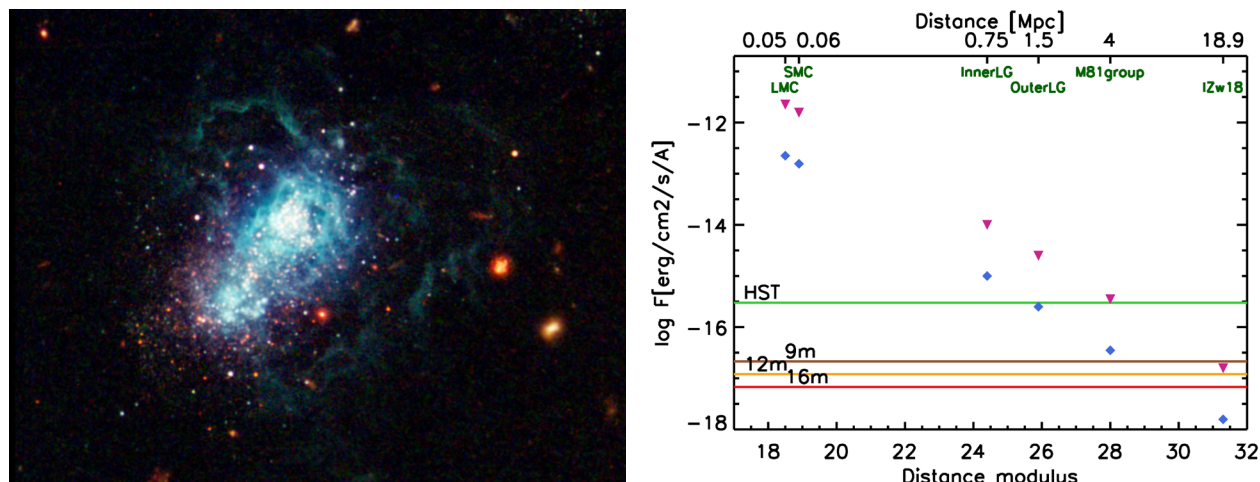


Figure A-46. Left: Resolving massive stars in the ultra-metal poor galaxy I Zw 18 at 18 Mpc is a long-standing goal for studies of stellar evolution. Right: UV fluxes (1500\AA) for massive stars (triangles = B-type supergiants; diamonds = O-type stars) at increasing distances, compared to five orbits of HST spectroscopy (at $R \sim 2000$). At least a 12m aperture is required for UV spectra of individual massive stars in I Zw 18..

of individual stars, will be feasible with future ground-based, multi-object spectrographs aided by adaptive optics (e.g., TMT, ELT). However, UV data are crucial to build the complete description of the stars.

Such observations require the sensitivity and spatial resolution of *at least a 12-m aperture facility in space* (see **Figure A-46**). High-quality UV spectroscopy over $1200 - 1800\text{\AA}$ of individual luminous stars will constrain their mass-loss rates, shocks, structure, and velocity fields of their winds. Only with access to UV spectra of these objects can we fully characterize their natures and test theoretical predictions for the properties of such stars in the early Universe.

A.28.3 The science program

LUMOS onboard LUVUOIR will enable the first thorough characterization of the winds of metal-poor (from 10% down to 2–3% solar) massive stars with mid-resolution ($R = \lambda/\Delta\lambda \geq 5000$) UV spectroscopy. The combination of the large aperture of LUVUOIR and the multiplex of LUMOS will allow us to mine metal-poor galaxies out to the outer edges of the Local

Program at a Glance

Science goal: The physical properties of massive stars at very low metallicities, akin to those in the early Universe.

Program details: UV spectroscopy of individual massive stars in the galaxy I Zw18 at a distance of 18 Mpc.

Instrument(s) + configuration(s): Multi-object spectroscopy with LUMOS (G155L).

Key observation requirements: UV spectroscopy spanning 1000 to 2000\AA (essential), to 2500\AA (desirable).; $R \geq 5000$; $S/N > 20$ per resolution element at 1500\AA .

Group, other neighboring groups, and ultimately I Zw18 (see **Figure A-46**). The data will provide definitive answers to pressing questions regarding the properties and evolution of high-mass stars including:

- The first observational parameterization of radiation-driven winds at very low metallicities ($<10\%$ solar), with consequences for models of Pop III stars and stellar evolution in the early Universe, and population-synthesis models used to interpret observations of high- z galaxies.
- Direct tests of ‘chemically-homogeneous evolution’ at such low metallicities, and a characterization of their winds. This evolutionary channel has been invoked to explain the binary system in the first LIGO detections (e.g., de Mink & Mandel, 2016) but lacks observational confirmation.

References

- Abbott et al. 2016, *Phys. Rev. Lett.*, 116, 061102
Bouret et al. 2015, *MNRAS*, 449, 1545
Bresolin et al. 2007, *ApJ*, 671, 2028
Camacho et al. 2016, *A&A*, 585, A82
de Mink & Mandel, 2016, *MNRAS*, 460, 3545
Evans et al. 2007, *ApJ*, 659, 1198
Fullerton et al. 2006, *ApJ*, 637, 1025
Garcia et al. 2014, *ApJ*, 788, 64
Haiman & Loeb, 1997, *ApJ*, 483, 21
Herrero et al. 2012, *A&A*, 543, A85
Kudritzki & Puls, 2000, *ARA&A*, 38, 613
Leitherer et al. 2001, *ApJ*, 550, 724
Mokiem et al. 2007, *A&A*, 473, 603
Prochaska et al. 2003, *ApJL*, 595, L9
Robertson & Ellis 2012, *ApJ*, 744, 95
Sundqvist et al. 2014, *A&A*, 568, A59
Tramper et al. 2011, *ApJL*, 741, L8
Venn et al. 2003, *AJ*, 126, 1326
Vílchez & Iglesias-Paramo 1998, *ApJ*, 508, 248

A.29 White dwarfs as probes of fundamental astrophysics

Martin Barstow (University of Leicester) & Boris Gänsicke (University of Warwick)

A.29.1 Introduction

White dwarfs (WDs) are the remnants of all stars with initial masses less than $8 M_{\odot}$, and they provide important laboratories for the study of stellar evolutionary processes and the behaviour of matter at extremes of temperature and density. As some of the oldest objects in the Galaxy they are useful cosmological clocks, placing strong limits on the ages of globular clusters and disk populations. They are implicated in the production of Type Ia supernovae, on which the cosmological distance scales and the existence of Dark Energy are predicated, even though the precise mechanism(s) remain unresolved.

In the strong gravitational fields associated with white dwarfs, it is predicted that their atmospheres should be pure H or He (depending on the prior evolution), devoid of heavier elements, which sink out of the surface layers. However, many studies (e.g., Barstow et al. 1993, 2003) have demonstrated that white dwarf atmospheres containing metals are ubiquitous (**Figure A-47**). While the presence of this material was initially attributed to the effect of radiative levitation, this mechanism was unable to explain the detailed abundances or the presence of metals in cool white dwarfs, where the radiative effects are negligible. It is now evident that many white dwarfs are accreting material from extrasolar planetary debris (e.g., Jura et al. 2009, 2012; Gänsicke et al. 2012; Barstow et al. 2014). Consequently, the study of white dwarf atmospheres provides a unique opportunity to determine the composition of these bodies.

It has been shown theoretically, in theories of quantum gravity, that fundamental constants, such as the fine structure constant (α) and the electron/proton mass ratio (μ) can vary

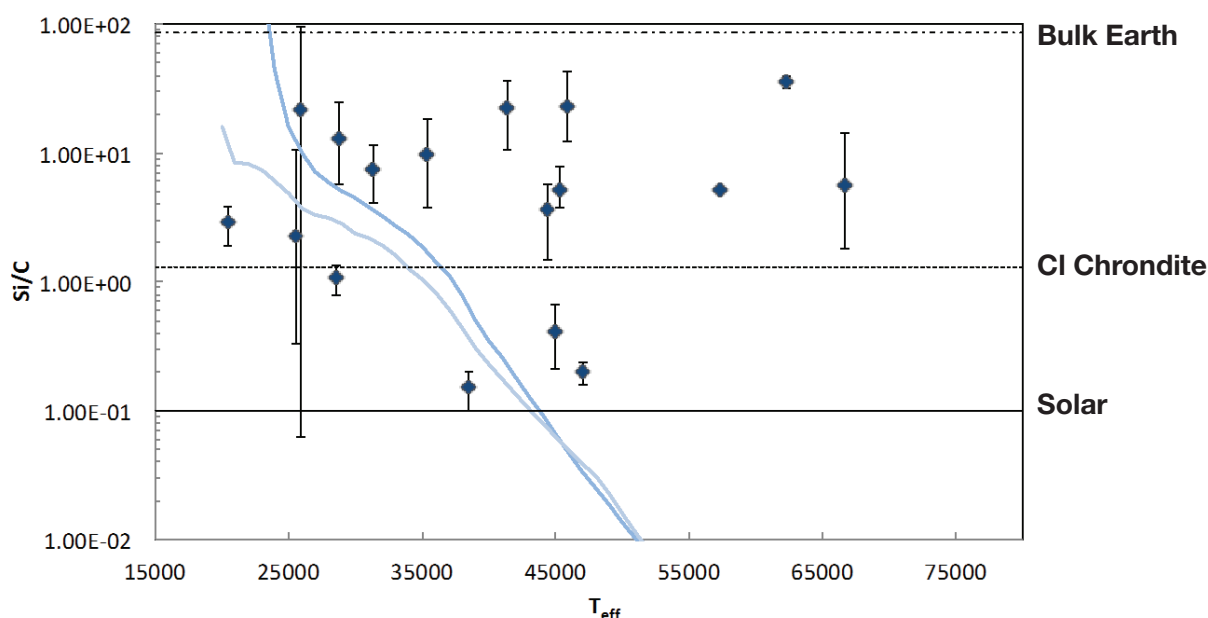


Figure A-47. Si to C ratio for a sample of 17 white dwarfs observed in the far-UV by FUSE. Most stars show evidence for accretion of rocky material.

in the presence of a strong gravitational field. Such variations are expected to manifest as small shifts in the wavelengths of atomic and molecular transitions. With UV spectra containing the absorption lines of many such transitions, white dwarfs have been used to study the potential effects (Berengut et al. 2013; Bagdonaite et al. 2014) but the work is limited to a few of the very brightest white dwarfs.

A.29.2 The role of LUVOIR

White dwarfs have been studied in the UV for around 40 years, initially by IUE and then HST. While this work has yielded many important and exciting scientific results, it has generally been limited to a small and heavily biased sample. White dwarfs are Earth-sized, and hence intrinsically faint, and even with the improved throughput of COS, high-resolution ultraviolet spectroscopy can only be obtained for either very nearby (<20 pc) or young (<100 Myr) and therefore hot white dwarfs, severely limiting our understanding of the underlying physics, and the wider diagnostic power of these stellar remnants. LUVOIR will provide a unique opportunity to address these shortcomings. The larger aperture will observations of fainter objects, increasing the accessible sample, but also yield reduced data collection times making the collection of suitable stellar samples more efficient. In addition, the dramatic improvement in the diffraction limited resolution enabled by the larger aperture, coupled with coronagraphic capability for the most extreme luminosity ratios, will open up the possibility of resolving binary systems with smaller separations and/or at greater distances.

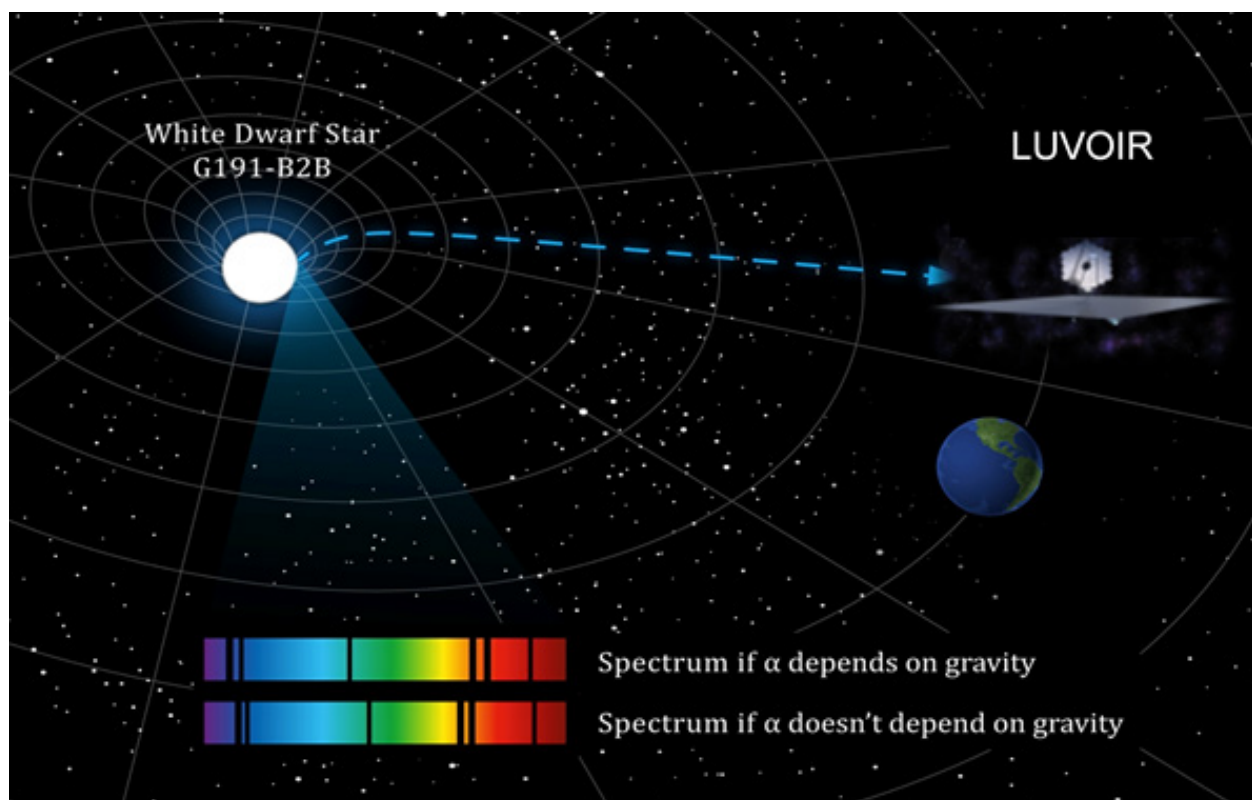


Figure A-48. Schematic illustration of the effect of a dependence of the fine structure constant on gravity (image courtesy of Julian Berengut).

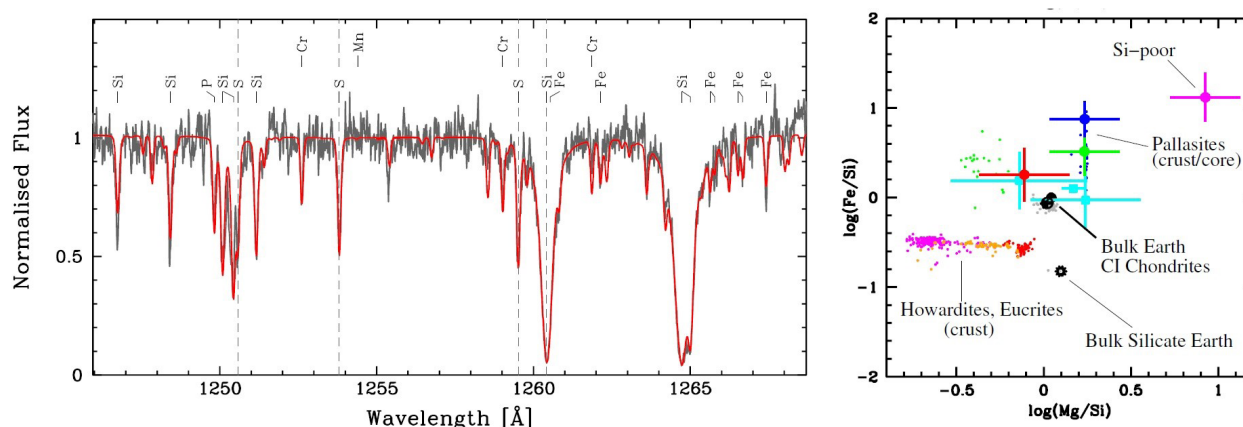


Figure A-49. The bulk abundances of disrupted exoplanetary bodies measured from far-ultraviolet spectroscopy of white dwarfs (left) are consistent with rocky parent bodies (right: large dots = white dwarfs, small dots = solar system meteorites).

A.29.3 The science program

Knowledge of the WD ages is important in measuring the ages of stellar populations. However, such results depend on a thorough understanding of the evolution of WDs themselves and on predictions of the cooling rates. In turn, the masses, radii, and photospheric compositions affect these rates. Studies of WDs in binary systems potentially represent a direct test of the evolutionary models and the mass-radius relation, since the WD mass can be independently determined from the orbital and physical elements of the system. In practice, however, few such systems have been available to be studied in sufficient detail to make these comparisons. An important science goal is to build up statistically significant samples of binary systems where orbits can be determined and follow-up spectroscopy carried out.

Priorities in exoplanet research are rapidly moving from finding planets to characterizing their physical properties. Of key importance is their chemical composition, which feeds back into our understanding of planet formation. Mass and radius measurements of transiting planets yield bulk densities, from which interior structures and compositions can be deduced (Valencia et al. 2010). However, those results are model-dependent and subject to degeneracies (Rogers & Seager 2010; Dorn et al. 2015). Transmission spectroscopy can provide insight into the atmospheric compositions (Sing et al. 2013; Deming et al. 2013), though cloud decks detected in a number of super earths systematically limit the use of this method (Kreidberg et al. 2014). For the foreseeable future, far-ultraviolet spectroscopy of white dwarfs accreting planetary debris remains the only way to directly and accurately measure the bulk abundances of exoplanetary bodies. Significant progress will be made through the acquisition of a large sample of high-resolution UV spectra to provide these measurements.

Observing potential variations in the fine structure constant in white dwarf spectra is very challenging, requiring extremely high S/N and deep understanding of systematic wavelength calibration effects. Statistically, there is also benefit in observing a significant sample of objects to compare results between them. Any observed effect should be reproduced in stars of similar gravity. Furthermore, extending the sample to the extreme range of white dwarf gravities allows exploration of the dependence of α & μ on gravity, or at least places important limits, which can constrain the possible range of theories.

Program at a Glance

Science goal: Understanding the physical properties of white dwarfs, their evolution and their composition—leading to new insights into fundamental physics and the composition of rocky extra-solar planets.

Program details: High resolution UV spectra, some with polarimetry; High resolution imaging; coronagraphic imaging for a subset of systems

Instrument(s) + configuration(s): LUMOS/HDI/ONIRS/POLLUX

Key observation requirements: 25:1 in spectra for most surveys, but 100:1 + for fine structure constant studies; diffraction limited imaging at $v \sim 20$

A large UVOIR telescope in the 10 to 16-m aperture range will enable high S/N observations of several thousand white dwarfs, increasing potential sample sizes for the above programs by 1 to 2 orders of magnitude. The length of typical exposures (approx. 0.1 hour) will likely be small compared to observational overheads. Therefore, attention will need to be paid to minimizing target acquisition and readout times and optimizing the pattern of slews between targets to achieve a high observing efficiency so that projects requiring large numbers of short exposure are not too costly.

References

- Bagdonaite, J., et al. 2014, *Phys. Rev. Lett.*, 113, id. 123001
 Barstow, M.A., et al. 1993, *MNRAS*, 264, 16
 Barstow, M.A., et al. 2003, *MNRAS*, 341, 870
 Barstow, M.A., et al. 2014, *MNRAS*, 440, 1607
 Berengut, J.C., et al. 2013, *Phys. Rev. Lett.*, 111, id. 010801
 Deming, D., et al. 2013, *ApJ*, 774, 95
 Dorn, C., et al. 2015, *A&A*, 577, 83
 Gänsicke, B., et al. 2012, *MNRAS*, 424, 333
 Jura, M., et al. 2009, 694, 805
 Jura, M., et al. 2012, *ApJ*, 750, 69
 Kreidberg, L., et al. 2014, *Nature*, 505, 69
 Rogers, L.A., & Seager, S. 2010, *ApJ*, 716, 1208,
 Sing, D. K., et al. 2013, *MNRAS*, 436, 2956
 Valencia, D., et al. 2010, *A&A*, 516, 20

A.30 Characterizing the nuclear outflow at the galactic core

Andrew J. Fox (STScI), Rongmon Bordoli (NSCU), F. Jay Lockman (Green Bank)

A.30.1 Introduction

Two giant lobes of gamma-ray emitting plasma, known as the Fermi Bubbles, extend 12 kpc above and below the Galactic Center (GC). Since their discovery (Su et al. 2010), the Bubbles have been the subject of intense research, and their origin via AGN activity or nuclear star formation is still debated. Imaging at gamma-ray, X-ray, microwave, and radio wavelengths has revealed their morphology and energetics. Recently, UV absorption-line spectroscopy with the Cosmic Origins Spectrograph (COS) and Space Telescope Imaging Spectrograph (STIS) on the Hubble Space Telescope has opened a new UV window on the Fermi Bubbles and allowed us to study the spatial extent, kinematics, chemical abundances, and physical conditions of the nuclear outflow (Fox et al. 2015, Bordoloi et al. 2017, Savage et al. 2017, Karim et al. 2018). However, with HST, we are still limited to pointing at single background sources (AGN or massive stars). Furthermore, foreground dust limits the number of UV-bright sources in the GC region observable with HST/COS, particularly at low Galactic latitude.

A.30.2 The role of LUVUOIR

The multiplexing capability and high sensitivity of LUVUOIR/LUMOS would open up the study of *multiple* background sources (massive stars and AGN) in the GC region in each pointing. With a higher density of sources covered (LUMOS can easily reach FUV magnitudes of 20), we will map out the morphology, kinematics, and chemical abundances in the foreground absorbing gas more efficiently and comprehensively than is currently possible with HST. **Figure A-50** illustrates the geometry of the experiment.

A.30.3 The science program

This LUVUOIR program would have several primary goals:

- spatially mapping out the nuclear outflow with LUMOS/MSA around multiple stellar and AGN directions in the Galactic Center region.
- probing the physical conditions of cool clouds embedded in the outflow, via measurements and analysis of low-ion (Si II, C II, O I, S II, Fe II) and high-ion (C IV, Si IV, N V) UV metal-absorption seen toward the background targets.
- deriving the mass outflow rate, by modeling the absorbing clouds detected at various Galactic latitudes with kinematic models (Bordoloi et al. 2017).

The analysis would require high S/N and high-resolution ancillary 21 cm spectra from radio facilities (e.g. the Green Bank Telescope) to derive the reference H I column densities in each direction at high sensitivity ($\sim 10^{17} \text{ cm}^{-2}$) and resolution ($\sim 1 \text{ km s}^{-1}$). The value of the LUVUOIR/LUMOS data would be enhanced by these radio data.

LUVUOIR/LUMOS observations with the G120M grating ($R=30400$) will cover the wavelength range 1000–1480 Å over a field of view of 3×1.6 arcmin. Using the micro-shutter array will allow us to observe tens of massive stars in the high-density regions near the GC.

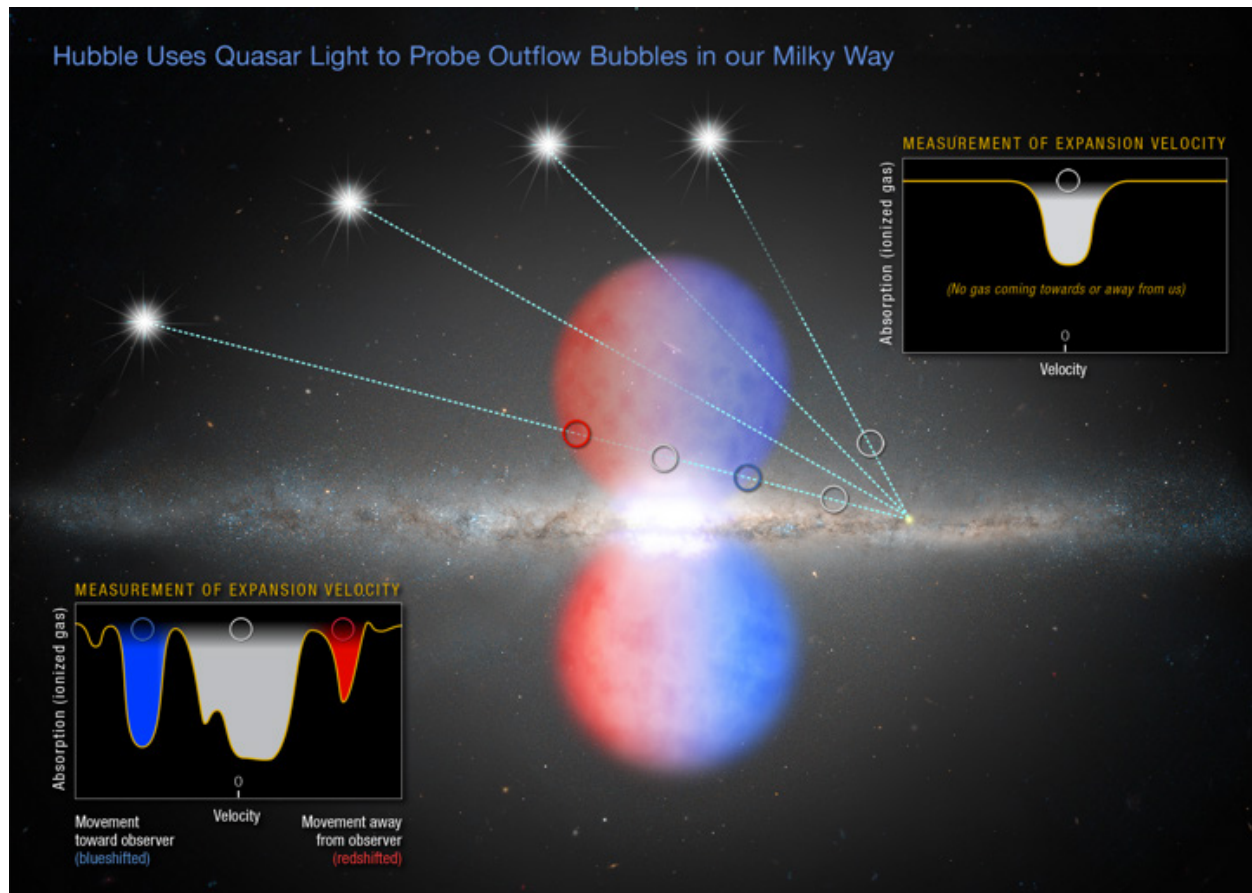


Figure A-50. Graphic illustrating our HST experiment to study the Fermi Bubble in UV absorption (courtesy Ann Field/STScI). The front- and rear sides of the Fermi Bubbles have different kinematic signatures.

Program at a Glance

Science goal: Map the galactic center nuclear outflow, probe cool clouds embedded in the outflow, and derive mass outflow rate.

Program details: LUVOIR UV spectroscopy will enable the study of multiple background sources (massive stars and AGN) to map the abundance, morphology, and kinematics of foreground gas in conjunction with ground-based 31 cm radio observations.

Instrument(s) + configuration(s): LUMOS spectroscopy G120 M grating

Key observation requirements: 1000–1480 nm, $R = 30000$, $S/N = 15$

Using the LUMOS ETC, we determine that with a 1-hr pointing and a 15 aperture, we can reach $S/N=15$ at 1300 Å for an O5V star with an FUV magnitude of 20 (AB system). For comparison, the HST/COS ETC shows that reaching $S/N=15$ on the same target with COS (G130M grating, 1291 setting) would take 8.3 hours. Therefore, this LUVOIR program represents an efficiency gain of a factor of almost an order of magnitude over what is possible

with HST/COS. Adding the effect of multiplexing further strengthens the case, since multiple massive stars may lie in the field of view.

References

- Bordoloi, R., Fox, A. J., Savage, B. D., Jenkins, E. B., et al. 2017, *ApJ*, 834, 191
Fox, A. J., Bordoloi, R., Savage, B. D. et al. 2015, *ApJL*, 799, L7
Karim, M. T, Fox, A. J., Jenkins, E. B., et al. 2018, *ApJ*, 860, 98
Savage, B. D., Kim, T.-S. Fox, A. J., Massa, D., et al. 2017, *ApJ*, 232, 25
Su, M., Slatyer, T. R., Finkbeiner, D. P. 2010, *ApJ*, 724, 1044

A.31 Ultraviolet haloes around edge-on galaxies

Benne W. Holwerda (University of Louisville) in collaboration with the SKIRT team (University of Gent)

A.31.1 Introduction

In the latest iterations of radiative transfer models of edge-on galaxies across from ultraviolet to the sub-millimeter regime (e.g., Popescu+ 2011, Holwerda+ 2012, Recently, De Geyter+ 2015, Mosenkov+ 2016, 2018), it has become clear that there is a dust-obscured ultraviolet component as well as a diffuse halo (see e.g., Seon+ 2014 and Seon & Draine, 2016, **Figure A-51**).

Models of the ultraviolet radiative transfer are complicated by both the localized nature of the origin in galaxies and the scatter from the dusty ISM (see **Figure A-52**). Similarly, the diffuse ultraviolet emission from inter-arm regions can either be from localized O-stars or scattered (Crocker+ 2015).

A way to test the nature of the diffuse UV emission in any of these galaxies that is completely independent from the panchromatic radiative transfer analysis is UV polarimetry, suggested by Baes & Viane (2016), Hodges-Kluck & Bregman (2014). If the UV halo emission is dominated by scattered radiation, we would expect a strong linear polarisation signature, similar as seen in reflection nebulae. Unfortunately, there is currently no UV polarisation instrument available. The total emission at these wavelengths is probably dominated by direct light from the stellar halo, but it is possible that the signature of a very extended dust distribution might still be visible in polarised light. Detailed polarised radiative transfer simulations should be used to test this.

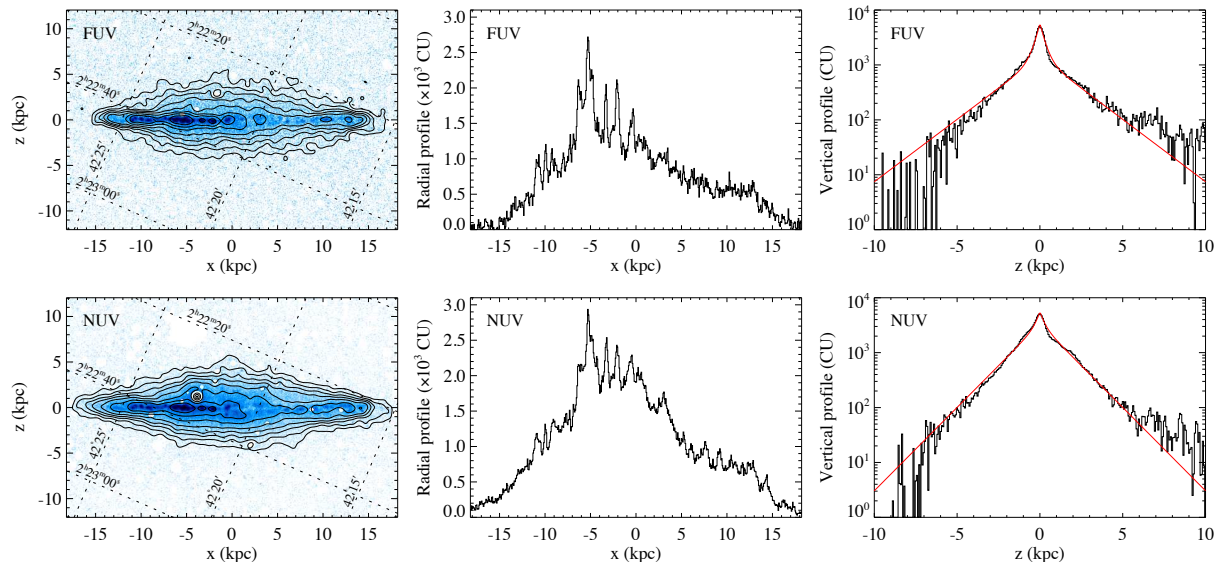


Figure A-51. *The NGC 891 ultraviolet halo from Seonet al. (2014).*



LUVOIR can observe the diffuse ultraviolet haloes in imaging, obtain spectra to identify the predominant stellar population behind them and polarization observations of the halo to determine how much of the light is scattered or not.

Program at a Glance

Program details: To detect and characterize the ultraviolet halo, one targets edge-on spiral disk galaxies (e.g., NGC 891) and the inter-arm regions in well-resolved face-on galaxies.

LUMOS spectroscopy – to determine the predominant stellar type responsible for the diffuse ultraviolet emission.

Key observation requirements: Key requirements are both FUV and NUV imaging to extremely low surface brightnesses ~ 32 mag/arcsec², R=3000 spectroscopy for stellar populations. A polarimeter to measure polarized light fraction.

A.31.3 The science program

The science program consists of deep imaging to detect ultraviolet haloes around galaxies.

Ultraviolet spectroscopy of the haloes will determine the dominant stellar populations and polarization imaging will be of extreme importance as well. Exposure times depend on the surface brightnesses needed for each galaxy.

References

- Crocker et al. 2015, *AJ*, 808, 76
Baes & Viane, 2016, *A&A*, 587, 86
De Geyter et al. 2015, *MNRAS*, 451, 1728
Hodges-Kluck & Bregman, 2014, *AJ*, 789, 13
Holwerda et al. 2012, *A&A*, 541, 5
Mosenkov et al. 2016, *A&A*, 592, 71
Mosenkov et al. 2018, in prep.
Popescu et al. 2011, *A&A*, 527, 109
Seon et al. 2014, *ApJ*, 785, 18
Seon & Draine, 2016, *ApJ*, 833, 201

A.32 The attenuation relation in overlapping galaxies

Benne. W. Holwerda (University of Louisville)

A.32.1 Introduction

Chance overlap of two galaxies (**Figure A-53**) is a relatively rare occurrence ($\sim 0.05\%$ of a redshift survey, see Holwerda et al. 2015) but the ones that do overlap can be used to constrain the dust content and distribution in the foreground disk (Keel & White, 1992, **Figure A-54**).

Attenuation curves could in principle be obtained using high-resolution, multi-wavelength data: high enough spatial sampling to resolve the ISM structure and well-spaced along the ultra-violet-optical-near-infrared to map the shape of the attenuation curves (**Figure A-55**).

Overlapping pairs have shown how dust is distributed in disk galaxies in unprecedented detail using the Hubble Space Telescope (e.g., Keel et al. 2001a,b, Holwerda et al., 2009) but ultra-violet information is currently only available for a single pair (Keel et al. 2014).



Figure A-53. An example of an overlapping pair of galaxies observed with the Hubble Space telescope (Howerda et al. 2009). The attenuation curve of this object is approximately Milky Way with ample variance. However, bluer information (e.g. UV coverage) would have revealed more detail in the attenuation curves. The study of overlapping pairs is moving from single objects such as these to galaxy population studies.

A.32.2 The role of LUV0IR

High spatial resolution and ultraviolet coverage would spell success in this particular project.

Other wavelength regimes can map the dust attenuation distribution but with LUV0IR observations of overlapping pairs, one can constrain the attenuation curves and spatial dependence with the foreground disk to the detail of structure of the ISM (e.g. parsec scale dust

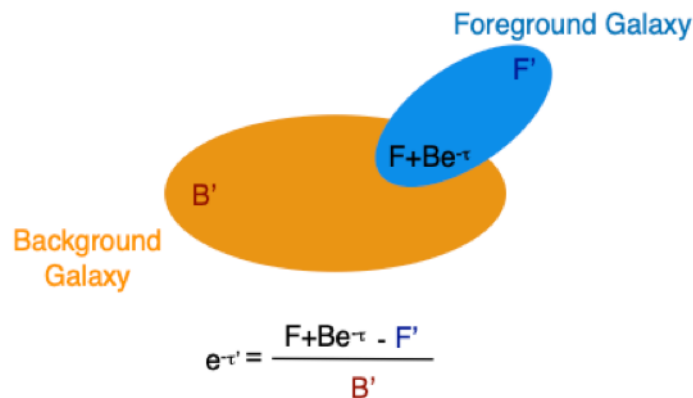


Figure A-54. The overlapping galaxy pair method. In a single image, flux measurement in the background (B') and foreground (F') galaxy on corresponding opposing sides to the overlap region ($F + Be^{-\tau}$) can be directly compared, assuming rotational symmetry of both systems.

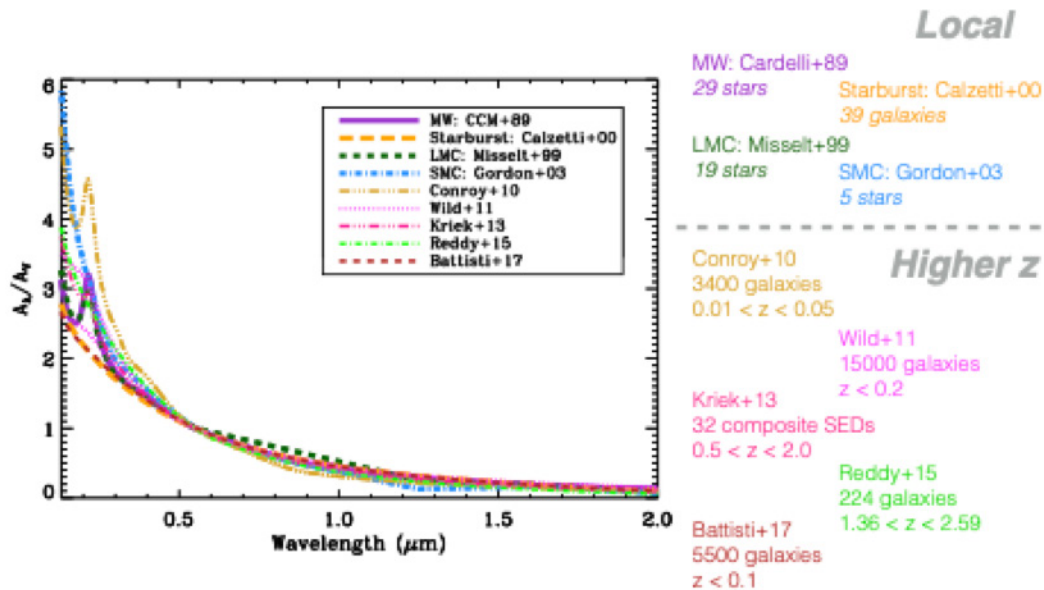


Figure A-55. The range of attenuation curves from different authors inferred for nearby and high redshift samples. The critical distinguishing features all lie below 3 μm . Figure courtesy of Lea Hagen.

clouds). This project would map the typical and variance of attenuation curves in galaxies, out to redshifts much greater than practical now ($z > 0.2$).

A.32.3 The science program

To truly distinguish between attenuation curves, one requires ultraviolet information. The presence or absence of the 2100 Angstrom bump in this wavelength regime is the critical distinguishing feature between Milky Way like attenuation curves and Magellanic Cloud ones (**Figure A-55**). The key deliverable will be a series of attenuation curves with both the mean and variance in attenuation curves in nearby galaxies as well as the prevalence of the UV “bump” and the dependence of these dust characteristics on galaxy properties (radius, mass, star-formation etc).

Program at a Glance

Science goal: To characterize the dust attenuation in overlapping galaxy pairs.

Program details: High resolution imaging of overlapping pairs in multiple filters, with one (medium) filter centered on the 2100 Angstrom “bump.”

Instrument(s) + configuration(s): Imaging, for detection and characterizing the event.

Key observation requirements: Key requirements are both FUV and NUV imaging to extremely low surface brightness ~ 32 mag/arcsec² and medium band filters to match the 2100 Angstrom bump at the redshift of the foreground galaxy. Alternatively, an ultraviolet IFU could be used.

References

- Holwerda et al. 2007, *AJ*, 134, 2385
Holwerda et al. 2009, *AJ*, 137, 3000
Holwerda et al. 2013a, *MNRAS*, 433, 47
Holwerda et al. 2013b, *A&A*, 556, A42
Holwerda et al. 2015, *MNRAS*, 449, 4277
Keel & White, 1992. *Nature*, 359, 6391
Keel et al. 2013, *PASP*, 125, 2
Keel et al. 2014, *AJ*, 147, 44

A.33 Quest for the first quasars

Yoshiki Matsuoka (Ehime University)

A.33.1 Introduction

One of the greatest achievements of modern optical/infrared astronomy is the discovery of ubiquitous supermassive black holes (SMBHs) throughout the universe (e.g, Kormendy & Ho 2013). Almost all massive galaxies in the local universe harbor a central SMBH, as evidenced by stellar and gaseous kinematic measurements. In the more distant universe, we know the presence of numerous quasars and active galactic nuclei (AGNs), whose energetic radiation is believed to originate from mass accretion onto a SMBH. As such, SMBHs are recognized as a major constituent of the baryonic universe. Furthermore, they may well control the fate of the host galaxies, as implied from the correlation between SMBH mass and galaxy bulge mass, and powerful gas outflows observed in quasar host galaxies, among other observational facts.

On the other hand, the origin of SMBHs is not yet known. The discoveries of SMBHs exceeding a billion solar masses (M_{sun}) at $z > 6$, where the universe is less than a billion years old, have provoked controversy on their seeding mechanism; SMBHs may be born as (i) remnants of the first stars with 10^2 – $10^3 M_{\text{sun}}$, which must be followed by extremely efficient mass accretion over a long time, (ii) products of runaway collapse of primordial star clusters, resulting in 10^3 – $10^4 M_{\text{sun}}$ seeds, or (iii) massive seeds with 10^4 – $10^5 M_{\text{sun}}$, resulting from direct collapse of primordial gas (e.g., Volonteri 2012). Observations of "the first quasars," representing the earliest stage of SMBH assembly from one or more types of the above seeds, are undoubtedly a key to disentangling the origin of SMBHs (see **Figure A-56**).

A.33.2 The role of LUVOIR

Quasars are expected to be extremely faint at the early stage of SMBH mass assembly, which took place in the very distant universe ($z > 10$). For example, a $10^5 M_{\text{sun}}$ SMBH at $z = 10^{-20}$, radiating at the Eddington limit, will have a rest-frame UV magnitude of 30–32 AB mag, which will be observed in near-IR wavelengths at $\lambda < 3 \mu\text{m}$. LUVOIR will be the first telescope with sufficient photometric sensitivity to detect such faint and distant signals.

A.33.3 The science program

The High Definition Imager (HDI) will be used for a square-degree scale imaging survey through a few near-IR bands. The survey field should overlap other multi-wavelength data sets, obtained by other space and ground-based instruments, in order to maximize various scientific potential when combined with the LUVOIR data. We will select $z > 10$ sources with the dropout technique; any source at $z > 10$ will be completely dark at $\lambda < 1.3 \mu\text{m}$ due to IGM absorption, which gives rise to a strong spectral break identifiable with near-IR multi-band photometry. Candidate first quasars will be searched for with broadband colors and inferred luminosity. Unfortunately, the emergent spectrum from a first quasar has been poorly studied so far. It may have an extremely red optical/IR color, if surrounding hydrogen gas heavily obscures the SMBH (Pacucci et al. 2015). On the other hand, if there are escape paths of photons from the vicinity of the SMBH, then they would make the first quasars appear much bluer. Most luminous dropout sources at the relevant cosmic epoch may simply

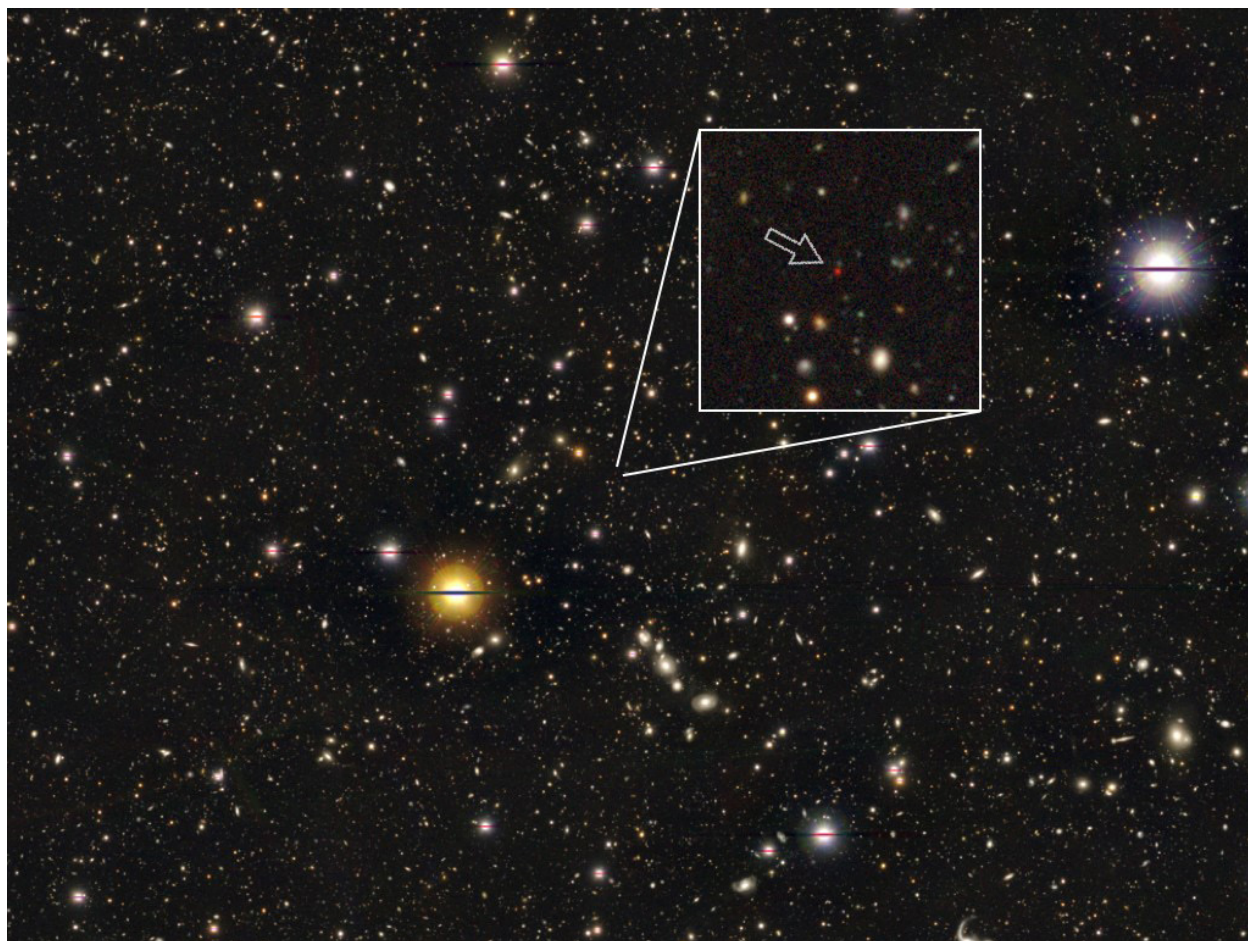


Figure A-56. A distant quasar discovered at $z \sim 6$, where the universe is less than a billion years old (Matsuoka et al. 2016, *ApJ*, 828:26). LUV OIR will probe even more distant universe, where the first quasars are being formed.

Program at a Glance

Science goal: We aim to discover “first quasars”, which represent the early evolutionary stage of supermassive black holes, with HDI extremely deep imaging.

Program details: a square-degree scale imaging survey in multi near-IR bands

Instrument(s) + configuration(s): HDI, imaging (+ grism spectroscopy)

Key observation requirements: 10σ depth of ~ 32 AB mag

be the first quasars, if a coeval (proto-) galaxy cannot produce a similar amount of radiation energy; this is indeed the case at the current observational frontier of $z = 6-7$, where virtually all sources with high luminosity (rest-frame UV absolute magnitude $M_{1450} < -24$ mag; Matsuoka et al. 2016) are quasars. The candidate first quasars thus identified will be followed up with ground-based extremely large telescopes, which will confirm the nature of the candidates through high-resolution near-IR spectroscopy. The grism mode of HDI may also be used to narrow down the photometric candidates. Ultimately, the spectroscopic

information and statistical properties, such as the number density as a function of SMBH mass and redshift, will be compared with theoretical predictions to disentangle the seeding mechanisms of SMBHs.

References

Kormendy & Ho 2013, *ARA&A*, 51, 511

Matsuoka et al. 2016, *ApJ*, 828, 26

Pacucci et al. 2015, *MNRAS*, 454, 3771

Volonteri 2012, *Science*, 337, 544

A.34 Exploring the high energy processes in microquasars as an exemplar case for high time resolution astrophysics

Warren Skidmore (Thirty Meter Telescope) and members of the TMT Time Domain ISDT

A.34.1 Introduction

High time resolution (between a few seconds to a few milliseconds) spectroscopic observing capabilities spanning the UV into the optical have applications across many areas of astrophysics, from the solar system to the high redshift universe. Here we describe one exemplar science case that requires observing capabilities that can be applied to many other cases.

Black hole X-ray binaries have a stellar mass black hole (a few to M_{\odot}) around which an accretion disk exists that is fed from a mass losing secondary star (**Figure A-57**). In many systems, high-speed jets of material are expelled in a situation very similar to that in AGN, this earns these systems the name of microquasars. Microquasars provide an opportunity to study the poorly understood jet acceleration mechanism and the mysterious process that harnesses the energy and angular momentum of accretion disk material to drive the jets. In AGN the region in which these processes are taking place are hidden by dust and gas but in microquasars they are directly visible however the timescales involved demand special capabilities from astronomical instruments.

In microquasars there are multiple processes occurring simultaneously; shocks at the base of the jets, flares from the accretion disk, reprocessing of X-rays to lower energies, synchrotron and cyclotron processes involving optically thick and optically thin emitting materials. Each process has different temporal and spectral characteristics. To disentangle the observed signals from each of the processes it is necessary to examine both the temporal and spectral characteristics together using time resolved spectroscopy that includes the UV and has the largest coverage to longer wavelengths.

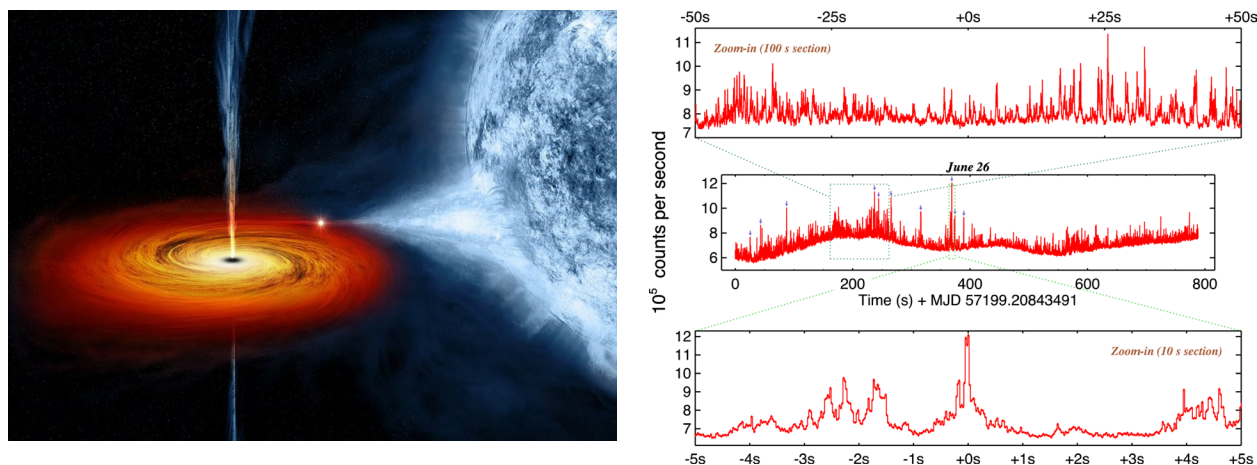


Figure A-57. Left: Artist's impression of the micro-quasar Cygnus X-1, showing material flowing from the mass-losing star and forming an accretion disk and the jets being driven out from the vicinity of the black hole. Right: Rapid optical variations in V404 Cyg observed with ULTRACAM on the 4.2-m WHT. Credit: Gandhi et al. (2016)

Program at a Glance

Science goal: Identify the observable signals of the stages of the process of converting accretion energy into power to drive the jets in microquasars and characterize each of those stages.

Program details: 100 to 400 nm, $R = 500$ LUMOS observations of a science target and 2 to 4 local field stars with $T_{\text{exp}} = 0.033$ s (100 to 400 nm) and 0.01 s (200 to 1000 nm)

Instrument(s) + configuration(s): 1. LUMOS multi-object (up to 5 targets) with fast read-out modes and G145 LL grating; 2. HDI grism multi-object (up to 5 targets) with fast read-out modes

Key observation requirements: Wide wavelength coverage, low spectral resolution, short exposure and fast readout modes.

A.34.2 The role of LUVOIR

Target brightness is $R \sim 12$, $B \sim 13.6$, however much of the variability may be constrained to emission lines. A large space based telescope with a moderate resolution UV/optical spectrograph is necessary in order to have the necessary wavelength coverage and acceptable S/N at the required sampling frequencies.

- **Far UV to blue (100 to 400 nm):** Sampling frequency of ~ 30 Hz with spectral resolution of $R \sim 500$.
- **Near UV to near IR (200 to 1000 nm):** Sampling frequency of ~ 100 Hz with spectral resolution of $R \sim 500$.

A.34.3 The science program

1. We would separately observe 4 microquasar targets (target brightness $R \sim 12$, $B \sim 13.6$, plus 2 to 4 local field stars to act as local photometric standards) using the LUMOS spectrograph with the G145 LL grating in a low multiplexing, wide wavelength coverage mode (100 to 400 nm). Each target would be observed for a duration of 2 hours with integration times of 0.033 sec giving $S/N \sim 20$.
2. As above (4 separate targets and local standards), except using the $R \sim 500$ GRISM mode on HDI and integration times of 0.01 s giving $S/N \sim 10$ to 20.

Further advances could be made using:

- Time resolved spectropolarimetric observations, as some of the variable emission is likely to be highly polarized.
- Coordinated simultaneous observations between X-ray to look at reprocessed signals and map the system (cross correlating to accuracies of ~ 1 millisecond)

However, these observations are not described here except to note the importance of high accuracy time stamps (better than ~ 10 μ s).

References

Gandhi, P., et al. 2016, *MNRAS*, 459, 554

A.35 Uncovering the transition between the cosmic dark age and the cosmic dawn

Masami Ouchi (University of Tokyo), Shotara Kikuchihara (University of Tokyo)

A.35.1 Introduction

Over the past two decades, studies of galaxy formation have made significant progress driven by deep observations with large ground-based telescopes, the spaceborne programs of Hubble/Sptizer Space Telescopes, and so on. These studies have photometrically and spectroscopically identified galaxies at up to redshift ~ 10 (Zitrin et al. 2015, Oesch et al. 2016), and they continue investigating galaxies at the redshift range of $z \sim 0.10$. These studies have provided details on the properties and the key cosmological evolutionary process of cosmic reionization when ionized atoms filled intergalactic space. Evolution of major galaxy quantities (including abundance and morphology) is revealed at this redshift range (Shibuya et al. 2015). Although there exist large uncertainties in physical parameters of galaxies, most observational results suggest that star-forming galaxies at $z > 6$ are major sources of cosmic reionization (Robertson et al. 2015). Interestingly, simple physical equations have consistently succeeded in explaining independent observational measurements of the cosmic star-formation rate density, stellar mass density, metal abundance, and cosmic microwave background (CMB) Thomson scattering optical depth (Madau & Dickinson 2014, Ishigaki et al. 2017). This indicates that a rough observational picture of galaxy formation and cosmic reionization is being established.

However, there remains a large missing piece in our understanding of galaxy formation: the formation of the first stars. Because the first stars formed from primordial gas with no efficient metal coolants, their formation process is highly unknown. Theoretical studies predict that the first stars preferentially had very high-mass stars within a star cluster, where gas collapsed due to the inefficient gas cooling, with large uncertainties regarding feedback effects caused by the stellar radiation heating the gas (Hirano et al. 2015). Such high mass stars might evolve into black hole binary systems whose merger events may be the source of the type of gravitational wave (Kinugawa et al. 2014) recently identified with the advanced LIGO experiment (Abbot et al. 2016). Moreover, such metal-free high mass stars should have a high production efficiency of hydrogen-ionizing photons with an energy of > 13.6 eV that are sources of cosmic reionization. Due to the limited sensitivities of the present-day large telescopes and the planned next generation telescopes (e.g. TMT, GMT, JWST, and WFIRST), only LUVOIR could explore the first stars found in the epoch of the transition between the cosmic dark age and cosmic dawn.

A.35.2 The role of LUVOIR

Given the extremely high sensitivities of LUVOIR in conjunction with gravitational lensing magnification, the first stars/clusters and the cosmic reionization process will be investigated for the first time. We outline three scientific cases below.

1. LUVOIR has the capability to detect the first stars and clusters at $z \sim 10$ beyond $M \sim -10$ mag using gravitational lens magnification from massive galaxy clusters. **Figure A-58** presents the observational parameter space covered by LUVOIR A (15.1m primary),

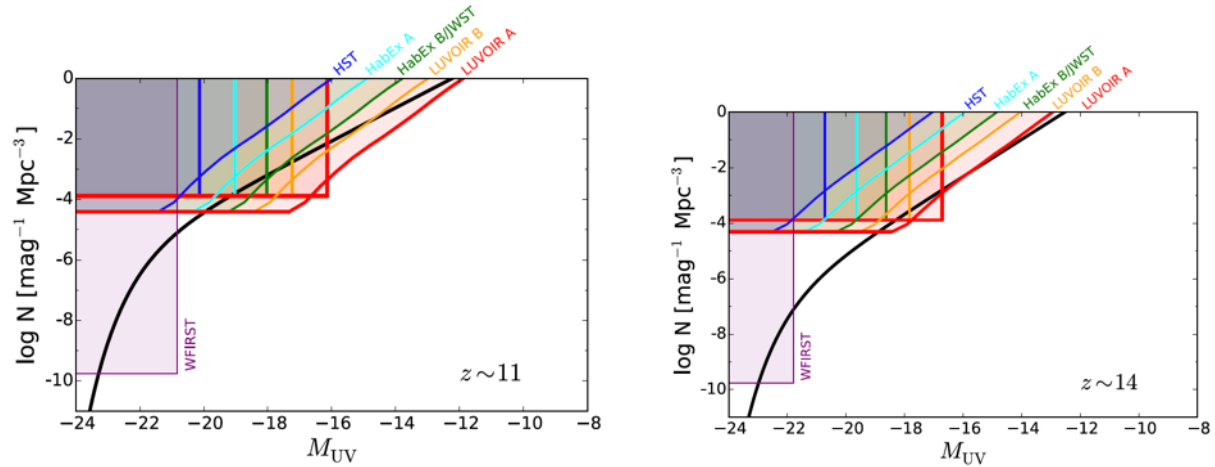


Figure A-58. (Left) Observational parameter space of LUVUOIR A (red lines), LUVUOIR B (yellow lines), HabEx B/JWST (green lines), HabEx A (cyan lines), WFIRST (magenta line), and HST (blue lines) that are compared with the estimated luminosity function of galaxies (black line) at $z \sim 11$. The vertical (diagonal) line part of the red, yellow, green, cyan, magenta, and blue lines indicate the observational parameter space accomplished by ~ 100 hour on-source integration in a blank field (in a galaxy-cluster field with gravitational lensing effects). (Right) Same as the left panel, but for galaxies at $z \sim 14$.

LUVUOIR B (9.2m), a hypothetical HabEx B/JWST (6.5m), HabEx A (4.0m), and HST (2.4m) compared with the expected luminosity function of galaxies at $z \sim 11$ and 14. Here, we assume the massive cluster lensing studies conducted in the past Hubble Frontier Fields (HFF; PI: J. Lotz) studies (Ishigaki et al. 2015, 2017). Although HabEx B/JWST will identify galaxies at this redshift range, the detection limit of HabEx B/JWST is not deep enough to detect either the first star clusters or the first stars even with a high gravitational lensing magnification of ~ 10 – $100\times$. The high latitude survey of WFIRST may pinpoint a lensed cluster of the first stars with a very high magnification factor, but successful identification may be extremely difficult (e.g. Zackrisson et al. 2015). In conjunction with gravitational lensing magnification in massive galaxy cluster fields, it is likely that identification of the first stars and star clusters at $z \sim 10$ – 14 near/below $M \sim -10$ mag needs LUVUOIR's capability of extremely deep near-infrared observations.

2. For the first time, the extremely deep imaging capability of LUVUOIR can identify the true faint ends of luminosity functions below $M \sim -15$ mag at $z \sim 10$, where a truncation of the luminosity function is expected. Theoretical studies suggest the truncation is a key quantity needed for understanding feedback from by star-formation/AGN activities and UV background radiation. The feedback of the UV background radiation has a tight correlation with the history of cosmic reionization.
3. If LUVUOIR includes an imaging capability of $\sim 1\%$ -width narrow bands with central wavelengths of $\sim 1\mu\text{m}$, there is a possibility to map out the $\text{Ly}\alpha$ intensity distribution (and evolution) that originated from cosmic HII bubbles that existed at the epoch of reionization (EoR). Because the field-of-view of LUVUOIR is probably not large, one may need to target the moderately early phase of the EoR, say at $z \sim 8$ – 10 . The $\text{Ly}\alpha$ intensity distribution

Program at a Glance

Science goal: Explore the early days of galaxy formation at the epoch of the transition between the cosmic dark age and cosmic dawn.

Program details: Detect the first stars at $z \sim 10$ using gravitational lensing. Identify the faint end of the stellar luminosity function below $M \sim -15$ at $z \sim 10$. Map out Ly α intensity from cosmic HII bubbles during the epoch of reionization.

Instrument(s) + configuration(s): HDI imaging + grism for deep NIR observing.

Key observation requirements: S/N ~ 5 for first stars/clusters. NIR imaging and spectroscopy. Narrow band ($\sim 1\%$) filters near $1 \mu\text{m}$ for Ly α mapping of HII bubbles.

will allow us to understand topology of reionization that depends on ionizing sources such as star-forming galaxies (stars), faint AGN, etc. These LUVOIR results will be complementary to those from the next-generation 21cm observations such as SKA that map out HI distribution at EoR. Because the feasibility of the cosmic HII bubble mapping is not clear yet, the feasibility should be investigated soon for the LUVOIR program.

A.35.3 The science program

We will address the three issues detailed above the three scientific cases, exploiting the extremely high sensitivities of LUVOIR. This will involve NIR imaging and spectroscopy of deep epochs of cosmological time. LUVOIR would target faint-end objects including the first stars/clusters that cannot be reached by the present-day and the planned next generation telescopes that study bright objects with a magnitude of ~ 20 mag.

References

- Abbot, et al. 2016. *ApJL*, 826, L13.
 Hirano, S., *ApJ*, 814, 1.
 Ishigaki, M. 2017, *MNRAS*, 468, 3.
 Ishigaki, M 2015. *PASJ*, 67, 3.
 Kinugawa, T. et al. 2014. *MNRAS*, 442, 4.
 Madau, P and Dickinson, M. *Annu. Rev. Astron. Astrophys.*, 52, 416.
 Oesch, M. et al. 2016, *ApJ*, 819, 129.
 Robertson, B. et al. 2015, *ApJL*, 802, L19
 Shibuya, T. et al. 2015, *ApJ Suppl.* 219, 15.
 Zackrisson et al. 2015, *ApJ*, 810, 1.
 Zitrin, A. et al. 2015, *ApJL*, 810, 12.

APPENDIX B. DESIGN REFERENCE MISSIONS

B.1 The LUVOIR science simulation tools

The LUVOIR team has produced a set of online software tools to enable quick, accurate performance estimation and facilitate team and community input to the LUVOIR concept study. Since many of the science return calculations included in these Design Reference Mission documents utilized these tools, we briefly describe them here. These tools evolved during the course of the LUVOIR study as the observatory designs matured. However, all of them may also be used to estimate performance of observatories that differ from the exact LUVOIR-A and LUVOIR-B designs. This functionality was used to aid design trades during the LUVOIR study and make the tools useful for multiple purposes.

The tools were developed by the LUVOIR Simulations Working Group, led by Jason Tumlinson (STScI), with major contributions from Giada Arney (NASA GSFC), Graham Kanarek (STScI), Tyler Robinson (NAU), and Geronimo Villanueva (NASA GSFC). All but one of the tools are hosted by STScI and are accessible through the LUVOIR website at <https://asd.gsfc.nasa.gov/luvoir/> (**Figure B-1**). Planetary Spectrum Generator is hosted by GSFC. For all tools, the aim has been to make them easy to grasp for first-time users. Each one includes an “Info” tab that describes its usage and assumptions. The user may save plots and other results.

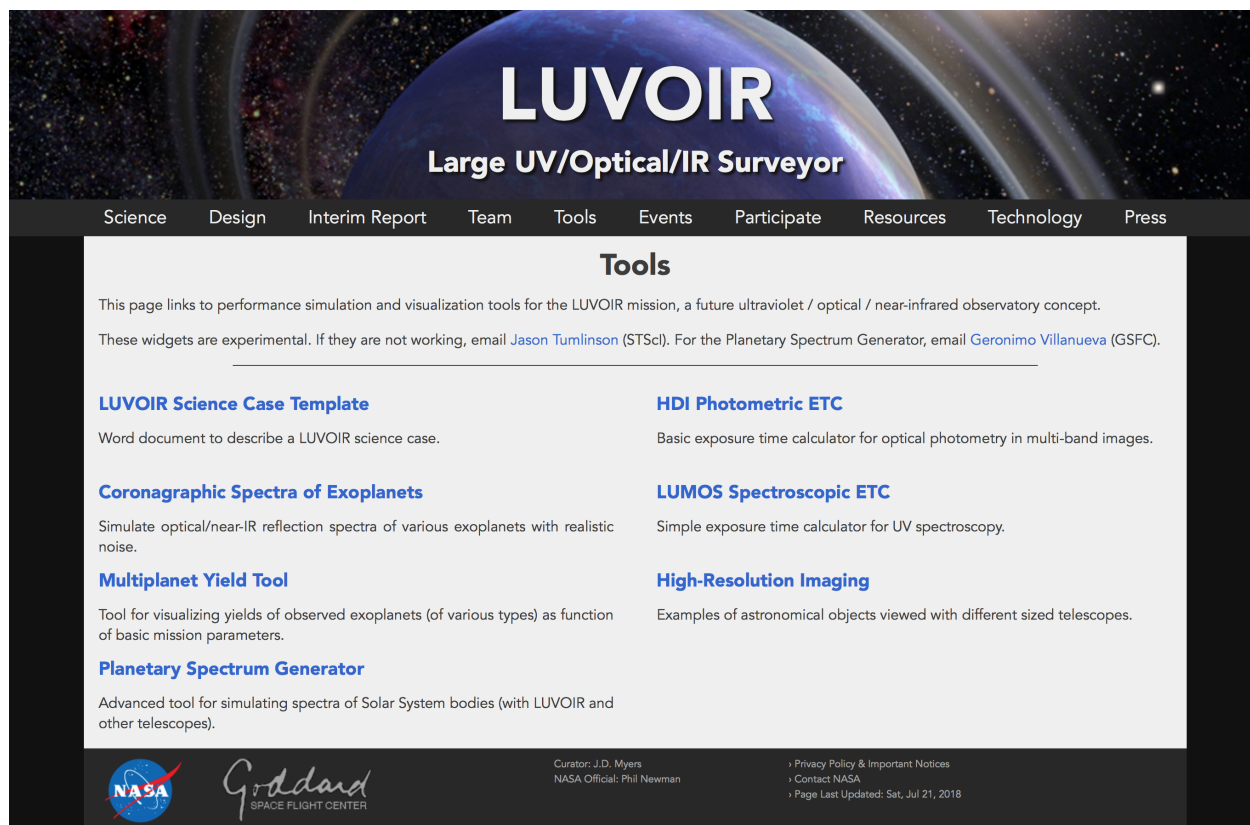


Figure B-1. Online LUVOIR Science Simulation Tools front page at <https://asd.gsfc.nasa.gov/luvoir/tools/>

The tools are written in python and make extensive use of the bokeh python library (bokeh.pydata.org). The underlying code is all open-source and available at github.com/tumlinson/luvoir_simtools. The GitHub repository includes instructions for how to use the code in local mode and its dependencies, as well as an ipython notebook with basic usage of the tools that can be adapted to many purposes.

B.1.1 Coronagraphic spectra of varied exoplanets

This richly featured tool is based upon the coronagraph noise model from Robinson et al. (2016) and calculates realistic, noisy direct spectra of many kinds of planets for an ECLIPS-like coronagraph (**Figure B-3**). Many model planet spectra are available, and both LUV OIR and ground-based spectra can be simulated. The library of planetary spectra allows users to select a wide range of planetary spectra, including as Earth-like worlds at different periods of Earth history, other solar system planets, false positive biosignature planets, mini-Neptunes, and warm Jupiters.

Noise terms include thermal radiation from the telescope, detector dark current and read noise, zodiacal light, exozodiacal light, and stellar light leakage. The ground-based mode also includes thermal radiation from the atmosphere and the wavelength-dependent transmissivity of Earth's atmosphere. Users can adjust these noise terms and can also change basic parameters such as the size of the planet, the semi-major axis of the planet's orbit, the

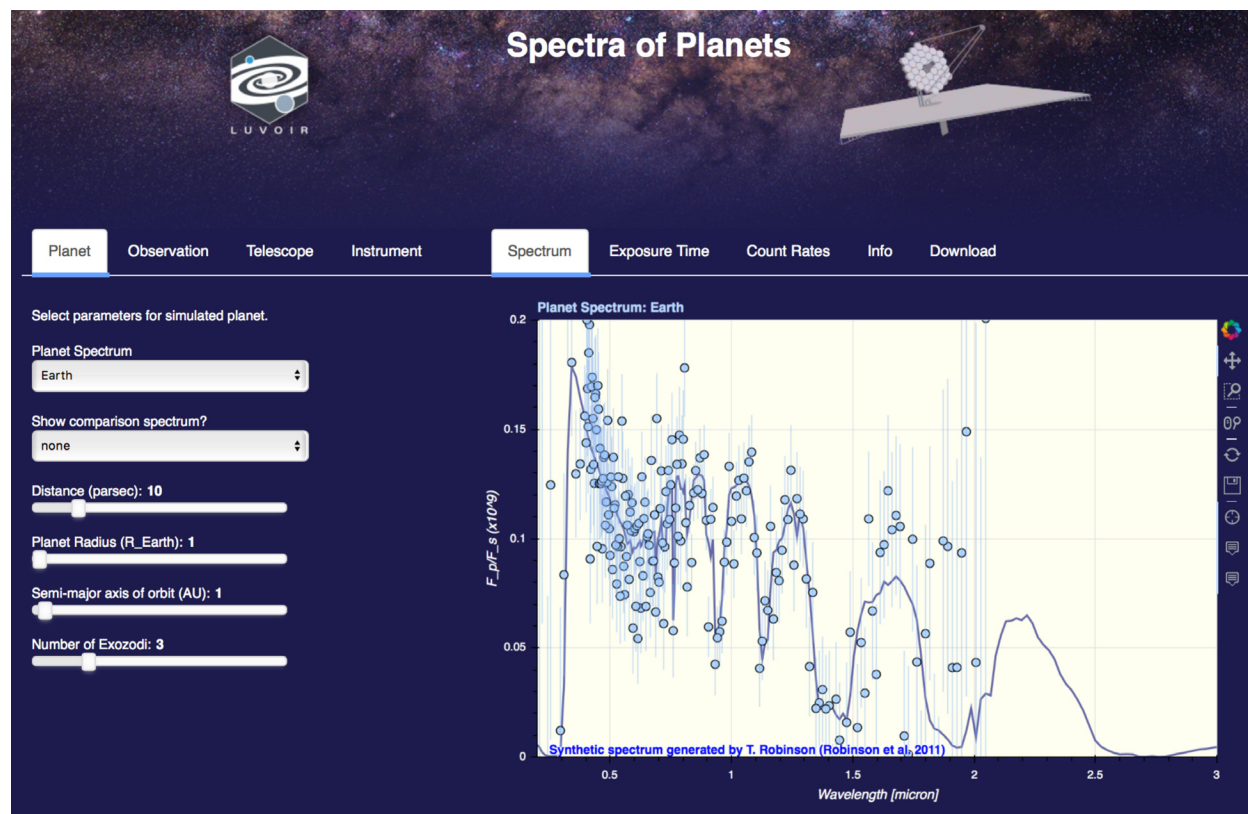


Figure B-2. Simulated coronagraphic exoplanet spectra. The "Spectrum" tab shows the spectrum of the selected planet with added noise. The "Exposure Time" tab shows the wavelength-dependent exposure time required to obtain a user-specified SNR. The "Count Rates" tab shows the wavelength-dependent planet flux and noise terms in counts/second.

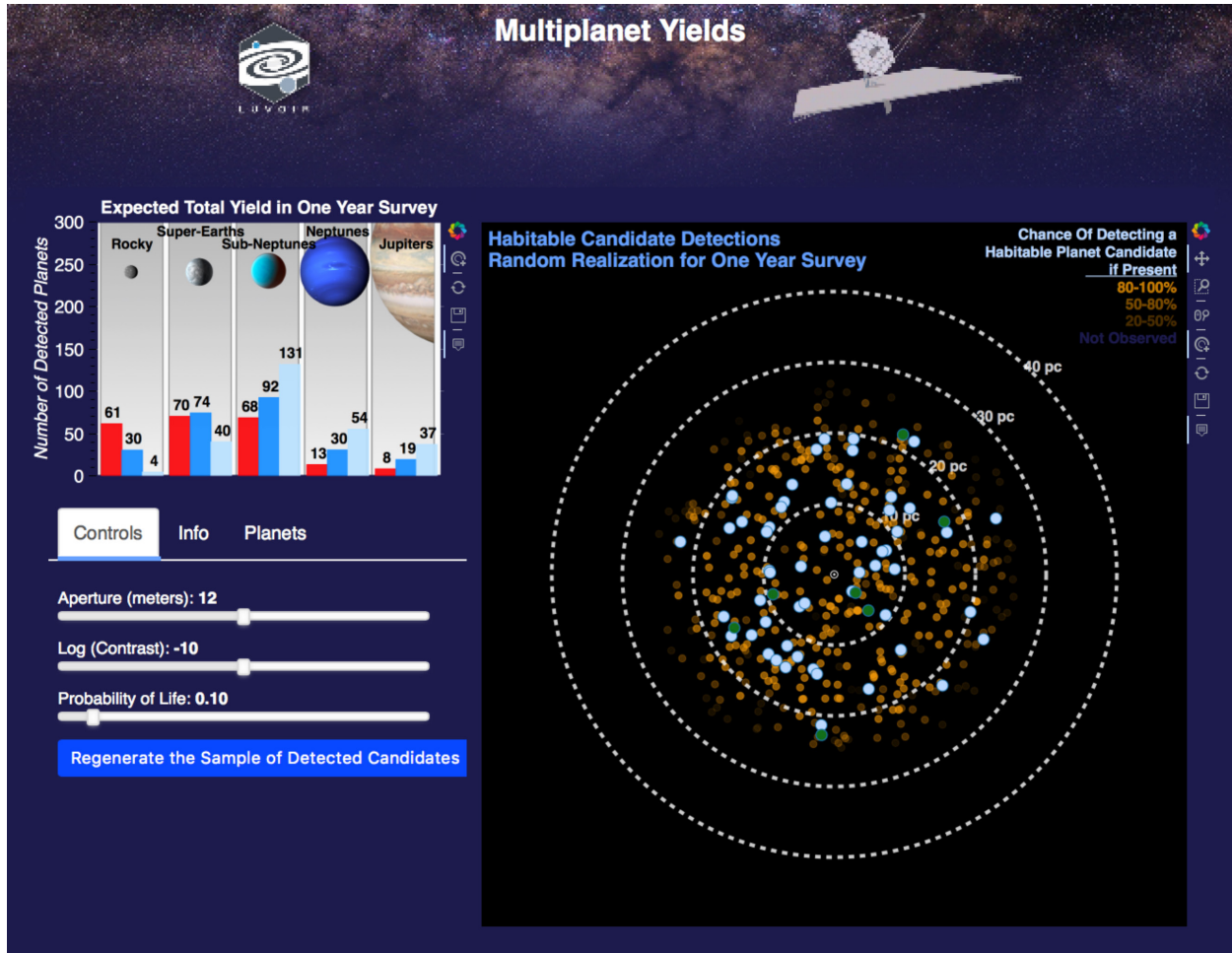


Figure B-3. Multi-planet yields visualization tool, which displays the user-selected telescope, instrument and planet/target properties in the bottom-left tabs, the expected yield in the top-left area, and a generated map of the odds of detecting a habitable planet candidate, assuming one is present, for stars within 40 pc of the Sun.

observer-system separation distance, the telescope diameter, the inner and outer working angles, the exposure time, the telescope temperature, throughput terms, and spectral resolution. Users may also choose to set all telescope and instrument parameters to the current LUVOR-A and LUVOR-B values. The desired signal-to-noise ratio (SNR) may also be selected, which the tool uses to calculate the exposure time required as a function of wavelength to achieve this SNR value.

B.1.2 Multi-planet yield tool

This tool visualizes multi-planet yield calculations based on the work in Stark et al. (2014, 2015, 2016). These yields assume one year of science exposure time (1.5 to 2 years total time including overheads) and the planet mass / orbit bins shown under the “Planets” tab (**Figure B-3**). The bar chart at left shows the expected numbers of different kinds of planets observed.

In the main panel, the planets colored in gold are shaded according to the fractional “yield” for that star (i.e., completeness) in the altruistic yield calculation. These estimated (probabilistic) yields are then sampled with random draws to highlight a hypothetical

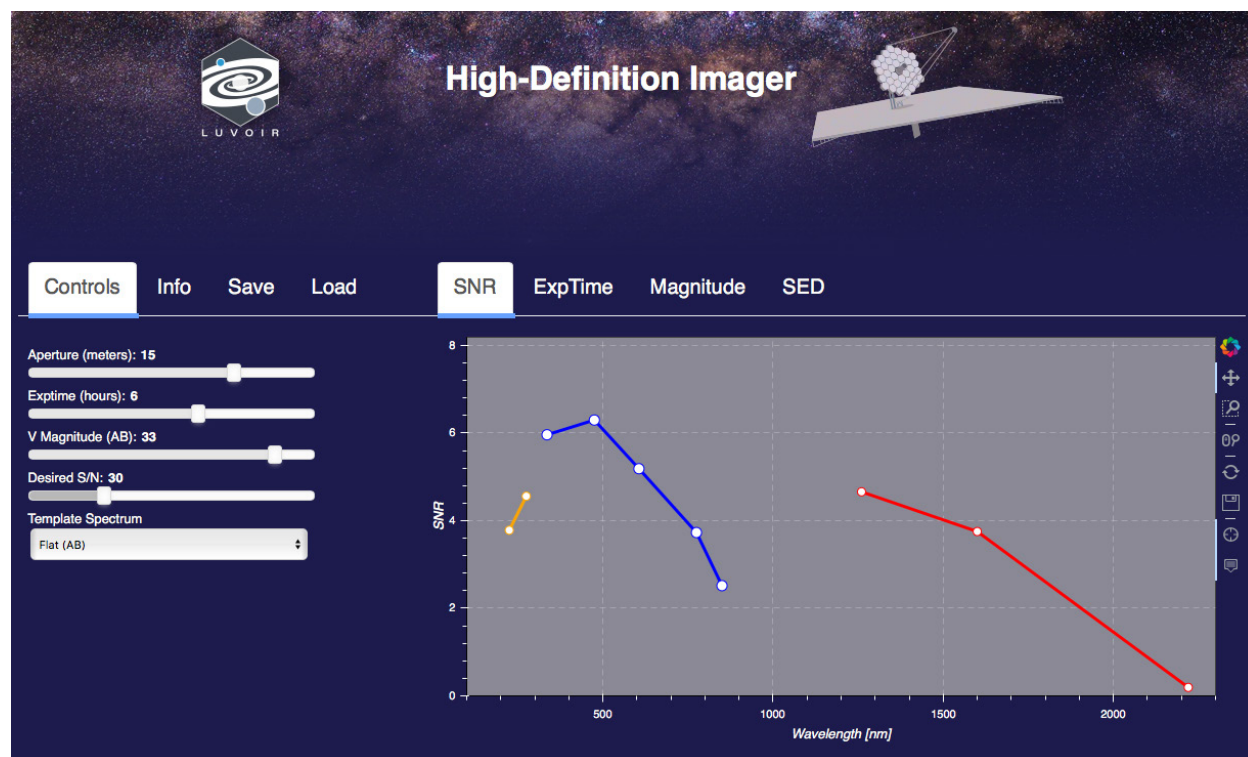


Figure B-4. HDI exposure time calculator results. For a flat continuum source normalized to AB = 33 mag, the signal-to-noise ratio returned in the V band is SNR=5. The “ExpTime” and “Magnitude” tabs show alternate results.

sample of detected “warm rocky” planets, which are marked in light blue. This sample is randomly drawn again according to the “probability of life” slider, which specifies the fraction of warm rocky planets with remotely detectable biosignature gases, which are marked in flashing green.

This tool demonstrates why dozens of habitable planet candidates are needed to perform a survey for habitable conditions and life in the nearby galaxy that can provide a statistically meaningful answer even if it is a null result. However, this is a generic tool to help understand how yields scale with three simple parameters (telescope aperture, coronagraph contrast, and probability of biosignatures). This tool was not however used to determine total exoplanet yields for the specific LUVOIR-A and LUVOIR-B designs. A full description of those more detailed calculations appears in **Section B.2**.

B.1.3 The High-Definition Imager exposure time calculator

This tool computes SNR limits and exposure times for imaging with HDI and LUVOIR-like telescopes with different aperture diameters (**Figure B-4**). A range of input spectral energy distributions are available. Users may save and restore their session by supplying a unique string that permits the user to save and restore their specific calculations. By supplying a unique string, the user names a file that will be stored on the STScI server.

B.1.4 The LUMOS exposure time calculator

This tool uses input template spectra of astronomical objects provided by the STScI pysynphot package to calculate SNR values for the UV modes of LUMOS paired with LUVOIR-like

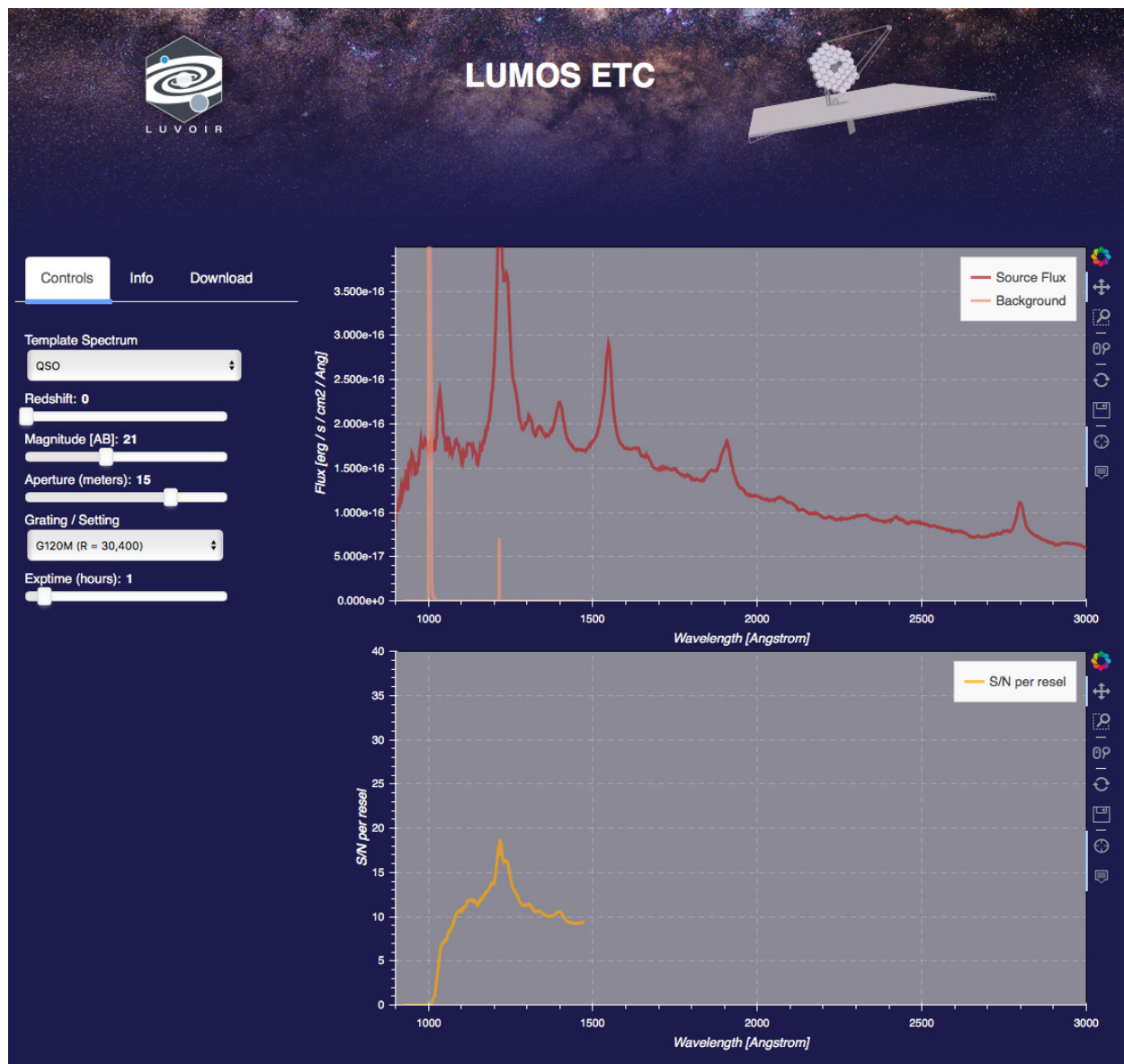


Figure B-5. LUMOS exposure time calculator.

telescopes of different sizes (Figure B-5). Normalization of template spectra is done in the GALEX FUV band. SNR is always given per resolution element.

B.1.5 High-resolution imaging gallery

This simple tool compares images at Hubble and LUVOIR-like spatial resolutions to illustrate the gains in image quality going from a 2.4 to a 12-m UV/optical telescope (Figure B-6).

B.1.6 Planetary spectrum generator

The Planetary Spectrum Generator (PSG) is a sophisticated online tool for synthesizing planetary spectra (atmospheres and surfaces) for a broad range of wavelengths (Figure B-7). The tool covers wavelengths from the extreme UV to the radio (50 nm to 100 mm), from any observatory (e.g., JWST, ALMA, Keck, SOFIA), any orbiter (e.g., MRO, ExoMars, Cassini, New

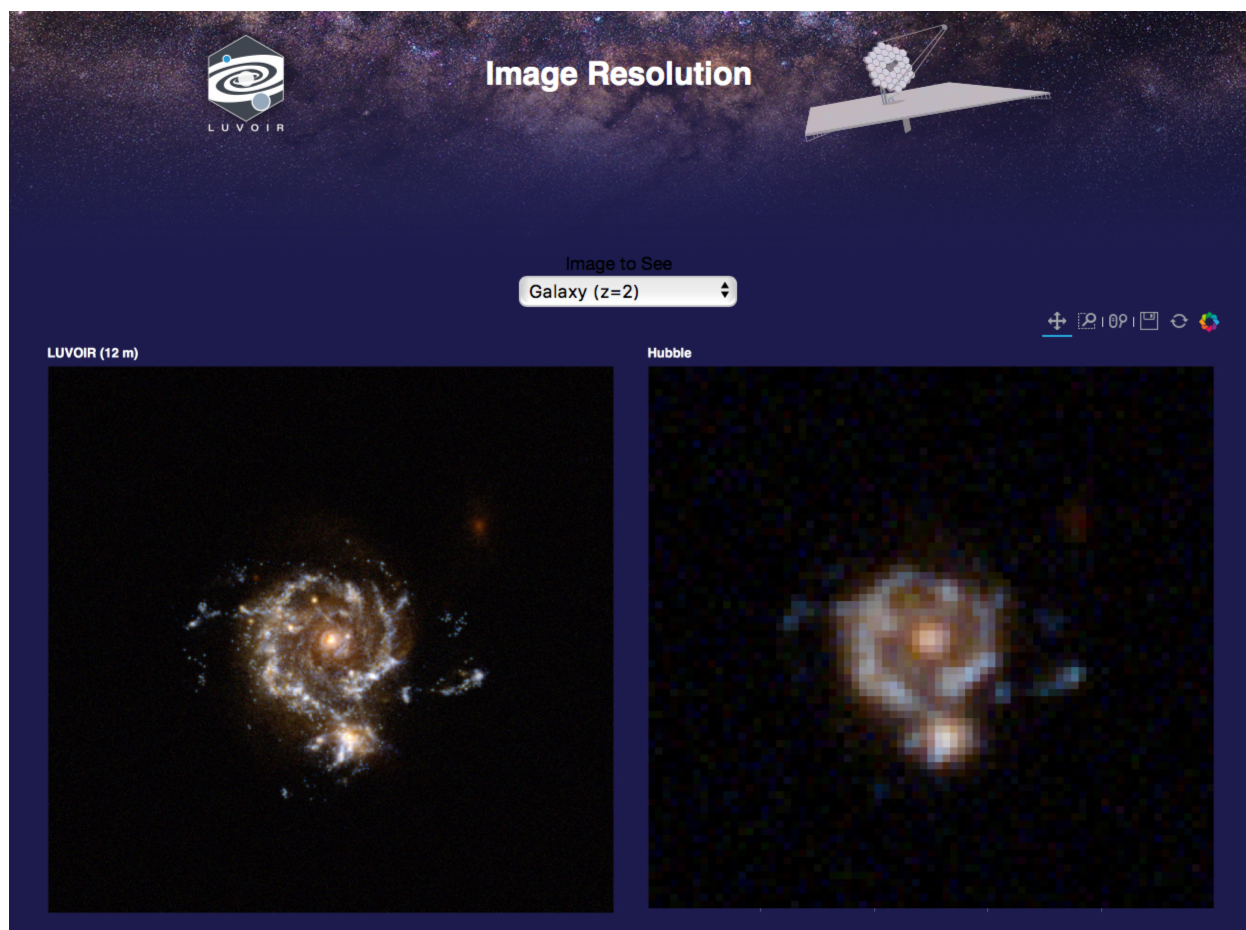


Figure B-6. Gallery of imaging simulations to visualize LUV OIR's spatial resolution.

Horizons), or any lander (e.g., MSL). This is achieved by combining several state-of-the-art radiative transfer models, spectroscopic databases and planetary databases (i.e., climatological and orbital).

The tool has the following capabilities:

- A 3D (three-dimensional) orbit calculator for most bodies in the solar system, and all confirmed exoplanets. The orbital calculator calculates all possible geometric parameters needed for computing spectroscopic fluxes. Possible observing scenarios are: observatory, from surface, nadir, limb, solar occultation and stellar occultation.
- Billions of spectral lines of almost 1,000 species from several spectroscopic repositories (e.g., HITRAN, JPL, CDMS, GSFC-Fluor).
- Atmospheric templates (vertical profiles of temperature and abundances) for the main atmospheres (Venus, Earth, Mars, Titan, Neptune, Uranus), and general atmospheric and surface parameters are available for the other bodies. For Earth and Mars several templates are available (Tropical, Polar, etc.). The code has a simplified model for cometary outgassing and dust distribution.

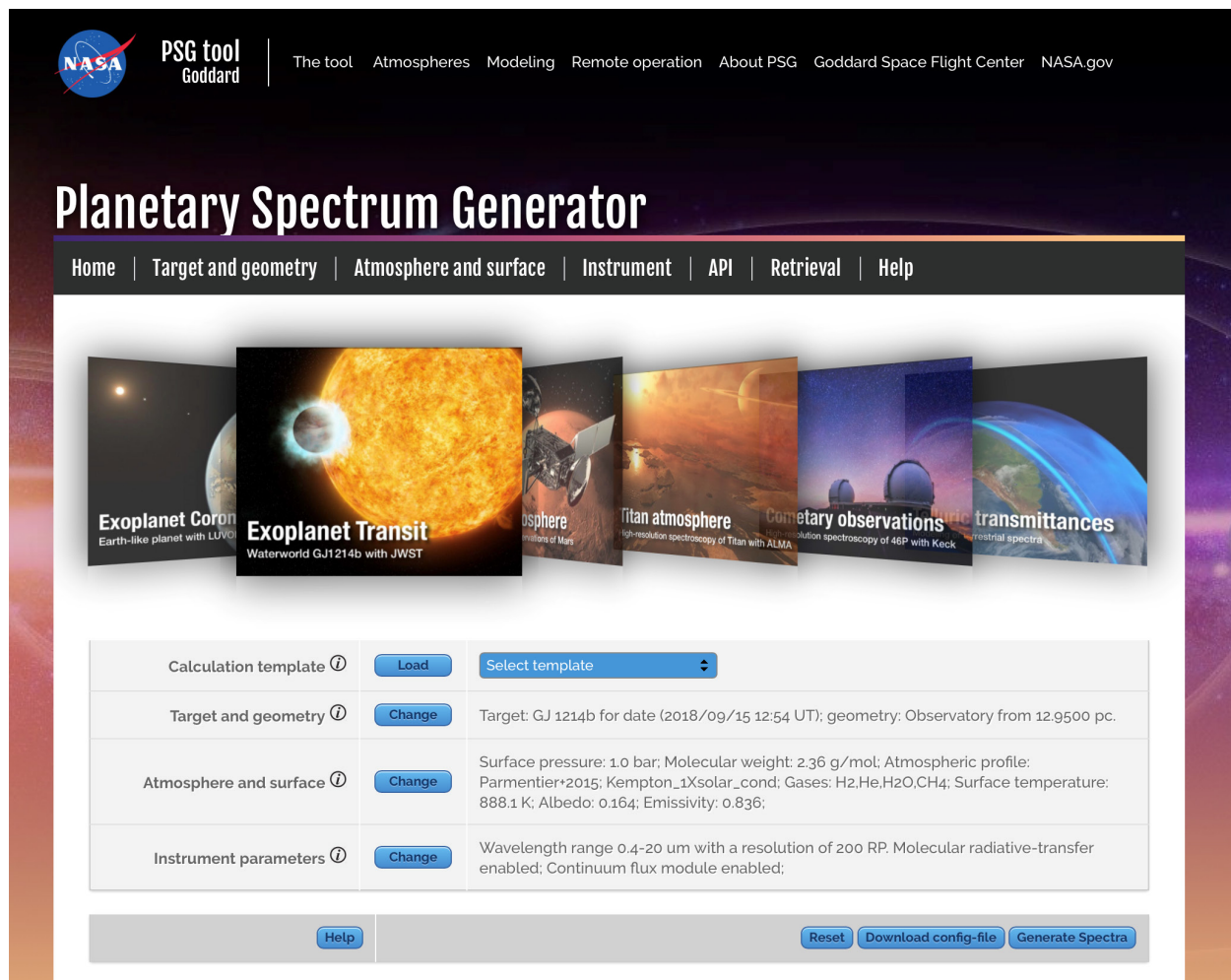


Figure B-7. Planetary Spectrum Generator.

- Radiative transfer analysis can be performed with several models:
 - Line-by-line and scattering, PUMAS
 - Correlated-k and scattering, PUMAS
 - Line-by-Line (LTE) Cometary Radio Model
 - Line-by-Line (non-LTE) Cometary Fluorescence Model
 - Generalized Continuum Model
- The code synthesizes spectra in any desired radiance unit (spectral radiance, spectral intensity, spectral flux, radiant energy density, irradiance, spectral irradiance, magnitude, etc.) and transmittance output—conversions between K, Jy, W/m²/sr, magnitude, can be useful.
- It includes the possibility to integrate stellar templates by adopting the Kurucz 2005 stellar templates (0.15–300 μ m), and the high-resolution ACE Solar spectrum (2–14 μ m) when considering the G-type template.

- The code allows application (or simply display) of terrestrial transmittances for a broad range of conditions (altitude and water vapor columns, also from SOFIA).
- PSG includes a realistic noise calculator for quantum and thermal detectors, that integrates several key instrument/instrument models (e.g., JWST, Keck, ALMA, SOFIA, IRTF, HST) and typical detector templates (CCD, heterodyne detectors, bolometers, etc.).

B.2 Signature Science Case #1: Finding habitable exoplanet candidates

B.2.1 Abstract

We quantify LUVOIR’s ability to detect and perform preliminary characterization of potentially Earth-like planets by simulating the execution of a 2-year survey optimized for exoEarths. We include community-consensus occurrence rates of exoplanets, all known sources of astrophysical noise, and high-fidelity simulations of instrument designs. Both versions of LUVOIR will detect and perform preliminary characterization on dozens of potentially Earth-like planets; LUVOIR-A will detect 54 such planets, while LUVOIR-B will detect 28. Newer coronagraph designs could potentially increase the LUVOIR-B yield by ~50%.

Program contact(s)

Christopher Stark (STScI)

Brief description

ECLIPS high-contrast optical imaging of hundreds of stars to discover 54 habitable planet candidates with LUVOIR-A and 25 with LUVOIR-B

Total observing time

LUVOIR-A: 2 years

LUVOIR-B: 2 years

B.2.2 Observations overview

To estimate the yield of directly imaged planets, we assume that LUVOIR must conduct a blind high-contrast imaging survey to search for and characterize potentially Earth-like exoplanets. While the efficiency of the LUVOIR exoplanet survey and the quality of its data products would benefit from a precursor survey identifying potentially Earth-like planets, we conservatively assume such a survey does not exist at the time of launch. Thus, the yield of such a blind survey is a probabilistic quantity, which depends on LUVOIR’s coronagraphic capabilities, the occurrence rate of planets of various types, their detectability, and the unknown distribution of planets around individual nearby stars.

To calculate expected exoplanet yields, we used the Altruistic Yield Optimization (AYO) code described in Stark et al. (2014, 2015), which employs the completeness techniques introduced by Brown (2005). Briefly, for each star in the LUVOIR master target list, we randomly distribute a large number of synthetic planets of a given type, forming a “cloud” of synthetic planets around each star, as shown in **Figure B-8**. Planet types are defined by a range of radii, albedo, and orbital elements.

We calculate the reflected light flux from each synthetic planet given its properties, orbit, and phase, and then determine the time required to detect it at SNR=7 with ECLIPS. This conservative SNR value was chosen to reduce false positive and negative detection rates to a negligible level and to budget for yet unknown systematics. Based on these detection times and the exposure time of a given observation, we calculate the fraction of the synthetic planets that are detectable (i.e., the completeness) as a function of exposure time. The completeness simply expresses the probability of detecting that planet type, if such a planet exists. The average yield of an observation is the product of the completeness and the occurrence rate of a given planet type.

We repeat this process for every observation until the total program lifetime is exceeded, arriving at an average total mission yield. In reality, yields may vary from this average due to the random distribution of planets around individual stars; we incorporate this source of

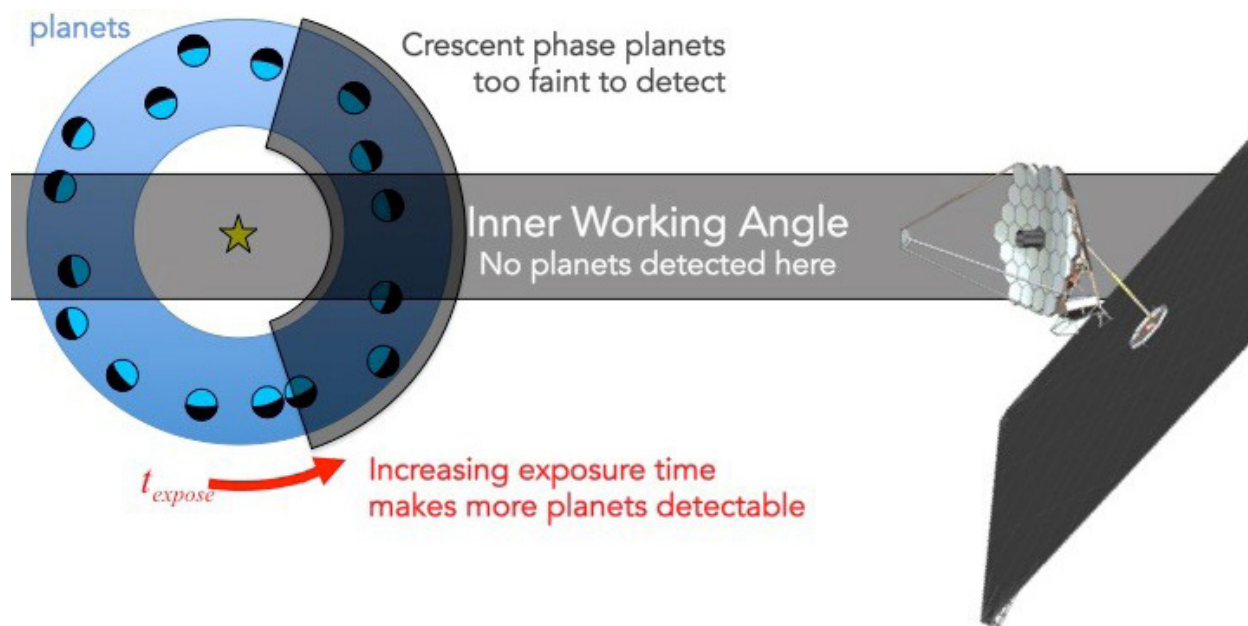


Figure B-8. *The completeness of an observation is the fraction of detectable planets to total planets and is a function of the exposure time. The yield of an observation is the product of completeness and the probability that such a planet actually exists (the occurrence rate).*

uncertainty in our yield calculations by accounting for the Poisson probability distribution of planets and exozodi for each star.

We employ the techniques of Stark et al. (2015) and Stark et al. (2016), which optimize the observation plan to maximize the yield of potentially Earth-like planets. For a coronagraph-based search, this involves optimizing the targets selected for observation, the exposure time of each observation, the delay time between each observation of a given star, the number of observations of each star, and the planet phase for spectral characterization (Stark et al. 2015). We do not explicitly schedule the observations. We expect the ability to schedule the observations will have a negligible impact on the exoplanet yield given LUV0IR's extremely large field of regard and rapid retargeting capabilities.

B.2.3 Targets

Our input star catalog was formed using the methods of Stark et al. (2019). Briefly, the target list is equivalent to the union of the Hipparcos New Reduction catalog and the GAIA TGAS catalog. For each star, we adopted the most recent measured parallax value from the Hipparcos, GAIA TGAS, and GAIA DR2 catalogs, then down-selected to stars within 50 pc. BVI photometry and spectral types were obtained from the Hipparcos catalog. Additional bands and missing spectral types were supplemented using SIMBAD. We filtered out all stars identified as luminosity class I-III, leaving only main sequence stars, sub-giants, and a few unclassified luminosity classes.

While the accuracy of any individual star's parameters may be important when planning actual observations, yield estimates can be very robust to these inaccuracies, as their effects average out when considering a large target sample (Stark et al. 2019). Given LUV0IR's

large sample size of hundreds of stars, inaccuracies in the target catalog will have a negligible impact on yield.

B.2.4 Exposure times & overheads

We adopted a total of 2 years for the exoEarth survey time (including overheads). We assigned each coronagraph observation a conservative 1 hour overhead in total for slew and settle time, based on the combination of the JWST slew rate and a preliminary analysis of thermal and dynamical settling times. In addition, we assigned each observation a static 1.6 or 2.0 hour overhead for wavefront sensing and control (WFSC) for LUVOIR A or B, respectively, along with a 10% tax on science time to account for a single touch-up iteration of WFSC after slewing to the science target. WFSC times were estimated from the WFIRST CGI operations concept scaled to the photon collection rate of LUVOIR. Total exposure time and overheads were required to fit within the exoplanet science time budget.

For planet detections, we required an $\text{SNR}=7$ evaluated over the full bandpass of the detection instrument, where both signal and noise are evaluated in a simple photometric aperture of $0.7 \lambda/D$ in radius (where in this case, D is the diameter of the outer edge of the Lyot stop projected onto the primary mirror). The SNR was evaluated according to Eq. 7 of Stark et al. (2014), which includes a conservative factor of 2 on the background Poisson noise to account for a simple background subtraction. We also included a background term for detector noise, as discussed below. For spectral characterizations, we required a spectrum with $R=70$ and $\text{SNR}=5$ per spectral channel which we evaluated at a wavelength of 1 micron, to search for water vapor in all detected exoEarth candidates. These cursory spectral characterizations to search for water vapor were included in the 2 years of exoEarth survey time.

B.2.5 Inputs & assumptions

Yield estimates require simulating the execution of a mission at a high level. They are therefore dependent on a large number of assumptions about the target stars, the planetary systems they host, and the capabilities of the mission. Given the inherent uncertainties in many of these assumptions, consistency between yield analyses is of primary importance. We adopt inputs and assumptions that are consistent with the choices made by the Exoplanets Standard Definitions and Analysis Team and those made by the HabEx STDT. We now review and justify our fiducial assumptions about the parameters that affect the yield.

B.2.5.1 Astrophysical assumptions

Planet types & occurrence rates. We followed the planet categorization scheme of Kopparapu et al. (2018), which consists of a 3 by 5 grid of planets binned by temperature (hot, warm, and cold) and planet radius (“rocky,” “super-Earths,” “sub-Neptunes,” “Neptunes,” and “Jupiters”), as shown in **Figure B-9**. Each planet was assigned an albedo defined by its radius (bins given in **Figure B-9**), a Lambertian phase function, and all planets were assumed to be on circular orbits. We assume that the semi-major axis boundaries that define the temperature bins of each planet type scale with the bolometric stellar insolation, such that they scale with the square root of the bolometric stellar luminosity.

For exoEarth candidates we adopted the green outlined region in **Figure B-9**. By this definition, exoEarth candidates are on circular orbits and reside within the conservative HZ, spanning

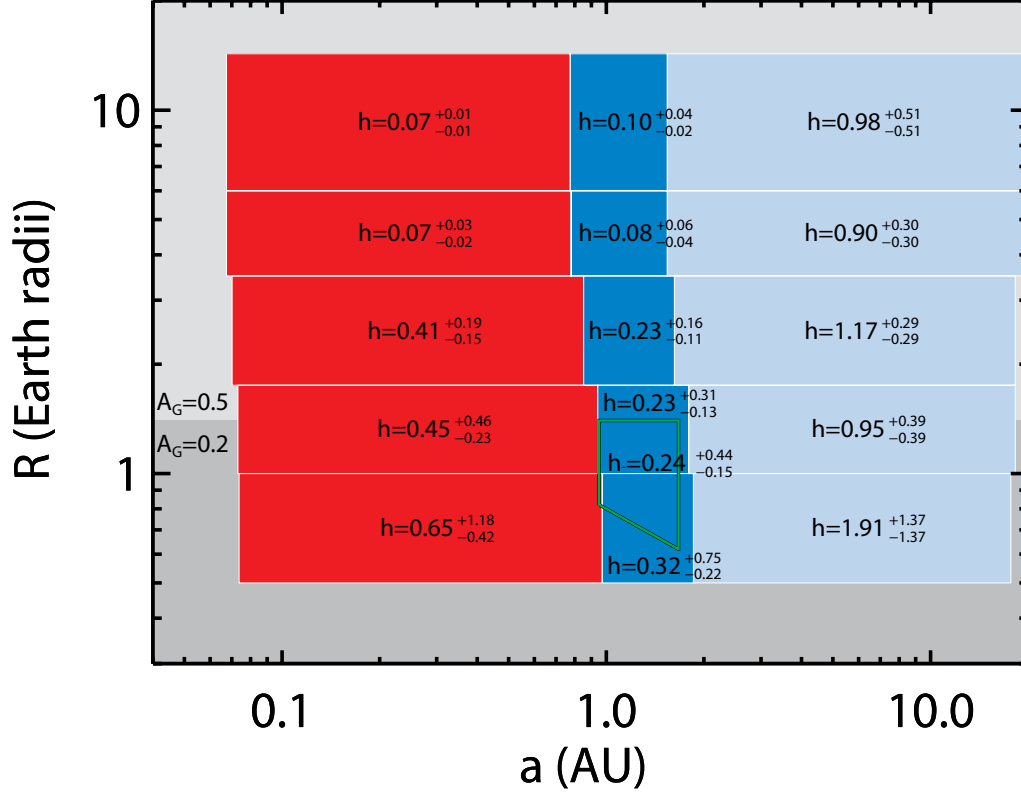


Figure B-9. Planet classifications used for yield modeling, including bin-integrated occurrence rates (η) and geometric albedos (A_G). Planets are binned into hot (red), warm (blue), and cold (ice blue) temperature bins and rocky, super-Earth, sub-Neptune, Neptune, and Jupiter size bins. The green outline indicates the boundaries of exoEarth candidates. The semi-major axis boundaries shown are for a solar-twin star; for other types of stars, semi-major axis boundaries are scaled to maintain a constant bolometric stellar insolation.

0.95–1.67 AU for a solar-twin star (Kopparapu et al. 2013). We only include planets with radii < 1.4 Earth radii and radii $\geq 0.8 a^{-0.5}$, where a is semi-major axis for a solar-twin star. The lower limit on our definition of the radius of exoEarth candidates is derived from an empirical atmospheric loss relationship derived from solar system bodies (Zahnle & Catling 2017). The upper limit on planet radius is a conservative interpretation of an empirically measured transition between rocky and gaseous planets at smaller semi-major axes (Rogers 2015). All exoEarth candidates were assigned Earth’s geometric albedo of 0.2, assumed to be valid at all wavelengths of interest.

We adopted the exoplanet occurrence rate values from the analysis by Dulz et al. (2019, in preparation), hereafter D19. The results in D19 are based on the NASA ExoPAG SAG13 meta-analysis of Kepler data (Kopparapu et al. 2018), given by

$$\frac{d^2 N(R, P)}{d \ln R d \ln P} = \Gamma R^\alpha P^\beta$$

where $N(R, P)$ is the number of planets per star in a bin centered on radius R and period P , R is in Earth radii and P is in years, and $[\Gamma, \alpha, \beta] = [0.38, -0.19, 0.26]$ for $R < 3.4 R_{\text{Earth}}$ and $[\Gamma, \alpha, \beta] = [0.73, -1.18, 0.59]$ for $R \geq 3.4 R_{\text{Earth}}$. D19 update the SAG13 occurrence rates to

address two notable limitations. First, the SAG13 occurrence rates of planets larger than $10 R_{\text{Earth}}$ are uncertain and are roughly a factor of 2 less than measured RV occurrence rates; D19 adopt the occurrence rates of Fernandes et al. (2019) for these planets. Second, extrapolating the SAG13 fit to our cold planets results in dynamically unstable systems; D19 impose simple stability criteria to constrain the occurrence rates of cold planets assuming maximally-packed systems. **Figure B-9** lists the occurrence rates when integrating over the boundaries of each planet type. Within each planet type, we adopted the D19 radius and period distribution. With this distribution, within a given planet temperature bin, small planets outnumber large planets.

The adopted occurrence rates of D19 are based on the SAG13 meta-analysis, which is a crowd-sourced average of published and unpublished occurrence rates, averaged over FGK spectral types. Uncertainties on the SAG13 occurrence rates are not well understood and are simply set to the standard deviation of the crowd-sourced values. Because of the large uncertainties in the SAG13 occurrence rates, we have weak constraints on how occurrence rates change with spectral type. Thus, we simply assume that the occurrence rates for each planet type bin are independent of spectral type.

In particular, for exoEarths in the HZ of sunlike stars, the resulting occurrence rate estimate is $\eta_{\text{Earth}} = 0.24^{+0.46}_{-0.16}$. This value is consistent with what is arguably the most careful estimate of η_{Earth} (and its statistical and systematic uncertainties) by the Kepler team itself (Burke et al. 2015). This paper notes, however, that different but equally plausible methods of treating various systematic errors can change this value by factors of several in either direction. Partly this is due to the fact that any estimate of η_{Earth} from the Kepler survey is necessarily

Table B-1. *Summary of astrophysical assumptions*

Parameter	Value	Description
η_{\oplus}	0.24	Fraction of Sun-like stars with an exoEarth candidate
R_p	$[0.6, 1.4] R_{\oplus}$	Planet radius ^a
a	$[0.95, 1.67] \text{ AU}$	Semi-major axis ^b
e	0	Eccentricity (circular orbits)
$\cos i$	$[-1, 1]$	Cosine of inclination (uniform distribution)
ω	$[0, 2\pi)$	Argument of pericenter (uniform distribution)
M	$[0, 2\pi)$	Mean anomaly (uniform distribution)
Φ	Lambertian	Phase function
A_G	0.2	Geometric albedo of planet surface from $0.55\text{--}1 \mu\text{m}$
z_c	$23 \text{ mag arcsec}^{-2}$	Average V band surface brightness of zodiacal light for coronagraph observations ^c
z_s	$22 \text{ mag arcsec}^{-2}$	Average V band surface brightness of zodiacal light for starshade observations ^c
x	$22 \text{ mag arcsec}^{-2}$	V band surface brightness of 1 zodi of exozodiacal dust ^d
n	3	Number of zodi for all stars

^a Distribution is a function of a according to the SAG13 occurrence rates

^b a given for a solar twin. The habitable zone is scaled to $\sqrt{L_*/L_{\odot}}$

^c Local zodi calculated based on ecliptic pointing of telescope. On average, starshade observes into brighter zodiacal light

^d For Solar twin. Varies with spectral type, as zodi definition fixes optical depth.

an extrapolation. Nevertheless, pending a more robust estimate of η_{Earth} accounting for all Kepler data, this study adopts the SAG 13 value and uncertainty. **Table B-1** summarizes the key astrophysical assumptions underlying our exoEarth candidate yield calculations.

Exozodiacal & zodiacal dust. Exozodiacal dust adds background noise, thereby reducing the SNR of a planet detection relative to the case of no exozodiacal dust. Recent results from the LBTI HOSTS survey for exozodiacal dust provide constraints on the exozodi distribution. Yield calculations herein adopt the freeform distribution that best fits LBTI HOSTS data, which has a median of 4.5 zodis of dust and appears bi-modal, with relatively few stars hosting extreme amounts of dust (Ertel et al. 2018). We assigned each star an exozodi level randomly drawn from this distribution.

The LBTI HOSTS survey detected dust around four potential LUV0IR targets: 297 zodis around Eps Eri, 148 zodis around Tet Boo, 588 zodis around 72 Her, and 235 zodis around 110 Her. For yield calculations, we assigned these stars their LBTI-measured exozodi levels.

Our definition of 1 zodi is a uniform (optically-thin) optical depth producing a V band surface brightness of 22 mag arcsec⁻² at a projected separation of 1 AU around a solar twin. Thus, the exozodi surface brightness drops off as the inverse square of the projected separation (Stark et al. 2014). Because the HZ boundaries scale by the *bolometric* stellar insolation, the V band surface brightness of 1 zodi of exozodi varies with spectral type (Stark et al. 2014).

The solar system’s zodiacal brightness varies with ecliptic latitude and longitude; the closer one observes toward the Sun, the brighter the zodiacal cloud will appear. We calculated the zodiacal brightness for each target star by making simple assumptions about typical telescope pointing (Leinert et al. 1998). We assume the coronagraph can observe near where the local zodi is minimized and adopted a solar longitude of 135 degrees for all targets.

B.2.5.2 Stray light from binary stars

Detecting exoplanets in binary star systems presents additional challenges. Light from companion stars outside of the coronagraph’s field of view, but within the field of view of the telescope, will reflect off the primary and secondary mirrors. Due to high-frequency surface figure errors and contamination, some of this light is scattered into the coronagraph’s field of view. For some binary systems, this stray light can become brighter than an exoEarth.

We directly calculate the stray light from binary stars in the final image plane. We adopt the numerical stray light models of Sirbu et al. (2019, in preparation). These models predict the power in the wings of the PSF at large separations assuming a $\lambda/20$ RMS surface roughness and an f^3 envelope, where f is the spatial frequency of optical aberrations. We assume that the stray light can be measured or modeled and include it simply as an additional source of background noise.

We make no artificial cuts to the target list based on binarity and allow the benefit-to-cost optimization in the AYO yield code to determine whether or not stray light noise makes a target unobservable. In practice, the AYO prioritization does reject a number of binary systems with contrast ratios close to unity and/or close separations. We note that including the full amount of light scattered by the companion is actually conservative, as the companion scattered starlight could be actively reduced with specialized observation methods. For

example, LUVOIR could use multi-star or super-Nyquist wavefront control coronagraphic techniques (Thomas et al. 2015; Sirbu et al. 2017).

B.2.5.3 Propagation of astrophysical uncertainties

All major known sources of astrophysical uncertainty are propagated through the yield calculations: uncertainty in occurrence rates, uncertainty in exozodi level, and the Poisson noise associated with the planet population and exozodi level of individual stars. Yield is calculated using the nominal best-fit exozodi distribution from LBTI data, as well as the $\pm 1\sigma$ distributions. For each exozodi distribution, 20 yield calculations are performed to sample the Poisson noise associated with individual exozodi levels.

For each exozodi distribution, yield calculations are performed for the pessimistic, nominal, and optimistic occurrence rates, for a total of 180 yield calculations. Each of the 180 yield calculations results in a list of optimized observations with associated completeness. Monte Carlo draws are then performed for each individual simulation to determine whether a planet is detected in a given observation, sampling the Poisson noise associated with planet populations of individual stars. The number of draws is weighted by the probability distribution of occurrence rate values and exozodi distribution. The detailed shape of these probability distributions is unknown. We assume normal distributions and weight the nominal and $\pm 1\sigma$ values accordingly; we ignore the tails of the distributions beyond $\pm 1.5\sigma$, which we expect to minimally impact the estimated uncertainties.

B.2.5.4 Instrument performance assumptions

LUVOIR-A coronagraph assumptions. Coronagraph performance was estimated via a wave propagation model, assuming an idealized optical system and perfect wavefront control. We adopted two coronagraphs designed for the LUVOIR-A segmented, on-axis primary: an apodized pupil Lyot coronagraph (APLC) and a charge 6 apodized vortex coronagraph (AVC). The APCL coronagraph consisted of 3 masks: a small-IWA mask (10% bandwidth, $3.8\text{--}12\lambda/D$ working angle), a medium-IWA mask (15% bandwidth, $6\text{--}20\lambda/D$ working angle), and a large-IWA mask ($11\text{--}33\lambda/D$ working angle). To each star we independently assigned either one of the APCL masks or the AVC coronagraph, based on the wavelength of observation and a cost-to-benefit ratio. We simulated the leaked starlight as a function of stellar diameter and the off-axis PSFs as a function of angular separation, providing inputs to the yield calculations according to the standards of Stark & Krist (2017).

The wave propagation model does not include some known systematic noise sources, such as residual spatial speckle noise caused by dynamic wavefront errors. Realistic estimates would require full end-to-end simulations of a well-defined telescope, instrument, and observing procedure. These effects will impact the coronagraph noise floor, the properties and frequency of false positives, and the final yield, though preliminary estimates suggest these effects are minor.

The APCL coronagraph design consists of a binary apodizer mask in the entrance pupil, followed by an image plane coronagraph mask, followed by a Lyot stop (N'Diaye et al. 2016). The apodizer is optimized to maximize coronagraph throughput while achieving 10^{-10} raw contrast over a desired range of working angles (e.g., Zimmerman et al. 2016). In the end, we designed three separate masks with overlapping working angles, allowing us to maximize the throughput for any size habitable zone. The resulting APCL designs are robust

Table B-2. Summary of adopted coronagraph performance for LUVUOIR-A, shown for the APLC and the VC coronagraph designs. Listed contrast is for a theoretical point source; contrasts used in simulations included the effects of finite stellar diameter. While only the spatially averaged raw contrast and coronagraph throughput are indicated, AYO simulations used their actual values at the planet angular separation.

Parameter	APLC ₁	APLC ₂	APLC ₃	VC	Description
ζ	4×10^{-11}	5×10^{-11}	5×10^{-11}	3×10^{-10}	Raw contrast ^a
$\Delta\text{mag}_{\text{floor}}$	26.5	26.5	26.5	26.5	Systematic floor noise (faintest detectable point source)
T_{core}	0.19	0.26	0.26	0.17	Coronagraphic core throughput ^a
T	0.23	0.23	0.23	0.23	End-to-end VIS channel detection throughput (including QE, excluding core throughput)
IWA	3.8	6.3	11.4	3.7	Inner working angle (λ/Δ) ^b
OWA	11.5	19.5	33	10	Outer working angle (λ/Δ)
$\Delta\lambda$	10%	15%	15%	20%	Bandwidth

^aAverage value between IWA and OWA.

^bSeparation at which core throughput reaches half the maximum value.

to stellar diameter and jitter (tolerance ~ 1 mas stellar diameter and ~ 0.5 mas jitter respectively for the LUVUOIR Architecture A primary at 600 nm).

The apodized vortex coronagraph design (Mawet et al. 2013) consists of a grayscale apodizer mask in the entrance pupil, followed by a vortex phase mask in the focal plane (Mawet et al. 2009), and an annular Lyot stop. We chose a charge 6 vortex mask to balance sensitivity to low-order aberrations and throughput at small angular separations (Ruane et al. 2017). We used the Auxiliary Field Optimization algorithm (Jewell et al. 2017) to optimize the grayscale apodizer and reduce the diffracted starlight due to the central obscuration, the secondary mirror support structures, and gap between mirror segments in an annular region about the star.

Table B-2 summarizes the coronagraph performance that we adopted for LUVUOIR-A. We note that although these metrics may provide a useful high-level understanding of coronagraph performance, some metrics should be interpreted with caution. For example, the inner working angle (IWA) estimates where the planet's throughput reaches 50% of the maximum value, but this does not mean that there is no planet signal interior to the IWA. On the contrary, the vortex coronagraph provides useful (albeit lower) throughput down to $\sim 2 \lambda/D$, such that bright, short-period planets may be detectable interior to the quoted $3.7 \lambda/D$ IWA.

The bandpass of the APLC designs is limited by the design of the apodized masks and was chosen based on a throughput-bandwidth tradeoff analysis. To work with a segmented on-axis telescope, the vortex coronagraph design also uses an apodized mask, which was designed assuming 20% bandwidth. All of these bandwidths are less than or equal to the expected simultaneous bandwidth of the wavefront control system. High Contrast Imaging Testbed results indicate that surpassing a bandwidth of $\Delta\lambda/\lambda = 0.2$ is challenging with a conventional dual DM coronagraph layout, thereby justifying our adopted maximum bandwidth of 20%.

The total throughput of the system in **Table B-2** is evaluated at visible wavelengths and includes the reflectivity of all optical surfaces, the detector quantum efficiency (QE), detector

Table B-3. Summary of adopted coronagraph performance for LUVOIR B, using the DMVC coronagraph.. Listed contrast is for a theoretical point source; contrasts used in simulations included the effects of finite stellar diameter. While only the spatially averaged raw contrast and coronagraph throughput are indicated, AYO simulations used their actual values at the planet angular separation.

Parameter	DMVC	Description
ζ	1.5×10^{-10}	Raw Contrast ^a
$\Delta\text{mag}_{\text{floor}}$	26.5	Systematic noise floor (faintest detectable point source)
T_{core}	0.40	Coronagraphic core throughput ^a
T	0.25	End-to-end VIS channel detection throughput (including QE, excluding core throughput)
IWA	3.8	Inner working angle (λ/D) ^b
OWA	27	Outer working angle (λ/D)
$\Delta\lambda$	20%	Bandwidth

^aAverage value between the IWA and OWA.

^bSeparation at which core throughput reaches half the maximum value within the dark hole.

readout inefficiencies in photon-counting mode, IFS throughput, and a 5% contamination budget. Detector parameters are discussed below. This throughput metric does not include the core throughput of the coronagraph, which was accounted for separately via the off-axis PSF simulations discussed above.

LUVOIR-B coronagraph assumptions. LUVOIR-B coronagraph performance was estimated in the same way as LUVOIR-A. However, the off-axis design of LUVOIR-B allows for the use of higher performance coronagraphs. We adopted a DM-assisted Vortex Coronagraph (DMVC) as our nominal coronagraph design for LUVOIR-B. The DMVC design uses the DMs to “fill in” the segment gaps of the primary mirror, such that the traditional vortex coronagraph downstream sees a monolithic primary mirror whose size is given by the primary’s inscribed diameter. As long as segment gap size is kept small ($<0.1\%$), the reduction in DMVC performance is modest compared to the ideal VC (Ruane et al. 2018, Stark et al. 2019). The downstream VC consists of a vortex phase mask in the focal plane (Mawet et al. 2009), and an annular Lyot stop. We chose a charge 6 vortex mask to balance sensitivity to low order aberrations and throughput at small angular separations (Ruane et al. 2017). We used the Auxiliary Field Optimization algorithm (Jewell et al. 2017) to optimize the DM shapes and reduce the diffracted starlight due to the segment gaps in an annular region about the star. **Table B-3** summarizes the nominal coronagraph performance that we adopted for LUVOIR-B.

We also examined a PIAA coronagraph as an alternative design for LUVOIR-B. Traditionally PIAA coronagraph designs have provided very high throughput and small IWA, but have not been sufficiently robust to low order aberrations and stellar diameter. Very recent PIAA designs have attempted to solve this robustness problem by adopting a simple opaque focal plane mask and optimizing the DM shape to maximize robustness and contrast. As a result, new PIAA designs appear sufficiently robust to stellar diameter and still

Table B-4. *Photon-counting CCD noise parameters adopted for yield modeling.*

Parameter	Value	Description
ξ	3×10^{-5} counts pix ⁻¹ sec ⁻¹	Dark current
RN	0 counts pix ⁻¹ read ⁻¹	Read noise (N/A)
τ_{read}	1000s	Read time (N/A)
CIC	1.3×10^{-3} counts pix ⁻¹ clock ⁻¹	Clock induced charge

achieve very high throughput near $3 \lambda/D$. These promising designs could improve the yield of LUVUOIR-B by a remarkable $\sim 50\%$.

Detector & other performance assumptions. Table B-4 lists the detector noise parameters that we adopted for yield calculations. We calculated the total detector noise count rate in the photometric aperture as

$$CR_{\text{b,detector}} \approx n_{\text{pix}} (\xi + RN^2/\tau_{\text{expose}} + 6.73 f \text{ CIC}),$$

where f is the photon counting rate and n_{pix} is the number of pixels contributing to the signal and noise. We tuned f to each individual target, such that our photon-counting detector time-resolves photons from sources 10 times as bright as an Earth-twin at quadrature.

We assumed the IFS splits the core of the PSF into 4 lenslets at the shortest wavelength, each of which are dispersed into 6 pixels per spectral channel for a total of 24 pixels per spectral channel at the shortest wavelength. For broadband coronagraphic detections using the imager, we adopted 4 pixels for the core of the planet. We note that the assumed detector noise is sufficiently low that small changes to the number of pixels have a negligible impact on yield.

B.2.6 Operations concepts

Yield is commonly thought of as the number of planets detected and/or characterized. As shown by Stark et al. (2016), the yield of a mission is very sensitive to precisely what measurements are required for “characterization,” and how the mission goes about making those measurements. Thus, the yield depends on the science products desired and how the mission conducts the observations.

B.2.6.1 Desired science products

LUVUOIR is designed to be capable of obtaining many exoplanet data products. For the exoplanet yield analysis, we considered three primary data products on planets identified as exoEarth candidates:

1. Photometry: to detect planets and measure brightness and color
2. Spectra: to assess chemical composition of atmospheres
3. Orbit measurement: to determine if planet resides in HZ and measure spectro-photometric phase variations

In the following sections, we describe how LUVUOIR will obtain these data products in an efficient manner to maximize the yield of the mission.

B.2.6.2 Dealing with confusion

Upon initial detection of a possible companion, the nature of the source may be unclear. We will have only photometry, possibly one color, and a stellocentric separation to determine the nature of the object. Color, brightness, and the fact the source is unresolved may allow us to discriminate between many background galaxies and exoplanets. However, recent work has shown that other planets can mimic the color of exoEarth candidates (e.g., Krissansen-Totton et al. 2016). Further, planets that most easily mimic Earth are small, hot terrestrial planets, which have even higher occurrence rates than exoEarth candidates (van Gorkom & Stark, in prep); planet-planet confusion may be common. However, performing costly characterizations on all planets mimicking an Earth could decrease the efficiency of the exoplanet survey and reduce the yield of exoEarth candidates; we may need to disambiguate point sources to identify high priority planets. LUVOIR is capable of dealing with these expected sources of confusion without significantly impacting the yield.

B.2.6.3 Order of operations

The order in which observations are conducted will impact the final yield of the mission. For example, taking spectra of every object consistent with an exoEarth candidate immediately upon discovery would be costly, as spectral characterization times can be long and we are likely to find many other planets at coincidental phases that mimic exoEarths. A more efficient order of operations would play to the strengths of the coronagraph, e.g., by first following up initial detections with orbit measurements, followed by spectra of interesting systems when planets are known to be at advantageous phases.

Ultimately these decisions will depend on uncertain quantities, like η_{Earth} for nearby FGK stars and the rate of confusion with background objects. A precise operations concept will require further detailed study and will surely be adapted “on the fly” during mission operations.

B.2.6.4 Simulating operations concepts

To simulate a given operations concept, we would need to generate a fictitious universe and simulate the execution of the mission one observation at a time, adapting to the detections, non-detections, and false positives as we go using decision-making logic. While current yield codes are capable of doing most of this (Savransky & Garrett 2016), the critical decision-making logic step is extremely complex and in its infancy. Realistic decision-making processes require simulating the precision of multiple types of measurements, estimating the likelihood that a planet is an exoEarth versus a background object or another planet, and determining the optimum criteria for decision-making.

In light of these complexities, we relied on the findings of Stark et al. (2016), wherein the impact of different operations concepts on yield was estimated by adopting general rules that define the observation plan. For example, to include orbit determination, Stark et al. (2016) required each planetary system be observed at least six times to a depth consistent with detecting an exoEarth. Using these methods, Stark et al. (2016) found that for coronagraph-based missions like LUVOIR, orbit determination is not particularly costly while spectral characterization can be very costly.

Therefore, we adopted the following operations scenario:

1. Detect planets using two bands within the UV and VIS coronagraph channels simultaneously (~450–500 and 500–550 nm), providing color information for the majority of detections.
2. Revisit all systems as necessary with the coronagraph until the orbits of high-priority planets are sufficiently constrained (~6 times each on average, over the course of months to years)
3. Based on the color, orbit, brightness, and phase variations, identify high-priority targets for spectral characterization.
4. Schedule and conduct spectral characterization observations on each exoEarth candidate at an optimized orbital phase to search for the presence of water vapor in the planet's atmosphere.

This operations scenario is both realistic and robust to error. By requiring orbit measurement regardless of what is detected, the operations concept is straightforward, does not rely on any confusion mitigation immediately after a detection, and proper motion will be established for free for all detected planets. Because the LUVUOIR coronagraph's field of regard is greater than a hemisphere at any given time, we expect that the revisit schedule for each star can easily be optimized to maximize detections, constrain orbits, and minimize characterization time without detailed consideration of whether or not the targets are inaccessible.

B.2.7 Results

The yields of habitable planet candidates and non-habitable exoplanets returned by the analysis described here appear in **Sections 1.3.1** and **3.4**.

B.2.8 Exoplanet yield-informed trades

Exoplanet yield was considered continuously while designing both LUVUOIR-A and LUVUOIR-B. Four major design trades were made based at least in part on yield studies:

B.2.8.1 Optimizing the primary mirror geometry

Concurrent with the LUVUOIR-A design study, the Segmented Coronagraph Design Analysis (SCDA) study concluded that two major factors greatly impacted the yield of coronagraphs for segmented apertures: the obscuration ratio of the secondary mirror and the inscribed diameter of the primary. The LUVUOIR design team and the SCDA team at STScI (PI: R. Soummer) studied 10 possible apertures for LUVUOIR, ranging from engineering-optimized designs to coronagraph-optimized designs. The studied apertures produced a range of yields that varied by a factor of two. The final aperture was selected based on its high yield and scalability.

B.2.8.2 IFS vs. fiber-fed spectrograph

Two proposed options were considered to obtain spectra of exoplanets: an integral field spectrograph (IFS) and a fiber-fed spectrograph. Both of these instruments have design strengths and weaknesses. The former has heritage from the WFIRST CGI, but packaging

considerations and detector size place limitations on the field of view and maximum resolution. The latter is compact and provides potentially higher resolution, but only provides spectra of one source at a time and requires a potentially complex operations concept. In the end, a yield study revealed that the throughput reduction required for the fiber-red spectrograph significantly reduced exoplanet yields to an unacceptable level.

B.2.8.3 NUV coronagraph channel

In addition to introducing additional engineering challenges, the presence of a NUV coronagraph channel reduces the throughput of all coronagraph channels by ~40%, as it requires all optical surfaces after the telescope and prior to the dichroics to be aluminum. In addition, the end-to-end throughput of the NUV channel coronagraph is roughly half that of the visible channel. We considered replacing the NUV coronagraph channel with a second visible channel and co-adding the coronagraph channels to double the detection bandwidth. We found that this trade increased yield by ~20%. However, the STDT determined that NUV coronagraphic capability was a higher priority than a 20% increase in exoplanet yield.

B.2.8.4 TMA vs. Cassegrain telescope design

The current LUVOIR-A telescope is a TMA design with 4 optics (primary, secondary, tertiary, and fine-steering mirror). By switching to a Cassegrain design, potentially two aluminum surfaces could be removed, increasing the throughput of all instruments by ~18%. We determined that an 18% increase in throughput would increase yield by ~6%. The STDT and design team determined that a 6% increase in yield did not warrant the increased complexity of the Cassegrain design given the timeline of the study.

B.3 Signature Science Case #2: Searching for biosignatures and confirming habitability

B.3.1 Abstract

Determining whether a potentially habitable exoplanet is actually habitable and whether it hosts life will be one of the greatest astronomical challenges in the coming decades. LUVUOIR's access to a broad swath of UV-visible-NIR wavelengths will enable searches for a diverse range of habitability indicators and biosignature features. **Chapter 3** describes the spectral features LUVUOIR will target to determine whether an exoplanet is habitable, whether it has life, and what features may indicate any potential biosignatures are false positives.

We anticipate detecting approximately 50 and 30 exoEarth candidates with LUVUOIR-A and -B, respectively. These candidates are rocky planets in their stars' habitable zones, and will be searched for water vapor in the imaging survey (Signature Science Case #1). However, not all habitable planet candidates will be actually habitable. Habitability depends on the availability of surface liquid water, which in turn depends on volatile delivery, planetary evolution, etc. Therefore, only a fraction of these candidates (η_{water}) may show signs of habitability via atmospheric water absorption features.

Our characterization strategy is outlined in **Figure 3-11** and accompanying text. We calculated the times required to obtain direct spectra of sufficient quality for confirming habitable conditions and detecting biosignatures on Earth-like exoplanets. The number of Earth-like exoplanets for which these direct spectra can be obtained in a 6-month program vary based on the number of planets chosen for spectral characterization and the fraction of the total wavelength range included in the nominal program. We emphasize that this DRM does not describe an optimized observing program, but rather represents a proof-of-concept to establish feasibility and uncover avenues for further exploration.

The strategy that obtains the largest number of planetary spectra involves observing spectra of all exoEarth candidates in order of lowest hanging fruit. If η_{water} is small, exoEarths will on average be farther away from us and will require longer integration times to characterize; in such a scenario piece-wise spectra that strategically focus on specific molecular signatures may be a better strategy than the "full" spectral characterization strategy laid out here. Further, in a low η_{water} scenario, some time may be shifted from the 2 year nominal exoEarth search survey to the 6 month characterization DRM, as a 6 month reduction in the nominal survey is expected to decrease the exoEarth candidate yield by only 10%, while it would double the time available for characterization. Maximizing the number of planets

Program contact(s)

Jacob Lustig-Yaeger (UW), Giada Arney (NASA GSFC), Kevin France (U Colorado – Boulder))

Brief description

ECLIPS high-contrast NUV/optical/ NIR spectroscopy of habitable planet candidates

LUMOS point-source UV spectroscopy of habitable planet candidate host stars (54 with LUVUOIR-A, 28 with LUVUOIR-B)

Total observing time

LUVUOIR-A: 6 months + 18 days = 6.5 months

LUVUOIR-B: 6 months + 9 days = 6.2 months

observed can enable powerful comparative planetology, so we choose a nominal program that obtains spectra of as many planets as possible.

We also calculated the observing times to obtain UV/optical spectra of all exoEarth candidate host stars with LUMOS. These stellar spectra are required for accurate modeling of photochemical effects in planet atmospheres and ruling out false positive biosignatures. As these stars are nearby and bright, the total required times are relatively short (2 weeks for LUVOIR-A and 1 week for LUVOIR-B).

Part of our full habitable planet candidate characterization strategy includes measuring planet masses using on-board astrometry with HDI. The time required for these measurements is included in the DRM for Signature Science Case #5: The formation of planetary systems (**Appendix B.6.2**).

B.3.2 Observations overview

Our primary goal is to obtain a spectrum of each exoEarth candidate that has sufficient wavelength coverage and SNR to detect signs of habitability and life, and to rule out potential false positives for any observed spectroscopic biosignatures. Obtaining a spectrum across the bulk of the ECLIPS wavelength range is sufficient to accomplish this goal. **Figure B-10** displays a characteristic modern Earth spectrum with the expected noise for the observations described in this program. This wavelength range is also sufficient to characterize and detect life on an Archean or Proterozoic Earth analog, as described in **Chapter 3**.

We perform our nominal exposure time calculations assuming a planet with a wavelength-independent 20% albedo (a “gray” planet with the Earth average albedo). This gray spectrum is agnostic to specific molecular features, allowing us to estimate the integration time required to obtain a given SNR on the mean spectral continuum at any wavelength. However, we also consider the detectability of key individual molecular bands on modern Earth, and for this we use a partially cloudy Earth spectrum (Robinson et al. 2011).

We require SNR=8.5 on the continuum across the complete LUVOIR spectral range (0.2–2.0 μm) to detect and place abundance constraints on atmospheric gases, based on work by Feng et al. (2018). Feng et al. (2018) performed atmospheric retrievals from 0.4–1.0

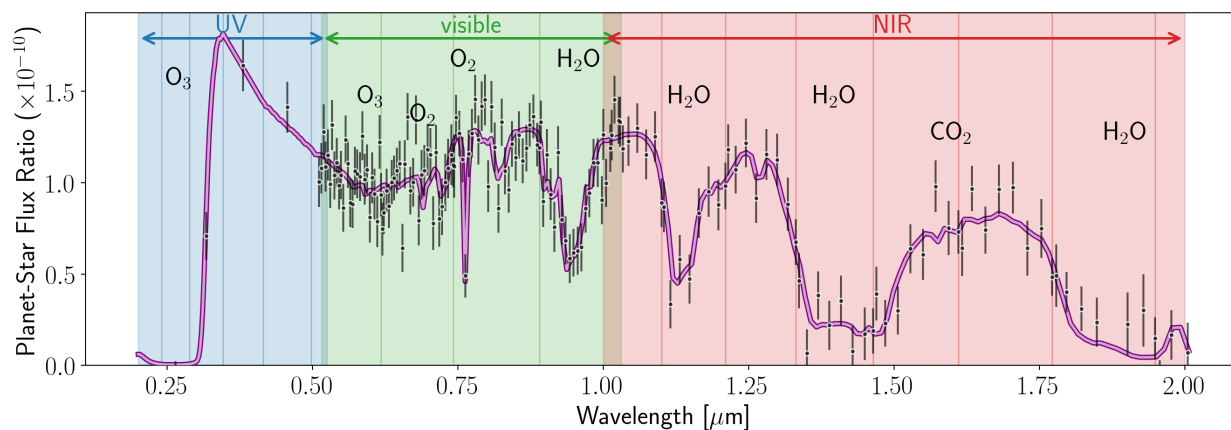


Figure B-10. Simulated spectrum of an Earth analog exoplanet observed with LUVOIR in this DRM observing program (SNR = 8.5). The shaded background regions indicate the wavelength ranges of the UV (blue) and visible (green), and NIR (red) channels. The vertical lines show 20% bandpasses in the UV and visible channels and 10% bandpasses in the NIR channel. Credit: J. Lustig-Yaeger (UW)

μm at a spectral resolution of $R=140$ (the same as LUVVOIR in the visible channel) for a range of SNR values. However, a subtlety of the Feng et al. results is that their quoted SNR values are calculated at a standard wavelength of $0.55 \mu\text{m}$, not at the continuum near the spectral feature of interest. Therefore, the equivalent SNR on the continuum at other wavelengths will be different from the Feng et al. SNR values at $0.55 \mu\text{m}$.

For instance, Feng et al. find that $\text{SNR}=10$ at $0.55 \mu\text{m}$ can place order-of-magnitude constraints on O_2 abundance. We find that $\text{SNR}=10$ at $0.55 \mu\text{m}$ corresponds to $\text{SNR}=8.5$ near the O_2 A band at $0.76 \mu\text{m}$. Based on the assumption that the O_2 A band is one of the more challenging spectral features we will retrieve (Feng et al. show that constraints on O_2 are weaker than those on H_2O and O_3 at a given SNR), we apply this $\text{SNR}=8.5$ requirement for O_2 across our spectrum, where our $\text{SNR}=8.5$ is equivalent to Feng et al.'s $\text{SNR}=10$ at $0.55 \mu\text{m}$ for O_2 retrieval.

LUVVOIR's broad wavelength coverage extends farther into the UV and farther into the NIR than the spectrum from the Feng et al. (2018) study, enabling access to a range of biosignatures and biosignature false positives. Specifically, this enables LUVVOIR to access features like the strong Hartley-Huggins ozone band ($0.2\text{--}0.3 \mu\text{m}$), which is a critical biosignature for planets with low oxygen abundances, like the mid-Proterozoic Earth (Planavsky et al. 2014; Reinhard et al 2017). LUVVOIR can also access the $1.6 \mu\text{m}$ CO_2 band which, together with CH_4 and/or organic haze (with spectral features across the visible and NIR), form a biosignature for Archean Earth-like planets (Arney et al. 2018; Krissansen-Totton et al. 2018).

B.3.3 Targets

Based on the exoEarth yields anticipated for LUVVOIR-A and B (54 planets for LUVVOIR-A; 28 planets for LUVVOIR-B), we perform a biased draw of targets from the total list of stars observed in the exoEarth imaging surveys (**Section B.2**), weighted towards stars with higher habitable zone completeness. This becomes our biased catalog of systems with exoEarth candidates.

B.3.4 Exposure times & overheads

We adopt the nominal telescope and ECLIPS instrument parameters for the LUVVOIR-A and LUVVOIR-B architectures, with 20% bandpasses across the LUVVOIR UV and visible spectral range and 10% bandpasses across the NIR. Simultaneous observations in two channels at a time were accounted for in the reported total exposure times. It is assumed the third channel will be for wavefront sensing, although observations in all three channels simultaneously may become possible in future with technological improvements.

The coronagraph simulations were performed using a modified version of the model developed by Robinson et al. (2016), which is available on GitHub (<https://github.com/jlust-igy/coronagraph>) and as an online interactive interface (**Section B.1.1**). This model uses analytic relations to calculate the photon count rates for a variety of astrophysical, telescope, and instrumental noise sources, including coronagraph speckles, zodiacal and exozodiacal dust, telescope thermal emission, dark current, and read noise. The exozodi level is set to the same value drawn from the LBTI exozodi distribution for each target system used in the initial detection survey (Signature Science Case #1), which ranges from about $0.1\text{--}100$ zodis.

The coronagraph model was also upgraded to include the dependence of the coronagraph contrast and throughput on the separation between the planet and star as a function of λ/D . This functional relationship is different for each coronagraph design so we use specific relationships for the APLC on LUVOIR-A, and the DMVC on LUVOIR-B. The APLC has multiple masks for different planet-star separations; we use the mask with the minimum exposure time for each star and for each bandpass.

We also account for overheads on our observations. For each target, we assume 1-hour for the combination of slew, dynamic settle, and thermal settle time. We then add 0.6 (1.25) hours for architecture A (B) to dig the dark hole for each bandpass observed. Finally, we impose a 10% overhead on the total science time for one assumed iteration of the wavefront control system.

We assume that the exoplanet being observed is Earth-radius at quadrature phase and located at the inner edge of the habitable zone (moist greenhouse; Kopparapu et al. 2013) for the star about which it orbits. Blackbodies are assumed for each stellar spectrum, set by the known stellar effective temperature; 90% of our stellar catalog is comprised of FGK stars for which a blackbody is a reasonable assumption.

For each star in the biased catalog of exoEarth candidates, we calculate the exposure time in each bandpass necessary to observe an exoEarth at $\text{SNR}=8.5$. Bandpasses that are not entirely observable when considering the IWA and OWA are not included in exposure time calculations. However, this approach overestimates decreases in spectral completeness, which we quantify as the percentage of the total LUVOIR wavelength range (0.2–2.0 μm) that is observable for any given exoEarth target. We also consider science program cases that omit bandpasses, which decreases spectral completeness.

To examine how our spectral yields are impacted by observations that target only a fraction of the full sample of exoEarth candidates, we randomly sample N_{draw} exoEarth candidates from the biased catalog, where N_{draw} is set by the fraction of water-vapor-bearing targets in the biased catalog, η_{water} . We use the precomputed exposure times per bandpass to calculate the total exposure time to get the full spectrum available for each planet. In addition to reporting the total integration time to characterize a complete N_{draw} set of planets, we calculate the maximal number of exoEarth spectra that could be obtained in a time-limited program, for which we prioritize targets with shorter exposure times.

B.3.5 Results

Bandpass exposure times vary significantly, both from one wavelength to another, and at a given wavelength depending on the specific stars in the sample that host the target exoEarth candidates. **Figure B-11** shows the range of exposure times required in each bandpass to observe the LUVOIR-A (top panel) and LUVOIR-B (bottom panel) exoEarth candidates. The percentage of exoEarth candidates in the biased draw catalog for which spectra in each bandpass may be obtained given IWA and OWA constraints is also shown.

LUVOIR-A and LUVOIR-B offer nearly complete coverage at UV and visible wavelengths for our set of target stars, but the IWA leads to decreasing spectral completeness towards longer NIR wavelengths. The longest NIR bandpass requires relatively long exposure times, but only ~40–70% of the stars in the biased catalog may have access to this entire bandpass given the coronagraph IWA. The large tails seen in the 95% confidence intervals (**Figure B-11**) that extend to lower exposure times is caused by the small handful of very nearest

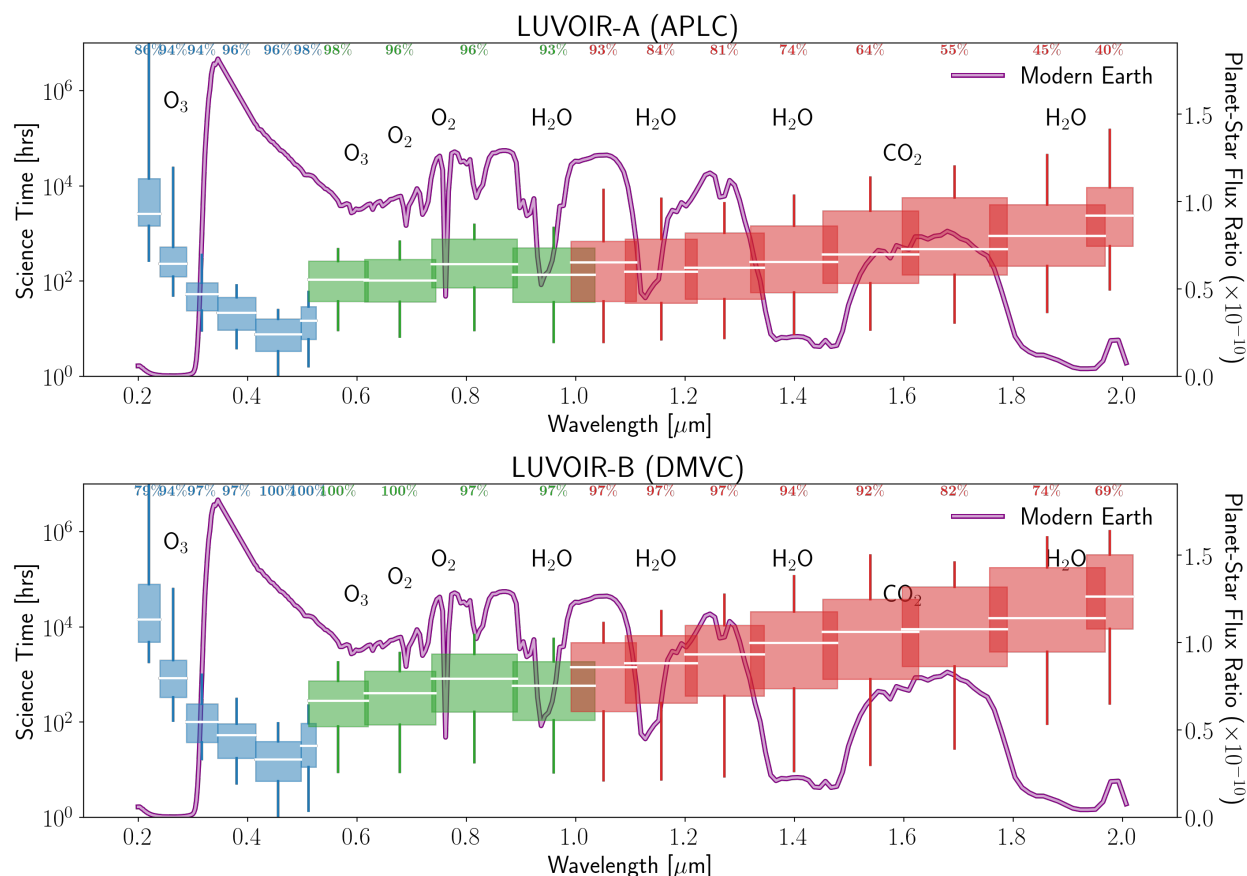


Figure B-11. Required science exposure time per bandpass (left axis) to reach $\text{SNR}=8.5$ for LUVUOIR-A (top panel) and LUVUOIR-B (bottom panel). The blue (UV channel), green (visible channel), and red (NIR channel) “boxes and whiskers” show the 50% (box extent) and 95% (whisker extent) confidence intervals about the median (white bar) science time required to observe the spectrum shown in **Figure B-10**, for the targets in the biased catalog of exoEarth candidates. The percentage of stars in the target catalog that can be completely observed in each bandpass—considering IWA and OWA constraints is displayed above each box. Exposure times required to achieve a fixed precision on the spectrum can vary by orders of magnitude.

targets in the sample that are only a few parsecs away, which require only a few hours to observe in this bandpass.

The shortest UV bandpass is particularly costly to observe for exoEarth planets, primarily due to the lack of reflected photons available and the low coronagraph throughput here. The large tail seen in the 95% confidence interval of the bluest UV bandpass that extends roughly two orders of magnitude higher in exposure time for LUVUOIR-B is caused by the latest type stars (late K and M dwarfs) in the sample which have a low UV flux.

Omitting the most time intensive bandpass(es) allows for spectra to be obtained for more targets in significantly less observing time, without sacrificing significant scientific yield. These expensive bandpasses could be observed later as part of a follow-on program for the most interesting planets that exhibit signs of habitability and life. Hundreds of days of observing time can be saved if these costly bandpasses are not included in the nominal science program.

Moreover, the two bluest UV bandpasses may not be immediately necessary for ozone detection on a modern Earth-like planet, which has the ozone Chappuis band between 0.5–0.7 μm (Feng et al. 2018) and can also access the long wavelength shoulder of the UV ozone Hartley-Huggins band in the third shortest UV bandpass at $\sim 0.3 \mu\text{m}$. For a Proterozoic Earth-like planet where the Chappuis band is not detectable, the third shortest UV band should be able to detect the spectral darkening from ozone.

Meanwhile, the reddest NIR bandpasses may provide leverage for the detection of water and/or methane, but both of these molecules have bands at shorter wavelengths that may be more easily detected. Archean Earth in particular may have had a methane-rich atmosphere able to produce CH_4 spectral features even in the visible channel. These reddest bandpasses are most valuable for detecting methane at low modern Earth-like abundances, but this type of expensive observation would likely only be sought once other signs of biosignatures were detected at shorter wavelengths. These bandpasses also allow access to CO_2 near 1.6 μm , which could be targeted as part of the nominal program for planets with shorter integration times, or part of an extended program if integration times are lengthy.

If only a subset of “interesting” targets according to η_{water} are observed, the value of η_{water} strongly affects the number of spectra that may be obtained in a time-limited science program. **Figure B-12** shows contours of the average number of spectra that can be acquired as a function of the total observing time and interesting target fraction, η_{water} . Low values for η_{water} (e.g., 10%) yield only a few exoEarth targets slated for follow-up in this program, which, on average, require long exposure times due to the lower probability of nearby targets. On the other hand, optimistic estimates for η_{water} yield many interesting targets for follow-up, which can be prioritized by distance such that many spectra are able to be observed even for a relatively modest observing program duration.

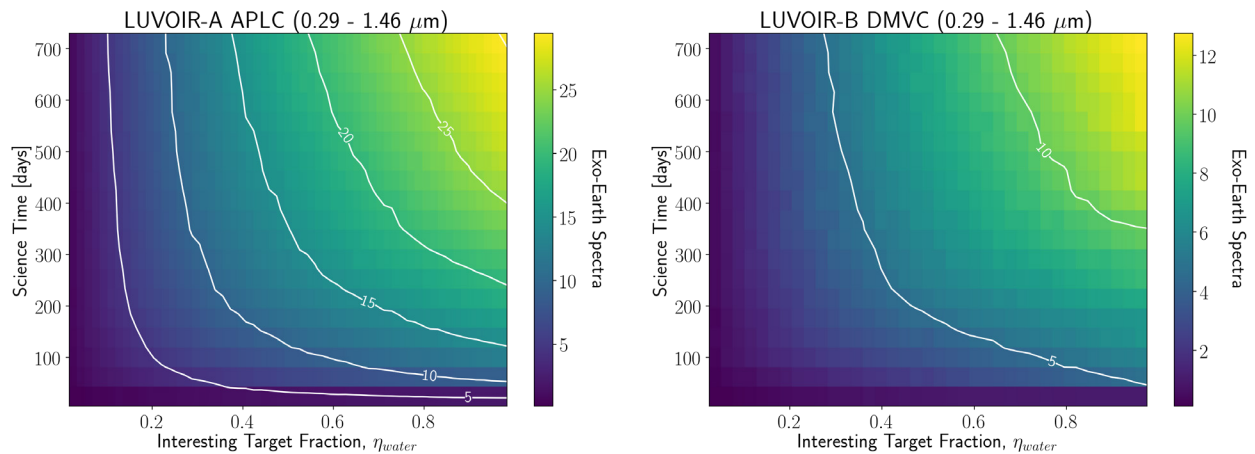


Figure B-12. Number of spectra (color map and contour lines) that may be observed by LUVUOIR-A (left panel) and LUVUOIR-B DMVC (right panel) as a function of both total observing time and fraction of “interesting” targets in the exoEarth candidate sample, η_{water} . The two shortest wavelength UV bandpasses and the four longest NIR bandpass are not included, so the spectrum spans 0.29–1.46 μm . A higher fraction of candidate targets increases the probability that nearby, more easily observed, stars are included in the exoEarth candidate sample, which yields more complete spectra in shorter duration programs.

Table B-5 and **Table B-6** report the number of exoEarth spectra that may be obtained for LUVUOIR-A and LUVUOIR-B, respectively, for different assumed interesting target fractions η_{water} and for different wavelength coverage cases for our nominal program observing all exoEarth candidates in order of shortest to longest observing time. Results are presented for both 12-month and 6-month habitable exoplanet characterization science program durations. The yield values for LUVUOIR-B may increase substantially (by up to 50%) with new PIAA coronagraph designs. For the nominal time allocation of this DRM (6 months), we choose to report yields for programs designed to acquire spectra from 0.29–1.46 μm , which we find strikes a balance between spectral completeness, observing time, and scientific yield.

Parallels

- ☐ Do not execute parallels with this program
- ☐ Parallels required for this program
- ☐ Can be executed as parallel to another program
- ☒ Possible to execute parallels with this program

Table B-5. Median number of spectra ($\text{SNR}=8.5$) observable in a 6-month or 12-month LUVUOIR-A habitable exoplanet characterization program for different wavelengths. These values represent our nominal program targeting as many exoEarths as possible; if only a subset of planets according to η_{water} are observed, the average number of spectra obtained decreases according to $N_{\text{spec}} \approx N_0 (\eta_{\text{water}}/100\%)^{0.71} (t_{\text{exp}}/365 \text{ days})^{0.37}$ where N_0 is the number in the second or third column. This relation is exact for the 0.29–1.46 μm range and approximate for the others.

LUVUOIR-A (APLC)	Number of spectra (6 months)	Number of spectra (12 months)
O ₂ -A (0.74–0.89 μm)	36	44
UV-vis 0.29–1.03 μm	23	30
0.29–1.46 μm	18	24
0.24–1.77 μm	11	15
0.24–2.0 μm	8	12
Full: 0.2–2.0 μm	5	8

Table B-6. Median number of spectra ($\text{SNR}=8.5$) observable in a 6-month or 12-month LUVUOIR-B habitable exoplanet characterization program for different wavelengths. These values represent our nominal program targeting as many exoEarths as possible; if only a subset of planets according to η_{water} are observed, the average number of spectra obtained decreases according to $N_{\text{spec}} \approx N_0 (\eta_{\text{water}}/100\%)^{0.76} (t_{\text{exp}}/365 \text{ days})^{0.39}$ where N_0 is the number in the second or third column. This relation is exact for the 0.29–1.46 μm range and approximate for the others.

LUVUOIR-B (DMVC)	Number of Spectra (6 months)	Number of Spectra (12 months)
O ₂ -A (0.74–0.89 μm)	18	23
UV-vis: 0.29–1.03 μm	11	15
0.29–1.46 μm	8	11
0.24–1.77 μm	5	6
0.24–2.0 μm	4	5
Full: 0.2–2.0 μm	2	2

Target of opportunity / time-critical

- ☐ Is a ToO program
- ☒ Is time-critical

Observations timed so that planet is at quadrature (or gibbous phase) to increase planet brightness.

B.3.6 Stellar spectroscopy

The planetary effective surface temperature alone is insufficient to accurately interpret biosignature gases, particularly for planets orbiting low-mass stars (K and M dwarfs). The UV stellar spectrum drives and regulates the upper atmospheric heating and chemistry on Earth-like planets, is critical to the definition and interpretation of oxygen species and other biosignature gases (e.g., Seager et al. 2013). As discussed in **Chapter 3**, the specifics of the stellar spectrum may produce false-positives in our search for biologic activity (Hu et al. 2012; Tian et al. 2014; Domagal-Goldman et al. 2014; Harman et al. 2015). This observing program will provide panchromatic stellar characterization and variability analysis of the host stars for all exoEarth candidates.

Observations overview. We will obtain low- to medium-resolution point-source spectroscopy of all stars with LUMOS, using the G155L, G300M, and G700L gratings to cover a total wavelength range of 100 to 1000 nm. The observations are:

1. **Characterization:** one complete spectrum over the whole bandpass
2. **High-cadence monitoring:** 8 FUV spectra (G155L) obtained sequentially to evaluate short-term flaring activity
3. **Low-cadence monitoring:** 3 FUV spectra (G155L) spread over the prime mission lifetime to evaluate longer-term stellar variability

These observations will require four visits per star.

Targets. All host stars with potentially habitable planet candidates from the exoEarth survey (adopting 50 stars for LUVOIR-A and 25 stars for LUVOIR-B).

Exposure times & overheads. For the characterization observation, the science exposure time is 1.25 hours per star. This time will return high quality spectra ($\text{SNR} > 50$ in the continuum) of these nearby bright stars ($V = 3$ to 11), more than sufficient to measure the strengths of all major stellar emission lines and providing information on the line shapes. The science exposure time for the high-cadence monitoring observations is 8×0.5 hours = 4 hours per star, sufficient to measure the strengths of emission lines arising from stellar activity. For the low-cadence monitoring, the science exposure time is 3×0.5 hours = 1.5 hours per star.

We adopt the same science exposure times for both LUVOIR-A and LUVOIR-B. This will result in lower but still sufficient SNR values for the LUVOIR-B spectra. We have likely overestimated the time needed for the LUVOIR-A spectra; this will be more carefully addressed in future. For now, the total science exposure time per star is 6.75 hours. All visits may be executed immediately before or after a coronagraphic observation of the system with ECLIPS. Therefore, we simply estimate the overhead time as 25% of the science time, for changing instruments and calibration exposures.

Results. The total time for the LUVUOIR-A program is 8.44 hours x 50 stars ~ 18 days. The total time for LUVUOIR-B is 8.44 hours x 25 stars ~ 9 days.

Parallels

- ☐ Do not execute parallels with this program
- ☐ Parallels required for this program
- ☐ Can be executed as parallel to another program
- ☒ Possible to execute parallels with this program

Target of opportunity / time-critical

- ☐ Is a ToO program
- ☒ Is time-critical

Observations to be scheduled in concert with ECLIPS coronagraphic observations for maximum efficiency.

B.4 Signature Science Case #3: The search for habitable worlds in the solar system

B.4.1 Abstract

The detection of subsurface liquid water in the icy moons of the outer solar system represented an important step in our search for habitable conditions and life outside the Earth. The surfaces of these ocean worlds betray signs of geologic activity, including disruption of their icy shells and the release of subsurface liquids. This activity produces surface albedo changes and, in some cases, plumes. We propose to investigate these potentially habitable worlds in two ways.

1. High-quality spectral imaging of FUV emission from Europa's plumes over long timescales and general auroral emission over one orbit around Jupiter at high cadence
2. Optical/NIR imaging of solar system ocean moons to record changes in surface albedo and composition caused by geologic activity

Thus LUVOIR will advance our understanding of the strength and frequency of plume activity, the interaction of Europa with Jupiter's magnetosphere, and geologic activity in the outer solar system.

B.4.2 UV spectral imaging of Europa plumes

Plumes from Europa have been inferred from observations with Hubble and Galileo (e.g., Roth et al. 2014, Sparks et al. 2016, Jia et al. 2018) and evidence of water was obtained from spectroscopic measurements of plume-like emission from hydrogen (H) and oxygen (O) with HST/STIS at ultraviolet wavelengths (Roth et al. 2014). The detected emission from hydrogen Lyman- α at 121.6 nm and neutral oxygen at 130.4 nm in December 2012 (**Figure B-13**) resulted from prompt emission following electron-impact dissociation of H₂O by Jupiter's electromagnetic field, and estimates of plume release suggested an output of several thousand tons of H₂O per second.

Observations taken in October 1999 and November 2012 did not show significant plume emission, demonstrating that strong plume activity is intermittent. However, since the current detections are near the sensitivity limit of HST, the presence of fainter plumes at the active location or other locations cannot be determined. Thus, the strength and frequency of plume activity from Europa is unknown. Providing a glimpse into the moon's interior, the plumes are of such great scientific interest that a UV spectroscopic capability to observe them was incorporated into the Europa Clipper mission. However, the spacecraft instrument is optimized for plume detection only during flybys and will therefore make primarily serendipitous discoveries. With a planned launch date in 2023, Europa Clipper is expected to

Program contact(s)

Aki Roberge (NASA GSFC), Marc Neveu (NASA GSFC), Britney Schmidt (Georgia Tech), Walter Harris (U of Arizona), Lucas Paganini (NASA GSFC)

Brief description

LUMOS multi-epoch FUV spectral imaging of Europa plume and general auroral emission
HDI multi-band, multi-epoch imaging of solar system ocean moons

Total observing time

LUVOIR-A: 11 days + 5 days = 16 days
LUVOIR-B: 27 days + 5 days = 32 days

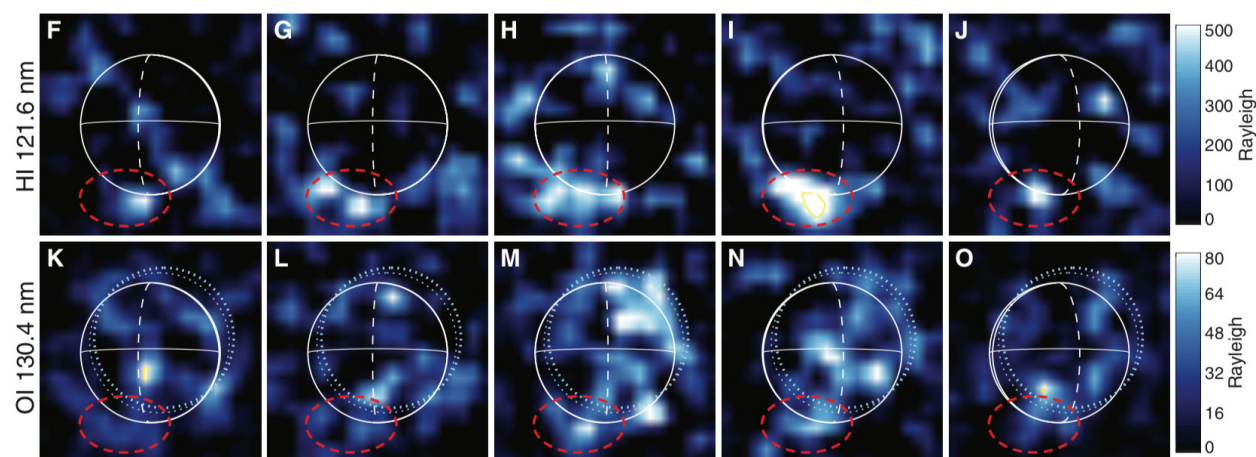


Figure B-13. Individual STIS images of Europa during five HST orbits in December 2012. Panels F to J show hydrogen Lyman- α emission and panels K to O show oxygen emission. Solar reflectance emission has been subtracted. The persistent plume-like emission is highlighted by the dashed red circles (Roth et al. 2014).

arrive in the Jupiter system in either 2026 or 2029 (depending on launch vehicle capabilities) and operate for at least three years.

LUVOIR will be in a position to serve three important supplemental roles in the effort to characterize the Europa plumes. First, with a 100x increase in sensitivity, a 6-fold improvement in spatial resolution, and a wide field of view, LUVOIR will be sensitive to plume activity over the whole surface with a vastly greater dynamic range than HST. This will enable characterization of a wider range of total mass production, cycles and patterns of activity, and topographic distribution. Second, LUVOIR will be in a position to follow up Europa Clipper discoveries with a regular cadence of observations over a longer time baseline, providing supplemental measurements of regions of interest and monitoring of changes in the global plume network under different tidal heating conditions. Third, LUVOIR could provide reconnaissance for subsequent spacecraft that might be in-system in the 2040s. Thus, we have created a preliminary plan for a Europa monitoring program using the sensitive far-UV spectral imaging capabilities of LUVOIR.

Observations overview. LUMOS FUV spectral imaging. Each observation will target the moon with the multi-object spectrograph (MOS) and the G155L grating, simultaneously covering a wavelength range (100 nm to 200 nm) that includes the hydrogen Lyman-alpha emission line (121.6 nm) and the neutral oxygen emission line (130.4 nm). An advantage of LUMOS is that the entire moon and a large area around it will remain within the MOS field-of-view. This allows all flux from anywhere in the region to be collected at all times without choosing a specific spectroscopic slit orientation, providing robustness to changing emission morphology.

To achieve the spatial resolution assumed in the Europa spectral imaging simulations shown in **Figures 1-10** and **3-20**, we will need to assemble mosaics out of dithered images. Exactly how many will be needed must be simulated in detail at a later date. For now, we adopt the strategy used for the best HST mosaics of Pluto (Buie et al. 2010), a 16-exposure dither pattern that optimally fills a unit pixel cell. Furthermore, the FUV PSF will have to be modeled out of the data. This was done for the HST Pluto mosaics, but at blue optical wavelengths. The LUVOIR telescopes will produce a much more stable and higher quality

PSF than HST at all wavelengths. Therefore, we believe this post-processing is feasible for LUVOIR+LUMOS, but it must be properly modeled in future.

Targets. Europa, visited once every two months over 5 years plus one visit of high cadence observations over one orbital period around Jupiter (3.5 days).

Exposure times & overheads. The time for each exposure with LUVOIR-A was estimated from far-UV observations of Europa in 2012 with HST. Those observations used the STIS instrument with the G140L grating. Two exposures were collected in five consecutive orbits during each visit, resulting in a 4- σ detection of Lyman- α plume emission and a 2.4- σ detection of neutral oxygen emission in the combined image with a total exposure time of 164 min (Roth et al. 2014).

Assuming Poisson statistics, we apply the following equations to estimate the times to obtain 3- σ detections of the neutral oxygen emission in each LUMOS exposure,

$$t_{LUMOS-A} = t_{STIS} \times \left(\frac{A_{STIS}}{A_{LUMOS-A}} \right) \times \left(\frac{R_{LUMOS}}{R_{STIS}} \right) \times \left(\frac{SNR_{LUMOS}}{SNR_{STIS}} \right)^2 \quad (1)$$

$$t_{LUMOS-A} \approx t_{STIS} \times \left(\frac{2\% \times 45238.93 \text{ cm}^2}{1.5 \times 10^5 \text{ cm}^2} \right) \times \left(\frac{11,600}{1000} \right) \times \left(\frac{3}{2.4} \right)^2 \quad (2)$$

$$t_{LUMOS-A} \approx 164 \text{ min} \times (0.006) \times (11.6) \times (1.56) = 18 \text{ min} \quad (3)$$

where A is the effective area of the observing mode, R is the spectral resolution $((\lambda)/(\Delta\lambda))$, and SNR is the signal-to-noise ratio of the emission. Specifications for the G140L mode of STIS are from Chapter 13 of the HST STIS Instrument Handbook for Cycle 27¹. Since the plume emission was unresolved to HST, the higher spatial resolution of LUVOIR may result in higher SNR than this in the individual exposures. Furthermore, the SNR in the individual Lyman- α images will be higher and the SNR in both final mosaics will be much higher.

The exposure time to observe Europa with LUVOIR-B is estimated by scaling the LUVOIR-A time by the ratio of collecting areas, 155 m² for LUVOIR-A and 43.8 m² for LUVOIR-B. Therefore, the LUVOIR-B exposure time is:

$$t_{LUMOS-B} = t_{LUMOS-A} \times \left(\frac{A_{LUVOIR-A}}{A_{LUVOIR-B}} \right) = 18 \text{ min} \times \frac{155 \text{ m}^2}{43.8 \text{ m}^2} = 64 \text{ min}$$

We estimate the overheads on these programs by assuming 1 hour per visit, primarily for retargeting slews.

Results. Assuming 16 exposures per visit, the science time per visit is 4.8 hours for LUVOIR-A and 17.1 hours with LUVOIR-B. Adding overheads brings the total time per visit to 5.8 hours for LUVOIR-A and 18.1 hours with LUVOIR-B. Therefore, the total time for the long-term Europa monitoring program with LUVOIR-A is 5.8 hours \times 6 visits per year

¹ http://www.stsci.edu/hst/stis/documents/handbooks/current/HB/c13_specref15.html

$\times 5$ years ≈ 7 days. The total long-term program time with LUVVOIR-B is 18.1 hours $\times 6$ visits per year $\times 5$ years ≈ 23 days.

To these totals, we add 4 days for a single visit of continuous high cadence observations of Europa over one whole orbit around Jupiter (3.5 day period). These data will be used to examine Europa's interaction with the Jovian magnetosphere via non-plume-related auroral emissions. About 20 mosaics can be obtained over this time period with LUVVOIR-A and 5 with LUVVOIR-B.

Therefore, the total time for the Europa program is 11 days with LUVVOIR-A and 27 days with LUVVOIR-B. This preliminary program is intended to demonstrate feasibility of FUV monitoring of Europa with LUVVOIR on various time scales and will no doubt benefit from further study and future optimization.

Parallels

- ☒ Do not execute parallels with this program
- ☐ Parallels required for this program
- ☐ Can be executed as parallel to another program
- ☐ Possible to execute parallels with this program

Since the exposures will be dithered to produce mosaics, this program is not suitable for parallel observations.

Target of opportunity / time-critical

- ☐ Is a ToO program
- ☒ Is time-critical

Multiple visits required, with cadence described above.

B.4.3 Optical/NIR imaging of ocean moons

Plumes from Enceladus were observed with the Cassini spacecraft (e.g., Hansen et al. 2006). The plumes from the southern polar region are about four times brighter when Enceladus is at apocenter in its orbit around Saturn, compared to at pericenter, suggesting a connection with tidal stresses induced by Enceladus' eccentric orbit (Hurford et al. 2007). Observations from Cassini-VIMS verified that Enceladus' tidal activity varies on an orbital timescale (Hedman et al. 2013). However, it is currently unknown whether the Enceladus plumes, which supply Saturn's E ring with material, are always active or whether geyser activity is an intermittent phenomenon on decadal or longer timescales.

The Enceladus plumes are tenuous (releasing a few hundred kg of H₂O per second; Hansen et al. 2006) and have never been observed with remote telescopes. Given the different magnetic environment at Saturn, it is difficult to predict whether Europa-like FUV emission will be detectable with LUVVOIR. Therefore, we chose to focus upon optical/NIR imaging of Enceladus and other ocean moons of the outer solar system, leveraging the high spatial resolution of LUVVOIR to look for changes in surface morphology caused by cryo-volcanism over long timescales.

Table B-7. *Ocean moons imaging targets*

Target	V mag	Angular diameter in 2040 (arcsec)	Diameter (km)	LUVOIR-A V band resolution (km)	LUVOIR-B V band resolution (km)
Europa	5.29	0.83	3122	28	52
Ganymede	4.61	1.4	5268	28	52
Callisto	5.65	1.28	4821	28	52
Enceladus	11.7	0.07	504	56	106
Titan	8.2	0.74	5151	56	106
Triton	13.47	0.12	2707	192	359

Future work will investigate the feasibility of detecting Enceladus's plumes in optical/NIR scattered light with LUVOIR. The bright surface of this moon makes it difficult to detect the faint plumes emanating from its surface. One advantage offered by the HDI instrument is the ability to read out different portions of the detectors at different rates, which will increase the dynamic range of the imaging observations.

Observations overview. Multi-band HDI imaging. Images will be obtained in narrow-band filters centered upon and bracketing absorption features of particular surface materials (e.g., water ice at 1100 and 1400 nm and methane ice at 1700 nm). For each visit, several images with slightly shifted pointing will be obtained, to create final mosaics with the best possible spatial resolution.

Targets. Outer solar system moons that show evidence of sub-surface oceans. For the present, we include the moons in **Table B-7**. Each moon will be observed twice per year over 5 years.

Exposure times & overheads. These targets are extremely bright for LUVOIR. With either LUVOIR-A or LUVOIR-B, a 10 sec HDI image of the faintest target (Triton) in a 1% filter centered near V band returns $\text{SNR} \approx 23$ per pixel. We expect our primary consideration will be to prevent saturation. Fortunately, HDI has high-speed readout capabilities and includes neutral density filters. Therefore, we simply allot 1 hour per target per epoch and adopt 1 hour of overhead per visit, primarily for retargeting slews.

Results. The total program time with both LUVOIR-A and -B is $6 \text{ moons} \times 2 \text{ visits per year} \times 5 \text{ years} \times 2 \text{ hours} = 120 \text{ hours} = 5 \text{ days}$. This simple observing program is intended to establish the feasibility of monitoring moons in the outer solar system; further details will be added at a later date.

Parallels

- ☒ Do not execute parallels with this program
- ☐ Parallels required for this program
- ☐ Can be executed as parallel to another program
- ☐ Possible to execute parallels with this program

Since the exposures will be dithered to produce mosaics, this program is not suitable for parallel observations.

Target of opportunity / time-critical

- ☐ Is a ToO program
- ☒ Is time-critical

Revisits twice per year over 5 years.

B.5 Signature Science Case #4: Comparative atmospheres

B.5.1 Abstract

The goal of this science case is to explore the diversity of planetary atmospheres. This will be done in three ways:

1. Optical/NIR direct spectroscopy of cold to warm giant planets
2. Optical/NIR transit spectroscopy of warm to hot super-Earth and sub-Neptune planets
3. UV transit spectroscopy of hot giant planets

With these observing programs, we will study atmospheric composition, cloud & haze properties, and atmospheric escape rates over a wide range of planet and star parameters.

B.5.2 Direct spectroscopy

We first focus on the direct spectroscopy program to observe a diverse set of 30 planets with known masses constrained with the radial velocity technique. We chose a set of planets with equilibrium temperatures that span the range from ammonia clouds to water clouds to no clouds. This will allow us to explore the role of condensation processes in shaping exoplanet spectra, as well as determine atmospheric composition and abundance of key absorbers.

Observations overview. We will use ECLIPS to obtain high-contrast spectra of these planets over a broad wavelength range (400–1000 nm). The goals are to use these spectra to constrain cloud layers and atmospheric molecular abundances well enough to provide meaningful constraints on bulk abundances and C/O ratios. These goals can be achieved with SNR~15, R=140 ECLIPS spectra (e.g. Lupu et al. 2016).

By observing planets orbiting stars with a variety of spectral types we will test for the influence of photochemical processes on planetary composition and aerosols, particularly searching for sulfur and carbon photochemical products. This survey will map out, for the first time, the degree of complexity of gas and ice giant planetary atmospheres cooler than those which can be probed by transit methods. We expect our results to provide new insights into planet formation, atmospheric chemistry, dynamics, and cloud and photochemical processes.

Targets. We constructed a list of known exoplanets with previous mass measurements by downloading the Composite Planets Table from the NASA Exoplanet Archive¹ on 20 November 2018. We removed targets that were either too far or too close to their stars to

Program contact(s)

Courtney Dressing (UC – Berkeley), Mark Marley (NASA Ames), Avi Mandell (NASA GSFC), Eric Lopez (NASA GSFC)

Brief description

ECLIPS high-contrast optical/NIR spectroscopy of 30 non-Earth-like exoplanets

HDI low-resolution optical/NIR point-source transit spectroscopy

LUMOS UV point-source transit spectroscopy of 16 Neptune to super-Earth exoplanets

Total observing time

LUVOIR-A: 18 days + 23 days + 5 days
= 46 days

LUVOIR-B: 21 days + 23 days + 5 days
= 49 days

¹ <https://exoplanetarchive.ipac.caltech.edu/cgi-bin/TblView/nph-tblView?app=ExoTbls&config=composite-pars>

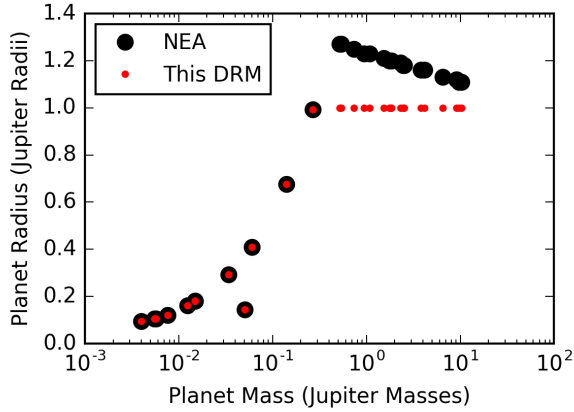


Figure B-14. Radii and masses of selected targets. The calculated radii provided via the NASA Exoplanet Archive (NEA; large black circles) are too large for massive planets. For this DRM, the assumed planet radii (smaller red circles) were capped at $1 R_J$.

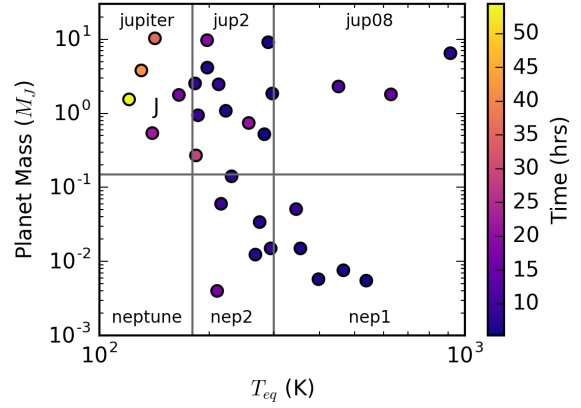


Figure B-15. Assumed atmospheric models for the selected targets. The points are colored based on the total required observation time (science integration time + overhead).

obtain complete spectral coverage from 400 to 1000 nm. We then calculated planetary equilibrium temperatures assuming a geometric albedo of 0.5.

Next, we refined the planet radii. The Composite Planet Table contains theoretical radius values based on the empirically-derived mass-radius relation published by Chen & Kipping (2017). Although these estimates are reasonable for less massive planets, they are unrealistically large for more massive planets. Accordingly, we revised the calculated radii so that no planets were assigned radii larger than Jupiter. The radii assumed for the planets we ultimately selected are shown in **Figure B-14**.

We then assigned model atmospheres to each planet using the classifications shown in **Figure B-15** and **Table B-8**. The atmospheric models include a warm Jupiter at 0.8 AU (“jup08”; Cahoy et al. 2010), a warm Jupiter at 2 AU (“jup2”; Cahoy et al. 2010), warm Neptune at 2 AU (“nep2”; Hu & Seager 2014), and a cloudy warm Neptune at 1 AU (“cloudy_nep1”; model provided by Renyu Hu). Planets with calculated equilibrium temperatures cooler

Table B-8. Science time and overheads required for each component of the LUV0IR-A non-earth direct spectroscopy program. The program requires 424 hours to investigate the compositions of 30 planets

Mass	$T_{eq} \leq 180 \text{ K}$	$180 < T_{eq} \leq 300 \text{ K}$	$T_{eq} > 300 \text{ K}$
$M_p > 0.15 M_J$	5 planets science: 132 hrs overhead: 38 hrs total: 171 hrs Model atmosphere = “jupiter”	11 planets science: 65 hrs overhead: 62 hrs total: 127 hrs Model atmosphere = “jup2” (warm Jupiter at 2 AU from Cahoy et al. 2010)	3 planets science: 18 hrs overhead: 17 hrs total: 35 hrs Model atmospheres= “jup08” (warm Jupiter at 0.8 AU from Cahoy et al. 2010)
$M_p \leq 0.15 M_J$	0 planets science: 0 hrs overhead: 0 hrs total: 0 hrs Model atmosphere = “neptune”	6 planets science: 18 hrs overhead: 17 hrs total: 35 hrs Model atmosphere = “nep2” (warm Neptune at 2 AU from Hu & Seager 2014)	5 planets science: 7 hrs overhead: 26 hrs total: 33 hrs Model atmosphere = “cloudy_nep1” (cloudy warm Neptune at 1 AU from Hu & Seager 2014)

than 180 K are assumed to have atmospheres similar to Jupiter or Neptune.

Exposure times & overheads. We calculated exposure times to obtain the desired spectra using LUVOIR-A and LUVOIR-B. The times required to obtain spectra with a median SNR=15 across each of the five visible bands and the three bluest NIR bands were calculated using the offline version of the ECLIPS simulation tool (**Section B.1.1**). The telescope and instrument parameters used appear in **Table B-9**. The planets were viewed at quadrature against a background of 3 zodis of exozodi. A breakdown of the time required for each planet category with LUVOIR-A appears in **Table B-8**.

The estimated overheads include an allocation of one hour for slewing, dynamic settling, and thermal settling, as well as a total of four hours for digging the coronagraph dark hole (assuming 30 minutes per band for five visible and three NIR band). An additional tax of 10% of the science time is added to account for ongoing wavefront control maintenance. For most targets, the estimated overhead is dominated by the time to dig the dark hole. If less time is required when switching bands or if the spectra can be obtained at a lower contrast, then these overheads would be significantly reduced. As a result, the overall program could be accomplished in much less time or the program could be expanded to incorporate observations of many more planets within the allotted time.

Results. Of the original set of possible exoplanets, we rejected all that required more than 120 hours total (science + overhead) time. For LUVOIR-A, this resulted in a set of 30 planets that efficiently sample temperature-radius space (**Figure B-16**). The selected planets and their exposure times are listed in **Table B-10**. When possible, we prioritized planets in multi-planet systems so that we could compare the compositions of planets that formed from the same disk. The full set of multi-planet systems is shown in **Figure B-17**. Even though multiple planets in a system might be visible at the same time, we did not decrease our estimated integration times to account for the possibility of simultaneous spectroscopic observations using the ECLIPS IFS. The total estimated time to observe the full set of 30 planets with LUVOIR-A is 424 hours ~ 18 days.

The planet exposure times for LUVOIR-B appear in **Table B-11**. To keep the total program time reasonable, we decided to observe 19 targets, resulting in a total estimated time of 499 hours ~ 21 days.

Table B-9. Telescope and ECLIPS parameters for exposure time calculations

Parameter	LUVOIR-A	LUVOIR-B
Encircled mirror diameter (D)	13.5 m	6.7 m
Contrast	1×10^{-10}	1×10^{-10}
IWA	$3.5 \lambda D$	$3.5 \lambda D$
OWA	$33 \lambda D$	$27 \lambda D$
Core throughput (Vis)	0.20	0.40
Core throughput (NUV)	0.20	0.40
Core throughput (NIR)	0.20	0.40
Optical throughput (NUV)	0.23	0.25
Optical throughput (Vis)	0.23	0.25
Optical throughput (NIR)	0.23	0.25
Resolution (NUV)	7	7
Resolution (Vis)	140	140
Resolution (NIR)	70	70
Dark current (NUV)	3×10^{-5}	3×10^{-5}
Dark current (Vis)	3×10^{-5}	3×10^{-5}
Dark current (NIR)	2×10^{-3}	2×10^{-3}
Read noise (NUV)	1×10^{-2}	1×10^{-2}
Read noise (Vis)	1×10^{-2}	1×10^{-2}
Read noise (NIR)	2.5	2.5
Clock-induced charge (NUV)	1.3×10^{-3}	1.3×10^{-3}
Clock-induced charge (Vis)	1.3×10^{-3}	1.3×10^{-3}
Clock-induced charge (NIR)	0	0

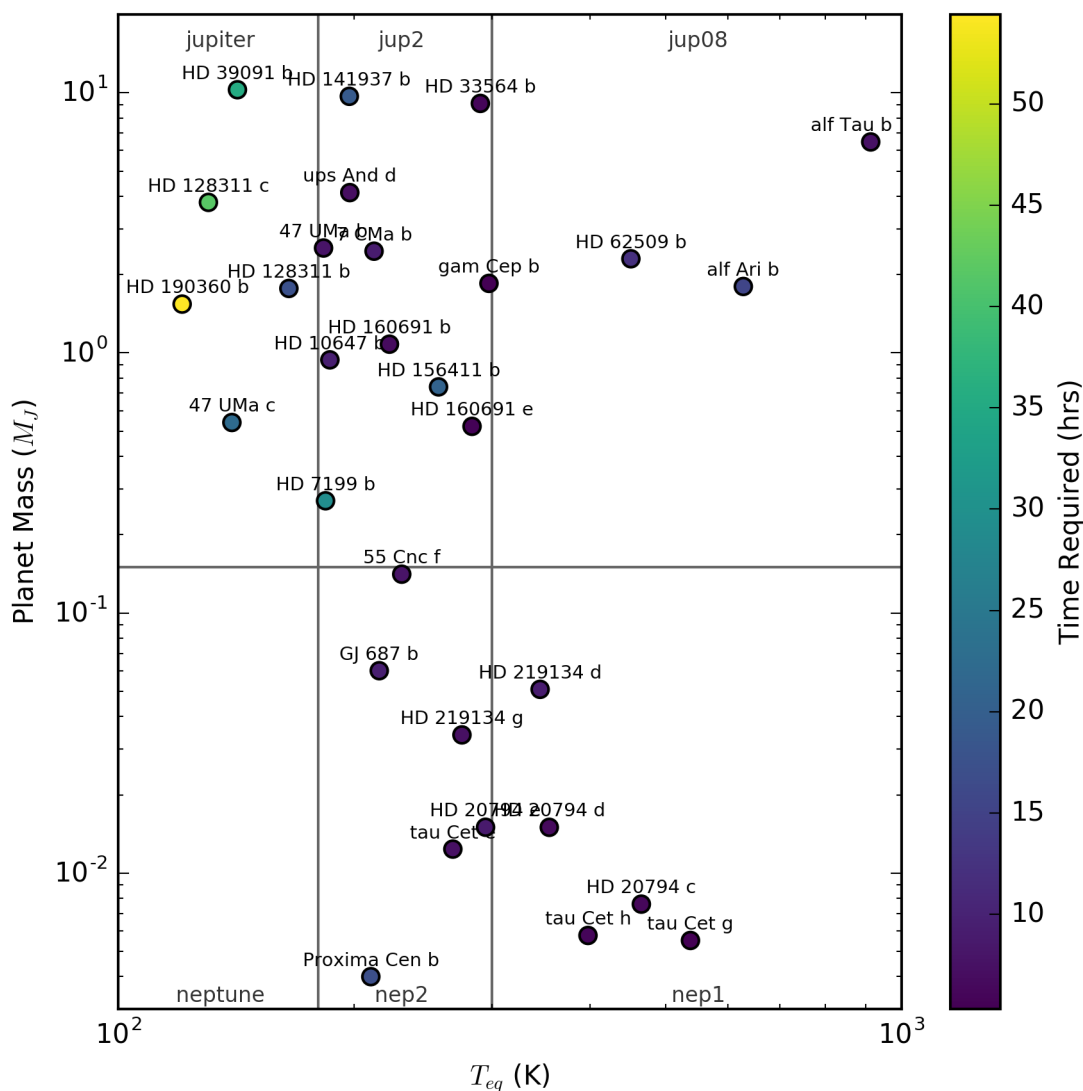


Figure B-16. Masses and equilibrium temperatures of the 30 planets in the LUVUOIR-A direct spectroscopy program. The planets are colored by the total time required (science + overhead). The grid cells indicate the selected model atmosphere (labeled at top and bottom).

Table B-10. Planets selected for our 424-hour non-Earth atmospheric characterization program with LUVUOIR-A. VIS = visible science exposure time; NIR = NIR science exposure time; OH = overheads; Target = total time for star; Cum. = cumulative total program time

Planet Properties					Star Properties				Time Required (Hours)				
Name	Mass (M_J)	R (R_J)	A (AU)	Teq (K)	Type	Teff (K)	R (R_J)	Dist (pc)	VIS	NIR	OH	Target	Cum.
tau Cet g	0.055	0.11	0.13	538	G8V	5310	0.83	3.6	0.23	0.06	5.03	5.3	5.3
gam Cep b	1.85	1	2.05	297	K1 IV	4744	4.9	13.54	0.35	0.09	5.04	5.5	10.8
HD 160691 e	0.52	1	0.92	283	G5 V	5807	1.33	15.61	0.41	0.17	5.06	5.6	16.4
HD 33564 b	9.1	1	1.10	290	F7 V	6250	1.44	20.97	0.65	0.31	5.10	6.1	22.5
tau Cet h	0.0058	0.11	0.24	398	G8V	5310	0.83	3.6	0.76	0.21	5.10	6.1	28.6
HD 20794 c	0.0076	0.12	0.20	465	G8V	5401	0.92	6	0.86	0.27	5.11	6.2	34.8

Planet Properties					Star Properties				Time Required (Hours)				
Name	Mass (M _J)	R (R _J)	A (AU)	Teq (K)	Type	Teff (K)	R (R _⊙)	Dist (pc)	VIS	NIR	OH	Target	Cum.
HD 20794 d	0.015	0.18	0.35	355	G8 V	5401	0.92	6	1.09	0.31	5.14	6.5	41.4
HD 160691 b	1.08	1	1.50	222	G5 V	5807	1.33	15.61	1.11	0.46	5.16	6.7	48.1
ups And d	4.13	1	2.51	197	F8 V	6183	1.56	13.41	1.27	0.60	5.19	7.1	55.1
HD 219134 g	0.034	0.29	0.38	275	K3 V	4699	0.78	6.55	1.73	0.41	5.21	7.4	62.5
tau Cet e	0.012	0.16	0.54	267	G8 V	5310	0.83	3.6	1.67	0.54	5.22	7.4	69.9
alf Tau b	6.47	1	1.46	914	K5 III	4055	45.1	20.43	0.05	2.24	5.23	7.5	77.4
55 Cnc f	0.14	0.68	0.79	230	G8 V	5196	0.94	12.59	2.02	0.61	5.26	7.9	85.3
47 UMa b	2.53	1	2.10	183	G0 V	5892	1.23	13.8	1.88	0.82	5.27	8.0	93.3
HD 20794 e	0.015	0.18	0.51	294	G8 V	5401	0.92	6	2.43	0.85	5.33	8.6	101.9
7 CMa b	2.46	1	1.93	212	K1 III	4792	2.3	19.82	2.85	0.78	5.36	9.0	110.9
HD 219134 d	0.051	0.14	0.24	346	K3 V	4699	0.78	6.55	3.01	0.65	5.37	9.0	119.9
GJ 687 b	0.06	0.41	0.17	215	M3 V	3340	0.43	4.55	3.72	0.26	5.40	9.4	129.3
HD 10647 b	0.94	1	2.02	186	F9 V	6218	1.1	17.34	2.68	1.35	5.40	9.4	138.8
HD 62509 b	2.3	1	1.64	451	K0 III	4946	8.31	10.34	0.16	6.35	5.65	12.2	150.9
alf Ari b	1.8	1	1.20	628	K1 IIIb	4553	13.9	20.21	0.18	9.18	5.94	15.3	166.2
Proxima Cen b	0.004	0.1	0.05	210	M5.5 V	3050	0.14	1.29	10.46	0.47	6.09	17.0	183.2
HD 128311 b	1.77	1	1.08	165	K0 V	4863	0.76	16.52	8.47	2.95	6.14	17.6	200.8
HD 141937 b	9.69	1	1.50	197	G2/3 V	5870	1.03	33.39	8.53	4.39	6.29	19.2	220.0
HD 156411 b	0.74	1	1.88	256	F8 IV/V	5900	2.16	56.96	9.11	5.23	6.43	20.8	240.8
47 UMa c	0.54	1	3.60	140	G0 V	5892	1.23	13.8	9.76	5.88	6.56	22.2	263.0
HD 7199 b	0.27	0.99	1.36	184	K0 IV/V	5371	0.97	36.19	15.25	6.80	7.20	29.2	292.2
HD 39091 b	10.27	1	3.38	142	G1 V	5950	1.17	18.28	16.26	11.28	7.75	35.3	327.5
HD 128311 c	3.79	1	1.74	130	K0 V	4863	0.76	16.52	23.77	9.52	8.33	41.6	369.2
HD 190360 b	1.54	1	3.97	121	G6 IV	5552	1.14	16.01	27.28	17.64	9.49	54.4	423.6

Table B-11. Planets selected for our 499-hour non-Earth atmospheric characterization program with LUVOIR-B. VIS = visible science exposure time; NIR = NIR science exposure time; OH = overheads; Target = total time for star; Cum. = cumulative total program time

Planet Properties					Star Properties				Time Required (Hours)				
Name	Mass (M _J)	R (R _J)	A (AU)	Teq (K)	Type	Teff (K)	R (R _⊙)	Dist (pc)	VIS	NIR	OH	Target	Cum.
WASP-53 c	16.35	1	3.73	93	K3 V	4953	0.80	202.5	0.10	0.01	5.00	5.2	5.2
gam Cep b	1.85	1	2.05	297	K1 IV	4744	4.9	13.54	0.44	0.12	5.06	5.6	10.8
tau Cet h	0.0058	0.11	0.24	398	G8 V	5310	0.83	3.6	1.06	0.35	5.14	6.5	17.3
HD 160691 b	1.08	1	1.50	222	G5 V	5807	1.33	15.61	1.43	0.63	5.21	7.3	24.6
ups And d	4.13	1	2.51	197	F8 V	6183	1.56	13.41	1.64	0.81	5.25	7.7	32.3
tau Cet e	0.012	0.16	0.54	267	G8 V	5310	0.83	3.6	2.21	0.79	5.30	8.3	40.6
47 UMa b	2.53	1	2.10	183	G0 V	5892	1.23	13.8	2.44	1.12	5.36	8.9	49.6
HD 20794 e	0.015	0.18	0.51	294	G8 V	5401	0.92	6	3.39	1.43	5.48	10.3	59.9

Planet Properties					Star Properties				Time Required (Hours)				
Name	Mass (M_J)	R (R_J)	A (AU)	Teq (K)	Type	Teff (K)	R (R_\odot)	Dist (pc)	VIS	NIR	OH	Target	Cum.
HD 10647 b	0.94	1	2.02	186	F9 V	6218	1.1	17.34	3.50	1.92	5.54	11.0	70.8
alf Tau b	6.47	1	1.46	914	K5 III	4055	45.1	20.43	0.09	8.31	5.84	14.2	85.1
HD 10697 b	6.21	1	2.13	212	G5 IV	5680	1.81	32.6	8.62	5.70	6.43	20.8	105.8
HD 62509 b	2.30	1	1.64	451	K0 III	4946	8.31	10.34	0.22	14.67	6.49	21.4	127.2
47 UMa c	0.54	1	3.60	140	G0 V	5892	1.23	13.8	12.97	8.78	7.18	28.9	156.1
HD 219134 h	0.34	1	3.11	95	K3 V	4699	0.78	6.55	18.49	6.43	7.49	32.4	188.6
HD 39091 b	10.27	1	3.38	142	G1 V	5950	1.17	18.28	22.23	18.03	9.03	49.3	237.8
HD128311 c	3.79	1	1.74	130	K0 V	4863	0.76	16.52	32.92	15.21	9.81	57.9	295.8
HD 164922 b	0.31	1	2.10	148	G9 V	5372	0.97	22.13	30.80	20.78	10.16	61.7	357.5
HD 95872 b	3.74	1	5.15	87	K0 V	5312	0.84	7.56	33.78	19.81	10.36	64.0	421.5
HD190360 b	1.54	1	3.97	121	G6 IV	5552	1.14	16.01	37.71	28.14	11.58	77.4	498.9

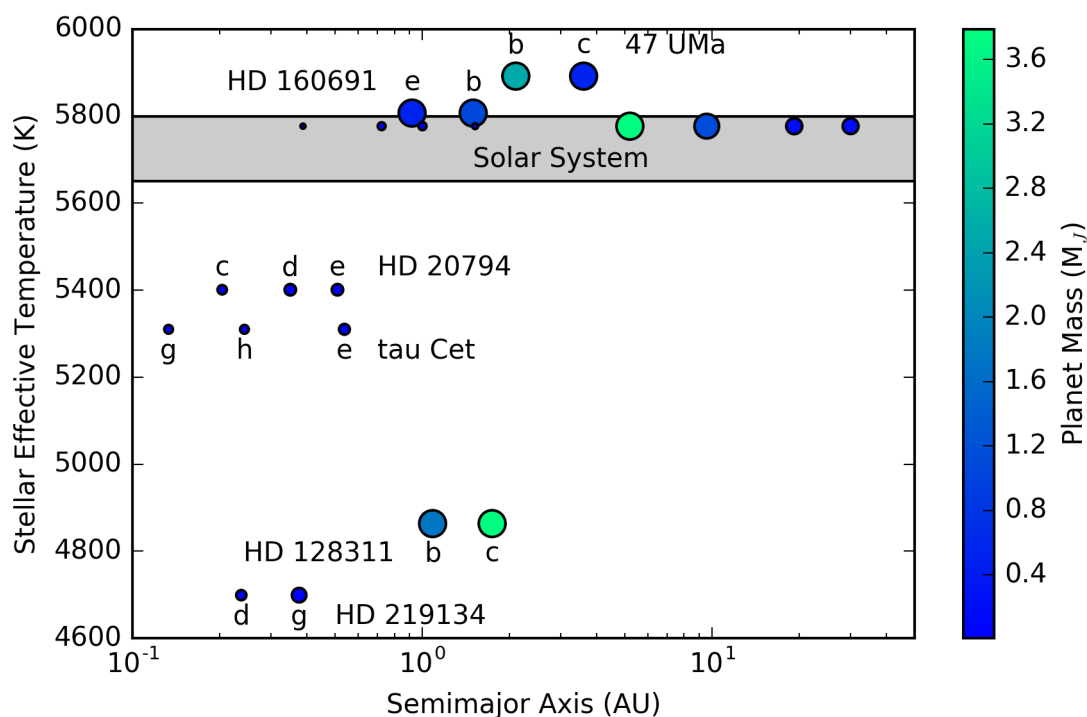


Figure B-17. Multiplanet systems in our LUV01R-A target sample for which LUV01R will obtain spectra of multiple planets. The target list also includes observations of only one planet in other known multiplanet systems.

Parallels

- ☐ Do not execute parallels with this program
- ☐ Parallels required for this program
- ☐ Can be executed as parallel to another program
- ☒ Possible to execute parallels with this program

Target of opportunity / time-critical

- ☐ Is a ToO program
- ☐ Is time-critical

B.5.3 Optical/NIR transit spectroscopy

LUVOIR will be a capable transit science successor to JWST for both hot and warm gas-rich planets as well as hot and warm rocky planets. LUVOIR-A will have a collecting area 178 m², a factor of 7x larger than JWST, and observations will reach the same SNR with 2.7x less integration time. LUVOIR will improve on JWST measurements between 0.8 and 2.5 μm , a band which covers molecular features of H₂O, CH₄, CO and hydrocarbons such as HCN. LUVOIR will therefore provide strong constraints on the bulk composition and oxidation state of the atmosphere. At shorter wavelengths (0.2–0.8 μm), LUVOIR’s capabilities will be unique. In particular, measurements of Rayleigh scattering and atomic metal lines will be key diagnostics of atmospheric properties for a wide range of planets, and O₂ at 720 nm and O₃ at 200–300 nm will enable the first searches for these key biomarkers of photosynthetic life.

Observations overview. The primary instrument for transit spectroscopy with LUVOIR will be the High Definition Imager (HDI), due to the broad simultaneous wavelength coverage (200 nm–2.5 μm) and the ability to spatially scan the spectra of bright stars across the large focal plane detectors. All observations will be taken with the HDI low-resolution optical/NIR grisms. HDI includes both a beamsplitter and a dichroic; the dichroic provides maximum throughput and full coverage from 400–1600 nm, while the beamsplitter provides half the flux in both the optical and NIR channels (200–950 nm and 800 nm–2.5 μm). For this Design Reference Program, we will use the beamsplitter for the giant planet observations and the dichroic for the rocky planets with high mean molecular weight atmospheres.

Targets. Hundreds of high-quality targets in the gas-rich regime are already known, and the TESS mission and other transit missions are currently rapidly increasing the number of high-quality rocky planet targets. In order to make a direct comparison to JWST, we decided to utilize targets from the JWST GTO target list, since these same targets will most likely be some of the first targets examined with LUVOIR. The sample targets are listed in **Table B-12**.

Exposure times & overheads. The total survey time is set by the transit duration for each planet and the number of targets. We will observe a single transit for the hot Jupiter/Saturn planets, 5 transits for hot Neptune/Uranus planets and ultra-hot rocky planets such as 55 Cnc e, and 50 transits for a few warm/temperate rocky planets such as TRAPPIST-1 e and LHS1140 b. For each visit, we will need to observe continuously over one full transit using HDI with an additional 50% margin on each side of the transit in order to establish stellar flux baselines before ingress and after egress.

To estimate the strength of spectral features, we assumed an Earth-like atmosphere for rocky planets, a 100x solar metallicity atmosphere for Neptunes, and a Jupiter-like atmosphere for Saturns and Jupiters. We calculated the expected SNR per resolution element on the combined H₂O and CH₄ feature at 1.8 μm ; the spectral feature is dominated by CH₄ in gas-rich atmospheres vs H₂O in Earth-like atmospheres. The resolving power was

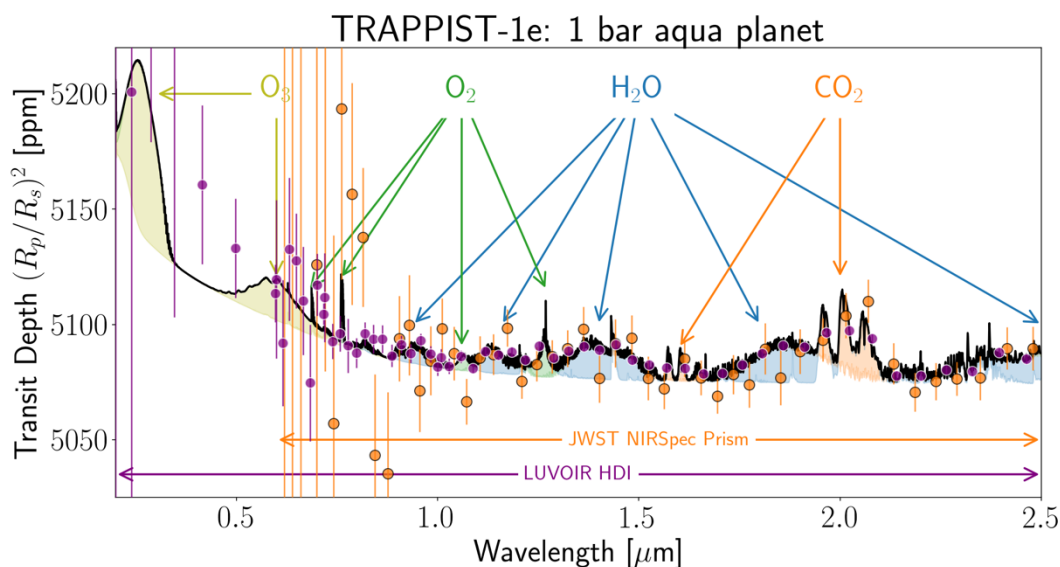


Figure B-18. Simulated spectra of TRAPPIST-1 e for 50 observed transits with JWST's NIRSpec prism (orange points) and 50 transits observed with LUVOIR-A HDI (purple points), assuming a water-covered planet with a 1 bar atmosphere (Lincowski et al. 2018). The NIRSpec spectrum was generated using the PandExo code (Batalha et al. 2017). Credit: J. Lustig-Yaeger (UW).

determined by the SNR—when possible, we chose a higher resolving power. Simulated transit spectra of TRAPPIST-1 e with JWST and LUVOIR-A appear in **Figure B-18**.

Results. The results of the SNR calculations for our sample target list are shown in **Table B-12**. With LUVOIR-A, we were able to achieve $\text{SNR} \gtrsim 7$ for H_2O feature with $R=15$ for each of the warm rocky planets (TRAPPIST-1 e, LHS 1140 b, and GJ 1132 b) by combining 50 transits. For all the other planets, we were able to achieve much higher SNR with 1-5 transits. Since the exposure times are set by the transit durations, the total survey time is the same for LUVOIR-A and LUVOIR-B, with the per target SNR scaling proportionally by telescope effective area. For our 16 targets, we estimate a total of 366 science hours and 549 total hours ~ 23 days with overheads.

Parallels

- ☐ Do not execute parallels with this program
- ☐ Parallels required for this program
- ☐ Can be executed as parallel to another program
- ☒ Possible to execute parallels with this program

Target of opportunity / time-critical

- ☐ Is a ToO program
- ☒ Is time-critical

Stars must be observed continuously during the transits of each planet.

B.5.4 Atmospheric escape via UV transit spectroscopy

High SNR FUV spectroscopy with LUVOIR LUMOS will enable us to detect exospheric absorption and measure atmospheric escape for ~ 16 transiting exoplanets. For ~ 10

Table B-12. A sample target list for optical/NIR transit spectroscopy, based on the expected GTO targets for JWST. The SNR per resolution element for the $\text{H}_2\text{O}/\text{CH}_4$ spectral feature at $1.8\ \mu\text{m}$ is calculated for LUVOIR-A and a specific resolving power.

Planet	Mass (M_\oplus)	Radius (R_\oplus)	Dens. (g cm^{-3})	T_{eq} (K)	Sp. type	# transits	Exp. Time (hr)	R	SNR @ $\text{H}_2\text{O}/\text{CH}_4$ LUVOIR-A
TRAPPIST-1 e	0.62	0.9	4.4	251	M8	50	100	15	18.0
GJ-1132	1.7	1.2	6	409	M4.5	50	80	15	6.8
LHS-1140	7	1.7	7.5	234	M4.5	50	100	15	7.1
55 Cnc e	8.1	1.9	6.4	1958	K0	1	3.2	500	18.0
K2-18	8	2.4	3.3	235	M2.5	5	26	100	11.6
GJ-3470	14.1	4.3	0.9	615	M1.5	1	3.8	500	25.8
HAT-P-26	18.7	6.3	0.4	1001	K1	1	5	500	45.8
GJ-436	22.1	4.2	1.8	686	M2.5	1	2	500	24.6
WASP-107	38	10.4	0.2	736	K6	1	5.4	500	140.0
HAT-P-12	66.1	10.7	0.3	963	K4	1	4.6	500	35.5
WASP-69	80	11.9	0.3	963	K5	1	4.4	500	78.9
WASP-17	163	22.3	0.1	1740	F4	1	8.8	500	23.2
HAT-P-1	168	14.8	0.3	1322	G0	1	5.6	500	38.5
WASP-80	172	11.2	0.7	825	K7	1	4.2	500	32.6
HD-209458	217	15.2	0.3	1450	G0	1	5.2	500	259.6
WASP-79	270	20.4	0.2	1900	F4	1	8	500	56.4
Total							366		

sub-Neptune to Neptune-sized exoplanets around nearby Sun-like stars, we will be able to detect exospheric absorption from hydrogen, carbon, and oxygen in a single transit. This will allow us to fully map the density and velocity structure of these planets' exospheres, constrain the physics of atmospheric escape, and measure atmospheric abundances, including C/O for material above any cloud layers. Additionally, for ~6 sub-Neptunes and super-Earths around nearby M dwarfs, we will measure hydrogen escape via Lyman-alpha observations, enabling us to understand escape rates for planets close to the habitable zone. For further details see **Section 3.1.4**.

Observations overview. All observations will be done with the LUMOS G120M grating mode to obtain medium resolution FUV spectra ($R > 40,000$). These spectra will simultaneously include all three of the targeted stellar emission lines: Lyman-alpha at 121.6 nm, OI at 130.4 nm and CII at 133.5 nm.

Targets. Targets are notional, based on the Barclay et al. (2018) simulated TESS catalog (**Figure B-19**). For each planet, we will need to observe continuously over one full transit using LUMOS with an additional 50% margin on each side of the transit in order to establish stellar flux baselines before ingress and after egress.

Exposure times & overheads. The total survey time is set by the transit duration for each planet and the number of targets. For each notional planet, we estimated the time required for its Hill sphere to transit and then doubled this time to obtain good coverage of ingress and egress. The best targets will typically have short orbital periods between 1–20 days,

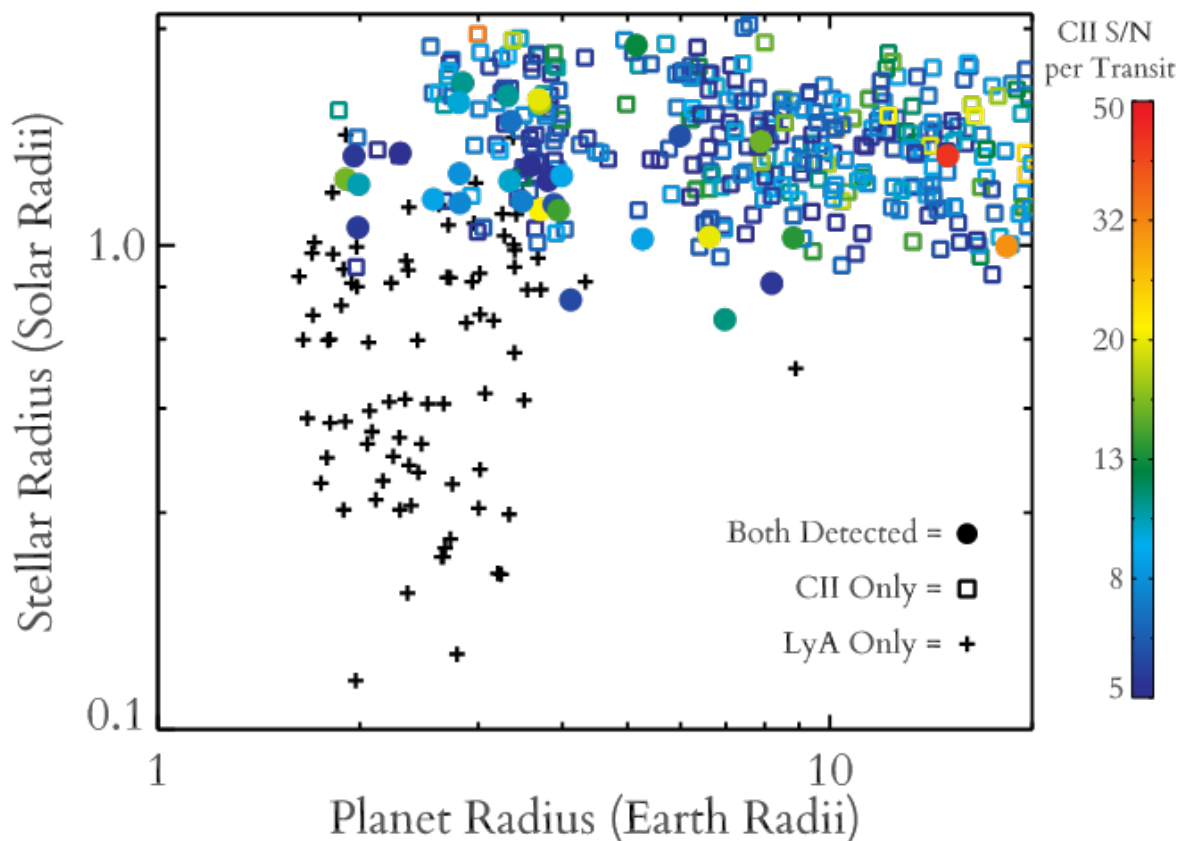


Figure B-19. Predictions for the number of TESS planets for which LUV0IR should be able to detect transiting exospheres. Points show simulated TESS planets taken from the Barclay et al. (2018) simulated TESS catalog for which LUV0IR could detect exospheric absorption at >5 sigma integrated over a single transit. For planets where a CII exosphere can be detected, points are color coded by the S/N of the planets CII absorption signal integrated over the transit. The axes show radii of these planet candidates and their host stars. The black crosses show planets where the exosphere can only be detected in Lyman Alpha, which are typically around nearby M dwarfs. The open squares show planets where the exosphere can only be detected in CII at 133nm, and the filled circles show simulated planets where both Lyman Alpha and CII can be detected.

resulting in relatively short transit durations of 1–4 hours. We calculated the expected SNR of each planet’s CII absorption given the transit duration.

Results. Due to stellar variability in the FUV between transits, it may not be helpful to co-add multiple transits. Therefore, the total survey time is the same for LUV0IR-A and LUV0IR-B, with the per target SNR scaling proportionally by telescope effective area. For our 16 targets, we estimate a total of 76 science hours and 114 total hours \sim 5 days with overheads.

Parallels

- ☐ Do not execute parallels with this program
- ☐ Parallels required for this program
- ☐ Can be executed as parallel to another program
- ☒ Possible to execute parallels with this program

Target of opportunity / time-critical

- ☐ Is a ToO program
- ☒ Is time-critical

Stars must be observed continuously during the transit of each planet.

B.6 Signature Science Case #5: The formation of planetary systems

B.6.1 Abstract

The goal of this science case is to understand the formation and evolution of planetary systems, from young planet-forming disks to mature exoplanet systems. This will be done in three ways:

1. UV spectroscopy of large numbers of protoplanetary disks in the Orion Star Forming Region to measure the primary molecular species and trace dispersal of primordial material via disk winds.
2. High contrast imaging of young planetary systems (debris disks) to probe early dynamical evolution and the timing of planet formation.
3. High precision astrometry to measure the masses and orbits of all planets in systems with habitable planet candidates. These measurements will also provide masses of habitable planet candidates needed for modeling of their atmospheres (Signature Science Case #2).

Program contact(s)

Kevin France (U of Colorado), Karl Stapelfeldt (JPL), Diana Windemuth (U of Washington), Marc Postman (STScI)

Brief description

LUMOS multi-object UV spectroscopy of protostars within 5 areas with different ages in the Orion Star-Forming Region

ECLIPS high contrast optical imaging of 25 debris disks

HDI high precision astrometry to measure masses and orbits of planets in ~54 systems with LUV OIR-A and ~28 with LUV OIR-B

Total observing time

LUV OIR-A: 9 days + 6 days + 10 days = 25 days

LUV OIR-B: 24 days + 22 days + 13 days = 59 days

These studies will provide essential information for developing models of the formation and dynamical evolution of planetary systems, as well as placing extrasolar systems in context with our own better studied system.

B.6.2 Protoplanetary disks

LUV OIR's multi-object, high-resolution spectroscopic capability ($R > 30,000$, > 4 square arc-minutes per LUMOS field) enables emission line surveys and absorption line spectroscopy of high-inclination ($i > 60$ degrees) protoplanetary disks. UV absorption line spectroscopy is the only direct observational technique to characterize co-spatial populations of molecules with respect to the most abundant species (H_2). This approach allows us to make absolute abundance and temperature measurements without having to rely upon molecular or gas-to-dust conversion factors nor geometry-dependent model results as with emission line spectroscopy. Such a program will, for the first time, trace the evolution and dispersal of the main molecular carriers of C, H, and O during planet assembly in the terrestrial and giant-planet forming regions, trace molecular and low-ionization metals from disk winds, and provide the absolute abundance patterns in disks as a function of age.

Observations overview. In this program, LUMOS will be used to obtain complete FUV and NUV spectra of protostars in the Orion complex, enabling the detection of the most abundant molecular species in disks, e.g., H_2 , CO, H_2O , and OH.

Targets. Observe 5 areas within the Orion star-forming region of different ages.

1. Orion Nebular Cloud: ~ 1 Myr, $\sim 24'$ size, 6 pointings
2. NGC1980: ~ 1 – 2 Myr, $\sim 16'$ size, 4 pointings
3. σ Ori: ~ 3 – 5 Myr, $\sim 33'$ size, 9 pointings
4. λ Ori: 4 – 8 Myr, $49'$ size, 13 pointings
5. 25 Ori: ~ 7 – 10 Myr, $33'$ size, 9 pointings

Exposure times & overheads. Using the LUMOS exposure time calculator (Section B.1.4), we find that 1 hour of science exposure time with LUMOS on LUVOIR-A will reach $\text{SNR} = 10$ per resolution element (assumed average $R = 40,000$) over a $2' \times 2'$ field for a spectral intensity of $F_\lambda = F(1100 \text{ \AA}) = 2 \times 10^{-16} \text{ erg cm}^{-2} \text{ s}^{-1} \text{ \AA}^{-1}$. This is typical of the continuum flux from young stars in Taurus scaled to the distance of the Orion complex (see Figure B-20).

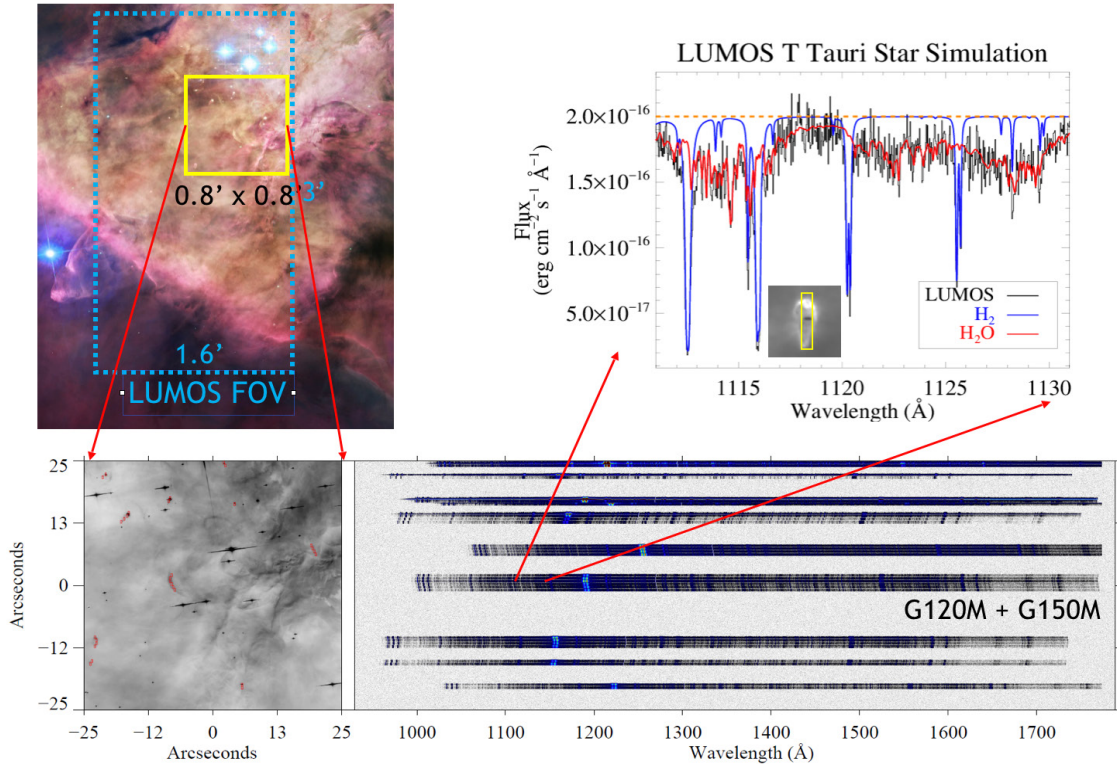


Figure B-20. Multi-object FUV spectroscopy of protoplanetary disks in the Orion Nebula. Upper left: HST-ACS image of the Orion Nebula (color credit, Robert Gendler), showing the full FOV of the LUMOS spectrograph (France et al. 2016). Lower panels zoom in on a $\sim 0.8 \times 0.8$ arcmin region showing ~ 30 protostellar/protoplanetary systems (Bally et al. 1998) and the apertures of the LUMOS microshutter array overplotted (slits are oversized for display). The two-dimensional spectra of the protoplanetary disk and accreting protostar are shown at right. In the upper right, we show a zoom in on the 1111 – 1132 \AA spectral region containing strong lines of H_2 and H_2O . The combination of spectral coverage, large collecting area, and multiplexing capability make LUVOIR ideal for surveying the composition of the planet-forming environments around young stars.

The total science exposure time per field is 30 minutes for FUV pre-imaging of the target field to locate the protostars and verify their brightnesses, followed by 1 hour in each of two FUV gratings (G120M and G150M) and 1 hour in the NUV (G300M). This gives 3.5 hours of science exposure time per field with LUVUOIR-A.

Scaling by the ratio of the collecting areas for LUVUOIR-A and -B (155 m^2 and 43.8 m^2 , respectively), LUMOS on LUVUOIR-B will require 12.4 hours per field. We simply assume a 50% overhead allocation for this program, to account for grating changes, wavelength calibration, and the relatively small repointing maneuvers.

Results. With a total of 41 pointings to cover the all five areas within the Orion complex, the total science exposure time with LUVUOIR-A is 3.5 hours per field \times 41 fields = 144 hours. The total LUVUOIR-A program time with overheads is 144 hours + 72 hours = 216 hours. For LUVUOIR-B, the total science exposure time is 12.4 hours per field \times 41 fields = 508 hours. The overheads for both programs should be about the same, so the total program time with overheads is 508 hours + 72 hours = 580 hours.

Parallels

- ☐ Do not execute parallels with this program
- ☐ Parallels required for this program
- ☐ Can be executed as parallel to another program
- ☒ Possible to execute parallels with this program

Target of opportunity / time-critical

- ☐ Is a ToO program
- ☐ Is time-critical

B.6.3 Young planetary systems

The final accretion of rocky terrestrial planets is believed to take place within a gas-depleted circumstellar debris disk during the first ~ 30 million years of a star's life. Planetary migration, giant impacts, gravitational stirring of the planetesimal disk by exterior gas giant planets, outgassing of magma oceans, and delivery of volatiles from beyond the snow line are all thought to play a role in determining the final arrangement and atmospheric compositions of the resulting rocky worlds.

High-contrast imaging of reflected light from these newly-formed planets and interplanetary debris dust can provide unique insights into the important physical processes. Only LUVUOIR can provide the small inner working angle and high spatial resolution needed to perform such studies for targets in nearby young stellar associations. This program will use ECLIPS to observe a sample of several dozen young stars of different spectral types. The science goals are to detect giant planets near the ice line, image the gravitational imprints of rocky planets on dust structures interior to the ice line, and constrain the abundances of volatile gases in the region of rocky planet formation.

Observations overview. ECLIPS optical coronagraphic imaging for every target. The images will be taken in a single optical band near 500 nm; an additional image in another channel (NUV or NIR) will be simultaneously obtained. Each target will be observed at two roll angles executed consecutively or as close in time as operational constraints allow.

Targets. At least 5 stars in each of the AFGKM spectral type bins (25 total stars). Targets are members of the Beta Pictoris, TW Hydrae, and Tucana/Horologium young associations at distances of 20–60 pc. The central stars range in V mag from 4 to 8.

Exposure times & overheads. The optical imaging exposure times are estimated to achieve SNR=60 at the ansae of a 200 zodi debris ring at 2.5 AU, giving ~ 1 hour per image and ~ 2 hours per star. We simply estimate the overhead time as 50% of the science time.

Results. For LUVOIR-A, the optical imaging program requires 2 hours per star \times 25 stars = 50 science hours, plus 25 hours for overheads. For a subset of targets (those with the brightest inner disks or highest stellar UV flux), NUV coronagraphy will be performed to measure the brightness of cometary OH emission as a signature of volatile delivery to the habitable zone. We allocate 50 science hours for NUV high-contrast imaging, plus 25 hours for overheads. The total time for the LUVOIR-A program is therefore 150 hours ~ 6 days.

We estimate the LUVOIR-B time by scaling the LUVOIR-A time by the ratio of the effective areas to keep the SNR roughly constant. Therefore, the total science exposure time with LUVOIR-B is 100 hours \times (155 m² / 43.8 m²) = 354 hours and the total program time is 531 hours ~ 22 days.

Parallels

- ☐ Do not execute parallels with this program
- ☐ Parallels required for this program
- ☐ Can be executed as parallel to another program
- ☒ Possible to execute parallels with this program

Target of opportunity / time-critical

- ☐ Is a ToO program
- ☐ Is time-critical

B.6.4 Exoplanet masses via astrometry

This program will measure masses and orbits of all planets in systems with habitable planet candidates discovered in Signature Science Case #1. Mass measurements are critical to exoplanet characterization. They provide a key observational parameter in statistical planet population studies to inform formation and evolution processes, and contextualize the physical and chemical state of individual planet candidates prioritized for detailed atmospheric abundance studies. Both LUVOIR mission concepts are uniquely poised to achieve the sub- μ s precision astrometry necessary to measure the masses of exoEarths or other rocky worlds. We aim to measure the masses of 1M_⊕ exoplanets to 25% precision using relative astrometry.

B.6.4.1 Observations overview

This program requires both internal and external calibration to reduce detector-based and optics-based systematics. The external calibrations necessitate position measurements of reference background sources in the HDI field-of-view to map all geometric distortions. In addition, sub- μ s precision for exoEarth detection requires an astrometric calibration system within HDI to measure detector-based systematic errors.

B.6.4.2 Targets

All habitable planet candidates from the initial, blind 2-year direct imaging survey. Here, we assumed 54 targets for LUVVOIR-A and 28 targets for LUVVOIR-B, based on preliminary expected yields from Stark et al. (2014)'s Altruistic Yield Optimization formalism.

B.6.4.3 Exposure times & overheads

Astrometric signal and sources of noise. Detecting the signals of terrestrial worlds around solar-type stars requires sub- μ as capabilities, achievable with LUVVOIR. From Kepler's laws, the predicted astrometric wobble for a planet with mass M_p in a circular orbit around a star with mass M_s at distance d is:

$$\theta = 3 \mu\text{as} \left(\frac{M_p}{M_\oplus} \right) \left(\frac{M_s}{M_\odot} \right)^{-\frac{2}{3}} \left(\frac{P}{\text{yr}} \right)^{\frac{2}{3}} \left(\frac{d}{\text{pc}} \right)^{-1} \quad (1)$$

The left panel of **Figure 16-21** shows, as a function of distance, the astrometric wobble of a solar-twin star due to various exoplanets orbiting at 1 AU: An Earth, a 10 Earth-mass sub-Neptune, and a Jupiter. For reference, the astrometric amplitude of an Earth-Sun twin at 10 pc is 0.3 μ as. We note that these astrometric signals assume systems consisting of a star with a single planet. The blended signals from multi-planet systems may increase the SNR requirements discussed below; extraction of those signals will need to be fully modeled at a later date.

Several factors affect the precision and accuracy of diffraction-limited astrometric measurements; these uncertainties propagate to the inferred mass, as well as the orbital properties, of an exoplanetary system. In the ideal case of a perfect detector and optics, the precision with which stellar centroid positions may be measured depends on the observational uncertainty, which is determined by the angular resolution of the telescope and the signal to noise ratio (SNR) of the observation; in this limit, the single-epoch astrometric precision in radians is

$$\sigma_{\text{obs}} = \left(\frac{\lambda}{2D_{\text{tel}}} \right) \left(\frac{1}{\text{SNR}} \right) \quad (2)$$

where λ is the wavelength of observation, D_{tel} is the effective diameter of the telescope, and the signal-to-noise ratio goes as

$$\text{SNR} = \sqrt{N_{\text{obs}} t_{\text{exp}} A_{\text{tel}} F_0 10^{-0.4m_s} \text{QE}} \quad (3)$$

Here, N_{obs} is the number of observations per epoch, t_{exp} is the exposure time per observation (s), A_{tel} is the effective area of the telescope (m^2), QE is the total system quantum efficiency, m_s is the apparent magnitude of the target star, and F_0 is the corresponding photon flux of a 0th mag star ($\text{photons m}^{-2} \text{s}^{-1}$) in the same magnitude system. Combining Eq. 2 and 3, the

astrometric observational noise scales as the inverse of the telescope diameter squared ($\sigma_{\text{obs}} \propto 1/D_{\text{tel}}^2$)—one power of D_{tel} from diffraction-limited angular resolution term and one power of D_{tel} from Poisson-limited light collecting term.

This is the observational uncertainty in centroiding a single point source. In relative or differential astrometry, the position of the target star is computed relative to a grid of background reference sources at separate epochs. A large number of reference points M is advantageous to average out correlated measurements of the target star position relative to the reference sources (e.g., Cameron et al. 2009, Sahlmann et al. 2013). In the limit of large M (≥ 100), the single-epoch precision from relative astrometry is comparable to the single-epoch astrometric precision for the point source target star.

Based on star counts from URAT (Zacharias et al. 2015) and Gaia (Gaia Collaboration et al. 2018) catalogues, the expected number of stars at $V=24$ mag with LUVOIR's $2' \times 3'$ field of view ranges from >100 at lower galactic latitudes ($b \lesssim 30^\circ$) to a few 10s at higher galactic latitudes ($b \gtrsim 60^\circ$). Therefore, we set the single-epoch observation time to the limiting integration time to observe point sources down to $V=24$ mag at $S/N=25$, roughly 10 sec and 50 sec for LUVOIR-A and LUVOIR-B, respectively¹.

In reality, the astrometric accuracy is limited by instrumental (detector + optical) systematics. In particular, geometric distortions in the optics system and sub-pixel positional errors on the CCD degrade stellar centroiding precision and bias astrometric measurements. These require additional calibration observations, which are further described below. The expected instrumental systematic error σ_{sys} is $0.34 \mu\text{as}$ and $0.65 \mu\text{as}$ for the LUVOIR-A and -B architectures, respectively.

In addition to instrumental systematics, photometric perturbations of the stellar surface from stellar activity, such as starspot modulation, will be a source of noise in stellar PSF centroiding. Several studies have evaluated the effects of stellar activity on astrometric measurements and found that a solar analog at 10 pc will exhibit $\sim 0.08 \mu\text{as}$ jitter (Eriksson & Lindegren 2007, Makarov et al. 2009, Lagrange et al. 2011). Here, we adopt a simple scaling relation for the astrometric noise of Sun-like stars from Makarov et al (2009):

$$\sigma_s = \frac{0.88 \mu\text{as}}{\sin i} \left(\frac{P_{\text{rot}}}{P_{\text{rot},\odot}} \right) \left(\frac{d}{\text{pc}} \right)^{-1} \quad (4)$$

Detection criterion, mass constraint, and synergy with direct imaging observations. An unambiguous astrometric detection (1% false alarm probability) requires an end of mission signal-to-noise ratio $SNR \approx 6$, corresponding to a 25% mass error (Catanzarite et al. 2006, Malbet et al. 2012). We define

$$SNR = \frac{\theta \sqrt{N_{\text{ep}}}}{\sigma} \quad (5)$$

where θ is the astrometric wobble or signal, σ is the single-epoch noise, and N_{ep} is the number of epochs observed. Here we treat each noise source described above

¹ LUVOIR HDI Photometric exposure time calculator: <https://asd.gsfc.nasa.gov/luvoir/tools/>

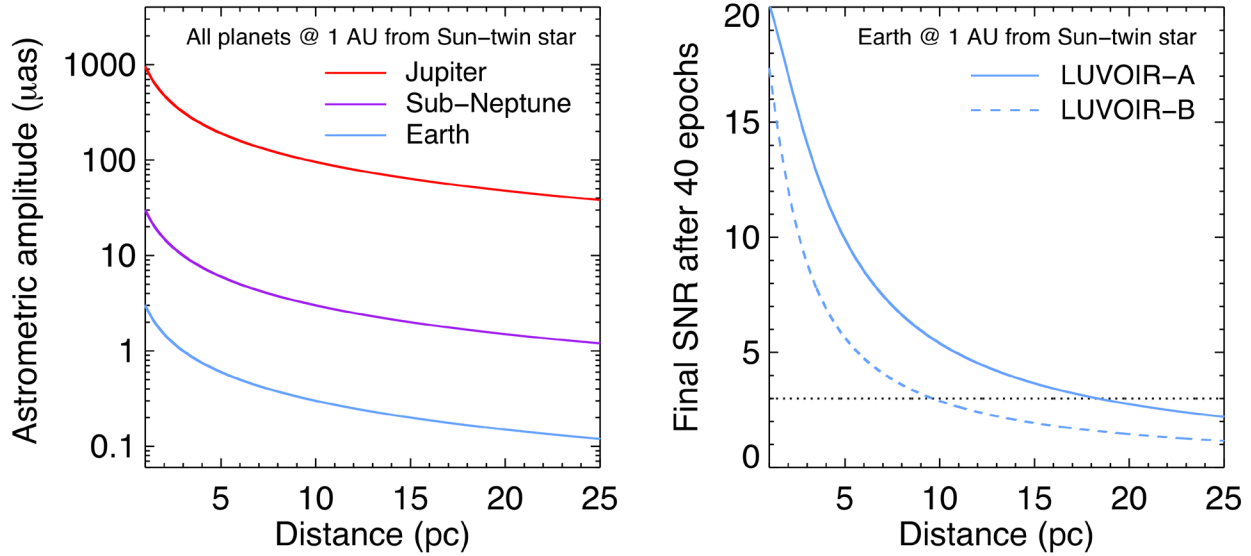


Figure B-21. LUV0IR can measure the astrometric signals of Earth-mass planets orbiting Sun-like stars and provide critical mass measurements for habitable and non-habitable planets. Left panel: Solid colored lines show the astrometric wobbles of a solar analog star due to a Jupiter-twin (red), a 10 Earth-mass sub-Neptune (purple), and an Earth-twin (blue), all with an orbital semi-major axis of 1 AU. Right panel: Predicted SNR for astrometric detections of Earth-twins around solar analogs for LUV0IR-A (solid line) and LUV0IR-B (dashed line). The curves assume 40 epochs of observations and noise from stellar jitter due to star spots, systematic noise set by detector metrology, and observational uncertainty. Using astrometry+direct imaging, a mass measurement with 25% precision requires SNR=3. Credit: D. Windemuth (UW) / A. Roberge (NASA GSFC).

(astrophysical, observational, and instrumental) as independent from one another, such that $\sigma^2 = \sigma_s^2 + \sigma_{\text{obs}}^2 + \sigma_{\text{sys}}^2$. We expect that the systematic errors from detector metrology will add in quadrature with other error terms (M. Shao, personal communication), but this assumption will need to be verified with full modeling of the astrometric error budget at a later date. The right panel of **Figure B-21** shows the expected astrometric SNR of an Earth-Sun analog as a function of distance, given 40 pointings spread over a year and including the sources of error discussed above. The systematic error dominates the preliminary noise budget for both LUV0IR-A and -B.

Torres (1999) and more recently Guyon et al. (2013) demonstrated that coupling astrometric measurements of the target star to direct imaging observations of its companion reduces the uncertainty in the companion's mass. The effective end-of-mission astrometric SNR threshold decreases by a factor of 2 with near-simultaneous direct imaging + astrometric observations. The intuitive explanation for this is that when both types of observations are available, the system is effectively a double-lined binary: the astrometric solution yields the star's semi-major axis with respect to its barycenter, which is sensitive to the mass ratio of the system, while the direct imaging solution yields the planet's semi-major axis relative to its host star, which is sensitive to the total mass of the system. For this reason, the planet and stellar mass, as well as their orbital properties, may be measured to higher precision.

Since our astrometric follow-up targets for exoplanet characterization will be determined from a direct imaging blind exoEarth search, they will already have ~6 epochs of SNR=7 coronagraphic observations. Consequently, we require an end-of-mission astrometric SNR=3

to measure the masses of exoEarth candidates with 25% precision (Case 1). For comparison, we also show the required science times for SNR=6, i.e., assuming astrometric measurements independent of directly imaged exoplanet orbits (Case 2).

Imaging observations. The astrometric observations will be made using the UVIS channel in the High Definition Imager (HDI) instrument. The observational challenge is to maximize the dynamic range necessary to detect both bright target stars ($V=4-7$ mag) and fainter background reference stars ($V>10$ mag), gathering enough photons for the latter without saturating the former. We propose two possible strategies to achieve this.

In the first strategy—direct stare mode—we would acquire two sequences of images. First, to get SNR=25 on the central target star ($V=4-7$ mag), we would use either an ultra-narrow band filter ($\Delta\lambda = 0.06$ nm) or a 500–800 nm broadband filter in conjunction with a 10-magnitude neutral density filter. The total exposure time to acquire the data would be a few seconds but acquired with a dozen or so very short (0.5 sec) exposures.

Next, the image of the reference field stars would be obtained using a broadband filter but also performed by accumulating many very short (0.5–1 sec) exposures. Obtaining SNR=25 for a broadband image of a $V=24$ mag star requires ~ 10 and ~ 50 sec of total integration time for LUVOIR-A and -B, respectively.

In the second strategy—spatial scanning mode—the telescope slews at a user-defined direction and rate during a longer exposure, so that light, including that of the host star, is spread over many pixels. This technique has demonstrated success for astrometry with the Hubble Space Telescope (e.g., McCullough & MacKenty 2012, Reiss 2014).

Overheads. Our program is heavily slew time dominated. We estimate this overhead time by computing an optimized route for our target sample, i.e., applying an open-ended traveling salesman algorithm that minimizes the total angular distance traveled. For the ~ 50 targets with LUVOIR-A, the minimum total angular distance is ~ 1180 degrees. Thus, at the LUVOIR slew rate goal of 3 degrees per minute, the total slew time is 6.6 hours per epoch for observing our entire sample. With LUVOIR-B, the minimum total angular distance for 29 targets is ~ 660 degrees, or 3.7 hours per epoch. We note that these slew time calculations are upper limits to the overhead time, and that achieving higher overhead efficiency may be possible by interleaving astrometric observations with those of other programs.

Laser-based pixel geometry calibration system requirements. In addition to the time allocated for science observations, the astrometric detection of exoplanets requires an calibration program to achieve $0.34 \mu\text{s}$ and $0.65 \mu\text{s}$ instrumental systematic error for LUVOIR-A and LUVOIR-B, respectively (corresponding to an astrometric accuracy of 0.0001 pixels). Using the planned internal laser-based calibration system, we will need to average 4 patterns of 20 co-added fringe images (10 in the x-direction, 10 in the y-direction) with 2.5×10^7 photons per pixel per pattern. The square root of the total number of photons per pixel, summed over all patterns, is the inverse of the desired fractional pixel precision. This will require of order 1000 co-added exposures per fringe image per pattern, assuming we limit each pixel to 50% of its 50,000 electron full well capacity. The amount of time required to calibrate the internal pixel positions with a single use of the laser system scales inversely as the square of the fractional pixel accuracy.

With a sensor pixel readout rate of 500 kHz and 32 readout ports per sensor we can complete the required HDI internal astrometric calibration sequence with a total allocation of ~ 12 hours. The number of times this calibration sequence would need to be done will

depends on the thermal and mechanical stability of the focal plane. Given LUVVOIR's overall stability requirements, we estimate that this calibration sequence would need to be done only in proximity to the execution of high precision astrometric observations. We envision dedicated astrometry campaigns once per month, in which these and other astrometric measurements are performed (e.g., Signature Science Case #8: Constraining dark matter using high precision astrometry; **Section B.9**). In this scheme, the internal calibrations take ~144 hours per year for both LUVVOIR-A and LUVVOIR-B.

The HDI thermal radiator is sized to handle heat loads corresponding to a 500 kHz readout rate and there will be no impact on telescope wavefront control during the calibration process. Therefore, the internal pixel position calibrations can be performed in parallel while other LUVVOIR instruments (e.g., ECLIPS, LUMOS) are the primary instrument and when HDI is not requested as a parallel imaging instrument; this would dramatically reduce the total program time. For the time being, we account for the calibration time within this program.

B.6.4.4 Results

In order to optimally map out astrometric solutions, the observations should be at ~evenly spaced epochs over the course of at least a year, i.e., to trace out 1 orbital period for habitable zone planets around solar-type stars. **Table B-13** gives the total science time and mean number of epochs as a function of number of targets for both LUVVOIR architectures assuming near simultaneous direct imaging observations (Case 1). This program on LUVVOIR-A requires a total science exposure time of 10 sec per pointing \times 53 targets \times an average of 14 epochs per target ~ 2 hours. The total program time is 2 hours + 92 overhead hours + 144 hours for laser calibration = 238 hours \approx 10 days.

For LUVVOIR-B, the Case 1 program requires a total science time of 50 sec per pointing \times 29 targets \times an average of 39 epochs per target ~ 16 hours. The total program time is 16 hours + 147 overhead hours + 144 hours for laser calibration = 307 hours \approx 13 days. The roughly order of magnitude increase in science time is due to a combination of two effects: 1) longer exposure times to collect enough photons for faint reference stars with LUVVOIR-B's smaller aperture, and 2) greater number of epochs required per star due to higher systematic noise floor of LUVVOIR-B.

For comparison, **Table B-14** gives the total science time and mean number of epochs as a function of number of targets for both LUVVOIR architectures assuming no coronagraphic information (Case 2). This program on LUVVOIR-A requires 526 hours \approx 22 days (8 science hours + 374 overhead hours + 144 hours for laser calibration). The total LUVVOIR-B time is 778 hours \approx 33 days (63 science hours + 571 overhead hours + 144 hours for laser calibration).

These are the total times required to obtain ~25% mass precision assuming the nominal habitable planet candidate list from the prime direct imaging survey. Given the substantial time savings and the fact that we certainly will have coronagraphic imaging for these targets, we chose Case 1 to account for the total time for this Signature Science Case within the prime mission.

Table B-13. *Total science exposure times assuming near-simultaneous direct imaging*

Case 1: SNR=3 (near-simultaneous direct imaging)					
LUVOIR-A			LUVOIR-B		
# of targets	Tot. science time (hours)	Epochs per target	# of targets	Tot. science time (hours)	Epochs per target
5	0.20 ^{+0.05} _{-0.05}	10.8 ^{+3.3} _{-3.3}	3	1.59 ^{+0.59} _{-0.41}	28.4 ^{+14.1} _{-9.8}
13	0.51 ^{+0.06} _{-0.07}	12.3 ^{+1.7} _{-1.9}	7	3.79 ^{+0.71} _{-0.74}	31.3 ^{+7.3} _{-7.6}
21	0.82 ^{+0.08} _{-0.07}	12.9 ^{+1.4} _{-1.2}	12	6.53 ^{+0.76} _{-0.72}	34.8 ^{+4.6} _{-4.3}
29	1.15 ^{+0.07} _{-0.07}	13.3 ^{+0.9} _{-0.9}	16	8.64 ^{+0.85} _{-0.70}	35.7 ^{+3.8} _{-3.2}
37	1.46 ^{+0.07} _{-0.07}	13.5 ^{+0.7} _{-0.7}	20	10.93 ^{+0.64} _{-0.87}	36.2 ^{+2.3} _{-3.1}
45	1.77 ^{+0.05} _{-0.06}	13.7 ^{+0.4} _{-0.5}	25	13.65 ^{+0.50} _{-0.59}	37.6 ^{+1.4} _{-1.7}
53	2.09 ⁺⁰ ₋₀	14.2 ⁺⁰ ₋₀	29	15.73 ⁺⁰ ₋₀	39.1 ⁺⁰ ₋₀

Table B-14. *Total science exposure times without direct imaging*

Case 2: SNR=6 (no direct imaging assumed)					
LUVOIR-A			LUVOIR-B		
# of targets	Tot. science time (hours)	Epochs per target	# of targets	Tot. science time (hours)	Epochs per target
5	0.78 ^{+0.16} _{-0.16}	44.6 ^{+11.4} _{-11.4}	3	6.48 ^{+1.92} _{-1.98}	108.0 ^{+46.1} _{-47.6}
13	2.04 ^{+0.28} _{-0.26}	49.4 ^{+7.8} _{-7.1}	7	15.10 ^{+2.77} _{-2.80}	126.4 ^{+28.5} _{-28.8}
21	3.32 ^{+0.28} _{-0.30}	51.8 ^{+4.8} _{-5.2}	12	25.81 ^{+3.02} _{-2.84}	137.8 ^{+18.1} _{-17.0}
29	4.56 ^{+0.28} _{-0.31}	52.8 ^{+3.5} _{-3.8}	16	35.13 ^{+2.93} _{-3.08}	144.2 ^{+13.2} _{-13.9}
37	5.83 ^{+0.26} _{-0.27}	54.1 ^{+2.6} _{-2.6}	20	43.29 ^{+3.08} _{-3.14}	144.5 ^{+11.1} _{-11.3}
45	7.08 ^{+0.22} _{-0.22}	54.9 ^{+1.7} _{-1.8}	25	54.25 ^{+2.05} _{-2.37}	149.4 ^{+5.9} _{-6.8}
53	8.34 ⁺⁰ ₋₀	56.7 ⁺⁰ ₋₀	29	62.86 ⁺⁰ ₋₀	156.0 ⁺⁰ ₋₀

Parallels

- ☐ Do not execute parallels with this program
- ☐ Parallels required for this program
- ☒ Can be executed as parallel to another program
- ☒ Possible to execute parallels with this program

The internal HDI focal plane calibrations with the internal laser metrology system can be executed in parallel with other programs, provided those programs do not require use of the HDI for science observations. However, the astrometric science observations proposed here require specific targeted fields and cannot be executed in parallel.

Target of opportunity / time-critical

- ☐ Is a ToO program
- ☒ Is time-critical

Multiple visits spread over ~ 1 year.

B.7 Signature Science Case #6: Small bodies in the solar system

B.7.1 Abstract

The small bodies of the solar system contain records of its formation and early evolution. The goal of this science case is to uncover some particularly elusive clues with two observing programs.

1. Execute a deep, multi-band imaging survey to discover trans-Neptunian objects (TNOs) down to the currently unseen smallest bodies (2 km for LUVOIR-A and 4 km for LUVOIR-B).
2. Measure orbits of TNO binaries to constrain theories of their formation and evolution.

Program contact(s)

Rebekah Dawson (Penn State), Walter Harris (U of Arizona), Aki Roberge (NASA GSFC)

Brief description

HDI multi-band imaging survey for very small TNOs

HDI imaging to measure orbits of TNO binaries

Total observing time

LUVOIR-A: 150 days

LUVOIR-B: 150 days

B.7.2 TNO deep drill survey

The Kuiper Belt is only available remnant of the solar system's primordial planetesimal population available for direct study. The characteristics of this population, including both size and orbital distribution, are directly relevant to understanding process of planetesimal formation and the migration of the giant planets. Sky background limits make HST the most sensitive optical telescope ever built, with the ability to detect TNOs with diameters in the range of ~ 35 km at 40 AU. However, this limit may leave $\geq 99\%$ of the inner population invisible to observers, and makes practical study of the region beyond the Kuiper Cliff at 55 AU impossible.

In this LUVOIR TNO imaging survey, we will reach a limiting detectable TNO magnitude of $R=33$ (~ 2 km at 40 AU) with LUVOIR-A and $R=31.5$ (~ 4 km at 40 AU) with LUVOIR-B (**Figure B-22**). We will measure R-J colors of all detected objects and perform revisits to establish orbits. These size limits are well below those expected for any other current or future TNO deep drill project (**Figure B-22**), allowing LUVOIR to reach down into unknown territory and strongly constrain planetesimal formation theories. We emphasize that the observing program outlined here is a draft program to establish feasibility and could no doubt benefit from future optimization.

Observations overview. Images will be obtained using the R band filter in the HDI UVIS detector. A simultaneous image in a NIR band (likely J) will also be obtained. The TNOs are expected to be brighter in J than R, so objects detected in the R band image will also be detected in the J band image. Roughly following the observing plan in the OSSOS TNO survey, each field will be revisited 26 times on average, with initial high cadence then targeted revisits over 5 years to measure orbits of detected objects.

Targets. HDI has a $2 \text{ arcmin} \times 3 \text{ arcmin}$ field-of-view. The number of fields observed was set to obtain as large a sample of detected bodies as possible in a reasonable total time allocation. We will observe 7 HDI fields (0.012 sq. degrees) with LUVOIR-A and 10 HDI fields

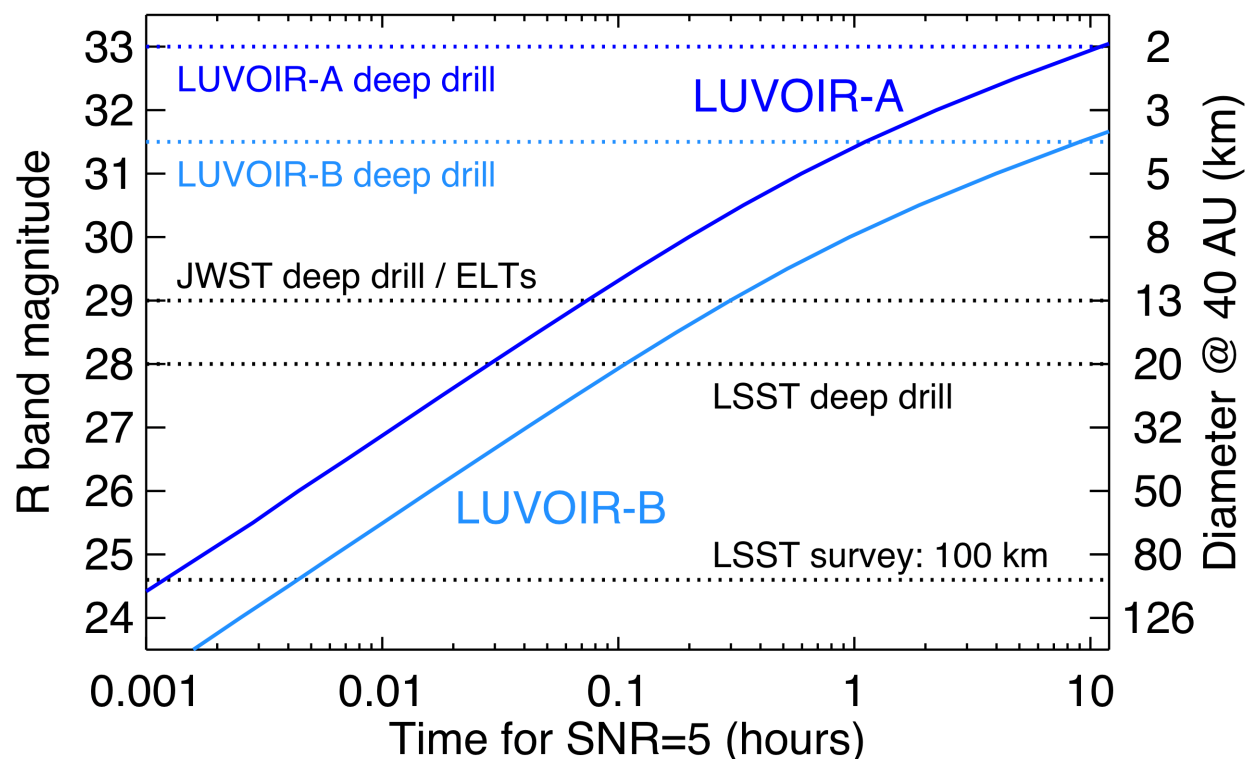


Figure B-22. LUNVOIR can reach down to smaller trans-Neptunian objects (TNOs) than any other current or planned facility. The solid curves show the R band apparent magnitude of TNOs detectable at SNR ~ 5 as a function of exposure time for LUNVOIR-A (dark blue) and LUNVOIR-B (light blue). The right y-axis shows the sizes of TNOs at 40 AU corresponding to the R magnitudes. These assume a single image that is depth-optimized to the Classical Kuiper-Edgeworth Belt by non-sidereal tracking. Horizontal dotted lines show limits for other TNO surveys. A 2 km object at 40 AU lies at R=33. Credit: R. Dawson (Penn State) / A. Roberge (NASA GSFC)

(0.017 sq. degrees) with LUNVOIR-B. The exact positioning of the fields will be determined at a future date.

Exposure times & overheads. The exposure time to reach R=33 with LUNVOIR-A is 11 hours and the time to reach R=31.5 with LUNVOIR-B is 9 hours. Therefore, the total exposure time per field is 11 hours × 26 visits = 11.9 days for LUNVOIR-A and 9 hours × 26 visits = 9.75 days for LUNVOIR-B. Including a 50% overhead allocation for this program, we obtain total times per field of 17.9 days with LUNVOIR-A and 14.6 days with LUNVOIR-B.

Results. Multiplying by the number of fields, the total program time is 17.9 days × 7 fields = 125 days with LUNVOIR-A and 14.6 days × 10 fields = 146 days with LUNVOIR-B. Given an extrapolated object frequency of 10,000 per sq. degree at R=33 and 1800 per sq. degree at R=31.5, we expect to detect 117 objects in the LUNVOIR-A survey and 30 objects in the LUNVOIR-B survey. Future analysis will establish what constraints may be placed on the small-end size distribution with these total samples.

Parallels

- ☐ Do not execute parallels with this program
- ☐ Parallels required for this program
- ☐ Can be executed as parallel to another program
- ☐ Possible to execute parallels with this program

Non-sidereal tracking limits the feasibility of parallel observations with this program.

Target of opportunity / time-critical

- ☐ Is a ToO program
- ☒ Is time-critical

26 visits to each field spread over 5 years.

B.7.3 Characterization of TNOs: binaries

The occurrence rates and properties of binary TNOs provide several critical constraints on how they form and evolve. Wide binaries are evidence of *in situ* formation for their components, as they would have been disrupted if formed elsewhere and scattered to their present locations. Different models for planetesimal formation make different predictions for component sizes, mass ratios, separations, and occurrence rates of binaries. Finally, binary orbits provide component masses, and are generally the only way to place constraints on the densities of small and distant TNOs.

Larger and brighter TNO binaries will likely be characterized with the upcoming ELTs. The smaller ones discovered in the LUVOIR TNO deep drill described above will remain beyond the reach of the ELTs. It is difficult to plan an observing program to characterize those binaries, as their frequency in the small TNO population is unknown. However, we briefly describe some ideas for observing them with LUVOIR and establish a notional time allocation for doing so.

Observations overview. In the TNO deep drill described above, the smallest bodies will be detected at $\text{SNR} = 5$, which may be insufficient to reveal them as binaries if their separations are small. However, with separations up to tens of thousands of km, some binaries may be spatially resolved (the spatial resolution in R band at 40 AU is 362 km for LUVOIR-A and 678 km for LUVOIR-B). The orbital periods will be on the order of a few to tens of days; thus the orbits of some binaries may be measured or constrained in the high cadence revisits that will occur for the deep drill fields. For any other binaries that are discovered but require further observations to measure their orbits, we will plan targeted revisits to obtain additional R and J band images.

Targets. Any TNO binaries discovered in the TNO deep drills described above that require additional observations to establish their orbits.

Exposure times & overheads. The exposure time to reach $R = 33$ at $\text{SNR} = 5$ with HDI on LUVOIR-A is 11 hours (as discussed in Section 16.7.2 above), while the time to reach $R = 31.5$ with LUVOIR-B is 9 hours. Adding 50% overheads, the total time for a pair of R and J band images is 16.5 hours with LUVOIR-A and 13.5 hours with LUVOIR-B.

Results. We chose to set a limit on the total time allocation for the whole solar system small bodies program (Signature Science Case #6) of 150 days for both LUVVOIR-A and -B. Subtracting 125 days for the TNO deep drill with LUVVOIR-A leaves a remainder of 25 days (600 hours) that can be devoted to follow-up of small binary systems; thus 36 additional revisits are possible with LUVVOIR-A. With LUVVOIR-B, only 4 days (96 hours) remain, permitting only 7 additional revisits. This appears insufficient for the faintest ~ 4-km bodies; however, even a small increase in size results in a large decrease in needed exposure time. Further investigation of the expected frequency and characteristics of small TNO binaries is required to determine whether this follow-up is feasible within the notional time allocation.

Parallels

- ☐ Do not execute parallels with this program
- ☐ Parallels required for this program
- ☐ Can be executed as parallel to another program
- ☐ Possible to execute parallels with this program

Non-sidereal tracking limits the feasibility of parallel observations with this program.

Target of opportunity / time-critical

- ☐ Is a ToO program
- ☒ Is time-critical

Targeted revisits to measure binary orbits.

B.8 Signature Science Case #7: Connecting the smallest scales across cosmic time

B.8.1 Abstract

Dwarf galaxies are the smallest luminous, dark-matter dominated objects known and are predicted to exist in orbit around all massive galaxies and in all environments. The spatial distribution of dwarf galaxies around their hosts provide novel and important constraints on the nature of the dark matter particle by probing the small-scale shape of the density fluctuation power spectrum. LUVOIR enables representative census surveys of luminous dwarfs around a handful of Milky Way analogs out to distances of 15 Mpc.

We use the abundance-matching framework to transform the observed dwarf population to a mass function, which is then compared with that predicted for the CDM-derived matter power spectrum. By targeting multiple host galaxies that are as similar to the Milky Way (MW) as possible, and assuming each survey is an effective “draw” on the underlying physics that results in the observed populations, we can estimate both the power spectrum’s amplitude and its measurement uncertainty on several spatial scales corresponding to those in the derived mass functions.

Program contact(s)

Marc Postman (STScI)

Brief description

HDI survey for dwarf galaxies around four Milky Way analog galaxies

Total observing time

LUVOIR-A: 12 days

LUVOIR-B: 57 days

B.8.2 Observations overview

The basic program strategy is to survey the region around four MW analogs within 15 Mpc to identify low-mass dwarf galaxies, then use the abundances of the dwarf systems to make an estimate of the matter power spectrum. Only LUVOIR has the sensitivity to survey MW analogs down to a limit where individual stars in the dwarf galaxies could be directly detected and used as an effective strategy for conducting a comprehensive census of extremely low-mass systems around larger host galaxies. We lay out two possible observing strategies to execute the surveys. Both assume that the field-of-view (FOV) of HDI is the same for LUVOIR-A and -B.

Option 1. This option uses only the UVIS channel of HDI. For each galaxy observed with LUVOIR-A, the central 100 kpc region will be imaged with a number of HDI pointings sufficient to cover 50% of the region. At each pointing, observations in the V (F606W) and i (F775W) bands will be obtained. The scale of 100 kpc corresponds to approximately half the virial radius for a MW mass system. Hence, this survey sampling will allow high completeness over a region where there should be significant numbers of satellite dwarf galaxies. To keep the total program time with LUVOIR-B reasonable, we reduced the size of the imaged region to 50 kpc.

Option 2. A second survey option takes advantage of the multiplexing capability of HDI’s UVIS and NIR channels. Because the UVIS and NIR channels are co-aligned (i.e., they see a nearly identical FOV), we can significantly reduce the time needed to complete each survey if we use a V-J (F606W-F125W) color to select the stars in the dwarf satellite galaxies

Table B-15. Survey parameters for LUVOIR-A probing central 100 kpc with 50% completeness, performed using two UVIS filters sequentially (Option 1)

Galaxy	Dist. (Mpc)	Number of HDI pointings	V Mag Limit	i Mag Limit	Integration time for this target (hours)	Cumulative time – no overheads (hours)	Cumulative time – 50% overheads (hours)
NGC5457	6.4	758	29.03	28.73	91	91	136
NGC891	10.0	313	30.00	29.70	95	186	279
NGC7331	11.7	229	30.34	30.04	98	284	426
NGC3810	14.2	156	30.76	30.46	103	387	581

Table B-16. Survey parameters for LUVOIR-B probing central 50 kpc with 50% completeness, performed using two UVIS filters sequentially (Option 1)

Galaxy	Dist. (Mpc)	Number of HDI pointings	V Mag Limit	i Mag Limit	Integration time for this target (hours)	Cumulative time – no overheads (hours)	Cumulative time – 50% overheads (hours)
NGC5457	6.4	190	29.03	28.73	76	76	114
NGC891	10.0	78	30.00	29.70	87	163	244
NGC7331	11.7	57	30.34	30.04	94	256	384
NGC3810	14.2	39	30.76	30.46	125	381	571

rather than a V-i (F606W-F775W) color. This allows us to survey a 100 kpc region around each galaxy with LUVOIR-B as well as LUVOIR-A.

B.8.3 Targets

The four MW analog galaxies chosen are NGC5457, NGC891, NGC7331, and NGC3810.

B.8.4 Exposure times

Option 1. The exposure times, calculated with the online HDI exposure time calculator (Section B.1.3), enable detection of a $M_V=0$ AB magnitude star at $\text{SNR} = 5$ in both the V and i bands assuming a color of $(V-i) = 0.30$ and $(V-J) = 0.35$. These photometric parameters are typical of stars in the Horizontal branch (HB) of the Hertzsprung-Russel (H-R) diagram. Dwarf galaxies are then detected as over-densities in the local star field. We will obtain a minimum of 3 exposures per band per pointing, with a maximum individual exposure time of 1200 sec.

Option 2. The J band exposure times are typically about 40% of the corresponding V band exposure times. Therefore, the time to survey each galaxy is set by the V band exposure times only (calculated as described for Option 1), dramatically reducing the total times compared to Option 1.

Overheads. We simply assume a 50% overhead allocation for this program, which will be largely devoted to repointing maneuvers.

B.8.5 Results

Option 1. Table B-15 and Table B-16 show, for LUVOIR-A and LUVOIR-B, the required total integration times per host galaxy target assuming V-i imaging, as well as the cumulative times to survey the 4 Milky Way analogs. The total program time is 581 hours for LUVOIR-A

Table B-17. Survey parameters for LUVOIR-A probing central 100 kpc with 50% completeness, performed using one UVIS filter and one NIR filter simultaneously (Option 2)

Galaxy	Dist. (Mpc)	Number of HDI pointings	V Mag Limit	i Mag Limit	Integration time for this target (hours)	Cumulative time – no overheads (hours)	Cumulative time – 50% overheads (hours)
NGC5457	6.4	758	29.03	28.68	45	45	68
NGC891	10.0	313	30.00	29.65	48	93	140
NGC7331	11.7	229	30.34	29.99	49	142	213
NGC3810	14.2	156	30.76	30.41	51	193	290

Table B-18. Survey parameters for LUVOIR-B probing central 100 kpc with 50% completeness, performed using one UVIS filter and one NIR filter simultaneously (Option 2)

Galaxy	Dist. (Mpc)	Number of HDI pointings	V Mag Limit	i Mag Limit	Integration time for this target (hours)	Cumulative time – no overheads (hours)	Cumulative time – 50% overheads (hours)
NGC5457	6.4	758	29.03	28.68	174	174	261
NGC891	10.0	313	30.00	29.65	202	376	564
NGC7331	11.7	229	30.34	29.99	220	596	894
NGC3810	14.2	156	30.76	30.41	310	905	1358

(100 kpc regions) and 571 hours for LUVOIR-B (50 kpc regions). If we chose to survey 100 kpc regions with LUVOIR-B, the total program time would be 2284 hours; hence the reduction in survey area.

With the 100 kpc regions surveyed using LUVOIR-A, we will measure the matter power spectrum and transfer functions on scales between 10–100 kpc at >4 sigma statistical significance (see Figure 5.2). We are currently assessing the impact of reducing each survey to the central 50 kpc region for the LUVOIR-B program on the derived constraint on the dark matter power spectrum.

Option 2. Table B-17 and Table B-18 show the same information as in the previous tables, assuming simultaneous imaging in the V and J bands. The total program time with is 290 hours for LUVOIR-A and 1358 hours for LUVOIR-B. Both programs survey 100 kpc regions; therefore, both LUVOIR-A and -B obtain the results given above for LUVOIR-A with Option 1. Given its greater science returns, we chose Option 2 to account for the total time for this Signature Science Case within the prime mission.

Parallels

- ☐ Do not execute parallels with this program
- ☐ Parallels required for this program
- ☐ Can be executed as parallel to another program
- ☒ Possible to execute parallels with this program

The LUMOS instrument could be used in parallel with HDI to acquire deep UV spectra of selected targets in the region. As the position angle of the HDI is not critical, one could have some freedom to select an orientation angle that facilitates slit alignment. Given that specific

targets and specific survey areas are required for this program, this program cannot be done as a parallel program when another instrument is prime.

Target of opportunity / time-critical

- ☐ 0 Is a ToO program
- ☐ 0 Is time-critical

B.9 Signature Science Case #8: Constraining dark matter using high precision astrometry

B.9.1 Abstract

The ability of dark matter to cluster in phase space is limited by intrinsic properties such as mass and kinetic temperature. Specifically, *the mean density profile of dwarf galaxies is a fundamental constraint on the nature of dark matter*. Current observations are unable to measure the density profile slopes within dwarf galaxies because of a strong degeneracy between the inner slope of the dark matter density profile and the velocity anisotropy of the stellar orbits. Radial velocities alone cannot break this degeneracy even if the present samples of radial velocities are increased to several thousand stars. The only robust way to break the anisotropy—inner slope degeneracy is to combine proper motions with radial velocities.

The required measurements are high precision proper motions for ~100 stars per galaxy. The necessary astrometric precision can be readily achieved by LUVOIR, given its multi-arc-minute field of view, high stability, and the pixel geometry calibration system within the HDI instrument. This same astrometric capability will also allow LUVOIR users to directly measure the 3-D motions of entire galaxies out to distances of up to 15 Mpc.

Program contact(s)

Marc Postman (STScI)

Brief description

HDI measurements of proper motions for ~100 stars in 20 dwarf galaxies to map dark matter distributions

Total observing time

LUVOIR-A: 1 month

LUVOIR-B: 3.5 months

B.9.2 Observations overview

We will obtain optical images of dwarf galaxies with HDI, with a few epochs of imaging for each galaxy. The proper motions of individual stars within the galaxies will be measured with a total precision better than ~10 km/sec (i.e., < 40 μ as/yr at 60 kpc).

B.9.3 Targets

20 dwarf spheroidal galaxies—10 within the Local Group (1 Mpc) and 10 beyond the Local Group (2–5 Mpc). Each galaxy will be imaged at 3 epochs to ensure good results, with those epochs ~evenly spread over 5 years.

B.9.4 Exposure times & overheads

Proper motion precision. The astrometric precision, in radians per epoch, achieved in a given image is given by the expression:

$$\sigma_{Acc} (rad) = \left(\frac{\lambda}{2D_T} \right) / \sqrt{t_{exp} F_{equiv}} \quad (1)$$

where λ is the wavelength of the observation in meters, D_T is the telescope diameter in meters, t_{exp} is the total exposure time per epoch in seconds, and F_{equiv} is the equivalent flux in photons per second. The equivalent flux, F_{equiv} , is:

$$F_{\text{equiv}} = F_0 10^{-0.4m_s} A_T QE N_s \quad (2)$$

where F_0 is the flux from a 0th mag star (photons $\text{m}^{-2} \text{sec}^{-1}$), m_s is the apparent magnitude of the stars being used for the astrometric measurement of tangential motion, A_T is the collecting area of the telescope in square meters, QE is the total system quantum efficiency, and N_s is the number of stars measured per epoch.

In the case where one is observing stars of various different magnitudes, Eq. (2) becomes:

$$F_{\text{equiv}} = F_0 A_T QE \sum_{i=1}^{N_s} 10^{-0.4m_i} \quad (3)$$

Because the equivalent flux is proportional to A_T , which is proportional to the square of the telescope diameter, the overall astrometric accuracy given in equation 1 scales as the inverse square of the telescope diameter—one power of D_T from the diffraction limit term and one power of D_T from the inverse square root of the total number of photons.

The error in the proper motion in units of arcseconds per year that one can then achieve given two separate epochs of observations is:

$$\sigma_{PM} ("/\text{yr}) = 206,264.8 \left(\frac{\sigma_{\text{Acc}} \sqrt{2}}{\Delta t_{\text{seq}}} \right) \quad (4)$$

where Δt_{seq} is the time difference between the two epochs expressed in units of years. The corresponding transverse velocity error achieved in km s^{-1} is:

$$\sigma_v (km s^{-1}) = \left(4.75 \frac{km}{pc} \frac{yr}{s} \right) \sigma_{PM} ("/\text{yr}) d(pc) \quad (5)$$

where d is the average distance to the target stars in parsecs. **Figure B-23** shows the 1σ velocity error as a function of telescope aperture for a survey observing 100 red giant branch (RGB) stars in a galaxy at a distance of 5 Mpc, assuming 2 epochs separated by 5 years.

Imaging observations. The observing sequence requires only one optical wide-band image per target per epoch. Each image will consist of 4 exposures for cosmic ray rejection, with individual exposure times not to exceed 1200 sec each.

The exposure time for the density profile study is driven by the desire to reach ~ 10 km/s accuracy on the target proper motion for ~ 100 stars in the dwarf galaxy being studied. This corresponds to a proper motion accuracy of $\sim 0.5 \mu\text{as/yr}$ at a distance of 4 Mpc, which can be achieved with LUVUOIR-A using two epochs separated by 5 years and an exposure time of 100 ksec per epoch. For LUVUOIR-B, the same observational parameters would allow us to achieve this velocity accuracy for galaxies out to a distance of 2.2 Mpc, with a corresponding

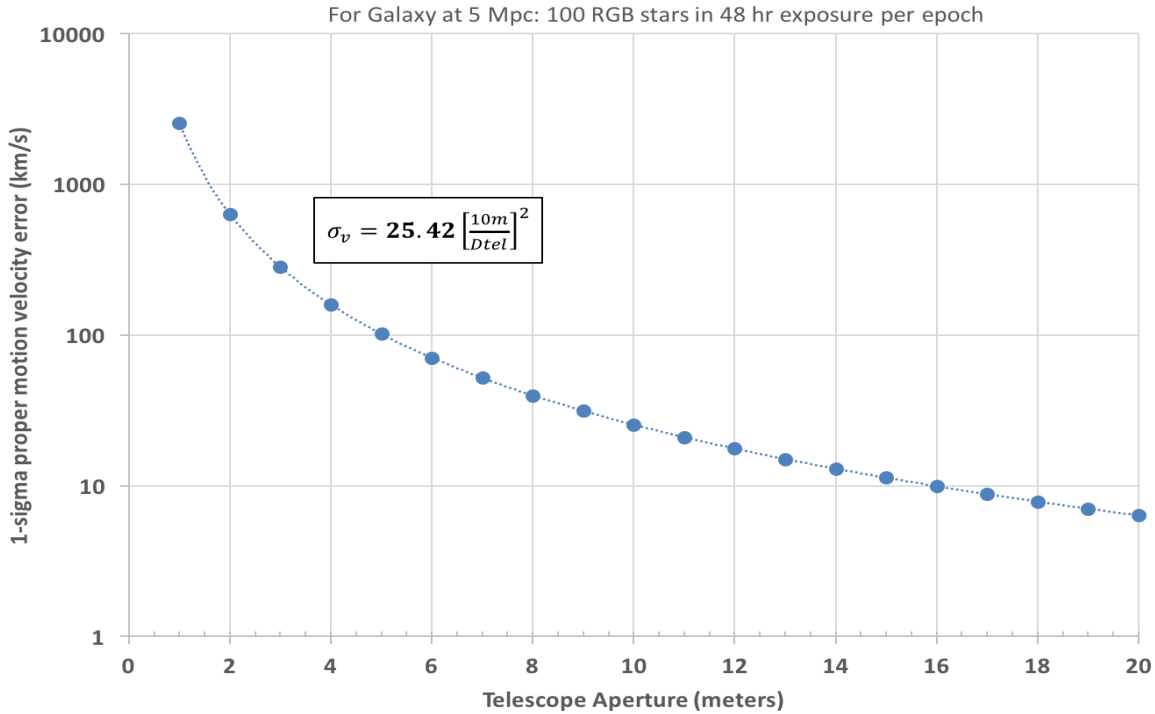


Figure B-23. 1σ proper motion velocity error as a function of telescope aperture for observations of RGB stars in a galaxy at a distance of 5 Mpc. Two epochs separated by 5 years are assumed here.

proper motion accuracy of $\sim 1 \mu\text{s/yr}$. This LUVOIR-A case would allow dwarf galaxies to be studied around a range of hosts, including M31 and M81. In this LUVOIR-B case, we'd be limited to studying primarily Local Group dwarf systems (see **Figure B-24** and **Figure B-25** for details).

In practice, we would need far less exposure time for nearby targets so the exact amount of telescope time will depend on the specific distribution of target distances. Specifically, the exposure time (in kiloseconds) required to achieve a given transverse velocity precision is:

$$t_{\text{exp}} = 0.3432 D_{\text{gal}}^4 \left(\frac{15 \text{ m}}{D_T} \right)^2 \left(\frac{10 \text{ km/s}}{\sigma_v} \right)^2 \quad (6)$$

where D_{gal} is the galaxy distance in Mpc, D_T is the telescope diameter in meters, and σ_v is the desired transverse velocity precision in km s^{-1} . A summary of the targets and exposure times appears in **Table B-19**.

Overheads. We simply assume a 50% overhead allocation for this program, which will be largely devoted to repointing maneuvers.

Laser-based pixel geometry calibration system requirements. The calibration program needed to achieve $\sim 10 \text{ km/s}$ proper motion precision over 5 years at a distance of 4 Mpc for LUVOIR-A or 2.2 Mpc for LUVOIR-B requires internal astrometric accuracies of ~ 0.0001 pixels, corresponding to $0.34 \mu\text{s}$ for LUVOIR-A or $0.65 \mu\text{s}$ for LUVOIR-B. Using the

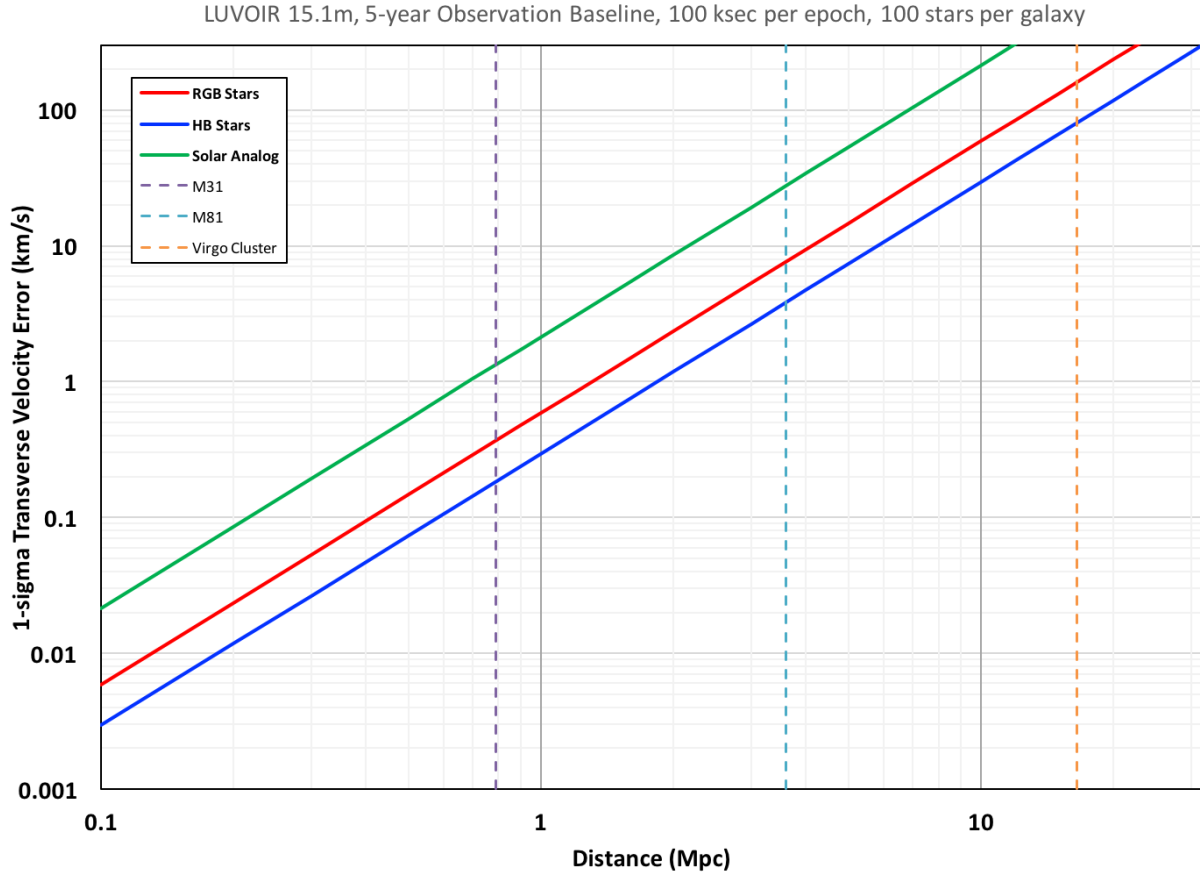


Figure B-24. Proper motion velocity error as a function of distance for 3 different stellar types. The errors here correspond to LUVUOIR-A with 100 ksec exposures per epoch, with three epochs over a 5-year baseline. The distances to the M31 and M81 galaxies, as well as the Virgo Cluster, are indicated with vertical dashed lines.

planned onboard laser-based calibration system, we will need to average 4 patterns of 20 co-added fringe images (10 in the x-direction, 10 in the y-direction) with 2.5×10^7 photons per pixel per pattern for both LUVUOIR-A and LUVUOIR-B. The square root of the total number of photons per pixel, summed over all patterns, is the inverse of the desired fractional pixel precision. This will require of order 1000 co-added exposures per fringe image per pattern, assuming we limit each pixel to 50% of its 50,000 electron full well capacity. The amount of time required to calibrate the internal pixel positions with a single use of the laser system scales inversely as the square of the fractional pixel accuracy.

Laser-based pixel geometry calibration system requirements. The calibration program needed to achieve ~ 10 km/s proper motion precision over 5 years at a distance of 4 Mpc for LUVUOIR-A or 2.2 Mpc for LUVUOIR-B requires internal astrometric accuracies of ~ 0.0001 pixels, corresponding to $0.34 \mu\text{as}$ for LUVUOIR-A or $0.65 \mu\text{as}$ for LUVUOIR-B. Using the planned onboard laser-based calibration system, we will need to average 4 patterns of 20 co-added fringe images (10 in the x-direction, 10 in the y-direction) with 2.5×10^7 photons per pixel per pattern for both LUVUOIR-A and LUVUOIR-B. The square root of the total number of photons per pixel, summed over all patterns, is the inverse of the desired fractional pixel precision. This will require of order 1000 co-added exposures per fringe image per pattern, assuming we limit each pixel to 50% of its 50,000 electron full well capacity. The amount

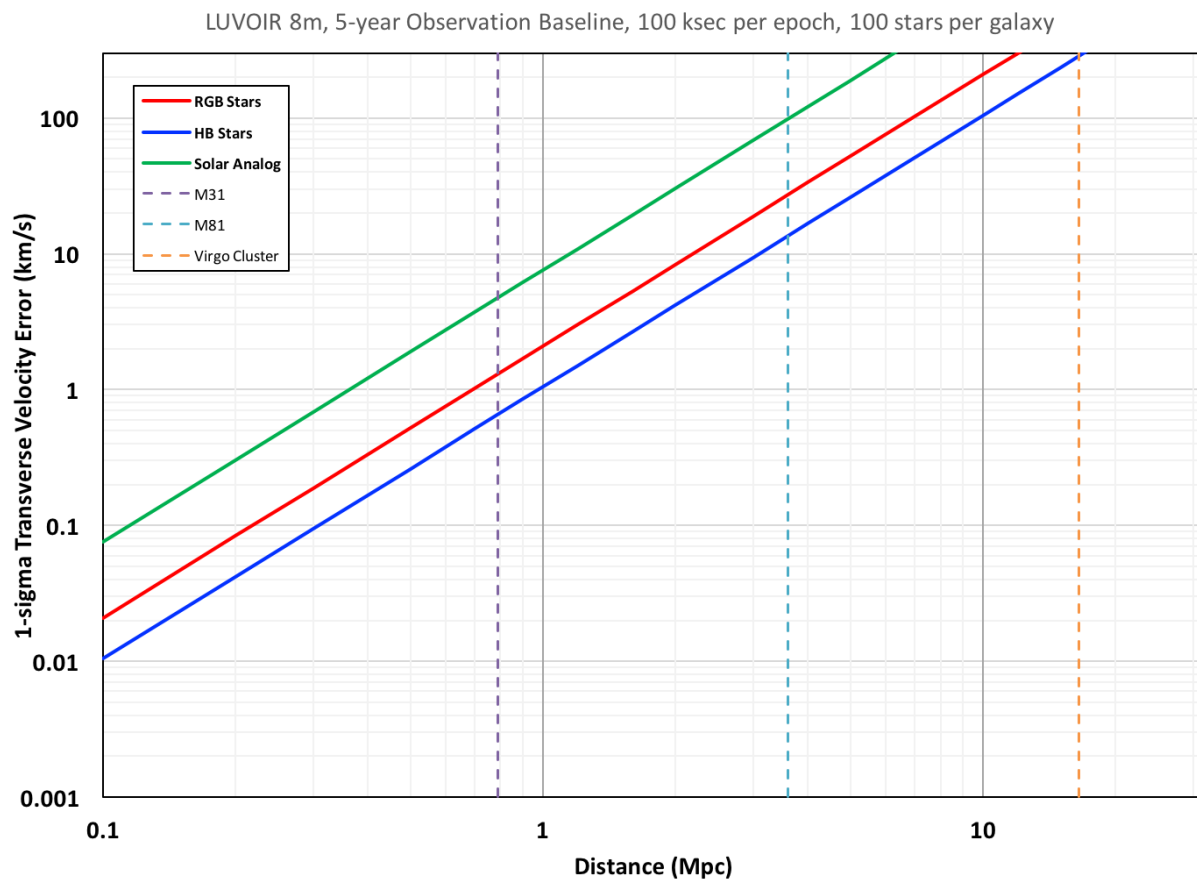


Figure B-25. Same as previous figure, but for LUVOIR-B.

of time required to calibrate the internal pixel positions with a single use of the laser system scales inversely as the square of the fractional pixel accuracy.

With a sensor pixel readout rate of 500 kHz and 32 readout ports per sensor we can complete the required HDI internal astrometric calibration sequence with a total allocation of ~11 hours for either LUVOIR-A or LUVOIR-B. The number of times this calibration sequence would need to be done depends on the thermal and mechanical stability of the focal plane. Given LUVOIR's overall stability requirements, we estimate that this calibration sequence would need to be done only in proximity to the execution of high precision astrometric observations. Therefore, the internal calibrations take about 11 hours per epoch for both LUVOIR-A and LUVOIR-B.

The HDI thermal radiator is sized to handle heat loads corresponding to a 500 kHz readout rate and there will be no impact on telescope wavefront control during the calibration process. Therefore, many of the internal pixel position calibrations can be performed in parallel while other LUVOIR instruments (e.g., ECLIPS, LUMOS) are the primary instrument and when HDI is not requested as a parallel imaging instrument; this would dramatically reduce the total program time. Furthermore, we envision dedicated astrometry campaigns once per month, in which these and other astrometric measurements (see Signature Science Case #5 in **Section B.6**) are performed, saving on calibration time. For the time being, however, we account for the needed calibration time within each program.

Table B-19. *Science exposure times per epoch for proper motion observations of stars in dwarf galaxies.*

Galaxy target	Distance (Mpc)	LUVOIR-A science time per epoch (hours)	LUVOIR-A cumulative time (hours)	LUVOIR-B science time per epoch (hours)	LUVOIR-B cumulative time (hours)
LG Dwarf 1	0.5	0.01	0.01	0.02	0.02
LG Dwarf 2	0.5	0.01	0.02	0.02	0.04
LG Dwarf 3	0.5	0.01	0.03	0.02	0.06
LG Dwarf 4	0.7	0.02	0.05	0.08	0.14
LG Dwarf 5	0.7	0.02	0.07	0.08	0.22
LG Dwarf 6	0.7	0.02	0.09	0.08	0.30
LG Dwarf 7	1.0	0.10	0.19	0.34	0.64
LG Dwarf 8	1.0	0.10	0.29	0.34	0.98
LG Dwarf 9	1.0	0.10	0.39	0.34	1.32
LG Dwarf 10	1.0	0.10	0.49	0.34	1.66
Dwarf 11	1.8	1.00	1.49	3.56	5.22
Dwarf 12	2.0	1.53	3.02	5.42	10.6
Dwarf 13	2.1	1.85	4.87	6.59	17.2
Dwarf 14	2.2	2.23	7.10	7.93	25.2
Dwarf 15	2.4	3.16	10.3	11.2	36.4
Dwarf 16	3.0	7.72	18.0	27.4	63.8
Dwarf 17	3.5	14.3	32.3	50.8	114.6
Dwarf 18	4.0	24.4	56.7	86.7	201.3
Dwarf 19	4.5	39.1	95.8	138.9	340.2
Dwarf 20	5.0	59.6	155.4	211.7	551.9

B.9.5 Results

For LUVOIR-A, the survey of 20 dwarf galaxies would require 3 epochs \times 155 hours = 465 hours of science time. This program on LUVOIR-B would require 3 epochs \times 552 hours = 1656 hours of science time. The total LUVOIR-A time would be 465 science hours + 233 overhead hours + (3 \times 11) hours for laser calibration \sim 1 month, while the total LUVOIR-B time would be 1656 science hours + 828 overhead hours + (3 \times 11) hours for laser calibration \sim 3.5 months. We note that both LUVOIR-A and B can conduct extensive astrometric surveys of the Local Group in just a few hours per epoch (see **Table B-19**).

Parallels

- ☐ Do not execute parallels with this program
- ☐ Parallels required for this program
- ☒ Can be executed as parallel to another program
- ☒ Possible to execute parallels with this program

The internal HDI focal plane calibrations with the internal laser metrology system can be executed in parallel with other programs, provided those programs do not require use of the

HDI for science observations. However, the astrometric science observations proposed here require specific targeted fields and cannot be executed in parallel.

Target of opportunity / time-critical

- ☐ Is a ToO program
- ☒ Is time-critical

Three visits to each dwarf galaxy, spread over 5 years.

B.10 Signature Science Case #9: Tracing ionizing light over cosmic time

B.10.1 Abstract

The goal of this science case is to investigate the reionization era, the time in cosmic history where the universe transitioned from being opaque to UV radiation to its present largely transparent state. This will be done in three ways.

1. Study the behavior of the galaxy luminosity function at the faint end, revealing the degree to which dwarf galaxies powered cosmic reionization.
2. Detect and quantify the evolution of ionizing radiation from low-redshift galaxies.
3. Map the escape of ionizing radiation from low-redshift galaxies and relate it to massive stellar populations and outflows.

Program contact(s)

Marc Postman (STScI), John O’Meara (Keck Observatory), Jane Rigby (NASA GSFC)

Brief description

HDI deep multi-band NIR imaging of 12 blank sky fields to find faint dwarf galaxies at high redshift
 LUMOS multi-object spectroscopy of 500 low-redshift galaxies per $\Delta z=0.2$ bin
 LUMOS multi-object spectroscopy of ~ 1000 star-forming regions within 100 low-redshift galaxies

Total observing time

LUV OIR-A: 120 days + 8 days + 7 days = 135 days (128 in parallel)
 LUV OIR-B: **Not feasible** + 15 days + 25 days = 40 days (15 in parallel)

With these programs, we will directly test the hypothesis that the UV background suppresses star formation, producing a significant turnover in the low-mass galaxy luminosity function, and characterize the ionizing radiation itself.

B.10.2 Dwarfs in the distant universe: probing the impact of reionization

The shape of the faint-end of the $z=7$ luminosity function is sensitive to the UV background, which can suppress star formation and produce a significant turnover in the low-mass galaxy luminosity function. Specifically, the rest-frame UV luminosity function may exhibit a turnover (e.g., Jaacks et al. 2013) that is detectable at absolute UV magnitudes $M \gtrsim -13.5$. Abundance-matching with current best estimates of the UV luminosity function implies that this corresponds to halo masses $\log (M/M_{\odot}) \approx 9$ at $z=7$, consistent with theoretical expectations for the suppression mass. Observationally, this deviation would start to be seen in NIR passbands at $AB \approx 33$ mag (**Figure B-26**). LUV OIR-enabled deep imaging surveys that reach the turnover in galaxy luminosity function, predicted to occur due to UV background feedback suppression, will directly test this hypothesis. Current theories predict that we should see this turnover in ionized regions, but not in neutral regions. Models of reionization are *extremely* sensitive to this, as the galaxies near this limit dominate the ionizing emissivity.

Observations overview. Deep imaging with HDI in the I-, J-, and H-bands to detect large numbers of faint dwarf galaxies at high redshift. The UVIS and NIR channels will observe the same field of view simultaneously.

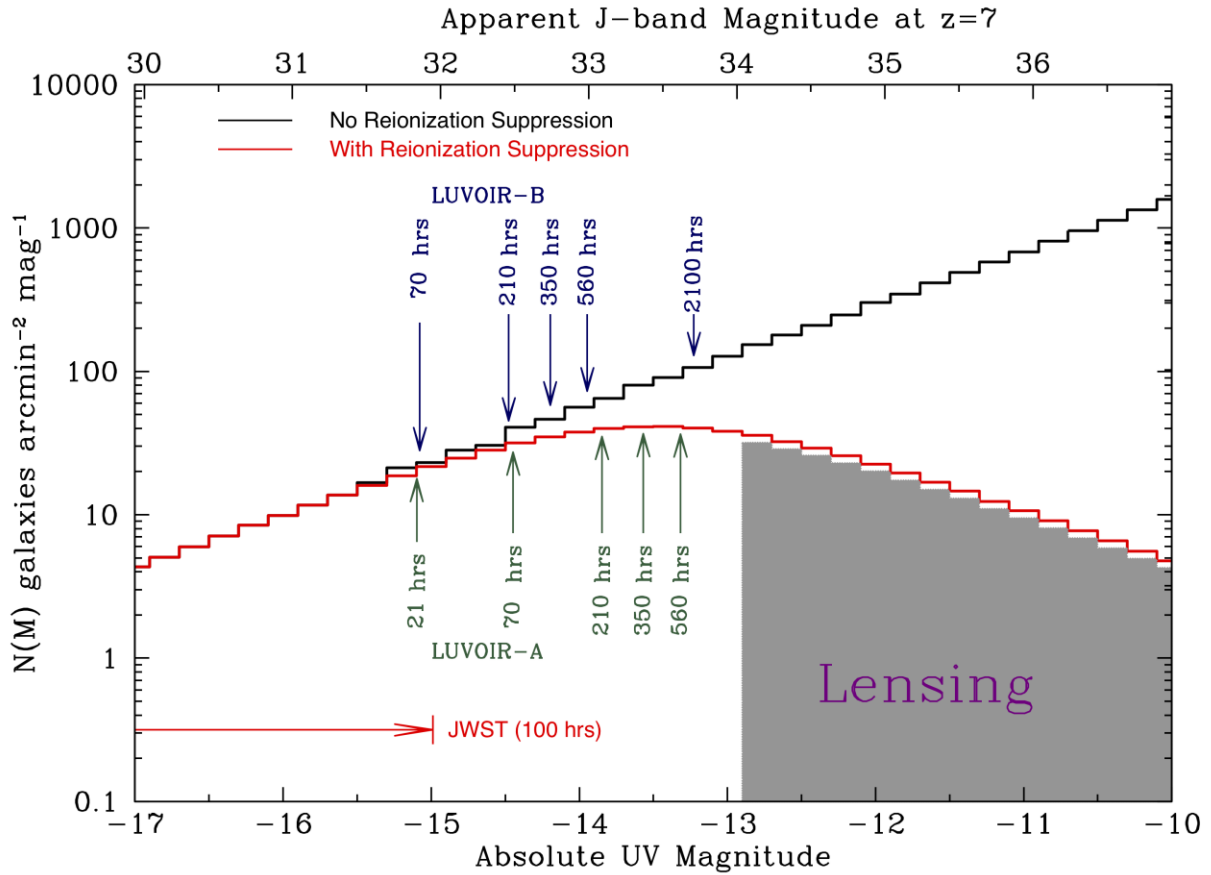


Figure B-26. Predictions for the number of $z=7$ galaxies per sq. arcmin. per magnitude for a model with reionization suppression (red histogram) and without reionization suppression (black histogram). Reionization suppression may introduce a detectable turnover in the luminosity function at an absolute UV magnitude around $M \approx -13.5$ mag. The SNR=4 depths reached in a 3-band survey with the two LUVIR concepts are shown, assuming simultaneous UVIS and NIR observations. This survey can be performed in parallel with the exoplanet spectroscopic characterization program. For reference, the SNR=4 depth for a 100 hour F200W JWST image is also shown. Credit: M. Postman (STScI)

Targets. Twelve blank sky fields to mitigate cosmic variance and allow us to study regions identified as being either ionized or neutral (as indicated by prior supporting deep 21 cm radio or Lyman-alpha imaging surveys).

Exposure times & overheads. The total survey time is set by identifying the depth at which the predicted difference between the differential rest-frame UV luminosity functions with and without re-ionization suppression of star formation reaches 5σ statistical significance. This corresponds to a J-band depth of approximately $AB = 32.75$ mag per field with galaxy counts summed over 12 fields (**Figure B-26**). The science time was allocated as follows: 70% in the F814W (I-band) filter, 15% in the F125W (J-band) filter, and 15% in the F160W (H-band) filter. The time allocations were derived assuming a source diameter of 100 milliarcsec (260 pc radius at $z=7$) and SNR=5 for a source with $AB = 32.75$ mag. The longer time allocated to the I-band is to ensure adequate depth for the dropout band, as the sources of interest will be identified using an I-band dropout selection criterion. The exposure times, calculated with the HDI exposure time calculator (**Section B.1.3**), appear in **Table B-20**.

Table B-20. *Exposure times for high-redshift galaxy luminosity function survey*

	LUVUOIR-A	LUVUOIR-B
UVIS exp. time, I-band (hours)	241	775
NIR exp. time, J- & H-bands (hours)	103	332
Science time per field (hours) **	241	775
Time per field with overheads (hours)	362	1163
Total time for 4 fields (hours)	1448	4652

** Exposure time per field is just the UVIS time since the NIR data are acquired simultaneously.

Both channels (UVIS, NIR) can be acquired simultaneously, as the two channels can have a common field of view. Thus, the total time for imaging a single field in all three bands is set by the UVIS integration time. We will implement occasional dithers to cover gaps in the detector array and allow rejection of hot / bad pixels. We will not need to dither to achieve Nyquist sampling since the HDI detector array is already Nyquist sampled at 500 nm. We simply assume a 50% overhead allocation for this program.

Results. As stand-alone programs, the total time comes to 2880 hours = 120 days with LUVUOIR-A and 9360 hours = 390 days with LUVUOIR-B. These would be very large investments of time to obtain these “LUVUOIR Ultra-Deep Fields.” However, these programs can be executed in parallel with long-duration ECLIPS observations, under the following constraints:

1. The ECLIPS target is at high galactic latitude.
2. The total science exposure time per HDI field is at least 160 hours with LUVUOIR-A and 520 hours with LUVUOIR-B.
3. There are at least 12 ECLIPS targets located in the sky such that the HDI FOV covers both ionized and non-ionized regions of the high-*z* universe.

Hundreds of field stars will be observed with ECLIPS multiple times during the 2-year habitable planet candidate survey (Signature Science Case #1). Therefore, Constraints #1 and #3 will be easily met.

Considering Constraint #2, the characteristics of the science exposure times in the 2-year habitable planet candidate survey with LUVUOIR-A are as follows:

1. Over a thousand “shallow” observations of hundreds of stars, with a mean science exposure time of ~ 8 hours. Each star visited ~ 6 times.
2. About 50 “deep” observations of a subset of stars, with a mean science exposure time of 70 hours. At least 12 of these targets will be observed for at least 160 hours. The average integration time for these 12 targets is 281 hours, with two fields being exposed for over 490 hours.

Therefore, constraint #2 will be met in the LUVUOIR-A habitable planet candidates survey. For LUVUOIR-B, it will be harder to obtain these “LUVUOIR Ultra-Deep Fields” in parallel with the habitable planet candidate survey. Too few stars will be observed for the 520 hours needed to reach the desired depth with LUVUOIR-B. For now, we assume that it is not feasible

to execute the current program with LUVOIR-B, either as a stand-alone program or as a parallel program.

Parallels

- ☐ Do not execute parallels with this program
- ☐ Parallels required for this program
- ☒ Can be executed as parallel to another program
- ☒ Possible to execute parallels with this program

See discussion above.

Target of opportunity / time-critical

- ☐ Is a ToO program
- ☐ Is time-critical

B.10.3 Characterizing ionizing radiation at low redshift

LUVOIR's investigation of the impact of reionization on structure formation extends to more recent periods in cosmic history as well with a characterization of the ionizing radiation that leaks from $z < 1$ galaxies. The emergence and sustenance of this ubiquitous background of ionizing radiation along with the accompanying evolution of large-scale structure are dependent on a key parameter, for which we have very little theoretical or observational guidance, namely the fraction of ionizing radiation escaping from these first and subsequent collapsed objects. LUVOIR can both determine the ultra faint-end shape of the luminosity function at high redshift and also characterize of the ionizing radiation itself by studying galaxies at much lower redshifts.

LUMOS will spatially resolve a large number of sources in a single observation over an extended field, allowing an in-depth characterization of the environmental factors that favor escape of far-UV radiation. Spatial resolution is important because Lyman continuum escape depends on the relative placement of the UV emitting region. LUVOIR observations will allow an accurate determination of the sources and sinks of the ionization background radiation field. Most importantly, LUVOIR will allow us to determine what kinds of massive stellar populations generate the ionizing radiation.

Observations overview. Low resolution multi-object spectroscopy of $0 \lesssim z \lesssim 1$ galaxies at wavelengths below the Lyman break, using LUMOS with the G145LL grating ($R=500$).

Targets. Random sky fields containing 500 galaxies with low escape fractions ($f_{900}^{\text{esc}} \leq 10\%$) per $\Delta z = 0.2$ bin.

Exposure times & overheads. We fix the exposure time per field to 10 hours and calculate the number of fields we must observe to get a sufficient number of galaxies per redshift bin. Galaxies must be detected at $\text{SNR}=5$ or greater over a 30 \AA window below the Lyman break. **Figure B-27** shows the cumulative number of star-forming galaxies in different redshift bins observed to the indicated escape fraction at the Lyman edge (5σ detection limit) in a 10-hour observation, as a function of the apparent UV magnitude. Using the cumulative number counts in **Figure B-27** and the effective areas for LUMOS on LUVOIR-A and LUVOIR-B, we arrive at the exposure time estimates to reach at least 500 objects with $f_{900}^{\text{esc}} \leq$

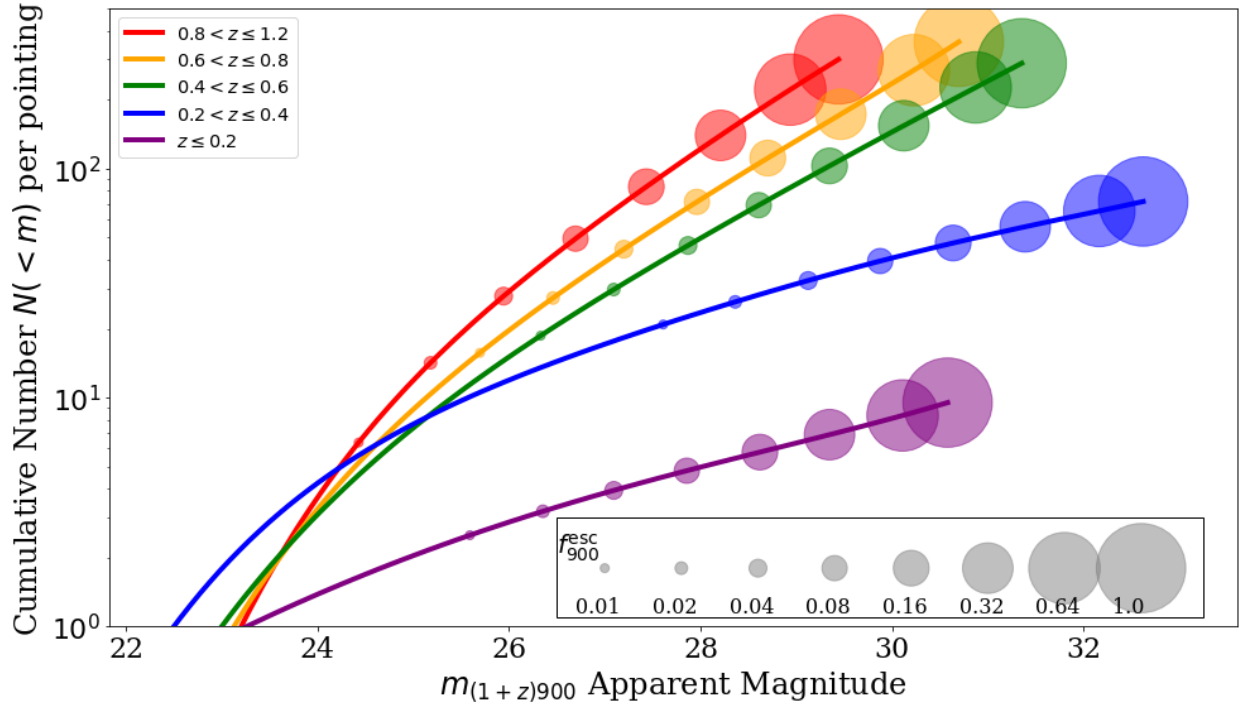


Figure B-27. The cumulative number of galaxies detected in a single LUMOS field-of-view vs the 5σ limiting flux in a 30 \AA interval shortward of $(1+z) * 911.8 \text{ \AA}$, assuming a 10-hour observation. Different redshift bins are shown with colored lines and escape fraction with different size circles.

10% per redshift bin shown in **Figure B-27**. We simply assume a 50% overhead allocation for this program.

Results. We constrain the observations to be at $0.2 < z < 1.2$, thus removing the most expensive bin in **Figure B-27**. In this scenario, we require a total science exposure time of 120 hours (12 fields) for LUV0IR-A and 230 hours (23 fields) for LUV0IR-B. Including overheads, the total program time is 180 hours \sim 8 days with LUV0IR-A and 345 hours \sim 15 days with LUV0IR-B.

Parallels

- ☐ Do not execute parallels with this program
- ☐ Parallels required for this program
- ☒ Can be executed as parallel to another program
- ☒ Possible to execute parallels with this program

This program does not require specific locations in the sky for the fields. It can therefore be executed in parallel as long as the LUMOS MOS remains pointed at same field for 10 hours.

Target of opportunity / time-critical

- ☐ Is a ToO program
- ☐ Is time-critical

B.10.4 Mapping the escape of ionizing radiation

By capturing both the ionizing and non-ionizing FUV, LUVOIR can link the massive stellar populations of galaxies to the ionized nebulae and outflows they power and the ionizing LyC radiation that may escape. To do so, LUVOIR must capture ionizing < 90 nm photons at any spectral resolution, as well as non-ionizing 120–160 nm rest-frame photons at $R > 5000$. This portion of the program will map, at high signal-to-noise and on the spatial scales of individual star-forming regions, how ionizing radiation escapes from galaxies, as a function of the age and metallicity of the massive stellar populations, the nebular conditions, and the strength of the outflow.

Observations overview. Multi-object spectroscopy of individual star-forming regions at rest-frame < 90 nm and 120–160 nm using LUMOS with the G155L grating ($R=11,600$).

Targets. 100 galaxies with redshifts in the range $z=0.25-0.3$, and selected to have GALEX integrated $FUV_{AB} = 19$ to enable high SNR. The LUMOS MOS apertures will be placed on as many individual star-forming regions within each galaxy as possible, approximately 1000 total.

Exposure times & overheads. For $R=11,000$, Chisholm et al. (2019) find that $SNR=12$ (4) per resolution element at $\lambda_r=140$ nm is required to determine the stellar age at the 10 (3) sigma level. Such SNR is sufficient to also detect faint nebular emission lines (Rigby et al. 2018). From the GALEX far-UV number counts (Xu et al. 2005), all-sky there are 10^5 galaxies brighter than $FUV_{AB} = 19$. Therefore, LUVOIR could target 100 fields with the LUMOS MOS, each field centered on a known $FUV_{AB}=19$ GALEX source in the redshift range $z=0.25-0.3$, with additional MOS apertures targeting fainter GALEX FUV sources with photometric redshifts in range. Using the LUMOS ETC, a 1-hour integration in G155L with LUVOIR-A on a $FUV_{AB}=19$ galaxy at $z=0.3$, with its flux divided into 15 equally bright star-forming regions each captured with a MOS aperture, would return $SNR=13$ per resolution element at $\lambda_r=140$ nm. LUVOIR-B requires 4 hours. We assume a 50% overhead allocation for this program.

Results. This program requires 100 hours (150 hours with overheads) for LUVOIR-A, and 400 hours (600 hours with overheads) for LUVOIR-B.

Parallels

- ☐ Do not execute parallels with this program
- ☐ Parallels required for this program
- ☐ Can be executed as parallel to another program
- ☒ Possible to execute parallels with this program

Target of opportunity / time-critical

- ☐ Is a ToO program
- ☐ Is time-critical

B.11 Signature Science Case #10: The cycles of galactic matter

B.11.1 Abstract

The goal of this science case is to understand the ways in which matter flows into and out of galaxies, controlling the evolution of star formation and determining the ultimate fates of galaxies. This will be done in three ways:

1. A quasar absorption line key program to measure baryons at 10 to 10^7 K across cosmic time.
2. A program to take a high definition view of the matter around a nearby galaxy
3. A program to resolve gas flows in nearby galaxies.

These unprecedented studies of the circumgalactic medium (CGM) will reveal the complex interplay between inflows of matter from the intergalactic medium (IGM) and outflows driven by stellar radiation, explosions, and active galactic nuclei (AGN).

Program contact(s)

John O'Meara (Keck Observatory), Jason Tumlinson (STScI)

Brief description

LUMOS UV spectroscopy of CGM / IGM absorption lines towards 100 quasars

LUMOS UV spectroscopy of 30 quasars behind a single nearby face-on spiral galaxy

LUMOS UV spectroscopy of inflows and outflows from ~ 1000 stellar clusters in nearby galaxies

Total observing time

LUVUOIR-A: 15 days + 6 days + 3 days = 24 days

LUVUOIR-B: 54 days + 18 days + 9 days = 81 days

B.11.2 Quasar absorption line survey

The primary objective of this program is to obtain column densities of ions sampling the full range of temperatures (10 – 10^7 K) and densities (10^{-6} – 10^2 cm $^{-3}$) in the intergalactic and circumgalactic medium. This will be achieved by obtaining LUMOS FUV+NUV spectra of 100 quasars at $z > 1$. The quasars are selected (via lack of strong intervening absorption and emission redshift) in part to facilitate measurement of many EUV lines such as NeVIII and MgX that sample high temperature, low density gas that may contain a significant reservoir of as of yet unseen baryons. Every quasar spectrum will provide simultaneous coverage of the $z \sim 1$ Lyman alpha forest, and the CGM of galaxies spanning several billion years of cosmic time. This program assumes a comprehensive absorption line campaign across a wide UV wavelength range. Smaller, more specific science programs will require significantly less time.

Observations overview. Each quasar would receive a single pointing and would be observed with each LUMOS M grating (G120M, G150M, G180M, G300M) to provide SNR $\gtrsim 20$ per resolution element over the entire $1000 < \lambda < 4000$ Å wavelength range.

Targets. 100 quasars at $z > 1$. As drawn from a cross-match between the SDSS DR7 and GALEX surveys, the example set of targets presented here would have $N = [18, 48, 34]$ quasars with GALEX FUV magnitudes of $[<18, 18-18.5, 18.5-19]$, respectively.

Exposure times & overheads. All exposure time calculations were done with the LUMOS exposure time calculator (Section B.1.4), assuming a flat spectral source. For reference,

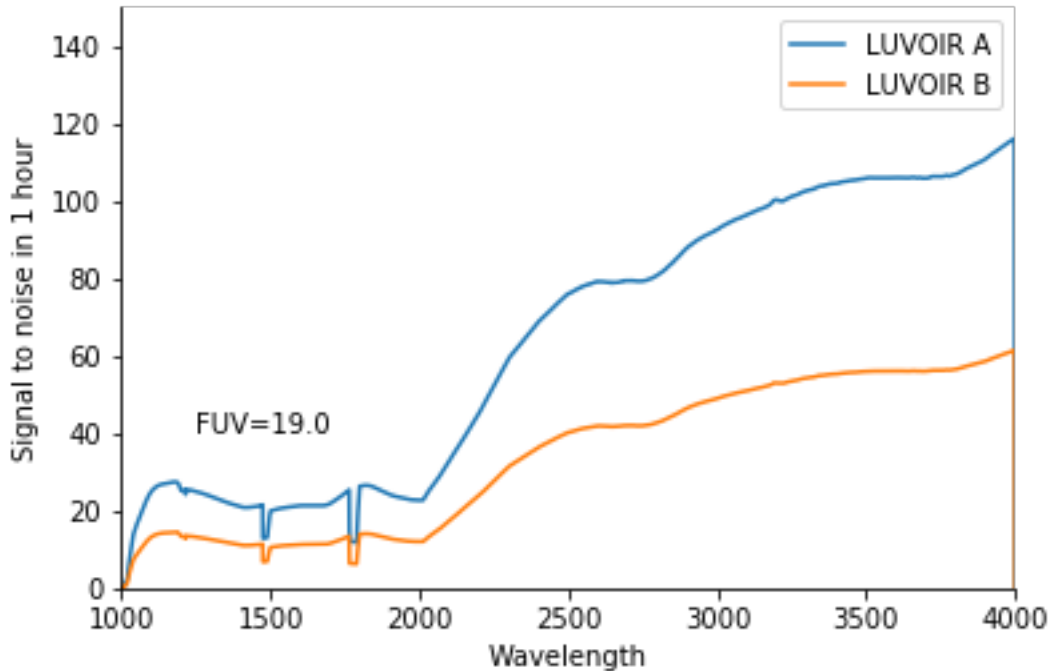


Figure B-28. Signal-to-noise ratio for a LUMOS-A spectral observation of a quasar with GALEX FUV magnitude = 19, assuming a flat spectrum and 1 hour per band (G120M, G150M, G180M, & G300M). The total science exposure time to acquire this spectrum would be 4 hours.

Figure B-28 shows the SNR delivered in 1 hour per band over the full range of wavelengths for a source with GALEX FUV magnitude = 19. Covering the full wavelength range for this source therefore requires 4 hours to observe in all 4 gratings. Relaxing the S/N requirement to be ≥ 20 everywhere, or choosing only certain gratings to focus on certain science, will significantly lower the total program time. We simply assume a 50% overhead allocation for this program.

Results. Using the example quasars with the numbers and GALEX FUV magnitudes given above, we find the total science exposure time for this program is 241 hours with LUVOR-A and 863 hours with LUVOR-B. Including overheads, the total program times are 362 hours = 15 days for LUVOR-A and 1294 hours = 54 days.

Parallels

- ☐ Do not execute parallels with this program
- ☐ Parallels required for this program
- ☐ Can be executed as parallel to another program
- ☒ Possible to execute parallels with this program

Target of opportunity / time-critical

- ☐ Is a ToO program
- ☐ Is time-critical

B.11.3 High definition view of a spiral galaxy

This program maps the halo gas (or CGM) of M51, a nearby face on spiral galaxy. The goal is to measure halo gas out to a radius of 200 kpc. With LUVOR / LUMOS sensitivity, we can

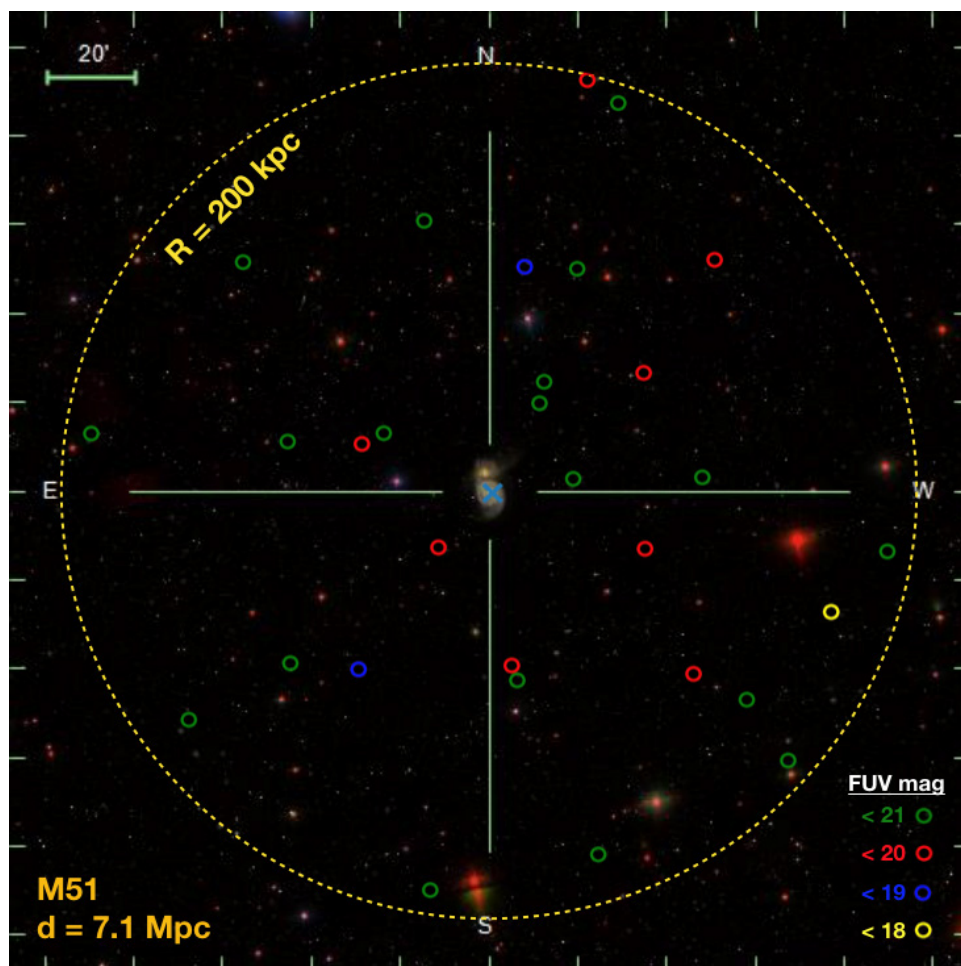


Figure B-29. The M51 field showing 30 QSOs within a projected separation of 200 kpc. These 30 sightlines will probe the mass content and kinematics of the CGM for this face on galaxy.

examine 30 quasar sightlines passing through M51's halo with complete medium-resolution UV spectra (**Figure B-29**). These data will map the spatial distribution, kinematics, metal content, and large-scale structures of the gas that feeds and is fed by this galaxy.

This program will move far past the science goals of the Hubble COS-Halos program, which used COS to observe the halos of 42 galaxies in a similar fashion. For COS-Halos, Tumlinson et al. (2013) selected QSOs with $FUV_{mag} < 18$, which are far fewer in number than those with $FUV < 21$. With a restricted QSO sample, the COS-Halos map of the CGM was built up by choosing a sample of galaxies with one QSO each, and summing up to obtain an averaged map of the diagnostic ions.

LUMOS will allow us to do the same, but for 30 sightlines around one single galaxy. This is now being done with Hubble for M31 (the AMIGA program), the only galaxy close enough for > 10 QSOs to lie in the background. LUMOS will combine the best attributes of COS-Halos and AMIGA to intensively probe the CGM of a single galaxy with all the key diagnostic lines in a reasonable allocation of time.

Observations overview. Complete point-source UV spectra of quasars behind a nearby spiral galaxy using the LUMOS M gratings ($R \sim 30,000$).

Table B-21. Science exposure times for complete LUMOS UV spectra of quasars behind the M51 galaxy.

Grating	Nominal Wavelength	Line of Interest	FUV < 21 (hours)	FUV < 20 (hours)	FUV < 19 (hours)	FUV < 18 (hours)
LUVOIR-A						
G120M	1040	OVI / Ly- β	4	1.5	0.5	0.2
G150M	1550	C IV	1.1	0.4	0.2	0.1
G180M
G300M	2800	Mg II	0.1	<0.1	<0.1	<0.1
Hours per quasar			5.2	2.0	0.8	0.4
# of quasars			19	8	2	1
Total science exposure time (hours)			99	16	1.6	0.4
LUVOIR-B						
G120M	1040	OVI / Ly- β	10	5	2	1
G150M	1550	C IV	4	1.5	0.6	0.3
G180M
G300M	2800	Mg II	1	0.4	0.2	0.1
Hours per object			15	7	2.8	1
# of quasars			19	8	2	1
Total science exposure time (hours)			285	56	5.6	1.4

Targets. Any nearby galaxy, at a distance of about 20 Mpc or less, will have numerous $AB_{\text{mag}} < 20$ quasars behind it. For concreteness, we have chosen the face-on spiral M51 at $d = 7.1$ Mpc. Other good examples are M82 (3.5 Mpc) and M101 (6.4 Mpc).

At the distance of M51, a projected sphere of radius $R = 200$ kpc subtends 1.61 degrees in radius, for a total projected surface area of 8.14 deg^2 . We derive a target list from the Sloan Digital Sky Survey QSO catalog, matched to the GALEX catalog to pre-select based on FUV magnitudes. This is, in fact, the same QSO catalog used to select targets for the COS-Halos program (Tumlinson et al. 2013), but LUVOIR allows us to go much deeper. Taking the entire set of objects that lie within 1.61 deg of M51 ($R = 200$ kpc projected) and with $FUV_{\text{mag}} < 21$, we find the 30 background quasars shown in **Figure B-29**.

Exposure times & overheads. Using the LUMOS exposure time calculator (**Section 16.1.4**), we produce a simple “exposure model” that bins quasars by magnitude and assigns nominal exposure times based on FUV magnitude. **Table B-21** shows the exposure times for $FUV_{\text{mag}} = 21, 20, 19$, and 18 . These are tuned to deliver $SNR = 10$ at OVI / Lyman- β ($1025\text{--}1040 \text{ \AA}$) and C IV (1550 \AA), and $SNR = 20$ at Mg II (2800 \AA). Objects within a magnitude bin with slightly brighter magnitudes will reach slightly higher SNR. We adopt a 25% overhead allocation for this program, allowing for small slews between targets, and otherwise assuming that LUMOS will reach efficiency for instrument-level overheads that is similar to HST/COS when Earth occultations are ignored.

Results. For LUVOIR-A, the per-object totals in the table show that the 30 selected objects will require 117 hours of science exposure time. The total LUVOIR-A time with overheads is $117 \text{ hours} + 29 \text{ hours} = 146 \text{ hours} \sim 6 \text{ days}$.

For LUVUOIR-B, the planned exposures take much longer. The total science exposure time is 348 hours, for a total of 435 hours ~ 18 days including overheads. This is expensive for a single-cycle large program. We therefore consider two descopes.

First, dropping the O VI / Lyman- β setting (G120M) saves 140 science hours, dropping the total to 112 hours for science and 140 hours total. This returns the program to the same overall length, but at the cost of a major scientific sacrifice by dropping access to the key UV diagnostic of highly ionized halo gas. Another compromise could be made in sample size, by dropping the faintest quasars. If we observe only 4 quasars in the $FUV_{\text{mag}} < 21$ bin, making the total sample 15 objects, then the required hours are 123 for science and 154 in total. Both descopes—dropping a key physical diagnostic or cutting the sample in half—would make this program far less compelling as a map of the low- z CGM.

Parallels

- ☐ Do not execute parallels with this program
- ☐ Parallels required for this program
- ☐ Can be executed as parallel to another program
- ☒ Possible to execute parallels with this program

Deep HDI images taken in parallel at random orients could provide useful imaging data on the stellar halo of the foreground galaxy, and on background galaxies at high redshift. Given typical exposure times of 1 hour, these images would reach AB ~ 31 in the optical bands of HDI.

Target of opportunity / time-critical

- ☐ Is a ToO program
- ☐ Is time-critical

B.11.4 Resolved gas flows

Gas outflows from galaxies are a key element of galaxy formation. They are believed to regulate the quantity of gas in galactic disks, distribute metals far into intergalactic space, and might be a major factor in the quenching of star formation in massive galaxies. Apart from the brief periods when AGN are dominant, feedback from star formation is the norm, but the effects of multiple, time varying outflows driven by correlated supernovae make it very difficult to unravel the mass loss rates and the energetics of the driving forces.

LUVUOIR's LUMOS spectrograph will enable exploration of "resolved flows." Using its multiplexing superpower, LUMOS will be able to observe hundreds of individual stellar clusters in nearby galaxies such as M83, M51, and M82 (**Figure B-30**). These observations will provide "down-the-barrel" measurements of galactic outflow and inflow with individual clusters as the sources. This technique will allow for dissection of gas flows and correlations of mass flow rates against cluster mass and age that will test specific theoretical predictions for the energetics and time evolution of the driving sources.

Observations overview. Complete multi-object UV spectra of stellar clusters in nearby spiral galaxies using the LUMOS M gratings ($R \sim 30,000$).

Targets. The multiplexing capability of LUMOS is key to the success of this observation. First, we must derive the number of clusters in a candidate galaxy. Two different methods

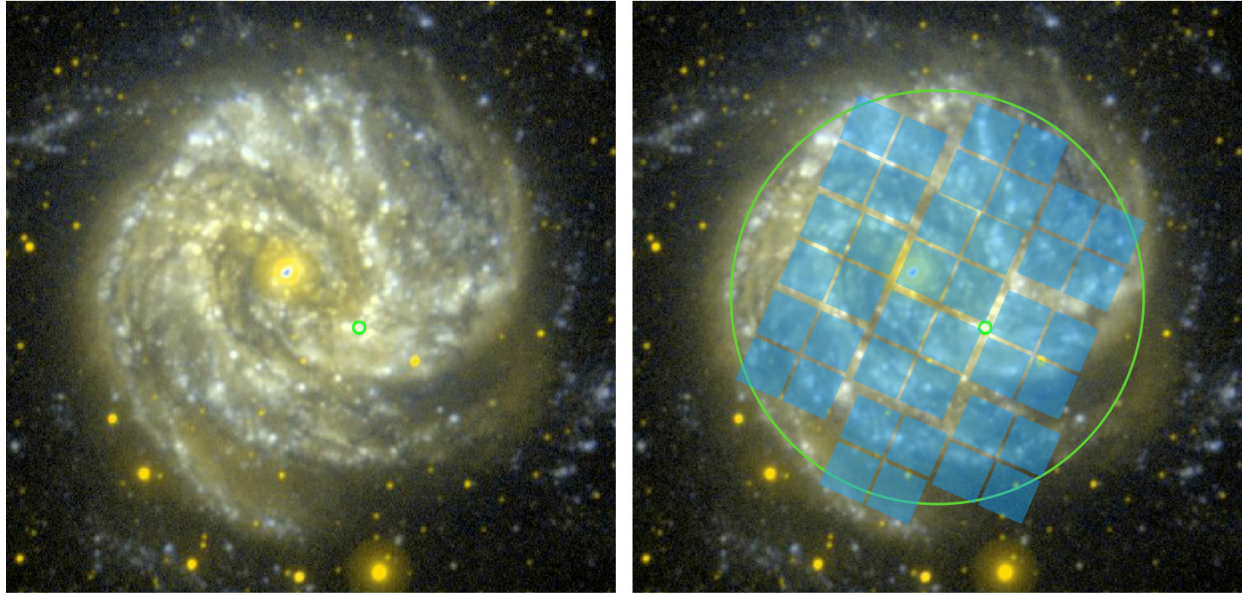


Figure B-30. GALEX FUV/NUV image showing a nominal layout for ten 2'x2' LUMOS footprints.

were employed using the face-on starburst M83 as a template, summarized here with further details provided below.

In Method 1, we use a GALEX source catalog covering a $R = 4.2$ arcmin circle encompassing most of the galaxy's disk. This catalog contains 120 sources with FUV mag < 18 , $N = 146$ for FUV mag < 19 and $N = 157$ with FUV mag < 20 (see **Figure B-31**). It seems likely that these deeper limits suffer from undercounting owing to confusion of the 5-arcsecond GALEX PSF. Thus, this catalog of relatively bright sources (FUV < 18) yields a conservative lower limit to the number of sources, $120 / 55 \text{ arcmin}^2 = 2.2$ per arcmin^2 . For the $2' \times 2'$ field-of-view (FOV) of LUMOS, we expect about 8–10 sources per field. Ten fields covering the disk of M83 will yield 80–100 sources.

In Method 2, an alternate catalog source is the Hubble-derived optical cluster catalog of Whitmore et al. (2015). They used the WFC3 optical bands to catalog the clusters and derive age and mass estimates. If we take their F225W photometry (the shortest band), we can use the slope of this “luminosity function” to correct for incompleteness in the GALEX catalog below FUV = 18. If we assume that the cluster UV luminosity function at FUV > 18 has the same slope as the F225W distribution, we obtain 360 total clusters in 10 fields, instead of 80–100.

Exposure times & overheads. Using the LUMOS exposure time calculator (**Section B.1.4**) and the parameters for LUVOIR-A, we produce a simple “exposure model” for that bins sources by magnitude and assigns nominal exposure times based on FUV magnitude. These are tuned to deliver SNR = 10 at O VI / Lyman- β (1025–1040 Å) and C IV (1550 Å), and SNR = 20 at Mg II (2800 Å). Brighter objects within a magnitude bin will reach higher SNR. The times for LUVOIR-B are simply scaled from the LUVOIR-A times by the ratio of the effective areas (LUVOIR-B time $\approx 3.5 \times$ LUVOIR-A time). The science exposure times per field for different limiting source magnitudes for LUVOIR-A and LUVOIR-B appear in **Table B-22**. We simply assume a 50% overhead allocation for this program, to account for grating changes, wavelength calibration, and repointing.

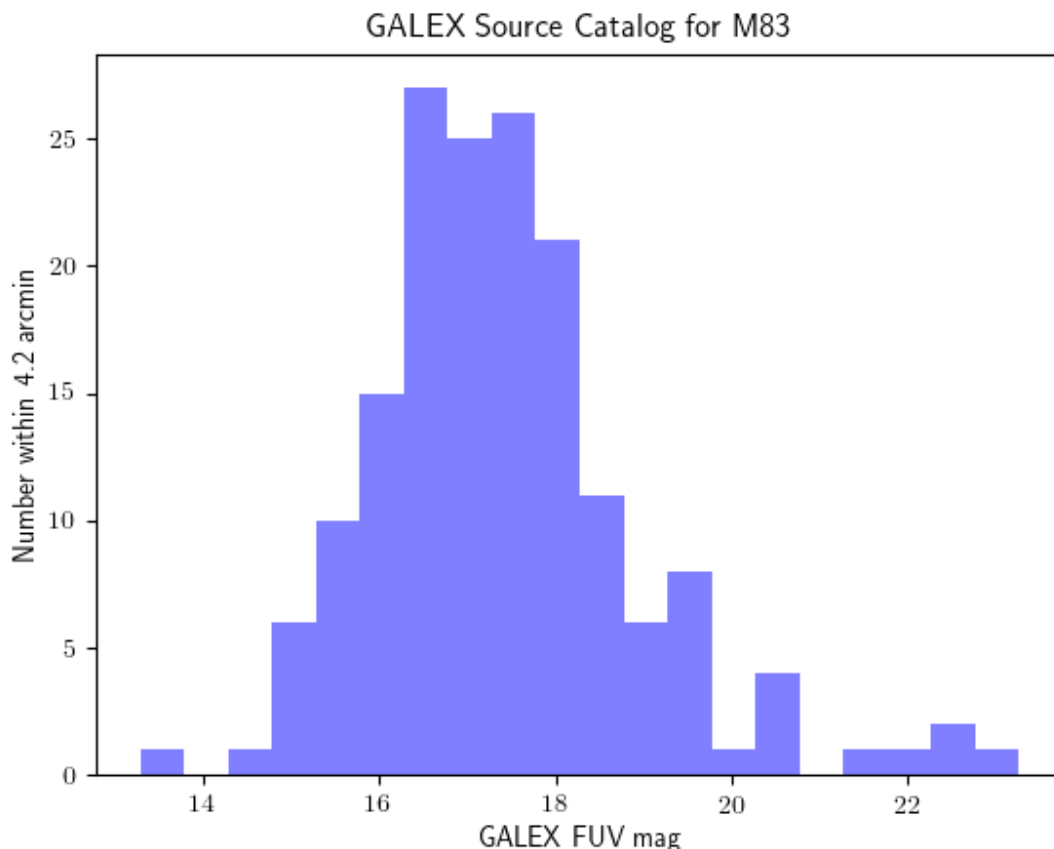


Figure B-31. *GALEX sources in the M83 Disk. A histogram of the GALEX catalog sources for $R < 4.2$ arcmin from the galaxy center. Completeness begins to be an issue near $FUV \sim 17$ because of confusion owing to the $5''$ GALEX PSF.*

Results. For Method 1, with its $FUV < 18$ sources, we require only about 0.5 hours per field to cover the full LUMOS spectroscopic bandpass (100–400 nm). We require about 0.5 hours \times 10 fields = 5 hours of science exposure time with LUVUOIR-A and 1.4 hours \times 10 fields = 14 hours of time with LUVUOIR-B to observe 80–100 sources per galaxy. Including overheads, the LUVUOIR-A time is 5 hours + 2.5 hours = 7.5 hours per galaxy and the LUVUOIR-B time is 14 hours + 7 hours = 21 hours per galaxy. With a set of 10 galaxies, the total program time is 75 hours \approx 3 days with LUVUOIR-A and 210 hours \approx 9 days with LUVUOIR-B to observe a total of \sim 800–1000 sources.

Hubble’s state-of-the-art observations of resolved outflows provide a useful comparison point. A program using the single-aperture, UV-optimized Cosmic Origins Spectrograph has obtained FUV-only (110–180 nm) spectra of 16 clusters in M83 (Program 14681, PI Aloisi). These 16 clusters required a total of 40 orbits of HST time (64 wall-clock hours). For LUVUOIR-A, the gain over Hubble is then: $(100 \text{ targets} / 16 \text{ targets}) \times (64 \text{ hours} / 7.5 \text{ hours}) = 53$. Therefore, LUVUOIR-A executes its outflow survey about 53 times more efficiently than Hubble.

For Method 2, we have to integrate 5x longer per field to maintain the same SNR for the fainter $FUV \sim 20$ sources, but get ~ 2.5 x better SNR at $FUV \sim 18$. Therefore, we require about 2 hours \times 10 fields = 20 hours of science exposure time with LUVUOIR-A and 7 hours

Table B-22. *Science exposure times for complete LUMOS UV spectra of sources in M83*

Grating	Nominal Wavelength	Line of Interest	FUV < 20 (hours)	FUV < 19 (hours)	FUV < 18 (hours)
LUVOIR-A					
G120M	1040	OVI / Ly- β	1.5	0.5	0.2
G150M	1550	C IV	0.4	0.2	0.1
G180M
G300M	2800	Mg II	<0.1	<0.1	<0.1
Hours per field			2.0	0.8	0.4
LUVOIR-B					
G120M	1040	OVI / Ly- β	5	2	1
G150M	1550	C IV	1.5	0.6	0.3
G180M
G300M	2800	Mg II	0.4	0.2	0.1
Hours per field			7	2.8	1.4

$\times 10$ fields = 70 hours of time with LUVOIR-B to observe ~ 360 sources per galaxy. The overheads should be the same as for Method 1. Therefore, the LUVOIR-A time is 20 hours + 2.5 hours = 22.5 hours per galaxy and the LUVOIR-B time is 70 hours + 7 hours = 77 hours per galaxy. Using the same total program allocations as in Method 1 (75 hours with LUVOIR-A and 210 hours with LUVOIR-B), we could observe 3 galaxies for a total of ~ 1080 sources.

It will be up to individual users to decide where they need to be in the sample-size / SNR / galaxy trade-space. This analysis shows that large samples of down-the-barrel measurements of resolved galactic gas flows are enabled with LUMOS' multiplexing superpower.

Parallels

- ☐ Do not execute parallels with this program
- ☐ Parallels required for this program
- ☐ Can be executed as parallel to another program
- ☒ Possible to execute parallels with this program

Target of opportunity / time-critical

- ☐ Is a ToO program
- ☐ Is time-critical

B.12 Signature Science Case #11: The multiscale assembly of galaxies

B.12.1 Abstract

The goals of this science case are to study galaxy evolution on spatial scales of 100pc—the sizes of large star-forming regions—across cosmic time. This will be accomplished in three ways:

1. A deep search for the smallest ultra-faint dwarf galaxies at high redshift ($z \sim 7$), the building blocks of giant galaxies.
2. High resolution optical imaging of galaxies at moderate redshift ($z \sim 1-2$), to reveal the interior morphology of galaxies.
3. Multi-color imaging of individual dwarf and giant stars in low redshift galaxies to detect the main sequence turnoff in resolved stellar populations and reconstruct the galaxies' star formation history.

Program contact(s)

Marc Postman (STScI), Jane Rigby (NASA GSFC), Daniella Calzetti (U Mass)

Brief description

HDI deep multi-band NIR imaging of 12 blank sky fields to find faint dwarf galaxies at high redshift

HDI optical imaging of the same 12 blank sky fields to probe galaxies at moderate redshift

HDI optical/NIR imaging of individual stars in low-redshift galaxies to measure stellar ages via detection of main sequence turnoffs

Total observing time

LUVUOIR-A: 120 days + 2 days + 17 days = 139 days (122 days in parallel)

LUVUOIR-B: **Not feasible** + 15 days + 20 days = 35 days (15 days in parallel)

The first program can be accomplished with the ultra-deep survey for high- z dwarf galaxies in Signature Science Case #9 (**Section B.9.2**). The second represents an augmentation of that NIR survey with additional 400 and 600 nm broad-band imaging to obtain thousands of galaxies at $z \leq 2$.

B.12.2 Galaxy assembly at the faint frontier

This science program aims to detect galaxies at the scale of the ultra-faint dwarf galaxies when they are still forming stars. This will reveal the grand sweep of galaxy formation to the earliest times, permitting full reconstruction of mass functions and merger trees. The program requires detections of ultra-faint dwarf galaxies at high redshift ($z \sim 7$), with a limiting magnitude of $AB \sim 33$ mag. The observational requirements are the same as those for the Signature Science Case #9 program “Dwarfs in the distant universe: probing the impact of reionization” (**Appendix B.10.2**).

No additional observing time is required for this program with LUVUOIR-A. This is an instance of a single rich dataset serving multiple scientific purposes. The deep NIR imaging (J, H, & K) in Signature Science Case #9 was judged to require unfeasibly long times with LUVUOIR-B. In future, we will investigate what can be achieved in parallel during the LUVUOIR-B habitable planet candidate survey. For now, we assume that it is not feasible to execute the current program with LUVUOIR-B.

Table B-23. *Exposure times for optical supplement to deep NIR survey*

Bands	On-target science integration time per field (hours)	# of fields	Total science time for this program (hours)	Total allocated time with overhead (hours)
LUVOIR-A				
F390W R=5	1.12	12	13.44	20.16
F606W R=5	1.27	12	15.24	22.86
LUVOIR-B				
F390W R=5	8.64	12	103.68	155.52
F606W R=5	11.48	12	137.76	206.64

B.12.3 Seeing inside galaxies as they form and transform

LUVOIR can measure the morphology of galaxies anywhere in the universe down to ~ 100 pc scales, revealing how the morphologies of galaxies change as they quench, and separating the star formation of distant galaxies into individual star-forming regions. Doing so requires rest-frame optical images to capture the older stellar populations, and rest-frame ultraviolet images to capture the young stellar population. Doing so over much of cosmic time requires a multi-band survey. The spatial resolution of LUVOIR is more important than depth, as Hubble already detects the light of many of these structures, hopelessly blurred together.

Observations overview. The I-, J-, and H-band images in the Signature Science Case #9 program “Dwarfs in the distant universe: probing the impact of reionization” (**Section B.10.2**) are much deeper than needed for the science goal in the current program. To trace the evolution to lower redshift, we add HDI images at 400 and 600 nm to those same fields, to capture the rest-frame UV for galaxies at moderate redshift ($z \sim 1-2$).

Targets. The same 12 blank sky fields as in the Signature Science Case #9 program “Dwarfs in the distant universe: probing the impact of reionization.”

Exposure times & overheads. We scale from the highly magnified lensed galaxy of Johnson et al. (2017), which was observed at ~ 1 orbit depth with HST/WFC3 in the F390W and F606W bands. For LUVOIR to capture star-forming regions in any distant un-lensed galaxy as clearly as HST can for lensed galaxies lensing, LUVOIR must image to depths of $AB = 30$ mag in F390W and F606W at $SNR \sim 25$. This is ~ 60 times fainter than HST/WFC3-UVIS reaches in 1 orbit.

The LUVOIR ETC yields the exposure times shown in **Table B-23**. We have assumed the sources are resolved (at $z=2$) and the SNR ratio of 25 is achieved within regions of 100 pc in size. We have assumed the total integration is made by summing individual exposures of 1200 seconds. We adopt a 50% overhead allocation for this program.

Results. Covering the 12 fields to $AB = 30$ mag $SNR=25$ (on scales of 100 pc) in each of the 400 and 600 nm bands, with overheads, requires a total of 43 hours ~ 2 days for LUVOIR-A and 362 hours ~ 15 days for LUVOIR-B. We note that the complimentary deep NIR imaging (I, J, & H) in Signature Science Case #9 was judged to require unfeasibly long times with LUVOIR-B. However, those images were designed to be far deeper than required for the science goal in the current program. We expect that the NIR imaging required here can be achieved in parallel with LUVOIR-B exoplanet observations. Therefore, this program can be executed in parallel for both LUVOIR architectures.

Parallels

- ☐ Do not execute parallels with this program
- ☐ Parallels required for this program
- ☒ Can be executed as parallel to another program
- ☐ Possible to execute parallels with this program

Can be done in parallel with coronagraphic exoplanet observations.

Target of opportunity / time-critical

- ☐ Is a ToO program
- ☐ Is time-critical

B.12.4 Dissecting galaxies one star at a time

Resolved stellar populations are cosmic clocks and assay meters that can assess the age and metallicity of their galaxies using well-defined relationships obeyed by stellar luminosity and color. Their most direct and accurate age diagnostic comes from resolving both the dwarf and giant stars, including the main sequence turnoff (MSTO). This program will detect the MSTO in a benchmark sample of up to 6 galaxies out to distances significantly beyond the Local Group and thus extend our study of the star formation histories of galaxies to important new galactic environments.

The HDI instrument on LUVUOIR has the sensitivity to reach down to below 34 AB mag for point sources in uncrowded stellar environments. We apply this capability to the detection of the MSTO in large spiral galaxies and, most importantly, to the nearest large elliptical galaxies that are located between 4–11 Mpc from the Milky Way. No current or planned facility has the capability to measure the stellar ages in these systems using the MSTO. Access to the MSTO in such systems will provide a robust and accurate (~ 0.1 dex) estimate of the ages of the stellar populations of these galaxies.

Observations overview. We will use the (V-J) color-magnitude diagram of the resolved stellar populations in the outskirts of a number of galaxies to determine the location of the MSTO and, hence, derive the age of that stellar population. The choice to use an optical/NIR color combination allows us to employ the simultaneous observing mode in HDI for data requiring both UVIS and NIR channel information and thus cuts the total observing time down significantly.

Targets. We select 8 large (M^* range) galaxies within the range 3–10 Mpc from the Milky Way galaxy. We focus on these larger galaxies to provide a sample that has not previously been accessible for resolved stellar population studies using the MSTO age estimator. The specific targets and estimated exposure times for each are given in **Table B-24** below.

Exposure times & overheads. We adopt the detection of a solar analog star in each of the target galaxies as the required limiting apparent magnitude we will need to reach in order to determine a reliable MSTO detection. We need to detect this solar analog star at a $\text{SNR} = 5$ in both the V and J band. The LUVUOIR ETC yields the exposure times shown in **Table B-24**. For the UVIS band, we have assumed the total integration is made by summing individual exposures of 1200 seconds. For the NIR band, we have assumed the total integration is made by summing individual exposures of 500 seconds. We assume both the UVIS and NIR

Table B-24. Target list and exposure time estimates for MSTO survey of local galaxies

Target	Distance (Mpc)	Galaxy Type	V-band app. mag of solar analog	V-band time for SNR=5 (hours)	J-band time for SNR=5 (hours)	HDI time without overhead (hours)
LUVOIR-A						
NGC 253	3.50	Sc	32.36	2.5	3.7	3.7
NGC5128	4.00	S0/E (Cen A)	32.65	4.3	6.3	6.3
NGC2403	4.55	Scd	32.93	7.1	10.5	10.5
NGC4736	4.70	Sab	33.00	8.0	12.0	12.0
NGC3627	7.05	Sb	33.88	39.8	60.1	60.1
NGC1291	9.25	S0/a	34.47	117.1	177.5	177.5
NGC3115	9.70	S0	34.57	141.6	214.6	214.6
NGC3379	11.22	E	34.89	252.8	383.9	383.9
LUVOIR-B						
NGC 253	3.50	Sc	32.36	31.0	46.5	46.5
NGC4945	3.60	Scd	32.42	34.6	52.1	52.1
NGC5128	4.00	S0/E (Cen A)	32.65	52.6	79.2	79.2
NGC2403	4.55	Scd	32.93	87.7	132.5	132.5
NGC5236	4.66	Sc	32.98	96.6	145.7	145.7
NGC4736	4.70	Sab	33.00	99.9	150.8	150.8
NGC4826	5.30	Sab	33.26	161.0	243.6	243.6
NGC5457	6.40	Scd	33.67	341.4	517.5	517.5

Table B-25. Total program times for LUVOIR-A survey options

Number of Targets	Number of Pointings per target	On-target science integration time (hours)	Total allocated time with overhead (hours)	Baselined Program
All 8 galaxies	1	869	1304	
Nearest 7		485	728	
Nearest 6		271	407	X
Nearest 5		93	140	
All 8 galaxies	2	1738	2607	
Nearest 7		970	1455	
Nearest 6		542	813	
Nearest 5		186	279	

bands are acquired simultaneously using the dichroic mode in HDI. In **Table B-25**, we give the total program times for various survey options with LUVOIR-A. In **Table B-26**, we give the total program times for various survey options with LUVOIR-B.

Results. Our baseline programs are the survey options that can be performed in under 500 hours. Using LUVOIR-A, observers will be able to survey 6 galaxies with a single pointing per galaxy in 407 hours, and could survey the nearest 5 galaxies in the sample with two

Table B-26. *Total program times for LUV OIR-B survey option*

Number of Targets	Number of Pointings per target	On-target science integration time (hours)	Total allocated time with overhead (hours)	Baselined Program
All 8 galaxies	1	1368	2052	
Nearest 7		851	1277	
Nearest 6		608	912	
Nearest 5		457	686	
Nearest 4		311	467	X
Nearest 6	2	1216	1824	
Nearest 5		914	1371	
Nearest 4		622	933	
Nearest 3		356	534	

pointings per target in 279 hours. We baseline the former (nearest 6 galaxies in sample) since we want to ensure to include at least 2 early type galaxies for study. Because these observations are well within the background-limited regime, the exposure times scale as D^4 , where D is the telescope aperture diameter. Hence, LUV OIR-A can accomplish a given suite of observations about 12.6 times faster than LUV OIR-B.

Therefore, we identify a different set of galaxies to observe with LUV OIR-B (see **Table B-24**) that are on average less distant but also less diverse in their properties—only one early type galaxy is accessible. Using LUV OIR-B observers would be able to survey the nearest 4 galaxies in the sample with a single pointing per galaxy in 467 hours, and could survey the nearest 3 galaxies in the sample with two pointings per target in 534 hours. With either telescope, one can reach at least one large early type galaxy (Centaurus A), providing a robust and detailed study of the star formation history of the kind of massive galaxy that does not exist in the Local Group.

Parallels

- ☐ Do not execute parallels with this program
- ☐ Parallels required for this program
- ☐ Can be executed as parallel to another program
- ☒ Possible to execute parallels with this program

Target of opportunity / time-critical

- ☐ Is a ToO program
- ☐ Is time-critical

B.13 Signature Science Case #12: Stars as the engines of galactic feedback

B.13.1 Abstract

The goals of this science case are to provide crucial information on galaxy feedback due to stars themselves, which is currently lacking due to the low sensitivity and spatial resolution of previous investigations. This will be done with two distinct observing programs:

1. An HDI imaging survey to find very massive stars in nearby galaxies, followed by LUMOS spectroscopy to assess their impact on star forming environments and galaxy evolution.
2. A multi-epoch HDI imaging survey of multiple/binary star systems in nearby galaxies to measure orbital parameters, followed by single-epoch UV spectroscopy to measure other stellar parameters.

Program contact(s)

Daniella Calzetti (UMass Amherst)

Brief description

HDI + LUMOS imaging and spectroscopic survey of VMSs in nearby LIRGs and ULIRGs (40 with LUVOIR-A and 15 with LUVOIR-B)

HDI multi-epoch imaging and LUMOS single-epoch spectroscopy of binary star systems in 7 regions within 5 nearby galaxies

Total observing time

LUVOIR-A: 18 days + 7 days = 25 days

LUVOIR-B: 24 days + 18 days = 42 days

B.13.2 Very massive stars

Very Massive Stars (VMSs) are stars that exceed the standard limit of $150 M_{\odot}$. One needs to observe very young massive star clusters in order to detect their presence, due to small number statistics at the high end of the initial mass function (IMF) and rapid evolutionary timescales. Yet these stars can heavily influence their surrounding environment; for instance, they can provide between 25% and 50% of the ionizing photon flux from the host cluster.

The goal of this program is to obtain a census of VMSs by targeting the youngest (< 2 Myr), most massive ($> 10^5 M_{\odot}$) clusters within luminous infrared galaxies (LIRGs) and ultra-luminous infrared galaxies (ULIRGs). Key diagnostics of VMSs are: P Cygni NV (1240 Å) and CIV (1550 Å) profiles, broad He II (1640 Å) emission, blue-shifted OV (1371 Å) wind absorption, and absence of SiIV (1400 Å) P Cygni emission / absorption.

Observations overview. This program involves an HDI multi-band imaging survey to identify VMSs in LIRGs and ULIRGs, followed by multi-object spectroscopy of the objects over the whole LUMOS UV bandpass

Targets. Spectroscopy of ~30 out of 200 luminous infrared galaxies (LIRGs) and ~10 out of 20 ultra-luminous infrared galaxies (ULIRGs) within the local 150 Mpc.

Exposure times & overheads. Candidates VMSs within each galaxy will be identified via HDI imaging in nine NUV-to-K broad bands and three H α (656.3 nm), Pb (1282 nm) and Pa (1876 nm) narrow bands for a subsample of at least 40 out of 220 LIRGs and ULIRGs. The broad and narrow-band imaging will be used to perform spectral energy distribution (SED) modeling and identify candidates with “excess” ionizing photons relative to models. The 40 targets will be observed with minimum SNR=20 in each band. Using the HDI exposure time

calculator (**Section B.1.3**), we find that HDI on LUVUOIR-A can achieve the required SNR in 5.75 hours for all 12 filters for a candidate cluster with $m_{AB} = 28.5$. This is a limiting magnitude, and most clusters will require significantly less exposure time, around 1–2 hours. We chose a typical HDI science exposure time of 3.7 hours per galaxy with LUVUOIR-A.

The 40 galaxies will be observed with LUMOS to obtain spectra with minimum SNR~10 on the continuum of the selected VMSs. Using the LUMOS exposure time calculator (**Section B.1.4**), we find that in a science exposure time of 2 hours, LUMOS on LUVUOIR-A can achieve the required SNR at 160 nm for a compact cluster with $m_{AB}(FUV) = 23$ mag. This is the characteristic FUV magnitude for a 1 Myr old, $10^6 M_{\odot}$ cluster at a distance of 80 Mpc and embedded in 20 mags of extinction, as expected in Arp220. Most clusters will require 2 to 5 hours to achieve the required SNR in their UV spectra. We chose a typical LUMOS science exposure time of 3.5 hours per galaxy with LUVUOIR-A.

The times required for the observations with LUVUOIR-B are estimated by scaling the LUVUOIR-A time by the ratio of collecting areas, 155 m² for LUVUOIR-A and 43.8 m² for LUVUOIR-B. Therefore, the LUVUOIR-B science exposure times are 13 hours per galaxy for the HDI imaging and 12.3 hours for the LUMOS spectroscopy. We assume a 50% overhead allocation for this program, to account for grating changes, wavelength calibration, and repointing.

Results. The total LUVUOIR-A science exposure time for the HDI imaging survey to find VMSs in the target galaxies is 3.7 hours x 40 galaxies = 148 hours. The LUVUOIR-A total science exposure time for the LUMOS spectroscopy is 3.5 hours x 40 galaxies = 140 hours. Including overheads, the total program time with LUVUOIR-A is (148 hours + 140 hours + 144 hours for overheads) = 18 days.

With LUVUOIR-B, the times are greatly increased. The science exposure time is 13 hours x 40 galaxies = 520 hours for the HDI imaging survey and 12.3 hours x 40 galaxies = 492 hours for the LUMOS spectroscopy. This gives a total science exposure time of 1012 hours for this program on LUVUOIR-B. We therefore reduce the number of galaxies observed from 40 to 15, cutting the total science exposure time to (13 hours + 12.3 hours) x 15 galaxies = 380 hours. With overheads, the total program time on LUVUOIR-B is 570 hours ~ 24 days.

Parallels

- ☐ Do not execute parallels with this program
- ☐ Parallels required for this program
- ☐ Can be executed as parallel to another program
- ☒ Possible to execute parallels with this program

Target of opportunity / time-critical

- ☐ Is a ToO program
- ☐ Is time-critical

B.13.3 Stellar multiplicity

Knowledge of stellar multiplicity and binary frequency provides constraints on models of star formation and the IMF, and of star cluster evolution. Hydro-dynamical simulations show that the disks surrounding massive stars in formation tend to be unstable and break into complex systems. The resulting properties of the multiple star systems (number of companions,

distributions of separations, periods, mass ratios, and eccentricities, and their dependence on the stellar mass) are model-dependent.

LUVOIR will be a prime facility to obtain a census of long period massive binaries in galaxies other than the MW and the Magellanic Clouds. These targets require high angular resolution and very stable PSF and photometry across the entire \sim arcmin field-of-view, in order to increase efficiency by targeting each cluster with a single pointing and deliver proper motions as accurate as $10 \mu\text{as/year}$ over a few years.

Observations overview. The characterization of the members of multiple/binary systems at all stages of evolution requires measuring the resolved massive stars' winds and photospheric parameters, including bolometric luminosities and masses, with spatial resolution up to 1000s AU. We will obtain positions and proper motions for stars in multiple/binary systems via optical imaging with a cadence of once per year over at least 5 years. UV spectra of the stars in a single epoch will also be obtained to identify stars' spectral types and measure wind properties.

Targets. 1–2 regions of recent (<100 Myr) star formation in each of 5 galaxies within ~ 1 Mpc: NGC6822, IC1613, NGC3109, Gr8, and the unusual nearby bright starburst IC10. A total of 7 regions will be imaged once per year over 5 years to obtain positions and proper motions for the binary stars.

Exposure times & overheads. For each region and in each observing epoch, we will obtain HDI imaging in the U, V, B, and I filters. These images all use the NUV/Vis detector and will have to be obtained in sequence. Exposure times are set to obtain $\text{SNR}=50$ on an A0 star, giving 720 sec per filter with LUVOIR-A and 2548 sec per filter with LUVOIR-B.

Each region will also be observed once with the LUMOS G155L and G300M gratings to obtain $\text{SNR}=10$ spectroscopy sufficient to identify the stars' spectral types. This requires 5.5 hours per pointing with LUVOIR-A and 19.5 hours with LUVOIR-B. We require ~ 2 LUMOS pointings to completely cover each HDI field. We simply assume a 50% overhead allocation for this program, to account for filter and grating changes, wavelength calibration, and repointing.

Results. With LUVOIR-A, the total HDI science exposure time without overheads is $(720 \text{ sec per filter}) \times 4 \text{ filters} \times 7 \text{ regions} \times 5 \text{ epochs} = 28 \text{ hours}$. The total LUMOS science exposure time is $(5.5 \text{ hours per pointing}) \times 2 \text{ pointings} \times 7 \text{ regions} = 77 \text{ hours}$. Therefore, the total program time with LUVOIR-A is $(28 \text{ hours} + 77 \text{ hours} + 53 \text{ hours for overheads}) \sim 7 \text{ days}$.

With LUVOIR-B, the same HDI imaging program requires a science exposure time of $(2548 \text{ sec per filter}) \times 4 \text{ filters} \times 7 \text{ regions} \times 5 \text{ epochs} = 99 \text{ hours}$. The LUMOS spectroscopy science exposure time is $(19.5 \text{ hours per pointing}) \times 2 \text{ pointings} \times 7 \text{ regions} = 273 \text{ hours}$. Assuming the overheads take the same amount of time on LUVOIR-A and -B, the total program time is $(99 \text{ hours} + 273 \text{ hours} + 53 \text{ hours}) \sim 18 \text{ days}$.

Parallels

- ☐ Do not execute parallels with this program
- ☐ Parallels required for this program
- ☐ Can be executed as parallel to another program
- ☒ Possible to execute parallels with this program

Target of opportunity / time-critical

- ☐ Is a ToO program
- ☒ Is time-critical

Each region will be imaged with HDI once per year over 5 years.

APPENDIX C. COMPLETE SCIENCE TRACEABILITY MATRICES

The LUVOIR STDT was chartered to study the most capable UV-Vis-NIR, general-purpose observatory for the era of the 2020 Astrophysics Decadal Survey. This was a challenge, in part because so many of the constraints for that era are uncertain: budget levels, launch vehicle availability, technology development, and the capabilities of contemporaneous facilities. Thus, we developed LUVOIR as a concept that was responsive to different future scenarios. LUVOIR's two concepts demonstrate its flexible architecture. LUVOIR-A is a point design that would maximize the science returns for a future in which the SLS Block 2 Tall faring is available. LUVOIR-B is a point design that would maximize the science returns for a future in which only launch vehicles currently operational (e.g., Falcon Heavy, Delta IV Heavy) or in development (e.g., New Glenn, SLS Block 1) are be available.

Each of these architectures would revolutionize astronomy and answer questions we cannot yet think to ask. We have identified 12 Signature Science Cases as examples of high priority science programs LUVOIR could carry out in a nominal five-year prime mission lifetime. In reality, the LUVOIR Study Team expects that LUVOIR's observing time would largely be allocated via competitive proposals selected by a Time Allocation Committee. The Signature Science Cases (SSCs) represent proof-of-concept programs that would be capable of answering a wide range of high-profile scientific questions of the 2030s and beyond. To re-cap, these SSCs are:

1. Determine the occurrence rates of Earth-like conditions on rocky worlds around Sun-like stars (**Chapter 3**)
2. Search habitable exoplanet candidates for signs of life and confirm habitability (**Chapter 3**)
3. Characterize potentially habitable ocean moons in the solar system (**Chapter 3**)
4. Compare the atmospheres of a diverse set of exoplanets (**Chapter 4**)
5. Study planet formation via observations of planetary systems with a wide range of ages (**Chapter 4**)
6. Reveal clues to the formation of the solar system via study of its smallest bodies (**Chapter 4**)
7. Probe the smallest scales across cosmic time to constrain the properties of dark matter (**Chapter 5**)
8. Constrain the properties of dark matter via high precision astrometry (**Chapter 5**)
9. Trace ionizing light and its impact on structure over cosmic time (**Chapter 5**)
10. Understand the ways in which matter flows into and out of galaxies (**Chapter 6**)
11. Study the assembly of galaxies at multiple spatial scales (**Chapter 6**)
12. Probe the impact of star formation upon galaxy evolution (**Chapter 6**)

By addressing these SSCs, LUVOIR will reveal how the story of life is woven throughout the physics and processes of the universe. We can trace this story from the formation of cosmic structure, to matter flows between galaxies, to planet formation, to the origins on life

on distant habitable worlds. LUVUOIR's scientific ambitions span a wide range of size scales, from the smallest bodies of our solar system to the most massive galaxies. They span a wide range of distances, from the neighboring planets in the solar system to currently unresolved young galaxies at the edge of the observable universe. And finally, they span a range of disciplines; from astrobiology, to planetary science, to astrophysics, to cosmology.

These important scientific programs LUVUOIR will address must be considered in a rigorous, quantitative framework. Here, we present Science Traceability Matrices (STM) for the LUVUOIR-A and -B concepts. Details on the individual observing programs appear in **Appendix B**. Each STM was developed by defining the most compelling science goals achievable for that future reality, and then tracing those goals to specific observatory, telescope, and instrument capabilities.

The LUVUOIR-A and -B STMs are divided into 12 sections, one for each of our SSCs. Reading across each row, the SSCs are related to specific science objectives, then to scientific requirements linking physical parameters to specific observables. Lastly, we connect the observables to instrument requirements to meet our objectives, state the projected instrument performance, and identify mission-level requirements. In this scheme, the designs of the observatories and the designs of the US-studied instruments (ECLIPS, HDI, LUMOS) are directly traceable to individual scientific goals. The science goals and requirements for the mission-enhancing, European-studied POLLUX instrument appear in **Chapter 13** and **Appendix H**.

Table C-1. LUVOIR-A Science Traceability Matrix

Complete LUVOIR-A Science Traceability Matrix						
		Scientific Requirements				
Signature Science Case	Science Objectives	Physical Parameters	Observables	Instrument Requirements	Projected Performance	Mission Requirements
SSC1: Finding habitable planet candidates Determine the occurrence rate of Earth-like conditions on rocky worlds around Sun-like stars	SO1: Find at least 1 Earth-like planet orbiting a solar-type star (95% confidence) for occurrence rates $\geq 5\%$ by discovering and studying ≥ 54 habitable planet candidates Definition of candidates: 1. Solar-type stars have FGK spectral types 2. Planet orbit within stars' habitable zones (semi-major axis $0.95 \leq a \leq 1.67$ AU for Sun-twin star, scaled by $\sqrt{L_*/L_\odot}$ for other spectral types) 3. Planet likely to be rocky (planet radius $\leq 1.4 R_{\text{Earth}}$) 4. Planet likely to retain atmospheres over geologic times (planet radius $\geq 0.8 a^{-0.5} R_{\text{Earth}}$) 5. Planet likely to be Earth-like (geometric albedo = 0.2 between 550–1000 nm)	PP1: Cumulative habitable zone completeness $C \geq 54/\eta_{\text{Earth}} \geq 54/0.24 \geq 225$	O1: High-contrast images of faint ($M_V \approx 30$) point-sources around hundreds of FGKM target stars within 30 parsecs of the Sun	IWA $\lesssim 4 \lambda/D$ [O1, O2, O3, O4] OWA $\geq 10 \lambda/D$ [O1, O2, O3, O4] Coronagraph raw contrast $\lesssim 1 \times 10^{-10}$ [O1, O2, O3, O4] Coronagraphic imaging in two $\geq 10\%$ bands near 500 nm [O2, O3] Spatially resolved coronagraphic spectroscopy with R=70 over $\geq 10\%$ bandpass centered near 940 nm [O4]	IWA = $3.7 - 11.4 \lambda/D$ [O1, O2, O3, O4] OWA = $10 - 33 \lambda/D$ [O1, O2, O3, O4] Coronagraph raw contrast $\approx 4 \times 10^{-11} - 3 \times 10^{-10}$ [O1, O2, O3, O4] Coronagraphic imaging in two 10 – 20% bands (450–500 nm and 500–550 nm) [O2, O3] Spatially resolved coronagraphic spectroscopy with R=70 over 10 – 20% bandpass centered near 940 nm [O4]	Inscribed diameter of telescope aperture ≥ 13.5 m [O1, O2, O3, O4, O5] Field of regard $>$ entire anti-Sun hemisphere [O1, O3] ≥ 6 visits to each candidate target system [O3]
		PP2: Colors of candidates in reflected light to begin confusion discrimination	O2: Broadband photometry of candidates (SNR ≥ 7) at two optical wavelengths			
		PP3: Orbital semi-major axis, eccentricity, and inclination of each candidate with 10% accuracy	O3: Candidate positions at ≥ 4 different locations with position uncertainty ≤ 5 mas (SNR ≥ 7)			
		PP4: Detection of atmospheric water vapor at abundance comparable to modern Earth's (2.5% by volume)	O4: Planetary direct spectra with continuum SNR=5 per spectral resolution element and R=70 around water vapor absorption feature at 940 nm			
	SO2: Reserve time in prime mission for follow-up exoEarth observations and other science goals	PP5: Limit total survey time to 2 years	O5: Hundreds of direct observations of FGK stars within 2 years	Coronagraph core throughput $\geq 15\%$ [O5] Detector parameters: Dark current $\lesssim 2 \times 10^{-2}$ counts pix ⁻¹ s ⁻¹ Read noise $\lesssim 5$ counts pix ⁻¹ read ⁻¹ [O5]	Coronagraph core throughput = 17 – 26% [O5] Detector parameters: Dark current $\lesssim 3 \times 10^{-5}$ counts pix ⁻¹ s ⁻¹ Read noise $\lesssim 0$ counts pix ⁻¹ read ⁻¹ [O5]	End-to-end optical throughput $\geq 20\%$ [O5] Slew & settle time $\lesssim 1$ hour per target [O5] Overheads $\lesssim 1$ hour per bandpass [O5]
				Multi-Parameter Science Return Dependencies Habitable planet candidates found in high-contrast survey defined above (first 8 most important mission & instrument parameters) $Y \propto D^{1.97} IWA^{-0.98} T^{0.35} \Gamma^{-0.33} E^{0.32} \Delta\lambda^{0.30} C^{-0.10} OWA^{0.07}$		

Complete LUVOIR-A Science Traceability Matrix						
		Scientific Requirements				
Signature Science Case	Science Objectives	Physical Parameters	Observables	Instrument Requirements	Projected Performance	Mission Requirements
	Y = yield of candidates, D = inscribed diameter of telescope aperture, IWA = coronagraph inner working angle, T = end-to-end throughput, Γ = point-spread function sharpness, E = total exposure time, $\Delta\lambda$ = instantaneous coronagraph bandpass, C = raw contrast, OWA = coronagraph outer working angle					
SSC2: Searching for biosignatures and confirming habitability Search habitable exoplanet candidates for signs of life and confirm the presence of liquid surface water	SO3: Measure the physical and chemical states of the atmospheres of habitable planet candidates to establish disequilibrium conditions and thereby identify biosignature gases Habitable planet candidates identified in SO1	PP6: Spectral energy distributions of ~50 FGKM exoplanet host stars	O6: UV spectra of bright stars ($V = 2 - 11$) over 100–400 nm, with precise measurement of total Lyman- α flux ($R \gtrsim 10,000$ and $SNR \gtrsim 50$ near 121.5 nm)	Point-source spectra at $R \gtrsim 10,000$ from 100–400 nm [O6]	Point-source spectra at $R \approx 11,600$ from 100–200 nm (G155L) and $R \approx 28,000$ from 200–1000 nm (G300M) [O6]	Telescope mirror reflectivity > 60% at 105 nm [O6]
		PP7: Masses of ~50 habitable exoplanet candidates orbiting Sun-like stars within 30 pc of the Sun with $\lesssim 25\%$ precision	O7: Astrometric measurements of stellar wobble caused by 1 Earth-mass planets at 1 AU from Sun-like stars with $V = 2 - 11$ (wobble semi-amplitude = 0.3 μas for Sun-twin star at 10 pc) Requires: 1. Detection of astrometric signal at end-of-mission $SNR=3$, utilizing coronagraphic images obtained in SO1 2. Mean number of epochs per target = 14, spread over ~1 year 3. Detection of $V=24$ background sources for calibration of optical distortions	Optical imaging with systematic single-measurement position errors $\lesssim 0.34 \mu\text{as} \approx 0.0001$ pixels [O7] Imaging field-of-view $\gtrsim 6$ sq. arcmin [O7] Rapid VIS detector readout to prevent saturation on bright exoplanet host stars [O7]	Optical imaging with systematic single-measurement position errors = 0.34 $\mu\text{as} \approx 0.0001$ pixels, achieved with internal laser-based system to calibrate detector distortions [O7] Imaging field-of-view = 6 sq. arcmin [O7] Readout of regions on VIS detector at up to 500 Hz [O7]	Diameter of telescope aperture $\gtrsim 15$ m [O7] ~14 visits to each candidate target system [O7]
		PP8: Measurement of atmospheric H_2O	O8: Planetary direct spectra with	$IWA \lesssim 4 \lambda/D$	$IWA = 3.7 - 11.4 \lambda/D$	

Complete LUVOIR-A Science Traceability Matrix						
		Scientific Requirements				
Signature Science Case	Science Objectives	Physical Parameters	Observables	Instrument Requirements	Projected Performance	Mission Requirements
		abundances with ≤ 1 dex precision for abundances comparable to modern Earth's (2.5% by volume)	continuum $\text{SNR} \geq 8.5$ per spectral resolution element and $R \geq 70$ around water vapor absorption features between 900 nm and 1800 nm	[O8, O9, O10, O11, O12, O13] $\text{OWA} \geq 10 \lambda/D$ [O8, O9, O10, O11, O12, O13]	[O8, O9, O10, O11, O12, O13] $\text{OWA} = 10 - 33 \lambda/D$ [O8, O9, O10, O11, O12, O13]	Inscribed diameter of telescope aperture ≥ 13.5 m [O8, O9, O10, O11, O12, O13]
		PP9: Measurement of atmospheric CH_4 abundances with ≤ 1 dex precision for abundances comparable to Archean Earth's (0.01 – 1% of total atmosphere)	O9: Planetary direct spectra with continuum $\text{SNR} \geq 8.5$ per spectral resolution element and $R \geq 70$ around CH_4 absorption features between 700 nm and 1700 nm	Coronagraph raw contrast $\leq 1 \times 10^{-10}$ [O8, O9, O10, O11, O12, O13] Spatially resolved coronagraphic spectroscopy with $R \geq 70$ over $\geq 10\%$ bandpasses between 700 nm and 1800 nm [O8, O9, O12, O13]	Coronagraph raw contrast $\approx 4 \times 10^{-11} - 3 \times 10^{-10}$ [O8, O9, O10, O11, O12, O13] Spatially resolved coronagraphic spectroscopy with $R=140$ (vis) and 70 (NIR) over 10 – 20% bandpasses between 500 nm and 2000 nm [O8, O9, O12, O13]	
		PP10: Measurement of atmospheric O_2 abundances with ≤ 1 dex precision for abundances comparable to modern Earth's (21% by volume)	O10: Planetary direct spectra with continuum $\text{SNR} \geq 8.5$ per spectral resolution element and $R=140$ around O_2 A band absorption feature at 760 nm	Spatially resolved coronagraphic spectroscopy with $R=140$ over $\geq 10\%$ bandpass near 760 nm [O10]	Spatially resolved coronagraphic spectroscopy with $R=140$ over 10 – 20% bandpass near 760 nm [O10]	
		PP11: Measurement of atmospheric O_3 abundances with ≤ 1 dex precision for abundances comparable to Proterozoic Earth's (0.1% present atmospheric level)	O11: Planetary direct spectra with continuum $\text{SNR} \geq 8.5$ per spectral resolution element and $R \geq 6$ near strong O_3 absorption feature at 250 nm	Multi-color coronagraphic imaging with effective $R=6$ over $\geq 10\%$ bandpasses between 200 nm and 400 nm [O11]	Multi-color coronagraphic imaging with effective $R=6$ over 10 – 20% bandpasses between 200 nm and 500 nm [O11]	
		PP12: Constrain presence of false positive biosignature indicator gases (O_4 , CO_2 , CO)	O12: Planetary direct spectra with continuum $\text{SNR} \geq 8.5$ per spectral resolution element and $R \geq 70$ around absorption features of O_4 near 1060 and 1270 nm,	Point-source coronagraphic spectroscopy with $R=200$ over $\geq 10\%$	Point-source coronagraphic spectroscopy with $R=200$ over 10 – 20%	

Complete LUVOIR-A Science Traceability Matrix						
		Scientific Requirements				
Signature Science Case	Science Objectives	Physical Parameters	Observables	Instrument Requirements	Projected Performance	Mission Requirements
			CO ₂ near 1590 nm, and CO at 1600 nm	bandpass near 1590 nm [O13]	bandpass near 1590 nm [O13]	
	SO4: Calculate the surface temperatures of habitable planet candidates to establish the likelihood of liquid water Habitable planet candidates identified in SO1	PP13: Measurement of key atmospheric greenhouse gas (e.g., H ₂ O, CO ₂) abundances with ≤ 1 dex precision for abundances comparable to modern Earth's	O13: Planetary direct spectra with continuum SNR ≥ 8.5 per spectral resolution element, $R \geq 70$ between 900 nm and 1800 nm (H ₂ O) and $R \geq 200$ around absorption feature of CO ₂ near 1590 nm			
SSC3: The search for habitable worlds in the solar system Characterize plume activity from and cryo-volcanism on solar system ocean moons	SO5: Monitor Europa to determine the strength and frequency of plumes emanating from its surface. Study the moon's interaction with the Jovian magnetosphere in detail	PP14: Mapping of auroral emission from individual plumes and general non-plume-related auroral emission	O14: Spatially resolved spectra of Lyman- α (121.6 nm) and OI (130.4 nm) emission (SNR ≥ 5 and $R \geq 10,000$ at 130.4 nm)	Spatially resolved spectroscopy with $R \geq 10,000$ over about 115–140 nm [O14]	Spatially resolved spectroscopy with $R \approx 11,600$ over 100–200 nm (G155L) [O14]	Telescope aperture diameter ≥ 8 m [O14] Telescope mirror reflectivity $> 90\%$ at 115 nm [O14] Non-sidereal tracking at ≥ 60 mas/sec [O14, O15] Dithered observations with slightly shifted telescope pointing [O14, O15]
		PP15: Measurement of plume frequency and the moon's changing interaction with the Jovian magnetosphere over one full orbital period (3.5 days)	O15: Single visits to Europa once every two months over 5 years One 4-day visit to Europa for high-cadence observations			
	SO6: Characterize cryo-volcanism on six outer solar system ocean moons under changing heating conditions (Europa, Ganymede, Callisto, Enceladus, Titan, and Triton)	PP16: Mapping of surface morphology over long timescales at wavelengths centered on and bracketing expected surface spectral features (e.g., water ice at 1100 and 1400 nm, methane ice at 1700 nm)	O16: High-resolution, narrowband optical/NIR mosaics obtained twice per year over 5 years	Imaging in narrowband filters at several optical/NIR wavelengths [O16] Imaging field-of-view ≥ 7 sq. arcsec [O16]	Imaging in 1% optical/NIR filters (central wavelengths TBD) [O16] Imaging field-of-view = 6 sq. arcmin [O16]	Telescope aperture diameter ≥ 8 m [O16] Non-sidereal tracking at ≥ 60 mas/sec [O16] Dithered observations with slightly shifted telescope pointing [O16]

Complete LUVOIR-A Science Traceability Matrix						
		Scientific Requirements				
Signature Science Case	Science Objectives	Physical Parameters	Observables	Instrument Requirements	Projected Performance	Mission Requirements
SSC4: Comparative atmospheres Study the atmospheres of a diverse set of exoplanets in a variety of ways	SO7: Characterize dozens of exoplanets covering a wide range of sizes ($0.1 R_{\text{Jupiter}} \lesssim R \lesssim 2 R_{\text{Jupiter}}$) and orbital distances ($100 \text{ K} \lesssim T_{\text{eq}} \lesssim 2000 \text{ K}$) Planetary spectral template assumptions: 1. $M_p > 0.15 M_{\text{Jupiter}}$ and $T_{\text{eq}} \leq 180 \text{ K}$: Jupiter 2. $M_p > 0.15 M_{\text{Jupiter}}$ and $180 \text{ K} \leq T_{\text{eq}} \leq 180 \text{ K}$: warm Jupiter at 2 AU from Cahoy et al. (2010) 3. $M_p > 0.15 M_{\text{Jupiter}}$ and $T_{\text{eq}} > 300 \text{ K}$: warm Jupiter at 0.8 AU from Cahoy et al. (2010) 4. $M_p \leq 0.15 M_{\text{Jupiter}}$ and $T_{\text{eq}} \leq 180 \text{ K}$: Neptune 5. $M_p \leq 0.15 M_{\text{Jupiter}}$ and $180 \text{ K} \leq T_{\text{eq}} \leq 180 \text{ K}$: warm Neptune at 2 AU from Hu & Seager (2014) 6. $M_p \leq 0.15 M_{\text{Jupiter}}$ and $T_{\text{eq}} > 300 \text{ K}$: cloudy warm Jupiter at 1 AU from Hu & Seager (2014) 7. Rocky planets: Earth	PP17: Measurement of key atmospheric gas (e.g., CH ₄ , H ₂ O, CO ₂) abundances with ≤ 1 dex precision for 30 known warm to cold exoplanets	O17: Planetary direct spectra with continuum SNR ≥ 15 per spectral resolution element and $R \geq 70$ between about 500 nm and 1700 nm	IWA $\lesssim 4 \lambda/D$ [O17, O18] OWA $\geq 30 \lambda/D$ [O17, O18] Coronagraph raw contrast $\lesssim 1 \times 10^{-9}$ [O17, O18]	IWA = $3.7 - 11.4 \lambda/D$ [O17, O18] OWA = $10 - 33 \lambda/D$ [O17, O18] Coronagraph raw contrast $\approx 4 \times 10^{-11} - 3 \times 10^{-10}$ [O17, O18]	Inscribed diameter of telescope aperture $\geq 13.5 \text{ m}$ [O17, O18]
		PP18: Measurement of atmospheric haze scattering slopes for 30 known warm to cold exoplanets	O18: Planetary direct spectra with continuum SNR ≥ 5 per spectral resolution element and $R \geq 6$ between about 200 nm and 500 nm	Spatially resolved coronagraphic spectroscopy with $R \geq 70$ over $\geq 10\%$ bandpasses between 500 nm and 1700 nm [O17] Multi-color coronagraphic imaging with effective $R=6$ over $\geq 10\%$ bandpasses between 200 nm and 500 nm [O18]	Spatially resolved coronagraphic spectroscopy with $R=140$ (vis) and 70 (NIR) over 10 – 20% bandpasses between 500 nm and 2000 nm [O17] Multi-color coronagraphic imaging with effective $R=6$ over 10 – 20% bandpasses between 200 nm and 500 nm [O18]	
		PP19: Measurement of key atmospheric gas (e.g., CH ₄ , H ₂ O, CO) abundances with ≤ 1 dex precision for 16 known transiting warm to hot exoplanets	O19: Planetary transmission spectra during transits with SNR ≥ 7 , $15 \lesssim R \lesssim 500$ between 200–2500 nm (full wavelength range covered simultaneously)	Point-source stellar spectroscopy with $15 \lesssim R \lesssim 500$ between 200 nm and 2500 nm [O19] Rapid VIS detector readout to prevent saturation on bright exoplanet host stars [O19]	Point-source stellar spectroscopy with $15 \lesssim R \lesssim 500$ between 200 nm and 2500 nm [O19] Readout of regions on VIS detector at up to 500 Hz [O19]	Diameter of telescope aperture $\geq 15 \text{ m}$ [O19]
		PP20: Measurement of atmospheric escape rates for 16 hot known transiting exoplanets	O20: Planetary transmission spectra to observe Lyman- α (121.6 nm), OI (130.4	Point-source stellar spectroscopy with $R \geq 30,000$ between 100 nm and 140 nm	Point-source stellar spectroscopy with $R \approx 30,300$ between 100	Diameter of telescope aperture $\geq 15 \text{ m}$ [O20]

Complete LUVOIR-A Science Traceability Matrix						
		Scientific Requirements				
Signature Science Case	Science Objectives	Physical Parameters	Observables	Instrument Requirements	Projected Performance	Mission Requirements
		via observations of exospheric H, O, and C	nm), and CII (133.5 nm) emission during single transits with $SNR \geq 5$, $R \geq 30,000$ between about 100–140 nm (full wavelength range covered simultaneously)	[O20]	nm and 140 nm (G120M) [O20]	Telescope mirror reflectivity > 60% at 105 nm [O20]
SSC5: The formation of planetary systems Study planet formation over a wide range of system ages	SO8: Follow the evolution and dispersal of the main molecular carriers of C, H, and O during planet assembly in the terrestrial and giant-planet forming regions of protoplanetary disks, trace molecular and low-ionization metals from disk winds, and provide absolute abundance patterns in disks as a function of age	PP21: Locate protoplanetary disks within five areas of the Orion star-forming region Areas: 1. Orion Nebular Cloud: ~1 Myr, ~24' size 2. NGC1980: ~1-2 Myr, ~16' size 3. σ Ori: ~3-5 Myr, ~33' size 4. λ Ori: 4-8 Myr, 49' size 5. 25 Ori: ~7-10 Myr, 33' size	O21: FUV imaging from 100–200 nm covering five areas in the Orion star-forming region, with sensitivity to detect FUV continuum flux of a young T Tauri star at ~370 pc Areas: 1. Orion Nebular Cloud: 6 pointings 2. NGC1980: 4 pointings 3. σ Ori: 9 pointings 4. λ Ori: 13 pointings 5. 25 Ori: 9 pointings	FUV imaging field-of-view ≥ 4 sq. arcmin [O21] Neutral density filters for bright object protection [O21] Multi-object spectroscopy at $R \geq 30,000$ from 100–400 nm [O22] Spectroscopic field-of-view ≥ 4 sq. arcmin [O22]	FUV imaging field-of-view ≈ 4 sq. arcmin [O21] Neutral density filters for bright object protection [O21] Multi-object spectroscopy at $R \approx 30,300$ from 100–140 nm (G120M), $R \approx 37,800$ from 130–170 nm (G150M), and $R \approx 28,000$ from 200–400 nm (G300M) [O22] Spectroscopic field-of-view ≈ 4 sq. arcmin [O22]	Diameter of telescope aperture ≥ 8 m [O21, O22] Telescope mirror reflectivity > 60% at 105 nm [O21, O22]
		PP22: Measure the most abundant molecular species in (H ₂ , CO, H ₂ O, and OH) in Orion protoplanetary disks	O22: Spectroscopy of protoplanetary disks in Orion with $R \approx 30,000$ and $SNR \approx 10$ per resolution element from 100–170 nm and 200–400 nm Reference flux at 110 nm: $F_{\lambda} = 2 \times 10^{-16} \text{ erg s}^{-1} \text{ cm}^{-2} \text{ \AA}^{-1}$			
	SO9: Investigate the planetesimal distributions in 25	PP23: Morphology of warm dust structures	O23: High-resolution images of visible light	IWA $\lesssim 4 \lambda/D$	IWA = 3.7 – 11.4 λ/D	

Complete LUVOIR-A Science Traceability Matrix						
		Scientific Requirements				
Signature Science Case	Science Objectives	Physical Parameters	Observables	Instrument Requirements	Projected Performance	Mission Requirements
	exoplanet systems around young AFGKM stars and look for signs of newly formed planets (5 stars per spectral type bin)	in 25 young exoplanet systems (cold dust to be observed with ground-based radio facilities)	scattered by interplanetary dust	[O23, O24] OWA $\geq 30 \lambda/D$ [O23, O24]	[O23, O24] OWA = $10 - 33 \lambda/D$ [O23, O24]	Inscribed diameter of telescope aperture ≥ 13.5 m [O23, O24]
		PP24: Search for cometary OH emission in a subset of young exoplanet systems as a signature of volatile delivery to the habitable zone	O24: High-resolution images of NUV light emitted by interplanetary OH	Coronagraph raw contrast $\lesssim 1 \times 10^{-9}$ [O23, O24] Coronagraphic imaging in one $\geq 10\%$ band near 500 nm [O23] Coronagraphic imaging in one $\geq 10\%$ band near 250 nm [O24]	Coronagraph raw contrast $\approx 4 \times 10^{-11} - 3 \times 10^{-10}$ [O23, O24] Coronagraphic imaging in one 10 – 20% band (500–550 nm) [O23] Coronagraphic imaging in one 10 – 20% near 250 nm [O24]	
	SO10: Determine the orbits and masses of planets in ~50 mature exoplanet systems, as well as the locations of asteroid and comet (planetesimal) belts To increase efficiency, the systems will be those hosting habitable exoplanet candidates found in SO1 (Sun-like host stars within 30 pc)	PP25: Orbits and masses of planets in ~50 exoplanet systems with $\lesssim 25\%$ precision on mass measurement Results from this program also satisfy PP7	O25: Astrometric measurements of stellar wobble caused by 1 Earth-mass planets at 1 AU from Sun-like stars with $V = 2 - 11$ (wobble semi-amplitude = $0.3 \mu\text{as}$ for Sun-twin star at 10 pc) Requires: 1. Detection of astrometric signal at end-of-program SNR=3, leveraging coronagraphic images obtained in SO1 2. Mean number of epochs per target =	Optical imaging with systematic single-measurement position errors $\lesssim 0.34 \mu\text{as} \approx 0.0001$ pixels [O25] Imaging field-of-view ≥ 6 sq. arcmin [O25] Rapid VIS detector readout to prevent saturation on bright exoplanet host stars [O25]	Optical imaging with systematic single-measurement position errors = $0.34 \mu\text{as} \approx 0.0001$ pixels, achieved with internal laser-based system to calibrate detector distortions [O25] Imaging field-of-view = 6 sq. arcmin [O25] Readout of regions on VIS detector at up to 500 Hz [O25]	Diameter of telescope aperture ≥ 15 m [O25] ~14 visits to each candidate target system [O25]

Complete LUVOIR-A Science Traceability Matrix						
		Scientific Requirements				
Signature Science Case	Science Objectives	Physical Parameters	Observables	Instrument Requirements	Projected Performance	Mission Requirements
			14, spread over ~1 year 3. Detection of V=24 background sources for calibration of optical distortions			
		PP26: Locations of warm planetesimal belts in ~50 exoplanet systems (cold belts to be observed with ground-based radio facilities) Most data for this program obtained in PP1	O26: High-resolution images of visible light scattered by interplanetary dust	IWA $\lesssim 4 \lambda/D$ [O26] OWA $\gtrsim 30 \lambda/D$ [O26] Coronagraph raw contrast $\lesssim 1 \times 10^{-9}$ [O26] Coronagraphic imaging in two $\geq 10\%$ bands near 500 nm [O26]	IWA = $3.7 - 11.4 \lambda/D$ [O26] OWA = $10 - 33 \lambda/D$ [O26] Coronagraph raw contrast $\approx 4 \times 10^{-11} - 3 \times 10^{-10}$ [O26] Coronagraphic imaging in two 10 – 20% bands (450–500 nm and 500–550 nm) [O26]	Inscribed diameter of telescope aperture $\gtrsim 13.5$ m [O26]
SSC6: Small bodies in the solar system Study the smallest bodies in the outer solar system to investigate its formation and early evolution	SO11: Discover trans-Neptunian objects (TNOs) down to the currently unseen smallest bodies that distinguish between different planetesimal formation scenarios and measure their reflected light colors	PP27: Detection of ~100 TNOs with sizes $\gtrsim 2$ km out to 40 AU and measurement of their brightnesses in one optical band and one NIR band	O27: Detection of $R \leq 33$ mag objects at $\text{SNR} \gtrsim 5$ in a 0.012 deg^2 region imaged in R band and one NIR band	Imaging in one broadband filter near 775 nm [O27] Simultaneous imaging in one broadband filter near 1260 nm [O27] Imaging field-of-view $\gtrsim 6$ sq. arcmin [O27]	Imaging in one ~20% filter centered at 775 nm (R band) [O27] Simultaneous imaging in one ~20% filter centered at 1260 nm (J band) [O27] Imaging field-of-view = 6 sq. arcmin [O27]	Diameter of telescope aperture $\gtrsim 15$ m [O27] Non-sidereal tracking at a rate equivalent to a circular orbit at 40 AU (6 nanorad/sec) [O27] ~26 visits per field to estimate orbits of detected objects [O27]
	SO12: Measure the component sizes, mass ratios, separations, and occurrence rates of TNO binaries to constrain theories of their formation and evolution	PP28: Orbits of TNO binaries discovered in the previous row	O28: Repeated detection of $R \leq 33$ mag objects at $\text{SNR} \gtrsim 5$ in R band and one NIR band	Imaging in one broadband filter near 775 nm [O28]	Imaging in one ~20% filter centered at 775 nm (R band) [O28]	Diameter of telescope aperture $\gtrsim 15$ m [O28]

Complete LUVOIR-A Science Traceability Matrix						
		Scientific Requirements				
Signature Science Case	Science Objectives	Physical Parameters	Observables	Instrument Requirements	Projected Performance	Mission Requirements
				Simultaneous imaging in one broadband filter near 1260 nm [O28] Imaging field-of-view ≥ 6 sq. arcmin [O28]	Simultaneous imaging in one ~20% filter centered at 1260 nm (J band) [O28] Imaging field-of-view = 6 sq. arcmin [O27]	Non-sidereal tracking at ≥ 60 mas/sec [O28] Targeted revisits [O28]
SSC7: Connecting the smallest scales across cosmic time Investigate the properties of dark matter via the matter power spectrum	SO13: Discriminate between standard cold dark matter, interacting dark matter, and several warm dark matter models by measuring the shape of the matter power spectrum on small scales (<100 kpc)	PP29: Measure the spatial distribution of extremely low-mass dwarf galaxies around four Milky Way (MW) analog galaxies within 15 Mpc	O29: Images of 100 kpc regions around four MW analog galaxies in the V and J bands simultaneously, with sensitivity to detect $M_V = 0$ AB mag stars at SNR=5 Assumptions: Stellar color V-J = 0.35, typical of stars on the Horizontal Branch of the Hertzsprung-Russel diagram	Imaging in one broadband filter near 550 nm [O29] Simultaneous imaging in one broadband filter near 1220 nm [O29] Imaging field-of-view ≥ 6 sq. arcmin [O29]	Imaging in V filter centered at 550 nm [O29] Simultaneous imaging in J filter centered at 1220 nm [O29] Imaging field-of-view ≥ 6 sq. arcmin [O29]	Diameter of telescope aperture ≥ 8 m [O29]
SSC8: Constraining dark matter using high precision astrometry	SO14: Probe the nature of the dark matter particle by measuring the density profiles of dwarf galaxies	PP30: High precision astrometric measurements of proper motions for ~100 stars in 20 dwarf spheroidal galaxies, 10 within the Local Group (1 Mpc) and 10 beyond the Local Group (2 – 5 Mpc)	O30: Astrometric measurements of stellar proper motions with end-of mission proper motion accuracy of ~10 km/s Requires: 1. Three epochs per galaxy spread over 5 years 2. Detection of V=24 background sources for calibration of optical distortions	Optical imaging with systematic single-measurement position errors $\leq 0.85 \mu\text{as} \approx 0.00025$ pixels [O30] Imaging field-of-view ≥ 6 sq. arcmin [O30]	Optical imaging with systematic single-measurement position errors = $0.34 \mu\text{as} \approx 0.0001$ pixels, achieved with on-board laser-based system to calibrate detector distortions [O30] Imaging field-of-view = 6 sq. arcmin [O30]	Diameter of telescope aperture ≥ 8 m [O30] 3 visits to each target [O30]

Complete LUVOIR-A Science Traceability Matrix						
		Scientific Requirements				
Signature Science Case	Science Objectives	Physical Parameters	Observables	Instrument Requirements	Projected Performance	Mission Requirements
SSC9: Tracing ionizing light over cosmic time	SO15: Study the behavior of the faint end of the galaxy luminosity function to reveal the degree to which dwarf galaxies powered cosmic reionization	PP31: Measure counts per sq. arcmin of dwarf galaxies at high-redshift ($z = 7$), with sensitivity to detect difference between rest-frame UV luminosity functions with and without reionization suppression at 5σ significance ($M_{UV} \gtrsim -13.5$)	O31: Deep images of 12 blank sky fields in the I, J, and H bands to detect dwarf galaxies with J-band AB mag = 32.75 at SNR=5	Imaging in two broadband filters centered near 1220 nm and 1630 nm [O31] Simultaneous imaging in one broadband filter near 800 nm [O31] Imaging field-of-view $\gtrsim 6$ sq. arcmin [O31] Execute in parallel with exoplanet direct observations [O31]	Imaging in J and H filters centered at 1220 nm and 1630 nm [O31] Simultaneous imaging in I filter centered at 803 nm [O31] Imaging field-of-view = 6 sq. arcmin [O31] Appears possible to execute in parallel given sky distribution of exoplanet target stars and length of exoplanet science exposures [O31]	Diameter of telescope aperture $\gtrsim 15$ m [O31]
	SO16: Detect and quantify the evolution of ionizing radiation from low-redshift galaxies	PP32: Characterize ionizing UV radiation from star-forming galaxies at low-redshift ($0.2 \lesssim z \lesssim 1.2$), with 500 galaxies per $\Delta z = 0.2$ redshift bin	O32: Low-resolution FUV spectra covering 12 random sky fields to detect galaxies at SNR=5 over 30 Å wavelength bin below the Lyman break	Multi-object spectroscopy at $R \approx 500$ from 100–200 nm [O32] Spectroscopic field-of-view $\gtrsim 4$ sq. arcmin [O32] Execute in parallel with exoplanet direct observations [O32]	Multi-object spectroscopy at $R \approx 500$ from 100–200 nm (G145LL) [O32] Spectroscopic field-of-view ≈ 4 sq. arcmin [O32] Appears possible to execute in parallel given sky distribution of exoplanet target stars and length of exoplanet science exposures [O32]	Diameter of telescope aperture $\gtrsim 8$ m [O32] Telescope mirror reflectivity > 60% at 105 nm [O32]
	SO17: Map the escape of ionizing radiation from low-	PP33: Observe the distribution of both	O33: Spectra from 100–200 nm, with	Multi-object spectroscopy at $R \approx$	Multi-object spectroscopy at $R \approx$	Diameter of telescope aperture $\gtrsim 8$ m

Complete LUVOIR-A Science Traceability Matrix						
		Scientific Requirements				
Signature Science Case	Science Objectives	Physical Parameters	Observables	Instrument Requirements	Projected Performance	Mission Requirements
	redshift galaxies and relate it to massive stellar populations and outflows	ionizing (rest-frame wavelengths <90 nm) and non-ionizing (rest-frame wavelengths 120–160 nm) radiation within 100 galaxies at $z = 0.25 - 0.3$	SNR \approx 13 at 140 nm, of individual star-forming regions within galaxies selected to have integrated GALEX FUV mag < 19	10,000 from 100–200 nm [O33] Spectroscopic field-of-view \gtrsim 4 sq. arcmin [O33]	11,600 from 100–200 nm (G150L) [O33] Spectroscopic field-of-view \approx 4 sq. arcmin [O33]	[O33] Telescope mirror reflectivity > 60% at 105 nm [O33]
SSC10: The cycles of matter Understand the ways in which matter flows into and out of galaxies	SO18: Determine the abundances of baryons in the intergalactic and circumgalactic medium across cosmic time	PP34: Absorption column density measurements of ions with a wide range of temperatures ($10 - 10^7$ K) and densities ($10^{-6} - 10^2$ cm $^{-3}$) via UV spectroscopy of 100 high-redshift ($z > 1$) quasars	O34: Spectra at SNR \gtrsim 20, $R \gtrsim$ 30,000 over 100–400 nm for the following set of 100 quasars Target properties: 1. GALEX FUV mag < 18: 18 quasars 2. GALEX FUV mag = 18–18.5: 48 quasars 3. GALEX FUV mag = 18.5–19: 34 quasars	Point-source spectroscopy at $R \gtrsim$ 30,000 from 100–400 nm [O34]	Point-source spectroscopy at $R \approx$ 30,300 from 100–140 nm (G120M), $R \approx$ 37,800 from 130–170 nm (G150M), $R \approx$ 40,800 from 160–200 nm (G180M), $R \approx$ 28,000 from 200–400 nm (G300M) [O34]	Diameter of telescope aperture \gtrsim 8 m [O34] Telescope mirror reflectivity > 60% at 105 nm [O34]
	SO19: Determine the spatial distribution, kinematics, metal content, and large-scale structures of the halo around a nearby face-on spiral galaxy	PP35: Measurements of absorption column densities and velocities for hot halo gas (Lyman- β , OVI, CIV, and MgII) out to 200 kpc around M51 via examination of sight lines to 30 quasars through the CGM	O35: Spectra at SNR \gtrsim 10, $R \gtrsim$ 30,000 over 100–400 nm for the following set of 30 quasars Target properties: 1. GALEX FUV mag < 18: 1 quasar 2. GALEX FUV mag < 19: 2 quasars 3. GALEX FUV mag < 20: 8 quasars 4. GALEX FUV mag < 21: 19 quasars	Point-source spectroscopy at $R \gtrsim$ 30,000 from 100–400 nm [O35]	Point-source spectroscopy at $R \approx$ 30,300 from 100–140 nm (G120M), $R \approx$ 37,800 from 130–170 nm (G150M), $R \approx$ 40,800 from 160–200 nm (G180M), $R \approx$ 28,000 from 200–400 nm (G300M) [O35]	Diameter of telescope aperture \gtrsim 8 m [O35] Telescope mirror reflectivity > 60% at 105 nm [O35]
	SO20: Examine the morphology of	PP36: Measurements of hot gas emission	O36: Spectra of stellar clusters in 10 fields	Multi-object spectroscopy at $R \gtrsim$	Multi-object spectroscopy at $R \approx$	Diameter of telescope aperture \gtrsim 8 m

Complete LUVOIR-A Science Traceability Matrix						
		Scientific Requirements				
Signature Science Case	Science Objectives	Physical Parameters	Observables	Instrument Requirements	Projected Performance	Mission Requirements
	emission/absorption from resolved gas flows in nearby galaxies	and absorption (Lyman-β, OVI, CIV, and MgII) from ~1000 individual stellar clusters in nearby spiral galaxies	covering each galaxy with SNR≥10, $R \gtrsim 30,000$ from 100–400 nm	30,000 from 100–400 nm [O36] Spectroscopic field-of-view ≥ 4 sq. arcmin [O36]	30,300 from 100–140 nm (G120M), $R \approx 37,800$ from 130–170 nm (G150M), $R \approx 40,800$ from 160–200 nm (G180M), $R \approx 28,000$ from 200–400 nm (G300M) [O36] Spectroscopic field-of-view ≈ 4 sq. arcmin [O36]	[O36] Telescope mirror reflectivity > 60% at 105 nm [O36]
SSC11: The multi-scale assembly of galaxies	SO21: Search for ultra-faint dwarf galaxies at high redshift, the primordial seeds of large spiral galaxies Can be achieved with the observations in SO15	PP37: Detect ultra-faint dwarf galaxies at high-redshift ($z = 7$) with 3σ sensitivity for galaxies at $M_{UV} \gtrsim -13.5$	O37: Deep images of 12 blank sky fields in the I, J, and H bands to detect dwarf galaxies with J-band AB mag = 32.75 at SNR=5	Imaging in two broadband filters centered near 1220 nm and 1630 nm [O37] Simultaneous imaging in one broadband filter near 800 nm [O37] Imaging field-of-view ≥ 6 sq. arcmin [O37] Execute in parallel with exoplanet direct observations [O37]	Imaging in J and H filters centered at 1220 nm and 1630 nm [O37] Simultaneous imaging in I filter centered at 803 nm [O37] Imaging field-of-view = 6 sq. arcmin [O37] Appears possible to execute in parallel given sky distribution of exoplanet target stars and length of exoplanet science exposures [O37]	Diameter of telescope aperture ≥ 15 m [O37]
	SO22: Study the interior morphology of galaxies at moderate redshift at ~100 pc scales	PP38: Detect individual star-forming clusters in galaxies at $z \sim 1 - 2$	O38: Add B and V band images to observations in O37, with depth to detect star-forming regions with AB = 30 mag at SNR~25	Imaging in two broadband filters centered near 390 nm and 606 nm [O38]	Imaging in B and V filters centered at 390 and 606 nm [O38]	Diameter of telescope aperture ≥ 8 m [O38]

Complete LUVOIR-A Science Traceability Matrix						
		Scientific Requirements				
Signature Science Case	Science Objectives	Physical Parameters	Observables	Instrument Requirements	Projected Performance	Mission Requirements
				Imaging field-of-view ≥ 6 sq. arcmin [O38] Execute in parallel with exoplanet direct observations [O38]	Imaging field-of-view = 6 sq. arcmin [O38] Appears possible to execute in parallel given sky distribution of exoplanet target stars and length of exoplanet science exposures [O38]	
	SO23: Determine the star formation and metallicity histories of different types of large galaxies	PP39: Measure the age and metallicity of resolved stellar populations in nearby large galaxies by detecting the main sequence turnoff in color-magnitude diagrams	O39: Images in V and J bands with depth to detect solar-type stars with $AB \leq 34.5$ at SNR=5 within 6 large galaxies closer than 10 Mpc	Imaging in two broadband filters centered near 550 nm and 1220 nm [O39] Simultaneous imaging in the V and J bands [O39] Imaging field-of-view = 6 sq. arcmin [O39]	Imaging in V and J filters centered at 550 nm and 1220 nm [O39] Simultaneous imaging in the NUV/optical and NIR channels [O39] Imaging field-of-view = 6 sq. arcmin [O39]	Diameter of telescope aperture ≥ 15 m [O39]
SSC12: Stars as the engines of galactic feedback	SO24: Find very massive stars ($M_* > 150M_\odot$) and assess their impact on star-forming environments and galaxy evolution	PP40: Search for candidate very massive stars (VMSs) in ~30 luminous infrared galaxies and ~10 ultra-luminous infrared galaxies within 150 Mpc	O40: Images of ~40 galaxies in 9 NUV to NIR broad bands and three narrow bands (H- α at 656.3 nm, P- β at 1282 nm, and P- α at 1876 nm) to identify candidate VMSs with $m_{AB} = 28.5$ mag at SNR \approx 20 in each band	Imaging in 9 broadband filters centered between 200 nm and 2190 nm [O40] Imaging in three narrowband filters centered at 656 nm, 1282 nm, and 1876 nm [O40] Imaging field-of-view ≥ 6 sq. arcmin [O40]	Imaging in 9 broadband filters centered between 200 nm and 2190 nm [O40] Imaging in three narrowband filters centered at 656 nm, 1282 nm, and 1876 nm [O40] Imaging field-of-view = 6 sq. arcmin [O40]	Diameter of telescope aperture ≥ 15 m [O40, O41] Telescope mirror reflectivity > 60% at 105 nm [O41]
		PP41: Measure key diagnostics of VMSs in ~30 luminous infrared galaxies and ~10 ultra-luminous	O41: Spectra of VMSs with $m_{AB}(FUV) \geq 23$ mag in ~40 galaxies at $R \geq 10,000$ and continuum SNR \geq 10			

Complete LUVOIR-A Science Traceability Matrix						
		Scientific Requirements				
Signature Science Case	Science Objectives	Physical Parameters	Observables	Instrument Requirements	Projected Performance	Mission Requirements
		infrared galaxies within 150 Mpc Key diagnostics: 1. CIV (1550 Å) and NV (1240 Å) P Cygni profiles 2. Broad He II (1640 Å) emission 3. Blue-shifted OV (1371 Å) wind absorption 4. Absence of SiIV (1400 Å) P Cygni emission / absorption	per resolution element from 120–170 nm	Multi-object spectroscopy at $R \gtrsim 10,000$ from 120–170 nm [O41] Spectroscopic field-of-view $\gtrsim 4$ sq. arcmin [O41]	Multi-object spectroscopy at $R \approx 11,600$ from 100–200 nm (G155L) [O41] Spectroscopic field-of-view ≈ 4 sq. arcmin [O41]	
	SO25: Obtain a census of long period massive binaries in galaxies other than the Milky Way and the Magellanic Clouds to constrain models of star formation and the initial mass function	PP42: Constrain orbital parameters of long period binary stars (via measurements of positions and proper motions) in 7 regions of recent star formation in 5 galaxies within ~1 Mpc	O42: Multi-epoch images in the U, B, V, and I bands, once per year over 5 years, with depth to detect an A0 star at SNR=50	Imaging in four broadband filters centered near 365 nm, 445 nm, 550 nm, and 806 nm [O42] Imaging field-of-view $\gtrsim 6$ sq. arcmin [O42]	Imaging in U, B, V, and I filters centered at 365 nm, 445 nm, 550 nm, and 806 nm [O42] Imaging field-of-view = 6 sq. arcmin [O42]	Diameter of telescope aperture $\gtrsim 8$ m [O42, O43] Telescope mirror reflectivity > 60% at 105 nm [O43]
		PP43: Identify the spectral types and measure wind properties for stars in previous row	O43: Single-epoch spectra with $R \sim 10,000$ and SNR~10 from 100–400 nm	Multi-object spectroscopy at $R \gtrsim 10,000$ from 100–400 nm [O43] Spectroscopic field-of-view $\gtrsim 4$ sq. arcmin [O43]	Multi-object spectroscopy at $R \approx 11,600$ from 100–200 nm (G155L) and $R \approx 28,000$ from 200–400 nm (G300M) [O43] Spectroscopic field-of-view ≈ 4 sq. arcmin [O43]	

Table C-2. LUVOIR-B Science Traceability Matrix

Complete LUVOIR-B Science Traceability Matrix						
		Scientific Requirements				
Signature Science Case	Science Objectives	Physical Parameters	Observables	Instrument Requirements	Projected Performance	Mission Requirements
SSC1: Finding habitable planet candidates Determine the occurrence rate of Earth-like conditions on rocky worlds around Sun-like stars	SO1: Find at least 1 Earth-like planet orbiting a solar-type star (95% confidence) for occurrence rates $\geq 10\%$ by discovering and studying ≥ 28 habitable planet candidates Definition of candidates: 1. Solar-type stars have FGK spectral types 2. Planet orbit within stars' habitable zones (semi-major axis $0.95 \leq a \leq 1.67$ AU for Sun-twin star, scaled by $\sqrt{L_{\star}/L_{\odot}}$ for other spectral types) 3. Planet likely to be rocky (planet radius $\leq 1.4 R_{\text{Earth}}$) 4. Planet likely to retain atmospheres over geologic times (planet radius $\geq 0.8 a^{-0.5} R_{\text{Earth}}$) 5. Planet likely to be Earth-like (geometric albedo = 0.2 between 550–1000 nm)	PP1: Cumulative habitable zone completeness $C \geq 28/\eta_{\text{Earth}} \geq 28/0.24 \geq 117$	O1: High-contrast images of faint ($M_V \approx 30$) point-sources around >100 FGKM target stars within 30 parsecs of the Sun	IWA $\lesssim 4.0 \lambda/D$ [O1, O2, O3, O4] OWA $\geq 10 \lambda/D$ [O1, O2, O3, O4] Coronagraph raw contrast $\lesssim 2 \times 10^{-10}$ [O1, O2, O3, O4] Coronagraphic imaging in two $\geq 15\%$ bands near 500 nm [O2, O3] Spatially resolved coronagraphic spectroscopy with R=70 over $\geq 15\%$ bandpass centered near 940 nm [O4]	IWA $\approx 3.8 \lambda/D$ [O1, O2, O3, O4] OWA $\approx 27 \lambda/D$ [O1, O2, O3, O4] Coronagraph raw contrast $\approx 1.5 \times 10^{-10}$ [O1, O2, O3, O4] Coronagraphic imaging in two 20% bands (400–500 nm and 500–600 nm) [O2, O3] Spatially resolved coronagraphic spectroscopy with R=70 over 20% bandpass centered near 940 nm [O4]	Inscribed diameter of telescope aperture $\gtrsim 6.7$ m [O1, O2, O3, O4, O5] Field of regard $>$ entire anti-Sun hemisphere [O1, O3] ≥ 6 visits to each candidate target system [O3]
		PP2: Colors of candidates in reflected light to begin confusion discrimination	O2: Broadband photometry of candidates (SNR ≥ 7) at two optical wavelengths			
		PP3: Orbital semi-major axis, eccentricity, and inclination of each candidate with 10% accuracy	O3: Candidate positions at ≥ 4 different locations with position uncertainty ≤ 5 mas (SNR ≥ 7)			
		PP4: Detection of atmospheric water vapor at abundance comparable to modern Earth's (2.5% by volume)	O4: Planetary direct spectra with continuum SNR=5 per spectral resolution element and R=70 around water vapor absorption feature at 940 nm			
		SO2: Reserve time in prime mission for follow-up exoEarth observations and other science goals	PP5: Limit total survey time to 2 years	O5: Hundreds of direct observations of FGK stars within 2 years	Coronagraph core throughput $\gtrsim 40\%$ [O5] Detector parameters: Dark current $\lesssim 2 \times 10^{-2}$ counts $\text{pix}^{-1} \text{s}^{-1}$ Read noise $\lesssim 5$ counts $\text{pix}^{-1} \text{read}^{-1}$ [O5]	Coronagraph core throughput $\approx 40\%$ [O5] Detector parameters: Dark current $\lesssim 3 \times 10^{-5}$ counts $\text{pix}^{-1} \text{s}^{-1}$ Read noise $\lesssim 0$ counts $\text{pix}^{-1} \text{read}^{-1}$ [O5]
Multi-Parameter Science Return Dependencies Habitable planet candidates found in high-contrast survey defined above (first 8 most important mission & instrument parameters) $Y \propto D^{1.97} IWA^{-0.98} T^{0.35} \Gamma^{-0.33} E^{0.32} \Delta\lambda^{0.30} C^{-0.10} OWA^{0.07}$						

Complete LUVOIR-B Science Traceability Matrix						
		Scientific Requirements				
Signature Science Case	Science Objectives	Physical Parameters	Observables	Instrument Requirements	Projected Performance	Mission Requirements
	Y = yield of candidates, D = inscribed diameter of telescope aperture, IWA = coronagraph inner working angle, T = end-to-end throughput, Γ = point-spread function sharpness, E = total exposure time, $\Delta\lambda$ = instantaneous coronagraph bandpass, C = raw contrast, OWA = coronagraph outer working angle					
SSC2: Searching for biosignatures and confirming habitability Search habitable exoplanet candidates for signs of life and confirm the presence of liquid surface water	SO3: Measure the physical and chemical states of the atmospheres of habitable planet candidates to establish disequilibrium conditions and thereby identify biosignature gases Habitable planet candidates identified in SO1	PP6: Spectral energy distributions of ~28 FGKM exoplanet host stars	O6: UV spectra of bright stars ($V = 0 - 11$) over 100–400 nm, with precise measurement of total Lyman- α flux ($R \gtrsim 10,000$ and $SNR \gtrsim 50$ near 121.5 nm)	Point-source spectra at $R \gtrsim 10,000$ from 100–400 nm [O6]	Point-source spectra at $R \approx 11,600$ from 100–200 nm (G155L) and $R \approx 28,000$ from 200–1000 nm (G300M) [O6]	Telescope mirror reflectivity > 60% at 105 nm [O6]
		PP7: Masses of ~28 habitable exoplanet candidates orbiting Sun-like stars within 30 pc of the Sun with $\lesssim 25\%$ precision	O7: Astrometric measurements of stellar wobble caused by 1 Earth-mass planets at 1 AU from Sun-like stars with $V = 0 - 11$ (wobble semi-amplitude = 0.3 μas for Sun-twin star at 10 pc) Requires: 1. Detection of astrometric signal at end-of-mission $SNR=3$, utilizing coronagraphic images obtained in SO1 2. Mean number of epochs per target = 39, spread over ~1 year 3. Detection of $V=24$ background sources for calibration of optical distortions	Optical imaging with systematic single-measurement position errors $\lesssim 0.65 \mu\text{as} \approx 0.0001$ pixels [O7] Imaging field-of-view $\gtrsim 6$ sq. arcmin [O7] Rapid VIS detector readout to prevent saturation on bright exoplanet host stars [O7]	Optical imaging with systematic single-measurement position errors = 0.65 $\mu\text{as} \approx 0.0001$ pixels, achieved with on-board laser-based system to calibrate detector distortions [O7] Imaging field-of-view = 6 sq. arcmin [O7] Readout of regions on VIS detector at up to 500 Hz [O7]	Diameter of telescope aperture $\gtrsim 8$ m [O7] ~39 visits to each candidate target system [O7]
		PP8: Measurement of atmospheric H_2O	O8: Planetary direct spectra with	$IWA \lesssim 4.0 \lambda/D$	$IWA \approx 3.8 \lambda/D$	

Complete LUVOIR-B Science Traceability Matrix						
		Scientific Requirements				
Signature Science Case	Science Objectives	Physical Parameters	Observables	Instrument Requirements	Projected Performance	Mission Requirements
		abundances with ≤ 1 dex precision for abundances comparable to modern Earth's (2.5% by volume)	continuum $\text{SNR} \geq 8.5$ per spectral resolution element and $R \geq 70$ around water vapor absorption features between 900 nm and 1800 nm	[O8, O9, O10, O11, O12, O13] $\text{OWA} \geq 10 \lambda/D$ [O8, O9, O10, O11, O12, O13]	[O8, O9, O10, O11, O12, O13] $\text{OWA} \approx 27 \lambda/D$ [O8, O9, O10, O11, O12, O13]	Inscribed diameter of telescope aperture ≥ 6.7 m [O8, O9, O10, O11, O12, O13]
		PP9: Measurement of atmospheric CH ₄ abundances with ≤ 1 dex precision for abundances comparable to Archean Earth's (0.01 – 1% of total atmosphere)	O9: Planetary direct spectra with continuum $\text{SNR} \geq 8.5$ per spectral resolution element and $R \geq 70$ around CH ₄ absorption features between 700 nm and 1700 nm	Coronagraph raw contrast $\lesssim 2 \times 10^{-10}$ [O8, O9, O10, O11, O12, O13] Spatially resolved coronagraphic spectroscopy with $R \geq 70$ over $\geq 15\%$ bandpasses between 700 nm and 1800 nm [O8, O9, O12, O13]	Coronagraph raw contrast $\approx 1.5 \times 10^{-10}$ [O8, O9, O10, O11, O12, O13] Spatially resolved coronagraphic spectroscopy with $R=140$ (vis) and 70 (NIR) over 20% bandpasses between 500 nm and 2000 nm [O8, O9, O12, O13]	
		PP10: Measurement of atmospheric O ₂ abundances with ≤ 1 dex precision for abundances comparable to modern Earth's (21% by volume)	O10: Planetary direct spectra with continuum $\text{SNR} \geq 8.5$ per spectral resolution element and $R=140$ around O ₂ A band absorption feature at 760 nm	Spatially resolved coronagraphic spectroscopy with $R=140$ over $\geq 15\%$ bandpass near 760 nm [O10]	Spatially resolved coronagraphic spectroscopy with $R=140$ over 20% bandpass near 760 nm [O10]	
		PP11: Measurement of atmospheric O ₃ abundances with ≤ 1 dex precision for abundances comparable to Proterozoic Earth's (0.1% present atmospheric level)	O11: Planetary direct spectra with continuum $\text{SNR} \geq 8.5$ per spectral resolution element and $R \geq 6$ near strong O ₃ absorption feature at 250 nm	Multi-color coronagraphic imaging with effective $R=6$ over $\geq 15\%$ bandpasses between 200 nm and 400 nm [O11]	Multi-color coronagraphic imaging with effective $R=6$ over 20% bandpasses between 200 nm and 500 nm [O11]	
		PP12: Constrain presence of false positive biosignature indicator gases (O ₄ , CO ₂ , CO)	O12: Planetary direct spectra with continuum $\text{SNR} \geq 8.5$ per spectral resolution element and $R \geq 70$ around absorption features of O ₄ near 1060 and 1270 nm,	Point-source coronagraphic spectroscopy with $R=200$ over $\geq 15\%$ bandpass near 1590 nm	Point-source coronagraphic spectroscopy with $R=200$ over 20% bandpass near 1590 nm	

Complete LUVOIR-B Science Traceability Matrix						
		Scientific Requirements				
Signature Science Case	Science Objectives	Physical Parameters	Observables	Instrument Requirements	Projected Performance	Mission Requirements
			CO ₂ near 1590 nm, and CO at 1600 nm	[O13]	[O13]	
	SO4: Calculate the surface temperatures of habitable planet candidates to establish the likelihood of liquid water Habitable planet candidates identified in SO1	PP13: Measurement of key atmospheric greenhouse gas (e.g., H ₂ O, CO ₂) abundances with ≤ 1 dex precision for abundances comparable to modern Earth's	O13: Planetary direct spectra with continuum SNR ≥ 8.5 per spectral resolution element, $R \geq 70$ between 900 nm and 1800 nm (H ₂ O) and $R \geq 200$ around absorption feature of CO ₂ near 1590 nm			
SSC3: The search for habitable worlds in the solar system Characterize plume activity from and cryo-volcanism on solar system ocean moons	SO5: Monitor Europa to determine the strength and frequency of plumes emanating from its surface. Study the moon's interaction with the Jovian magnetosphere in detail	PP14: Mapping of auroral emission from individual plumes and general non-plume-related auroral emission	O14: Spatially resolved spectra of Lyman- α (121.6 nm) and OI (130.4 nm) emission (SNR ≥ 5 and $R \geq 10,000$ at 130.4 nm)	Spatially resolved spectroscopy with $R \geq 10,000$ over about 115–140 nm [O14]	Spatially resolved spectroscopy with $R \approx 11,600$ over 100–200 nm (G155L) [O14]	Telescope aperture diameter ≥ 8 m [O14] Telescope mirror reflectivity $> 90\%$ at 115 nm [O14] Non-sidereal tracking at ≥ 60 mas/sec [O14, O15] Dithered observations with slightly shifted telescope pointing [O14, O15]
		PP15: Measurement of plume frequency and the moon's changing interaction with the Jovian magnetosphere over one full orbital period (3.5 days)	O15: Single visits to Europa once every two months over 5 years One 4-day visit to Europa for high-cadence observations			
	SO6: Characterize cryo-volcanism on six outer solar system ocean moons under changing heating conditions (Europa, Ganymede, Callisto, Enceladus, Titan, and Triton)	PP16: Mapping of surface morphology over long timescales at wavelengths centered on and bracketing expected surface spectral features (e.g., water ice at 1100 and 1400 nm, methane ice at 1700 nm)	O16: High-resolution, narrowband optical/NIR mosaics obtained twice per year over 5 years	Imaging in narrowband filters at several optical/NIR wavelengths [O16] Imaging field-of-view ≥ 7 sq. arcsec [O16]	Imaging in 1% optical/NIR filters (central wavelengths TBD) [O16] Imaging field-of-view = 6 sq. arcmin [O16]	Telescope aperture diameter ≥ 8 m [O16] Non-sidereal tracking at ≥ 60 mas/sec [O16] Dithered observations with slightly shifted telescope pointing [O16]

Complete LUVOIR-B Science Traceability Matrix						
		Scientific Requirements				
Signature Science Case	Science Objectives	Physical Parameters	Observables	Instrument Requirements	Projected Performance	Mission Requirements
SSC4: Comparative atmospheres Study the atmospheres of a diverse set of exoplanets in a variety of ways	SO7: Characterize dozens of exoplanets covering a wide range of sizes ($0.1 R_{\text{Jupiter}} \lesssim R \lesssim 2 R_{\text{Jupiter}}$) and orbital distances ($100 \text{ K} \lesssim T_{\text{eq}} \lesssim 2000 \text{ K}$) Planetary spectral template assumptions: 1. $M_p > 0.15 M_{\text{Jupiter}}$ and $T_{\text{eq}} \leq 180 \text{ K}$: Jupiter 2. $M_p > 0.15 M_{\text{Jupiter}}$ and $180 \text{ K} \leq T_{\text{eq}} \leq 180 \text{ K}$: warm Jupiter at 2 AU from Cahoy et al. (2010) 3. $M_p > 0.15 M_{\text{Jupiter}}$ and $T_{\text{eq}} > 300 \text{ K}$: warm Jupiter at 0.8 AU from Cahoy et al. (2010) 4. $M_p \leq 0.15 M_{\text{Jupiter}}$ and $T_{\text{eq}} \leq 180 \text{ K}$: Neptune 5. $M_p \leq 0.15 M_{\text{Jupiter}}$ and $180 \text{ K} \leq T_{\text{eq}} \leq 180 \text{ K}$: warm Neptune at 2 AU from Hu & Seager (2014) 6. $M_p \leq 0.15 M_{\text{Jupiter}}$ and $T_{\text{eq}} > 300 \text{ K}$: cloudy warm Jupiter at 1 AU from Hu & Seager (2014) 7. Rocky planets: Earth	PP17: Measurement of key atmospheric gas (e.g., CH ₄ , H ₂ O, CO ₂) abundances with ≤ 1 dex precision for 19 known warm to cold exoplanets	O17: Planetary direct spectra with continuum SNR ≥ 15 per spectral resolution element and $R \geq 70$ between about 500 nm and 1700 nm	IWA $\lesssim 4.0 \lambda/D$ [O17, O18] OWA $\geq 25 \lambda/D$ [O17, O18] Coronagraph raw contrast $\lesssim 1 \times 10^{-9}$ [O17, O18] Spatially resolved coronagraphic spectroscopy with $R \geq 70$ over $\geq 15\%$ bandpasses between 500 nm and 1700 nm [O17] Multi-color coronagraphic imaging with effective $R=6$ over $\geq 15\%$ bandpasses between 200 nm and 500 nm [O18]	IWA $\approx 3.8 \lambda/D$ [O17, O18] OWA $\approx 27 \lambda/D$ [O17, O18] Coronagraph raw contrast $\approx 1.5 \times 10^{-10}$ [O17, O18] Spatially resolved coronagraphic spectroscopy with $R=140$ (vis) and 70 (NIR) over 20% bandpasses between 500 nm and 2000 nm [O17] Multi-color coronagraphic imaging with effective $R=6$ over 20% bandpasses between 200 nm and 500 nm [O18]	Inscribed diameter of telescope aperture $\geq 6.7 \text{ m}$ [O17, O18]
		PP18: Measurement of atmospheric haze scattering slopes for 19 known warm to cold exoplanets	O18: Planetary direct spectra with continuum SNR ≥ 5 per spectral resolution element and $R \geq 6$ between about 200 nm and 500 nm			
		PP19: Measurement of key atmospheric gas (e.g., CH ₄ , H ₂ O, CO) abundances with ≤ 1 dex precision for 16 known transiting warm to hot exoplanets	O19: Planetary transmission spectra during transits with SNR ≥ 4 , $15 \lesssim R \lesssim 500$ between 200–2500 nm (full wavelength range covered simultaneously)	Point-source stellar spectroscopy with $15 \lesssim R \lesssim 500$ between 200 nm and 2500 nm [O19] Rapid VIS detector readout to prevent saturation on bright exoplanet host stars [O19]	Point-source stellar spectroscopy with $15 \lesssim R \lesssim 500$ between 200 nm and 2500 nm [O19] Readout of regions on VIS detector at up to 500 Hz [O19]	
		PP20: Measurement of atmospheric escape rates for 16 hot known transiting exoplanets via observations of	O20: Planetary transmission spectra to observe Lyman- α (121.6 nm), OI (130.4 nm), and CII (133.5 nm) emission during	Point-source stellar spectroscopy with $R \geq 30,000$ between 100 nm and 140 nm [O20]	Point-source stellar spectroscopy with $R \approx 30,300$ between 100 nm and 140 nm (G120M) [O20]	

Complete LUVOIR-B Science Traceability Matrix						
		Scientific Requirements				
Signature Science Case	Science Objectives	Physical Parameters	Observables	Instrument Requirements	Projected Performance	Mission Requirements
		exospheric H, O, and C	single transits with $\text{SNR} \geq 3$, $R \geq 30,000$ between about 100–140 nm (full wavelength range covered simultaneously)			Telescope mirror reflectivity > 60% at 105 nm [O20]
SSC5: The formation of planetary systems Study planet formation over a wide range of system ages	SO8: Follow the evolution and dispersal of the main molecular carriers of C, H, and O during planet assembly in the terrestrial and giant-planet forming regions of protoplanetary disks, trace molecular and low-ionization metals from disk winds, and provide absolute abundance patterns in disks as a function of age	PP21: Locate protoplanetary disks within five areas of the Orion star-forming region Areas: 1. Orion Nebular Cloud: ~1 Myr, ~24' size 2. NGC1980: ~1-2 Myr, ~16' size 3. σ Ori: ~3-5 Myr, ~33' size 4. λ Ori: 4-8 Myr, 49' size 5. 25 Ori: ~7-10 Myr, 33' size	O21: FUV imaging from 100–200 nm covering five areas in the Orion star-forming region, with sensitivity to detect FUV continuum flux of a young T Tauri star at ~370 pc Areas: 1. Orion Nebular Cloud: 6 pointings 2. NGC1980: 4 pointings 3. σ Ori: 9 pointings 4. λ Ori: 13 pointings 5. 25 Ori: 9 pointings	FUV imaging field-of-view ≥ 4 sq. arcmin [O21] Neutral density filters for bright object protection [O21] Multi-object spectroscopy at $R \geq 30,000$ from 100–400 nm [O22] Spectroscopic field-of-view ≥ 4 sq. arcmin [O22]	FUV imaging field-of-view ≈ 4 sq. arcmin [O21] Neutral density filters for bright object protection [O21] Multi-object spectroscopy at $R \approx 30,300$ from 100–140 nm (G120M), $R \approx 37,800$ from 130–170 nm (G150M), and $R \approx 28,000$ from 200–400 nm (G300M) [O22] Spectroscopic field-of-view ≈ 4 sq. arcmin [O22]	Diameter of telescope aperture ≥ 8 m [O21, O22] Telescope mirror reflectivity > 60% at 105 nm [O21, O22]
		PP22: Measure the most abundant molecular species in (H_2 , CO, H_2O , and OH) in Orion protoplanetary disks	O22: Spectroscopy of protoplanetary disks in Orion with $R \approx 30,000$ and $\text{SNR} \approx 10$ per resolution element from 100–170 nm and 200–400 nm Reference flux at 110 nm: $F_\lambda = 2 \times 10^{-16} \text{ erg s}^{-1} \text{ cm}^{-2} \text{ \AA}^{-1}$			
	SO9: Investigate the planetesimal distributions in 25 exoplanet systems around young AFGKM stars and look	PP23: Morphology of warm dust structures in 25 young exoplanet systems (cold dust to	O23: High-resolution images of visible light scattered by interplanetary dust	IWA $\lesssim 4.0 \lambda/D$ [O23, O24]	IWA $\approx 3.8 \lambda/D$ [O23, O24]	Inscribed diameter of telescope aperture ≥ 6.7 m

Complete LUVOIR-B Science Traceability Matrix						
		Scientific Requirements				
Signature Science Case	Science Objectives	Physical Parameters	Observables	Instrument Requirements	Projected Performance	Mission Requirements
	for signs of newly formed planets (5 stars per spectral type bin)	be observed with ground-based radio facilities)		$OWA \geq 25 \lambda/D$ [O23, O24]	$OWA \approx 27 \lambda/D$ [O23, O24]	[O23, O24]
		PP24: Search for cometary OH emission in a subset of young exoplanet systems as a signature of volatile delivery to the habitable zone	O24: High-resolution images of NUV light emitted by interplanetary OH	Coronagraph raw contrast $\lesssim 1 \times 10^{-9}$ [O23, O24] Coronagraphic imaging in one $\geq 15\%$ band near 500 nm [O23] Coronagraphic imaging in one $\geq 15\%$ band near 250 nm [O24]	Coronagraph raw contrast $\approx 1.5 \times 10^{-10}$ [O23, O24] Coronagraphic imaging in one 20% band (500–600 nm) [O23] Coronagraphic imaging in one 20% near 250 nm [O24]	
	S10: Determine the orbits and masses of planets in ~28 mature exoplanet systems, as well as the locations of asteroid and comet (planetesimal) belts To increase efficiency, the systems will be those hosting habitable exoplanet candidates found in SO1 (Sun-like host stars within 30 pc)	PP25: Orbits and masses of planets in ~28 exoplanet systems with $\lesssim 25\%$ precision on mass measurement Results from this program also satisfy PP7	O25: Astrometric measurements of stellar wobble caused by 1 Earth-mass planets at 1 AU from Sun-like stars with $V = 0 - 11$ (wobble semi-amplitude = $0.3 \mu\text{as}$ for Sun-twin star at 10 pc) Requires: 1. Detection of astrometric signal at end-of-mission SNR=3, utilizing coronagraphic images obtained in SO1 2. Mean number of epochs per target = 39, spread over ~1 year 3. Detection of V=24 background sources for	Optical imaging with systematic single-measurement position errors $\lesssim 0.65 \mu\text{as} \approx 0.0001$ pixels [O25] Imaging field-of-view ≥ 6 sq. arcmin [O25] Rapid VIS detector readout to prevent saturation on bright exoplanet host stars [O25]	Optical imaging with systematic single-measurement position errors = $0.65 \mu\text{as} \approx 0.0001$ pixels, achieved with on-board laser-based system to calibrate detector distortions [O25] Imaging field-of-view = 6 sq. arcmin [O25] Readout of regions on VIS detector at up to 500 Hz [O25]	

Complete LUVOIR-B Science Traceability Matrix						
		Scientific Requirements				
Signature Science Case	Science Objectives	Physical Parameters	Observables	Instrument Requirements	Projected Performance	Mission Requirements
			calibration of optical distortions			
		PP26: Locations of warm planetesimal belts in ~28 exoplanet systems (cold belts to be observed with ground-based radio facilities) Most data for this program obtained in PP1	O26: High-resolution images of visible light scattered by interplanetary dust	IWA $\lesssim 4.0 \lambda/D$ [O26] OWA $\gtrsim 25 \lambda/D$ [O26] Coronagraph raw contrast $\lesssim 1 \times 10^{-9}$ [O26] Coronagraphic imaging in two $\geq 15\%$ bands near 500 nm [O26]	IWA $\approx 3.8 \lambda/D$ [O26] OWA $\approx 27 \lambda/D$ [O26] Coronagraph raw contrast $\approx 1.5 \times 10^{-10}$ [O26] Coronagraphic imaging in two 20% bands (400–500 nm and 500–600 nm) [O26]	Inscribed diameter of telescope aperture $\gtrsim 6.7$ m [O26]
SSC6: Small bodies in the solar system Study the smallest bodies in the outer solar system to investigate its formation and early evolution	SO11: Discover trans-Neptunian objects (TNOs) down to the currently unseen smallest bodies that distinguish between different planetesimal formation scenarios and measure their reflected light colors	PP27: Detection of ~30 TNOs with sizes $\gtrsim 4$ km out to 40 AU and measurement of their brightnesses in one optical band and one NIR band	O27: Detection of $R \leq 31.5$ mag objects at $\text{SNR} \gtrsim 5$ in a 0.017 deg^2 region imaged in R band and one NIR band	Imaging in one broadband filter near 775 nm [O27] Simultaneous imaging in one broadband filter near 1260 nm [O27] Imaging field-of-view $\gtrsim 6$ sq. arcmin [O27]	Imaging in one ~20% filter centered at 775 nm (R band) [O27] Simultaneous imaging in one ~20% filter centered at 1260 nm (J band) [O27] Imaging field-of-view = 6 sq. arcmin [O27]	Diameter of telescope aperture $\gtrsim 8$ m [O27] Non-sidereal tracking at a rate equivalent to a circular orbit at 40 AU (6 nanorad/sec) [O27] ~26 visits per field to estimate orbits of detected objects [O27]
	SO12: Measure the component sizes, mass ratios, separations, and occurrence rates of TNO binaries to constrain theories of their formation and evolution	PP28: Orbits of TNO binaries discovered in the previous row	O28: Repeated detection of $R \leq 31.5$ mag objects at $\text{SNR} \gtrsim 5$ in R band and one NIR band	Imaging in one broadband filter near 775 nm [O28] Simultaneous imaging in one broadband filter near 1260 nm [O28]	Imaging in one ~20% filter centered at 775 nm (R band) [O28] Simultaneous imaging in one ~20% filter centered at 1260 nm (J band) [O28]	Diameter of telescope aperture $\gtrsim 8$ m [O28] Non-sidereal tracking at ≥ 60 mas/sec [O28] Targeted revisits [O28]

Complete LUVOIR-B Science Traceability Matrix						
		Scientific Requirements				
Signature Science Case	Science Objectives	Physical Parameters	Observables	Instrument Requirements	Projected Performance	Mission Requirements
				Imaging field-of-view ≥ 6 sq. arcmin [O28]	Imaging field-of-view = 6 sq. arcmin [O27]	
SSC7: Connecting the smallest scales across cosmic time Investigate the properties of dark matter via the matter power spectrum	SO13: Discriminate between standard cold dark matter, interacting dark matter, and several warm dark matter models by measuring the shape of the matter power spectrum on small scales (<100 kpc)	PP29: Measure the spatial distribution of extremely low-mass dwarf galaxies around four Milky Way (MW) analog galaxies within 15 Mpc	O29: Images of 100 kpc regions around four MW analog galaxies in the V and J bands simultaneously, with sensitivity to detect $M_V = 0$ AB mag stars at SNR=5 Assumptions: Stellar color V-J = 0.35, typical of stars on the Horizontal Branch of the Hertzsprung-Russel diagram	Imaging in one broadband filter near 550 nm [O29] Simultaneous imaging in one broadband filter near 1220 nm [O29] Imaging field-of-view ≥ 6 sq. arcmin [O29]	Imaging in V filter centered at 550 nm [O29] Simultaneous imaging in J filter centered at 1220 nm [O29] Imaging field-of-view ≥ 6 sq. arcmin [O29]	Diameter of telescope aperture ≥ 8 m [O29]
SSC8: Constraining dark matter using high precision astrometry	SO14: Constrain the nature of the dark matter particle by measuring the density profiles of dwarf galaxies	PP30: High precision astrometric measurements of proper motions for ~100 stars in 20 dwarf spheroidal galaxies, 10 within the Local Group (1 Mpc) and 10 beyond the Local Group (2 – 5 Mpc)	O30: Astrometric measurements of stellar proper motions with end-of mission accuracy of ~10 km/s Requires: 1. Three epochs per galaxy spread over 5 years 2. Detection of V=24 background sources for calibration of optical distortions	Optical imaging with systematic single-measurement position errors $\leq 0.98 \mu\text{as} \approx 0.00015$ pixels [O30] Imaging field-of-view ≥ 6 sq. arcmin [O30]	Optical imaging with systematic single-measurement position errors $\leq 0.65 \mu\text{as} \approx 0.0001$ pixels, achieved with on-board laser-based system to calibrate detector distortions [O30] Imaging field-of-view = 6 sq. arcmin [O30]	Diameter of telescope aperture ≥ 8 m [O30] 3 visits to each candidate target system [O30]
SSC9: Tracing ionizing light over cosmic time	SO15: Study the behavior of the faint end of the galaxy luminosity function to reveal the degree to which dwarf galaxies powered cosmic reionization Not feasible with LUVOIR-B	PP31: Measure counts per sq. arcmin of dwarf galaxies at high-redshift ($z = 7$), with sensitivity to detect difference between rest-frame	O31: Deep images of 12 blank sky fields in the I, J, and H bands to detect dwarf galaxies with J-band AB mag = 32.75 at SNR=5	Imaging in two broadband filters centered near 1220 nm and 1630 nm [O31]	Imaging in J and H filters centered at 1220 nm and 1630 nm [O31]	Diameter of telescope aperture ≥ 15 m [O31]

Complete LUVOIR-B Science Traceability Matrix						
		Scientific Requirements				
Signature Science Case	Science Objectives	Physical Parameters	Observables	Instrument Requirements	Projected Performance	Mission Requirements
		UV luminosity functions with and without reionization suppression at 5σ significance ($M_{UV} \gtrsim -13.5$)		Simultaneous imaging in one broadband filter near 800 nm [O31] Imaging field-of-view $\gtrsim 6$ sq. arcmin [O31] Execute in parallel with exoplanet direct observations [O31]	Simultaneous imaging in I filter centered at 803 nm [O31] Imaging field-of-view = 6 sq. arcmin [O31] Not possible to execute in parallel given sky distribution of exoplanet target stars and length of exoplanet science exposures [O31]	
	SO16: Detect and quantify the evolution of ionizing radiation from low-redshift galaxies	PP32: Characterize ionizing UV radiation from star-forming galaxies at low-redshift ($0.2 \lesssim z \lesssim 1.2$), with 500 galaxies per $\Delta z = 0.2$ redshift bin	O32: Low-resolution FUV spectra covering 12 random sky fields to detect galaxies at SNR=5 over 30 Å wavelength bin below the Lyman break	Multi-object spectroscopy at $R \approx 500$ from 100–200 nm [O32] Spectroscopic field-of-view $\gtrsim 4$ sq. arcmin [O32] Execute in parallel with exoplanet direct observations [O32]	Multi-object spectroscopy at $R \approx 500$ from 100–200 nm (G145LL) [O32] Spectroscopic field-of-view ≈ 4 sq. arcmin [O32] Appears possible to execute in parallel given sky distribution of exoplanet target stars and length of exoplanet science exposures [O32]	Diameter of telescope aperture $\gtrsim 8$ m [O29] Telescope mirror reflectivity > 60% at 105 nm [O32]
	SO17: Map the escape of ionizing radiation from low-redshift galaxies and relate it to massive stellar populations and outflows	PP33: Observe the distribution of both ionizing (rest-frame wavelengths <90 nm) and non-ionizing (rest-frame wavelengths 120–160 nm) radiation	O33: Spectra from 100–200 nm, with SNR \approx 13 at 140 nm, of individual star-forming regions within galaxies selected to have integrated GALEX FUV mag < 19	Multi-object spectroscopy at $R \approx 10,000$ from 100–200 nm [O33] Spectroscopic field-of-view $\gtrsim 4$ sq. arcmin	Multi-object spectroscopy at $R \approx 11,600$ from 100–200 nm (G150L) [O33] Spectroscopic field-of-view ≈ 4 sq. arcmin	Diameter of telescope aperture $\gtrsim 8$ m [O33] Telescope mirror reflectivity > 60% at 105 nm [O33]

Complete LUVOIR-B Science Traceability Matrix						
		Scientific Requirements				
Signature Science Case	Science Objectives	Physical Parameters	Observables	Instrument Requirements	Projected Performance	Mission Requirements
		within 100 galaxies at $z = 0.25 - 0.3$		[O33]	[O33]	
SSC10: The cycles of matter Understand the ways in which matter flows into and out of galaxies	SO18: Determine the abundances of baryons in the intergalactic and circumgalactic medium across cosmic time	PP34: Absorption column density measurements of ions with a wide range of temperatures ($10 - 10^7$ K) and densities ($10^{-6} - 10^2 \text{ cm}^{-3}$) via UV spectroscopy of 100 high-redshift ($z > 1$) quasars	O34: Spectra at $\text{SNR} \geq 20$, $R \geq 30,000$ over 100–400 nm for the following set of 100 quasars Target properties: 1. GALEX FUV mag < 18: 18 quasars 2. GALEX FUV mag = 18–18.5: 48 quasars 3. GALEX FUV mag = 18.5–19: 34 quasars	Point-source spectroscopy at $R \geq 30,000$ from 100–400 nm [O34]	Point-source spectroscopy at $R \approx 30,300$ from 100–140 nm (G120M), $R \approx 37,800$ from 130–170 nm (G150M), $R \approx 40,800$ from 160–200 nm (G180M), $R \approx 28,000$ from 200–400 nm (G300M) [O34]	Diameter of telescope aperture ≥ 8 m [O34] Telescope mirror reflectivity > 60% at 105 nm [O34]
	SO19: Determine the spatial distribution, kinematics, metal content, and large-scale structures of the halo around a nearby face-on spiral galaxy	PP35: Measurements of absorption column densities and velocities for hot halo gas (Lyman- β , OVI, CIV, and MgII) out to 200 kpc around M51 via examination of sight lines to 30 quasars through the CGM	O35: Spectra at $\text{SNR} \geq 10$, $R \geq 30,000$ over 100–400 nm for the following set of 30 quasars Target properties: 1. GALEX FUV mag < 18: 1 quasar 2. GALEX FUV mag < 19: 2 quasars 3. GALEX FUV mag < 20: 8 quasars 4. GALEX FUV mag < 21: 19 quasars	Point-source spectroscopy at $R \geq 30,000$ from 100–400 nm [O35]	Point-source spectroscopy at $R \approx 30,300$ from 100–140 nm (G120M), $R \approx 37,800$ from 130–170 nm (G150M), $R \approx 40,800$ from 160–200 nm (G180M), $R \approx 28,000$ from 200–400 nm (G300M) [O35]	Diameter of telescope aperture ≥ 8 m [O35] Telescope mirror reflectivity > 60% at 105 nm [O35]
	SO20: Examine the morphology of emission/absorption from resolved gas flows in nearby galaxies	PP36: Measurements of hot gas emission (Lyman- β , OVI, CIV, and MgII) from ~1000 individual stellar clusters in nearby spiral galaxies	O36: Spectra of stellar clusters in 10 fields covering each galaxy with $\text{SNR} \geq 10$, $R \geq 30,000$ from 100–400 nm	Multi-object spectroscopy at $R \geq 30,000$ from 100–400 nm [O36]	Multi-object spectroscopy at $R \approx 30,300$ from 100–140 nm (G120M), $R \approx 37,800$ from 130–170 nm (G150M), $R \approx 40,800$ from 160–200	Diameter of telescope aperture ≥ 8 m [O36] Telescope mirror reflectivity > 60% at 105 nm

Complete LUVOIR-B Science Traceability Matrix						
		Scientific Requirements				
Signature Science Case	Science Objectives	Physical Parameters	Observables	Instrument Requirements	Projected Performance	Mission Requirements
				Spectroscopic field-of-view ≥ 4 sq. arcmin [O36]	nm (G180M), $R \approx 28,000$ from 200–400 nm (G300M) [O36] Spectroscopic field-of-view ≈ 4 sq. arcmin [O36]	[O36]
SSC11: The multi-scale assembly of galaxies	SO21: Search for ultra-faint dwarf galaxies at high redshift, the primordial seeds of large spiral galaxies Not feasible with LUVOIR-B	PP37: Detect ultra-faint dwarf galaxies at high-redshift ($z = 7$) with 3σ sensitivity for galaxies at $M_{UV} \gtrsim -13.5$	O37: Deep images of 12 blank sky fields in the I, J, and H bands to detect dwarf galaxies with J-band AB mag = 32.75 at SNR=5	Imaging in two broadband filters centered near 1220 nm and 1630 nm [O37] Simultaneous imaging in one broadband filter near 800 nm [O37] Imaging field-of-view ≥ 6 sq. arcmin [O37] Execute in parallel with exoplanet direct observations [O37]	Imaging in J and H filters centered at 1220 nm and 1630 nm [O37] Simultaneous imaging in I filter centered at 803 nm [O37] Imaging field-of-view = 6 sq. arcmin [O37] Not possible to execute in parallel given sky distribution of exoplanet target stars and length of exoplanet science exposures [O37]	Diameter of telescope aperture ≥ 15 m [O37]
	SO22: Study the interior morphology of galaxies at moderate redshift at ~ 100 pc scales	PP38: Detect individual star-forming clusters in galaxies at $z \sim 1 - 2$	O38: Images of 12 blank sky fields in the B and V band with depth to detect star-forming regions with AB = 30 mag at SNR~25 Obtain I, J, and H band images of same fields at similar depth	Imaging in two broadband filters centered near 390 nm and 606 nm [O38] Imaging field-of-view ≥ 6 sq. arcmin [O38]	Imaging in B and V filters centered at 390 and 606 nm [O38] Imaging field-of-view = 6 sq. arcmin [O38] Appears possible to execute in parallel	Diameter of telescope aperture ≥ 8 m [O38]

Complete LUVOIR-B Science Traceability Matrix						
		Scientific Requirements				
Signature Science Case	Science Objectives	Physical Parameters	Observables	Instrument Requirements	Projected Performance	Mission Requirements
				Execute in parallel with exoplanet direct observations [O38]	given sky distribution of exoplanet target stars and length of exoplanet science exposures [O38]	
	SO23: Determine the star formation and metallicity histories of different types of large galaxies	PP39: Measure the age and metallicity of resolved stellar populations in nearby large galaxies by detecting the main sequence turnoff in color-magnitude diagrams	O39: Images in V and J bands with depth to detect solar-type stars with $AB \leq 34.5$ at SNR=5 within 4 large galaxies closer than 5 Mpc	Imaging in two broadband filters centered near 550 nm and 1220 nm [O39] Simultaneous imaging in the V and J bands [O39] Imaging field-of-view = 6 sq. arcmin [O39]	Imaging in V and J filters centered at 550 nm and 1220 nm [O39] Simultaneous imaging in the NUV/optical and NIR channels [O39] Imaging field-of-view = 6 sq. arcmin [O39]	Diameter of telescope aperture ≥ 8 m [O39]
SSC12: Stars as the engines of galactic feedback	SO24: Find very massive stars ($M_* > 150 M_\odot$) and assess their impact on star-forming environments and galaxy evolution	PP40: Search for candidate very massive stars (VMSs) in ~11 luminous infrared galaxies and ~4 ultra-luminous infrared galaxies within 150 Mpc	O40: Images of ~15 galaxies in 9 NUV to NIR broad bands and three narrow bands (H- α at 656.3 nm, P- β at 1282 nm, and P- α at 1876 nm) to identify candidate VMSs with $m_{AB} = 28.5$ mag at SNR~20 in each band	Imaging in 9 broadband filters centered between 200 nm and 2190 nm [O40] Imaging in three narrowband filters centered at 656 nm, 1282 nm, and 1876 nm [O40] Imaging field-of-view ≥ 6 sq. arcmin [O40]	Imaging in 9 broadband filters centered between 200 nm and 2190 nm [O40] Imaging in three narrowband filters centered at 656 nm, 1282 nm, and 1876 nm [O40] Imaging field-of-view = 6 sq. arcmin [O40]	Diameter of telescope aperture ≥ 8 m [O40]
		PP41: Measure key diagnostics of VMSs in ~11 luminous infrared galaxies and ~4 ultra-luminous	O41: Spectra of VMSs with $m_{AB}(FUV) \geq 23$ mag in ~15 galaxies at $R \geq 10,000$ and continuum SNR ≥ 10	Multi-object spectroscopy at $R \geq 10,000$ from 120–170 nm [O41]	Multi-object spectroscopy at $R \approx 11,600$ from 100–200 nm (G155L) [O41]	Diameter of telescope aperture ≥ 8 m [O41]

Complete LUVOIR-B Science Traceability Matrix						
		Scientific Requirements				
Signature Science Case	Science Objectives	Physical Parameters	Observables	Instrument Requirements	Projected Performance	Mission Requirements
		infrared galaxies within 150 Mpc Key diagnostics: 1. CIV (1550 Å) and NV (1240 Å) P Cygni profiles 2. Broad He II (1640 Å) emission 3. Blue-shifted OV (1371 Å) wind absorption 4. Absence of SiIV (1400 Å) P Cygni emission / absorption	per resolution element from 120–170 nm	Spectroscopic field-of-view ≥ 4 sq. arcmin [O41]	Spectroscopic field-of-view ≈ 4 sq. arcmin [O41]	Telescope mirror reflectivity > 60% at 105 nm [O41]
	SO25: Obtain a census of long period massive binaries in galaxies other than the Milky Way and the Magellanic Clouds to constrain models of star formation and the initial mass function	PP42: Constrain orbital parameters of long period binary stars (via measurements of positions and proper motions) in 7 regions of recent star formation in 5 galaxies within ~1 Mpc	O42: Multi-epoch images in the U, B, V, and I bands, once per year over 5 years, with depth to detect an A0 star at SNR=50	Imaging in four broadband filters centered near 365 nm, 445 nm, 550 nm, and 806 nm [O42] Imaging field-of-view ≥ 6 sq. arcmin [O42]	Imaging in U, B, V, and I filters centered at 365 nm, 445 nm, 550 nm, and 806 nm [O42] Imaging field-of-view = 6 sq. arcmin [O42]	Diameter of telescope aperture ≥ 8 m [O42, O43] Telescope mirror reflectivity > 60% at 105 nm [O43]
		PP43: Identify the spectral types and measure wind properties for stars in previous row	O43: Single-epoch spectra with $R \sim 10,000$ and SNR~10 from 100–400 nm	Multi-object spectroscopy at $R \geq 10,000$ from 100–400 nm [O43] Spectroscopic field-of-view ≥ 4 sq. arcmin [O43]	Multi-object spectroscopy at $R \approx 11,600$ from 100–200 nm (G155L) and $R \approx 28,000$ from 200–400 nm (G300M) [O43] Spectroscopic field-of-view ≈ 4 sq. arcmin [O43]	

APPENDIX D. COMPLETED TECHNICAL TRADES

Over the course of the LUVOIR mission concept study, the study team conducted many trades that evolved both the architecture and the discrete concepts to what is presented in this report. In this appendix, we will review several of the more noteworthy trades that were conducted so that these can inform any future work that is done on LUVOIR.

Those trades include:

- Aperture geometry
- Telescope optical design
- Secondary mirror deployment
- Primary mirror baffle
- Attitude control systems and gimbal architectures

D.1 Aperture geometry

Problem addressed: The geometric layout of the aperture has a significant impact on coronagraph throughput, which in turn has a significant impact on exoplanet yield.

Early layouts for the primary mirror segments were similar to JWST, only with more segments. Early performance evaluations of the expected coronagraph performance—in terms of Earth-like exoplanet yield—used the nominal diameter of the primary mirror with no central obscuration for the secondary mirror. In later analyses, it was revealed, as shown in **Figure D-1**, that the coronagraph throughput is sensitive to the obscuration ratio, defined as

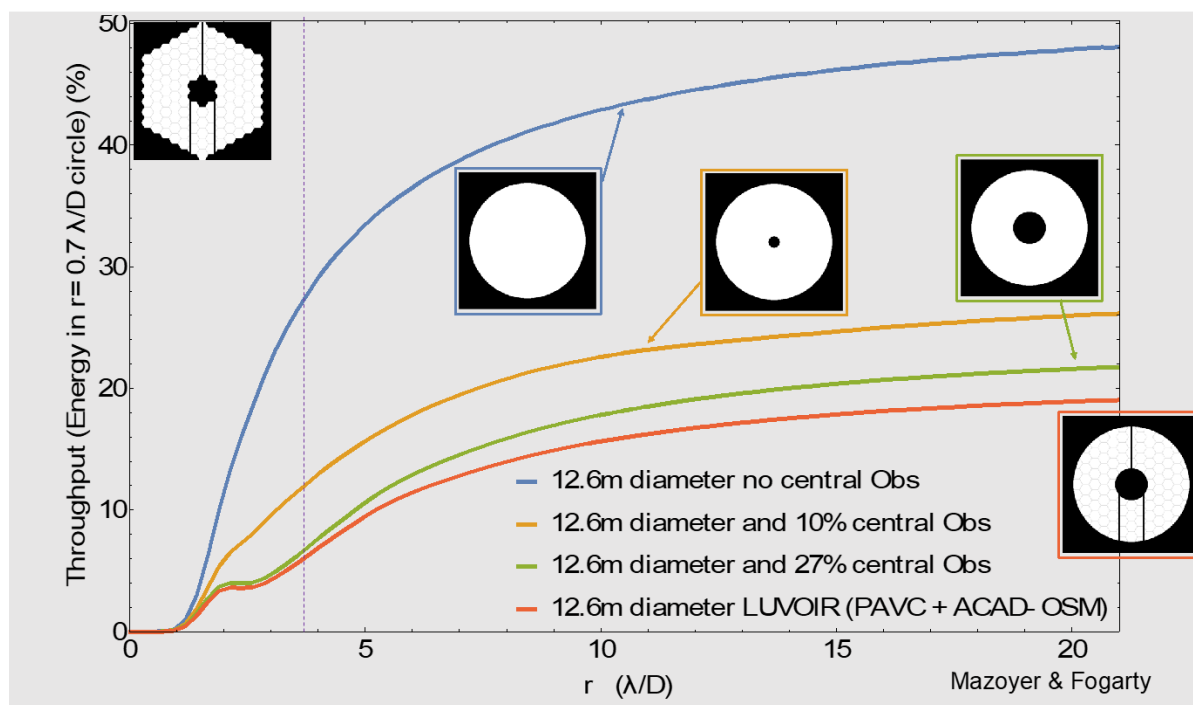


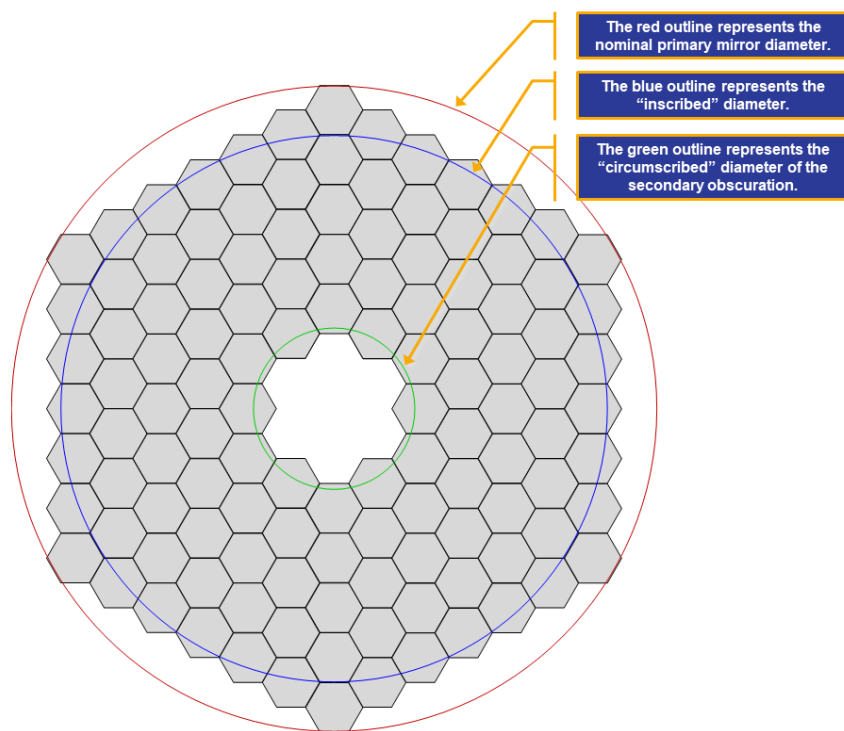
Figure D-1. Coronagraph throughput as a function of primary mirror obscurations. The presence and size of a central obscuration has a significant effect on the throughput, while segmentation and secondary mirror support struts do not.

the circumscribing diameter of the obscuration with the inscribing diameter of the primary mirror. Smaller obscuration diameters provide higher coronagraph throughput, with no obscuration yielding the best performance. It should also be noted that the impact on coronagraph performance due to primary mirror segment gaps, and secondary mirror support structures, was found to be negligible provided that each structure was kept smaller than a nominal value ($<0.05\%$ of the pupil diameter for segment gaps, and $<1\%$ of the pupil diameter for secondary mirror struts).

Figure D-2 below illustrates how the masked outer diameter (“inscribed diameter”) compares to the nominal diameter of the primary mirror. In the early designs, the nominal diameter was $\sim 15\text{m}$ but the inscribing circle that represents the mask over the primary mirror is $\sim 12.6\text{m}$. Complicating the problem is that we had not optimized the size of the central obscuration. In early designs, the diameter of the obscuration circumscribing circle is $\sim 3.7\text{m}$.

The trade involved multiple geometric layouts of the primary mirror hexagonal mirror segments as well as various ways for the secondary mirror to obscure the primary mirror. The performance of each iteration was compared to the performance of a monolithic primary mirror with an optimized central obscuration and a three-point mounting scheme for the secondary mirror. **Figure D-3** below shows some of the variations examined during the trade.

Figure D-4 through **Figure D-6** illustrate how the original layout of the primary mirror segments compares to a layout that more closely represents the final geometric layout of LUV OIR’s primary mirrors.



Early LUV OIR Primary Mirror Layout

Figure D-2. Masked inner and outer diameters

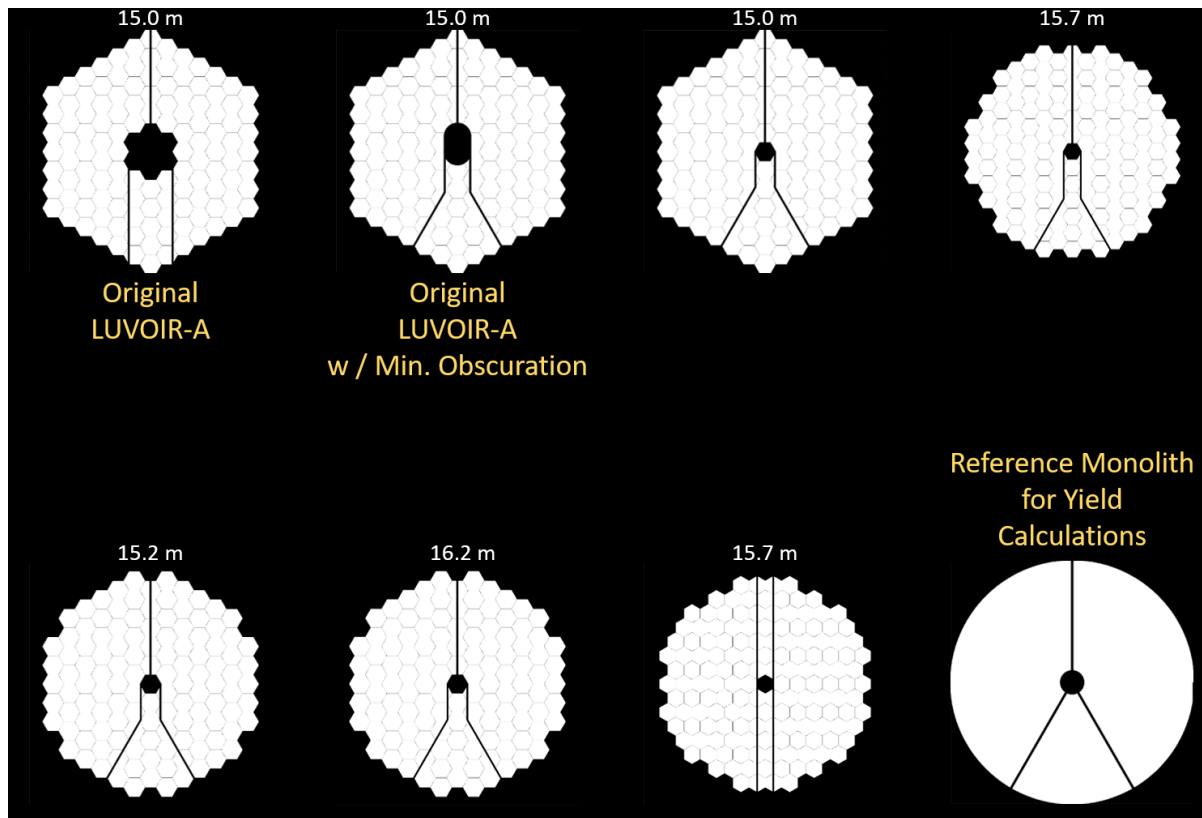


Figure D-3. Variations in the primary mirror pupil geometry studied as part of this trade.

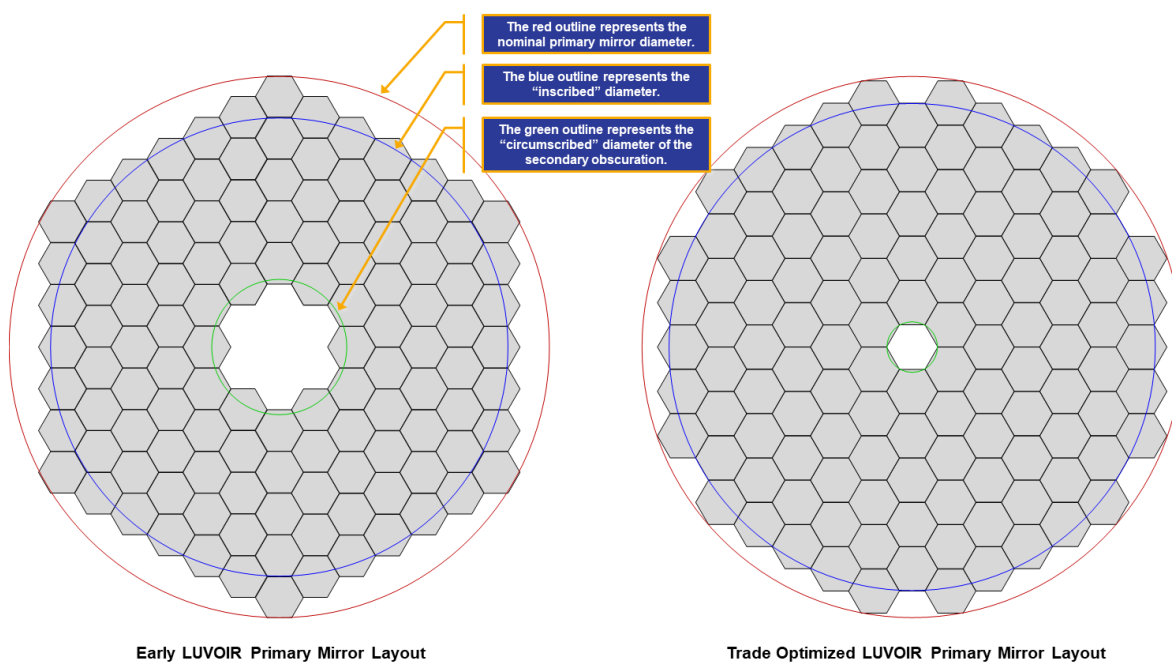


Figure D-4. Comparison of the original LUVOIR primary mirror to a more optimized layout

Table D-1. Results of the trade showing that the current layout is optimized for a given nominal diameter


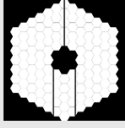
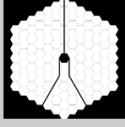
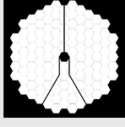
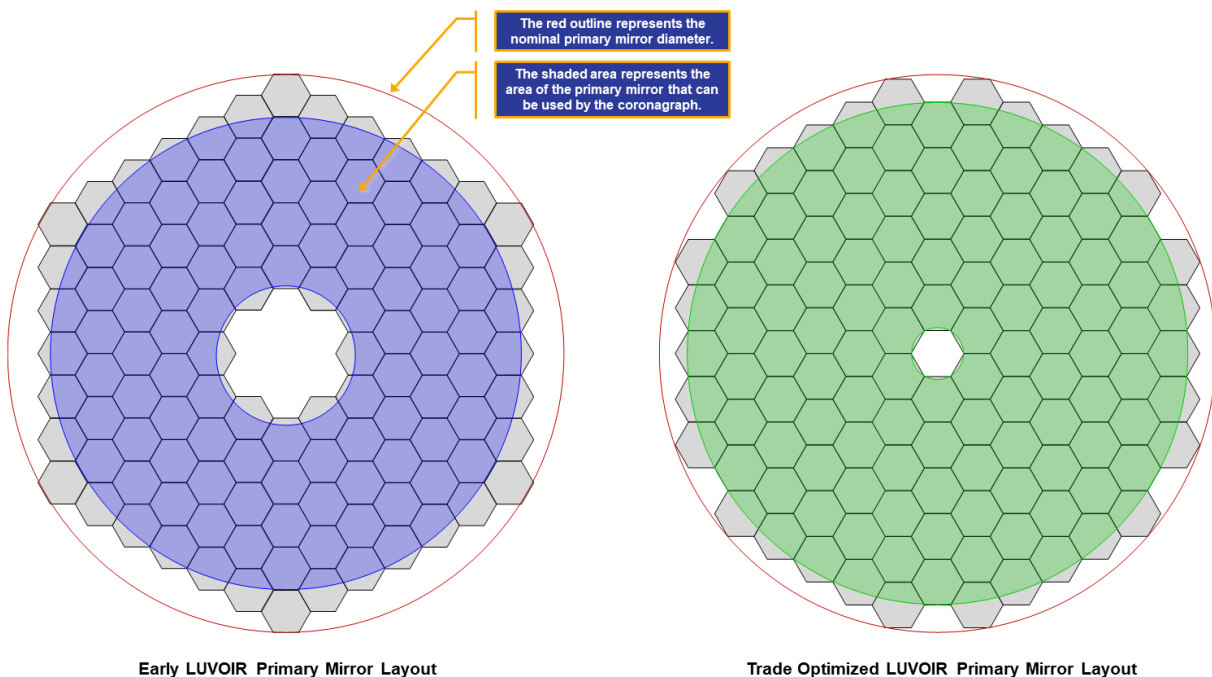
Description of Aperture	Aperture	Performance of Aperture
Monolith with 10% central obscuration Reference Aperture		Reference
Original LUVOIR-A layout		~64% of reference
Geometric layout identical to original LUVOIR-A with a smaller obscuration.		~87% of reference
Geometric layout "rounded"		~95% of reference

Table D-1 shows the trends found during this trade. It should be noted that the size of the primary mirror was also studied during this trade (as can be seen in the variations shown in **Figure D-3**). We attempted to maximize the size of the primary mirror from a packaging point of view. However, it turned out that mass was ultimately the driver for size, not packaging.

**Figure D-5.** Comparison of usable area between the original LUVOIR layout and more optimized version.

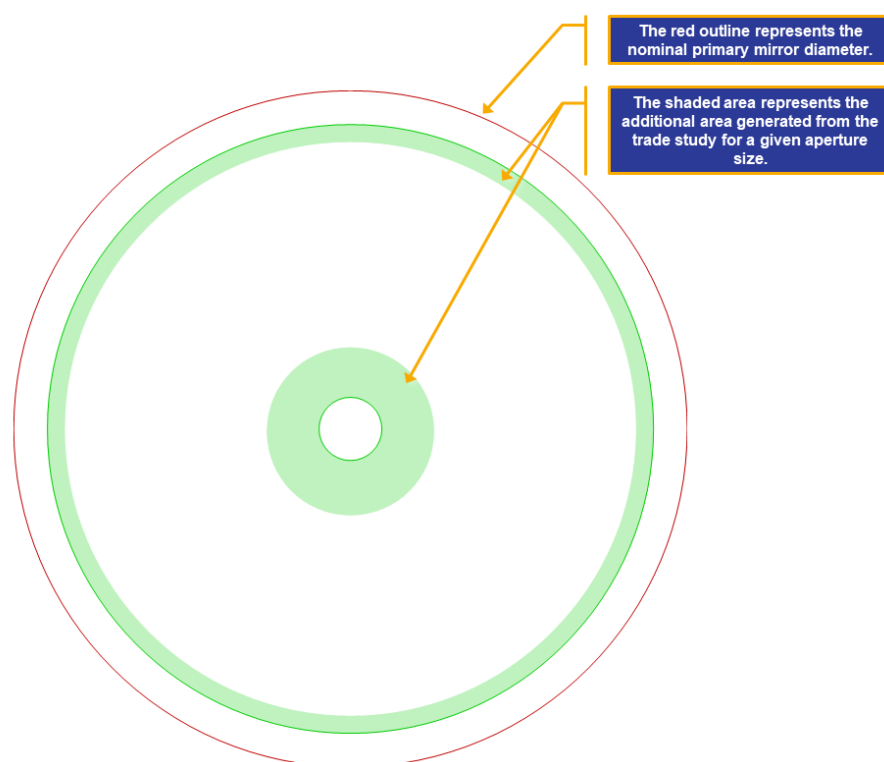
D.2 Telescope optical design

Problem addressed: Different telescope designs are better optimized for different instrument uses. This trade examined the pros and cons of various designs.

During the course of trying to optimize the performance of the telescope—throughput for the coronagraph and collecting area for the other instruments—four basic telescope designs were considered:

- Three-mirror anastigmat (TMA) with a fourth fast steering mirror (FSM).
- Two mirror Cassegrain design with fast steering mirrors inside each instrument as needed.
- Hybrid design with an intermediate Cassegrain focus for the coronagraph and a TMA/FSM for the other instruments.
- Off-axis, unobscured telescope which could take any of the aforementioned forms.

During this trade, the off-axis design was discarded for the larger LUVOIR-A concept for several reasons. First, in order to minimize the polarization aberrations, the secondary mirror would need to be much farther than 20m away from the primary mirror, creating structural issues. Second, the packaging requirements to stow the off-axis mirror would require a much smaller primary mirror than desired for LUVOIR-A. It should be noted that as



Increased Collecting Area for the Coronagraph

Figure D-6. Area gained for the same nominal diameter as a result of this trade

the design for the smaller LUVUOIR-B evolved, this off-axis design was reused to eliminate the central obscuration on the primary mirror, significantly improving the exo-Earth yield of LUVUOIR-B. In this case, because the primary mirror had already been reduced to optimize the mass and overall size of the telescope for a smaller launch vehicle, the distance between the primary mirror and the secondary mirror could be held to ~20 m, which is nearly the same as it is for the larger LUVUOIR-A concept.

The hybrid design was discarded due to throughput issues. Separating the TMA channel from the Cassegrain channel required us to add at least one fold mirror in at least one of the two telescope channels. Three mirrors in the Cassegrain channel wasn't a significant improvement over the four mirrors in the TMA/FSM layout. However, the need for five mirrors in the TMA/FSM channel caused unacceptable degradation in the UV instrument throughput.

As for the TMA vs the Cassegrain options, the TMA was chosen for its versatility and overall instrument accommodation. While the Cassegrain design showed better throughput, the TMA provided the wide field of view (FOVs) required by most of the instruments. Additionally, the need to add FSMs to each of the instruments—as opposed to one FSM for the telescope itself—needlessly increased the complexity of each instrument.

Ultimately, the TMA/FSM design was chosen.

D.3 Secondary mirror deployment

Problem addressed: Prior to completing integrated modeling runs of the secondary mirror support structure, there was a perception that the layout of the structure would not be stiff enough for performance requirements.

During the early design concepts for LUVUOIR-A, we used a JWST-like design for the secondary mirror support structure (SMSS), shown in **Figure D-7**, as well as for the deployment

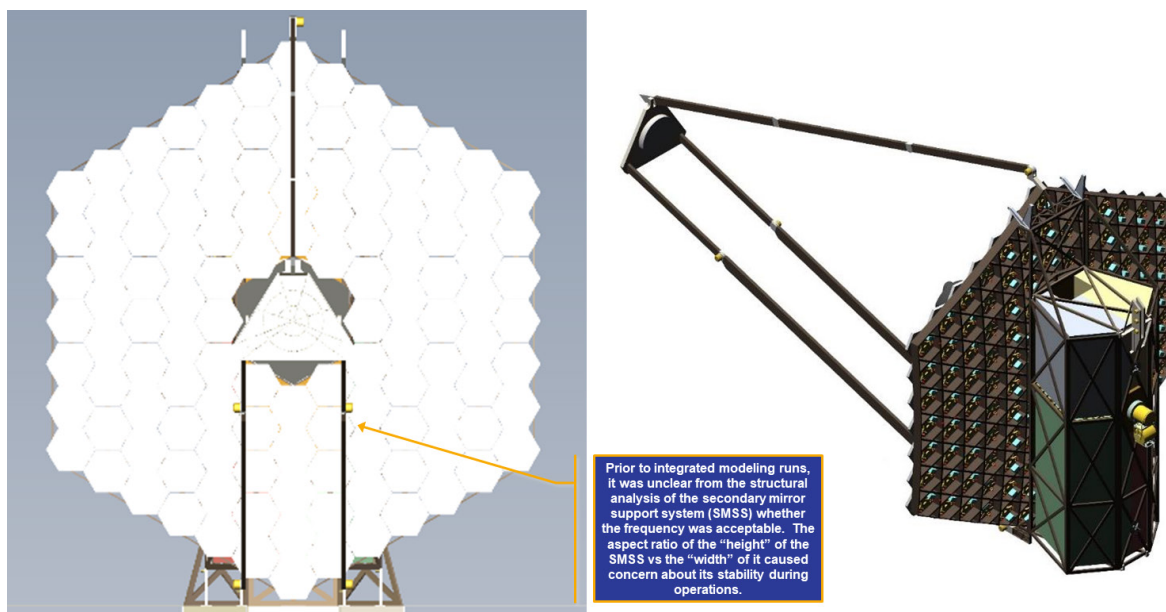


Figure D-7. Early concepts for LUVUOIR used a JWST-like secondary mirror support structure design and deployment scheme

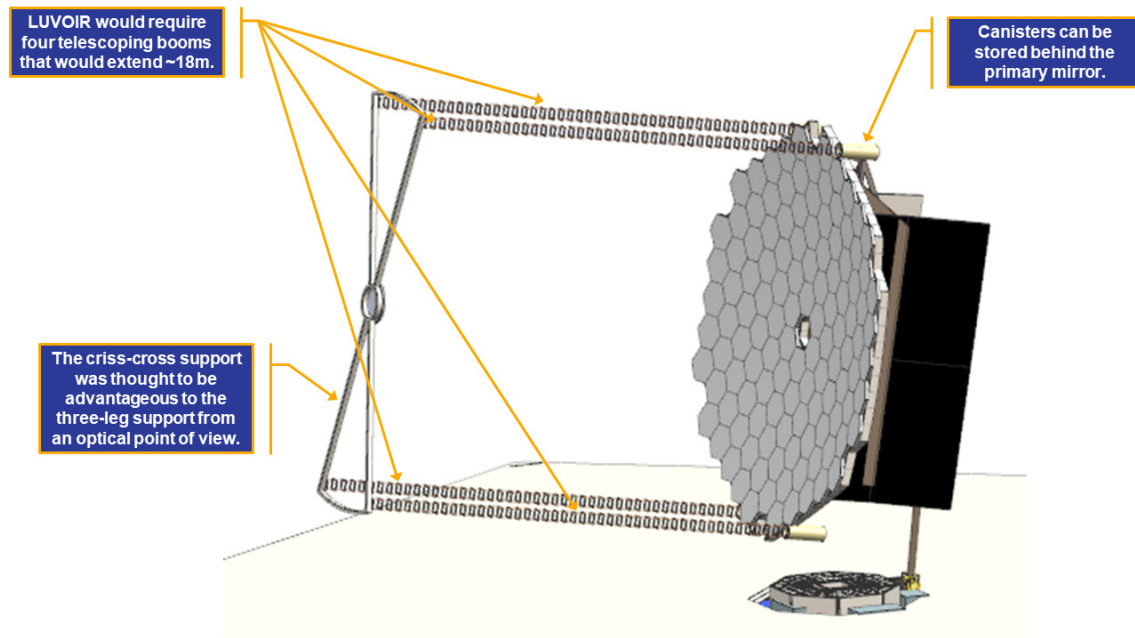


Figure D-8. *Alternative secondary mirror support structure and deployment scheme*

scheme. Given the size of the telescope, it wasn't clear whether that type of design would be stiff enough and so an alternative was explored.

The alternative involved the use of four telescoping booms with the secondary mirror attached to a cross-brace between the four booms as shown in **Figure D-8**. The booms used have been used on many missions for antenna deployments as well as solar sail deployments. Prior to analysis, it was believed that the cross bracing would be advantageous to the JWST-like structure in terms of how much the size of that design needed to be scaled.

Ultimately, structural analysis showed that the deployed frequency of the JWST-like design was higher than that of the deployable boom design. Furthermore, the deployable boom is a lattice structure which made modeling its distortion behavior challenging.

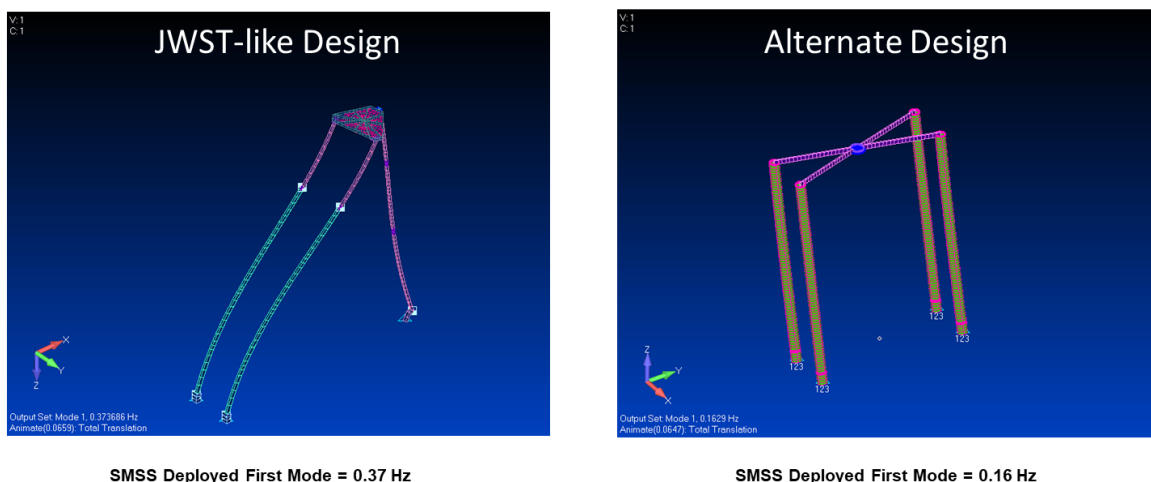


Figure D-9. *Comparison of stiffness between the two design alternatives*

The deployable boom concept was ultimately discarded in favor of a JWST-like SMSS design and deployment scheme.

D.4 Primary mirror baffle

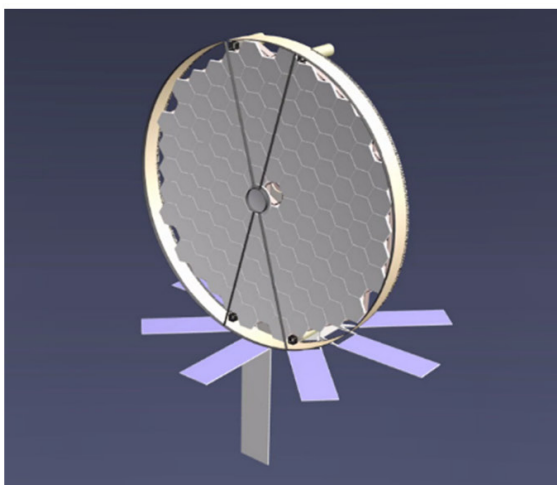
Problems addressed: Stray light and thermal control of the primary mirror.

During the course of the secondary mirror deployment trade study, we thought that we could leverage the deployable boom concept to reduce stray light access to the primary mirror and provide a more stable thermal environment via a large, primary mirror baffle tube. The baffle would be blankets that would be attached to the deployable booms and deploy with the secondary mirror.

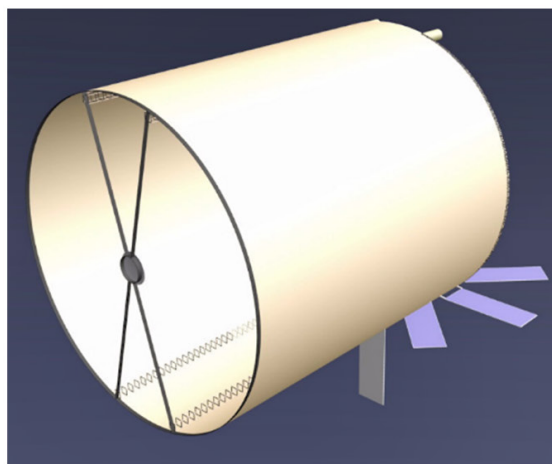
Ultimately, the deployable boom concept was not used for the deployment of the secondary mirror, eliminating the mechanism we thought would enable the primary mirror baffle.

That being said, initial stray light analysis showed insignificant improvement to a primary mirror without the baffle but with a frill around the primary mirror. Additionally, the primary mirror baffle did not eliminate the need for the telescope sunshade although it did marginally reduce the power needed to heat the primary mirror.

There was no demonstrated benefit to having the primary mirror baffle.



Deployable primary mirror baffle in the stowed configuration



Deployable primary mirror baffle in the deployed configuration

Figure D-10. During the secondary mirror deployment trade, the deployable boom concept was used to add a primary mirror baffle

D.5 Attitude control systems and gimbal architectures

Problems addressed: The center of pressure (CP) from the solar wind was offset from the center of gravity (CG) of the telescope requiring several momentum dumps per day.

In early designs of LUV OIR, there was an offset between the center-of-pressure of solar wind on the sunshade and the center-of-mass of the payload. This was primarily caused by the location of the payload gimbal hinge.

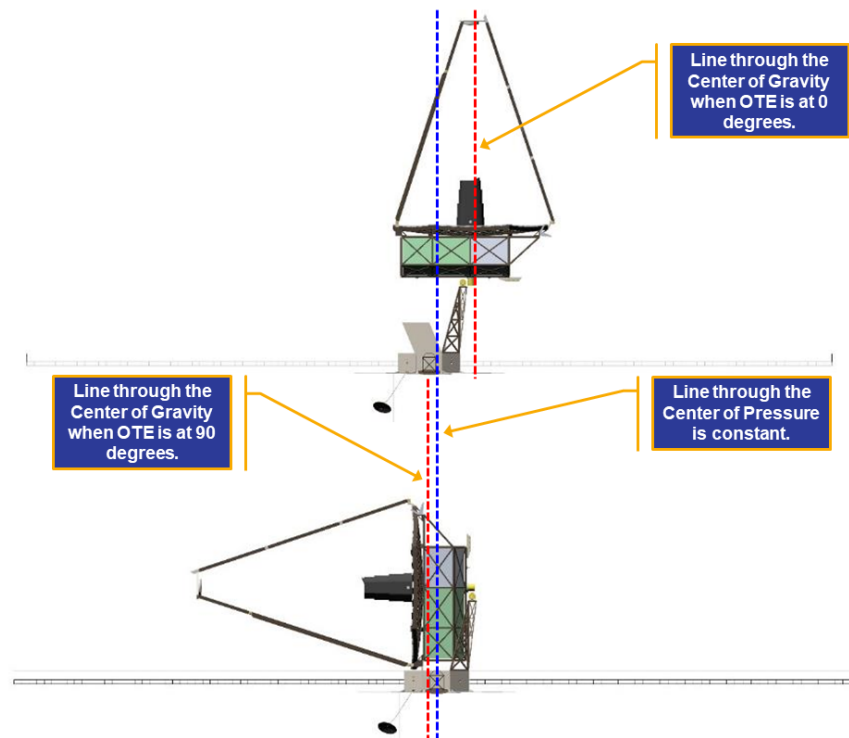


Figure D-11. The center of pressure of the solar wind on the sunshade does not line up with the CG of the payload

Assuming a uniform, symmetric sunshade, the CP is roughly at the geometric center of that shade. However, the gimbal tower, which holds about 2/3 of the observatory mass, is offset from this geometric center by the size of the spacecraft bus. This results in the CG of the payload being offset from the CP as shown in **Figure D-11**. In this configuration, momentum unloading would need to occur up to 2–3 times per day.

During this trade, the feasibility of using gimbals on either end of the telescoping arm, shown in **Figure D-12**, was studied to see if that could more readily line up the CG with the CP, reducing the frequency of momentum dumps.

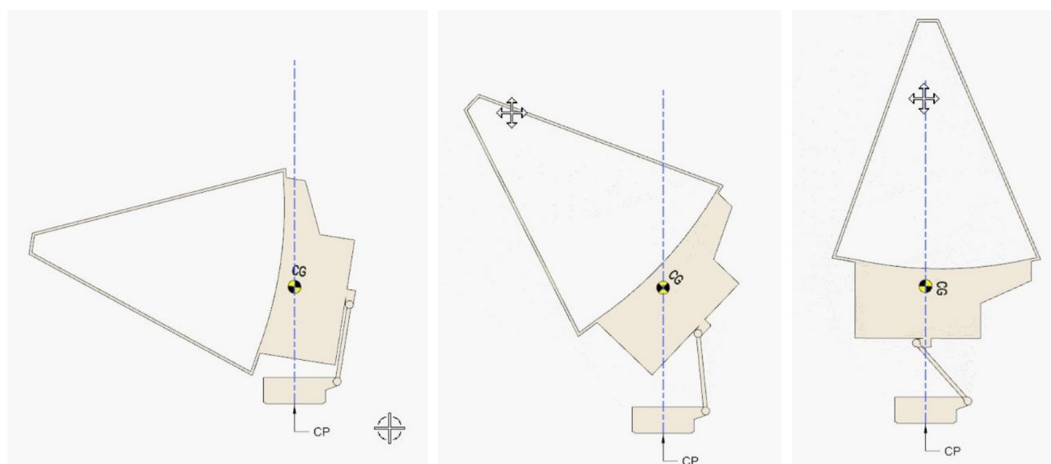


Figure D-12. Early concept showing that the CG and the CP could be aligned with gimbals at either end of the telescoping arm

Ultimately, this trade resulted in a fundamental design change to the telescoping arm and gimbals. The current design now maintains a line of action through the CG of the OTA / BSF / SIs, the CP on the sunshade, and a normal to the Sun that results in fewer momentum dumps (approximately once every three weeks).

APPENDIX E. DETAILED TECHNICAL BUDGETS

This appendix provides more detail on the technical resource allocations, assumptions, and designs presented in this report.

E.1 Mass

As discussed in **Section 12.3.3**, a uniform 30% mass growth allowance (MGA) is applied to the current best estimate mass (CBE) at the assembly level, according to

$$MEV = \frac{CBE}{1 - MGA},$$

where MEV is the maximum expected value. The primary mirror segment assemblies and the secondary mirror assembly each use a 20% MGA, due to the relatively high confidence in those designs based on decades of mirror assembly development. Propellant masses are based on the observatory MEV mass, so MGA is not applied to those values. Margin and reserve is applied to the MEV mass based on the launch vehicle capability.

Table E-1. LUVOIR mass budget for each concept.

Level	Element	Sub-System	Assembly	LUVOIR-A			LUVOIR-B		
				Current Best Estimate Mass [kg]	Mass Growth Allowance [%]	Maximum Expected Value Mass [kg]	Current Best Estimate Mass [kg]	Mass Growth Allowance [%]	Maximum Expected Value Mass [kg]
1	Payload	OTA	Primary Mirror Segment Assemblies (All)	7,616	20%	9,520	2,593	20%	3,241
1	Payload	OTA	PM Backplane Support Structure (PMBSS)	2,165	30%	3,092	813	30%	1,161
2	Payload	OTA	PMBSS, Structure Only	2,057	30%	2,938	692	30%	989
2	Payload	OTA	PMBSS, Hinges & Latches	108	30%	154	106	30%	151
2	Payload	OTA	PMBSS, Edge Sensor Data Router	11	30%	15	15	30%	22
1	Payload	OTA	Backplane Support Frame (BSF)	4,704	30%	6,720	1,997	30%	2,853
2	Payload	OTA	BSF, Structure Only	3,964	30%	5,663	1,538	30%	2,197
2	Payload	OTA	BSF, Radiator Panels	507	30%	725	295	30%	421
2	Payload	OTA	BSF, Wing Launch Locks	139	30%	199	96	30%	137
2	Payload	OTA	BSF, Servicing Hardware	93	30%	132	69	30%	99
1	Payload	OTA	Secondary Mirror Assembly (SMA)	57	20%	71	49	20%	62
1	Payload	OTA	Secondary Mirror Support Structure (SMSS)	188	30%	268	438	30%	626
2	Payload	OTA	SMSS, Structure Only	116	30%	166	416	30%	595
2	Payload	OTA	SMSS, Hinges & Latches	71	30%	102	22	30%	31
1	Payload	OTA	Aft-Optics System (AOS)	188	30%	268	159	30%	227
2	Payload	OTA	AOS, Structure Only	113	30%	162	116	30%	165
2	Payload	OTA	AOS, Optics and Mechanisms	74	30%	106	43	30%	62
1	Payload	OTA	Thermal Management System (TMS)	837	30%	1,196	471	30%	673

Level	Element	Sub-System	Assembly	LUVOIR-A			LUVOIR-B		
				Current Best Estimate Mass [kg]	Mass Growth Allowance [%]	Maximum Expected Value Mass [kg]	Current Best Estimate Mass [kg]	Mass Growth Allowance [%]	Maximum Expected Value Mass [kg]
1	Payload	OTA	Payload Power Distribution Unit (PPDU)	56	30%	81	42	30%	61
1	Payload	OTA	Payload Main Electronics Box (PMEB)	41	30%	58	37	30%	52
1	Payload	OTA	Laser Metrology Electronics Box (LMEB)	69	30%	98	59	30%	84
1	Payload	OTA	Harness	1,559	30%	2,227	559	30%	799
1	Payload	PAS	Vibration Isolation & Precision Pointing System (VIPPS)	75	30%	107	75	30%	107
1	Payload	PAS	Gimbal #1	68	30%	97	46	30%	66
1	Payload	PAS	Gimbal #2	67	30%	95	45	30%	64
1	Payload	PAS	Tower / Articulating Arm	272	30%	388	140	30%	200
1	Payload	HDI	High Definition Imager	671	30%	958	430	30%	615
1	Payload	ECLIPS	Extreme Coronagraph for Living Planetary Systems	807	30%	1,153	780	30%	1,114
1	Payload	LUMOS	LUVOIR Multi-object Spectrograph	874	30%	1,249	544	30%	778
1	Payload	POLLUX	POLLUX	375	30%	536	0	-	0
1	Payload	Misc	Miscellaneous Hardware	898	30%	1,284	376	30%	537
Payload Totals:				21,585	27%	29,465	9,655	28%	13,321
1	Spacecraft	Bus	Structure	1,828	30%	2,611	1,689	30%	2,413
1	Spacecraft	Bus	Thermal Management System (TMS)	72	30%	103	72	30%	103
1	Spacecraft	Bus	Attitude Control System (ACS)	251	30%	359	251	30%	359
1	Spacecraft	Bus	Propulsion System	161	30%	230	398	30%	569
1	Spacecraft	Bus	Command & Data Handling (C&DH)	56	30%	79	56	30%	79
1	Spacecraft	Bus	Communications	69	30%	98	62	30%	89
1	Spacecraft	Bus	Electrical Power System (EPS)	691	30%	987	752	30%	1,074
1	Spacecraft	Bus	Harness	88	30%	126	165	30%	236
1	Spacecraft	Sunshade	Deployable Boom Assemblies	384	30%	549	384	30%	549
1	Spacecraft	Sunshade	Blanket Assemblies	285	30%	408	202	30%	288
1	Spacecraft	Misc	Miscellaneous Hardware	194	30%	278	174	30%	248
1	Spacecraft	Propellant	Propellant	2,137	0%	2,137	1,272	0%	1,272
Spacecraft Totals:				6,216	22%	7,965	5,478	25%	7,280
Observatory Total:				27,801	26%	37,430	15,133	27%	20,602
Maximum Permissible Value (Launch Vehicle Capacity) [kg]:						44,300			37,000
Margin & Reserve [kg]:						6,870			16,398
Margin & Reserve [%]:						15.5%			44.3%
Total Mass Contingency (CBE to MPV) [kg]:						16,499			21,867
Total Mass Contingency (CBE to MPV) [%]:						37.2%			59.1%

Table E-2. *LUVOIR power budget for each concept.*

Level	Element	Sub-System	Assembly	LUVOIR-A						LUVOIR-B					
				Average Power			Peak Power			Average Power			Peak Power		
				Current Best Estimate Power [W]	Power Growth Allowance [%]	Maximum Expected Value [W]	Current Best Estimate Power [W]	Power Growth Allowance [%]	Maximum Expected Value [W]	Current Best Estimate Power [W]	Power Growth Allowance [%]	Maximum Expected Value [W]	Current Best Estimate Power [W]	Power Growth Allowance [%]	Maximum Expected Value [W]
1	Payload	OTA	Primary Mirror Segment Assemblies (All)	4,116	40%	6,861	5,316	40%	8,861	1,486	40%	2,477	3,447	40%	5,746
2	Payload	OTA	PMSA Support and Actuation System	0	-	0	10	40%	17	0	-	0	10	40%	17
2	Payload	OTA	PMSA Thermal System	24	40%	41	24	40%	41	17	40%	28	43	40%	71
2	Payload	OTA	PMSA Mirror Segment Control Electronics	10	40%	17	10	40%	17	10	40%	17	10	40%	17
1	Payload	OTA	Edge Sensor Data Routers	15	40%	25	15	40%	25	21	40%	35	21	40%	35
1	Payload	OTA	Secondary Mirror Assembly (SMA)	70	40%	116	80	40%	133	23	40%	38	33	40%	55
2	Payload	OTA	SMA Support and Actuation System	0	-	0	10	40%	17	0	-	0	10	40%	17
2	Payload	OTA	SMA Thermal System	65	40%	108	65	40%	108	18	40%	30	18	40%	30
2	Payload	OTA	SMA Mirror Control Electronics	5	40%	8	5	40%	8	5	40%	8	5	40%	8
1	Payload	OTA	Aft Optics System (AOS)	75	40%	125	75	40%	125	44	40%	73	44	40%	73
2	Payload	OTA	Tertiary Mirror Assembly	54	40%	90	54	40%	90	23	40%	38	23	40%	38
2	Payload	OTA	Fast Steering Mirror	21	40%	36	21	40%	36	21	40%	36	21	40%	36
1	Payload	OTA	Thermal Management System	1,486	40%	2,477	1,586	40%	2,643	1,242	40%	2,070	1,242	40%	2,070
1	Payload	OTA	Payload Power Distribution Unit (PDU)	2,311	40%	3,852	2,826	40%	4,710	1,346	40%	2,244	2,057	40%	3,428
1	Payload	OTA	Payload Main Electronics Box (MEB)	1,486	40%	2,477	1,852	40%	3,087	799	40%	1,331	1,330	40%	2,217
1	Payload	OTA	Laser Metrology Electronics Box	130	40%	217	130	40%	217	130	40%	217	130	40%	217
1	Payload	PAS	Vibration Isolation and Precision Pointing System	61	40%	102	115	40%	192	61	40%	102	115	40%	192
1	Payload	PAS	Payload Articulation Assembly	25	40%	42	100	40%	167	25	40%	42	100	40%	167
1	Payload	HDI	High Definition Imager	162	40%	270	254	40%	424	142	40%	237	192	40%	320

Level	Element	Sub-System	Assembly	LUVOIR-A						LUVOIR-B					
				Average Power			Peak Power			Average Power			Peak Power		
				Current Best Estimate Power [W]	Power Growth Allowance [%]	Maximum Expected Value [W]	Current Best Estimate Power [W]	Power Growth Allowance [%]	Maximum Expected Value [W]	Current Best Estimate Power [W]	Power Growth Allowance [%]	Maximum Expected Value [W]	Current Best Estimate Power [W]	Power Growth Allowance [%]	Maximum Expected Value [W]
1	Payload	ECLIPS	Extreme Coronagraph for Living Planetary Systems	1,036	40%	1,726	1,060	40%	1,766	1,032	40%	1,720	1,056	40%	1,760
1	Payload	LUMOS	LUVOIR Multi-object Spectrograph	438	40%	729	575	40%	958	365	40%	608	503	40%	838
1	Payload	POLLUX	POLLUX	130	40%	217	130	40%	217	0	-	0	0	-	0
Payload Totals:				11,541	40%	19,235	14,115	40%	23,525	6,716	40%	11,194	10,270	40%	17,117
1	Spacecraft	Bus	Structure	0	-	0	0	-	0	0	-	0	0	-	0
1	Spacecraft	Bus	Thermal Management System (TMS)	2,126	40%	3,544	2,126	40%	3,544	2,475	40%	4,125	2,475	40%	4,125
1	Spacecraft	Bus	Attitude Control System (ACS)	212	40%	353	212	40%	353	212	40%	353	212	40%	353
1	Spacecraft	Bus	Propulsion System	33	40%	55	260	40%	433	33	40%	55	260	40%	433
1	Spacecraft	Bus	Command & Data Handling (C&DH)	114	40%	191	114	40%	191	114	40%	191	114	40%	191
1	Spacecraft	Bus	Communications	217	40%	361	361	40%	602	130	40%	216	361	40%	602
1	Spacecraft	Bus	Electrical Power System (EPS)	71	40%	118	82	40%	137	77	40%	129	91	40%	151
1	Spacecraft	Bus	Harness	51	40%	85	82	40%	137	51	40%	85	82	40%	137
1	Spacecraft	Sunshade	Deployable Boom Assemblies	0	-	0	40	40%	67	0	-	0	40	40%	67
1	Spacecraft	Sunshade	Blanket Assemblies	0	-	0	0	-	0	0	-	0	0	-	0
Spacecraft Totals:				2,824	40%	4,706	3,278	40%	5,463	3,092	40%	5,154	3,635	40%	6,059
Observatory Total:				14,365	40%	23,941	17,393	40%	28,988	9,809	40%	16,348	13,906	40%	23,176
Margin & Reserve [W]:				7,980				9,663				5,449		7,725	
Margin & Reserve [%]:				25%				25%				25%		25%	
Maximum Permissible Value [W]:				31,922				38,650				21,797		30,902	
Total Power Contingency (CBE to MPV) [W]:				17,557				21,258				11,988		16,996	
Total Power Contingency (CBE to MPV) [%]:				55%				55%				55%		55%	

E.2 Power

A uniform 40% power growth allowance is applied to the current best estimate power at the assembly level. An additional 25% margin and reserve is then applied to the maximum expected average and peak powers.

E.3 Wavefront error

Figure E-1, **Figure E-2**, and **Figure E-3** show the top-level wavefront error budget summary for the HDI, ECLIPS, and LUMOS instruments, respectively.

E.4 Optical telescope assembly (OTA) and spacecraft thermal assumptions and budgets

The requirements for the thermal subsystem are defined by the temperatures and stabilities necessary to perform nominal data acquisition to realize LUVOIR's science goals. The driving requirements, therefore, are for the thermal design to achieve the actively-heated control setpoints per component while maintaining the desired thermal stability. The operational temperature and stability requirements for each major component are defined in **Table E-3**.

The following assumptions were made for the LUVOIR modeling and thermal analysis:

E.4.1 Environmental assumptions

LUVOIR orbits the sun 1.5 million km away from the Earth in the second Sun-Earth Lagrange point (SEL2) quasi-halo orbit.

- Infrared radiation and albedo from the Earth and Moon are negligible
- The thermal environment is favorable for passive cooling
- With the stability of the thermal environment at SEL2, steady-state thermal analysis can correctly capture the thermal behavior of LUVOIR during nominal operations
- Deployed sunshade presents a uniform, flat geometric surface
- All surfaces on each layer of the sunshade and all layers form the same angle to the solar vector

E.4.2 Configuration and orientation assumptions

- The coordinate system used in the thermal analysis is that defined for the “vertex” system shown in **Figure E-4**. That is, the origin is located at the primary mirror vertex, with V1 pointing towards the secondary mirror. V3 is aligned with the instrument column and pointing upward, with V2 completing the right-handed system.
- The worst-case steady-state thermal environments for LUVOIR are captured by the following configurations, as defined in **Figure E-5**: (a) sunshade pitch 0°, OTA pitch 90°; (b) sunshade pitch 0°, OTA pitch 0°; (c) sunshade pitch 45°, OTA pitch 90°.

E.4.3 OTA thermal modeling assumptions

- Backplane support frame (BSF) radiators are completely isolated from conductive parasitic heat leaks from the BSF structure.

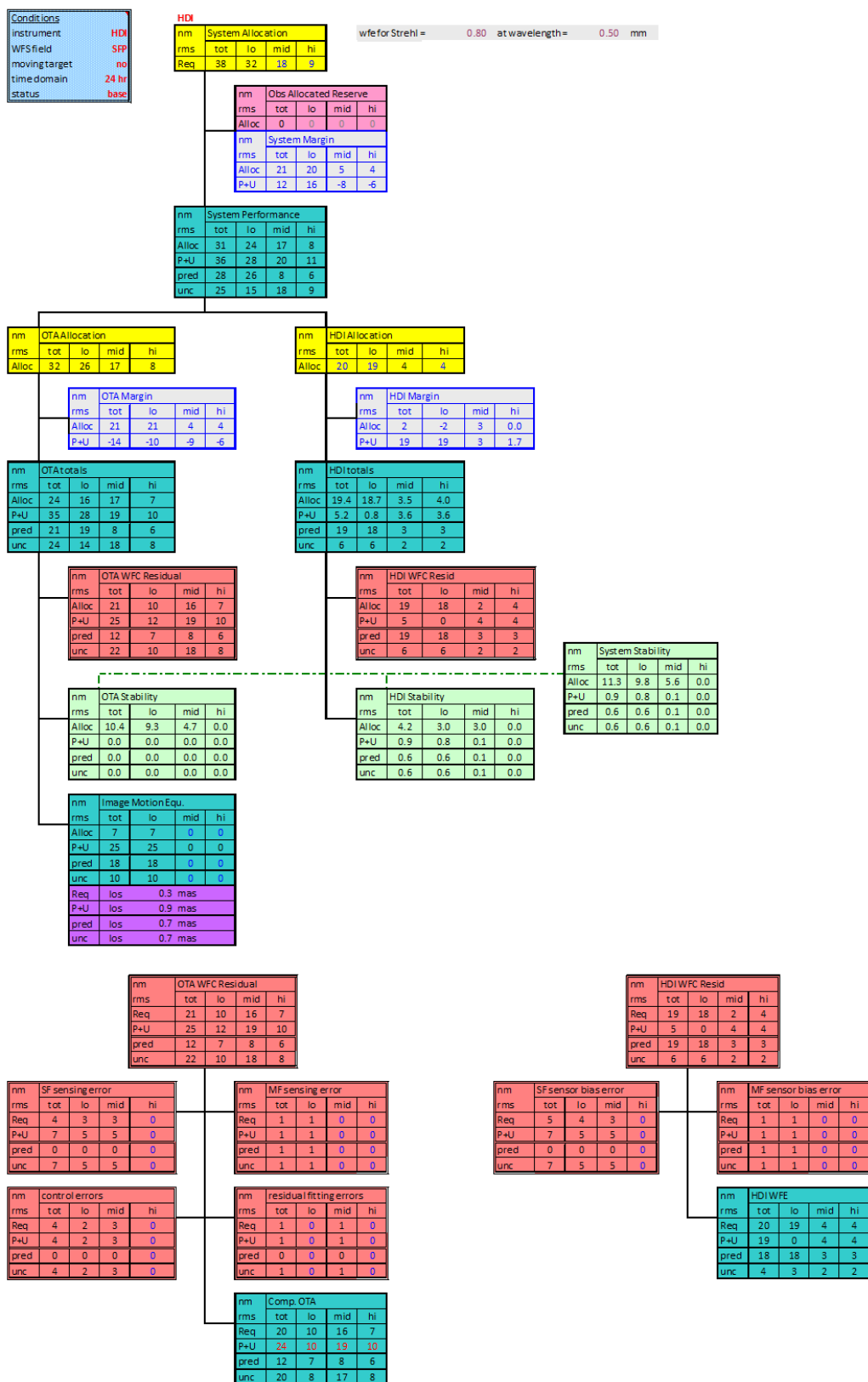


Figure E-1. HDI wavefront error budget, top-level summary.

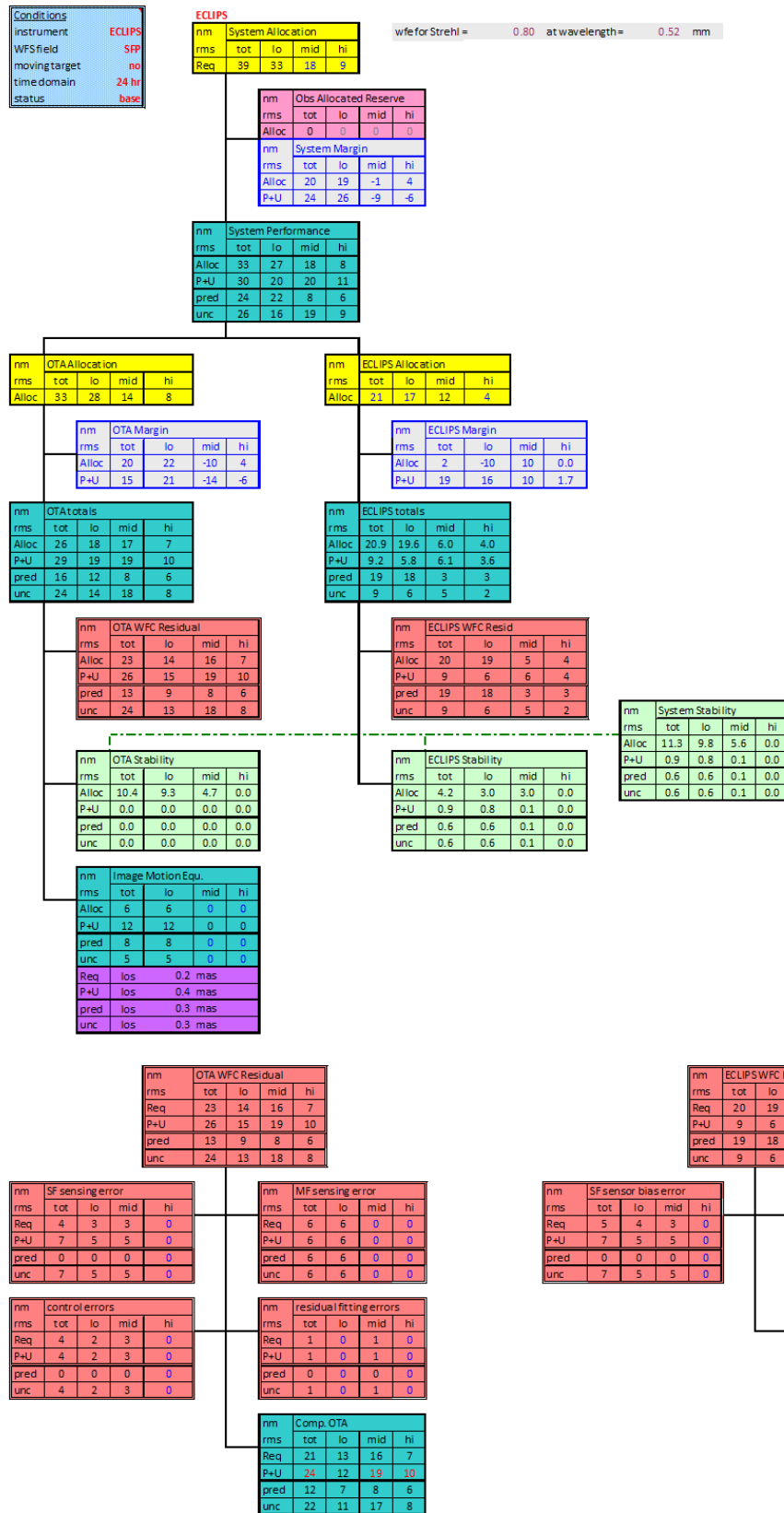


Figure E-2. ECLIPS wavefront error budget top-level summary.

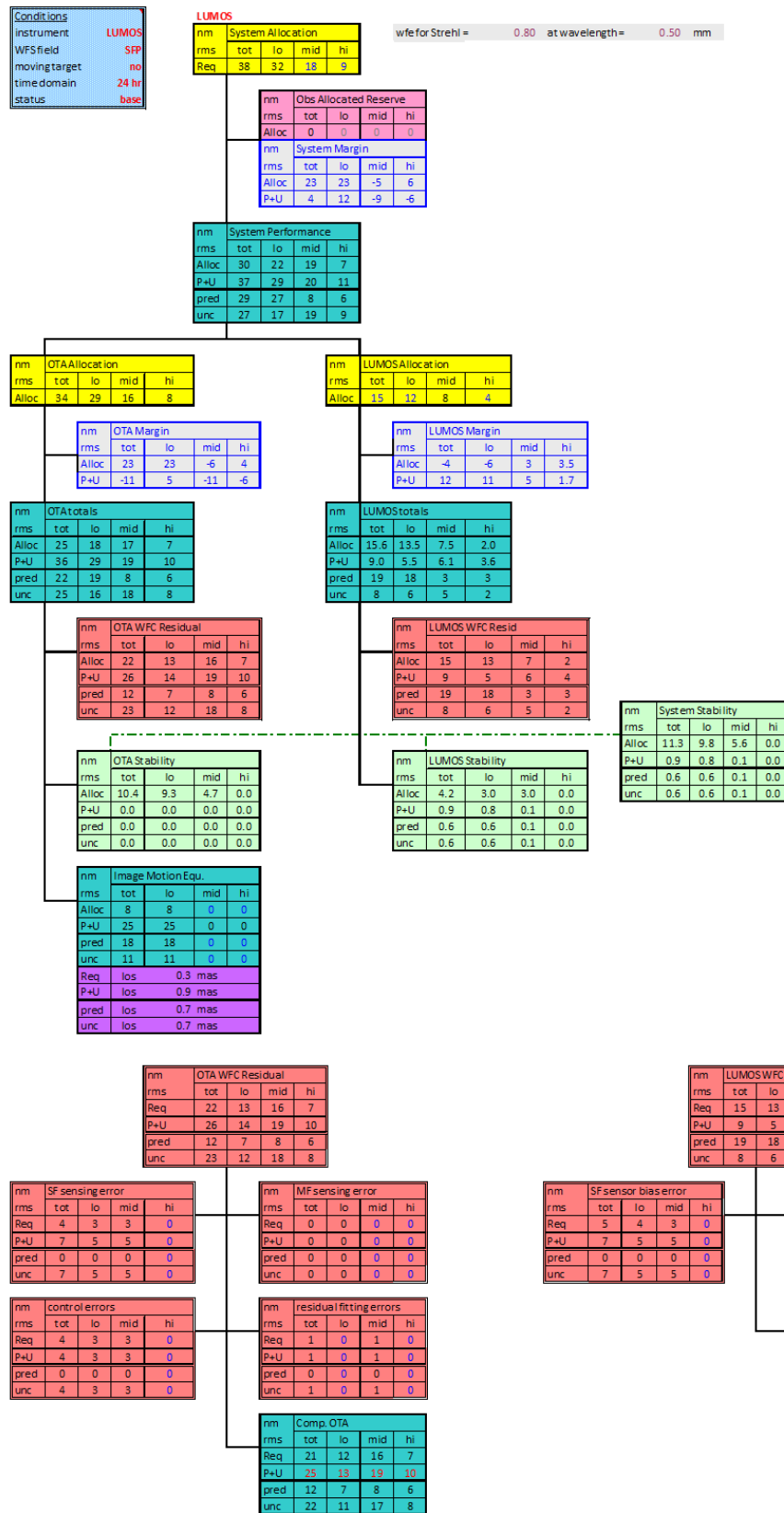


Figure E-3. *LUMOS* wavefront error budget top-level summary.

Table E-3. *Temperature and stability requirements.*

	Temperature Requirement (K)	Temperature Stability (K)
AOS Structure	270 K	± 0.001 K
BSF Structure	270 K	± 0.001 K
PMB Structure	270 K	± 0.001 K
SMA Housing	270 K	± 0.001 K
SMSS Structure	270 K	± 0.001 K
Mirrors (PM, SM, TM, FSM)	270 K	± 0.001 K
Spacecraft (SC) Bus Panels	Operationally Controlled to 270 K	± 3 K
	263–313 K survival	
Power Subsystem Electronics (PSE)	263 – 313 K	± 3 K
Command & Data Handling (C&DH)	263 – 313 K	± 3 K
Attitude Control Electronics (ACE)	263 – 313 K	± 3 K
Propulsion Subsystem	283 – 313 K	± 3 K
Batteries	263 – 313 K	± 3 K
Star Trackers	253 – 323 K	± 3 K
Control Moment Gyroscopes	253 – 333 K	± 3 K
Communications Boxes	249 – 334 K	± 3 K
Roll-Out Solar Arrays	56 – 379 K	

- The 170 K and 270 K radiators on the $\pm V2$ sides are shown as the same surface in the thermal model. These are actually separate surfaces with their own radiator temperatures.
- The BSF radiator blankets do not touch the BSF structure blankets.
- Multi-layer insulation (MLI) on the OTA and instruments perform with $\epsilon^* = 0.02$.
- The primary mirror backplane support structure (PMBSS) internal cavities and the internal space enclosed by composite tubes and housing have no radiative view to space.
- The uneven heat dissipation from the harness in the BSF, PMBSS, and secondary mirror support structure (SMSS) is compensated with heater output. There are no significant spatial temperature gradients within these structures.
- Harness power changes do not impact temperature stability in these structures.
- Heat from the payload main electronics box (PMEB), payload power distribution unit (PPDU), and laser metrology electronics box (LMEB) are completely transferred to their dedicated radiators through loop heat pipes. There is no heat lost which impacts the stability of the BSF heaters.
- Temperature is maintained uniformly with heater control across BSF joints.

E.4.4 Hardware assumptions

- Per heater circuit, there are four heaters, a pair of control sensors, and four corresponding thermostats.

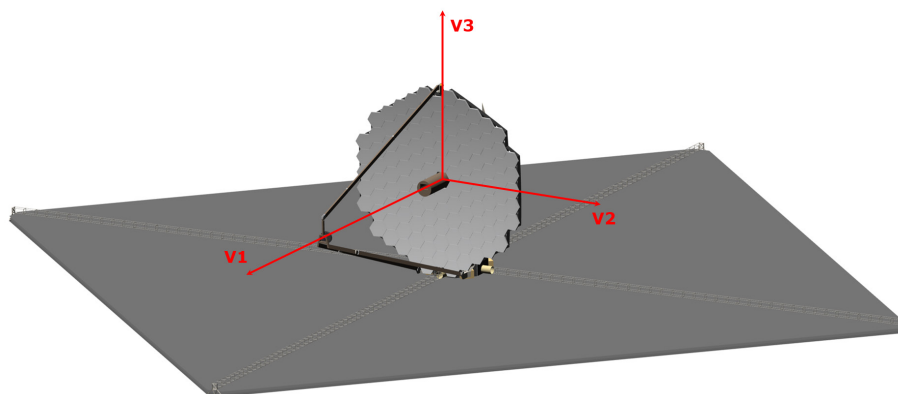


Figure E-4. LUVOIR “V” coordinate system.

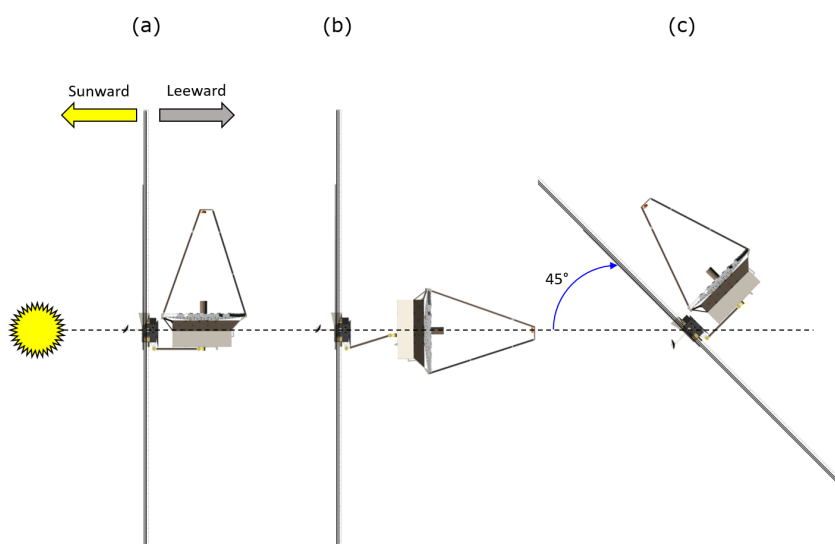


Figure E-5. LUVOIR operational orientations

- The control methodology and heater placement on the BSF, PMBSS, SMSS, secondary mirror assembly (SMA) housing, and aft optics subsystem (AOS) spread heat uniformly with acceptable spatial gradients.
- Radiator panels are aluminum facesheets with aluminum honeycomb core, with embedded heat pipes within the core, aligned in the V3 direction.
- For the fast steering mirror (FSM), the heater is mounted directly to the mirror rear surface.
- Black Kapton (BK) outer layer is used for MLI forward of the PMSAs in the thermal analysis. However, this may be substituted for germanium black Kapton (GBK) or Stamet coating if static charging is an issue.

E.4.5 Mirror thermal control assumptions for the PMSAs, SMA, TMA

- Heater plate has an unobstructed view to the diffuser plate, with emissivity of 0.85.
- Diffuser plate has an unobstructed view to the primary mirror (PM), with emissivity of 0.85.

- Per primary mirror segment assembly (PMSA), SMA, and tertiary mirror assembly (TMA), the rear side of the mirror, diffuser plate, heater plate, and low-emissivity shield (LES) are all spaced 2 cm away from each other.
- The LES walls extend as close to the mirror edge as possible, and it is assumed there are no significant heat losses from the gap between the LES and the mirror.
- For all mirrors, the stability requirement can be achieved with the use of the diffuser and heater plate assembly, as well as software algorithms for active control of heater power output.
- The control methodology and heater placement on the heater plates spreads heat uniformly with acceptable spatial gradients.

E.4.6 Spacecraft thermal modeling assumptions

- Blanketing on all surfaces of the spacecraft (SC) except the sun-facing side of the bus assumes an $\epsilon^* = 0.02$.
- High-temperature blanketing on the sun-facing side of the spacecraft bus assumes an $\epsilon^* = 0.01$.
- Harness heat load is spread evenly throughout the V1 and V2 panels of the spacecraft bus.
- All electronics boxes are mounted to the spacecraft bus panels with Nusil thermal interface material.
- Conduction from the Roll-Out Solar Arrays (ROSA) and sunshade booms to spacecraft bus is negligible.

E.4.7 Interface assumptions

- Conductive and radiative losses through the payload articulation system (PAS) are negligible.
- Energy exchange between the BSF and SC through the PAS interface are insignificant.
- Heat transfer is negligible between the following interfaces: SMSS to SMA Housing, SMSS to PMBSS, PMBSS to BSF, and PMBSS to AOS.
- Heat required for deployment mechanisms is assumed to be encompassed by the total structural heating budget.

E.4.8 Heater power summary

On an observatory level, the key thermal performance metrics evaluated in this study are heater power, radiator area, and mass. Lower values in each metric indicate greater efficiency in the thermal design. The following describes the impacts that each metric has on the effectiveness of the overall thermal design:

- Precise heater control is essential on LUVOIR's OTA and SC bus design to achieve the desired temperatures and stabilities. However, in an application of LUVOIR's size and scope, heater power efficiency is also vital to prevent power budgets from ballooning. Optimizations need to be made for a thermal design that maintains cold bias on the structures for positive heater control, yet insulates the structures enough

to prevent excessive loss of heat to space. In essence, the goal for minimizing heater power is to ensure that as much heat as possible generated by the heaters goes towards heating the structure, rather than being lost to inefficiencies.

- Minimization of radiator area is critical both to save mass as well as preclude the need for deployable radiator structures. Deployable radiators become necessary in case there is insufficient surface area on the BSF to mount fixed radiators, but the addition of deployables greatly increase mass and mechanical complexity, as well as present problems with efficient heat transport and rejection. To minimize radiator area, the parameters to optimize are reducing parasitic heat and achieving lower sink temperatures on the BSF $\pm V2$ and $+V3$ sides. However, another essential facet to consider in radiator area optimization is each radiator's ability to achieve the required sink temperatures for passive cooling of detectors and electronics boxes at 100 K, 170 K, and 270 K.
- Mass of a thermal system is on average 6–11% of the total observatory mass. The stringent temperature control requirements of LUVUOIR, however, require large amounts of thermal hardware, in which a majority of the thermal subsystem mass is consumed by MLI, heaters, and heat straps. In optimization of mass, the goal is to balance the quantity of heaters and MLI needed to achieve the lowest mass and power while still achieving design requirements. Also, the balance of copper heat strap mass versus transport heat pipe mass must be considered to ensure adequate heat transfer to the radiators while minimizing parasitics.

The thermal analysis on the currently optimized design for nominal operations is presented in the tables below. All of the analysis is performed in steady-state, since transient thermal effects during the mission operational phase are expected to be minimal given the stable thermal environment of SEL2. Also, given the high-level conceptual nature of the current study, these models were developed primarily to generate preliminary estimates for radiator area and heater power rather than to provide realistic responses over time to environmental perturbations or configuration changes.

To conservatively size the radiators at this conceptual phase, the 170 K component parasitics have a margin of 50% added, while for the 100 K component parasitics, a margin of

Table E-4. LUVUOIR-A OTA and spacecraft required heater powers.

	Required Heater Power (W)		
	Sunshade 0°, OTA 90°	Sunshade 0°, OTA 0°	Sunshade 45°, OTA 90°
Primary Mirror Backplane Support Structure	488	498	489
PM Segment Heater Plates	2,798	2,914	2,792
BSF	477	497	480
SMSS and SMA	346	348	346
AOS Structure, TM, and FSM	133	144	135
Spacecraft Bus	1,413	2,126	1,602
TOTAL CBE	5,655	6,527	5,844
TOTAL with 40% Heater Margin	9,425	10,878	9,740

Table E-5. *LUVOIR-B OTA and spacecraft required heater powers.*

	Required Heater Power (W)		
	Sunshade 0°, OTA 90°	Sunshade 0°, OTA 0°	Sunshade 45°, OTA 90°
Backplane	164	163	164
PM Segment Heater Plates	890	936	891
BSF	455	451	455
SMSS and SMA	531	534	531
AOS Structure, TM, and FSM	104	107	104
Spacecraft Bus	1,114	2,475	1,064
TOTAL CBE	3258	4666	3209
TOTAL with 40% Heater Margin	5,430	7,777	5,348

Table E-6. *Required radiator area for each LUVOIR concept.*

	LUVOIR-A		LUVOIR-B	
	Required Area (m ²)	Max Sink Temp (K)	Required Area (m ²)	Max Sink Temp (K)
250 K OTA Radiators	66.1	105	34.7	95
150 K OTA Radiators	6.9	105	5.7	95
80 K OTA Radiators	4.4	70	2.4	58
Spacecraft Bus Radiators	9.7	232	11.5	192

100% is added. For the heater powers, a 40% uncertainty margin is included in the predictions, per NASA GSFC GOLD rules (NASA-GSFC-STD-1000G, 2016).

E.4.9 Radiator area summary

Calculated radiator areas based on the heat dissipations and parasitics within each LUVOIR concept are tabulated for each OTA temperature zone and the spacecraft bus in **Table E-6**. For the OTA, LUVOIR-A has enough area on the BSF V2 sides for the 250 K and 150 K radiators, and also enough on the +V3 side to accommodate the required area for the 80 K radiator. On LUVOIR-B, while area on the +V3 side is sufficient for the 80 K radiator, the addition of a fixed V-shaped extension on the aft (-V1) side of the BSF is necessary to provide extra radiator space for the 150 K and 250 K zones. Fortunately, neither concept require the use of deployable radiators for extra area, greatly simplifying their design. Each radiator panel is embedded with a series of spreader heat pipes. Radiator panels exist on each panel of the spacecraft bus that contains an internally-mounted powered component, with MLI covering any areas where a radiator is not desired. All panels with heat-dissipating components also contain embedded ammonia spreader heat pipes to even gradients and prevent box baseplates from overheating.

E.5 Structural analysis

E.5.1 Finite element model description

The finite element model (FEM) of the LUVOIR A observatory deployed configuration is shown in **Figure E-6** and **Figure E-7**. It consists of the 5 major observatory components: secondary mirror assembly (SMA), primary mirror assembly (PMA), backplane support frame

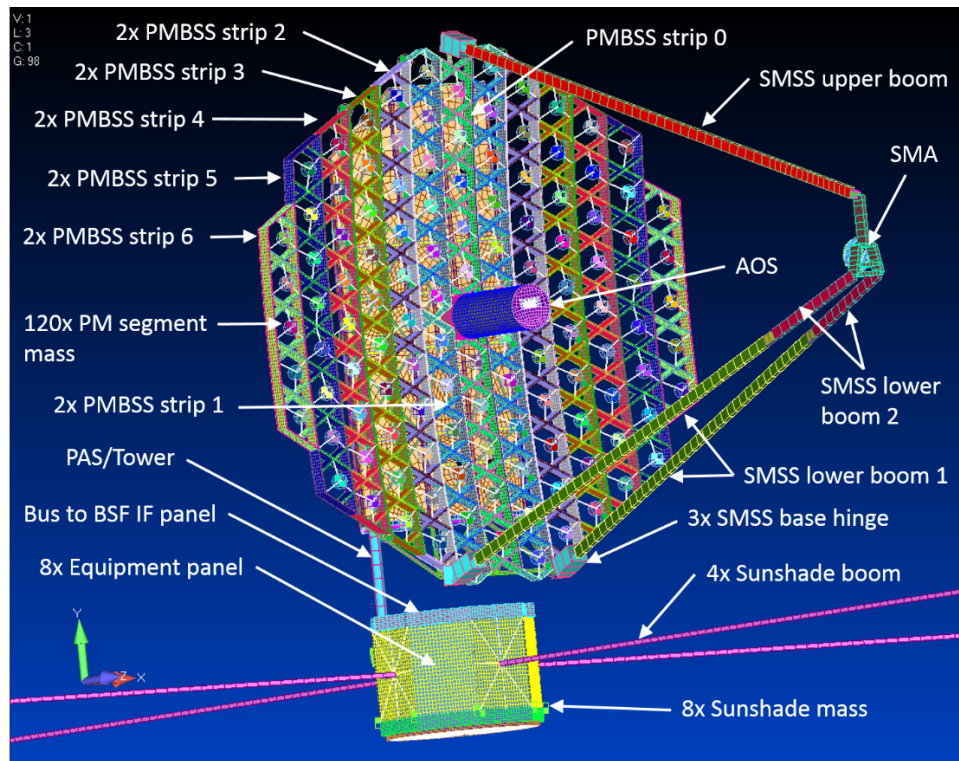


Figure E-6. *LUVOIR-A observatory deployed finite element model (+Z view).*

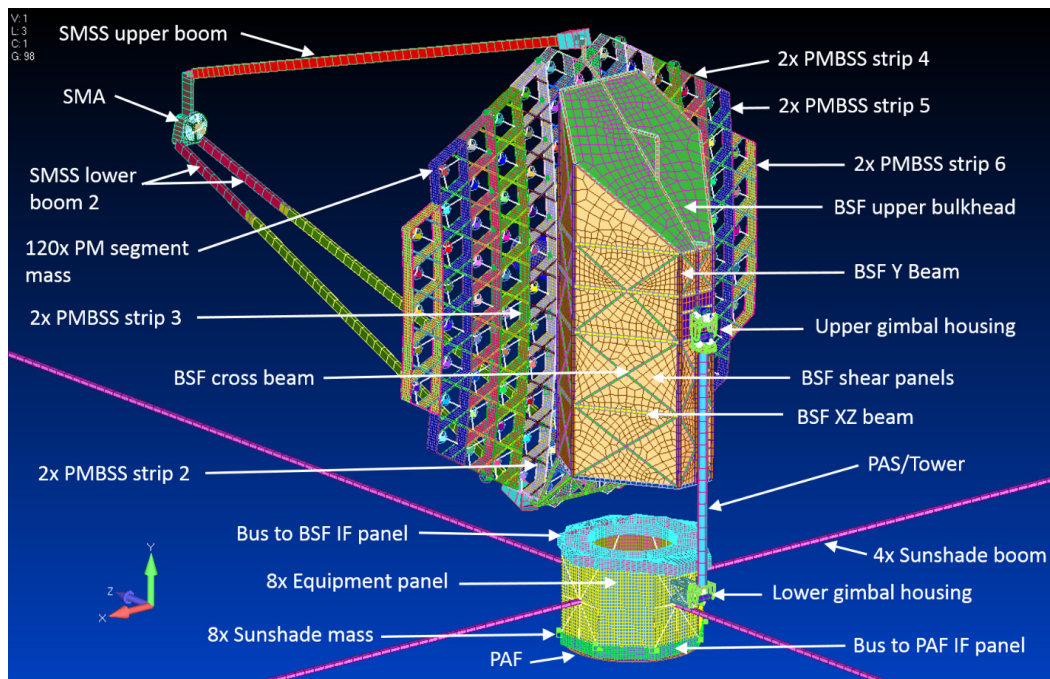


Figure E-7. *LUVOIR-A observatory deployed finite element model (-Z view).*

(BSF), gimbal tower, also called the payload articulation system (PAS), and spacecraft bus. The deployed model currently consists of 83,415 elements and 70,381 nodes.

The finite element model of the LUVOIR A observatory stowed configuration is shown in **Figure E-8** and **Figure E-9**. The stowed model currently consists of 84,427 elements and 69,287 nodes.

Similar models also exist for the LUVOIR-B deployed and stowed observatory configurations. The deployed model currently consists of 107,931 elements and 100,864 nodes. The stowed model currently consists of 96,071 elements and 90,005 nodes.

E.5.2 Structural analysis results

The FEM of the LUVOIR-A observatory in the stowed configuration was optimized to produce a maximum first mode frequency with a mass no greater than 33,000 kg. From that solution the model was tuned using engineering judgement to further reduce the mass and increase the first mode frequency. The result was a stowed observatory with a first lateral mode of 5.1 Hz. and a first axial mode of 17.2 Hz. with a mass of 32,573 kg.

The first lateral mode results from the structure rocking back and forth along the Z-axis. It is a combination of translation of 58% of the observatory mass in the Z-axis and a rotation of 95 % of the observatory mass about the X-axis. The maximum strain energy for this mode, which points to the structure driving the mode, is found in the Y beams of the BSF bending with the weight of the payload.

The first axial mode results from the SMSS and the center wing structure rocking along the Y-axis. It is caused by translation of 8% of the observatory mass in the Y-axis. The maximum strain energy for this mode, which points to the structure driving the mode, is found in the PMBSS wings. **Table E-7** shows modal effective mass fractions for major modes of the observatory stowed configuration. The major modes have greater than 5 % of the observatory mass involved in the mode.

Table E-7. *LUVOIR-A stowed configuration modal effective mass fractions.*

Mode	Frequency [Hz]	X-Axis Translation	Y-Axis Translation	Z-Axis Translation	X-Axis Rotation	Y-Axis Rotation	Z-Axis Rotation
1	5.071	0%	0%	58%	95%	0%	0%
2	5.164	48%	0%	0%	1%	2%	82%
43	6.221	8%	0%	0%	0%	0%	10%
55	8.566	0%	0%	0%	0%	6%	0%
90	10.299	0%	0%	1%	0%	5%	0%
135	12.111	0%	0%	0%	0%	5%	0%
136	12.877	0%	0%	0%	0%	10%	0%
141	13.876	1%	0%	0%	0%	7%	0%
150	16.882	0%	1%	0%	0%	6%	0%
151	17.229	0%	8%	0%	0%	0%	0%
167	20.827	0%	7%	0%	0%	0%	0%
171	21.891	1%	5%	0%	0%	0%	0%
186	24.001	0%	5%	1%	0%	0%	0%
192	24.810	0%	5%	0%	0%	0%	0%

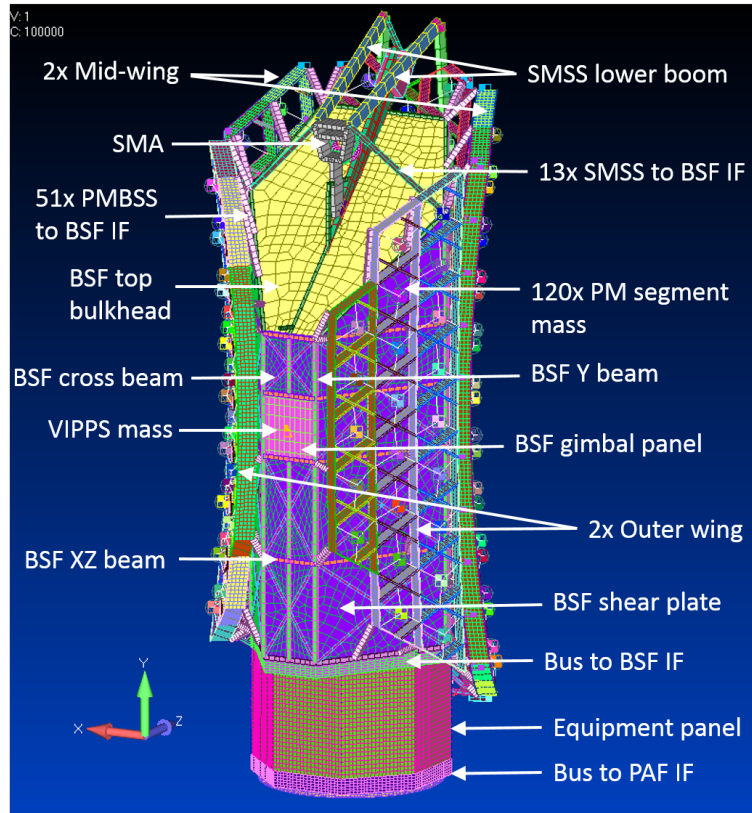


Figure E-8. *LUVOIR-A observatory stowed finite element model (-Z view).*

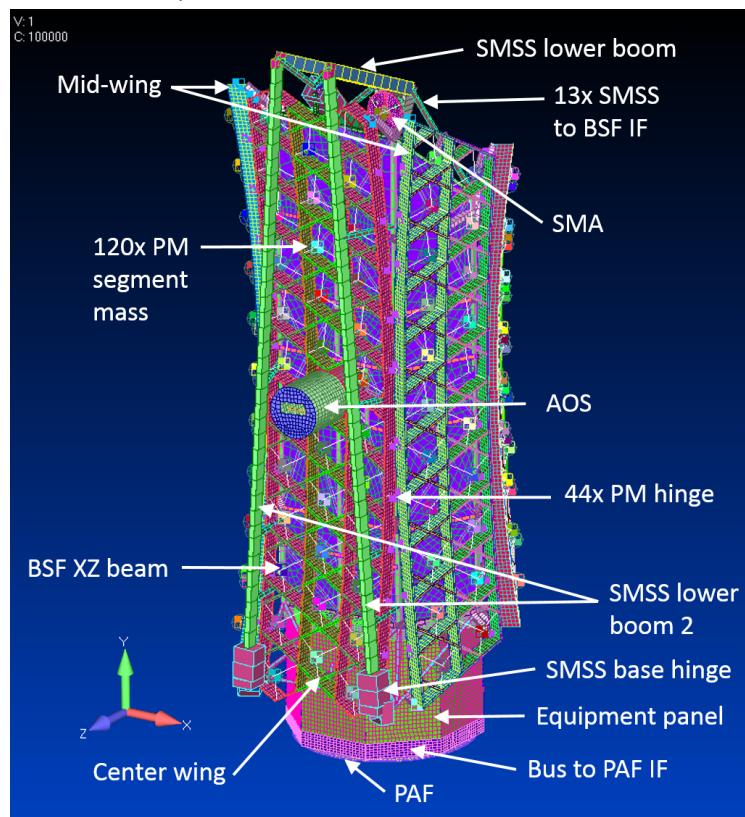


Figure E-9. *LUVOIR-A observatory stowed finite element model (+Z view).*

A normal mode solution with free boundary conditions was then run on the FEM of the LUVOIR-A observatory in the deployed configuration. The model properties matched the dimensions in the stowed model solution above. The result was an observatory with a first spacecraft bus mode of 0.05 Hz. and a first payload mode of 0.8 Hz with a mass of 32,573 kg.

The LUVOIR-A deployed first observatory mode results from the sunshade masts rocking back and forth in the Y-axis. The maximum strain energy for this mode, which points to the structure driving the mode, is found in the bus sunshade beams bending with the inertia of the tip masses at the ends.

The LUVOIR-A deployed first payload mode results from the secondary mirror assembly translating along the X-axis. This mode is driven by the BSF base to SMSS interface beams bending with the mass of the secondary mirror assembly and support structure. The maximum strain energy for this mode is found in the BSF base to SMSS interface beams which shows the structure driving the mode. Future modifications to this structure can be made to increase the frequency or change the behavior of this mode if necessary.

The FEM of the LUVOIR-B observatory in the stowed configuration was optimized to produce a maximum first mode frequency with a mass no greater than 19,000 kg. From that solution the model was tuned using engineering judgement to further reduce the mass and increase the first mode frequency. The result was a stowed observatory with a first lateral mode of 8.0 Hz and a first axial mode of 40.3 Hz with a mass of 19,031 kg.

The first lateral mode results from the structure rocking back and forth along the Z-axis. It is a combination of translation of 48% of the observatory mass in the Z-axis and a rotation of 92% of the observatory mass about the X-axis. The maximum strain energy for this mode, which points to the structure driving the mode, is found in the Y beams at the base of the BSF bending with the weight of the payload.

The first axial mode results from the structure rocking back and forth along the Y-axis. It is a result of translation of 5% of the observatory mass in the Y-axis. The middle bulkhead drumming in the Y-axis is the driver of this mode, which carries the BSF structure and the PMA wings along with it. The modal effective mass fractions of this mode can be found in **Table E-8**.

A normal modes solution with free boundary conditions was then run on the FEM of the LUVOIR-B observatory in the deployed configuration. The model properties matched the

Table E-8. *LUVOIR-B stowed configuration modal effective mass fractions.*

Mode	Frequency [Hz]	X-Axis Translation	Y-Axis Translation	Z-Axis Translation	X-Axis Rotation	Y-Axis Rotation	Z-Axis Rotation
1	8.02	1%	0%	48%	92%	0%	2%
2	8.14	49%	0%	1%	2%	7%	90%
4	13.47	0%	1%	1%	0%	11%	0%
5	13.69	0%	0%	0%	0%	5%	0%
6	14.22	2%	0%	0%	0%	9%	1%
14	19.93	0%	0%	0%	0%	12%	1%
147	40.27	0%	5%	0%	0%	0%	0%
150	40.79	0%	7%	0%	0%	0%	0%

dimensions in the stowed model solution above. The result was an observatory with a first spacecraft bus mode of 0.1 Hz. and a first payload mode of 1.4 Hz. with a mass of 19,031 kg.

The LUVOIR-B deployed first observatory mode results from the sunshade masts rocking back and forth in the Y-axis. The maximum strain energy for this mode, which points to the structure driving the mode, is found in the bus sunshade beams bending with the inertia of the tip masses at the ends.

The LUVOIR-B deployed first payload mode results from the entire payload rotating about the X-axis at gimbal 1. In turn, the secondary mirror assembly rotates about the interface hinge to the BSF. This interface can be stiffened up in future design modifications to reduce the effects of this mode. This mode is ultimately driven by the sunshade beams, so decoupling the spacecraft from the payload will also remove its effects.

E.6 Propulsion

Propulsion schematics for LUVOIR-A and LUVOIR-B are shown in **Figure E-10** and **Figure E-11**.

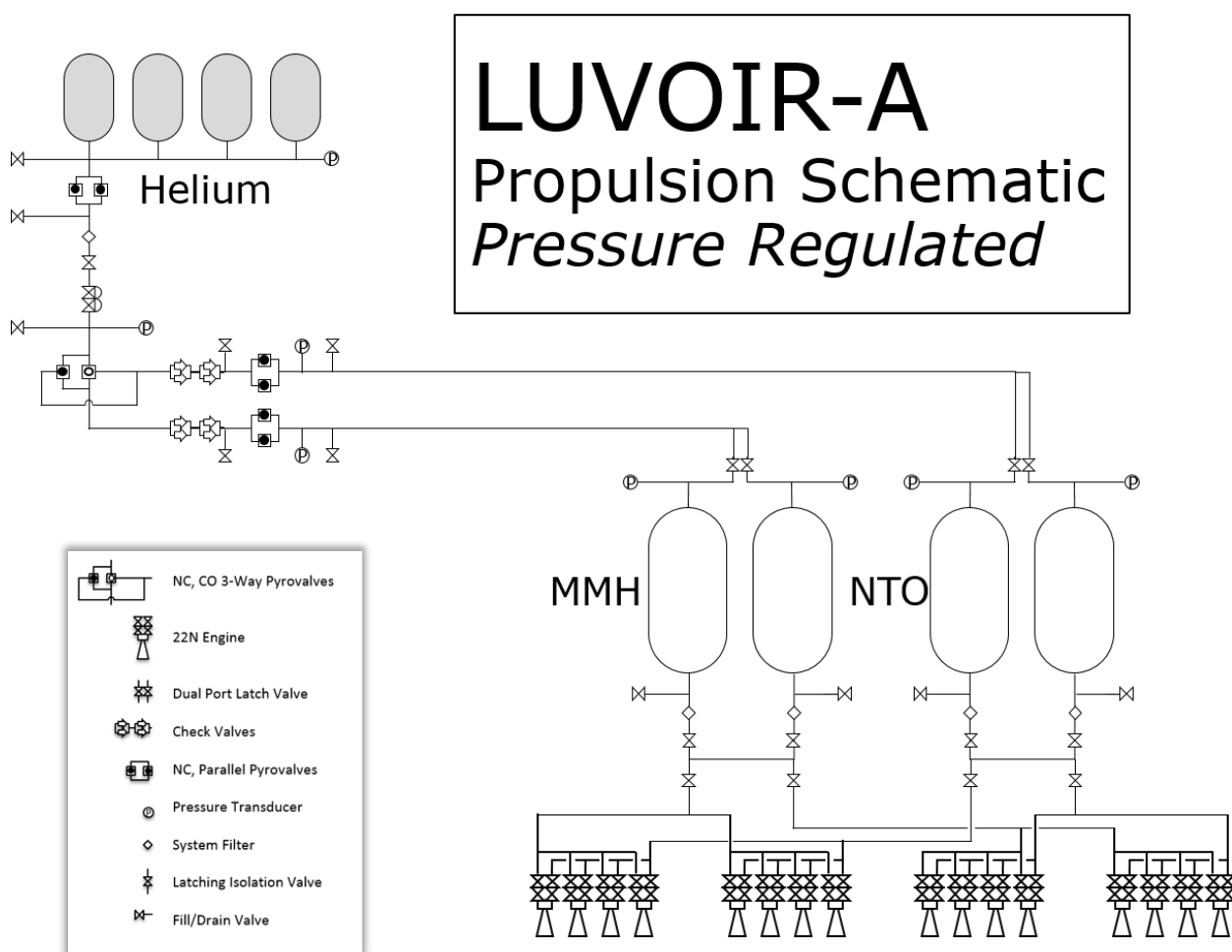


Figure E-10. Propulsion system schematic for LUVOIR-A's pressure-regulated system. MMH: monomethylhydrazine. NTO: Nitrogen tetroxide.

LUVOIR-B

Propulsion Schematic

Blowdown

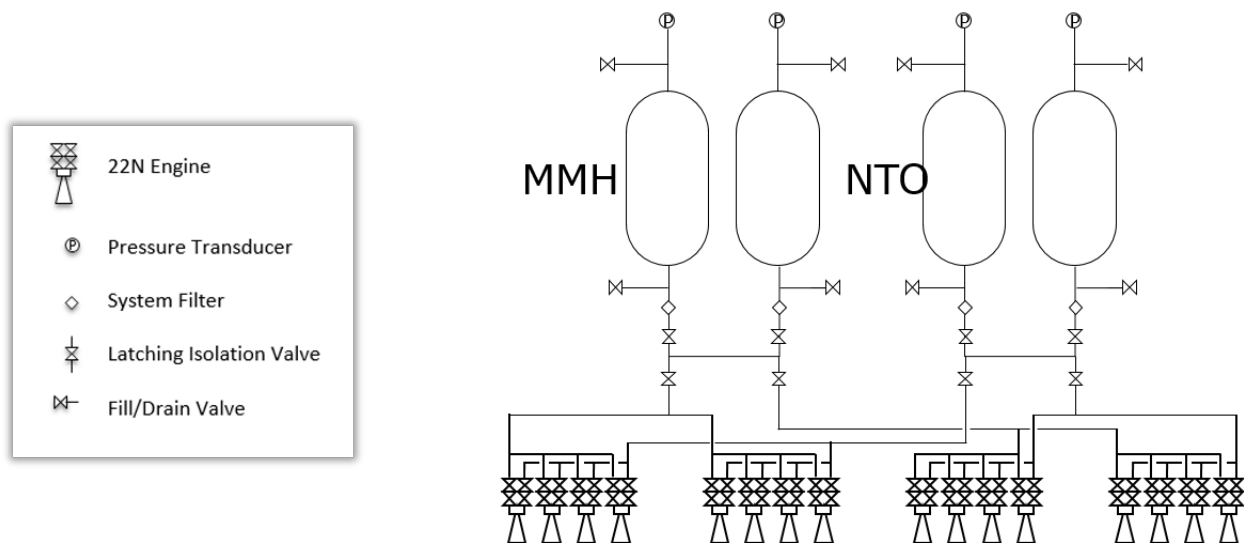


Figure E-11. Propulsion system schematic for LUVOIR-B's blowdown system.

APPENDIX F. HERITAGE

The LUVOIR design incorporates heritage elements from many missions, including the Hubble Space Telescope (HST), James Webb Space Telescope (JWST), and the Wide Field Infrared Survey Telescope (WFIRST). Use of heritage components establishes confidence in the design’s feasibility, as well as cost and schedule realism. Throughout the concept study, the LUVOIR team has sought to take advantage of heritage designs and components to the greatest extent possible to ensure an appropriate level of risk is constrained to truly new items or applications, i.e., technology.

Because LUVOIR is planned to launch in the late 2030s, ostensibly all of the missions we cite will have flight heritage as LUVOIR enters its implementation phase. However, at this phase of our study, we conducted an inheritance review to ensure we understand the scope of effort and magnitude of cost that is either implicit in our assumptions or explicit in our technology-development plan. We will conduct follow-up inheritance reviews in Pre-Phase A and beyond to update our assumptions and technology development plans as needed.

We define three types of heritage in order to be transparent about the risk associated with our assumptions: design, qualification, and flight. **Design heritage** is a form of “future heritage” that leverages hardware design efforts by projects that themselves are early in development, such as WFIRST. Most design heritage hardware has a TRL of 6. Design heritage hardware carries the greatest risk of the three categories, and we attempted to minimize its use in the LUVOIR designs.

Qualification heritage refers to hardware that has been designed, built, and fully flight qualified, but has not yet flown and operated in a space environment. An example of qualification heritage is most of the components in the LUVOIR design that leverage JWST. These components have received significantly more analysis and testing than the design heritage components, and so carry less risk, yet still have not been fully validated in an operational flight environment. Most qualification heritage hardware is TRL 7, however if it would require significant additional engineering to be used on LUVOIR, is assessed at TRL 6 instead.

Flight heritage refers to hardware that has successfully flown and operated in space. The TRL may vary between 7 and 9 depending on how much the flight environment and usage differ from LUVOIR’s. For example, HST clearly has flight heritage, and yet LUVOIR will have to ensure any HST-derived hardware is designed and qualified for the LUVOIR environment and operation. Another example is harnesses. The specific types of cables themselves are all TRL 9, but some degree of engineering is required to determine length, connectors, and routing. Only flight-proven items that are truly “off-the-shelf,” such as launch restraint mechanisms or thermostats, are assessed at TRL 9.

Table F-1 is a comprehensive listing of LUVOIR’s components (down to level 5 or lower, according the Master Equipment Lists) and identifies the heritage type, what mission(s) the heritage is derived from, and the current TRL of the items. Any item in the LUVOIR design that does not fall into one of the three heritage categories is considered part of the technology development effort of LUVOIR, and is listed in **Table F-2**, and included in the technology development plan, discussed in **Chapter 11**.

Table F-1. *LUVOR component-level heritage traceability*

Element	Sub-system	Assembly / Sub-assembly	Component / Item	Type	Sub-type	TRL (FY19)	Inherited From...
Payload	ECLIPS	Apodizing Mask Wheel Assembly	Wheel Mechanism	Heritage	Qualification	7	JWST MIRI Filter Wheel, JWST OSIM Pupil Wheel
Payload	ECLIPS	Calibration Lamp System	Calibration Lamps	Heritage	Flight	7	HST WFC3
Payload	ECLIPS	Control System Processor	Matrix Inversion / Virtex 5 FPGA Boards	Heritage	Flight	7	SpaceCube 2.0
Payload	ECLIPS	Focal Plane Mask Wheel Assy.	Wheel Mechanism	Heritage	Qualification	7	JWST MIRI Filter Wheel, JWST OSIM Pupil Wheel
Payload	ECLIPS	Harness	SpaceWire, 1553, LVDS, etc.	Heritage	Flight	7	Multiple
Payload	ECLIPS	Integral Field Spectrographs	Opto-mechanical Design	Heritage	Design	6	WFIRST CGI
Payload	ECLIPS	Low-order Wavefront Sensor	Low-order Wavefront Sensor	Heritage	Design	6	WFIRST CGI
Payload	ECLIPS	Lyot Mask Wheel Assy.	Wheel Mechanism	Heritage	Qualification	7	JWST MIRI Filter Wheel, JWST OSIM Pupil Wheel
Payload	ECLIPS	Main Electronics Box	LEON3FT Processor Card	Heritage	Qualification	7	PACE/OCI
Payload	ECLIPS	Main Electronics Box	Support Electronics	Heritage	Qualification	7	Mustang Electronics Development at GSFC
Payload	ECLIPS	NIR Channel	Protected Au coating	Heritage	Qualification	7	JWST
Payload	ECLIPS	Opto-mechanical System	Dichroics	Heritage	Flight	7	HST WFPC2, HST WFC3
Payload	ECLIPS	Opto-mechanical System	General Mirrors, Mounts, Benches	Heritage	Design	6-7	WFIRST CGI
Payload	ECLIPS	Selectable Optical Filter Assy.	Filters	Heritage	Flight	7	HST WFC3, JWST NIRCcam
Payload	ECLIPS	Selectable Optical Filter Assy.	SOFA Mechanism	Heritage	Flight	7	HST WFC3
Payload	ECLIPS	Servicing Hardware	Mech. / Data / Power / Thermal Blind Mate	Heritage	Flight	7	HST, ISS, RESTORE-L, Satellite Servicing Projects Division
Payload	ECLIPS	Servicing Hardware	Rails	Heritage	Flight	7	HST, ISS, RESTORE-L, Satellite Servicing Projects Division
Payload	ECLIPS	Thermal Management System	MLI, Heat Pipes, Heaters, Etc.	Heritage	Flight	7-9	OSIRIS-REX, GPM, Spitzer, JWST, HST, LandSat-8, ICESat-2, AURA, LADEE, etc.
Payload	ECLIPS	UV Channel	Enhanced Hot-deposited Al+MgF2	Heritage	Flight	7	ICON, GOLD
Payload	ECLIPS	Various	Flip-in Mechanisms	Heritage	Flight	7	SIRTF/IRAC, GLAS Laser Select mechanism, JWST PIL (Qualification heritage)
Payload	HDI	Calibration Lamp System	Calibration Lamps	Heritage	Flight	7	HST WFC3
Payload	HDI	Channel Select Wheel	Channel Select Wheel Mechanism	Heritage	Flight	7	HST WFC3, JWST NIRCcam Pupil Wheel (Qualification heritage)
Payload	HDI	Channel Select Wheel	Dichroic, Beamsplitter, Reflective elements	Heritage	Flight	7	Multiple
Payload	HDI	Contamination Control	Purge Hardware	Heritage	Flight	7	HST, FUSE
Payload	HDI	Harness	SpaceWire, 1553, LVDS, etc.	Heritage	Flight	7	Multiple
Payload	HDI	Main Electronics Box	LEON3FT Processor Card	Heritage	Qualification	7	Mustang Electronics Development at GSFC

Element	Sub-system	Assembly / Sub-assembly	Component / Item	Type	Sub-type	TRL (FY19)	Inherited From...
Payload	HDI	Main Electronics Box	Support Electronics	Heritage	Qualification	7	JWST
Payload	HDI	NIR Channel	Protected Au coating	Heritage	Qualification	7	JWST
Payload	HDI	Opto-mechanical System	General Mirrors, Mounts, Benches	Heritage	Flight	6-7	Hubble WFC3, WFIRST WFI (Design heritage)
Payload	HDI	Pixel Calibration System	Calibration System Components	Heritage	Design	6	
Payload	HDI	Pupil Imaging Lens	Pupil Imaging Lens	Heritage	Qualification	7	JWST NIRCam
Payload	HDI	Servicing Hardware	Mech. / Data / Power / Thermal Blind Mate	Heritage	Flight	7	HST, ISS, RESTORE-L, Satellite Servicing Projects Division
Payload	HDI	Servicing Hardware	Rails	Heritage	Flight	7	HST, ISS, RESTORE-L, Satellite Servicing Projects Division
Payload	HDI	Spectral Filter Wheel Assys.	Spectral Filter Wheel Mechanisms	Heritage	Flight	7	HST WFC3, JWST NIRCam (Qual. Heritage), JWST MIRI Filter Wheel (Qual. Heritage)
Payload	HDI	Spectral Filter Wheel Assys.	Spectral Filters	Heritage	Flight	7	HST WFC3
Payload	HDI	Thermal Management System	MLI, Heat Pipes, Heaters, Etc.	Heritage	Flight	7-9	OSIRIS-REX, GPM, Spitzer, JWST, HST, LandSat-8, ICESat-2, AURA, LADEE, etc.
Payload	HDI	UVIS Channel	Enhanced Hot-deposited Al+MgF2	Heritage	Flight	7	ICON, GOLD
Payload	LUMOS	Calibration Lamp System	Calibration Lamps	Heritage	Flight	7	HST COS, HST STIS
Payload	LUMOS	Filter Wheel Assy.	Filter Wheel Mechanism	Heritage	Flight	7	HST WFC3, JWST NIRCam (Qual. Heritage), JWST MIRI Filter Wheel (Qual. Heritage)
Payload	LUMOS	Filter Wheel Assy.	Reflective Filters	Heritage	Flight	7	HST COS, HST STIS, Sounding Rocket Missions (SISTINE, FORTIS...)
Payload	LUMOS	Grating Selection Assy.	Grating Selection Mechanism	Heritage	Flight	7	JWST NIRCam (similar to pupil imaging lens mechanism)
Payload	LUMOS	Harness	SpaceWire, 1553, LVDS, etc.	Heritage	Flight	7	Multiple
Payload	LUMOS	High Voltage Power Supply	HVPS	Heritage	Flight	7	Sounding Rocket / CubeSat Missions (CHESS, SISTINE, CUTE, FORTIS, SPRITE, etc.)
Payload	LUMOS	Main Electronics Box	LEON3FT Processor Card	Heritage	Qualification	7	Mustang Electronics Development at GSFC
Payload	LUMOS	Main Electronics Box	Support Electronics	Heritage	Qualification	7	JWST
Payload	LUMOS	Microshutter Control Elec.	RTAX-2000	Heritage	Flight	7	ISS Demo
Payload	LUMOS	Opto-mechanical System	General Mirrors, Mounts, Benches	Heritage	Flight	6-7	HST COS, HST STIS
Payload	LUMOS	Opto-mechanical System	UV Gratings	Heritage	Design	6	Sounding Rocket / CubeSat Missions (CHESS, SISTINE, CUTE, FORTIS, SPRITE, etc.)
Payload	LUMOS	Servicing Hardware	Mech. / Data / Power / Thermal Blind Mate	Heritage	Flight	7	HST, ISS, RESTORE-L, Satellite Servicing Projects Division
Payload	LUMOS	Servicing Hardware	Rails	Heritage	Flight	7	HST, ISS, RESTORE-L, Satellite Servicing Projects Division

Element	Sub-system	Assembly / Sub-assembly	Component / Item	Type	Sub-type	TRL (FY19)	Inherited From...
Payload	LUMOS	Thermal Management System	MLI, Heat Pipes, Heaters, Etc.	Heritage	Flight	7-9	OSIRIS-REX, GPM, Spitzer, JWST, HST, LandSat-8, ICESat-2, AURA, LADEE, etc.
Payload	OTA	AOS	AOS Deployment Mechanism	Heritage	Flight	7	Nothrop Grumman Storable Tubular Extendable Member (STEM) Drive
Payload	OTA	AOS	Fast Steering Mirror	Heritage	Flight	7	JWST
Payload	OTA	BSF	Mech. / Data / Power / Thermal Blind Mate	Heritage	Flight	7	HST, ISS, RESTORE-L, Satellite Servicing Projects Division
Payload	OTA	BSF	Radiators	Heritage	Flight	7	GPM, LandSat-8
Payload	OTA	BSF	Servicing Rails	Heritage	Flight	7	HST, ISS, RESTORE-L, Satellite Servicing Projects Division
Payload	OTA	BSF	Structure	Heritage	Qualification	6	JWST BSF
Payload	OTA	Edge Sensor Data Router	SpaceWire Router Card	Heritage	Design	7	Multiple
Payload	OTA	Harness	SpaceWire, 1553, LVDS, etc.	Heritage	Flight	7	Multiple
Payload	OTA	Main Electronics Box	RAD750	Heritage	Flight	7	Deep Impact, MRO, WorldView-1, Kepler, etc.
Payload	OTA	Main Electronics Box	Support Electronics	Heritage	Qualification	7	Mustang Electronics Development at GSFC
Payload	OTA	PMBSS	Backplane Structure	Heritage	Qualification	6	JWST PMBSS
Payload	OTA	PMBSS	Hook Latch / Catch Assembly	Heritage	Qualification	6	JWST Wing Latches
Payload	OTA	PMBSS	Motorized Hinges	Heritage	Qualification	6	JWST Wing Motorized Hinges
Payload	OTA	PMBSS	Passive Hinges	Heritage	Qualification	6	JWST Wing Passive Hinges
Payload	OTA	PMSA	Coarse / Fine Stage Actuator	Heritage	Qualification	7	JWST Bipod Actuators
Payload	OTA	SM	Coarse / Fine Stage Actuator	Heritage	Qualification	7	JWST Bipod Actuators
Payload	OTA	SM	Latch Assemblies	Heritage	Qualification	7	JWST SMSS Latches
Payload	OTA	SM	Motorized Hinge Assemblies	Heritage	Qualification	7	JWST SMSS Hinges
Payload	OTA	SM	SM Support Structure	Heritage	Qualification	7	JWST SMSS
Payload	OTA	Thermal Management System	MLI, Heat Pipes, Heaters, Etc.	Heritage	Flight	7-9	OSIRIS-REX, GPM, Spitzer, JWST, HST, LandSat-8, ICESat-2, AURA, LADEE, etc.
Payload	PAS	Articulation Arm	Telescoping Arm	Heritage	Flight	7	JWST Deployable Tower Assembly
Payload	PAS	Gimbals	Gimbals	Heritage	Flight	7	ISS Beta Gimbal Assemblies
Payload		Throughout	Launch Locks	Heritage	Flight	9	NEA 9100, NEA 9106B, etc.
Spacecraft	Bus	Attitude Control System	Coarse Sun Sensors	Heritage	Flight	9	Adcole Analog Units
Spacecraft	Bus	Attitude Control System	Control Moment Gyroscopes	Heritage	Flight	7	Honeywell M325

Element	Sub-system	Assembly / Sub-assembly	Component / Item	Type	Sub-type	TRL (FY19)	Inherited From...
Spacecraft	Bus	Attitude Control System	Inertial Reference Unit	Heritage	Flight	9	DTU
Spacecraft	Bus	Attitude Control System	Star Trackers	Heritage	Flight	9	DTU micro-ASC
Spacecraft	Bus	Avionics	C&DH, ACE, P&GD	Heritage	Flight	6	Mustang Electronics Development at GSFC
Spacecraft	Bus	Communication	Coilable Boom System	Heritage	Flight	7	Northrop Grumman
Spacecraft	Bus	Communication	Transponders, Electronics, Antenna, Etc.	Heritage	Flight	9	L-3 Cincinnatti Electronics
Spacecraft	Bus	Electrical Power System	Battery, Electronics, Harness	Heritage	Flight	7	Multiple
Spacecraft	Bus	Solar Array	Roll-out Solar Array	Heritage	Qualification	6	DSS ROSA, ISS
Spacecraft	Bus	Structure	Decks, Walls, Panels	Heritage	Flight	9	LRO
Spacecraft	Bus	Thermal Management System	MLI, Heat Pipes, Heaters, Etc.	Heritage	Flight	7-9	OSIRIS-REX, GPM, Spitzer, JWST, HST, LandSat-8, ICESat-2, AURA, LADEE, etc.
Spacecraft	Sunshade	Blanket Assembly	Blankets, Separation Material	Heritage	Qualification	6	JWST, Standard MLI / SLI
Spacecraft	Sunshade	Deployable Boom Assemblies	Coilable Boom System	Heritage	Qualification	6	Northrop Grumman, Rocco

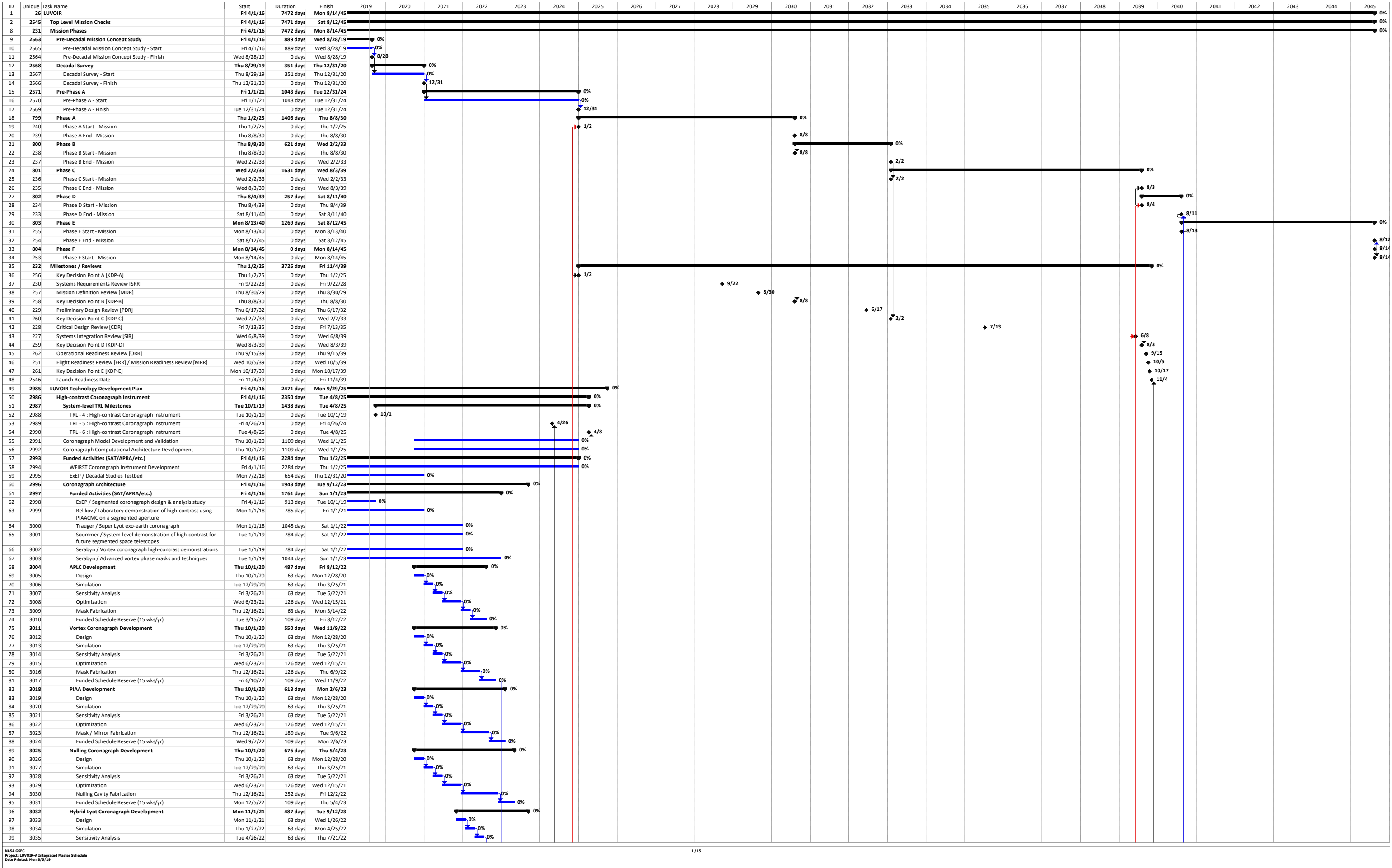
Table F-2. LUVUOIR component level technology listing. See Chapter 11 for a detailed technology development plan.

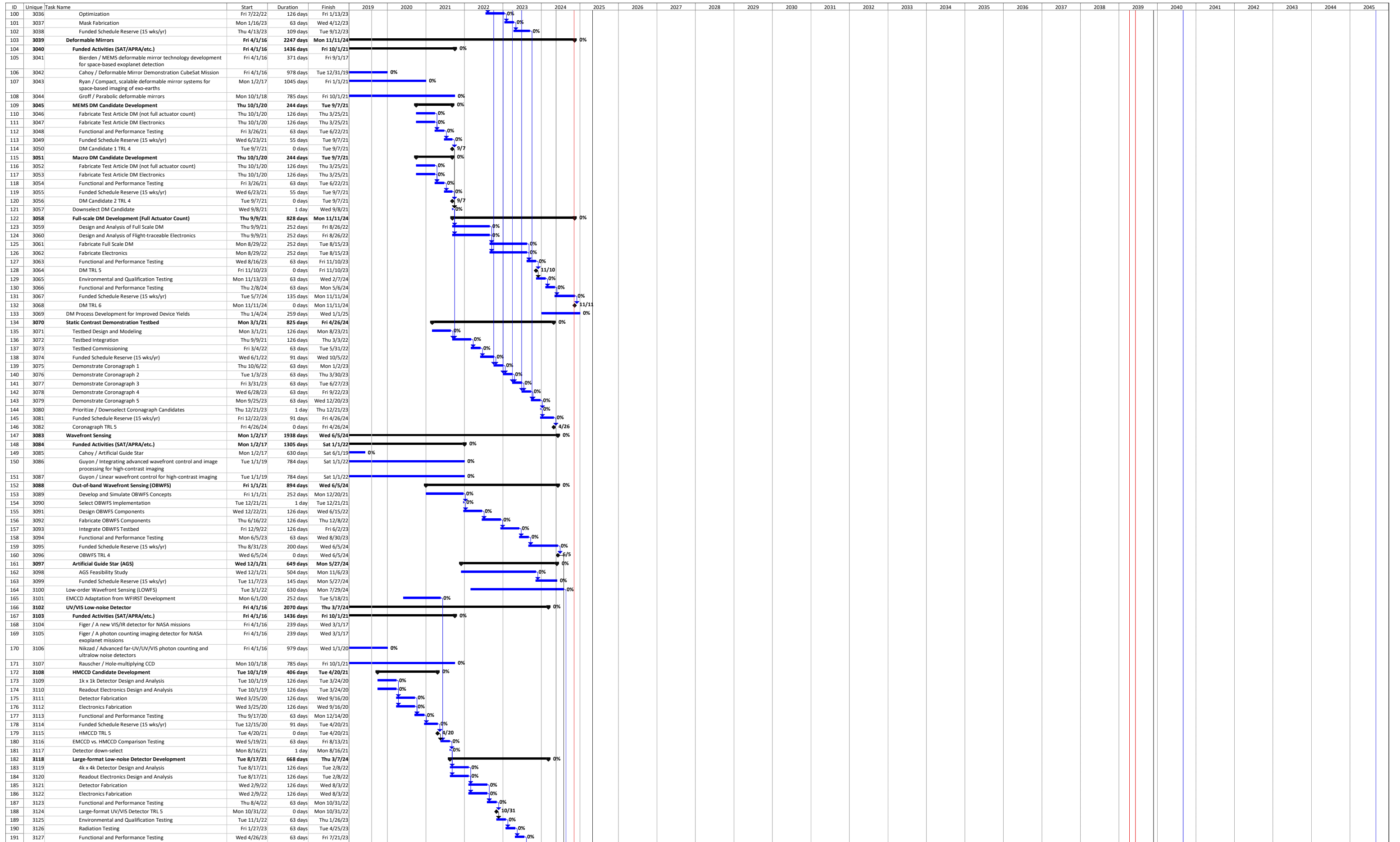
Element	Sub-system	Assembly / Sub-assembly	Component / Item	Type	Sub-type	TRL (FY19)	Technology Development
Payload	ECLIPS	Apodizing Mask Wheel Assembly	Apodizing Masks	Technology	Enabling	4	See Technology Development Plan
Payload	ECLIPS	Camera Detectors	1k x 1k EMCCD	Technology	Enabling	5	See Technology Development Plan
Payload	ECLIPS	Camera Detectors	4k x 4k EMCCD	Technology	Enabling	4	See Technology Development Plan
Payload	ECLIPS	Camera Detectors	H4RG-10	Technology	Enabling	5	See Technology Development Plan
Payload	ECLIPS	Contamination Control	Molecular Absorber Coating (MAC)	Technology	Enhancing	5	See Technology Development Plan
Payload	ECLIPS	Control System Processor	High Performance Space Computer	Technology	Enhancing	4	See Technology Development Plan
Payload	ECLIPS	Focal Plane Mask Wheel Assy.	Focal Plane Masks	Technology	Enabling	4	See Technology Development Plan
Payload	ECLIPS	Lyot Mask Wheel Assy.	Lyot Masks	Technology	Enabling	4	See Technology Development Plan
Payload	ECLIPS	Opto-mechanical System	Deformable Mirrors	Technology	Enabling	4	See Technology Development Plan
Payload	ECLIPS	Out-of-band Wavefront Sensor	Out-of-band Wavefront Sensor	Technology	Enabling	3	See Technology Development Plan
Payload	ECLIPS	VIS Channel	Ag+Al ₂ O ₃ +HfO ₂	Technology	Enhancing	5	See Technology Development Plan
Payload	HDI	Contamination Control	Molecular Absorber Coating (MAC)	Technology	Enhancing	5	See Technology Development Plan
Payload	HDI	NIR Detector	H4RG-10	Technology	Enabling	5	See Technology Development Plan
Payload	HDI	Opto-mechanical System	Freeform Mirrors	Technology	Enhancing	5	See Technology Development Plan
Payload	HDI	UVIS Detector	8k x 8k CMOS Detectors	Technology	Enabling	4	See Technology Development Plan
Payload	HDI	UVIS/NIR Detectors	ACADIA Readout ASIC	Technology	Enhancing	5	See Technology Development Plan
Payload	LUMOS	Contamination Control	Molecular Absorber Coating (MAC)	Technology	Enhancing	5	See Technology Development Plan
Payload	LUMOS	Far-UV Focal Planes	CsI Microchannel Plates	Technology	Enabling	6	See Technology Development Plan
Payload	LUMOS	Far-UV Focal Planes	GaN Microchannel Plates	Technology	Enabling	4	See Technology Development Plan
Payload	LUMOS	Near-UV Focal Planes	8k x 8k CMOS Detectors	Technology	Enabling	4	See Technology Development Plan
Payload	LUMOS	Opto-mechanical System	Freeform Mirrors	Technology	Enhancing	5	See Technology Development Plan
Payload	LUMOS	Opto-mechanical System	Microshutter Array	Technology	Enabling	3	See Technology Development Plan
Payload	LUMOS	Opto-mechanical System	Mirror / Grating Coatings	Technology	Enabling	3	See Technology Development Plan
Payload	OTA	AOS	Tertiary Mirror Substrate	Technology	Enabling	5	See Technology Development Plan
Payload	OTA	AOS	Tertiary, FSM Mirror Coating	Technology	Enabling	3	See Technology Development Plan
Payload	OTA	Laser Metrology Electronics Box	Laser & Phasemeter Electronics	Technology	Enabling	4	See Technology Development Plan
Payload	OTA	PMSA	Edge Sensor	Technology	Enabling	3	See Technology Development Plan

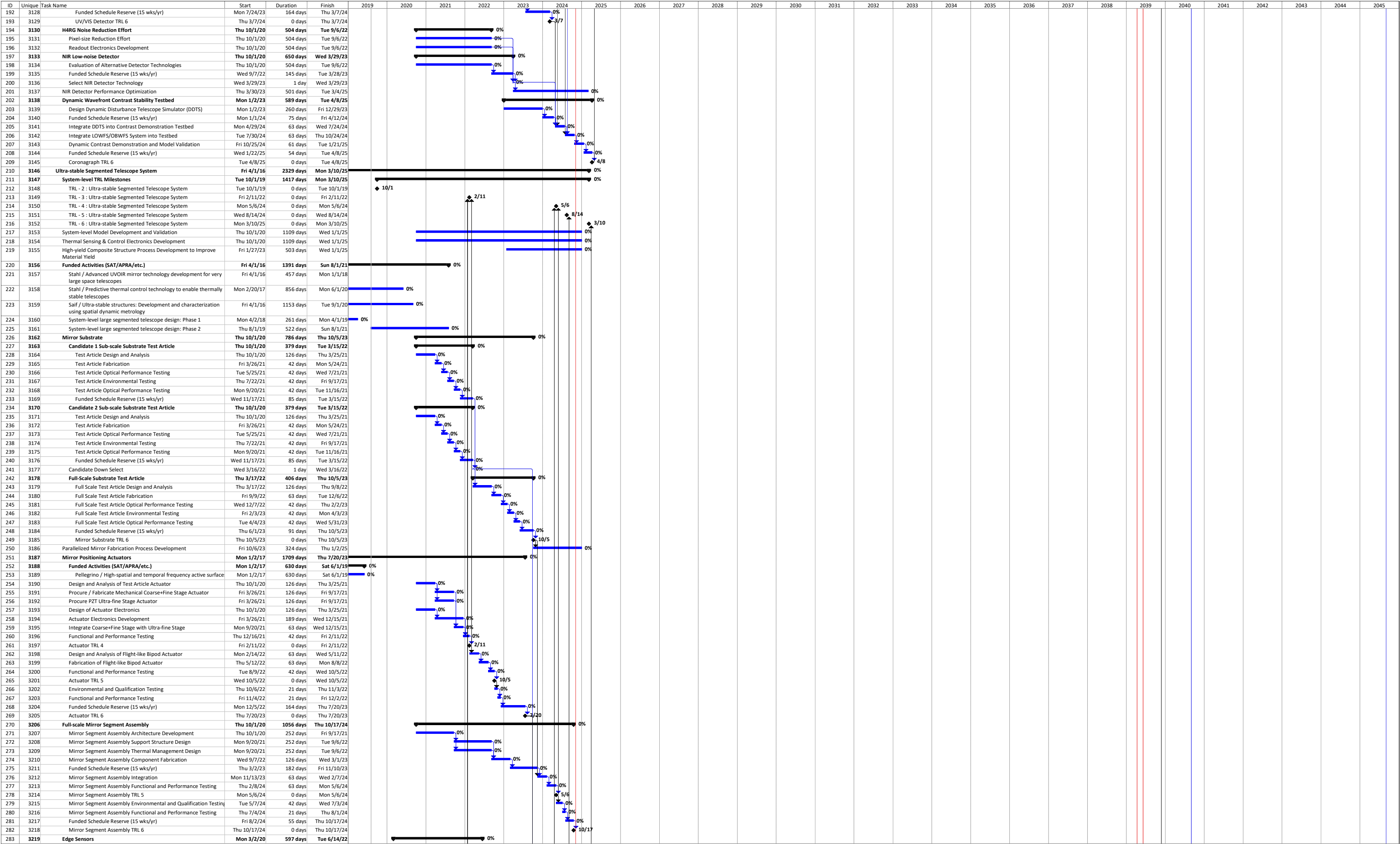
Element	Sub-system	Assembly / Sub-assembly	Component / Item	Type	Sub-type	TRL (FY19)	Technology Development
Payload	OTA	PMSA	Mirror Coating	Technology	Enabling	3	See Technology Development Plan
Payload	OTA	PMSA	Mirror Segment Substrate	Technology	Enabling	5	See Technology Development Plan
Payload	OTA	PMSA	PZT Ultra-fine Actuator	Technology	Enabling	3	See Technology Development Plan
Payload	OTA	SM	Mirror Coating	Technology	Enabling	3	See Technology Development Plan
Payload	OTA	SM	Mirror Substrate	Technology	Enabling	5	See Technology Development Plan
Payload	OTA	SM	PZT Ultra-fine Actuator	Technology	Enabling	3	See Technology Development Plan
Payload	OTA		Artificial Guide Star	Technology	Enhancing	3	See Technology Development Plan
Payload	PAS	VIPPS	VIPPS	Technology	Enabling	4	See Technology Development Plan
Payload		Throughout	Thermal Sensing & Control	Technology	Enabling	6	See Technology Development Plan

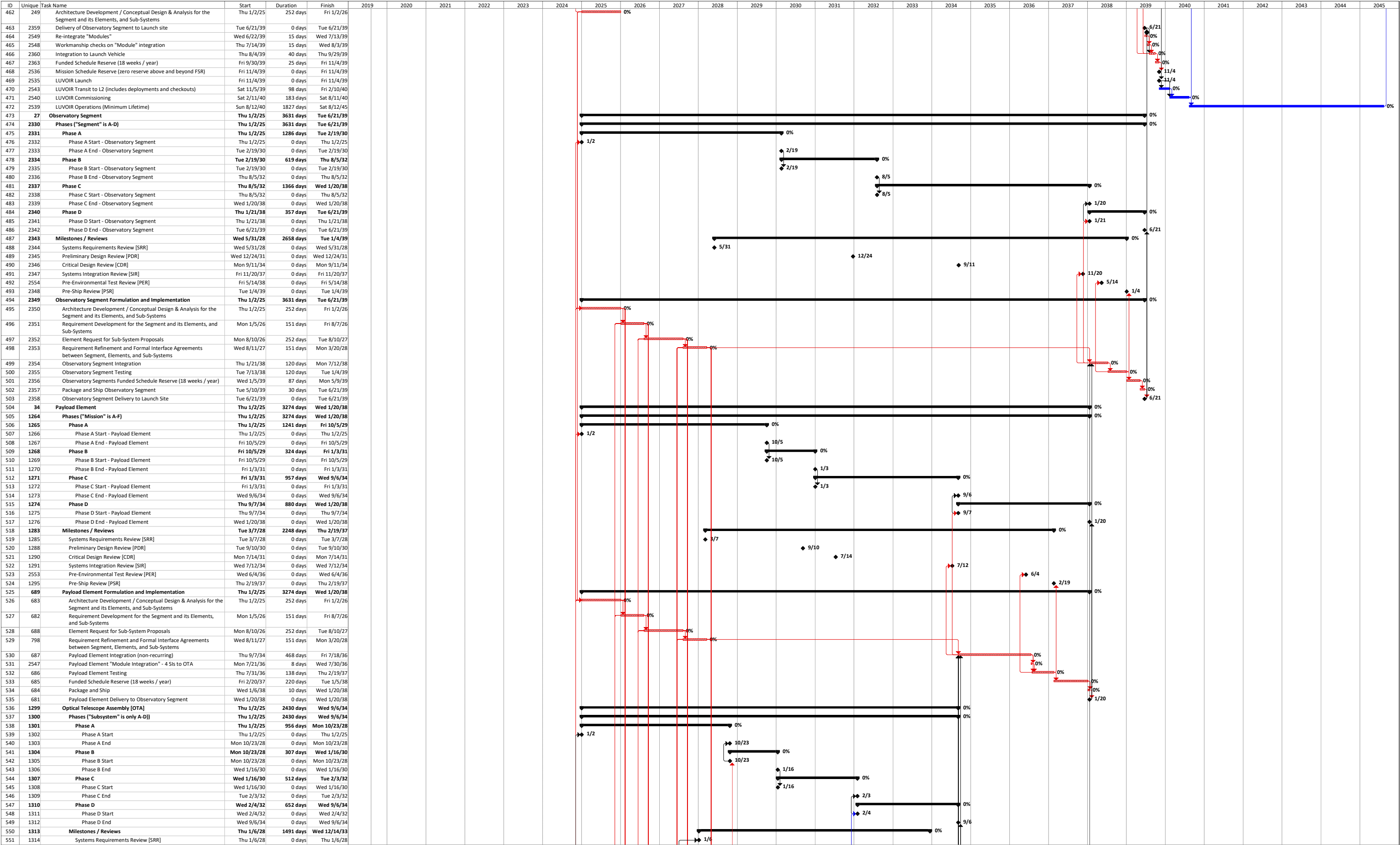
APPENDIX G. DETAILED SCHEDULE

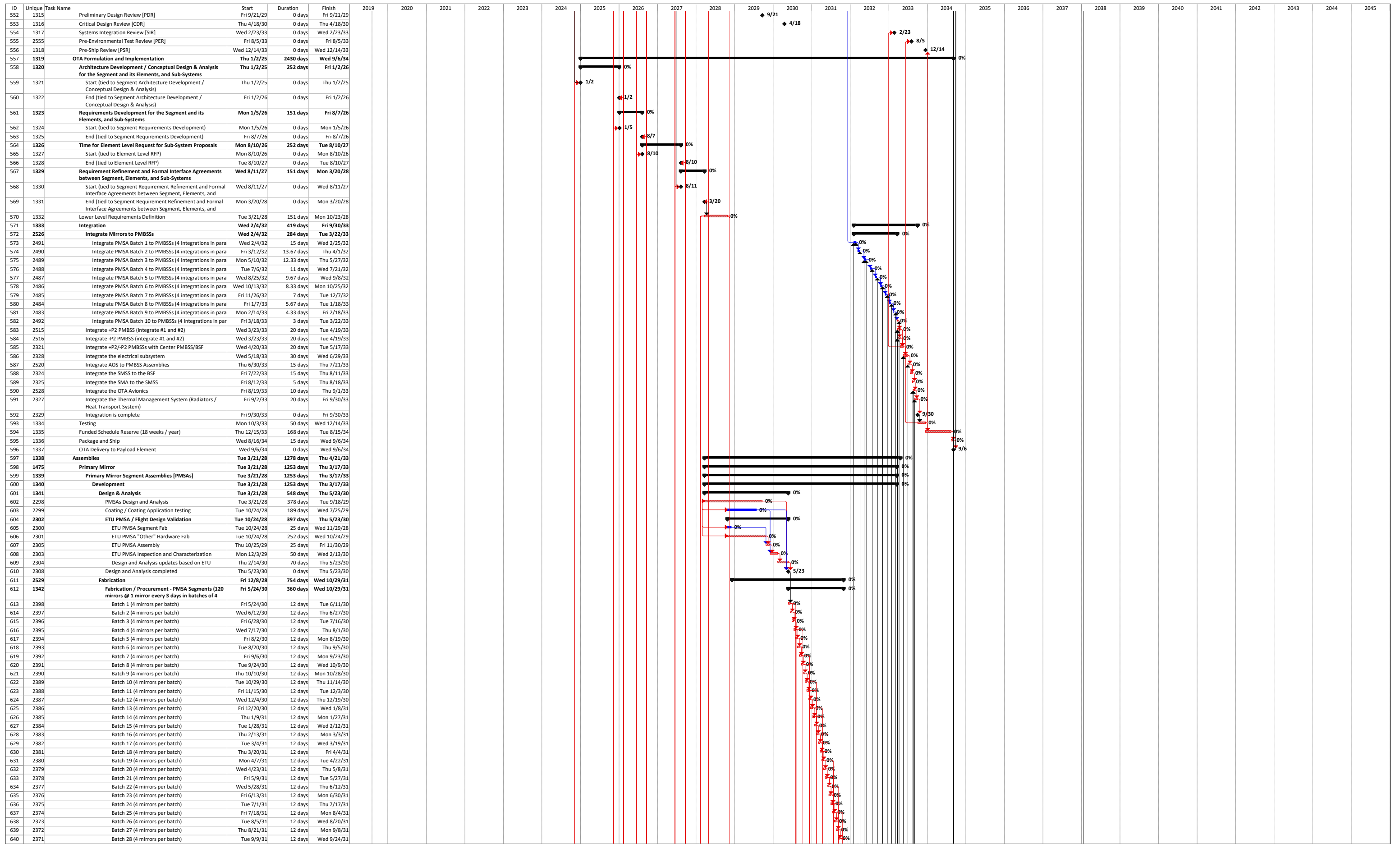
Table G-1. Complete LUVOR-A mission development schedule





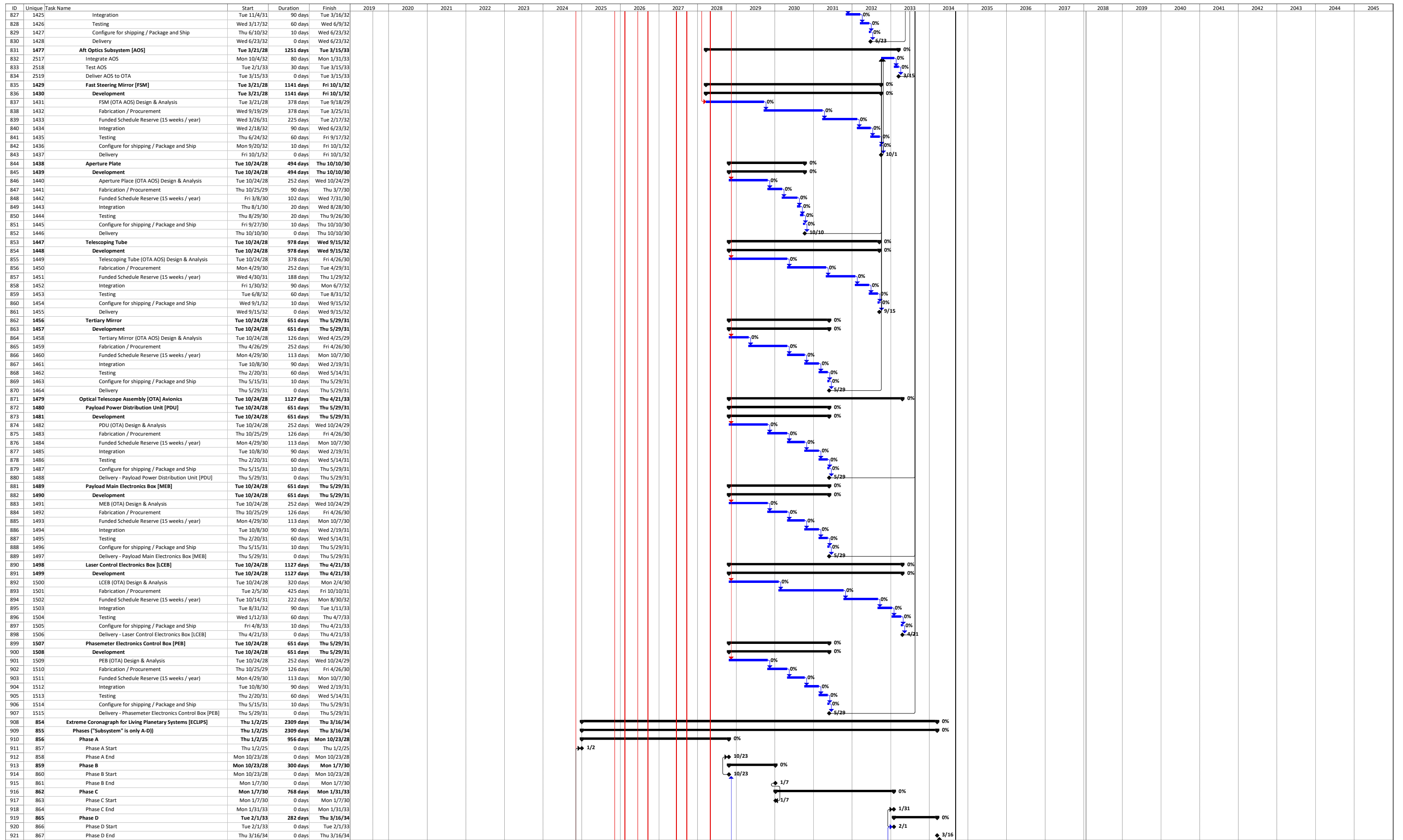






ID	Unique	Task Name	Start	Duration	Finish	2019	2020	2021	2022	2023	2024	2025	2026	2027	2028	2029	2030	2031	2032	2033	2034	2035	2036	2037	2038	2039	2040	2041	2042	2043	2044	2045
641	2370	Batch 29 (4 mirrors per batch)	Thu 9/25/31	12 days	Fri 10/10/31																											
642	2369	Batch 30 (4 mirrors per batch)	Tue 10/14/31	12 days	Wed 10/29/31																											
643	2367	Procure motors (720 + 6 = 726 total motors @ ~20 motors per month)	Fri 12/8/28	726 days	Wed 10/29/31																											
644	2418	NLT Start date required to procure all motors in time for assembly	Fri 12/8/28	0 days	Fri 12/8/28																											
645	2417	Batch 1 (20 motors per batch)	Fri 12/8/28	20 days	Tue 1/9/29																											
646	2416	Batch 2 (20 motors per batch)	Tue 1/9/29	20 days	Wed 2/7/29																											
647	2415	Batch 3 (20 motors per batch)	Wed 2/7/29	20 days	Thu 3/8/29																											
648	2414	Batch 4 (20 motors per batch)	Thu 3/8/29	20 days	Thu 4/5/29																											
649	2413	Batch 5 (20 motors per batch)	Thu 4/5/29	20 days	Thu 5/3/29																											
650	2412	Batch 6 (20 motors per batch)	Thu 5/3/29	20 days	Fri 6/1/29																											
651	2411	Batch 7 (20 motors per batch)	Fri 6/1/29	20 days	Fri 6/29/29																											
652	2410	Batch 8 (20 motors per batch)	Fri 6/29/29	20 days	Mon 7/30/29																											
653	2409	Batch 9 (20 motors per batch)	Mon 7/30/29	20 days	Mon 8/27/29																											
654	2408	Batch 10 (20 motors per batch)	Mon 8/27/29	20 days	Tue 9/25/29																											
655	2407	Batch 11 (20 motors per batch)	Tue 9/25/29	20 days	Wed 10/24/29																											
656	2406	Batch 12 (20 motors per batch)	Wed 10/24/29	20 days	Fri 11/23/29																											
657	2405	Batch 13 (20 motors per batch)	Fri 11/23/29	20 days	Fri 12/21/29																											
658	2404	Batch 14 (20 motors per batch)	Fri 12/21/29	20 days	Wed 1/23/30																											
659	2403	Batch 15 (20 motors per batch)	Wed 1/23/30	20 days	Thu 2/21/30																											
660	2402	Batch 16 (20 motors per batch)	Thu 2/21/30	20 days	Thu 3/21/30																											
661	2401	Batch 17 (20 motors per batch)	Thu 3/21/30	20 days	Thu 4/18/30																											
662	2400	Batch 18 (20 motors per batch)	Thu 4/18/30	20 days	Thu 5/16/30																											
663	2512	Batch 19 (20 motors per batch)	Thu 5/16/30	20 days	Fri 6/14/30																											
664	2511	Batch 20 (20 motors per batch)	Fri 6/14/30	20 days	Mon 7/15/30																											
665	2510	Batch 21 (20 motors per batch)	Mon 7/15/30	20 days	Mon 8/12/30																											
666	2509	Batch 22 (20 motors per batch)	Mon 8/12/30	20 days	Tue 9/10/30																											
667	2508	Batch 23 (20 motors per batch)	Tue 9/10/30	20 days	Tue 10/8/30																											
668	2507	Batch 24 (20 motors per batch)	Tue 10/8/30	20 days	Wed 11/6/30																											
669	2506	Batch 25 (20 motors per batch)	Wed 11/6/30	20 days	Fri 12/6/30																											
670	2505	Batch 26 (20 motors per batch)	Fri 12/6/30	20 days	Tue 1/7/31																											
671	2504	Batch 27 (20 motors per batch)	Tue 1/7/31	20 days	Wed 2/5/31																											
672	2503	Batch 28 (20 motors per batch)	Wed 2/5/31	20 days	Thu 3/6/31																											
673	2502	Batch 29 (20 motors per batch)	Thu 3/6/31	20 days	Thu 4/3/31																											
674	2501	Batch 30 (20 motors per batch)	Thu 4/3/31	20 days	Thu 5/1/31																											
675	2500	Batch 31 (20 motors per batch)	Thu 5/1/31	20 days	Fri 5/30/31																											
676	2499	Batch 32 (20 motors per batch)	Fri 5/30/31	20 days	Fri 6/27/31																											
677	2498	Batch 33 (20 motors per batch)	Fri 6/27/31	20 days	Mon 7/28/31																											
678	2497	Batch 34 (20 motors per batch)	Mon 7/28/31	20 days	Mon 8/25/31																											
679	2496	Batch 35 (20 motors per batch)	Mon 8/25/31	20 days	Tue 9/23/31																											
680	2495	Batch 36 (20 motors per batch)	Tue 9/23/31	20 days	Wed 10/22/31																											
681	2494	Batch 37 (6 motors in this batch for SMA)	Wed 10/22/31	6 days	Wed 10/29/31																											
682	2306	Fabrication / Procurement - "Other" PMSA hardware	Mon 6/10/30	350 days	Wed 10/29/31																											
683	2430	NLT Start date required to procure all "other" hardware required for PMSAs	Mon 6/10/30	0 days	Mon 6/10/30																											
684	2428	Batch 1	Mon 6/10/30	35 days	Tue 7/30/30																											
685	2427	Batch 2	Tue 7/30/30	35 days	Wed 9/18/30																											
686	2426	Batch 3	Wed 9/18/30	35 days	Thu 11/7/30																											
687	2425	Batch 4	Thu 11/7/30	35 days	Tue 12/31/30																											
688	2424	Batch 5	Tue 12/31/30	35 days	Fri 2/21/31																											
689	2423	Batch 6	Fri 2/21/31	35 days	Fri 4/11/31																											
690	2422	Batch 7	Fri 4/11/31	35 days	Mon 6/2/31																											
691	2421	Batch 8	Mon 6/2/31	35 days	Tue 7/22/31																											
692	2420	Batch 9	Tue 7/22/31	35 days	Wed 9/10/31																											
693	2419	Batch 10	Wed 9/10/31	35 days	Wed 10/29/31																											
694	1344	Integration / PMSA Assembly and coating (per batch : 4 segments in parallel, 3 sets of segments in series)	Tue 7/30/30	360 days	Tue 1/6/32																											
695	2441	Batch 1	Tue 7/30/30	48 days	Fri 10/4/30																											
696	2440	Batch 2	Mon 10/7/30	45.33 days	Thu 12/12/30																											
697	2439	Batch 3	Thu 12/12/30	42.67 days	Thu 2/13/31																											
698	2438	Batch 4	Fri 2/14/31	40 days	Fri 4/11/31																											
699	2437	Batch 5	Mon 4/14/31	37.33 days	Thu 6/5/31																											
700	2436	Batch 6	Thu 6/5/31	34.67 days	Thu 7/24/31																											
701	2435	Batch 7	Fri 7/25/31	32 days	Tue 9/9/31																											
702	2434	Batch 8	Wed 9/10/31	29.33 days	Wed 10/22/31																											
703	2433	Batch 9	Wed 10/22/31	26.67 days	Mon 12/1/31																											
704	2432	Batch 10	Tue 12/2/31	24 days	Tue 1/6/32																											
705	1345	Testing	Mon 10/7/30	317 days	Tue 1/13/32																											
706	2452	Batch 1	Mon 10/7/30	15 days	Mon 10/28/30																											
707	2451	Batch 2	Thu 12/12/30	13.89 days	Fri 1/3/31																											
708	2450	Batch 3	Fri 2/14/31	12.78 days	Wed 3/5/31																											
709	2449	Batch 4	Mon 4/14/31	11.67 days	Tue 4/29/31																											
710	2448	Batch 5	Thu 6/5/31	10.56 days	Thu																											

[illegible]



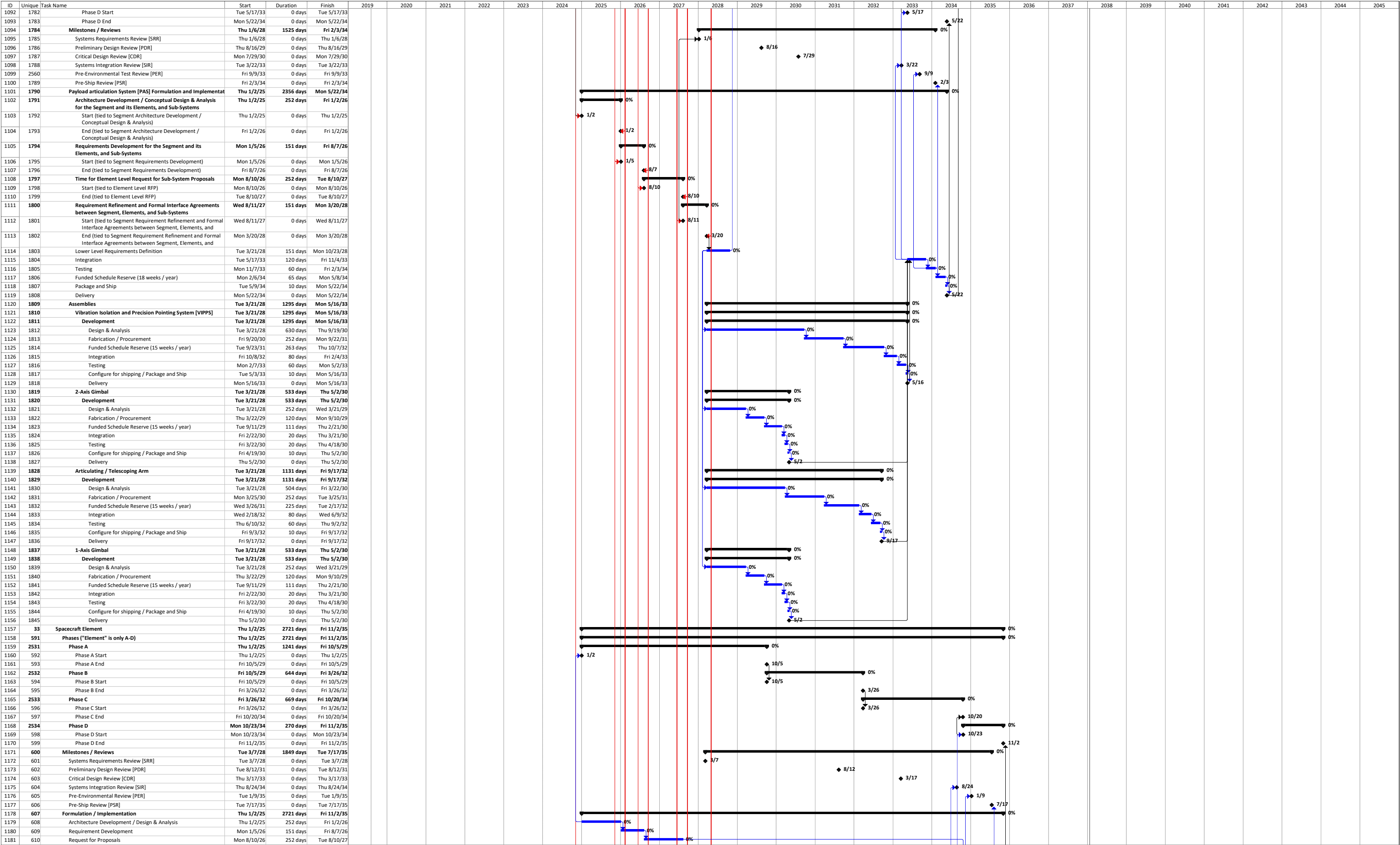
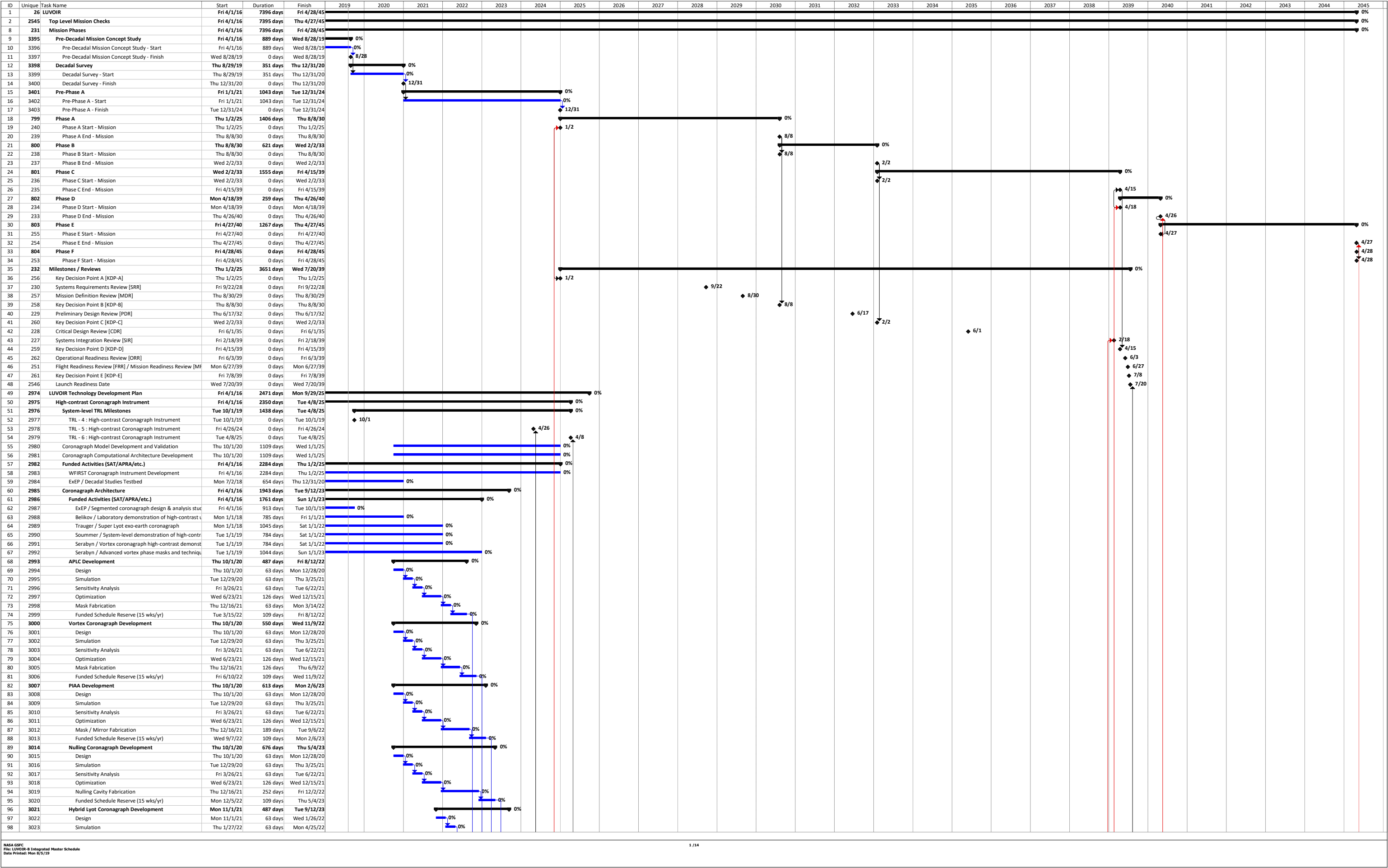
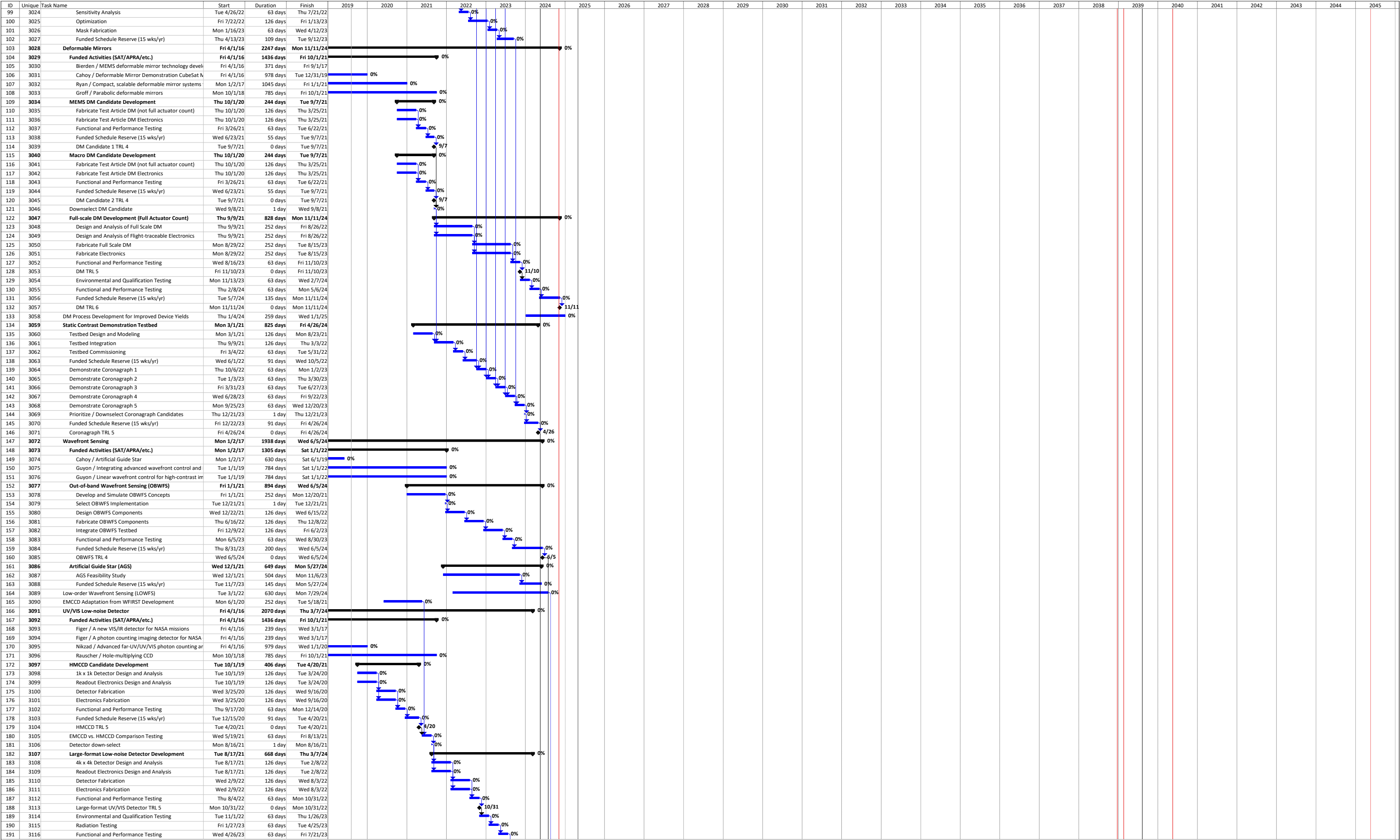
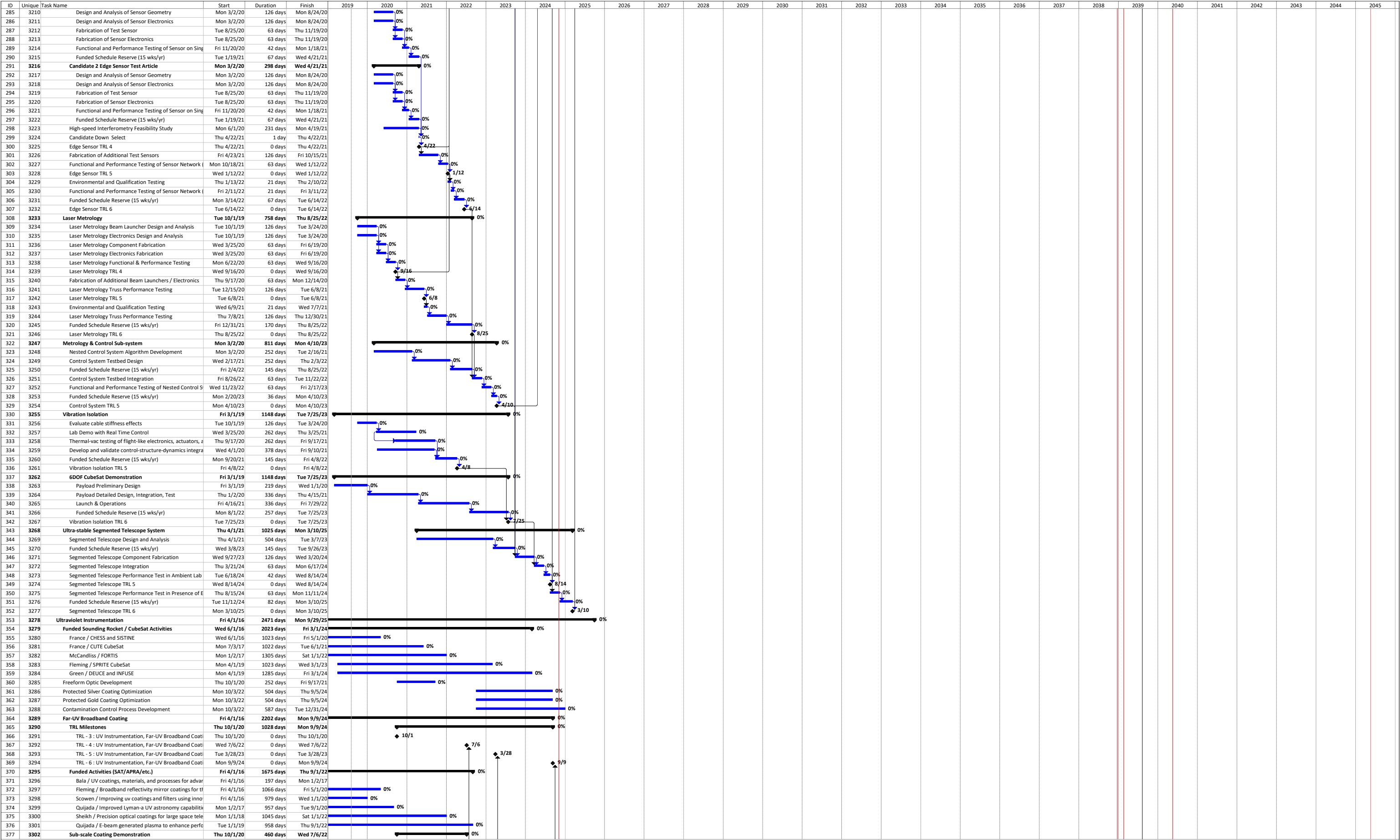


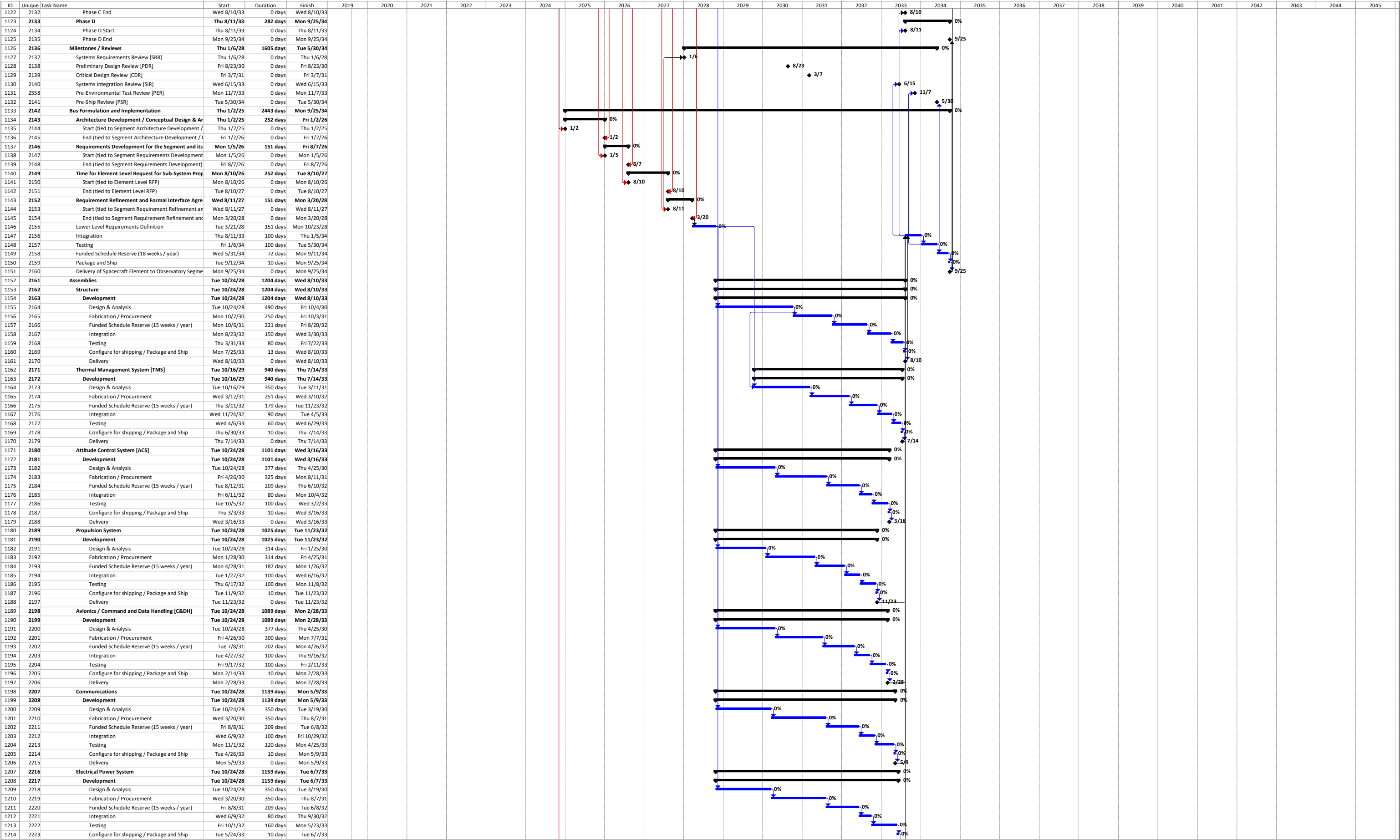
Table G-2. Complete LUVOIR-B mission development schedule







ID	Unique	Task Name	Start	Duration	Finish	2019	2020	2021	2022	2023	2024	2025	2026	2027	2028	2029	2030	2031	2032	2033	2034	2035	2036	2037	2038	2039	2040	2041	2042	2043	2044	2045
564	1326	Time for Element Level Request for Sub-System Prop	Mon 8/10/26	252 days	Tue 8/10/27																											
565	1327	Start (tied to Element Level RFP)	Mon 8/10/26	0 days	Mon 8/10/26																											
566	1328	End (tied to Element Level RFP)	Tue 8/10/27	0 days	Tue 8/10/27																											
567	1329	Requirement Refinement and Formal Interface Agree	Wed 8/11/27	151 days	Mon 3/20/28																											
568	1330	Start (tied to Segment Requirement Refinement an	Wed 8/11/27	0 days	Wed 8/11/27																											
569	1331	End (tied to Segment Requirement Refinement anc	Mon 3/20/28	0 days	Mon 3/20/28																											
570	1332	Lower Level Requirements Definition	Tue 3/21/28	151 days	Mon 10/23/28																											
571	1333	Integration	Tue 1/13/32	359 days	Wed 6/15/33																											
572	2526	Integrate Mirrors to PMBSs	Tue 1/13/32	96.14 days	Wed 5/26/32																											
573	2491	Integrate PMSA Batch 1 to PMBSs (4 integratio	Tue 1/13/32	30 days	Wed 2/25/32																											
574	2490	Integrate PMSA Batch 2 to PMBSs (4 integratio	Thu 2/26/32	23.3 days	Tue 3/30/32																											
575	2489	Integrate PMSA Batch 3 to PMBSs (4 integratio	Tue 3/30/32	16.6 days	Wed 4/21/32																											
576	2488	Integrate PMSA Batch 4 to PMBSs (4 integratio	Tue 4/27/32	6.6 days	Thu 5/6/32																											
577	2492	Integrate PMSA Batch 5 to PMBSs (4 integratio	Mon 5/24/32	2.14 days	Wed 5/26/32																											
578	2321	Integrate +P2/-P2 PMBSs with Center PMBS/BSF	Wed 5/26/32	20 days	Thu 6/24/32																											
579	2328	Integrate the electrical subsystem	Thu 6/24/32	30 days	Fri 8/6/32																											
580	2520	Integrate AOS to PMBS5 Assemblies	Wed 3/16/33	15 days	Tue 4/5/33																											
581	2324	Integrate the SMSS to the BSF	Wed 4/6/33	15 days	Tue 4/26/33																											
582	2325	Integrate the SMA to the SMSS	Wed 4/27/33	5 days	Tue 5/3/33																											
583	2528	Integrate the OTA Avionics	Wed 5/4/33	10 days	Tue 5/17/33																											
584	2327	Integrate the Thermal Management System (Radia	Wed 5/18/33	20 days	Wed 6/15/33																											
585	2329	Integration is complete	Wed 6/15/33	0 days	Wed 6/15/33																											
586	1334	Testing	Thu 6/16/33	50 days	Thu 8/25/33																											
587	1335	Funded Schedule Reserve (18 weeks / year)	Fri 8/26/33	147 days	Thu 3/30/34																											
588	1336	Package and Ship	Fri 3/31/34	15 days	Thu 4/20/34																											
589	1337	OTA Delivery to Payload Element	Thu 4/20/34	0 days	Thu 4/20/34																											
590	1338	Assemblies	Tue 3/21/28	1278 days	Thu 4/21/33																											
591	1475	Primary Mirror	Tue 3/21/28	1049 days	Fri 5/21/32																											
592	1339	Primary Mirror Segment Assemblies [PMSAs]	Tue 3/21/28	1049 days	Fri 5/21/32																											
593	1340	Development	Tue 3/21/28	1049 days	Fri 5/21/32																											
594	1341	Design & Analysis	Tue 3/21/28	548 days	Thu 5/23/30																											
595	2298	PMSAs Design and Analysis	Tue 3/21/28	378 days	Tue 9/18/29																											
596	2299	Coating / Coating Application testing	Tue 10/24/28	189 days	Wed 7/25/29																											
597	2302	ETU PMSA / Flight Design Validation	Tue 10/24/28	397 days	Thu 5/23/30																											
598	2300	ETU PMSA Segment Fab	Tue 10/24/28	25 days	Wed 11/29/28																											
599	2301	ETU PMSA "Other" Hardware Fab	Tue 10/24/28	252 days	Wed 10/24/29																											
600	2305	ETU PMSA Assembly	Thu 10/25/29	25 days	Fri 11/30/29																											
601	2303	ETU PMSA Inspection and Characterizat	Mon 12/3/29	50 days	Wed 2/13/30																											
602	2304	Design and Analysis updates based on E	Thu 2/14/30	70 days	Thu 5/23/30																											
603	2308	Design and Analysis completed	Thu 5/23/30	0 days	Thu 5/23/30																											
604	2529	Fabrication	Fri 10/5/29	342 days	Mon 1/27/31																											
605	1342	Fabrication / Procurement - PMSA Segme	Fri 5/24/30	168 days	Mon 1/27/31																											
606	2398	Batch 1 (4 mirrors per batch)	Fri 5/24/30	12 days	Tue 6/11/30																											
607	2397	Batch 2 (4 mirrors per batch)	Wed 6/12/30	12 days	Thu 6/27/30																											
608	2396	Batch 3 (4 mirrors per batch)	Fri 6/28/30	12 days	Tue 7/16/30																											
609	2395	Batch 4 (4 mirrors per batch)	Wed 7/17/30	12 days	Thu 8/1/30																											
610	2394	Batch 5 (4 mirrors per batch)	Fri 8/2/30	12 days	Mon 8/19/30																											
611	2393	Batch 6 (4 mirrors per batch)	Tue 8/20/30	12 days	Thu 9/5/30																											
612	2392	Batch 7 (4 mirrors per batch)	Fri 9/6/30	12 days	Mon 9/23/30																											
613	2391	Batch 8 (4 mirrors per batch)	Tue 9/24/30	12 days	Wed 10/9/30																											
614	2390	Batch 9 (4 mirrors per batch)	Thu 10/10/30	12 days	Mon 10/28/30																											
615	2389	Batch 10 (4 mirrors per batch)	Tue 10/29/30	12 days	Thu 11/14/30																											
616	2388	Batch 11 (4 mirrors per batch)	Fri 11/15/30	12 days	Tue 12/3/30																											
617	2387	Batch 12 (4 mirrors per batch)	Wed 12/4/30	12 days	Thu 12/19/30																											
618	2386	Batch 13 (4 mirrors per batch)	Fri 12/20/30	12 days	Wed 1/8/31																											
619	2369	Batch 14 (4 mirrors per batch)	Thu 1/9/31	12 days	Mon 1/27/31																											
620	2367	Procure motors (720 + 6 = 726 total moto	Fri 10/5/29	326 days	Mon 1/27/31																											
621	2418	NLT Start date required to procure all m	Fri 10/5/29	0 days	Fri 10/5/29																											
622	2417	Batch 1 (20 motors per batch)	Fri 10/5/29	20 days	Mon 11/5/29																											
623	2416	Batch 2 (20 motors per batch)	Mon 11/5/29	20 days	Wed 12/5/29																											
624	2415	Batch 3 (20 motors per batch)	Wed 12/5/29	20 days	Fri 1/4/30																											
625	2414	Batch 4 (20 motors per batch)	Fri 1/4/30	20 days	Mon 2/4/30																											
626	2413	Batch 5 (20 motors per batch)	Mon 2/4/30	20 days	Tue 3/5/30																											
627	2412	Batch 6 (20 motors per batch)	Tue 3/5/30	20 days	Tue 4/2/30																											
628	2411	Batch 7 (20 motors per batch)	Tue 4/2/30	20 days	Tue 4/30/30																											
629	2410	Batch 8 (20 motors per batch)	Tue 4/30/30	20 days	Wed 5/29/30																											
630	2409	Batch 9 (20 motors per batch)	Wed 5/29/30	20 days	Wed 6/26/30																											
631	2408	Batch 10 (20 motors per batch)	Wed 6/26/30	20 days	Thu 7/25/30																											
632	2407	Batch 11 (20 motors per batch)	Thu 7/25/30	20 days	Thu 8/22/30																											
633	2406	Batch 12 (20 motors																														



APPENDIX H. FURTHER POLLUX DETAILS

H.1 POLLUX consortium

The POLLUX payload Work Breakdown Structure is as follows:

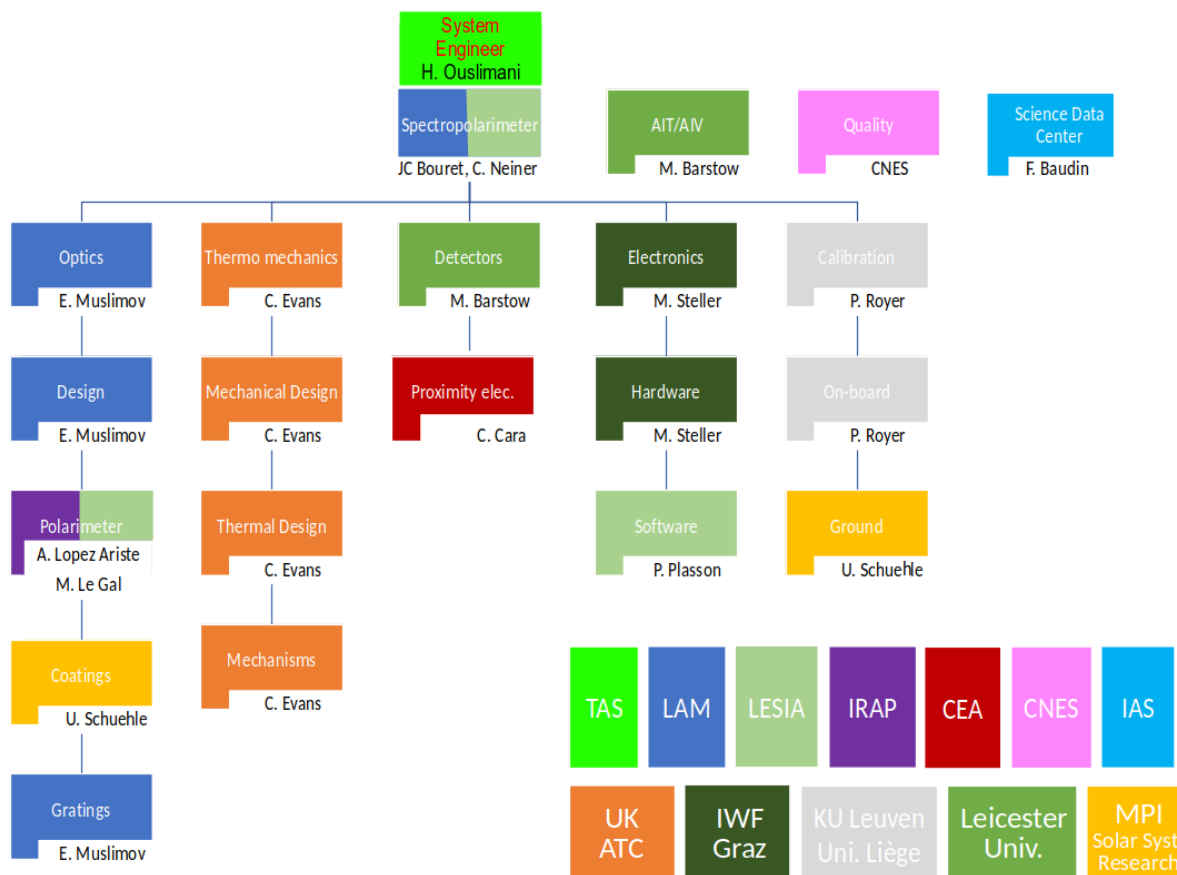


Figure H-1. *POLLUX payload Work Breakdown Structure*

The payload consortium currently consists of 5 laboratories (LAM, LESIA, IRAP, CEA and IAS), TAS, and CNES in France, as well as 6 institutes in other European countries: ATC and Leicester University in the UK, Space Research Institute in Graz in Austria, Leuven University and Liège University in Belgium, and Max Planck Institute for solar system research in Germany. See the Work Breakdown Structure above. Other European institutes have expressed their interest in participating in the POLLUX payload in the future, such as the Institute for Astrophysics at the University of Vienna in Austria, the Institute of planetary research at DLR in Germany, or INTA and the UCM in Spain.

POLLUX consortium members and their country of affiliation are listed below:

1. Evelyne Alecian	IPAG	France
2. João Alves	Univ. Vienna	Austria
3. Thierry Appourchaux.....	IAS.....	France
4. Ioannis Argyriou.....	Leuven Univ.	Belgium
5. Marc Audard.....	Geneva Obs.	Switzerland
6. Dietrich Baade	ESO	Germany
7. Francesca Baciotti	Arcetri	Italy
8. Martin Barstow.....	Univ. Leicester	UK
9. Mathieu Barthelemy	IPAG	France
10. Frédéric Baudin.....	IAS.....	France
11. Michel Berthé	CEA	France
12. Beth Biller.....	Univ. Edinburgh.....	UK
13. Pernelle Bernardi	LESIA.....	France
14. Javier Berzona Molina.....	TU Delft	Netherlands
15. Anthony Boccaletti.....	LESIA	France
16. Isabelle Boisse	LAM	France
17. Samuel Boissier.....	LAM	France
18. James Bolton	Univ. Nottingham	UK
19. Piercarlo Bonifacio.....	GEPI	France
20. Francois Boulanger	LP ENS.....	France
21. Jean-Claude Bouret	LAM	France
22. Vincent Bourrier.....	Univ. Geneve.....	Suisse
23. Jarle Brinchmann	IA-CAUP.....	Portugal
24. Matteo Brogi	Univ. Warwick.....	UK
25. Ross Burgon.....	Univ. Leicester	UK
26. Matthew Burleigh.....	Univ. Leicester	UK
27. José Antonio Caballero.....	CAB	Spain
28. Juan Cabrera	DLR.....	Germany
29. Christophe Cara	CEA	France
30. Sarah Casewell.....	Univ. Leicester	UK
31. Stéphane Charlot	IAP	France
32. Jean-Yves Chaufray	LATMOS.....	France
33. Andrea Chiavassa.....	OCA	France
34. Christopher Conselice.....	Univ. Nottingham	UK
35. Nick Cox.....	ACRI-ST	France
36. Orlagh Creevey	OCA	France
37. Patricio Cubillos.....	Space Research Institute.....	Austria
38. Tanausú del Pino Alemán.....	IAC	Spain
39. Magali Deleuil	LAM	France
40. Jean-Michel Desert.....	Univ. Amsterdam	Netherlands
41. Richard Desselle	CSL.....	Belgium
42. David Ehrenreich	Univ. Genève.....	Switzerland
43. Chris Evans	UKATC/STFC	UK

44. Annette Ferguson	Royal Obs. Edinburgh	UK
45. Marc Ferrari	LAM	France
46. Ignacio Ferreras	UCL	UK
47. Andrzej Fludra	STFC	UK
48. Colin Folsom	IRAP	France
49. Luca Fossati	Space Research Inst.	Austria
50. Wesley Fraser	Queen's Univ. Belfast	UK
51. Yves Frémat	ROB	Belgium
52. Michele Fumagalli	Durham Univ.	UK
53. Boris Gaensicke	Univ. Warwick	UK
54. Marina Galand	Imperial College	UK
55. Antonio Garcia Munoz	TU Berlin	Germany
56. Miriam García García	CAB	Spain
57. Stephan Geier	Univ. Potsdam	Germany
58. Brad Gibson	Univ. Hull	UK
59. Mareike Godolt	TU Berlin	Germany
60. Aaron Golden	NUI Galway	Republic of Ireland
61. Ana Ines Gomez de Castro	UCM	Spain
62. John Lee Grenfell	DLR	Germany
63. Denis Grodent	Univ. Liège	Belgium
64. Cécile Gry	LAM	France
65. Manuel Güdel	Univ. Vienna	Austria
66. Serge Habraken	CSL	Belgium
67. David Hall	Open Univ.	UK
68. Carole Haswell	Open Univ.	UK
69. Mats Holmstrom	Swedish Inst. Of Space Physics	Sweden
70. Hugues Jones	Univ. Hertfordshire	UK
71. Petr Kabath	Czech Academy of Sciences	Czech Republic
72. Maarit Käpylä	Max Planck Inst. for SSR	Germany
73. Franz Kerschbaum	Univ. Vienna	Austria
74. Pierre Kervella	LESIA	France
75. Kristina Kislyakova	Univ. Vienna	Austria
76. Christian Knigge	Univ. Southampton	UK
77. Oleg Kochukhov	Uppsala Univ.	Sweden
78. Rubina Kotak	University of Turku	Finland
79. Alvaro Labiano	CAB (CSIC-INTA)	Spain
80. Laurent Lamy	LESIA	France
81. Antonino Lanza	INAF-Catania Obs.	Italy
82. Jon Lapington	Univ. Leicester	UK
83. Francois Leblanc	LATMOS	France
84. Jacques Le Boulrot	LERMA	France
85. Maelle Le Gal	LESIA	France
86. Vianney Lebouteiller	CEA	France
87. Alain Lecavelier des Etangs	IAP	France
88. Jyri Lehtinen	Max Planck Inst. for SSR	Germany

89. Monika Lendl	Space Research Inst.	Austria
90. Simona Lombardo	LAM	France
91. Louise Lopes	CNES	France
92. Arturo Lopez Ariste	IRAP	France
93. Carlo Felice Manara	ESO	Germany
94. Laurent Mahy	Leuven Univ.	Belgium
95. Pablo Marcos Arenal	UCM	Spain
96. Frédéric Marin	Strasbourg Obs	France
97. Jean-Francois Mariscal	LATMOS	France
98. Tom Marsh	Univ. Warwick	UK
99. Fabrice Martins	LUPM	France
100. Elena Mason	INAF-Trieste Obs.	Italy
101. Stéphane Mathis	CEA	France
102. Paolo Mazzali	LJMU	UK
103. Sean McGee	Univ. Birmingham	UK
104. Bruno Milliard	LAM	France
105. David Montgomery	UKATC/STFC	UK
106. Christoph Mordasini	Univ. Bern	Switzerland
107. Julien Morin	LUPM	France
108. Carole Mundell	Univ. Bath	UK
109. Eduard Muslimov	LAM	France
110. Yael Nazé	Liège Univ.	Belgium
111. Coralie Neiner	LESIA	France
112. Pasquier Noterdaeme	IAP	France
113. Göran Östlin	Stockholm Univ.	Sweden
114. Roland Ottensamer	Univ. Vienna	Austria
115. René Oudmaijer	Leeds Univ.	UK
116. Hana Ouslimani	TAS	France
117. Isabella Pagano	INAF-Catania Obs.	Italy
118. Enric Pallé	IAC	Spain
119. Paul Palmer	Univ. Edinburgh	UK
120. Chris Pearson	STFC RAL Space	UK
121. Martin Pertenaïs	DLR	Germany
122. Céline Peroux	LAM	France
123. Pascal Petit	IRAP	France
124. Matthew Pieri	LAM	France
125. Juliet Pickering	Imperial Coll.	UK
126. Philippe Plasson	LESIA	France
127. Don Pollacco	Univ. Warwick	UK
128. Delphine Porquet	LAM	France
129. Norbert Przybilla	Innsbruck Univ.	Austria
130. Hadi Rahmani	GEPI	France
131. Theresa Rank-Lüftinger	Univ. Vienna	Austria
132. Heike Rauer	DLR	Germany
133. Gregor Rauw	Univ. Liège	Belgium

134. Jean-Michel Reess	LESIA	France
135. Philipp Richter	Univ. Potsdam.....	Germany
136. Loic Rossi	LATMOS.....	France
137. Philippe Rousselot	Besancon Obs.	France
138. Pierre Royer	Leuven Univ	Belgium
139. Sarah Rugheimer.....	Univ. Oxford.....	UK
140. Hugues Sana	Leuven Univ	Belgium
141. Ruben Sanchez Janssen.....	STFC.....	UK
142. Joop Schaye	Leiden Univ.	Netherlands
143. Christian Schneider	Hamburg Obs.....	Germany
144. Udo Schühle.....	Max Planck Inst. for SSR	Germany
145. Steve Shore	Univ. Pisa	Italy
146. Michael Smith.....	Univ. Kent.....	UK
147. Colin Snodgrass	Univ. Edinburgh.....	UK
148. Daphne Stam	TU Delft	Netherlands
149. Dimitris Stamatellos	Univ. Central Lancashire.....	UK
150. Manfred Steller.....	Space Research Institute.....	Austria
151. Beate Stelzer	Univ. Tuebingen.....	Germany
152. Luca Teriaca.....	Max Planck Inst. for SSR	Germany
153. Samantha Thompson	Univ. Cambridge.....	UK
154. Andrew Tkachenko	Leuven Univ	Belgium
155. Pier-Emmanuel Tremblay.....	Univ. Warwick.....	UK
156. Javier Trujillo Bueno	IAC	Spain
157. Juan C. Vallejo	UCM	Spain
158. Hans van Winckel	Leuven Univ	Belgium
159. Aprajita Verma	Univ. Oxford.....	UK
160. Aline Vidotto	Trinity Coll. Dublin.....	Republic of Ireland
161. Jorick Vink.....	Armagh Obs.	UK
162. William Wadsworth	Univ. Bath.....	UK
163. Klaus Werner	Univ. Tuebingen.....	Germany
164. Peter Wheatley.....	Univ. Warwick.....	UK
165. Glenn White	STFC.....	UK
166. Klaas Wiersema.....	Univ. Leicester	UK
167. Stephen Wilkins	Univ. Sussex	UK
168. Huirong Yan	DESY	Germany
169. Konstanze Zwintz	Innsbruck Univ	Austria

H.2 Cost of POLLUX

We present here the evaluation of the cost of POLLUX as performed by the POLLUX consortium. The cost of the various sub-systems has been provided by the leader of each sub-system. It includes costs related to the development plan. In addition, system-level cost has been added, as well as the cost for the Science Data Center (SDC), AIT/AIV, management and coordination of the interfaces between the various participants, and product assurance. The table below presents the details of the POLLUX cost evaluation.

Table H-1. *Details of POLLUX Cost Evaluation*

Element	Cost in Million euros (€)
3 UV spectrographs	48
3 UV polarimeters	8
3 δ -doped EMCCDs	15
3 front end electronics	10.2
Main electronic hardware	20
Main electronic software	2.9
Calibration	10.5
Structure	30
Harness	8
AIT/AIV	30
Science Data Center	7
Management	12
System and interface coordination	33
Product assurance	9
TOTAL	243.6
Contingency 20%	48.7
TOTAL with contingency	292.3

This cost corresponds to the cost of POLLUX if it were studied, built, and tested entirely by the POLLUX consortium. Would these activities be led by our industrial partner Thales Alenia Space (TAS) with sub-systems provided by the consortium, the cost would increase to 370 M€ (20% contingency included). This cost would nevertheless remain well below the maximum Cost at Completion of an M-class contribution by ESA, which is typically 550 M€.

H.3 UV polarimeters

H.3.1 Design for the POLLUX UV polarimeters

H.3.1.1 General design: temporal modulation

Current detectors being only sensitive to intensity, the polarization (Q, U, and V Stokes parameters) needs to be modulated into the intensity in order to be measured. POLLUX polarimeter designs are composed of two components: a modulator and an analyzer. The modulator is rotating around the optical axis at several specific and pre-defined positions. It introduces a phase shift between p and s polarizations. By rotating the modulator, we change this phase shift and thus the polarization. The analyzer filters the light polarized in a particular direction. The combination of both elements therefore creates a modulation of the polarization encoded in the light intensity. Indeed, the output of the polarimeter is then a linear combination of the Stokes parameters.

This method requires several measurements—at least 4—to retrieve the 4 Stokes parameters. Each measurement corresponds to an angular position of the modulator. The measurements are combined and demodulated with the help of the demodulation matrix in order to retrieve the input Stokes vector (IQUV). In the end, the observer obtains 4 spectra, one for each Stokes parameter.

The modulation and demodulation matrices are computed with the Mueller matrices of each optical components. This working principle is schemed in **Figure H-2**.

H.3.1.2 Polarimetric efficiencies

What is the impact of measuring the polarization of the incoming light on the SNR of the Stokes spectra? The best way to assess it is through the use of an efficiency parameter as the one introduced by del Toro Iniesta & Collados (2001). It determines how raw photon noise is transferred into the polarization measurement. An efficiency of 1 means that the SNR is

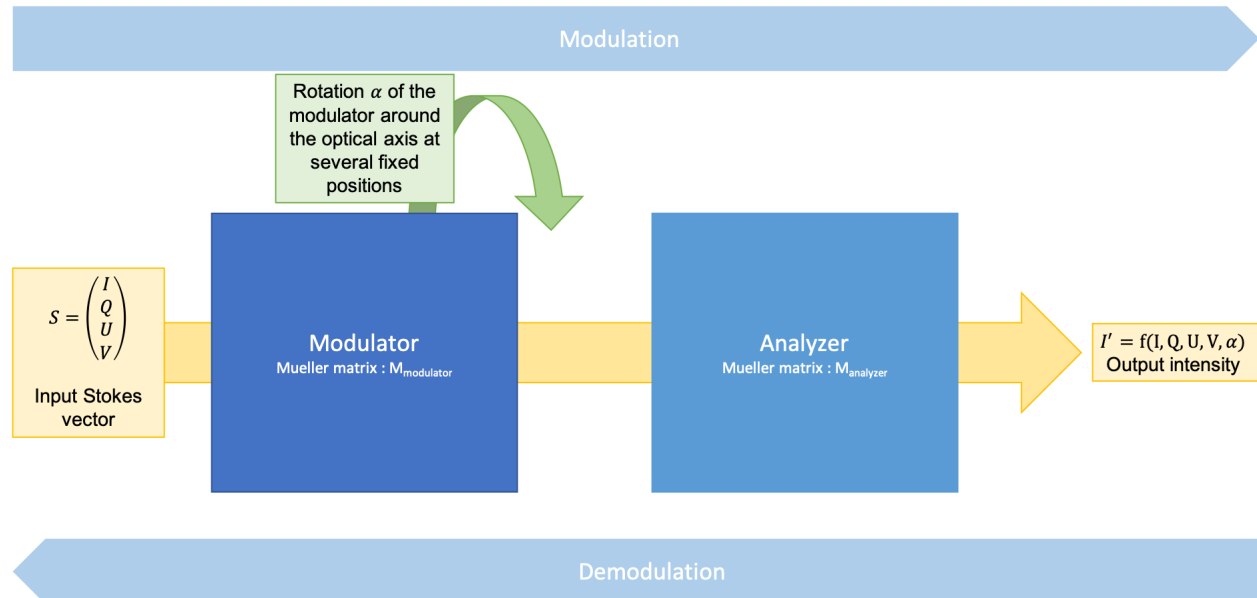


Figure H-2. Scheme of a polarimeter using temporal modulation

identical in the polarization and in the intensity measurements, but only half if the efficiency is 0.5. Since all the detected photons at a given wavelength are used for intensity measurements, but 3 different polarizations (Stokes QUV parameters) have to be measured, the sum of the squared efficiencies of the polarizations will add up to 1. This means that one can choose to measure one polarization, e.g., circular, with efficiency 1, but only at the prize of not measuring the two other, e.g., linear, polarizations.

Many science cases however require the measurement of all Stokes parameters. In such a case we require the three efficiencies to be similarly good, or around $1/\sqrt{3} \approx 0.57$. Moreover, since the optical design of LUVUOIR is not polarization-free, measuring all Stokes parameters will allow us to calibrate and disentangle the instrumental polarization introduced by LUVUOIR optics.

H.3.1.3 Designs for the POLLUX polarimeters

H.3.1.3.1 NUV

The POLLUX NUV polarimeter can work by transmission using birefringence, which is a standard way of building a polarimeter. The modulator is made of two plates of MgF_2 and the analyzer is a MgF_2 Wollaston prism. To optimize the polarimetric efficiencies at 0.57, the first plate of the modulator should be $e_1=12.8 \mu\text{m}$ thick and has a fast axis angle at $\alpha_1=32.6^\circ$. The second plate should be $e_2=3.7 \text{ mm}$ thick and has a fast axis angle at $\alpha_2=147.3^\circ$.

However, such thin plates cannot be built. Therefore, the solution is to replace each thin plate by a pair of thicker ($\sim 0.3 \text{ mm}$) plates perpendicular to each other. The global axis of the pair remains at the optimal calculated angle and we use a thickness difference between both plates of the pair corresponding to the optimal calculated thickness. In terms of polarization this produces the same effect as the thin plate. The design of the POLLUX NUV polarimeter is represented in **Figure H-3**.

The modulator takes 6 fixed angular positions: 2.3° , 36° , 50.4° , 69.9° , 112.6° and 147.7° (rather than 4 positions to introduce redundancy and improve the precision of the results). At the output of the Wollaston prism, both p and s polarizations are measured simultaneously. We thus record in total 12 measurements.

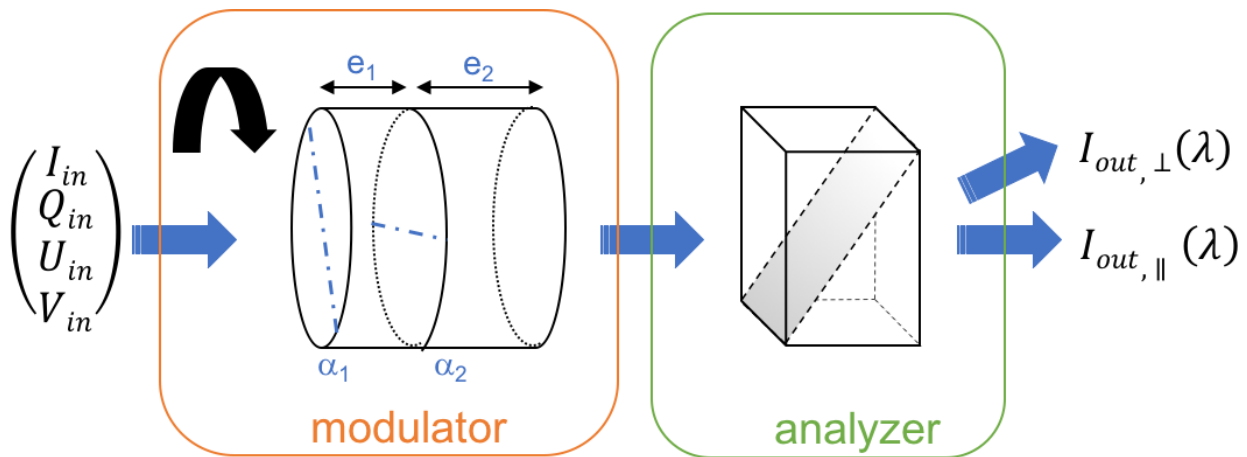


Figure H-3. NUV and MUV polarimeters design

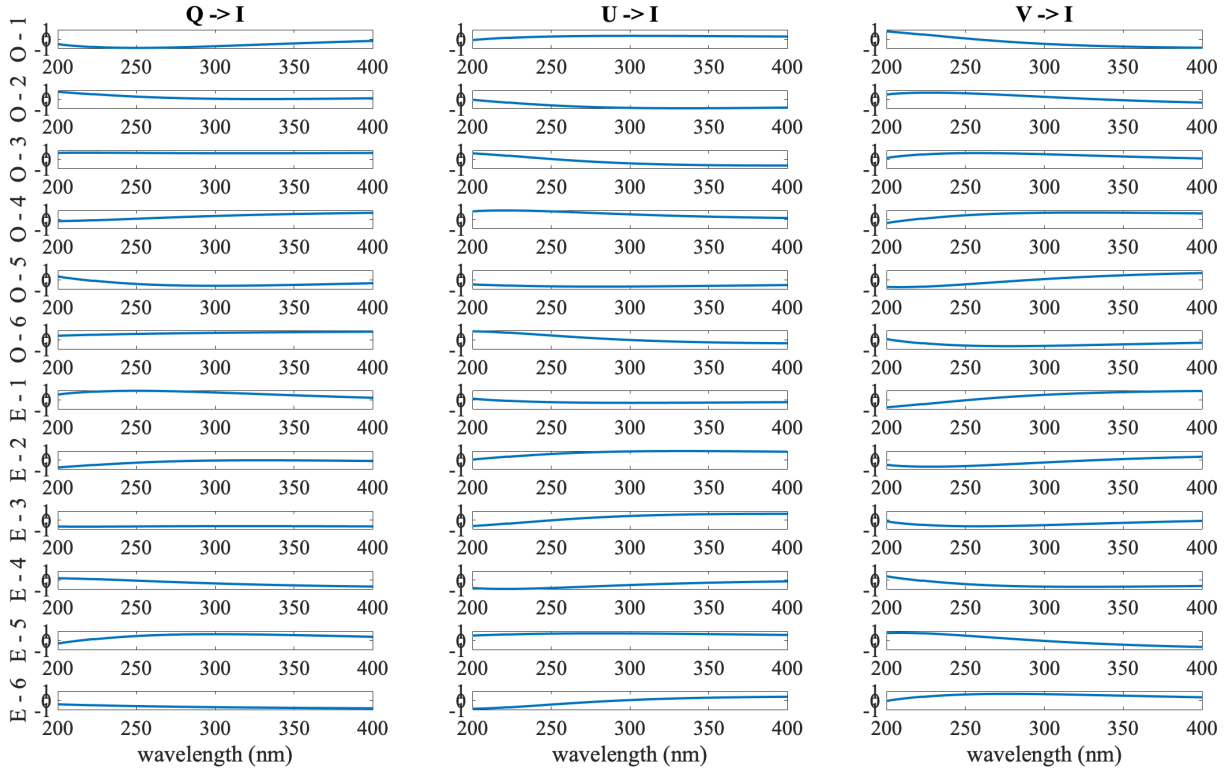


Figure H-4. Modulation matrix of the NUV channel polarimeter. Coefficients being normalized to intensity, the intensity modulation is equal to one at all wavelengths and is therefore not represented. Each line represents a measurement: there are 12 measurements due to the 6 angular positions and the 2 outputs of the Wollaston prism.

The modulation and demodulation matrices are shown in **Figure H-4** and **Figure H-5**. For this design, SiO_2 was considered as well but MgF_2 turned out to have better results (see Le Gal et al, 2018, SPIE). Efficiencies of this polarimeter are given in the main POLLUX chapter, **Figure 14-21** in **Section 14.2.8**. The results are very satisfying.

H.3.1.3.2 FUV

In the absence of transparent and birefringent materials in the FUV, POLLUX proposes the use of the retardance intrinsic to any reflection as a modulation mechanism. A 3-mirror device, dubbed K-device or K-mirror, that rotates around the optical axis has been studied satisfactorily. Retardance is introduced by the reflections on the 1st and 3rd mirrors and the equivalent of a fast axis for birefringent crystals is given by the incidence plane onto the 1st mirror. Altogether, the 3-mirror device mimics a rotating waveplate.

The performance of such a device is determined by both the angle of incidence on the first mirror and the material of the mirror. SiC, ta-C, and B4C are studied for this mirror. With the current data, SiC mirror seems to be optimal for the modulator. The optimal angle of incidence on the first mirror is 82° . It defines the incidence angle on all mirrors so that the modulator does not affect the optical axis of the instrument.

The modulator takes 4 angular positions which means that only 4 measurements are needed to measure the entire Stokes vector—contrary to the 6 measurements chosen for the

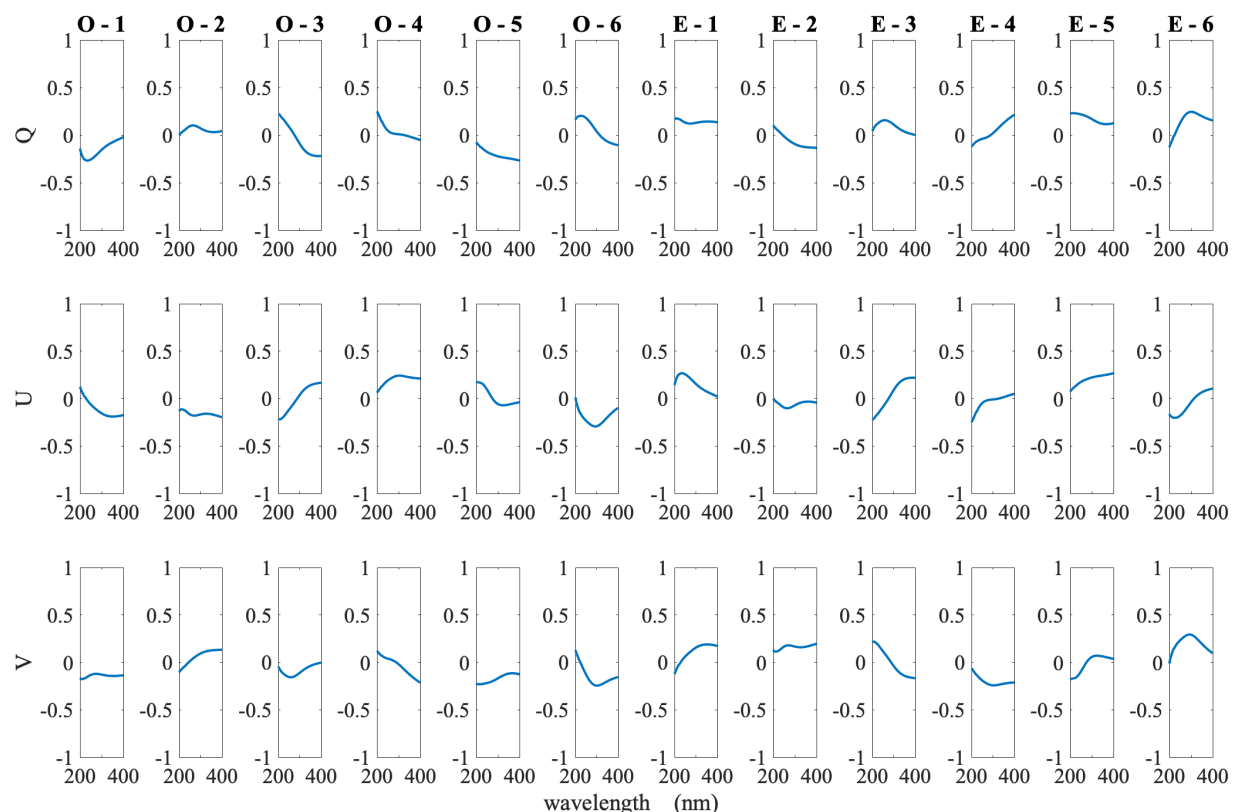


Figure H-5. Demodulation matrix of the NUV channel polarimeter. Coefficients being normalized to intensity; the intensity modulation is equal to one at all wavelengths and is therefore not represented. The demodulation matrix is the inverse of the modulation matrix.

transmissive NUV polarimeter. The FUV modulator positions are 20.2° , 66.3° , 113.7° and 159.8° .

The analyzer is also dramatically affected by the absence of any birefringent material usually employed in polarizing beam-splitters. Incidence at Brewster angles is left as the only polarizing mechanism in this wavelength domain. And yet, the Brewster angle changes with wavelength, so rigorously we can only impinge at Brewster angle at one single wavelength. At angles other than Brewster's, the polarization efficiency decreases, leaving us with a very imperfect analyzer. We therefore propose to use instead an analogous of the Brewster angle but on a metal instead of a crystal. This Brewster-like angle is more constant over the wavelength range even though it does not achieve 100% efficiency neither. Several materials have been considered. A plate of ta-C—a diamond like carbon (see Larruquert et al. 2013)—has been chosen as we achieve a polarizer with a 68% efficiency on average over the wavelength range at 73° incidence angle as shown in **Figure H-6** (left) with a reflectivity reaching almost 80% for 90 nm as one can see in **Figure H-6** (right). The design of the FUV polarimeter is represented in **Figure H-7**.

H.3.1.3.3 MUV

The MUV channel has legacy from the two other channels. Further studies are ongoing to decide whether a transmissive polarimeter as the NUV channel or a reflective polarimeter

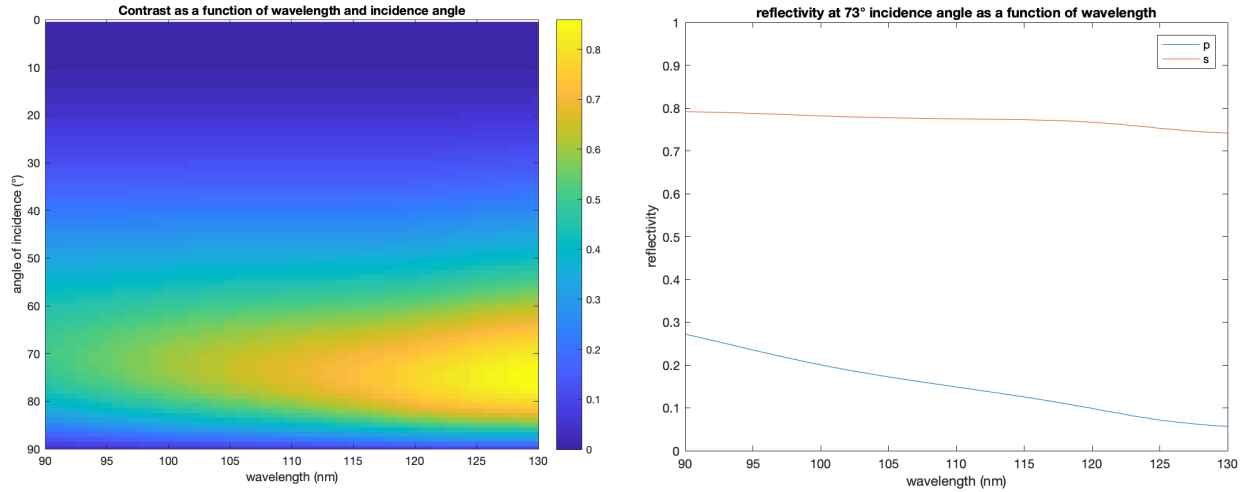


Figure H-6. Left: Contrast between p and s polarizations after a reflection on a ta-C plate as a function of wavelength (abscissa) and angle of incidence (ordinate). Right: Reflectivity of s and p polarizations on a mirror in ta-C.

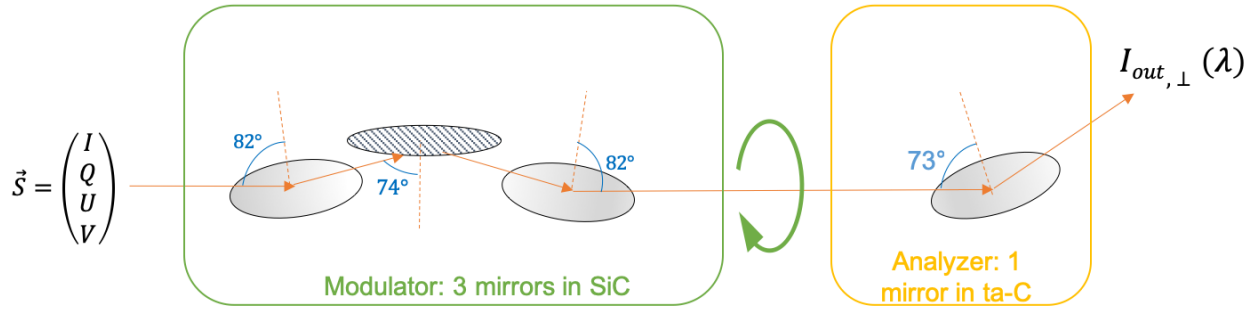


Figure H-7. Design of the FUV polarimeter. The modulator is made of three SiC mirrors; the first incidence angle is 82°, the second and third incidence angles are then 74° and 82° in order to align the input and output beam. The modulator does not affect the optical axis. The analyzer is a mirror in ta-C at 73°. It changes the optical axis.

as the FUV channel would be best for the MUV channel. Even though the transmissive solution requires to reduce the wavelength range for polarimetric measurements to above 123 nm due to the drop of MgF_2 birefringence at 119.5 nm, considering that the polarization of this part of the spectrum can be recorded in the FUV channel, we decided to settle for a polarimeter with MgF_2 plates. Indeed, this solution has already been tested with success and it no longer needs to prove its efficiency.

The current baseline design as described in the main chapter is therefore composed of two double plates of MgF_2 . The thickness difference of the first double plate is $e_1 = 9.6 \mu\text{m}$ and the global fast axis is $\alpha_1 = 6.4^\circ$. The thickness difference of the second double plate is $e_2 = 3.3 \mu\text{m}$ and the global fast axis is $\alpha_2 = 70.0^\circ$. The modulator is followed by a Wollaston prism. The design is thus the same as for the NUV channel, shown in **Figure H-3**. Future studies will show if the MUV polarimeter could be changed for a reflective polarimeter, increasing the efficiency in the low range of the studied spectrum.

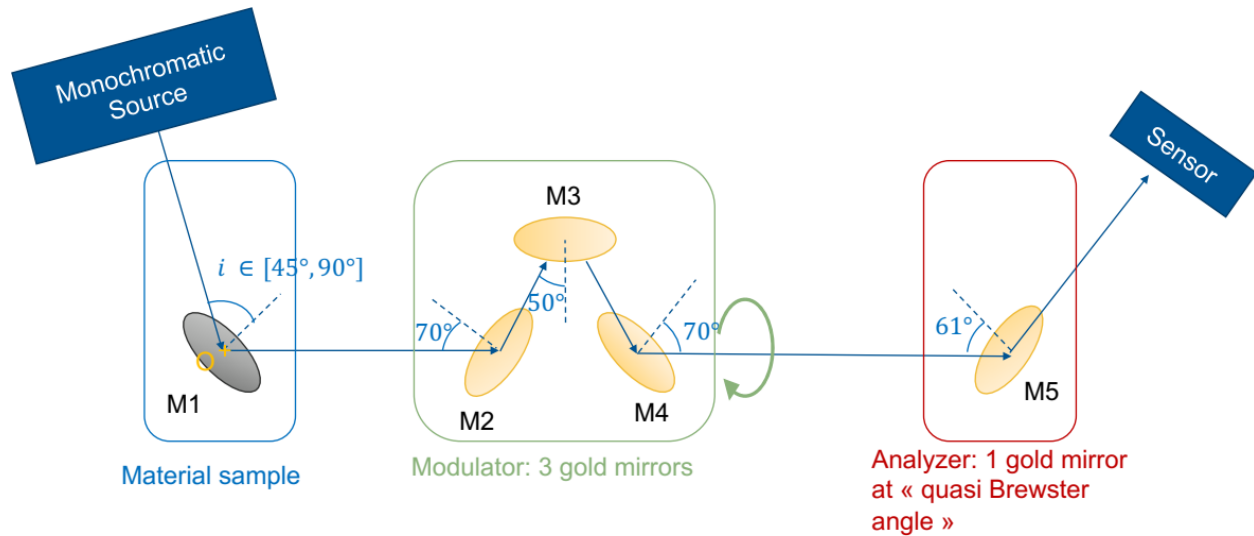


Figure H-8. Scheme of the experiment to select the best material for the FUV polarimeter.

H.3.2 On-going developments for UV polarimeters

R&D work on UV polarimeters is funded by CNES since 2011, first in the frame of the Arago space project proposed to ESA (Pertenis et al. 2017) and now for POLLUX. This work is led at the LESIA laboratory (Paris Observatory), with the collaboration of the IRAP, LERMA, and LATMOS laboratories (in France). Several experiments are currently being executed.

H.3.2.1 Test of materials for reflective polarimeters

A bench has been set up to measure polarimetric properties of various materials in order to choose the most efficient material for the mirrors of the FUV polarimeter of POLLUX and possibly of the MUV polarimeter. We have first identified candidate materials based on the little information available in the literature, on theoretical predictions, and on a study by SAFRAN REOSC funded by CNES to this aim.

Our current best candidates are SiC, B₄C, and ta-C. To measure the actual properties of these candidate materials, a polarimeter made of gold working in the FUV and MUV domain has been built at LESIA and installed in a vacuum chamber at LATMOS. Gold is not an efficient material and therefore it will not be used for POLLUX, but its properties are well known and reproducible irrespective of the supplier and environmental conditions. Therefore, it is a good material for a measurement bench. By placing a sample of a candidate material between the UV light source and the gold polarimeter, one can measure the polarization properties of the candidate material. This experiment has started and measurements are being acquired at the time of writing. We expect to be able to select the best material for the FUV polarimeter and the MUV polarimeter in a few months.

For the MUV, an efficiency trade-off will be made between the MUV polarimeter made of mirrors and the current baseline made of MgF₂ birefringent plates. The bench is represented in **Figure H-8** and actual pictures are shown in **Figure H-9**.

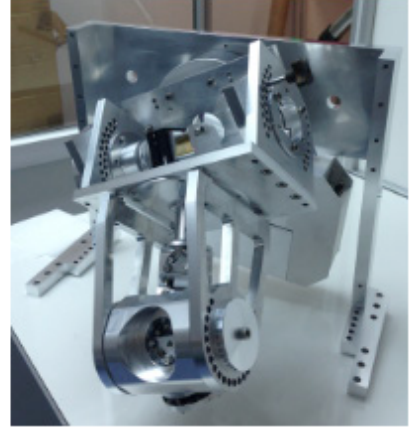


Figure H-9. Left: Bench and vacuum chamber at LATMOS. Right: Experiment built at LESIA for the FUV polarimeter, currently placed in the vacuum chamber.

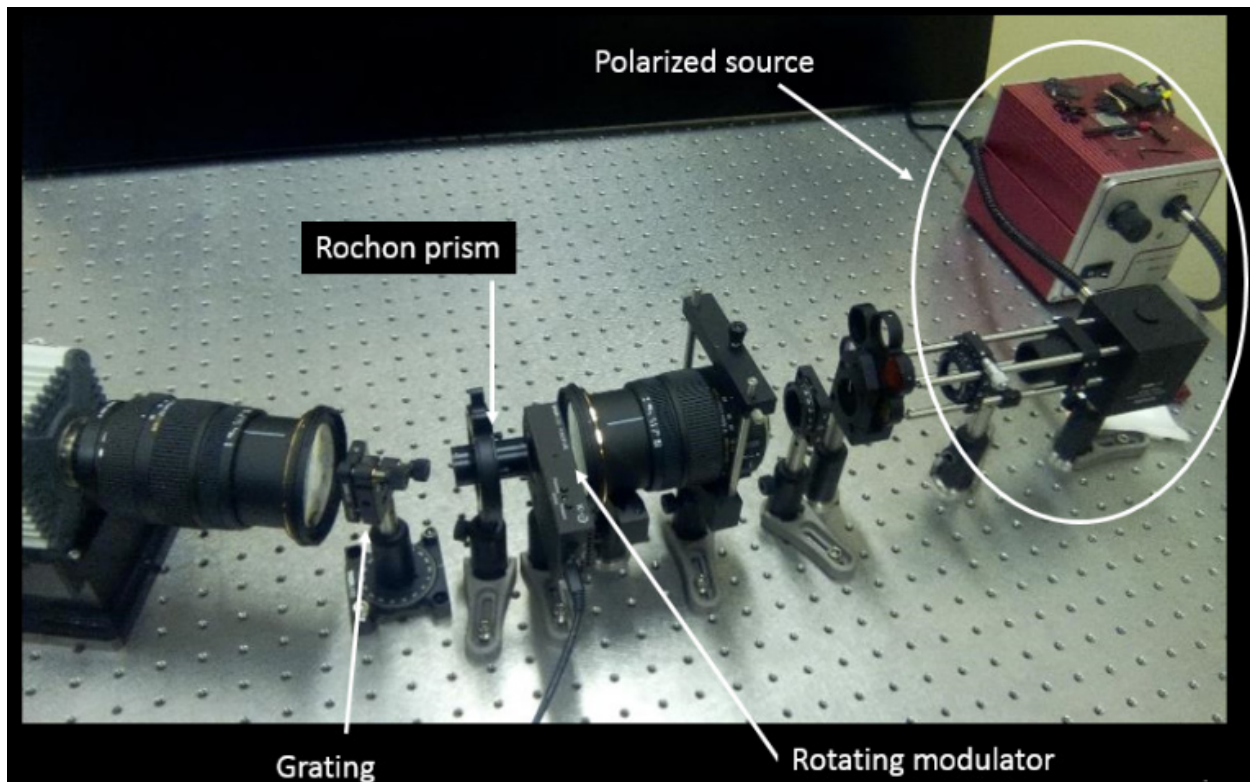


Figure H-10. Bench of the polarimeter with MgF_2 plates, during the tests in the visible domain.

H.3.2.2 Tests of MgF_2 polarimeters

A 10-m UV spectrograph available at LERMA at the Paris Observatory is being used to test the polarimeters made of birefringent MgF_2 plates in the UV. This design is the one chosen for the NUV polarimeter and the current baseline for the MUV polarimeter. We have already built and successfully tested a prototype in the visible domain (Pertenis et al. 2016). The visible test bench is shown in **Figure H-10**. In 2018 we built a set-up to mount the MgF_2 -plate polarimeter in front of the 10-m UV spectrograph (**Figure H-11**, left) to measure the

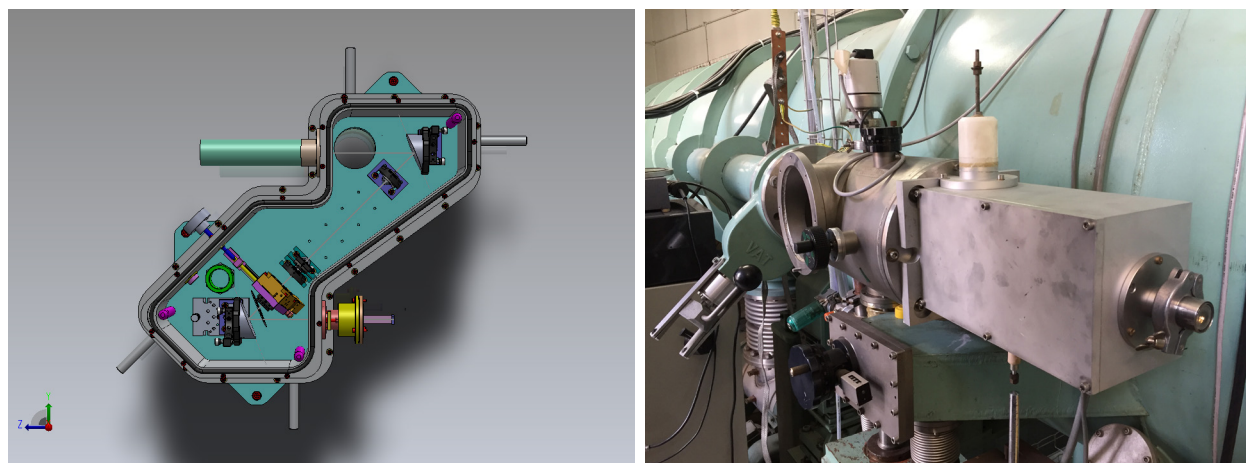


Figure H-11. Left: Design of the vacuum chamber and MgF_2 -plate UV polarimeter. Right: part of the 10-m UV spectrograph on which the MgF_2 -plate polarimeter will be mounted.

efficiency obtained in the POLLUX NUV and MUV wavelength ranges (Le Gal et al. 2018). The measurements started in May 2019. This bench is presented in **Figure H-11**, right.

H.3.2.3 Tests for thermal resistance

The efficiency of the MgF_2 -plate polarimeters is much better when the plates can be put in optical contact with molecular adhesion within the stack of plates rather than with air gaps

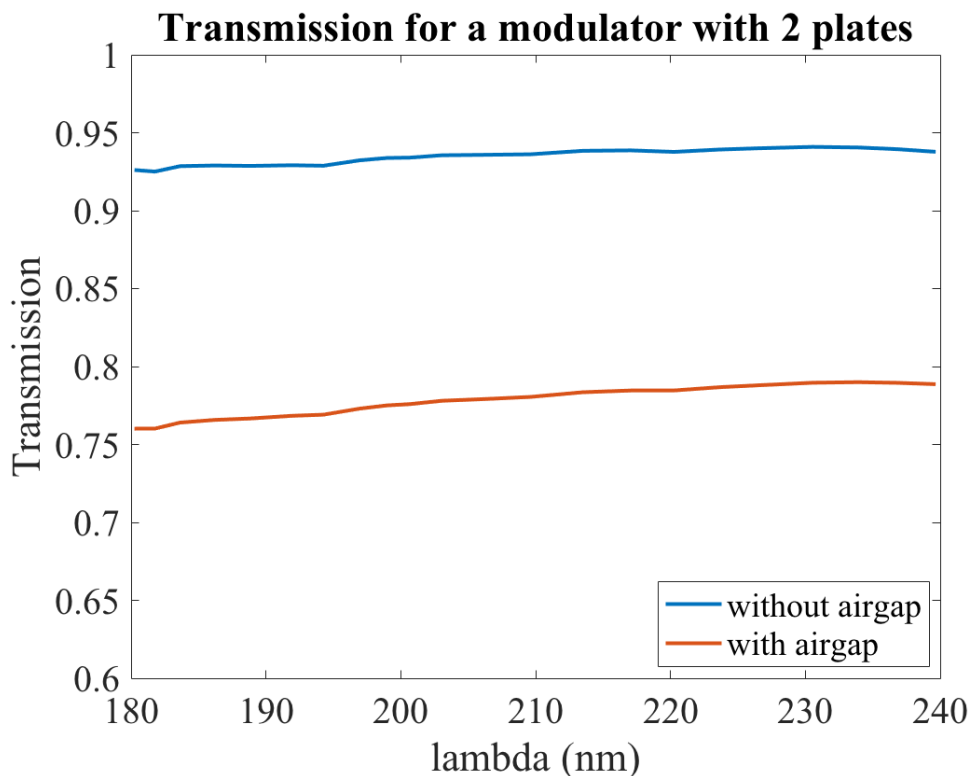


Figure H-12. Transmission curve for a MgF_2 polarimeter using 2 double plates for the modulator, either in optical contact (blue curve) or with air gaps (red curve).

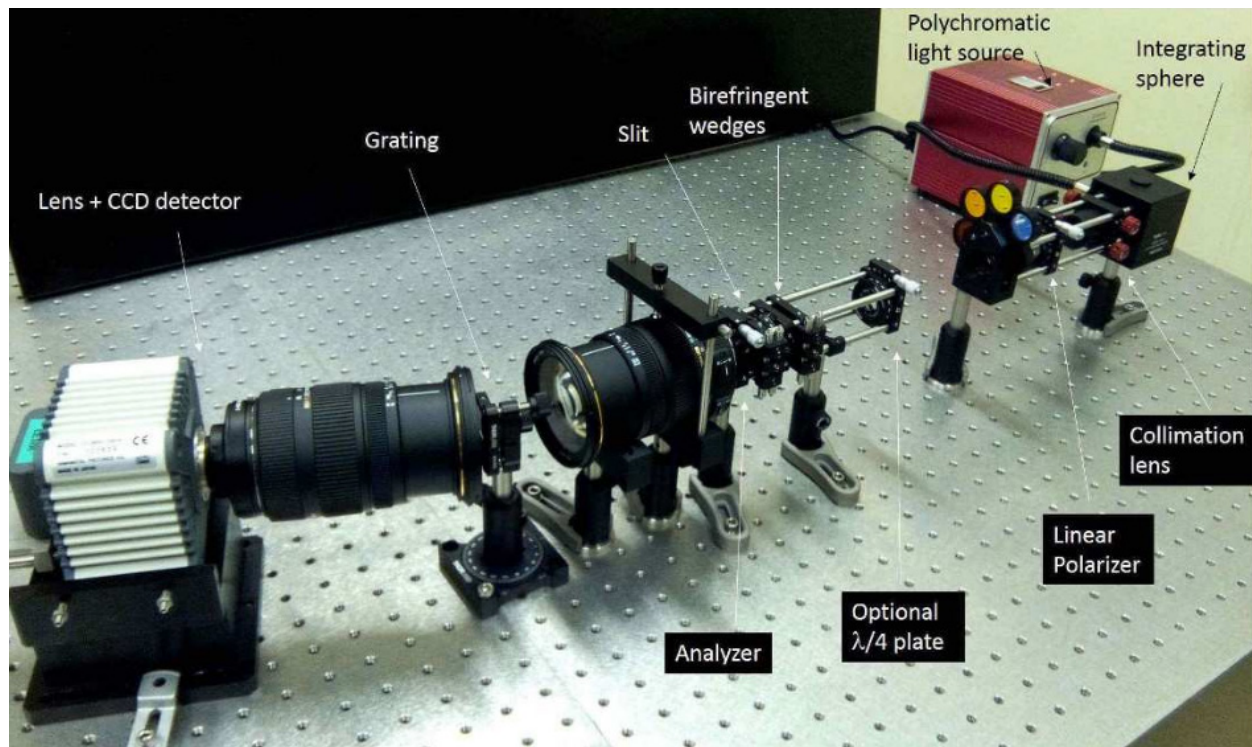


Figure H-13. Bench of the polarimeter with MgF_2 wedges, during the tests in the visible domain.

between the plates. Indeed, one can see in **Figure H-12** that the transmission reaches almost 95% with optical contact but drops to between 75 and 80% when airgaps are included. Moreover, the presence of air gaps mimics a Fabry-Perot and produces fringes which must be post-processed. However, since the MgF_2 plates are very thin and birefringent and their fast axes are in different orientations, thermal variations may break the plates or the molecular adhesion. We have devised a thermal cycling test of various configurations of the optically-contacted plates to test their resistance and qualify them for use in POLLUX. The plates are ready and tests started at LESIA in July 2019.

H.3.2.4 Static UV polarimeter

More prospective work is also being conducted to test an innovative type of polarimeters made of birefringent MgF_2 wedges (Sparks et al. 2010, Pertenais et al. 2015). This concept uses spatial modulation of the polarization instead of temporal modulation. The polarization is indeed modulated by the varying thickness of the wedge depending on the height at which the light crosses the wedge. As a consequence, this design includes no moving part. The drawback is that it requires larger detectors since each echelle order has a certain thickness and orders must thus be spread further apart. A prototype has already been built and successfully tested in the visible domain as one can see in **Figure H-13** (Pertenais et al. 2016). Some results are presented in **Figure H-14**.

We plan to perform tests of this static polarimeter in the UV domain on the 10-m UV spectrograph of the Paris Observatory in 2020.

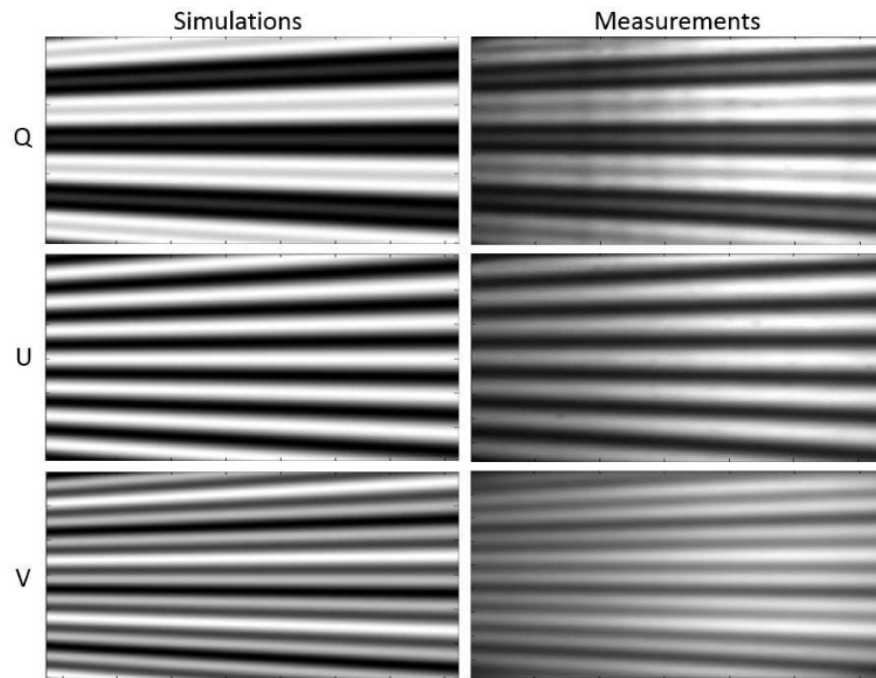


Figure H-14. Results obtained with the polarimeter made with MgF_2 wedges, in the visible domain. Left: simulations of a 100% Q, U and V polarized light, right: measurements with the prototype. The x-axis shows the wavelength while the y-axis corresponds to the height of the wedges. The patterns correspond to the modulation of the polarization observed in the spectrum.

H.4 Budgets

H.4.1 Data rates and interfaces

Each full image acquired by the POLLUX on-board software has a size of about 28.8 MB (14.4 Mpixels). The number of full calibration images (flat-fields, bias, dark) to be acquired per day when POLLUX is observing is 48. Moreover, 3 additional calibration images and 3 science images must be acquired per pointing for the pure spectroscopy mode (NUV+MUV and FUV), while 6 additional calibration images and 16 science images must be acquired per measurement for the spectropolarimetric mode. However, spectropolarimetric acquisitions are most of the time done as series of, typically 5, measurements to increase the SNR. As a consequence, a typical POLLUX observation will require about 4.2 GB per day, i.e., 33.64 Gb/d, without compression nor on-board processing, or 0.68 GB/d using a factor 4 lossless compression ratio and some on-board processing (averaging of the calibration frames). **Table H-2** below summarizes the telemetry budget for one typical POLLUX pointing in pure spectroscopy and spectropolarimetry modes. In comparison to the science data, the log files, metadata and other ancillary data have a marginal weight in the telemetry budget (less than 10%).

Table H-2. Summary of POLLUX Telemetry budget

Pure spectroscopy – budget for one pointing							
Mode	Data	Count	FUV	MUV	NUV	Total w/o averaging	Total with averaging
Calibration	flat-field	1	10	10	10	30	3
Calibration	bias	1	5	5	5	15	3
Calibration	dark	1	1	1	1	3	3
Calibration	wavelength	1	1	1	1	3	3
pure spectroscopy	spectra	1	1	1	1	3	3
Calibration	wavelength	1	1	1	1	3	3
Total (full images)						54	15
Data volumes (GBytes)						1.56	0.43
Data volume with compression (GBytes)						0.39	0.11
Spectropolarimetric mode – budget for one pointing							
Mode	Data	Count	FUV	MUV	NUV	Total w/o averaging	Total with averaging
Calibration	flat-field	1	10	10	10	30	3
Calibration	bias	1	5	5	5	15	3
Calibration	dark	1	1	1	1	3	3
Calibration	wavelength	1	1	1	1	3	3
Spectropolarimetric	spectra	5	4	6	6	80	80
Calibration	wavelength	1	1	1	1	3	3
Total (full images)						146	95
Data volumes (GBytes)						4.20	2.74
Data volume with compression (GBytes)						1.05	0.68

Among the science cases addressed by POLLUX, some require monitoring, especially the 3D magnetic mapping of circumstellar environments which requires measurements at 20 different stellar rotational phases. Assuming that all 20 measurements are obtained on the same day (i.e., that the stellar rotation period is short), the telemetry budget is 50.9 GB/d, without compression nor on-board processing, or 12.45 GB/d with compression and some on-board processing. Note that additional on-board processing could also be considered if necessary, such as windowing of the spectral orders.

The on-board software is embedded in the Data Processing Unit (DPU), itself part of the Instrument Control and Power Unit (ICPU).

H.4.2 Processing power

Several processing implemented in the POLLUX on-board software are time-consuming, in particular the compression algorithms. The management of the interfaces, due to the high input data rates, is also demanding in terms of processing power. A multi-core processor like the LEON4-FT GR740 processor seems to be at first glance well-sized for offering all the CPU resources needed by the software.

H.4.3 Memory resources

The POLLUX on-board software shall be able to acquire simultaneously up to two full images (28.8 MB x 2, i.e., 460 Mb). For managing the compression, the software shall also store in its working memory a set of reference full images. A memory space shall also be allocated for managing the full image averaging process. As a result, a total amount of 256 MB for managing the data (in SDRAM memory) is required. For the code execution itself, 32 MB (in SRAM memory) are needed.

H.4.4 Main budget for the Instrument Control and Power Unit

The Instrument Control and Power Unit (ICPU) consists of a power supply, the DPU board and most likely of another board providing analog circuitry for temperature measurement and of some electronics to operate the mechanisms. For the mass, a cold redundant unit is assumed ([power supply unit (PSU) + DPU + analogue board] x 2).

This power budget is for the ICPU only. If galvanic isolation for the sensor already inside the ICPU is needed, 20% to 25% of the sensor power may be added to the power dissipation of the ICPU (assuming 75 to 80% efficiency). The efficiency will strongly depend on demands for stability and accuracy. The converters for the sensors (high stability, accuracy,...) are usually not better than 60%.

However, the grounding is usually provided within the detector itself or its front end electronics.

H.4.5 Thermal load

The heat loads from the electronics and mechanisms in the current design are summarized in **Table H-3**. **Table H-4** shows the estimated cross-section for the wicks, while **Table H-5** summarizes the heat impact on the radiator temperature as a function of wicks size.

NB: please note that the EMCCD detectors present a peak power consumption of 10 W when used at 10 MHz in continuous readout (all output active).

Table H-3. *POLLUX ICPU budget*

	Dimensions (mm x mm x mm)	Mass (kg)	Power (W)	Comment
PSU	-	1.2	-	converter efficiency 80%
DPU	-	0.7	6	@50MHz
Analog board	-	0.6	4	
Housing	300 x 200 x 200	1.5	-	
Total	300 x 200 x 200	8	10	Including redundancy

Table H-4. *Summary of heat loads from the current design*

Source	Temp. zone (K)	Watts	Duty cycle	Ave. power (/hr)
NUV				
Detector FEE	270	11.8	Continuous	11.8
Detector FPA	170	1	Continuous	1
Collimator mechanism	270	2	(5 sec/hour)	2.8e-3
Polarimeter slide	270	2	(5 sec/hour)	2.8e-3
Polarimeter rotator	270	2	(30 sec/hour)	1.7e-2
MUV				
Detector FEE	270	11.8	Continuous	11.8
Detector FPA	170	1	Continuous	1
Collimator mechanism	270	2	(5 sec/hour)	2.8e-3
Polarimeter slide	270	2	(5 sec/hour)	2.8e-3
Polarimeter rotator	270	2	(20 sec/hour)	1.1e-2
FUV				
Detector FEE	270	11.8	Continuous	11.8
Detector FPA	170	1	Continuous	1
Polarimeter slide	270	2	(5 sec/hour)	2.8e-3
Collimator mechanism	270	2	(5 sec/hour)	2.8e-3
FUV input mirror	270	2	(3 sec/hour)	1.7e-3
Calibration unit				
CU input mirror	270	2	(5 sec/hour)	2.8e-3
CU selection mechanism	270	8	(20 sec/hour)	0.04
Flat lamp ignition	270	30	(1 sec/hour)	8.3e-3
Flat calibration	270	10	(120 sec/hour)	0.33
Wavecal lamp ignition	270	3	(1 sec/hour)	8.3e-4
Wavecal calibration	270	2	(120 sec/hour)	0.07
Other				
Detectors power supply	270	16.4	Continuous	16.4
On-board Computer	270	12	Continuous	12
Totals 170 K				3
Totals 270 K				64.3

Table H-5. Cross section for the cooling wicks, estimated for the conservative case of arrays at 170K.

Wick	Heat load (W)	Wick length (m)	DT (K)	Integrated Conductivity (W/m)	Cross section (m ²)
NUV	1	1+2	83	3.573e4	8.4e-5
MUV	1	1+2	83	3.573e4	8.4e-5
FUV	1	2+2	83	3.573e4	1.1e-4

H.4.6 Mass and Power budget for the calibration unit

The mass and power budgets for the calibration unit are presented in **Table H-7** and **Table H-8**. Full details about the calibration unit (550 mm x 300 mm x 270 mm) are available in

Table H-6. Radiator temperature versus size

Total heat load (W)	Radiator area (m ²)	Ambient (K)	Radiator temperature (K)
3	4	87	92
3	8	87	89
3	16	87	88

Table H-7. Preliminary mass budget for the CU, as currently evaluated

Calibration Unit Part		Mass (g)	Mass with 20% margin (g)
Deuterium arc lamp	Light source	600	720
Pt-Cr-Ne HCL	Light source	600	720
Wheel mechanism	Mechanism for lamp selection	2000	2000
Baffling block	Straylight reduction	800	960
Calibration unit's mechanical parts	Calibration unit housing	3 000	3600
Mirror assembly	Mirror and support	1000	1200
High voltage power supply	Power supply for HCL	4 000	4 800
TOTAL		12 000	14 400

Table H-8. Power budget of calibration unit

Calibration Unit Mode	Mode Description	Power (W)	Power with 20% margin (W)
Flat-field calibration	Lamp selection with wheel mechanism	8	9.6
	Lamp ignition	30	36
	Calibration with lamp in steady-state	10	12
Wavelength Calibration	Lamp selection with wheel mechanism	8	9.6
	Lamp ignition	3	3.6
	Calibration with lamp in steady-state	2	2.4
Scientific Observation Initialization	Calibration unit off	0	0

the dedicated **Appendix H.5**.

The aim of the power supply box (300 mm x 300 mm x 100 mm) is to provide power to the calibration lamps. These lamps work with high voltage current. Typically, hollow cathode lamps need about 300 V and 10 mA for ignition, and 200 V and 10 mA for steady-state operation; and deuterium arc lamps need about 300 V and 100 mA for ignition and 100 V and 100 mA for steady-state. Because the main electronics of POLLUX will provide power at 28 V, it will not be sufficient for our lamps. We thus need to design a custom power supply unit especially for the lamps.

H.4.7 Total Mass and Power budget for POLLUX

The overall payload budget is presented in the following **Table H-9** and **Table H-10**:

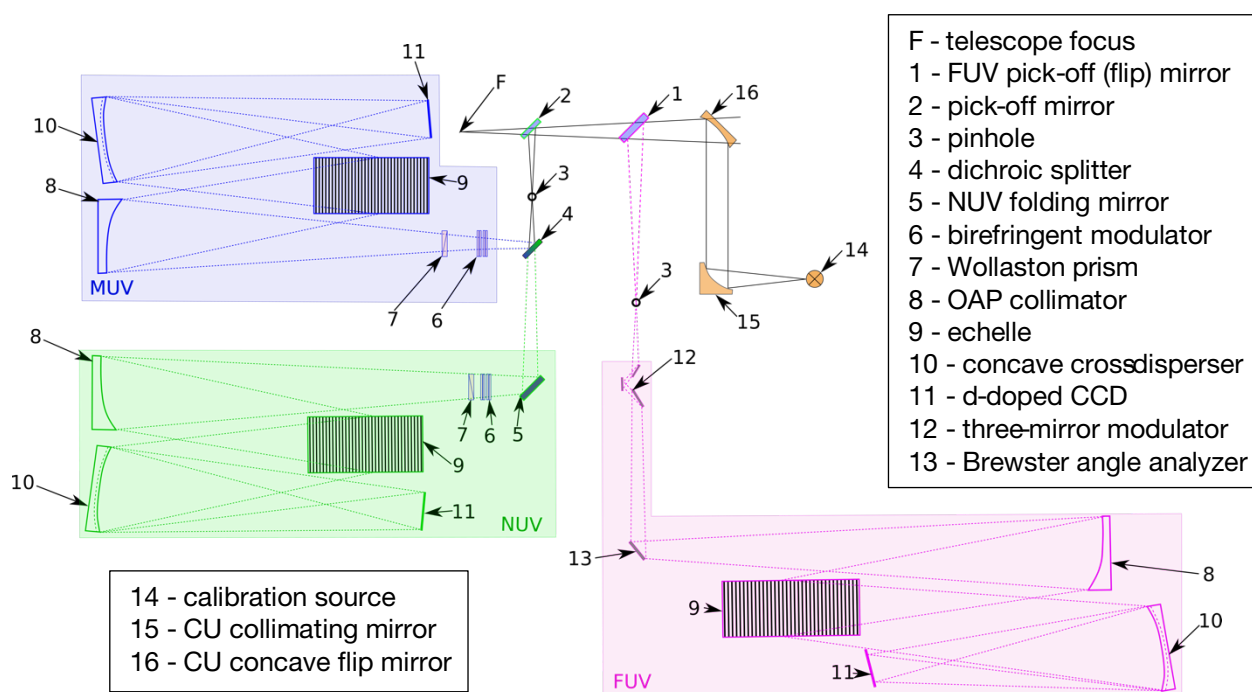
Table H-9. *POLLUX payload mass and volume budgets*

Designation number on the instrument optical layout (Figure H-15)		Mass (kg)	Volume (m ³)
Payload		375	5.2
Foreoptics		5.4	
1	FUV pick-off (flip) mirror	4.1	
2	NUV/MUV pick-off mirror	0.31	
3	Pinhole	0.25	
15	CU collimating mirror	0.36	
16	CU concave flip mirror	0.36	
NUV		51	0.355 x 0.280 x 1.550
structure	NUV chassis	39	
4	dichro	0.30	
5	NUV Folding mirror	0.30	
6 & 7	Polarimeter	0.44	
8	Collimator	1.9	
9	Echelle grating	4.0	
10	Cross-disperser	2.4	
11	Focal plane	3.2	
MUV		67	0.382 x 0.280 x 1.805
structure	MUV chassis	53	
6 & 7	Polarimeter	0.34	
8	Collimator	2.1	
9	Echelle grating	3.6	
10	Cross-disperser	4.5	
11	Focal plane	3.4	
FUV		179	0.500 x 0.665 x 3.317
structure	FUV chassis	142	
12 & 13	Polarimeter	4.3	
8	Collimator	8.0	
9	Echelle grating	5.0	
10	Cross-disperser	13.5	
11	Focal plane	6.5	

Designation number on the instrument optical layout (Figure H-15)	Mass (kg)	Volume (m ³)
Calibration unit	12	0.055 x 0.300 x 0.270
Common Structure / Support frame / electronics	61	0.650 x 0.796 x 3.500

Table H-10. *POLLUX* payload power budget

	Mass (kg)	Volume (m ³)	Power (W)
Payload	375	5.2	130
Detector electronics (per unit)	1.72	0.18 x 0.12 x 0.083	13
FEE power supply	2.33	0.18 x 0.12 x 0.083	16.4
ICPU	8	0.3 x 0.2 x 0.2	11
FCU	9.6	0.5 x 0.3 x 0.27	48
FCU power supply	4.8	0.3 x 0.3 x 0.1	16

Figure H-15. Schematics of the *POLLUX* instrument design

H.5 Calibration unit

This appendix describes the preliminary design of the in-flight calibration unit that should be implemented in the POLLUX instrument. The calibration unit is designed to inject the light of different well-known sources in the optical path of the instrument, allowing an in-flight calibration and monitoring.

Behind the entrance of POLLUX, a two-position mechanism holding a flip-mirror is placed to feed either the FUV channel or the MUV/NUV channels. The light from the calibration unit should be injected as early as possible in the optical chain in order to minimize the non-common path between science and calibration observations, i.e., at the flip-mirror level.

H.5.1 Calibration

In this section, we list the points that will be carried out by the calibration unit.

H.5.1.1 Flat-field

H.5.1.1.1 PRNU – Pixel Response Non Uniformity

The PRNU is commonly referred to as “pixel-to-pixel variation.” Most of these variations result from variations in the pixels’ effective detection surfaces, and are hence wavelength-independent. Consequently, to first order, this effect can be calibrated on the ground, by uniformly illuminating the detectors with white light.

The mean absorption depth of a photon in the detection layer of a CCD is wavelength dependent, so the PRNU may also have a small wavelength-dependent contribution. This, as well as the aging of the detector itself, needs to be monitored on a regular basis. A specific light source is required for this on-board. It needs to be as spectrally uniform as possible and it must illuminate all parts of the detectors that will be used for scientific or calibration purposes. It will hence be necessary to inject it before the polarimeter to calibrate the areas receiving the two polarizations from the sky.

H.5.1.1.2 Blaze function and cross-order profiles

The blaze functions and cross-order profiles will be calibrated via the flat-field light source.

H.5.1.1.3 Linearity

The detector linearity with flux can be estimated on the ground, and monitored in flight via series of flat-field measurements of varying duration, complemented by regular monitoring of celestial calibrators.

H.5.1.2 Wavelength calibration

The wavelength solution should be measured with a very high accuracy. The monitoring frequency shall be driven by the overall instrument stability (possibly demanding a measurement before and after every scientific acquisition, as assumed in **Section H.4.1**). It places requirements on the layout of the calibration unit and the light sources used for the wavelength

calibration: the sources must contain a sufficient number of spectral lines in every spectral order to guarantee an accurate wavelength solution.

H.5.1.3 Other points

Several calibration aspects have not been addressed because they are not directly impacting the definition of the calibration unit, as they are related to observation modes or other opto-mechanical parts of the instrument. We can cite:

- The detectors **dark current** is measured via series of dark exposures of various durations. The insertion of a shutter mechanism at the entrance of POLLUX is an option to avoid any light and/or stray light from the telescope to illuminate the detectors.
- The detector offset (**bias**) is measured via series of zero integration time exposures.
- The **Relative Spectral Response Function** (RSRF), i.e., the global spectral transfer function of the instrument, can be measured (and must be regularly monitored) via celestial standards of which the spectrum is known or can be modeled with sufficient accuracy.
- The optical elements most susceptible to ageing in flight include the main mirror and the entrance optics, all placed before any possible injection point of calibration sources. The **instrumental polarization** should be calibrated on-ground and monitored in-flight thanks to celestial standards.

H.5.2 Calibration Unit

The calibration unit will provide continuum flat-field (FF) source, in order to allow the calibration of pixel-to-pixel response variations, monitoring of the blaze function and estimation of the detector response linearity.

The calibration unit will also provide a spectral source, in order to do a wavelength calibration.

H.5.2.1 Flat-field calibration source

Deuterium arc lamps are very intense light sources covering a large part of the UV domain. In these lamps, a tungsten filament and an anode are placed inside a nickel box structure. An arc is created from the filament to the anode and excites the molecular deuterium contained within the bulb. The deuterium eventually emits light as it transitions back to its initial state.

Figure H-16 below presents the relative intensity spectrum of a commercial Deuterium lamp from Hamamatsu (Dever et al. 2002). This commercial lamp has its maximal intensity emission between 150 and 200 nm. Even if the relative intensity is not constant over the spectrum that will be covered by POLLUX, the variations are relatively smooth. Deuterium lamps are also the best identified solution to cover simultaneously the NUV and MUV channels

On the COS instrument on-board the HST, the FF calibration system consists of two deuterium lamps (nominal and redundant; Fischer et al. 2019). COS also has a FUV channel that goes down to 90 nm. However, it is specified in Fischer et al. (2019) that the deuterium lamps are not bright enough to map out the FF at FUV wavelengths. Therefore, they

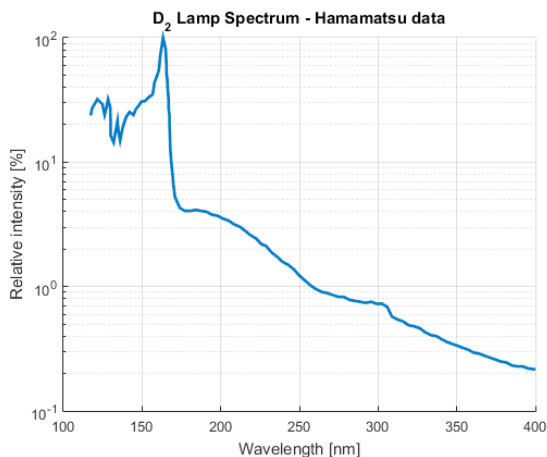


Figure H-16. Deuterium lamp spectrum

are performing the FUV flats by combining observations of bright white dwarfs. We propose the same approach.

H.5.2.2 Wavelength calibration source

A Hollow Cathode Lamp (HCL) consists of an anode and a cathode inside of a glass tube. An inert gas is placed inside the glass tube and when a high voltage is applied between the anode and the cathode, the gas starts ionizing, creating plasma. The ions are then accelerated into the cathode, sputtering off atoms from it. After that, both the gas and the sputtered cathode atoms are excited by col-

lisions with other particles in the plasma. Eventually, these excited atoms decay to lower states thereby emitting photons at precise wavelengths, depending on the inert gas and the cathode material.

The most suitable choice for the spectral calibration lamp is Platinum-Neon HCL. This kind of calibration lamp has the advantages to have a high heritage in space missions such as IUE and HST (with COS and STIS instruments) and to cover the UV spectral domain of 113 to 320 nm with more than 3000 spectral lines (Kerber et al. 2005b; Pascucci et al. 2010; Fischer et al. 2019). In order to cover a wider part of the UV spectral range with a high density of spectral lines, we can add about 10% Cr to the cathode to extend the wavelength coverage. This was done for the STIS instrument on-board the HST (see Kerber et al. 2005a)

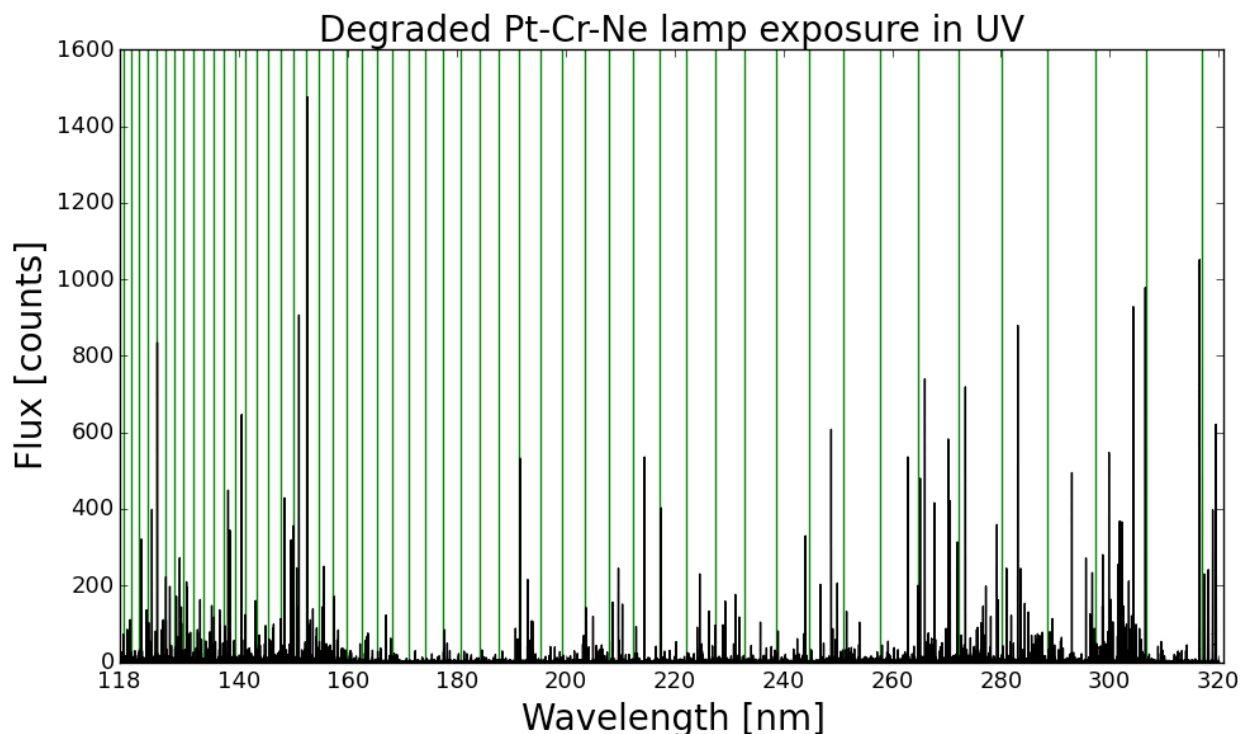


Figure H-17. Degraded Pt-Cr-Ne spectrum from Kerber et al. (2005a).

to get a continuous distribution of emission lines for the range 113–800 nm as it was specified for STIS. **Figure H-17** shows a reference calibration spectrum used on STIS (HST) which is just a small part of the spectrum. The full spectrum is presented in **Figure H-17** and **Figure H-18** in log scale (Kerber et al. 2005a).

H.5.2.3 Selection mechanism

We expect to design a selection mechanism inside the calibration unit. The mechanism will be used to select the calibration mode that should be used and more precisely, the lamp that should be used. As it is illustrated in the previous sections, at least two calibration lamps are needed for totally different purposes. Therefore, it is necessary to design a unit able to propose a FF calibration mode and a wavelength calibration mode.

Several solutions are possible:

- Place the lamps on a rigid support facing the mechanism. Mirrors are mounted on the mechanism assembly to select which lamp is used for the calibration. The mechanism is a wheel assembly with several positions. Each position is associ-

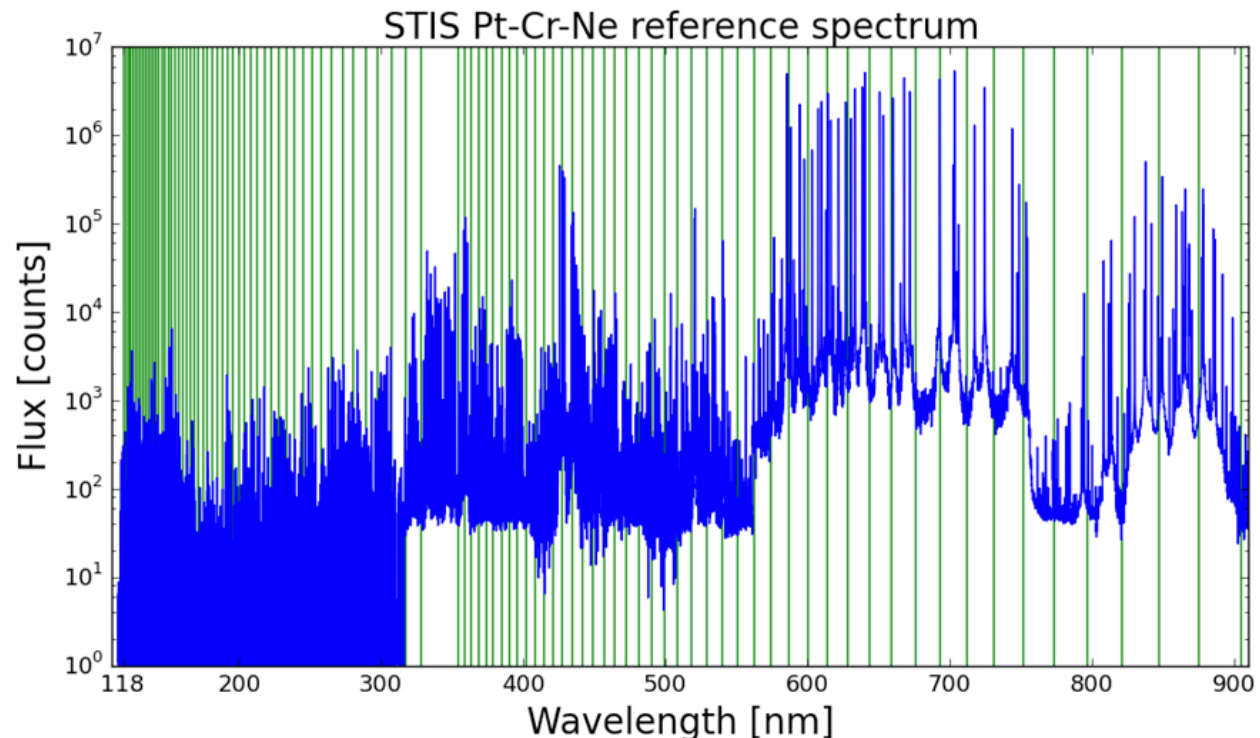


Figure H-18. *STIS Pt-Cr-Ne reference spectrum (Kerber et al. 2005a). As for the FF calibration, the Pt-Cr-Ne HCL is not able to cover the entire FUV channel spectral domain, only going down to 115 nm instead of 90 nm. The problem is also encountered on COS where they have to limit the achievable resolution at shorter wavelength because of the lack of calibration lines*

ated to a mirror which is also associated to a specific light source in front of the assembly.

- Place the mirror(s) on a rigid support facing the mechanism. In this case, the lamps are mounted on the wheel mechanism at each position of the wheel.

- Place the lamps on a rigid support facing a single mirror assembly mounted on a mechanism. The mirror is rotating around one axis in order to be able to scan all the lamps, as a turret assembly.

At this preliminary stage, we evaluate that the second solution is preferable because it is lighter than the first option and a priori smaller than the third option. Regarding the second solution, it is possible to design the system in such a way that only one mirror is placed in front of the mechanism assembly with the lamps. The first solution requires as many mirrors on the mechanism as input stimuli (i.e., more than two, considering redundancy). The third solution could also be interesting to investigate to compare the volume and mass with the second solution. The mechanism configuration will be study at the early stage of the project (Phase A) in order to select the most suitable and robust solution.

As stated above, the baseline for the mechanism concept is a wheel assembly. The wheel assembly should be associated to a stepper motor that allows rotating the wheel around its axis. This kind of mechanism assembly has already been used in space missions and is therefore not considered as a critical point for the design definition.

H.5.3 Block diagram

The block diagram of the calibration unit interfacing with the instrument is shown below. In the diagram below, the blue boxes are related to the telescope and the POLLUX instrument and are then not part of the calibration unit. However, it shows at which point of the instrument the signal from the calibration unit should be injected.

The calibration unit box has an “Optics” box inside because we will need to integrate at least a mirror assembly to create a collimated beam as the optical output of the calibration unit for the instrument. A simple off-axis parabola should be sufficient to create the collimated beam.

The “Calibration lamps & Selection Mechanism” box contains the deuterium and Pt-Cr-Ne lamps discussed in the previous sections. Considering redundancy and possible lifetime issues, we consider cold redundancy for all the lamps, which are tripled, for a total of six lamps. Redundant lamps will be used during the mission if the nominal ones break down or if the ageing effects do not allow the system to reach the required performance. It has to be noted that the ageing of the Pt-Cr-Ne lamps has been monitored and studied for STIS (Kerber et al. 2005a; Pascucci et al. 2010). Similar studies will be repeated for all lamps considered here during Phase A. The box in the diagram also contains the selection mechanism presented in **Section 14.3.3** because the lamps are mounted on this mechanism assembly. As it is stated in the previous section, we selected this configuration for the selection mechanism at this stage. The final design will be selected during phase A.

There is also a “High Voltage Power Supply” box associated to the calibration unit. This power supply is required because we intend to work with arc and hollow cathode lamps and as it is explained in the operation of these lamps, they need the application of high voltage between the anode and the cathode/filament for ionizing the gas inside the bulb of the lamp. For example, a classical off-the-shelf HCL would require: 3W for ignition using 10 mA and 300 V and 2W for steady-state using 10 mA and 200 V (Klose & Bridges 1987). The power needed for deuterium lamps is much higher according to information from Hamamatsu as

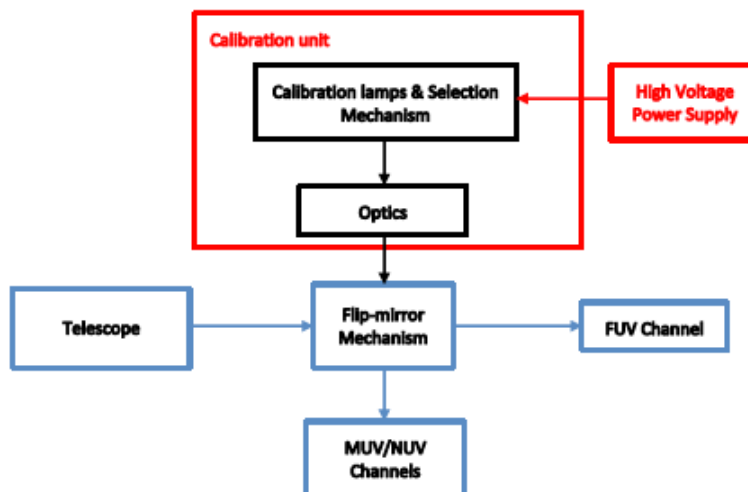


Figure H-19. Block diagram of the calibration unit

the high voltage is of the same order as for HCL (300 V) but the current is around 100 mA, leading to a peak power for ignition of 30W.

At this preliminary stage, we do not expect to have a high voltage power supply from the satellite for all the sub-units. Therefore, we consider that the high voltage needed for the lamps is under the responsibility of the calibration unit and we plan to integrate an electrical transformer to convert low voltage into high voltage.

H.5.4 Overview of the Calibration Unit Preliminary Design

Figure H-20 shows the 3D overview of the calibration unit. The wheel assembly supporting the nominal and redundant lamps is placed in front of the mirror assembly that inject the light beam toward the POLLUX instrument. A baffle block is placed between the wheel and the mirror in order to minimize the straylight that could be seen by the instrument while in calibration mode.

The envelope/size of the whole unit is detailed in (Dever et al. 2002). The calibration box size is 550 x 300 x 270 mm while the associated high voltage power supply (that is not presented in **Figure H-20**) is 300 x 300 x 100 mm.

H.5.5 Power Supply

The aim of the power supply box is to provide power to the calibration lamps. These lamps work with high voltage current. Typically, hollow cathode lamps need about 300 V and 10 mA for ignition and 200 V and 10 mA for steady-state operation and deuterium arc lamps need about 300 V and 100 mA for ignition and 100 V and 100 mA for steady-state.

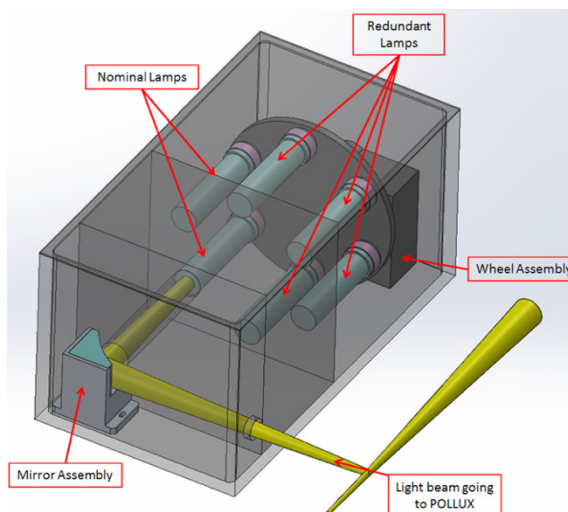


Figure H-20. Schematic rendering of a possible calibration unit of POLLUX.

Because the main electronics of POLLUX will provide power at 28 V, it will not be sufficient for our lamps. We thus need to design a custom power supply unit especially for the lamps. Some precautions have to be taken when using high voltage systems in space applications according to NTSS standards (corresponding to European ECSS-E-HB-20-05A).

Usually, high voltage power supplies are made of a transformer to step-up an AC voltage and to transfer electrical power by magnetic coupling between circuits while keeping DC isolation. Due to magnetic effects, the system should be isolated from the other parts of POLLUX. A suitable shielding will be designed for the transformer.

H.5.6 Power Budget

Concerning the power budget, we have to define some operating modes in order to quantify the instantaneous power consumption. It is done in **Table H-8** taking into account the calibration unit design and constraints.

H.5.7 Evaluation of Technology Readiness

The technology readiness level (TRL) of key technologies in the calibration unit of POLLUX instrument shall be evaluated to identify the potential risks and critical points for the development. They are summarized in **Table H-11**.

H.5.8 Conclusion and Open Points

The design of the calibration unit we propose consists of a set of six lamps (nominal + redundant) mounted on a wheel mechanism and place in front of a mirror that injects the light in the optical path of POLLUX. A high voltage power supply is also needed for the calibration lamps.

Section 14.1.7 shows that we have not identified high criticality or high risk for the development of the calibration unit. However, we assume that the development of the selection mechanism and the UV coating of the mirrors have medium criticality and risk. Concerning

Table H-11. Summary of technologies of the calibration unit with their associated criticality, the associated risk of the development and their evaluated TRL

Calibration Unit Part		Development criticality	Development risk	Remarks	TRL
Deuterium arc lamps	Light source	Low	Low	Characterization of the lamps and ageing – Normal work	>5, already flown
Pt-Cr-Ne HCLs	Light source	Low	Low	Characterization of the lamps and ageing – Normal work	>5, already flown
Reflective UV optics	Optics for light injection in the optical path	Low	Low	Mirrors are classical	>5, already flown
UV coating	Coating for the optics of the unit	Medium	Medium	The optics have to be coated and efficient for the NUV and MUV channels – Normal work	3 for MUV and NUV and >6 for the FUV. See Table 13-5 .
Selection mechanism	Mechanism for calibration mode selection	Medium	Medium	Specific development and qualification – Normal work	>5, similar systems already flown
High Voltage Power Supply	Power supply for HCLs	Low	Low	Specific development and qualification – Normal work	>5, already flown

the coating, we have to identify the best solution corresponding to the maximum reflectance of the mirrors over the full spectral range. The same concerns are valid for the mirrors of the instrument. Regarding the selection mechanism, it has to be noted that the qualification of the assembly should be strong because it corresponds to a single point of failure for the calibration unit. However, this will be mitigated via the introduction of a redundant drive and control of that mechanism.

Eventually it is demonstrated that the light sources that are proposed and that have been used in the past for the calibration of UV instruments are not able to cover a large part of the FUV channel. At this stage, there is consequently no internal optical stimuli foreseen for the calibration of the FUV channel. This will be performed via celestial calibrators (essentially white dwarfs).

H.6 Performances

H.6.1 Spectral resolution

It is assumed that the resolution difference between the two polarization states is smaller than the sampling in numerical modelling—see the spot diagrams below.

In order to account for possible misalignments due to switching from the pure spectroscopic mode to the spectropolarimetric one, the target spectral resolving power was set to 123,000 rather than the required 120,000. Typical values reached with the present POLLUX design are listed in **Table H-12**, and plotted in **Figure H-21**. Note that the theoretical

Table H-12. *Summary of spectral resolving power*

Wavelength (nm)	Order	Spectral resolving power	Spectral length of the order on the detector (nm)
NUV			
388.15	33	129,838	11.94
394.03		131,835	
400.09		133,832	
261.41	49	133,157	8.04
265.37		131,811	
269.45		130,467	
197.06	65	129,651	6.06
200.05		131,750	
203.12		130,736	
MUV			
193.52	30	125,973	6.56
196.74		131,178	
200.08		133,349	
145.14	40	132,854	4.92
147.56		131,214	
150.06		129,574	
116.11	50	125,450	3.93
118.04		131,145	
120.04		129,833	
FUV			
118.52	20	125,973	6.1
121.48		131,178	
124.59		133,349	
103.06	23	132,854	5.3
105.63		131,214	
108.34		129,574	
87.79	27	125,450	4.5
89.98		131,145	
92.29		129,833	

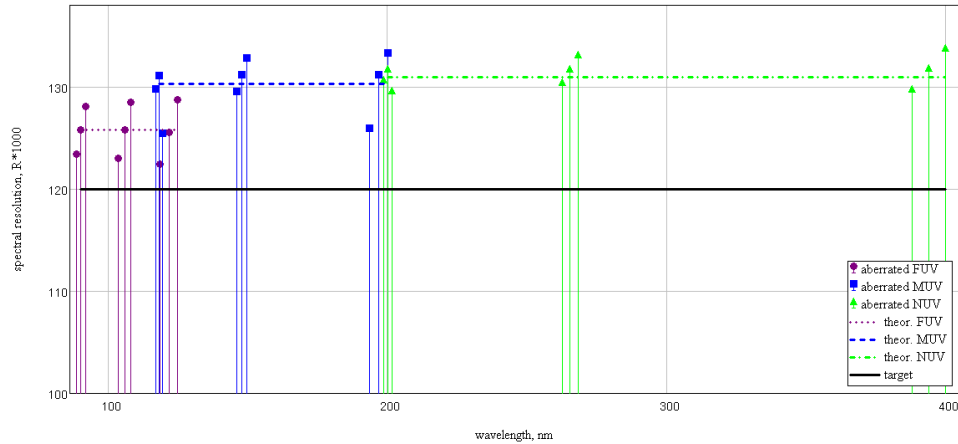


Figure H-21. *Spectral resolving power chart*

resolution of the FUV was intentionally decreased in order to fit the detector length limitations (see **Figure H-21**).

The spectral resolution for each order listed in **Table H-12** is for the trapezoid of wavelength that do not overlap, while the wavelengths on the first column (and the order length, last column) is provided for the full orders on the detectors.

Below we illustrate the efficiency of the different elements of POLLUX, that were considered for the computation of POLLUX total efficiency (see **Section 14.2.8**).

We note that most of these data came from the corresponding experts or working group. Corresponding references are provided whenever possible. We also note that in order to avoid issues with sampling difference, noises etc. in the initial data, all the efficiency data were interpolated. Hence, all the spectral dependences are presented by smoothed envelope curves.

H.6.2 Dichroic

Figure H-22 shows the efficiency of the dichroic separating the NUV and MUV ranges. See **Section 14.3** for the description of this element.

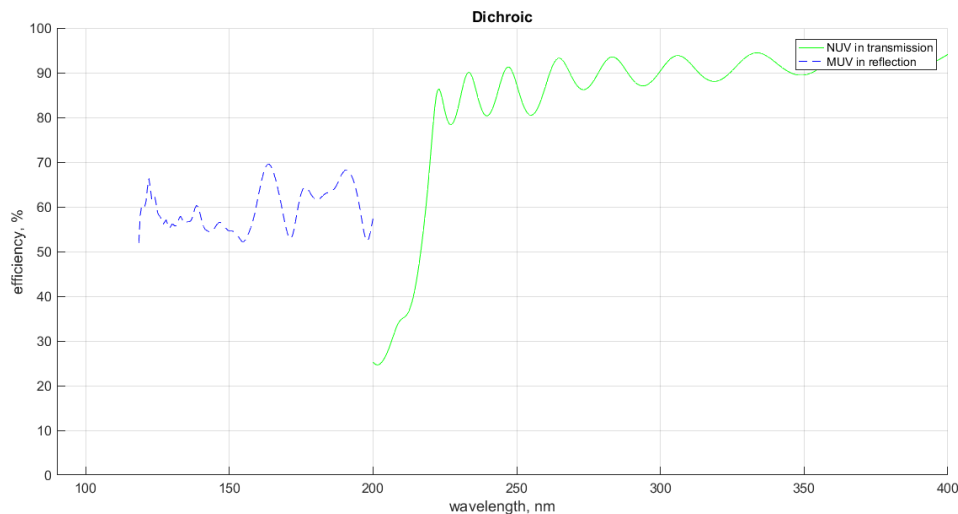


Figure H-22. *Efficiency of the dichroic separating the beams for NUV and MUV (resp.), from a preliminary study performed by Safran REOSC (see also Section 14.3)*

H.6.3 Echelle gratings

The customized echelle gratings can be produced on a Si substrate by means of photolithography and e-beam-etching (Tutt et al. 2016). Due to the material properties the peak of the triangular groove profile has an angle of 70.6 degrees instead of 90 degrees. Also, for the efficiency estimation the deviation from the Littrow mounting was neglected. Theoretically, the given result can be further improved after the profile etching optimization.

On the other hand, the technology has not been tested yet at gratings with sizes larger than 140×140 mm (see also Marlowe et al. 2016, McEntaffer et al. 2013). We must emphasize that at the current stage possible signal summation for the overlapping parts of adjacent orders is not accounted for. Thus, the minima on **Figure H-23** may be increased, though the maxima will remain the same.

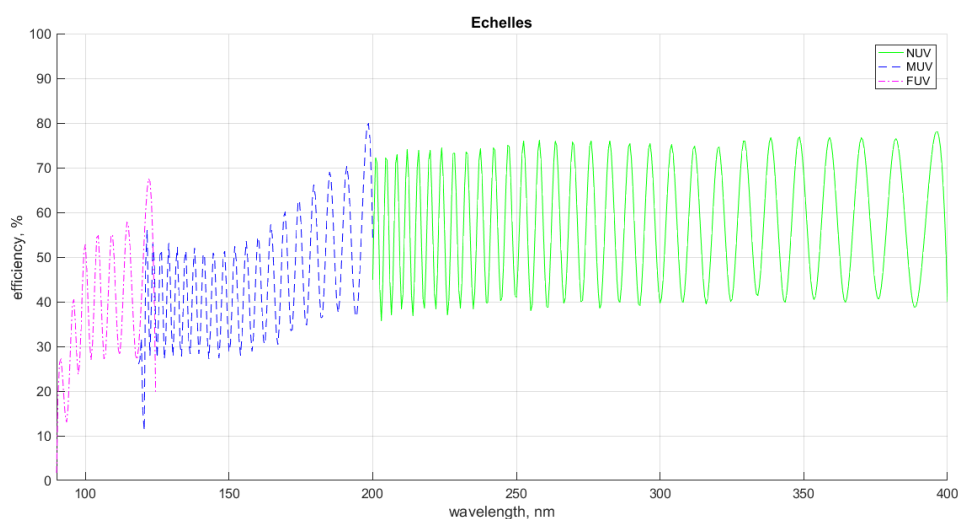


Figure H-23. Theoretical efficiencies of the customized echelle gratings for NUV, MUV, and FUV channels, from a preliminary study performed by the team of R. McEntaffer at Penn State University (see Section 14.3). Here, only the envelope curve is shown.

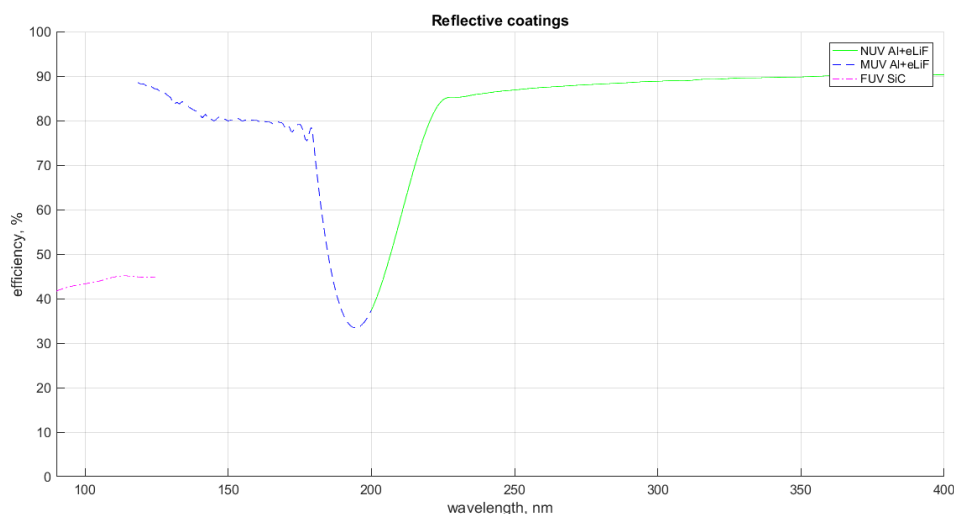


Figure H-24. Theoretical efficiencies of the eLiF coating (for NUV, MUV), and SiC (FUV), assumed for the pick-off mirrors and polarimetric modules of the three channels, respectively.

Al+eLiF reflectivity data was provided by the LUVUOIR Study Office. The data for SiC was taken from Fernández-Perea et al. (2006).

H.6.4 Birefringent materials

In the MUV and NUV channels the polarization units contain birefringent elements made of MgF_2 . **Figure H-25** shows their transmission which accounts for the thicknesses and spectral properties. The MgF_2 data are taken from Dodge (1984) and cross-checked with the Crystan database¹.

H.6.5 EMCCD detectors

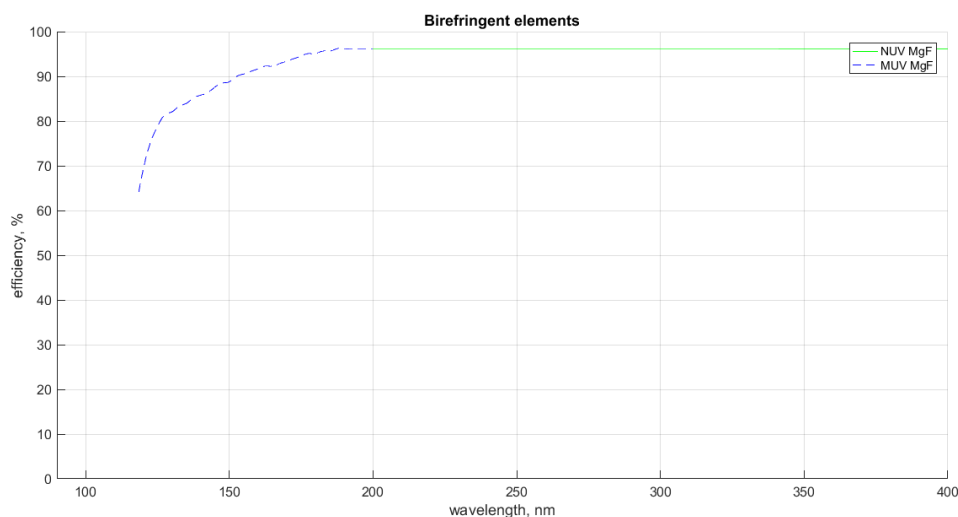


Figure H-25. Throughput of the birefringent optical elements.

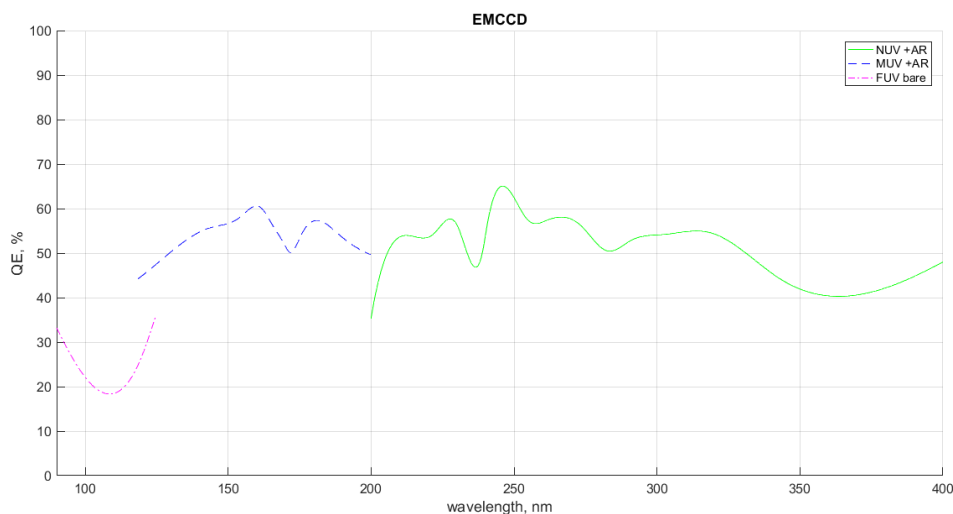


Figure H-26. Theoretical Efficiency of an AR coated δ -doped CCD.

As was stated before, the baseline implies use of δ -doped EMCCD's in all the channels. They have relatively high quantum efficiency down to the extreme UV (Nikzad et al., 2016, 2017). Here we apply the QE data for an AR coated EMCCD (Nikzad et al., 2016). The envelope efficiency curve is shown in **Figure H-26** (see also **Section 14.2.8**).

¹ <https://www.crystran.co.uk/userfiles/files/magnesium-fluoride-mgf2-data-sheet.pdf>

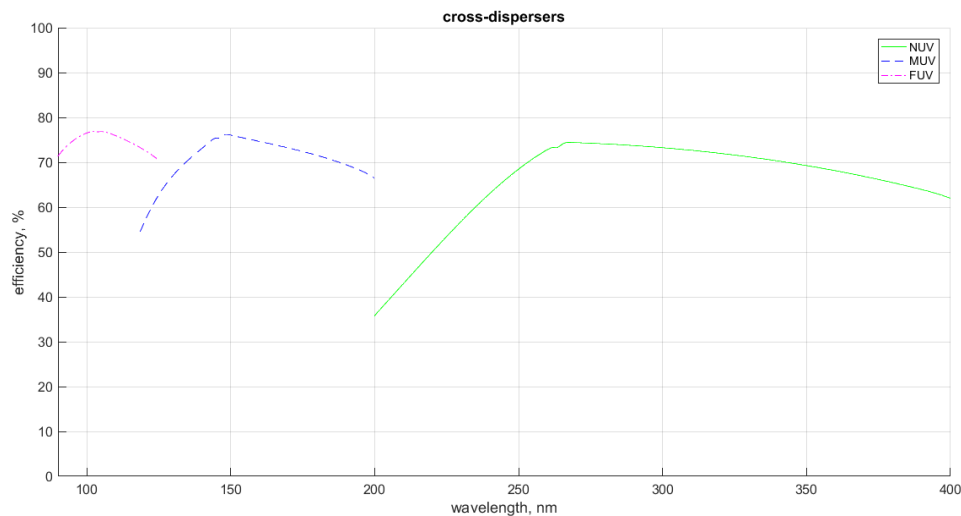


Figure H-27. Theoretical diffraction efficiencies of the cross-dispersers computed with the RCWA method.

H.6.6 Cross-dispersers

The cross-dispersers efficiencies were computed with use of the RCWA (rigorous coupled-wave analysis) method, implemented in the GD-calc software. The computation was performed as follows. For each channel, twelve control wavelengths were taken (the same ones as for the image quality analysis). In each beam 100 rays were generated in a regular grid to cover the footprint at the grating surface. For each point the real ray data including the direction cosines for the local normal vector, the incident and diffracted beams were extracted. The local changes of the groove frequency and curvature computation was simplified: the real aberrated recording wavefronts were replaced by the nearest spherical ones. Then using the GD-calc solver the diffraction efficiencies for two polarization states were computed. It was supposed that the groove profile is triangular blazed for the central wavelength for each sub-range and the profile depth is $\frac{1}{2}$ of this wavelength. After computation averaging for all rays and for two polarization states was performed and the spectral dependence was restored.

Note that the cross-dispersers are recorded by two oppositely directed laser beams. The front-illuminating beam is aberrated by an auxiliary mirror to compensate the aberrations. The mirrors are freeform, although we anticipate that they may be simplified to ordinary aspheres, if the astigmatism is controlled by the mirror tilt.

In the NUV and MUV schemes flat freeforms in parallel beams are used, but they have clear apertures close to that of the recorded grating. In the FUV case the auxiliary mirror is mounted in a diverging beam, so the clear aperture is smaller. The back-illuminating mirror comes from a collimator. To compensate the substrate influence this beam is slightly defocused. The incidence angles of the two beams are computed to provide a blazed groove profile. See **Figure H-28** and **Figure H-29**.

In principle, tilt angle of the auxiliary mirror may be used instead of ast3 summand in the surface equation. It could help to simplify the recording mounting, but requires an iterative re-design of the recording geometry.

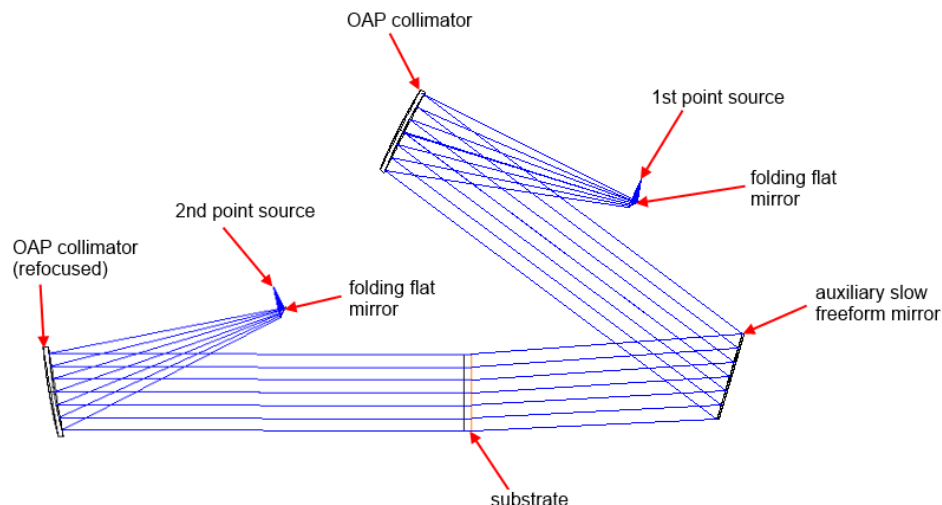


Figure H-28. Cross-disperser grating recording scheme for the NUV and MUV (OAP: Off-Axis Parabolic)

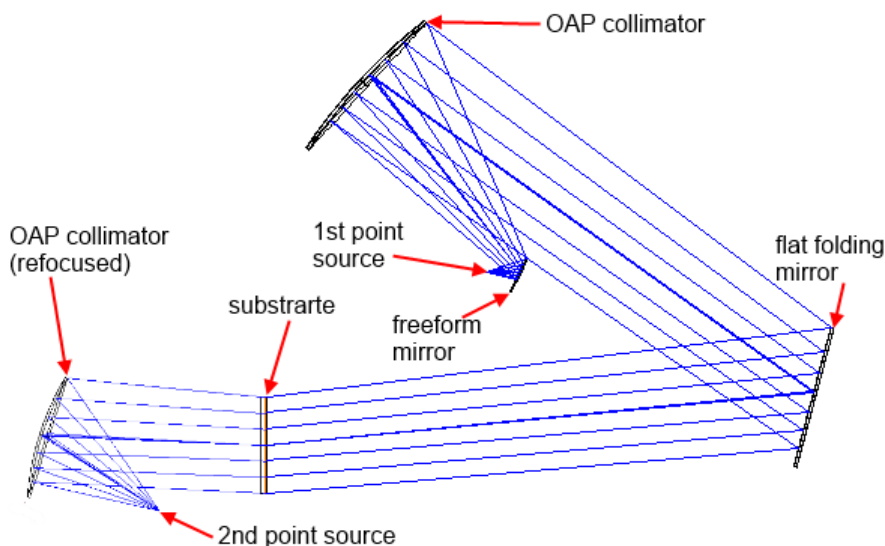


Figure H-29. Cross-disperser grating recording scheme for the FUV

H.6.7 Comparison with HST-COS

Figure H-30 and **Figure H-31** present a comparison of the effective area of POLLUX vs the COS spectrograph onboard HST (Fischer et al. 2019). POLLUX is superior to COS by several orders of magnitudes at most wavelengths except around ~ 200 nm:

H.6.8 Image Quality

The spot diagrams (**Figure H-32**, **Figure H-33**, **Figure H-34**) demonstrate a few important points. First, they show the achieved aberration correction. The spot size in the main dispersion direction (X axis on the plots) is small for all the cases and it is close to the pinhole width. Second, the diagrams are elongated in the cross-dispersion direction (Y axis). This elongation was allowed by decreasing the corresponding weight coefficient in optimization. This allows us to achieve the necessary resolution, and match all the boundary conditions.

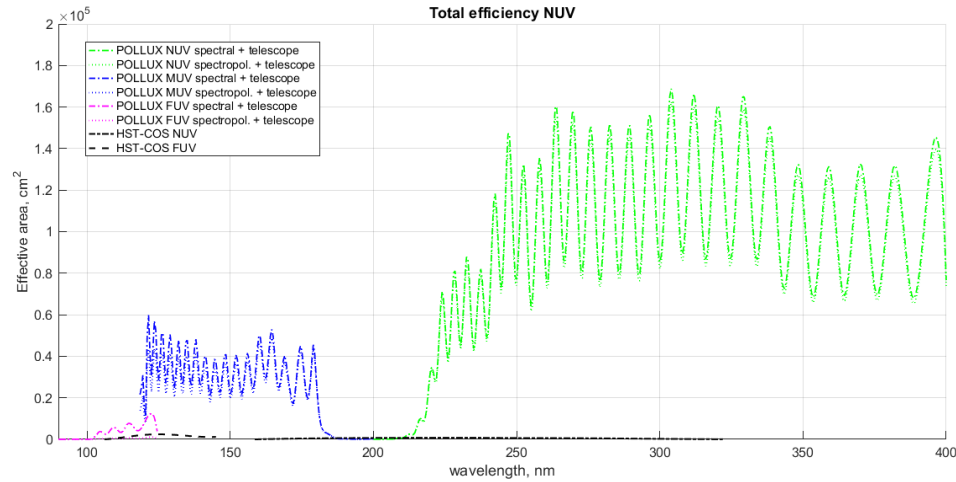


Figure H-30. Effective area of POLLUX channels (colors) vs HST/COS (black lines)

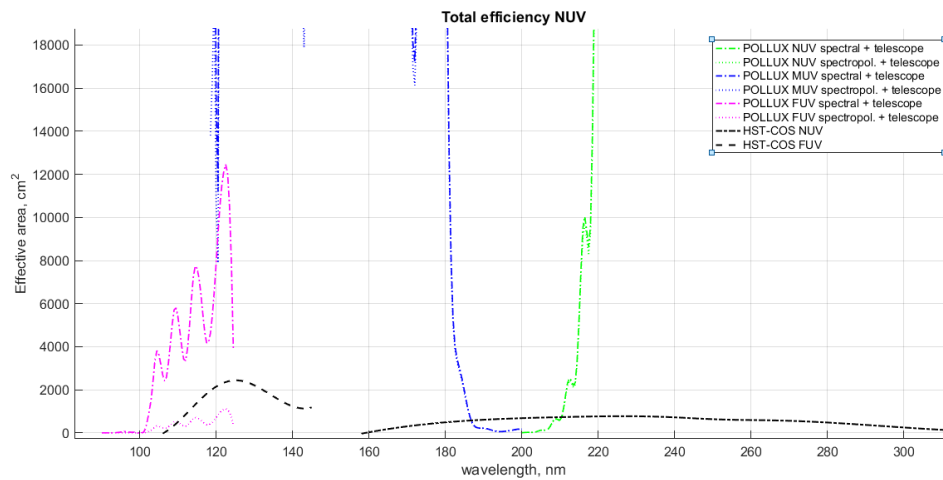


Figure H-31. Zoom of effective area of POLLUX channels (colors) vs HST/COS (black lines)

Third, the spot diagrams demonstrate that the image quality for the ordinary and extraordinary beams in the spectropolarimetric mode remains approximately the same. So hereafter we do not need to repeat image quality estimations for two polarization states.

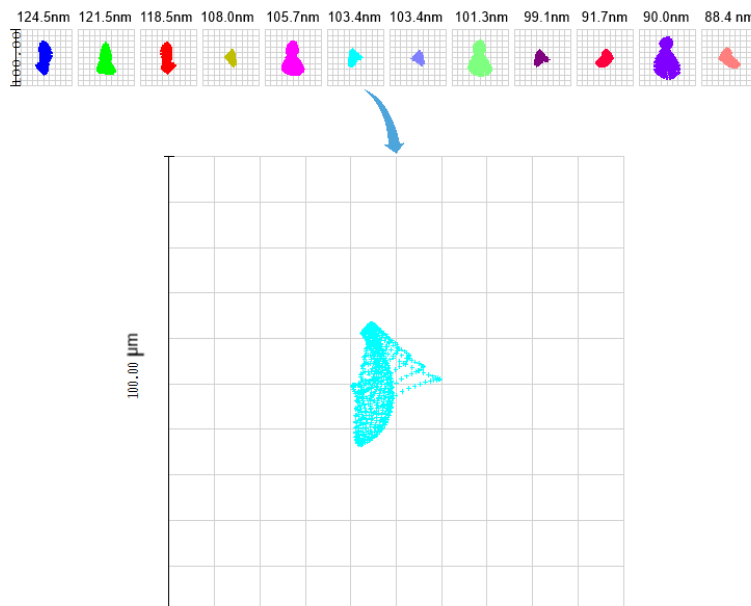


Figure H-32. FUV channel spot diagrams

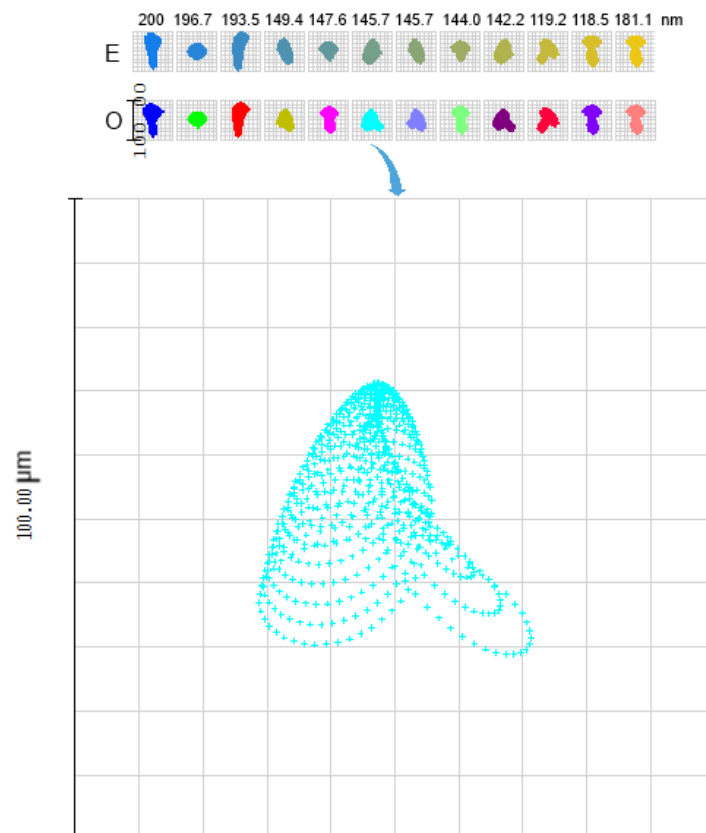


Figure H-33. MUV channel spot diagrams

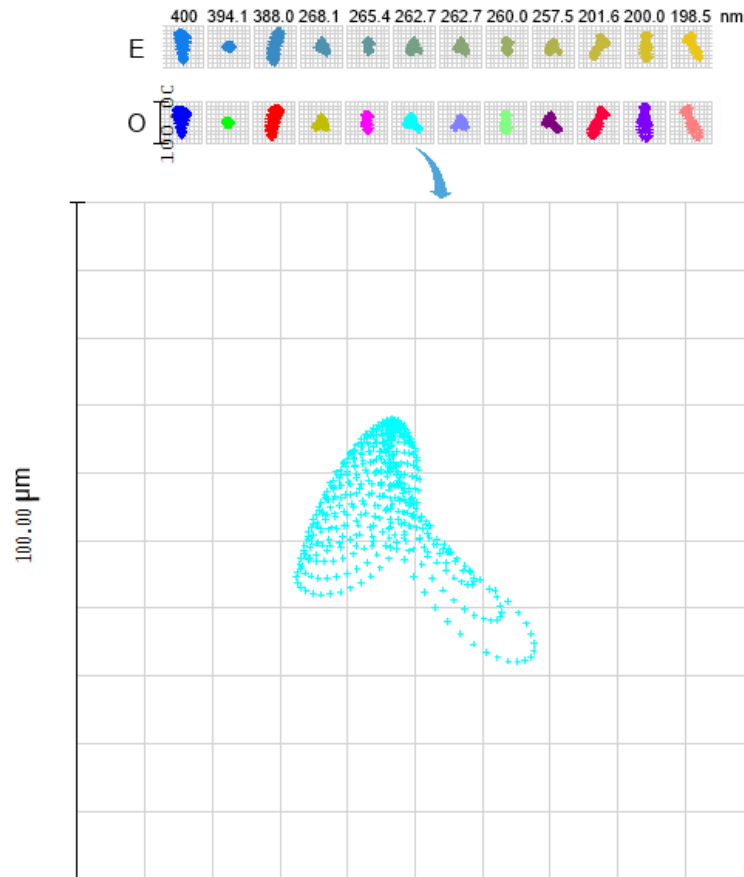


Figure H-34. *NUV channel spot diagrams*

H.7 A simulator for POLLUX

The POLLUX simulator can be downloaded at <https://github.com/Simlomb/PolluxSimTools>

In this package there are several modules, one can use. For example:

1. Run the web-ETC locally from a terminal as: `bokeh serve --show pollux_etc/`
2. Run the full simulator from a terminal as: `python main_pollux.py`

The web-ETC (which can be used also from https://polluxetc.lam.fr/pollux_etc) takes as input a series of parameters (aperture size, redshift, AB-magnitude of the object, exposure time) that can be set by the user. It also allows several possible SED templates as input and provides plots with the SNR (**Figure H-35**) for the selected observing channel/mode for POLLUX (NUV, MUV, FUV, both in spectropolarimetric and spectroscopic-only mode).

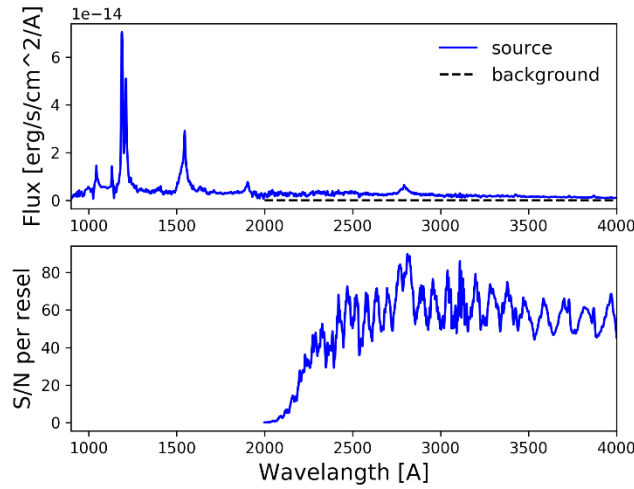


Figure H-35. Example of input SED and background (top panel), and corresponding SNR for the NUV channel of POLLUX (bottom panel). The input template is a Seyfert 1 template of 17.2 mag AB, integrated for 2.5 hrs at redshift 0. In order to avoid saturation of the sensor, 8 different exposures were added to reach the total exposure time of 2.5 hrs.

The detectors chosen for POLLUX are EMCCDs, which, when operated in Electron Multiplication mode (EM), provide an additional gain, G , up to $\times 1000$ and an additional noise term, the Excess Noise Factor (equal to $\sqrt{2}$ for gain of 1000). For an input spectrum (list of templates in **Table H-13** of flux ϕ (in counts/(s \cdot cm² \cdot Å)), background equivalent flux, BEF (in counts/(s \cdot cm² \cdot Å)), exposure time t_{exp} , the SNR equation used is:

$$SNR = \frac{I}{\sqrt{(I + B + D) \cdot ENF^2 + RON^2 \cdot N_{\text{pix}}}},$$

where $I = \phi \cdot A_{\text{eff}} \cdot t_{\text{exp}} \cdot \Delta\lambda$ is the input flux in counts as observed by POLLUX, $B = BEF \cdot A_{\text{eff}} \cdot t_{\text{exp}} \cdot \Delta\lambda$ is the astrophysical background (Earth-glow and interplanetary Ly α) in counts as observed by POLLUX, $A_{\text{eff}} = R_L^4 \cdot A_L \cdot T_{\text{Pollux}} \cdot QE_{\text{EMCCD}}$ is the effective area of the POLLUX channel considered, $D = D_c \cdot t_{\text{exp}} \cdot N_{\text{pix}}$ is the total dark noise in counts and $RON = RON/G$ is the readout noise of the EMCCD operated in EM mode.

In the previous equation we considered that the EMCCDs were used in imaging mode, we also considered that $\Delta\lambda = \lambda/R$ where R is the resolution of POLLUX, R_L is the reflectivity of the LUVOIR's mirrors and A_L is its aperture area, T_{pollux} is the efficiency of the POLLUX channel considered, QE_{EMCCD} is the quantum efficiency of the related EMCCD, D_c and RN are its dark and the readout noise respectively, and finally N_{pix} is the number of detector pixels within the FWHM of the object observed.

If the observations are made with the photon counting mode of the detectors, then the equation is:

$$SNR = \frac{DP \bullet I}{\sqrt{(I + B + D + C \bullet N_{\text{pix}} \bullet N_{\text{frame}}) \bullet DP}},$$

where DP is the detection probability, C is the clock induced charge noise, that becomes dominating when reading out fast, N_{frame} is the number of frames required to have a total exposure time of t_{exp} . For these calculations we assumed a $DP = 0.75$ for a gain of 1000, with a threshold at 250 counts/frame.

The simulator provides also a best observing strategy in case the required magnitude/exposure times will saturate the detectors. For a given total exposure time, it prints on the terminal the number of frames required and the duration of each of them. In case the

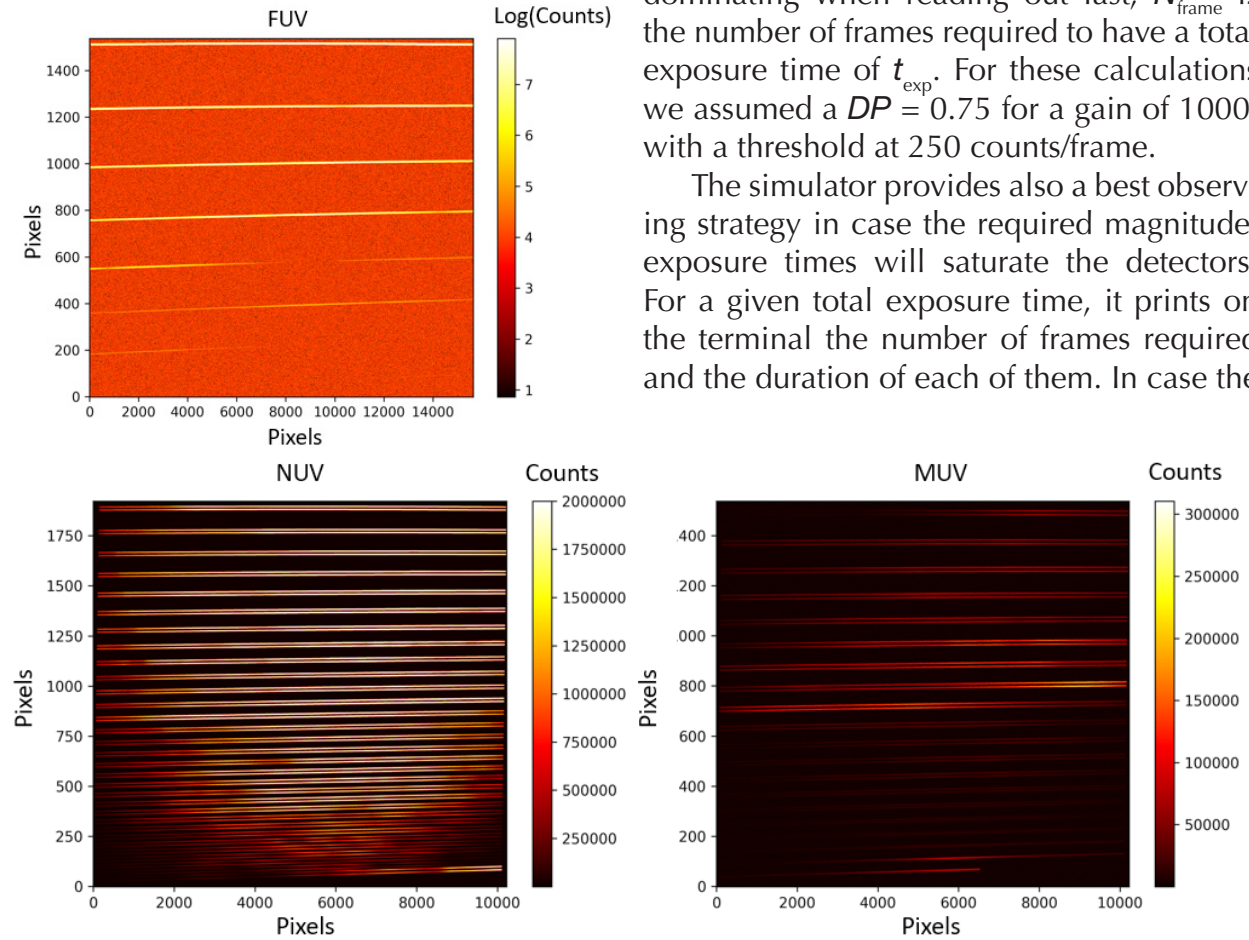


Figure H-36. 2D images from POLLUX simulations in polarimetric mode. The input template is a Seyfert 1, integrated for 2.5 hrs. Top left NUV channel image and top right MUV channel image: the object has 17.2 mag AB. The object is observed at the same time in these two channels. Bottom left: FUV channel image, the object has 11.2 mag AB. The x-axis and y-axis of the images are not plotted with their physical scales as the number of pixels in x-direction is too large and would make the rendering of the plot very difficult. Note that the FUV channel image is plotted in log scale to enhance the flux at the shortest wavelengths.

requested magnitude still generates too many photons, the SNR appears flat in the saturated regions.

The simulator `main_pollux.py` also allows to generate 2D images of POLLUX. These images show, for each channel, the positions of the echelle spectra generated (also for the two polarization states if the observing mode is with polarizers in). The simulator includes the BEF, the blurring effect due to the instrumental Point Spread Function (PSF), and some of the effect of the noise terms, such as EMCCD gain non-uniformity, readout and dark noise, saturation. The images produced are generated for the imaging mode and the photon counting mode of the EMCCDs.

For the simulation of the SNR and the 2D image, the user can insert a name with which the plots and the data files generated are saved in a directory within the package (`/pollux_tool/`). In the 2D image case, also a map of the wavelength position across the EMCCD is saved. An example of 2D images generated for a 2.5-hour observation of a Seyfert 1 of 17.2 mag AB (for NUV and MUV channel) and 11.2 mag AB (for FUV channel) is shown in **Figure H-36**. The images appear squared instead of rectangular (as the actual shape of the sensors), because the number of pixels in x-direction is too large and would make the rendering of the plot very difficult, hence different scales have been used for the X- and Y-axis.

A list of the options available for the simulator is accessed with `main_pollux.py -h`

When requesting the gain `-g 1`, the usage mode for the detectors switches automatically to imaging mode without any EM gain. This has consequences also on the smallest exposure time achievable (that becomes larger, 24 s) and on the readout noise.

Table H-13. *Table H-15: SED templates available as inputs in the POLLUX simulator*

Input for the simulator	Template used
o5v	O5V Star
hr1886	B1V Star
alplyr	A0V Star
alpcmi	F15V-V
g2v	G2V Star
gamdra	K5III
mdwarf	M1 Dwarf
mdwarf2	M3 Dwarf
ctts2	Classical TTauri
g191b2b	G191B2B (WD)
gd71	GD71 (WD)
gd153	GD153 (WD)
qso	QSO
s99	10 Myr Starburst
orion	Orion Nebula
nodust	Starburst, No Dust
ebv6	Starburst, $E(B-V)=0.6$
syfrt1	Seyfert 1
syfrt2	Seyfert 2
liner	Liner
flam	Flat in F_{λ}

H.8 Echelle gratings

H.8.1 Design of the POLLUX echelle gratings

In each channel of POLLUX, the echelle grating parameters were defined from the required spectral resolving power, working spectral range, sampling, slit size and the camera focal length. Also, the limitations on the detector size and overall volume were taken into account. It was supposed that the spectrograph works in Littrow mounting and the grating has regular triangular grooves.

The NUV and MUV echelles have an almost identical size and blazing angle. The groove frequencies differ approximately by a factor of 2. The groove frequencies and the angles correspond to currently achievable values. The size is larger than most known examples. The FUV echelle has unusual frequency and blazing angle. There is no evidence that such a grating has been ever produced before for the UV domain. Also, it is substantially larger than currently available gratings. These gratings are difficult to fabricate with the ordinary mechanical ruling technology, so the lithographic process was considered as the primary option.

The footprint diagrams are shown in **Figure H-37** below. One can note the rays separation in the NUV and MUV channels. For the MUV, pattern is blurred due to the MgF_2 birefringence nonlinearity.

H.8.2 Fabrication process for high-performance UV echelle gratings

The POLLUX echelle gratings are fabricated using standard techniques in nanofabrication. Electron beam (e-beam) lithography allows for customization of the groove period while anisotropic etching allows for customization of the blaze profile. The ability to choose unique groove densities and facet angles allows the performance of the echelles to be optimized for the specific wavelengths critical to the POLLUX science goals.

The steps in the fabrication process are outlined in **Figure H-38** (Miles et al., *ApJ*, 869, 95, 2018). The initial groove pattern is determined by programming the e-beam tool with the desired groove parameters for periodicity. The pattern is then transferred into a nitride hard mask using reactive ion etching. Chemical etching using KOH preferentially breaks Si crystal bonds in directions other than the $\langle 111 \rangle$ direction so that $\{111\}$ crystal planes are exposed during the etch. Prolonged etching can “undercut” the nitride mask features and maximize the fraction of the groove period covered by the active facet. Illumination of the resulting triangular profile in the Littrow configuration then optimizes diffraction efficiency.

H.8.3 First tests

A prototype POLLUX grating was recently fabricated by PSU on a single silicon substrate of 6” diameter for the MUV channel using these processes (**Figure H-39**). A 10 nm thick chromium (Cr) coating has been deposited on the whole substrate.

The target parameters for this grating are a period of 3.455 μm , blaze angle of 54.7°, clear aperture of 25x25 mm, and diffraction efficiency >50% over the 118–195 nm band. Following fabrication, the profile was measured using atomic force microscopy (AFM) as shown in **Figure H-40**. The resulting triangular profile is remarkably pristine. The measured value of periodicity is 3.48 μm with a blaze angle of 54.8°, both within the tool’s accuracy to the desired parameters. The KOH undercut left a plateau at the top of the groove with a

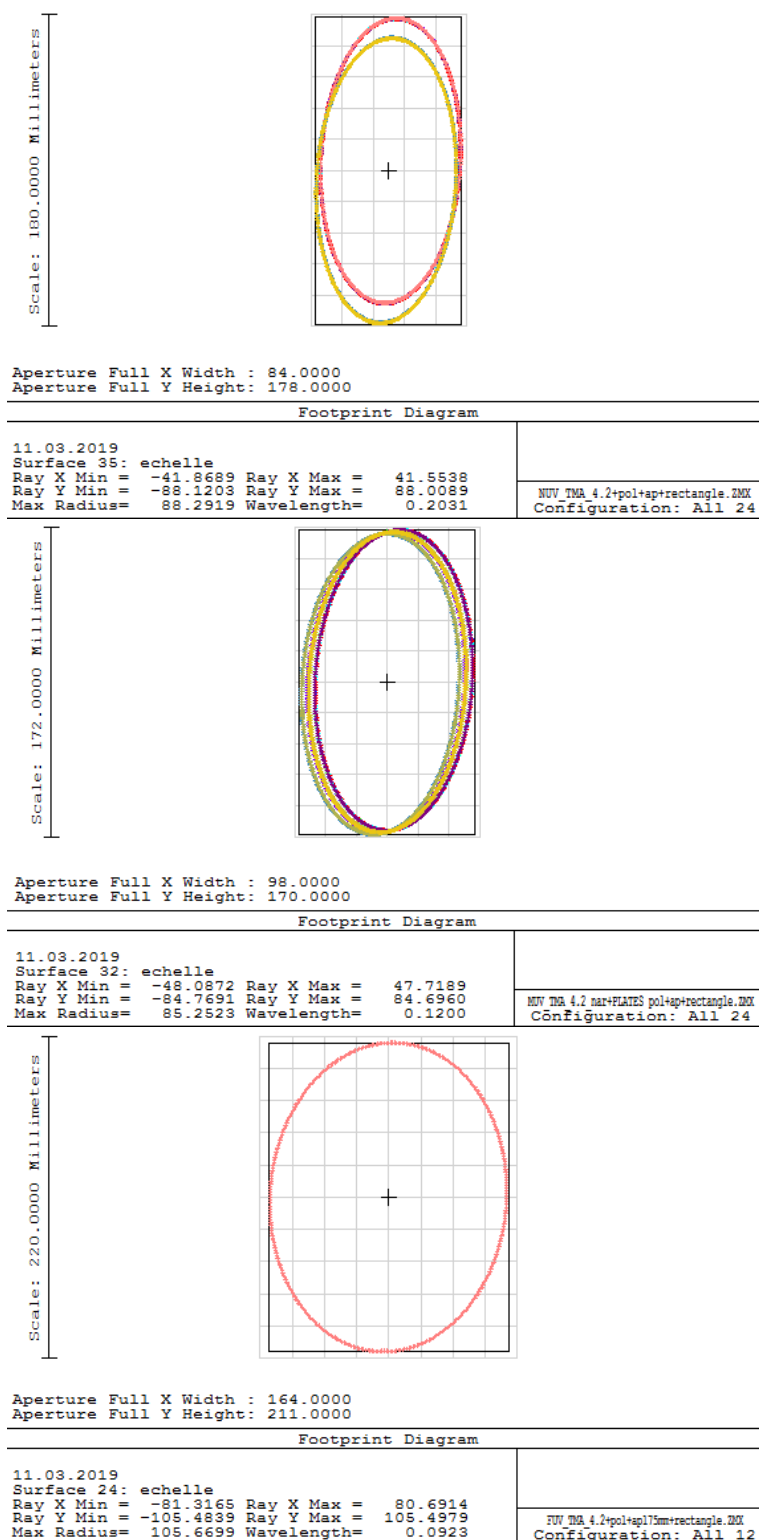


Figure H-37. Beam footprint at the POLLUX echelles: top – NUV, middle – MUV, bottom – FUV. As part of a feasibility study, we initiated a collaboration with the group of Professor Randy McEntaffer at Penn state University (PSU) in 2018. Their methodology was originally developed to fabricate X-ray reflection gratings, but it is very well suited to produce UV gratings with non-standards characteristics such as those we need for POLLUX.

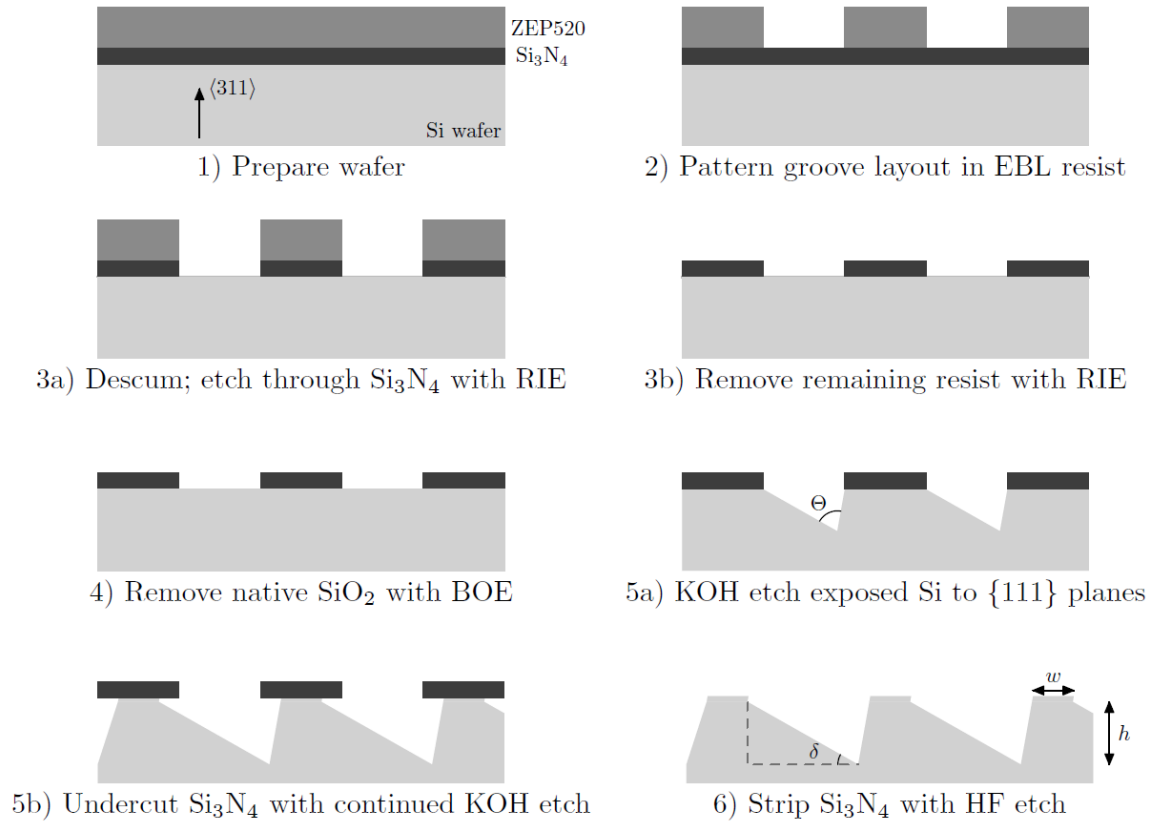


Figure H-38. Fabrication process for the POLLUX echelle gratings.

width of 110 nm. Additional performance could be realized by limiting this width even further. A photograph of the two prototypes is shown in **Figure H-41** along with a top-down scanning electron microscope (SEM) image demonstrating the excellent groove quality over a large area.

The POLLUX prototype grating was tested for diffraction efficiency at the Laboratory for Atmospheric and Space Sciences at the University of Colorado, Boulder. The measured data are shown in **Figure H-42**. The performance easily met the desired requirement of >50%

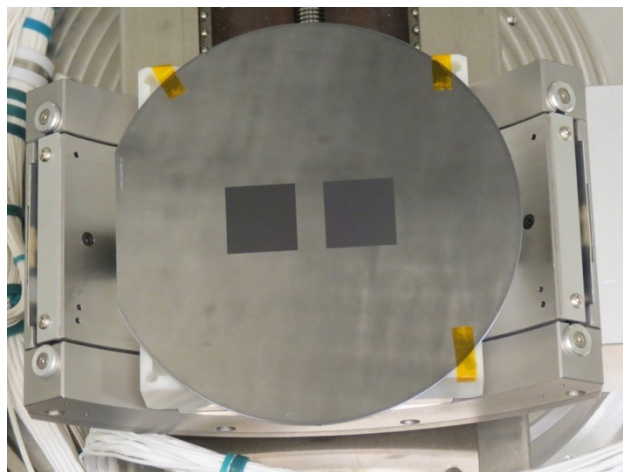
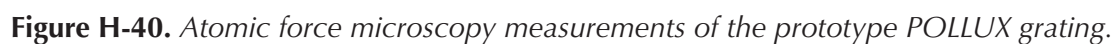


Figure H-39. Picture of both grating prototypes manufactured on a 100 mm diameter silicon wafer.



and maintained efficiency $>70\%$ over the desired band with a peak efficiency $>90\%$. This efficiency is nearly a factor of 2 better than the HST COS grating operating in the same wavelength regime (Osterman et al., Proc SPIE, 4485, 2002). This extremely high performance can be increased even further through reduction of the 110 nm plateau on top of the grating profile.

This fabrication process not only allows for customization of the groove period and blaze, but also allows for high temperature deposition processes for optimized UV coatings (Quijada et al. 2014, Fleming et al. 2017). Coating prototype gratings with these new processes will be part of the technology development for the echelles. In addition, the echelle technology development will address further customization of the groove profiles

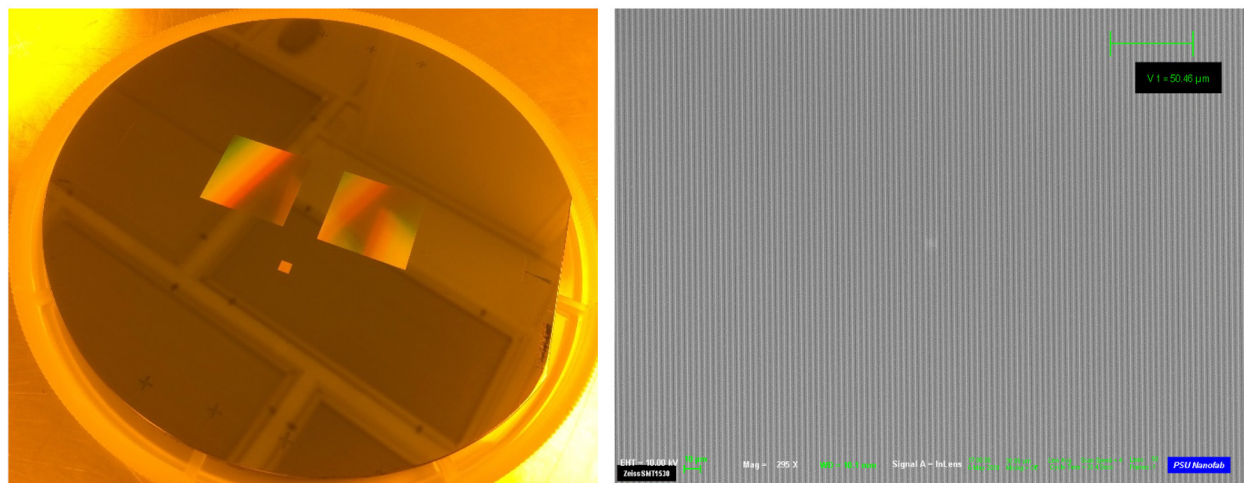


Figure H-41. *Left – Photograph of the prototype grating wafer. Right – Top-down SEM image of the grooves.*

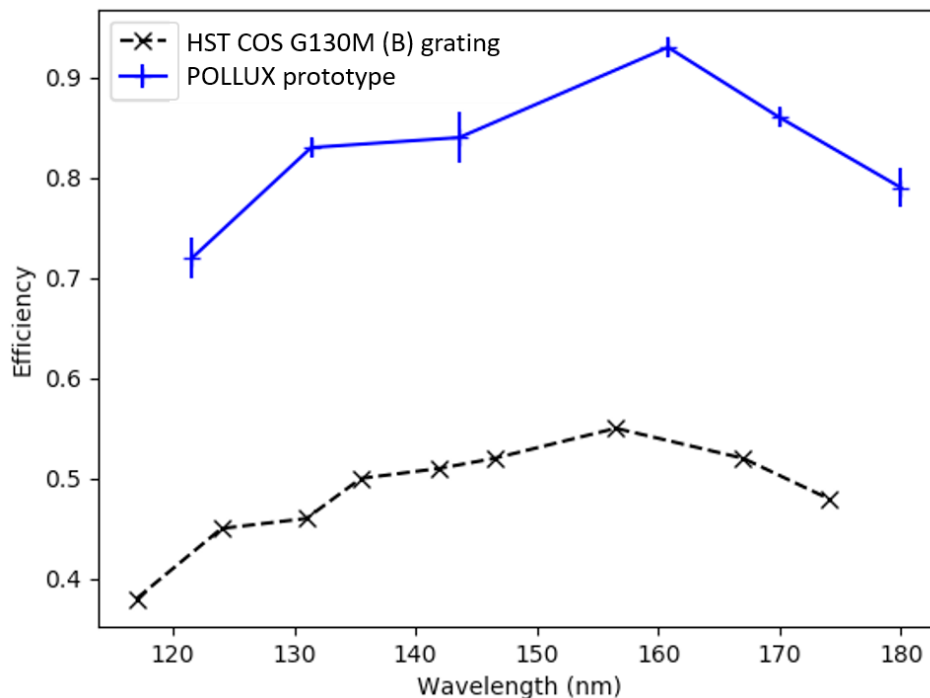


Figure H-42. Measured diffraction efficiency for the POLLUX prototype in comparison to an HST COS grating.

for the NUV and FUV channels and assess the accuracy to which period and blaze can be controlled. Finally, while large area gratings have been fabricated on 150 mm wafers (Miles et al 2018), the echelle gratings for POLLUX must be larger. Therefore, future technology development will address applying these processes to areas consistent with POLLUX requirements.

H.8.4 Future development

The NUV and MUV channel echelles can be fabricated on 200 mm wafers. The processes used to create the prototype can easily be transferred to this slightly larger format so no significant hurdle is anticipated here. However, the FUV channel echelle is considerably larger than a 200 mm wafer, therefore requiring either a new fabrication method, or stitching together of two gratings made using the same methods as the prototype. These two development paths will be studied early in the POLLUX program.

H.9 Detectors for POLLUX

H.9.1 Detector Technology Trade-offs

H.9.1.1 Microchannel plate versus solid-state detectors

The choice of detectors for POLLUX lies between microchannel plate-based detectors and solid-state devices such as CMOS, CCDs and EMCCDs. Traditionally, microchannel plates (MCPs) have been the solution of choice owing to their higher quantum efficiency in conjunction with UV photocathodes, single photon counting capability, lower noise and larger physical formats. Developments in solid state detectors, however, such as the development of EMCCDs with an intrinsic gain stage allowing photon counting operation, larger device sizes with smaller pixel dimensions, and entrance window technologies such as δ -doping, have raised their potential competitiveness.

The large imaging area coupled with high spatial resolution requirement of the POLLUX instrument place demanding constraints on the detector. Traditional MCPs have been manufactured at sizes of typically up to $100 \times 100 \text{ mm}^2$, e.g., the Chandra HRC detector. More recently within the Large-Area Picosecond Photodetector (LAPPD) Collaboration, MCP manufacturing techniques using borosilicate glass and atomic layer deposition have been developed which allow production of large format MCPs, up to $200 \times 200 \text{ mm}^2$, see **Figure H-43** (Adams et al. 2015).

Thus far the largest LAPPD MCPs ($200 \times 200 \text{ mm}^2$) have only been manufactured with $20 \text{ }\mu\text{m}$ pore size, limiting ultimate spatial resolution, and their internal support structures generate additional dead-space within the active imaging area. For POLLUX such detectors would need to be open-faced for the FUV channel, requiring a deployable door, or a sealed tube construction for the MUV and NUV channels, the size making the proximity focusing of the photocathode over such a large format problematic. Tiling detectors can alleviate this problem, but this introduces dead-space, for example the LUMOS MOS MCP detectors require a 12 mm gap between active areas (France et al. 2017).

Whereas early solid-state imaging detectors were limited in size, pixel format, noise and quantum efficiency, especially at UV wavelengths, enormous investment has led to

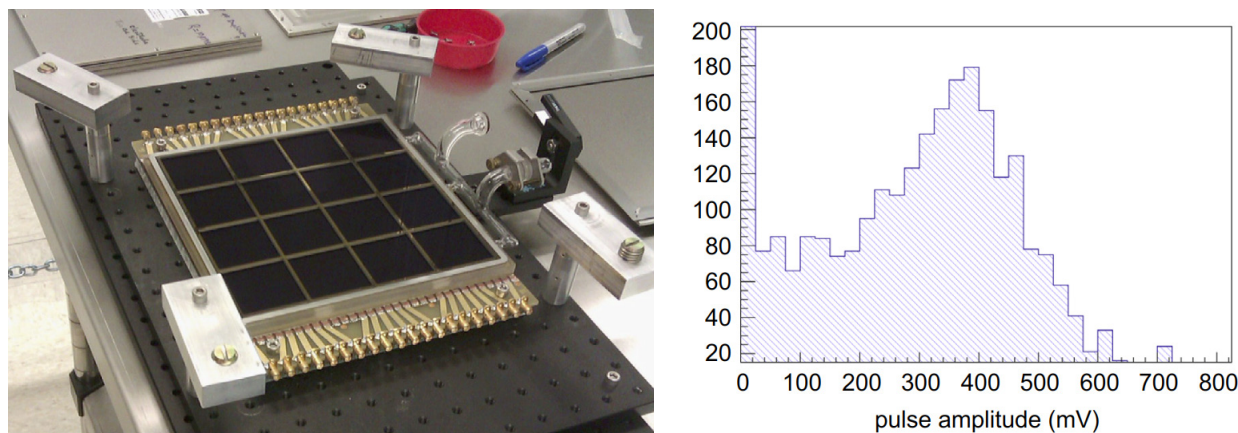


Figure H-43. A photograph of a $200 \times 200 \text{ mm}^2$ LAPPD MCP detector. The plot on the right-hand side shows the pulse height distribution at a gain of 3×10^7 electrons.

development of large-format high-resolution imaging arrays. Pixel sizes have been reduced, photon-counting capability has been achieved using built-in gain, and UV quantum efficiency of 60%-80% achieved using δ -doping (Nikzad et al. 2016; **Figure H-44**).

Sensor size has also increased significantly, and even when tiling is unavoidable, mechanical gaps and thus dead-space can be significantly smaller than for their vacuum tube counterparts. Previous limitations of solid-state detectors, such as lack of photon-counting ability and out-of-band rejection have been overcome by the development of the Electron Multiplying CCD (EMCCD) with its built-in gain, and integrated metal dielectric filters which can provide enhanced visible rejection.

H.9.1.2 Trade-offs between CMOS and CCDs

The choice of solid-state detector technology for POLLUX lies between: CMOS active pixel sensors, which typically include their charge measurement circuitry within every pixel, and; the charge-coupled device (CCD), a more mature technology which shifts pixel charge sequentially to a readout node(s) at the periphery of the imaging area. While CMOS sensors are now ubiquitous in consumer electronics, their heritage in space is undeveloped and their theoretical performance advantages for space applications are yet to be proven.

CMOS and CCDs can be manufactured on silicon wafers up to 8" in size, allowing active dimensions up to 180 mm depending on the particular manufacturer/foundry. They typically require cooling to ~ 170 K to achieve their best performance. CMOS and CCD technologies both suffer from radiation damage but in different ways; the main mechanism for CCDs being degradation of the charge transfer efficiency (CTE), whereas CMOS devices are more likely to develop hot pixels. CMOS devices benefit from lower complexity drive electronics than CCDs, and EMCCD requirements are even more complex due to the higher voltage EM stage. CMOS devices have lower dynamic range (70–80 dB) than CCDs (100 dB) but this is reduced for EMCCDs in photon-counting mode due to the increased charge per photon. However, the EM mode of EMCCDs can be turned off and the device operated as a conventional CCD to mitigate this limitation, providing enhanced operational flexibility.

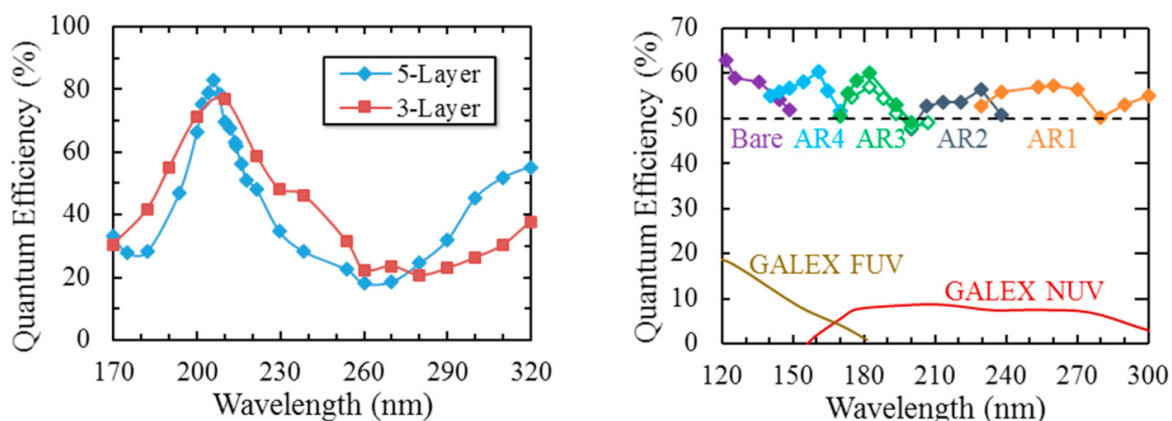


Figure H-44. : (left) QE data of δ -doped conventional (closed diamonds) and EMCCDs (open diamonds) enhanced with single layer AR coatings [34]. (right) QE data from two superlattice-doped CCD201s (e2v's 1k \times 2k EMCCD) optimized for the 200–220 nm wavelength range; the device designs included a three-layer AR coating (red squares) and a five-layer AR coating (blue diamonds). Figure from [3]

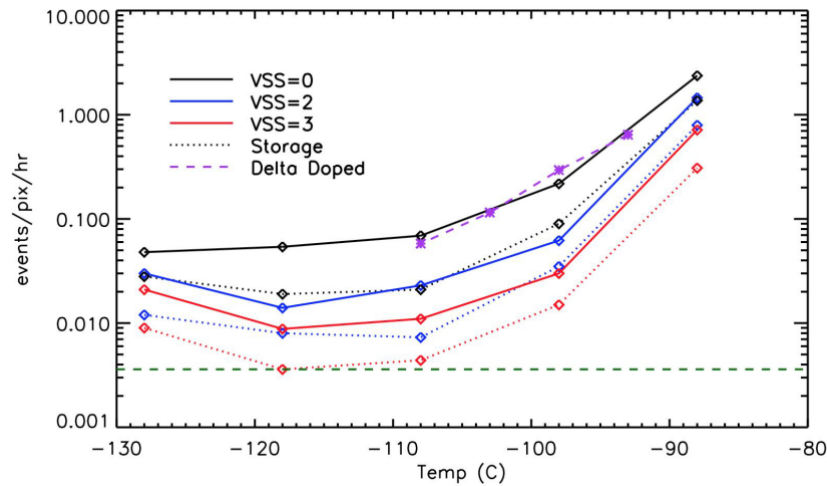


Figure H-45. Measured values of dark current vs. temperature. Solid lines indicate dark current for image area while dotted lines indicate dark current for storage area. Colours represent different substrate voltages. Initial dark current measurements of a δ -doped device are shown in purple at a substrate voltage of 0.0 V. Figure from Hamden et al. (2015).

In terms of noise performance current CMOS devices compete directly with scientific CCDs (sCCD) both having a typical noise of 2–3 e^- , however CMOS is still under development and performance in all areas will inevitably improve. For example, the lowest CMOS noise reported thus far, of 0.1 $e^-/\text{pix}/s$ (P. Jerram, Teledyne-e2v, private communication), has been measured on the Transneptunian Automated Occultation Survey (TAOS II) ground-based camera. Given the current trend it is expected that CMOS sensors will reach a noise level of 0.5 e^- within 5 years whereas CCD noise performance has probably plateaued.

H.9.2 Performance and Specification of POLLUX EMCCD

While the prospects for further development of CMOS to the point where they could become suitable candidate detectors in the future are high, the requirement for a current technology providing single photon counting capability has driven the baseline choice for POLLUX to the EMCCD.

The built-in gain of the EMCCD reduces the photon-counting noise way below the levels achievable either using sCMOS or sCCD sensors. **Figure H-45** shows a plot of measured noise versus temperature of the conventional and δ -doped EMCCDs utilized for the Faint Intergalactic-medium Redshifted Emission Balloon (FIREBall-2) mission, the data indicating the very low noise levels achievable in EM mode. An EMCCD was chosen to replace the previously used MCP detector for this mission to increase throughput while maintaining low detector noise. Quantum efficiency can also now match MCP detectors: the predicted quantum efficiency of POLLUX EMCCDs being shown in **Figure H-46**, based on QE measurements from the JPL δ -doping process.

The negligible noise of the EMCCD allows for long integration times but requires operation at low temperature, typically 170 K. The EM stage also has drawbacks including: reduced dynamic range, increased power dissipation, increased noise factor over non-EM mode, and can produce an ageing effect in the device, though the latter can be offset by calibration or increased voltage. However, these can be mitigated since the mode of the

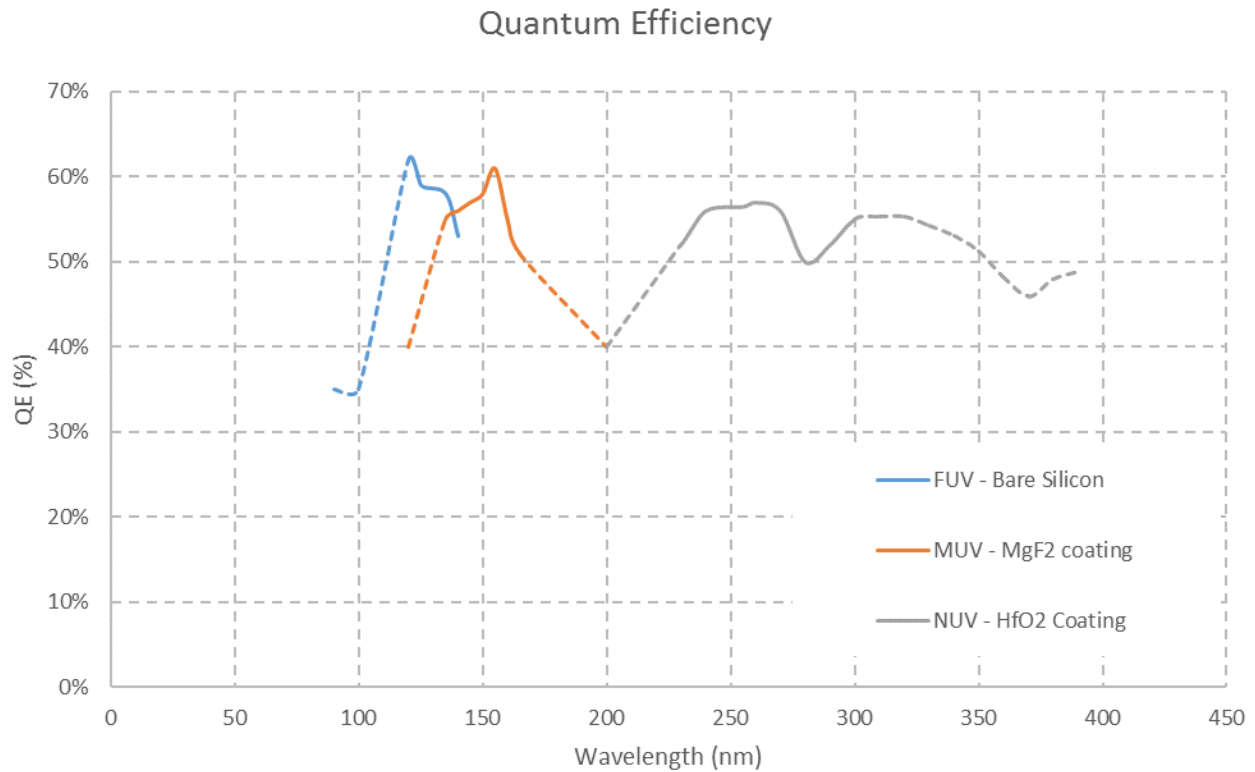


Figure H-46. The expected quantum efficiency of the EMCCDs covering the FUV, NUV and MUV channels for POLLUX. Dotted line is extrapolated from measurements. This data is based on QE measurements from the JPL δ -doping process (Nikzad et al. 2012).

EMCCD can be selectable depending on the input characteristics to allow operation either as a conventional CCD, or as a photon-counting EMCCD.

Table H-14 shows the specifications of an EMCCD design solution for POLLUX from Teledyne-e2v using currently available technologies. The frame transfer devices have a pixel size of 13 μm in a 7800 \times 1800 format per detector, the dead-space between EMCCD tiles

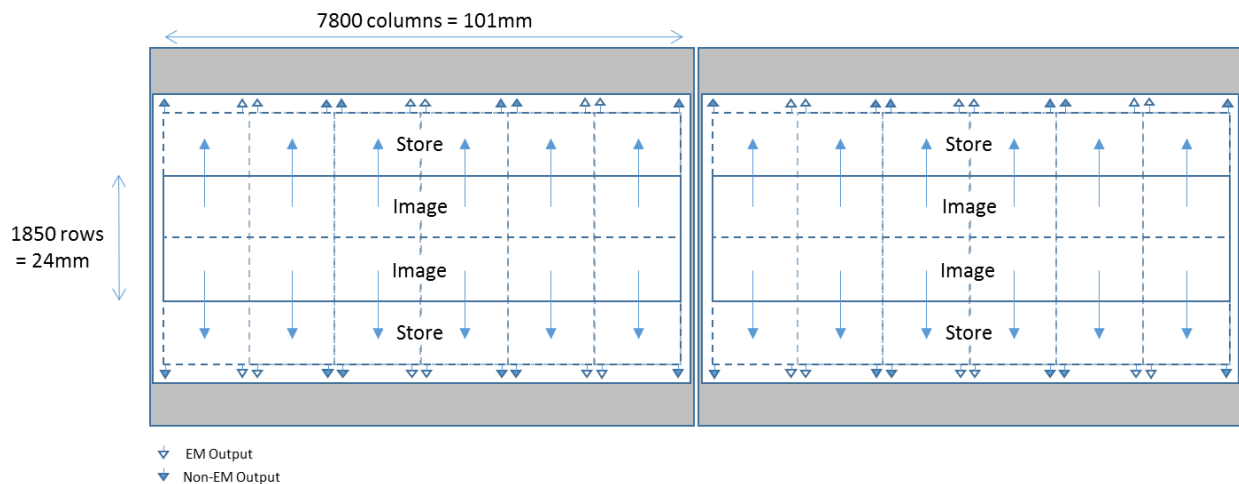


Figure H-47. Focal plane layout of one design alternative for POLLUX: a Teledyne-e2v tiled array of two frame-transfer EMCCD, giving an active area of $\sim 200 \times 24 \text{ mm}^2$.

Table H-14. Preliminary specifications of one design alternative for POLLUX: a Teledyne-e2v EMCCD large-area photon counting sensor design.

Parameter	EMCCD
Pixel pitch	13 μm
Image area rows	1850
Image area columns	7800
Number of outputs	12 EM + 12 Non-EM
Mode	Split Frame Transfer
Die Size	103mm x 54mm
Dead space at sides of chip	1 mm
Chip edge to package edge distance	50 μm
Package format	PGA, buttable on 2 sides
High Speed (EM) Output	
CVF	1.4 $\mu\text{V}/\text{e}$
Output / Register Charge Handling Capacity	500 ke
Amplifier Noise @ 10MHz	50 e
Input-referred noise @ 1000x multiplication gain	0.05 e
Low Noise (Non-EM) Output	
CVF	5.3 $\mu\text{V}/\text{e}$
Output / Register Charge Handling Capacity	280 ke
Amplifier Noise @ 50kHz	3.1 e
Data rate (using low-responsivity outputs with EM gain)	10 Mpix/s per output
Min. frame time @ 10MHz readout	120 ms
Data rate (using high-responsivity outputs without EM gain)	50 kpix/s per output
Min. frame time @ 50kHz readout	24 s
Peak power consumption (10MHz continuous readout, all outputs active)	10 W
Image FWC	80 ke
Dark Signal @ 20°C (Inverted Mode)	260 e/pix/s
Dark Signal @ -100°C (Non-Inverted Mode)	1 e/pix/hour
Clock-Induced Charge @ -100°C (Non-Inverted Mode)	0.005 e/pix/frame

being 2.05 mm. Each device uses 24 readout nodes equally split between low gain (conventional CCD) mode and high gain (EM) mode to flexibly accommodate the expected signal dynamic range. The Teledyne-e2v CCD process only supports 6" silicon wafers, limiting the maximum active length to ~130 mm. **Figure H-47** shows the layout including dead-space of a tiled arrangement allowing an active area of 200 x 24 mm².

H.10 DRMs

H.10.1 Exoplanets

TITLE: Unveiling Exoplanetary Aerosol Properties and Coverage: UV Atmospheric Characterization of Exoplanet Atmospheres through Polarimetry

PROGRAM CONTACT: Luca Fossati, Austrian Academy of Sciences, luca.fossati@oeaw.ac.at

ABSTRACT: The polarization state of starlight reflected by a planetary atmosphere uniquely enables to reveal the presence, coverage, particle size, and composition of aerosols as well as changing cloud patterns and/or exo-rings/trojans/moons. Observations in reflected unpolarized light or in transmission are unable to provide similar information. Furthermore, polarization observations give access to probing the atmosphere of planets independently of the orbital geometry (i.e., transiting and non-transiting planets). The fraction of polarized reflected starlight strictly depends on the system parameters and planetary orbital phase, with its maximum reached when a planet is close to quadrature ($90^\circ/270^\circ$), although the specifics depend on the actual atmospheric properties.

The combined high spectral resolution and polarimetric capabilities of POLLUX enable to simultaneously study the polarimetric properties of the continuum and to look for and characterize the polarimetric signal due to scattering from single molecules (see **Section 14.1.1**). Aerosols appear to be ubiquitous in exoplanetary and solar system planet atmospheres, and a description of their optical properties and vertical distribution is critical for constraining models of chemistry, dynamics, and energy budget of these planets. This program will therefore provide the information necessary for observationally constraining the formation, occurrence, and distribution of aerosols in (exo-)planetary atmospheres.

NOMINAL TIME ALLOCATION (hours): 720 hours (480 science hours and 220 overhead hours with POLLUX). This is 3 hours for NUV linear spectropolarimetry repeated 8 times over a planet orbital phase, that is 3 x 8 hours (24 hours) per target. Considering the sample of currently known exoplanets, the target list comprises 20 targets (20 targets x 24 hours are 480 hours of shutter time).

TARGETS / POINTINGS DESCRIPTION: The target list comprises planets with masses larger than Saturn to ensure Jupiter-like planetary radii (e.g., Hatzes & Rauer 2015), orbital periods shorter than 3 days, and orbiting stars hotter than the Sun and closer than 200 pc. These constraints lead to a list of 20 targets, though a number of additional (possibly better) targets is expected to become available following the results of the Gaia, TESS, and PLATO missions. More than half of the targets are transiting planets, thus POLLUX observations will ideally complement transmission and emission observations conducted across the electromagnetic spectrum.

OBSERVATION DETAILS:

1. POLLUX:

- a) Spectropolarimetry: near-UV linear polarization
- b) Observing plan: 8 pointings per target uniformly distributed in planetary orbital phase and each pointing consisting of 3 hours of shutter time, possibly split into multiple consecutive exposures to avoid saturation

Total science integration time: 480 hours

PARALLELS: Check all that apply.

- ☐ Do not execute parallels with this program
- ☐ Parallels required for this program
- ☐ Can be executed as parallel to another program (list constraints below)
- ☒ Possible to execute parallels with this program

Parallels constraints:

TARGET OF OPPORTUNITY / TIME CRITICAL: Check all that apply and describe below.

- ☐ Is a ToO program
- ☒ Is time-critical

ToO / time critical description: The observations need to uniformly cover the planetary orbital phase. It is crucial that some of the observations are obtained as close as possible to the expected phases of maximum polarization (i.e., close to quadrature).

H.10.2 Interstellar and circumgalactic medium

TITLE: POLLUX study of the magnetic field structure in relation with the different phases of the ISM

PROGRAM CONTACT: Huirong Yan, hyan@mail.desy.de ; Cecile Gry, cecile.gry@lam.fr

ABSTRACT: The POLLUX spectropolarimeter will detect linear polarization in many UV absorption lines through Ground State Alignment (GSA, Yan & Lazarian 2006) and will open up access to the third dimension of the magnetic field, by measuring its orientation in different clouds, on limited distances along the lines of sight and on small scales. Recent dust polarization measurements by e.g., Planck have represented a huge step forward in the knowledge of the Galactic magnetic field in terms of sensitivity, sky coverage and statistics. However, they tell us nothing on the distance of the magnetic field and its distribution in the different components or phases. In a 100 observing hours program, observing several hundreds of hot stars with a SNR of 500 to measure linear polarization at a level of a few % from optically thin absorption lines, will help understand the role played by the magnetic field in the relation between the different phases. By discerning magnetic fields in gas with different dynamical properties, the high spectral resolution of POLLUX will allow the first study of interstellar magnetic turbulence (Zhang & Yan 2018).

NOMINAL TIME ALLOCATION (hours): 150 hours (100 science hours and 50 overhead hours).

TARGETS / POINTINGS DESCRIPTION: 500 stars, types O and early B (up to B3-B4), with distances less than 500 pc and magnitudes typically $V=5$, from $V=1$ to $V=10$.

OBSERVATION DETAILS: UV Spectropolarimetry with POLLUX: 500 pointings, 2 exposures per pointing to cover the spectrum from FUV to NUV in linear polarization, exposure times from a few seconds to a few minutes per exposure, to achieve a SNR between 300 and 1000 depending on the position of the line on the detector.

Total science integration time: 100 hours

PARALLELS: Check all that apply.

- ☐ Do not execute parallels with this program
- ☐ Parallels required for this program
- ☐ Can be executed as parallel to another program (list constraints below)
- ☒ Possible to execute parallels with this program

Parallels constraints:

TARGET OF OPPORTUNITY / TIME CRITICAL: Check all that apply and describe below.

- ☐ Is a ToO program
- ☐ Is time-critical

ToO / time critical description:

H.10.3 Stellar physics

TITLE: Magnetic fields across the HR diagram

PROGRAM CONTACT: Chris Evans, UK ATC, chris.evans@stfc.ac.uk

ABSTRACT: Magnetic fields play a significant role in stellar evolution because they control the angular momentum budget and mediate evolution of accretion processes and wind outflows; they are also an important factor in both planet and star formation. We need POLLUX spectropolarimetry to identify and characterize these magnetic fields across all stellar masses. A 100-hour LUVOIR-POLLUX program would be transformational in our understanding of the role of magnetic fields in stellar evolution. This is an illustrative example of a 100-hour (on-source time) stellar program.

NOMINAL TIME ALLOCATION (hours): 150 hours (100 hours on sources + 50 hours overheads)

TARGETS / POINTINGS DESCRIPTION: Tens of bright ($V < 10$) Galactic OB-type stars (well distributed across the sky) and observations of the 20 brightest T Tauri stars.

OBSERVATION DETAILS: The two components envisaged are observations of the ~20 brightest T Tauri stars and observations of tens of Galactic massive stars, as follows:

- *T Tauri stars:* NUV_POL spectropolarimetry to investigate the interface of the star and disk via, e.g., the Mg 2800Å doublet, CII] quintuplet at 2325Å and FeI lines at 2330Å (e.g., López-Martínez & Gómez de Castro, 2014). For an illustrative magnitude of $m_{\text{FUV}} = 17$ and using the classical TT spectrum in the POLLUX ETC, we recover SNR ~100 in the continuum at 2800Å in 2 hrs/star (assuming four polarimeter configs) for the 15-m LUVOIR-A aperture.
- *Massive stars:* MUV_POL spectropolarimetry will provide the first assessment of the presence/strength of weak magnetic fields in main-sequence massive stars. The required SNR (>1000) is demanding, but these are bright Galactic stars ($V < 10$ mag) so observing a first sample of about 20 objects (drawn from, e.g., Fossati et al. 2015) is well within the reach of ~60 hours of a large program with LUVOIR-A.

Total science integration time: 100 hours split as ~40 hours for *T Tauri* stars and ~60 hours for weak magnetic fields in *Massive stars*.

PARALLELS: Check all that apply.

- ☐ Do not execute parallels with this program
- ☐ Parallels required for this program

- ☐ Can be executed as parallel to another program (list constraints below)
- ☒ Possible to execute parallels with this program

Parallels constraints:

TARGET OF OPPORTUNITY / TIME CRITICAL: Check all that apply and describe below.

- ☐ Is a ToO program
- ☐ Is time-critical

ToO / time critical description:

H.10.4 Physics of active galactic nuclei

TITLE: Determining how nearby Active Galactic Nuclei form, evolve, and impact galaxy evolution thanks to UV spectropolarimetry

PROGRAM CONTACT: Frédéric Marin, Astronomical observatory of Strasbourg, CNES, University of Strasbourg, CNRS, frederic.marin@astro.unistra.fr

ABSTRACT: POLLUX will offer the possibility to reveal the physics of Active Galactic Nuclei (AGNs) UV-emitting/absorbing regions, arising from either the accretion disk, synchrotron emission in jet-dominated AGNs or large-scale outflows. Key accretion disk signatures are indeed revealed only in polarized light, and with higher contrast at UV wavelengths. In particular linear and circular polarimetry will provide measurements of the geometry of the system, insights on the mineralogy, structure and alignment of the smallest dust grains, together with the line-of-sight magnetic field. The structure of outflowing winds in nearby broad absorption lines systems and the properties of young star forming regions, directly related to AGN activity, will be in the reach of the instrument. POLLUX will also allow to constrain the nature and lifetime of particles in relativistic plasma for a variety of jet models that are responsible for galactic feedback. By focusing on bright, low redshift AGNs, it will be possible to obtain, for the first time, high resolution data providing striking insights on AGN physics and structure. Complemented with the optical and infrared instruments on-board of LUVOIR, POLLUX will undoubtedly constitute a very powerful tool to uncover the unresolved and poorly understood physics of AGNs.

NOMINAL TIME ALLOCATION (hours): 900 hours (600 science hours and 300 overhead hours with POLLUX).

TARGETS / POINTINGS DESCRIPTION: Most targets will be bright AGNs in the Local Universe ($z < 0.1$). All targets are scheduled for a MUV+NUV POLLUX coverage (2 channels: MUV, NUV; acquired simultaneously) and the brightest targets will also be observed in the FUV channel. We aim at observing diverse flavors of AGNs: radio-loud and radio-quiet, pole-on and edge-on objects.

OBSERVATION DETAILS: Many AGNs show linear optical polarization degrees of the order of a percent or less before removing the contribution of unpolarized parasitic light (starlight, starburst light, interstellar polarization). Although it is known that the AGN polarization fraction increases in the UV band due to lesser starlight dilution, we require to measure a polarization level similar to that of the linear polarization observed in the optical band with a precision of $P/\sigma_P \geq 3$ for conservative purposes. We used the POLLUX ETC tool with the 15 meters aperture configuration and single observations. Blazing sources require repeated observations while more stable AGNs do not. The time-dependence of UV polarization is critical to assess the physics of inner accretion disks and must be provided for a limited number of sources. Compiling the brightest AGN sources from the Swift/BAT survey (Ricci et al. 2011), the brightest AGNs from the 12th Véron-Cetty catalog (V-band), the

highly-polarized Seyferts-1s from the catalog of Goodrich & Miller (1994), and a few more bright AGNs gives a sample of 40 potential targets.

Not all targets are suitable for FUV observations and several AGNs require large observing times even for the NUV+MUV band. We thus restrict ourselves to the most promising targets, i.e., AGNs with high optical linear polarization and “low” estimated exposure times. We ended up selecting 20 AGNs for NUV+MUV exposures, including 5 AGNs for additional FUV exposures.

1. POLLUX:

- a) Spectropolarimetry: 20 different targets/pointings, 1 exposure per pointing (although it could be split for low variability sources), 1–50 hours per NUV+MUV exposure, 15–50 hours per FUV exposure, simultaneous linear + circular polarization
- b) High resolution spectroscopy: the total flux spectrum acquired during spectropolarimetric observations will be sufficient
- c) About 5 repeated NUV exposures for at least 2 blazing AGNs. The time separation is of the order of weeks/months.

PARALLELS: Check all that apply.

- ☐ Do not execute parallels with this program
- ☐ Parallels required for this program
- ☐ Can be executed as parallel to another program (list constraints below)
- ☒ Possible to execute parallels with this program

Parallels constraints:

TARGET OF OPPORTUNITY / TIME CRITICAL: Check all that apply and describe below.

- ☐ Is a ToO program
- ☐ Is time-critical

H.10.5 Solar system

TITLE: UV polarisation of the solar system

PROGRAM CONTACT: Jean-Yves Chaufray, LATMOS, chaufray@latmos.ipsl.fr

ABSTRACT: The UV spectropolarimetric observations of the objects of the solar system is crucial to investigate a large area of phenomena from the surface to the atmospheres and magnetospheres in the frame of space weather and exobiology/habitability fields. Very few UV polarimetric observations were obtained so far (e.g., Fox et al. 1997, Esposito and Travis 1982). The UV measurements of the surface albedo and polarisation can provide information on the surface activity (volcanisms, plumes) of icy bodies like satellites of Jupiter and Saturn, and their composition in water ices / organic matter. For example; the Wisconsin Ultraviolet Photopolarimeter Experiment (WUPPE) observations of Io has revealed a surface spatially covered by 25% SO₂ frost with polarization variations associated to different volcanic regions. Io volcanism is of importance also for magnetospheric studies, since it is the main source of plasma in the Jovian magnetosphere and some strong events have been associated to brightening of jovian aurorae. UV Polarimetric observations of the Moon show a transition in the scattering of the UV light near 220 nm with a scattering from grains surface for wavelength < 220 nm and volume scattering for wavelength > 220 nm (Fox et al. 1998). These processes are not well understood due to the lack of measurements, and therefore systematic observations of the UV polarisation of the surface of different objects in the solar system could open a new field of investigation to constrain the surface properties (refractive index, surface roughness, particle size,...), and help to diagnose the surface properties of objects that cannot be reached by spacecrafts and can't be target of sample returns.

The UV measurements are also a very useful tool to investigate the composition of the planetary atmospheres and aerosols content, especially for objects far from the Sun where in-situ missions will not be sent in the future. For example, a difference in polarisation of dark and bright UV regions of the Venusian atmosphere has been measured and was used to constrain the optical thickness of haze, while UV polarization observations of Mars were used to derive successfully its surface pressure. Extensions of such studies to less studied objects of the solar system will provide fundamental parameters of their atmospheres.

Finally, UV studies (for example from HST) have provided a large amount of information on the planetary magnetospheres of the giant gas planets Jupiter and Saturn and their electromagnetic interaction with their satellites that can be extended to giant ices planets (Uranus and Neptune) and used to interpret possible weakest detection of exoplanets auroal emissions.

NOMINAL TIME ALLOCATION (hours): 500

TARGETS / POINTINGS DESCRIPTION: All objects of the solar system could be targets for POLLUX. POLLUX will measure the polarized solar reflected light from planetary surfaces/atmospheres. Its high sensitivity is necessary to track any organic and ice composition of the crust of comets and Kuiper Belt objects from their UV spectrum. Spectral UV albedos of

object as faint as Pluto can be derived from POLLUX. For objects like Io, Encelade, Europa, Ganymede, tidal stress is responsible of volcanoes or plume activity at the surface, and this activity varies with the orbital position of the satellite. Therefore, to investigate the variations of surface activity, and the surface properties, it would be needed to observe these bodies at different time along their orbit. To catch transient event, long observations over several days (the orbital period is ~ 1.8 days for Io and ~ 3.6 days for Europa) would be needed for each object.

OBSERVATION DETAILS: For bright icy objects like Io, Europa, Ganymede, and Enceladus, the flux can be measured with a $\text{SNR} > 10$ in a 5-min integration with a spectral resolution of 1 nm. The polarisation of Io can be measured for one hour integration with a $\text{SNR} > 5$ and a resolution of 1 nm for wavelengths > 240 nm (**Figure H-48**) and in 5 minutes for a resolution of 10 nm. Therefore, for most icy satellites of Jupiter and Saturn, one hour of observations should be sufficient to obtain UV albedos and polarisation with a good spectral resolution.

To study spatial and temporal variations (different regions at the surface and orbit of Io around Jupiter), we need to target several times each object. Therefore 20 hours of observations per object should be used to have a high spectral resolution of polarization for a minimum of 5 positions around the planet and 4 regions at the surface. To catch transient events, longer period of observations should be used for each object (~ 100 hours/object).

Total science integration time: ~ 500 hours

PARALLELS: Check all that apply.

- ☐ Do not execute parallels with this program
- ☐ Parallels required for this program
- ☐ Can be executed as parallel to another program (list constraints below)
- ☒ Possible to execute parallels with this program

UV mapping of the surface by LUMOS in close time proximity with POLLUX observations would be an advantage to place the polarimetric observations in a global context.

Parallels constraints:

TARGET OF OPPORTUNITY / TIME CRITICAL: Check all that apply and describe below.

- ☐ Is a ToO program
- ☐ Is time-critical

ToO / time critical description:

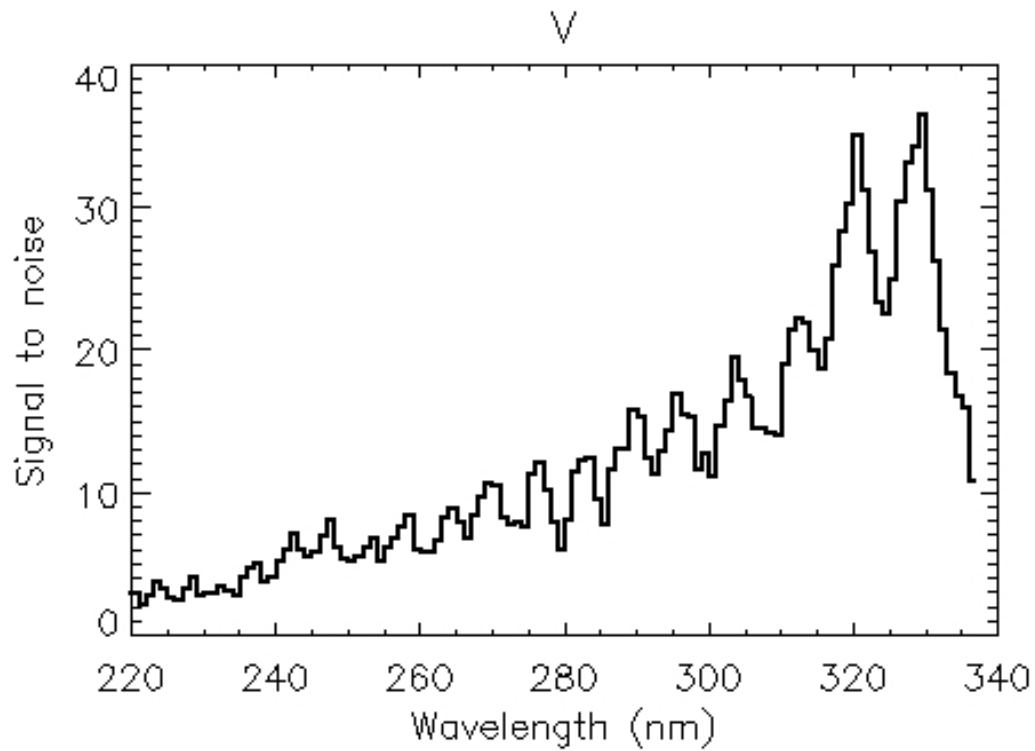


Figure H-48. Simulated SNR for the Stokes parameter V for an observation of Io surface during an integration time of one hour and a resolution of 1 nm by POLLUX

APPENDIX I. ADDITIONAL LUVOIR INSTRUMENT CONCEPTS

Here we present information on some possible alternate and/or second-generation instrument concepts for LUVOIR.

I.1 Starshades for LUVOIR

Eric Cady (JPL) & Aki Roberge (NASA GSFC)

I.1.1 Introduction

Starshades are a relatively new idea for providing the extreme high-contrast needed for exoplanet direct observations. They have strengths and weaknesses that are complementary to those of coronagraphs. A starshade is an independent spacecraft flying in formation with the telescope (**Figure I-1**). The goal is to keep the telescope in the shadow cast by the starshade, and keep both spacecraft aligned with the target star. The larger the telescope, the larger the starshade needs to be. The edges of a starshade have a very particular shape to control diffraction and deepen the shadow at the location of the telescope. A lecture on the Theory and Development of Starshades given at the 2014 Sagan Summer Workshop is available here: https://www.youtube.com/watch?feature=player_detailpage&v=h5w6z0jow1Q#t=0

A starshade blocks the unwanted bright light from an exoplanet host star before it enters the telescope, while allowing light from nearby planets to pass nearly unattenuated. Therefore, internally scattered light reaching the detector is minimized. Telescope segments and obstructions do not need to be masked out and the wavefront does not need to be

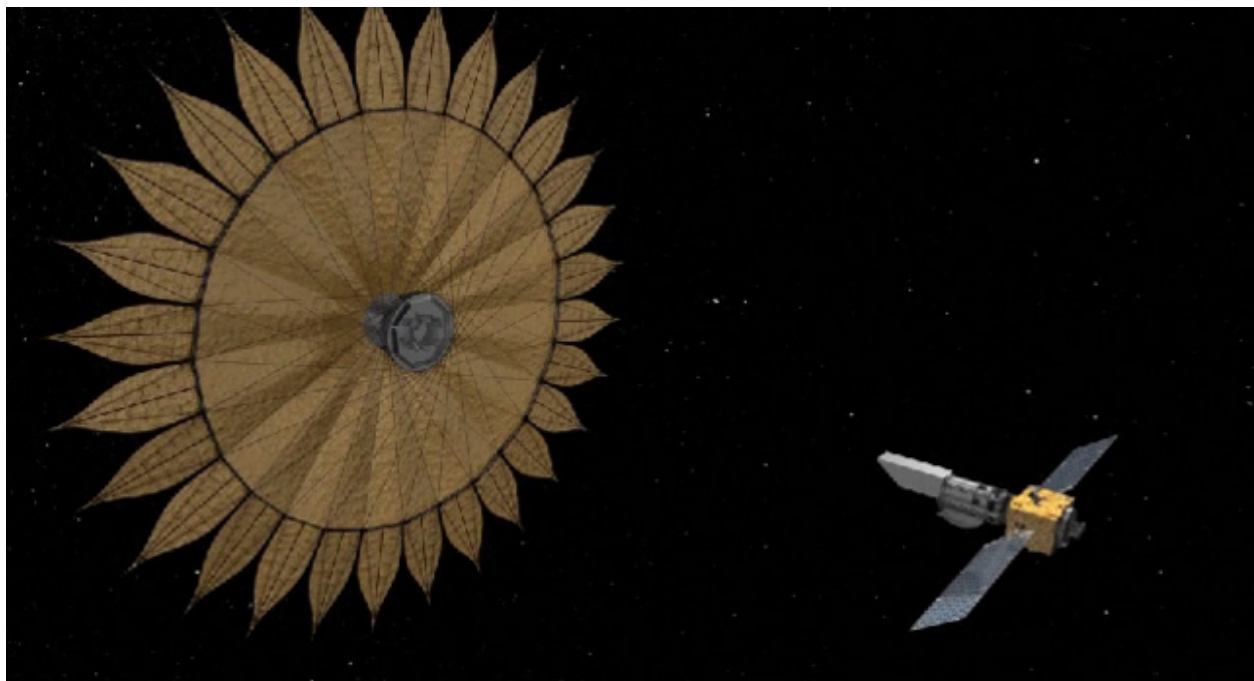


Figure I-1. Artist's conception of the Exo-S mission concept, a starshade paired with a small telescope. The image captures a moment just after starshade deployment. The full deployment video can be viewed at <https://exoplanets.nasa.gov/resources/1015/>. Credit: NASA / JPL / Caltech.

corrected with deformable mirrors. A starshade can provide a very small inner working angle (IWA), approximately given by the starshade radius (R) divided by the starshade-telescope separation (z), down to around the diffraction limit of the telescope ($\sim 1.2 \lambda/D$). For planets in habitable zones of nearby sun-like stars, the starshade-telescope separations are tens to hundreds of thousands of km.

Starshades have no intrinsic outer working angle (OWA). They can be designed to operate over large bandpasses (a few times larger than today's coronagraph bandpasses) and to provide small IWAs at virtually any wavelength. For a fixed IWA and contrast level, the required starshade size increases with wavelength. Since the starshade is not part of the optics train, internal reflections are kept to a minimum and total throughput is high. This makes them excellent for deep spectroscopy, especially in the NIR where coronagraphs struggle to provide small IWAs.

On the weaknesses side, the need to slew the starshade over huge arcs to realign it with different target stars means there are long intervals (days to weeks) between the high-contrast observations and the total number of observations is fuel-limited. The telescope can do other kinds of astronomical observations in the intervals, but starshades are relatively inefficient for high-contrast imaging surveys. The starshade and telescope must be precisely aligned during observations to maintain high contrast. Keeping the telescope in the darkest part of the starshade shadow generally translates to lateral position precision of about a meter (the separation precision is much less stringent).

Full-scale end-to-end system tests on the ground are not possible, although sub-scale tests are being done in the lab and in the field (e.g., Cady et al. 2010; Smith et al. 2016). The large sizes of starshades means that they must be folded up for launch and deployed in space. The exact shape of the optical edge must be accurate (on the order of $100 \mu\text{m}$ tolerance for contrast in the 10^{-10} range) after deployment. Further, the thin edge of the starshade must be engineered to minimize sunlight scattering back into the telescope. More information on starshade technology development is at <https://exoplanets.nasa.gov/exep/technology/technology-overview/>

1.1.2 Scope of LUVUOIR starshade study

Starshades have several attractive features, and their strengths complement those of coronagraphs. Therefore, a series of starshade designs for LUVUOIR were investigated. Here we discuss the design parameters and constraints, the optimization methodology, and the results.

Performance constraints. Starshade designs were created for 7 architectures with the constraints shown in **Table I-1**. Cases 1, 2, 5, and 6 were studied in May/June 2017. At this time, preliminary designs for the LUVUOIR apertures were used, with a diameter of 9 m for LUVUOIR-B. Cases 3, 4, and 7 were studied in April/May 2019 and used the final LUVUOIR apertures. The operating wavelength ranges and IWAs were fixed. We set a requirement that the mean contrast in a $1.0 \lambda/D$ annulus centered at the IWA in the final telescope focal plane be no greater than 5×10^{-12} . The same metric was used for HabEx starshade designs in separate work and is consistent with producing 10^{-10} contrast after running through an error budgeting process with achievable tolerances.

Engineering constraints. Each starshade was optimized for a diameter 2-m larger than the telescope aperture, to allow ~ 1 -m formation-flying offset between starshade and telescope in all directions. Petal tip sizes and inter-petal gaps were bounded at ≥ 1 mm.

Table I-1. *Starshade design architectures studied*

	Case 1	Case 2	Case 3	Case 4	Case 5	Case 6	Case 7
Design Name	-	OM11	UK13	UM8	-	OH22	UL14
Telescope Diameter	15 m	15 m	15 m	15 m	9 m	9 m	8 m
Short Wavelength Cutoff (nm)	250	250	300	250	250	250	300
Long Wavelength Cutoff (nm)	2500	1000	850	400	2500	1000	850
Starshade Diameter (tip-to-tip)	>200 m	160 m	67 m	46 m	>200 m	95 m	57 m
Starshade-Telescope Separation	-	687,549 km	113,277 km	94,882 km	-	244,939 km	94,815 km
Geometric IWA (center-to-tip)	-	24 mas	61 mas	50 mas	-	40 mas	62 mas
Optical IWA (50% throughput at central wavelength)	-	-	51 mas	41 mas	-	-	51 mas

Starshade diameter, petal number, and petal length were permitted to float as part of the overall optimization.

I.1.3 Starshade size and shape optimization

The optimization procedure used for the LUVOIR starshades has been covered in other works (e.g., Cady et al. 2009). Very briefly, a smoothly varying radial apodization function, $A(r)$, is approximated with a binary shape that has transmission of 1 or 0 everywhere (**Figure I-2**). To select an appropriate $A(r)$ for a LUVOIR starshade, we chose scientific constraints (e.g., IWA, contrast, science bandpass, telescope diameter) and engineering constraints (e.g., minimum feature sizes, edge smoothness, formation-flying tolerance). These parameters are sufficient to populate a constrained linear optimization with a min-max cost function.

The optimization was performed using the geometric IWA as a constraint, which is defined as $\theta = \arctan(R/z) \approx R/z$, where R is the starshade radius and z is the starshade-telescope separation. We chose θ based on science goals for a particular starshade, and let the

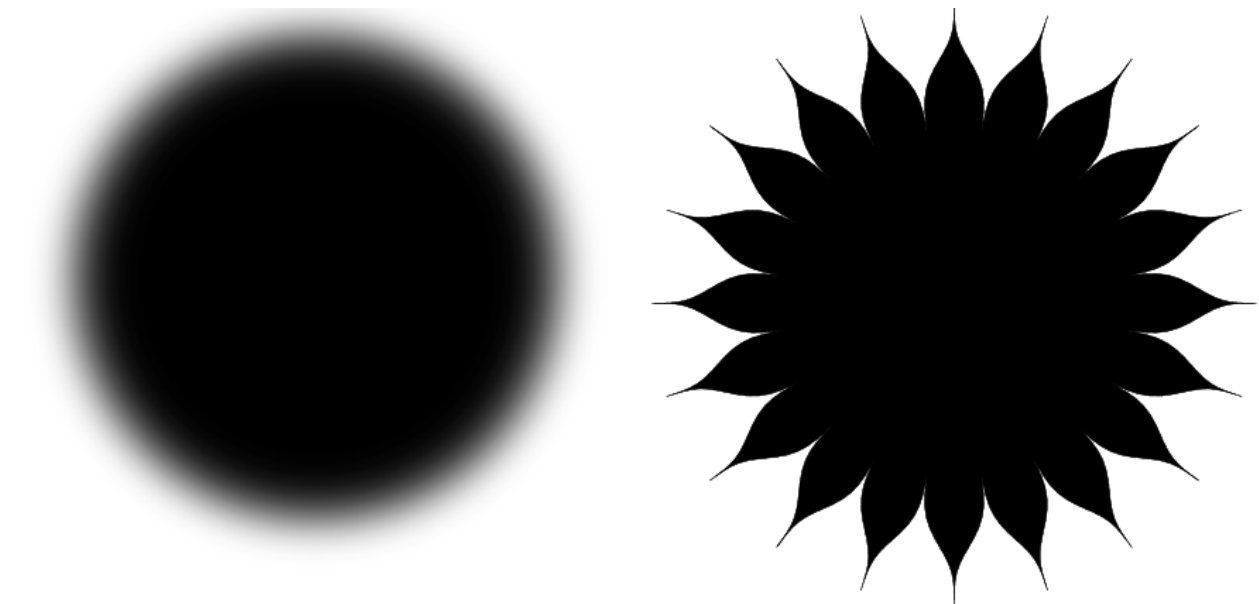


Figure I-2. An apodizer is converted into a binary starshade by replacing the tapering outer annulus with a series of N binary structures (“petals”).

distance z float as R/θ . There are two advantages of using the geometric IWA during design optimization. First, the parameter is independent of $A(r)$, and so is known prior to beginning the optimization. Second, since the starshade has no structure beyond the geometric IWA, errors in starshade manufacturing will only appear as sources from inside the angular extent of the starshade. Therefore, using the geometric IWA during design optimization means the ultimate performance will be much less sensitive to manufacturing errors.

However, the optical IWA, determined after the starshade design is finalized, is more relevant for calculation of its scientific performance. The optical IWA is also more comparable to IWAs as defined for coronagraphs. Unfortunately, the optical IWAs were not calculated during the first design round and these values are not currently available for Cases 1, 2, 5, and 6.

Implicit in these designs is an assumption that the apodization is solid in the center and tapers monotonically outward, with that taper occurring over a sub-region of the radial extent. Leaving a solid central disk is a practical choice, as the spacecraft bus can be located there without interfering with the apodization profile. Manufacturing considerations require that $A(r)$ cannot go smoothly to 0 at R or 1 at the radius of the central disk, as the petal tips or gaps between petals would become impossibly narrow. We prevent this by constraining feature sizes directly in the optimization.

Linear optimizations provide globally optimal solutions for their constraints, so in practice we iterate on the scientific and engineering parameters and rerun linear optimizations until an apodization function consistent with the science case is produced. Once a promising apodization is identified, it is propagated through the target telescope to the focal plane using a propagator that runs on the exact locus of edge points, rather than the azimuthally symmetric approximation used for the optimization. Final evaluation of the starshade performance is done in the focal plane.

I.1.4 Results

The results of the design runs appear in **Table I-1**. For Cases 1 and 5, which have the longest wavelength of operation (2500 nm), no designs that satisfied the science constraints were found for starshade diameters < 200 m. Therefore, these Cases were not studied further. Cases 2 and 6 were designed for the 250–1000 nm bandpass; these two designs are shown in **Figure I-3**. The sizes of these shades are still quite large: 160 m in diameter for LUVUOIR-A (Case 2) and 95 m in diameter for LUVUOIR-B (Case 6).

Given the large sizes of these designs, an investigation was done to look at the effect on geometric IWA of fixing the Case 6 diameter to 70 m. This raised the geometric IWA from 40 mas to 57 mas. For this 70 m case, loosening the science constraints only produced weak improvement in IWA. For example, raising the permitted contrast by 10x only decreased the geometric IWA to 53 mas, while separately raising the short wavelength cutoff to 500 nm decreased the geometric IWA to 54 mas.

These initial experiments very clearly showed the strong impact of the long wavelength cutoff on the required starshade diameter. Therefore, in the second round of designs done in 2019, we examined starshades intended for use at shorter wavelengths. Reducing the long wavelength cutoff to 850 nm resulted in starshades with diameters of 67 m for LUVUOIR-A (Case 3) and 57 m for LUVUOIR-B (Case 7).

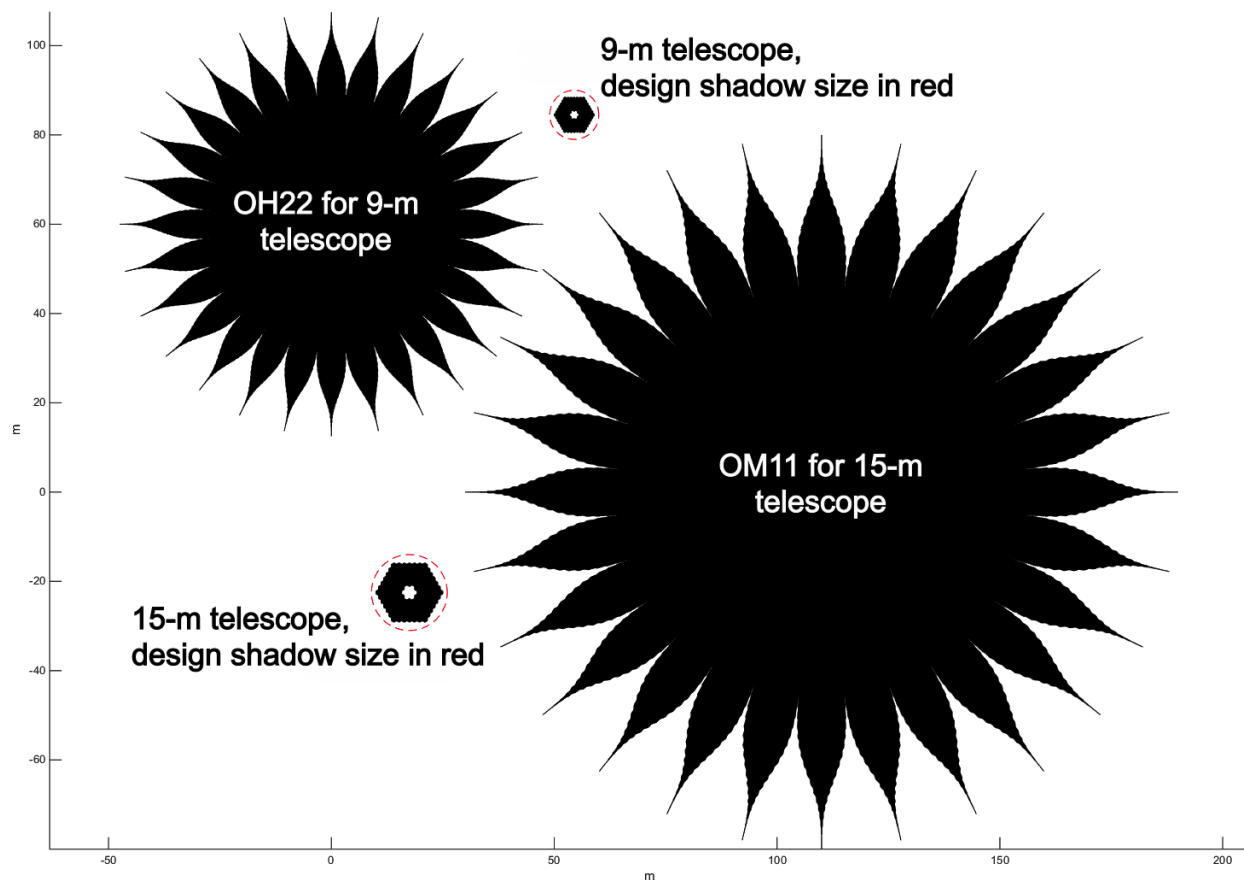


Figure I-3. The two starshades for a 250–1000 nm bandpass, to scale, along with the telescope apertures and shadows they were designed to.

Case 4 is particularly interesting; with an NUV/blue bandpass of 250–400 nm, the starshade diameter was only 46 m for LUVOIR-A. The LUVOIR Team set a high priority on high-contrast spectroscopy at these wavelengths, as they are required for observation of ozone in habitable exoplanet candidates and hazes in all exoplanets. However, including a NUV channel in the LUVOIR coronagraphs reduces the throughput of all the channels, due to additional aluminum mirrors within the instrument (instead of silver). The possibility of covering these wavelengths separately with a starshade is an interesting trade study that could be performed at some later date.

We conclude the following from these preliminary starshade studies:

1. Starshades that reach into the NIR (beyond 1000 nm) are unfeasibly large for both LUVOIR architectures.
2. A starshade that spans the entire optical bandpass (< 1000 nm) is likely unfeasible for LUVOIR-A. Such a starshade may be a viable option for LUVOIR-B, albeit one that surpasses the current “nominal” maximum starshade size of ~70 m.
3. NUV/blue starshades appear to be viable—and interesting—options for both LUVOIR-A and -B.

I.2 Extension of LUVUOIR's capabilities to 5 μm or beyond

Michael Werner (Caltech-JPL)

We present the scientific rationale and technical implications for the use of LUVUOIR out to at least 5 μm . We consider primarily the benefits of such an extension to the study of exoplanets, which is a pillar of the LUVUOIR scientific case. We discuss two possible realizations of LUVUOIR (9.2-m, $T = 293\text{ K}$) and (12-m, $T = 273\text{ K}$) and also present a simple instrument concept that could achieve our scientific objectives with limited impact on the rest of the facility. This section is based on Werner et al. (2016) (hereafter W16), which provides considerably greater detail. The examples below thus underestimate the power of the 15-m LUVUOIR-A architecture.

I.2.1 Introduction

The rationale for operating LUVUOIR out to at least 5 μm may be summarized as follows. One can be confident that, whenever LUVUOIR launches, the study of exoplanet atmospheres will be an exciting and crucial scientific discipline. Numerous molecular species likely to be important probes of exoplanet atmospheres have bands in the infrared beyond $\sim 2\text{ }\mu\text{m}$ including H_2O , CO , CO_2 , CH_4 , NH_3 , and O_3 . Many of these same species are abundant in the Earth's atmosphere and are difficult to access from the ground but are easily studied by a space telescope such as LUVUOIR. In addition, recent developments suggest that atmospheric hazes or clouds may be common in exoplanet atmospheres and that they can interfere with our ability to determine molecular abundances using optical and near-infrared measurements only (e.g., Sing et al. 2016). Observations further into the infrared have the potential to improve constraints on molecular abundances by either punching through the haze or better defining its properties and extent. As a general principle, the study of exoplanet atmospheres will benefit greatly from inclusion of the widest range of molecules over the widest wavelength range. LUVUOIR's infrared capabilities would inform our overall understanding of exoplanet atmospheres and, in ways which may be difficult to foresee at present, support our quest to identify habitable or potentially habitable planets through atmospheric studies. Of course, an infrared-capable LUVUOIR could also carry out exciting studies of targets other than exoplanets.

I.2.2 Use of a warm telescope for infrared exoplanet studies from space

Sensitivity is not the only rationale for an infrared space telescope. Here we consider instead the benefits of a 273–300 K space telescope, in comparison to a comparable- or even larger-sized telescope at a mountaintop observatory. For present purposes, these benefits come in four categories:

Access to the entire infrared spectrum. From outside the Earth's atmosphere, we can access the entire infrared spectrum and all infrared-active molecular species. This may include important species with critical diagnostic features longward of 5 μm , as well as the prominent species with spectral features in the 2–5 μm band discussed here.

Clear skies and long observations. Many exoplanet observations—for example, transits, eclipses, and phase curves—will be of long duration and have timing constraints. A space

telescope, operating always under cloudless skies and easily able to observe a particular target for days rather than hours, provides great practical advantages for this type of study.

Stability. The study of exoplanet spectra using combined light spectroscopy (i.e., transit spectroscopy) requires achieving a measurement precision on the order of parts per million (ppm) for the most difficult cases. Achieving such photometric precision on a large, warm telescope in space would certainly be easier than on a similar telescope on the ground, looking through the warm and turbulent atmosphere.

Sensitivity. A large space telescope should achieve higher sensitivity than a comparably sized telescope on the ground because of the absence of atmospheric absorption and emission and the routine achievement of diffraction-limited performance.

The scientific, technical, and functional considerations outlined above motivated us to explore extending the wavelength range of LUVOIR to 5 μm , without imposing a constraint on the telescope temperature, but by adding an instrument. We begin by exploring the scientific benefits of this extended wavelength coverage. We also present a strawman design for an infrared spectrometer, covering the 1–5 μm wavelength range with resolving power $R = 200$, which could execute the science described below with minimal system impact. The 5- μm cutoff reflects current detector technology. A more thorough study should explore longer wavelengths, noting, for example, that the 5–8 μm spectral interval is largely inaccessible from the ground. It could also include exploration of eclipse spectroscopy; here we consider only transit spectroscopy.

1.2.3 Exoplanet atmospheric characterization with transit spectroscopy

Telescope size can trump background noise. Transit spectroscopy thrives on observations of the brightest stars, for which the main noise source, even with a warm telescope, can be the photon noise of the star itself. For these observations of bright stars there is nothing gained, in principle, by cooling the telescope. In **Figure I-4**, we consider the time taken (or inverse sensitivity) for three telescope configurations to detect a similar small (10 ppm at $R=200$) and narrow feature at 4 μm , as a function of the stellar magnitude at that wavelength. The configurations are two versions of LUVOIR and JWST (6.5-m, cryogenic telescope). LUVOIR is more sensitive than JWST for bright host stars, with the 12-m LUVOIR telescope taking $\sim 4\times$ less time to make the same observation for stars brighter than $[L]\sim 9$ mag, as is to be expected in the stellar photon-limited case. The 15-m LUVOIR would be about 40% faster than the 12-m version. For transit spectroscopy, a large warm telescope becomes more powerful than a smaller but cooler one.

There will be targets. Exoplanet direct imaging is a major driver of the LUVOIR concept, which includes coronagraphy to obtain direct images and low-resolution spectra of exoplanets. The infrared functionality discussed here would provide a powerful complement to this direct imaging work through the use of combined light studies, greatly increasing the scope and wavelength coverage of LUVOIR exoplanet studies. Observations of transiting exoplanets with LUVOIR can yield an enormous scientific return due to the combination of a large aperture and thousands or tens of thousands of targets, each presenting a different scientific puzzle.

In addition to Kepler, K2, and TESS, the PLATO mission, to be launched by ESA in 2028 with a 4-year prime mission lifetime, will yield planets for study by LUVOIR. Based on information provided by David Brown of the PLATO team, PLATO should find over 3400

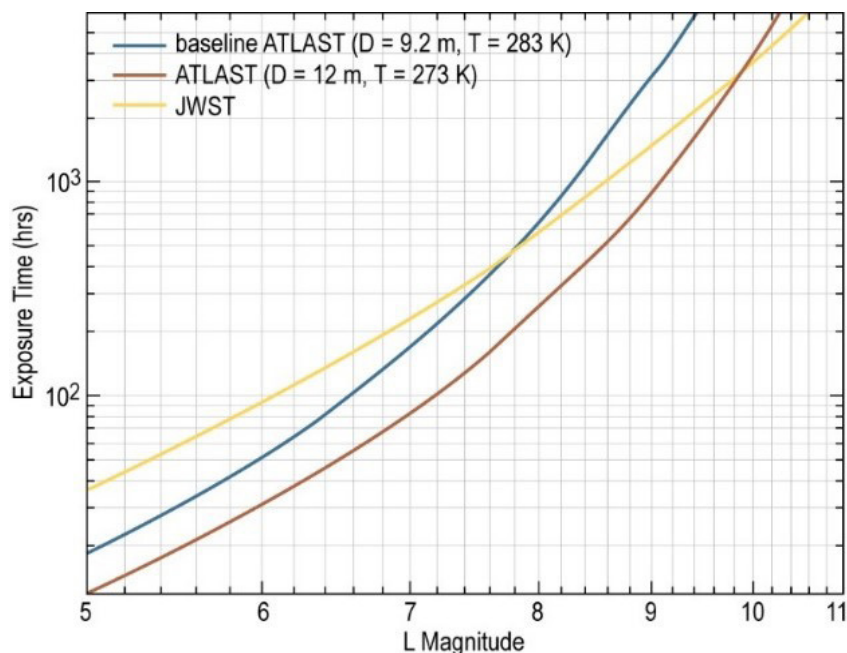


Figure I-4. Exposure time (or inverse sensitivity) as a function of stellar magnitude for detection of a small and narrow feature (10 ppm at $R=200$) at $4\ \mu\text{m}$ due to a transiting exoplanet. Three telescope configurations are shown: 9.2-m and 12-m LUV0IRs [called ATLAST in W16] and JWST. LUV0IR is more sensitive than JWST for bright host stars, with the 12-m LUV0IR telescope taking $\sim 4\times$ less time to make the same observation, as is to be expected in the stellar photon limited case. For the LUV0IR configurations, a total photon throughput of 0.35 and a (single mode) background with emissivity 0.2 is assumed; these parameters are commensurate with those of the instrument described below. For JWST, the actual expected performance of the NIRCAM grism (Greene et al. 2007) is adopted. The specific example adopted here is quite stressing in terms of photometric precision requirement, but the gain of the large warm telescope would be preserved in less demanding observations as well.

transiting planets around stars brighter than 11th magnitude in the visible. The predicted S/N per hour vs. planet size for the some of the most readily studied exoplanets which PLATO might discover is shown in **Figure I-5**. We take $S/N > 100$ as our target, because only a portion of the total transit signal is contributed by the atmosphere. This is readily achieved in a single transit for Jovian planets with $R \sim 10 R_{\text{Earth}}$. A handful of smaller planets will orbit stars of ~ 5 th mag, and their spectra can be readily obtained. Co-adding transits will reach still smaller planets. The 5th magnitude star can be observed with LUV0IR and the $R=200$ spectrometer described below without saturating the detectors, provided that frame rates faster than 1 Hz are achievable.

Abundance constraints: an example. A critical performance metric for characterizing exoplanet atmospheres via spectroscopy is the degree of constraint the measurements provide on the abundance of detected species, also termed the atmospheric mixing ratio. W16 evaluated the effects of the LUV0IR wavelength range on the constraints that LUV0IR transit spectroscopy might provide. We note a recent paper by Greene et al. (2016), which, for the specific case of JWST, shows the importance of observations longward of $2.5\ \mu\text{m}$ for characterizing exoplanet atmospheres. As an illustrative example, W16 considered the

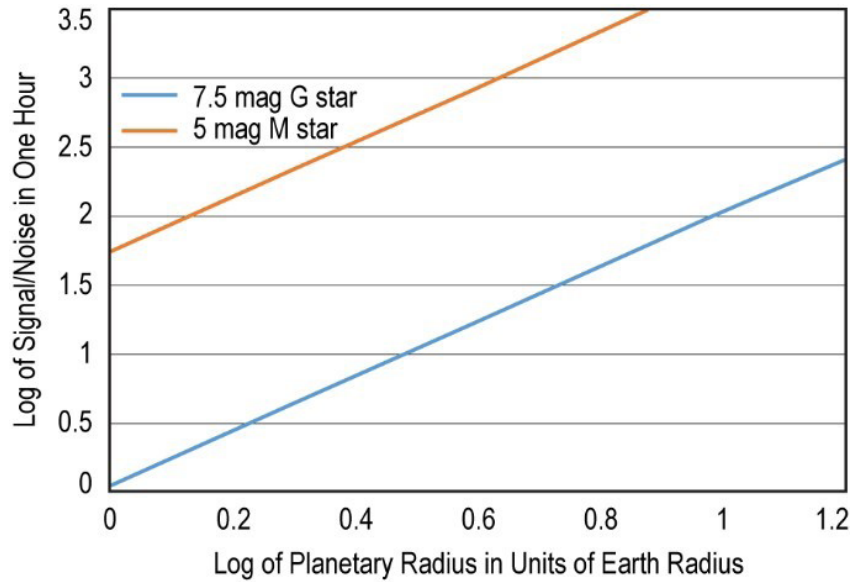


Figure I-5. Signal/noise on the transit depth for each resolution element in one hour for planetary transits at $4\ \mu\text{m}$. A 9.2-m, 293 K telescope and the $R=200$ fiber-fed spectrograph described below were adopted for the calculation.

case of a $2.6 R_{\text{Earth}}$, $6.1 M_{\text{Earth}}$ transitional super-Earth/sub-Neptune planet with a 600 K atmosphere orbiting a K star, assuming solar metallicity, thermal equilibrium chemistry, and a clear atmosphere, observed with the 9.2-m LUVOIR. A number of independent observations were simulated and the results analyzed with a multi-parameter MCMC retrieval using the CHIMERA code.

The results of these experiments are presented in **Table I-2**, which shows that with 0.4–5.0 μm spectral coverage, LUVOIR has the potential to determine the abundance of water and methane in many TESS/K2/PLATO targets. If the spectral coverage were limited to 2.5 μm , brighter stars are required, so substantially fewer targets would become available for study. This demonstrates the benefits of the enhanced wavelength range we are proposing, particularly for the high mean molecular weight atmosphere, which approximately corresponds to an Earth-like atmosphere. In this case, a very bright star ($[H] < 6.3\ \text{mag}$) is required for abundance determinations with less than an order of magnitude uncertainty; stars this bright that harbor transiting planets may be rare statistically. As expected, the lower mean molecular weight atmosphere, with its larger scale height, would be much more readily observed. Several recent papers (Misra, Meadows, & Crisp 2014; Betremieux & Kaltenegger

Table I-2. Limiting magnitude for determination of molecular abundances with an overall uncertainty of less than one order of magnitude for a $2.6 R_{\text{Earth}}$ super-Earth/sub-Neptune ($T \sim 600\ \text{K}$) orbiting a K star, assuming 24 hours of observation time spread over a number of transits.

	Molecule	0.4–2.5 μm	0.4–5 μm
Mean mol. weight 2.3	H_2O	$H_{\text{mag}} < 10.3$	$H_{\text{mag}} < 11.3$
	CH_4	$H_{\text{mag}} < 10.3$	$H_{\text{mag}} < 12.3$
Mean mol. weight 28	H_2O	$H_{\text{mag}} < 6.3$	$H_{\text{mag}} < 8.3$
	CH_4	$H_{\text{mag}} < 6.3$	$H_{\text{mag}} < 8.3$

2014) have highlighted the effects of refraction in the lower part of an exoplanet's atmosphere on our ability to study abundances using transit measurements. The importance of this effect depends on both the size of the star and the star-planet distance, and it will have to be taken into consideration in more sophisticated predictions.

Studying a true Earth analog. A major thrust of exoplanet studies is, of course, the push to identify and study potentially habitable Earth-like planets. Recent work has shown that simply identifying O₂ and O₃ in a particular atmosphere is not adequate. Other molecular species, notably CH₄ but also N₂, CO, and CO₂, may have to be studied in order to rule out or confirm the potential habitability of a particular planet which shows O₂ and O₃. Understanding the prevalence of these species (all of which have strong spectral features longward of 2.5 μm) in exoplanet atmospheres thus takes on special interest, even if it may not in general be possible to search for all of these molecules in the atmosphere of the same planet.

The detection of biosignatures in the atmosphere of a true Earth analog presents major challenges. This is a difficult detection, so we present it as a limiting case; studying larger planets with more extended atmospheres should be much easier. The average methane volume mixing ratio in the Earth's atmosphere is quite low (1.7 ppm), a factor of 200 less than CO₂, but it is the major source of departure from thermodynamic equilibrium if the atmosphere is considered as a closed system (without oceans and rocks). The strong methane 3.4 μm feature will be blended with a water absorption at low R, but nonetheless contributes up to 10 km (a little more than the 8 km scale height) of extra absorption in the transmission spectrum of an Earth. The weaker methane features at shorter wavelengths are yet more heavily blended. In atmospheres with high cloud coverage, the strong IR molecular features absorb at altitudes above the cloud deck, which is another major advantage of long wavelength spectroscopy.

We have computed the transit spectrum of an Earth analog orbiting a late type star, exploiting the advantages conferred by M stars for transit measurements; in addition, the refraction effect mentioned above is much less of a concern for M stars than for solar type stars. Conservatively assuming that the occurrence of habitable zone rocky planets is 0.2 around late type stars, the nearest M-dwarf with a favorable transit will be about ~15 pc away.

In **Figure I-6** we show a simulated LUVUOIR R=20 transit spectrum of an Earth transiting an M4V star (distance 15 pc, Lmag = 7.7) in the 2–5 μm region; the underlying model simply uses an Earth transit spectrum and the instrument prescription described in this paper, for which the spectral resolution can be degraded from 200 to 20 with a $\sqrt{10}$ increase in S/N per resolution element. While the total time required for the spectrum shown in **Figure I-6** (~60 transits or 120 hours) is large, it is not outrageously so (two exoplanets have had similar amounts of Hubble time awarded). The orbital period of a habitable zone planet around our M4 star is 16 days, so about 2.5 years would be required to obtain spectra similar to that shown in **Figure I-6**.

I.2.4 Summary of infrared capability for LUVUOIR

We have demonstrated that a ~10-m diameter telescope operating in space at room temperature would be able to make unique and important scientific measurements in the infrared out to at least 5 μm. By using the technique of transit spectroscopy, where for bright stars

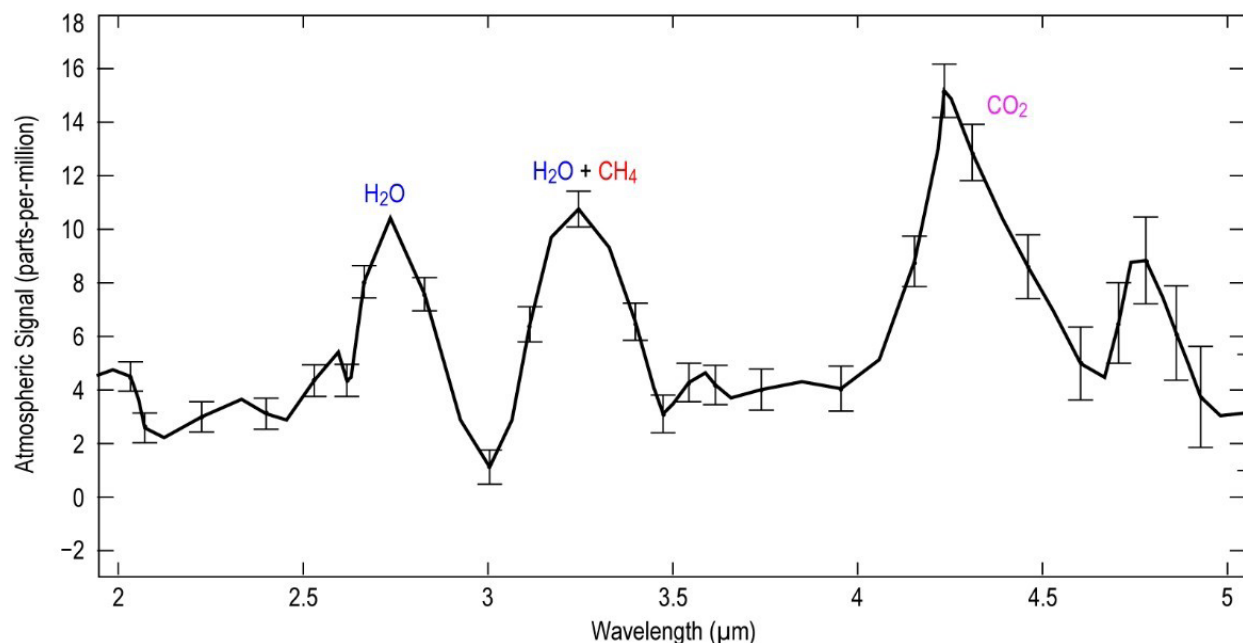


Figure I-6. A 2–5 μm $R \sim 20$ model transmission spectrum of a $1 R_{\text{Earth}}$ habitable zone planet with an Earth-like oxidizing atmosphere transiting an M4V star ($R_{\text{star}} = 0.32 R_{\text{Sun}}$, $T_{\text{star}} = 3100 \text{ K}$) 15 pc from Earth. The 1-sigma errors per wavelength bin, obtained with the smaller LUVOIR design ($D=9.2 \text{ m}$, $T=273 \text{ K}$), are plotted along with the model. The total integration time is 120 hours in transit, corresponding to 60 transits of about 2 hours each. Features of H_2O , CH_4 , and CO_2 are detected (this spectrum does not include the effects of refraction). CH_4 is blended with H_2O at $\sim 3.3 \mu\text{m}$ and determining its independent presence and total column would require full atmospheric retrieval; in the Earth's atmosphere, CH_4 and H_2O contribute roughly equally to the $3.3 \mu\text{m}$ feature. A total throughput of 0.35 and an emissivity of 0.2 is assumed here. The y-axis is labelled in parts per million (ppm) relative to the total signal produced by the star. The overall depth of the transit for this case would be about 800 ppm; the features shown in the spectrum would be manifest as changes in the transit depth with wavelength. The precision of a few ppm called for here would be a challenging target for IR detector technology.

the noise is set by the stellar photons rather than the thermal background, such a telescope could outperform smaller but lower temperature telescopes. It would also be capable of obtaining spectra of millions of infrared sources from the WISE catalog and provide new information about the formation of solar systems, which would link directly to exoplanet observations. We feel that such a capability should be carefully considered for incorporation into LUVOIR, now or in the future, particularly if further studies of instrument concepts such as that presented below show that they can be easily incorporated into the payload.

I.2.5 A fiber-fed infrared spectrometer for LUVOIR

W16 describe a fiber-fed IR spectrometer for LUVOIR. The spectral resolving power of 200 was chosen to permit disambiguation of molecular features in exoplanet atmospheres and also to permit study of the profiles of solid-state absorption features in galactic protostellar and protoplanetary disks. We emphasize that other spectrograph designs and means of feeding the spectrograph could provide equivalent performance, and that coupling the starlight into and out of the fiber could stress the LUVOIR pointing system and perhaps other design

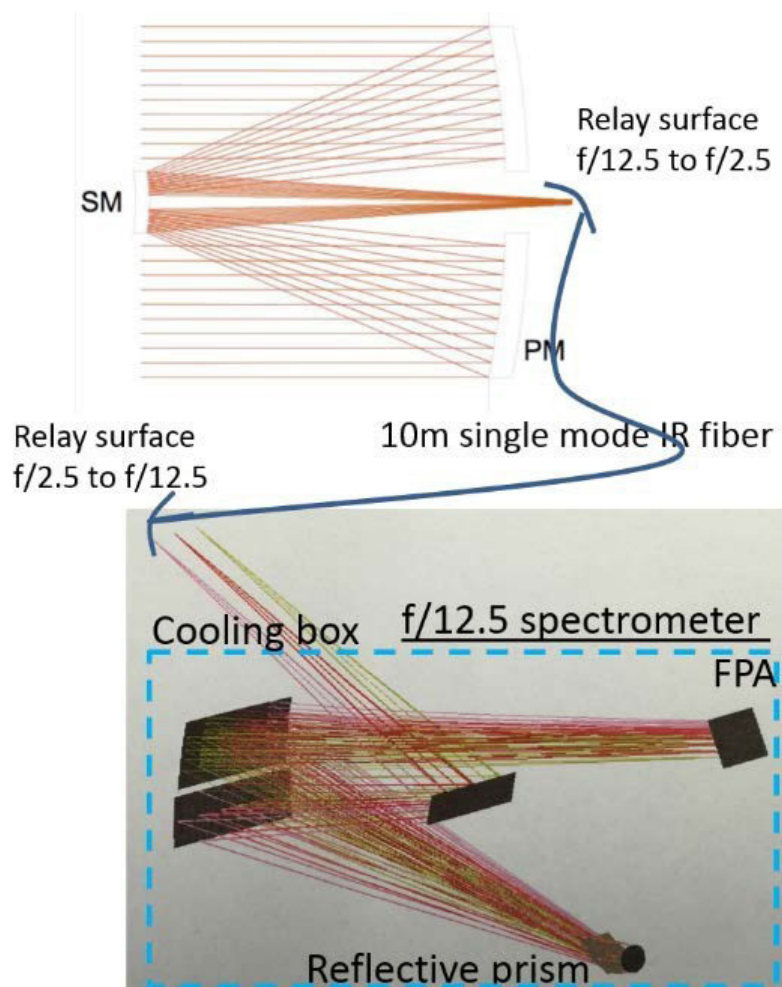


Figure I-7. *Fiber-fed, prism-based IR spectrometer configuration.*

parameters. An alternative approach using mirrors instead of fibers to feed the spectrograph ought certainly to be considered, for example.

This particular approach was chosen because, on the surface at least, it appears to minimize the system impact of the thermal infrared capability. **Figure I-7** is a concept sketch of the system. A pick-off mirror will be inserted into the LUVOIR telescope focal plane to relay the star signal into a prism-based spectrometer system ($f/12.5$), featuring a MWIR FPA ($5\ \mu\text{m}$ -cutoff H2RG from Teledyne). The reflective prism is made of calcium fluoride. A 10 m IR fiber (Fluoride Fiber ZBLAN SM from Le Verre Fluore) is used to carry the light from the telescope to the spectrometer, which is mounted on the exterior structure of LUVOIR so that it can cool radiatively. To get optimal fiber coupling, 2 relay mirrors with power ($f/12.5$ to $f/2.5$) are utilized. To minimize the spectrometer background noise, a cold shield box covers the full spectrometer system, and the second relay surface illuminates the spectrometer slit, which is mounted on the side of the otherwise sealed cold shield box. The performance of this system is detailed in W16 and used in the calculations presented above.

The design of the spectrometer described here was supported by a grant from the JPL Research and Technology Development fund. Portions of the work described in this paper were carried out at the Jet Propulsion Laboratory, California Institute Technology, under a contract with the National Aeronautics and Space Administration.

I.3 JAXA transit spectrometer for LUVOIR

Taro Matsuo (Osaka Univ./NASA Ames Research Center), Thomas Greene (NASA Ames Research Center), Takahiro Sumi, Satoshi Itoh (Osaka Univ.), Tomoyasu Yamamuro (OptCraft), & Toru Yamada (JAXA ISAS)

I.3.1 Summary

We propose a highly stable spectrograph for LUVOIR, aiming to measure the habitability and biosignatures of nearby transiting planets orbiting late-type stars (**Figure I-8**). The instrument applies the densified pupil spectrograph that provides multiple spectra of a planet and its host star on a detector plane and provides spectroscopy stable against any wave-front errors including telescope pointing jitter and deformation of the primary mirror figure. Simulations show that a densified pupil spectrograph on a telescope with the large aperture of LUVOIR could observe a number of nearby transiting planets orbiting bright stars such as those discovered by the Transiting Exoplanet Survey Satellite (TESS). In addition, the electrical variation in a detector system can be reduced to a random term. Thus, the LUVOIR transit spectrometer is designed to reduce the systematic noise down to a few parts-per-million (ppm) and nearly achieves ideal photon-noise-limited performance.

The LUVOIR transit spectrometer with three 1k x 1k HgCdTe detectors simultaneously covers 0.6 to 2.5 μm as the baseline specification and 0.7 to 4.0 μm as the extended one at one time measurement, respectively. The resolving power is set to more than 200 over the entire wavelength range. The volume of the LUVOIR transit spectrometer is approximately 2 x 1.2 x 0.2 m (length x width x thickness). Thanks to the strong light-gathering power of LUVOIR-A and -B, the LUVOIR transit spectrometer allows us to measure signs of the habitability and biosignatures of nearby potentially habitable transiting planets that will be discovered by TESS.

I.3.2 Science

Characterization of the atmospheres of Earth-like planets in the near- and mid-infrared wavelength region is an important approach to search for life in the universe. Signs of nonequilibrium atmospheric chemistry that indicate biological activity can be confirmed through measurements of oxidized species such as O_2 and O_3 , and reduced species such as CH_4 . Other biosignatures such as N_2O have also been proposed. **Figure I-8** shows a transmission spectrum of an Earth-like planet orbiting a late M-type star such as TRAPPIST-1.

There are several absorption features of the biosignatures in the wavelength range of the proposed LUVOIR transit spectrometer: O_2 at 0.76 and 1.28 μm , O_3 at 0.6 and 3.26 μm , CH_4 at 2.35 and 3.3 μm , and N_2O at 2.9 and 3.9 μm . The depths for most of these absorption features are 30–40 ppm in transmission for a late M-type star and 15–20 ppm for a middle M-type star, respectively. Thus, if the LUVOIR transit spectrometer achieves the photon-noise-limited performance, we can investigate whether there is biological activity on nearby potentially habitable planets orbiting the late and middle M-type stars. The LUVOIR spectrometer can also investigate habitability via detecting the H_2O absorption features at 1.4 and 1.9 μm and CO_2 absorption features at 2.0 and 2.75 μm .

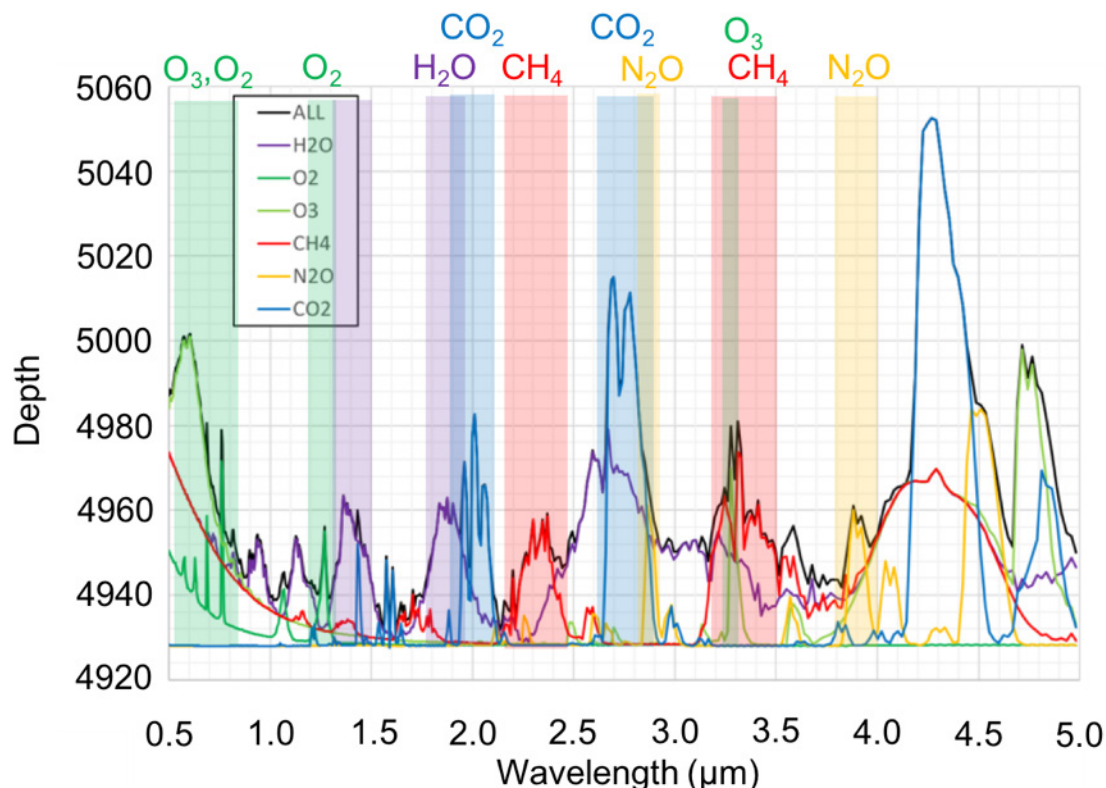


Figure I-8. Theoretical transmission spectrum of an Earth-like planet orbiting late M-type star. The y axis has units of ppm.

I.3.3 Instrument concept

This instrument uses the densified pupil spectrograph, composed of a pupil densification system and a spectrograph (Matsuo et al. 2016). An overview of this instrument appears in **Figure I-9**. The densified pupil has a key role in performing stable spectroscopy. The densification factor is determined by multiplication of the division number of a pupil slicer and the pupil densification of two concave mirrors after the pupil slicer. The densified sub-pupils after the pupil densification system correspond to the entrance of the spectrograph.

Thanks to the large densification factor, each densified sub-pupil acts as a point source and each beam is collimated by a collimator mirror. A dispersive device put in the collimated beam spreads the light in one dimension as a function of the wavelength. The densified pupil spectrograph performs stable spectroscopy with the dispersive element put on the focal plane and is essentially same as those of existing focal-plane spectrographs. Finally, the densified pupil spectrograph generates the spectra of the divided primary mirrors on the detector plane.

I.3.4 Advantages

The densified pupil spectrograph optimized for the LUV0IR concept provides the following advantages over general-purpose spectrographs:

1. Stable spectroscopy against wavefront errors including pointing jitter and deformation of the primary mirror

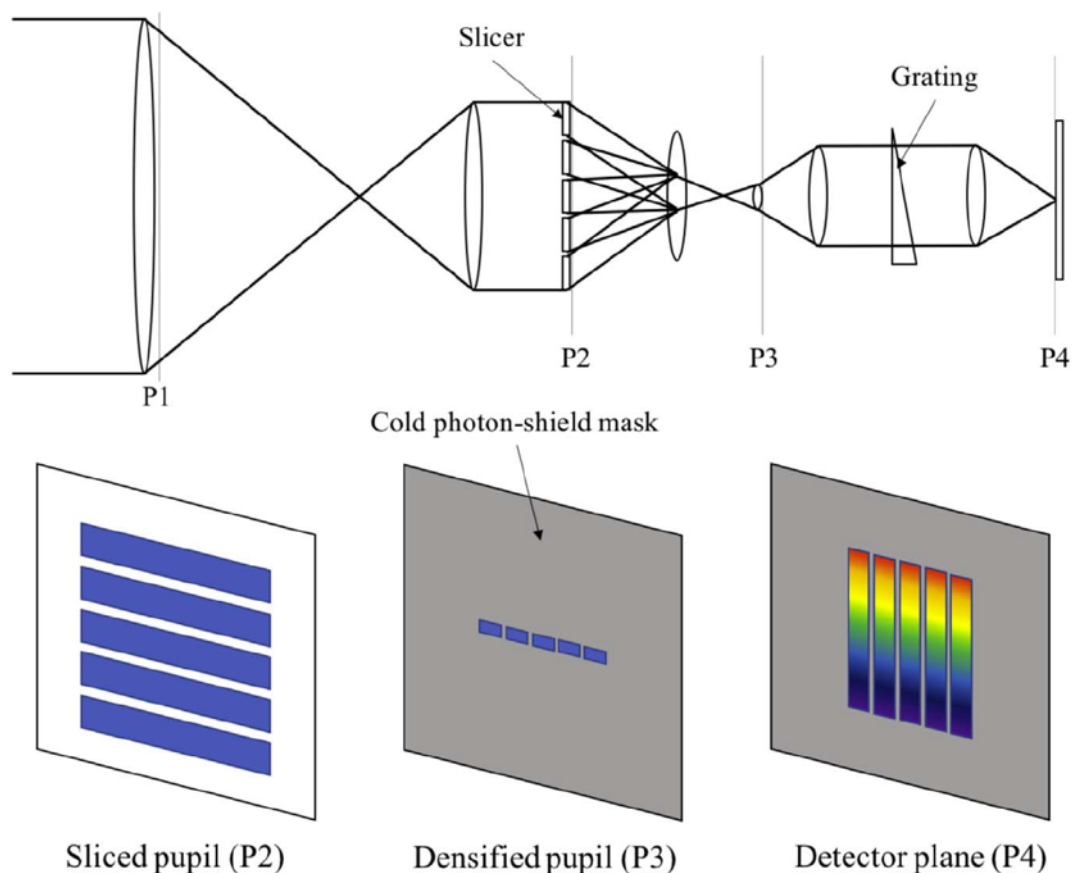


Figure I-9. Overview of the densified pupil spectrograph (Goda & Matsuo 2018). *P* shows the pupil plane that is optically conjugated to the primary mirror. *P1* is the primary mirror of the telescope, *P2* is the plane of the pupil slicer, *P3* is the plane on which the densified pupil images are formed, and *P4* is the detector plane.

2. Observations of bright stars with multiple detector samples without saturation
3. Suppression of hot/warm pixels, cosmic rays, and gain variation in the detector system, improving transit measurement stability

Wavefront error. One of the limitations on transit spectroscopy is image movement and deformation on the inter- and intra-pixel variations of the detector plane. The detector plane in the densified pupil spectrograph is optically conjugated to the primary mirror; the LUVOIR transit spectrometer generates spectral images of the primary mirror on the detector plane. As a result, the spectra are not principally affected by any wavefront errors such as the telescope pointing jitter and deformation of the primary mirror. In addition, the number of samplings for each resolved spectral element is much larger than that of a general-purpose spectrograph. Based on the analytical estimation provided by Matsuo et al. (2016), the photometric variation due to PSF movement and deformation induced by wavefront error is much smaller than 1 ppm with a sufficiently large field stop before the pupil densification system.

Saturation limit. Due to the large number of star and planet spectra formed on the detector plane and an increase in the number of detector reads, the number of incident photons is limited even with the large aperture of the LUVOIR telescope because the detector

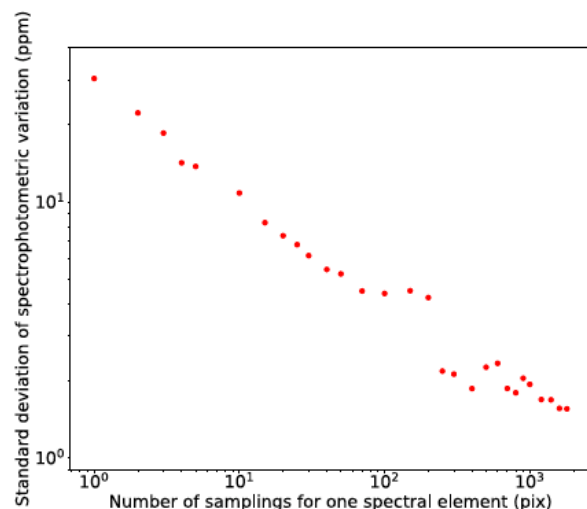


Figure I-10. Standard deviation of spectrophotometric variation as a function of the number of samplings for each spectral element. The flat-field uncertainty of the Wide-field Infrared Survey Explorer (WISE) W3 data collected during the WISE cryogenic mission was used for this evaluation.

the science pixels (**Figure I-10**). Only common time-variation components over the science pixels remain. Considering that the detector plane is optically conjugated to the pupil plane, a pupil mask can completely block astronomical light coming into residual pixels (i.e., reference pixels). The common time-variation components are reconstructed with the reference pixels and mostly reduced into a random term (**Figure I-11**).

will saturate. Since the number of samplings for a given resolved spectral element is set to around 1000, the saturation limit for the LUV0IR transit spectrometer is 100 times brighter compared to general-purpose spectrographs if the number of detector reads increases. This fully allows characterization of nearby potentially habitable transiting planets that will be discovered by TESS.

Electrical variation in a detector system.

The transit signal is affected not only by image movement and deformation due to wavefront error but also by electrical variation in the detector system. The densified pupil spectrograph can reduce the impact of electrical variation on the transit signal (Goda & Matsuo 2018). A group of pixels exposed to the star light (i.e., science pixels) at the same wavelengths allows pixel-to-pixel gain variations to be smoothed out through average of

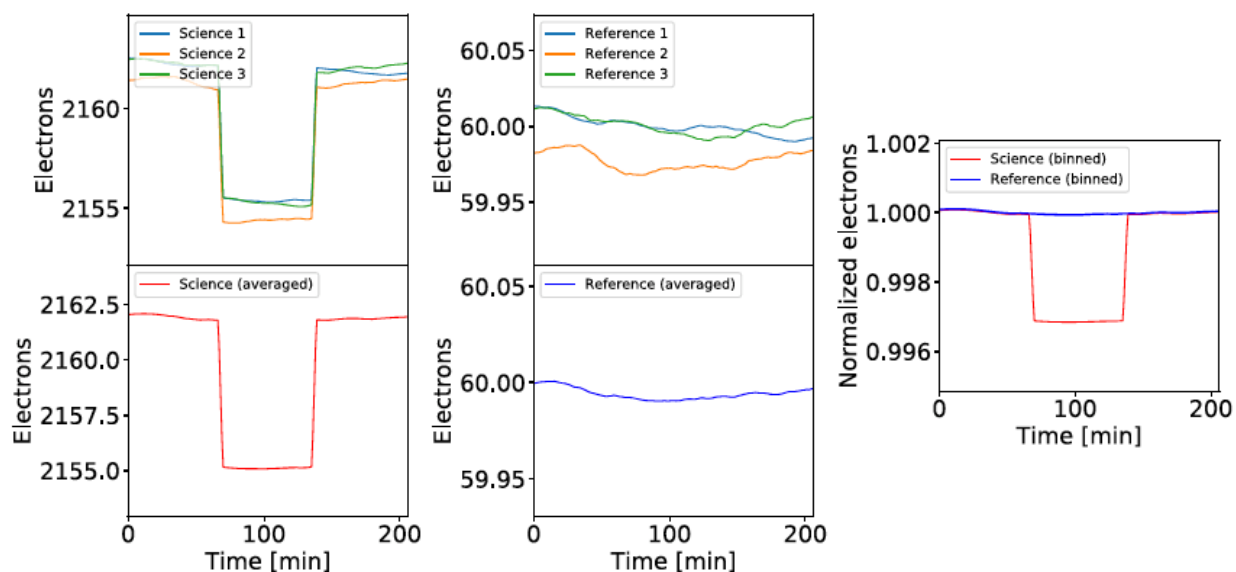


Figure I-11. Comparison of the science pixel data with the reference pixel data without shot noise. The pixel-to-pixel time variations of each data example are almost smoothed out. The averaged reference data accurately trace the time-variation components associated with the science data (Goda & Matsuo 2018).

I.3.5 Overview of the LUVOIR transit spectrometer

The optical design of the instrument is based on the Origins Space Telescope (OST) Mid-Infrared Spectrometer Coronagraph (MISC). The densified pupil spectrograph designed for the OST MISC covers a wide wavelength range of 2.8 to 20 μm at one time using two 1k x 1k HgCdTe detectors and one 1k x 1k Si:As IBC detector (Matsuo et al. 2018). The instrument proposed for the LUVOIR telescope covers 0.6 to 2.5 μm as the baseline specification and 0.7 to 4.0 μm as the extended option. The light is divided into three channels and each divided beam is sent to a detector: 0.6–1.0, 0.9–1.7, and 1.5–2.5 μm for the baseline instrument and 0.7–1.25, 1.15–2.2, and 2.1–4.0 μm for the extended option. The minimum spectral resolved wavelength, $\Delta\lambda$, is set to almost 0.005 times the central wavelength range, almost corresponding to a spectral resolving power of 200 for the general-purpose spectrographs. Note that, while the general-purpose spectrographs provide a constant $\lambda/\Delta\lambda$, $\Delta\lambda$ is fixed for the densified pupil spectrograph. This occurs because the diameter of the point spread function imaged on the diffraction grating is proportional to the wavelength.

The instrument is mainly composed of following three subsystems: 1. the relay optical system, 2. the pupil densification part, and 3. the spectrograph. **Figure I-12** shows the block diagram for one optical channel of the LUVOIR transit spectrometer. The optical components necessary for stable spectroscopy are located in the pupil and focal planes. **Figure I-13** shows the details of the pupil densification and spectrograph components of **Figure I-12**. The volume of the LUVOIR transit spectrometer is approximately 2 x 1.2 x 0.2 m (length x width x thickness) and the volume for the pupil densification part and spectrograph is 1.1 x 0.5 x 0.3 m. Because the spectrum of the primary mirror is measured on the detector plane, the volume for the pupil densification part and spectrograph is independent of the diameter of the primary mirror. In contrast, the volume of the relay optical system does depend on the diameter of the primary mirror.

The relay optical system is designed such that the beam diameter is reduced to 10 mm, corresponding to the diameter of the pupil slicer. A field stop puts the focal plane in the relay optical system. The field of view is defined by the annular radius of a field stop put on the focal plane. However, the point spread function is partially blocked by the field stop and photometric variation is induced by the telescope pointing jitter (Itoh et al. 2017). This photometric variation is called “PSF motion loss.” **Figure I-14** shows the photometric variation due to the PSF motion loss induced by the telescope pointing jitter as a function of the field of view. The radius of the field stop is determined such that the photometric variation of the PSF motion loss is less than 1 ppm. Assuming that the pointing jitter of LUVOIR-B is 10 mas, the optimal field stop radius is set to 3.5". Note that the photometric variation due to the PSF

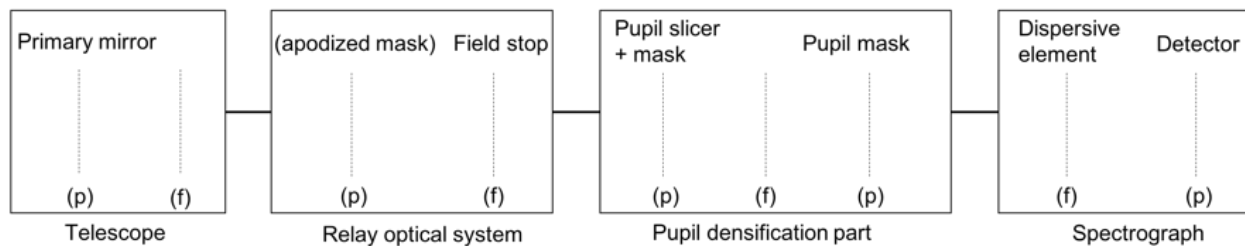


Figure I-12. Block diagram of the key components for the LUVOIR transit instrument. (p) and (f) represent the pupil and focal planes, respectively.

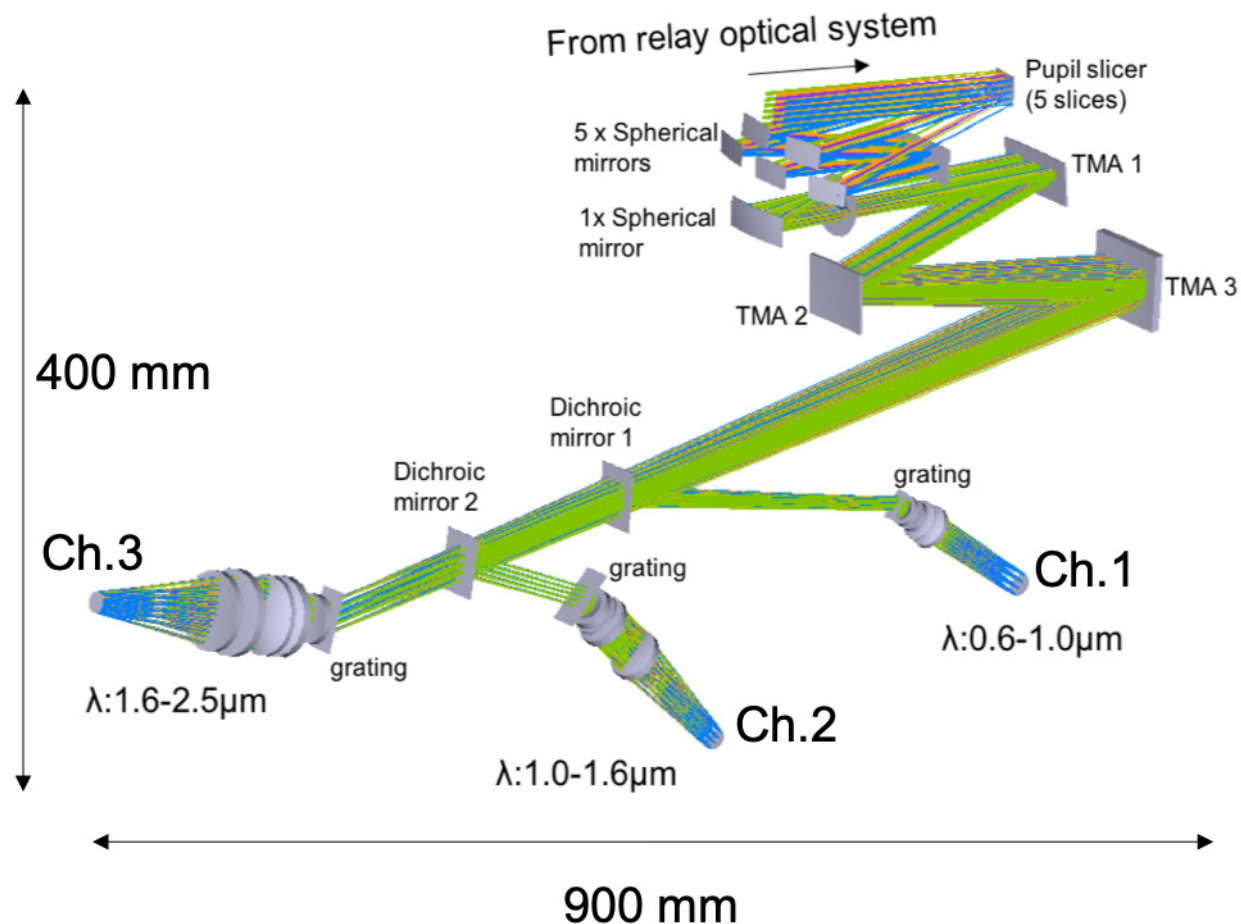


Figure I-13. Three-dimensional design of the LUVOIR transit spectrometer.

motion loss was calculated based on a diffraction-limited image of a circular aperture. We are currently deriving a pupil mask function suitable for segmented space telescopes such as LUVOIR-B based on a general analytical expression for the point spread function of a segmented telescope derived by Itoh et al. (2018).

The role of the pupil densification part is to divide the pupil into 5 sub-pupils with a pupil slicer composed of 5 slice mirrors and align the divided pupils in a straight line. Each divided beam is densified with two concave mirrors. As an extended option, the pupil can be divided in tune with the figure of the segmented mirror (see **Figure I-15**). The sub-pupils are imaged onto the entrance of the spectrograph. A pupil mask outside of the sub-pupils blocks any background or scattered light. After the pupil densification part, the densified sub-pupils are collimated by a three-mirror assembly (TMA) and divided into three channels by two dichroic mirrors. A transmission grating and a camera optical system are employed in each channel. The camera optical system is composed of four or five CaF_2 lenses. The aberration of the point spread function can be ignored; the size is fully smaller than 1 pixel. For the baseline specification, two 1k x 1k HgCdTe detectors with a 1.7 μm cutoff wavelength and with a 2.5 μm cutoff wavelength are applied for the short and middle wavelength channels and the long one, respectively. For the extended option, a 1k x 1k HgCdTe detector with a 1.7 μm cutoff wavelength, one with a 2.5 μm cutoff wavelength, and one with a 5.5 μm

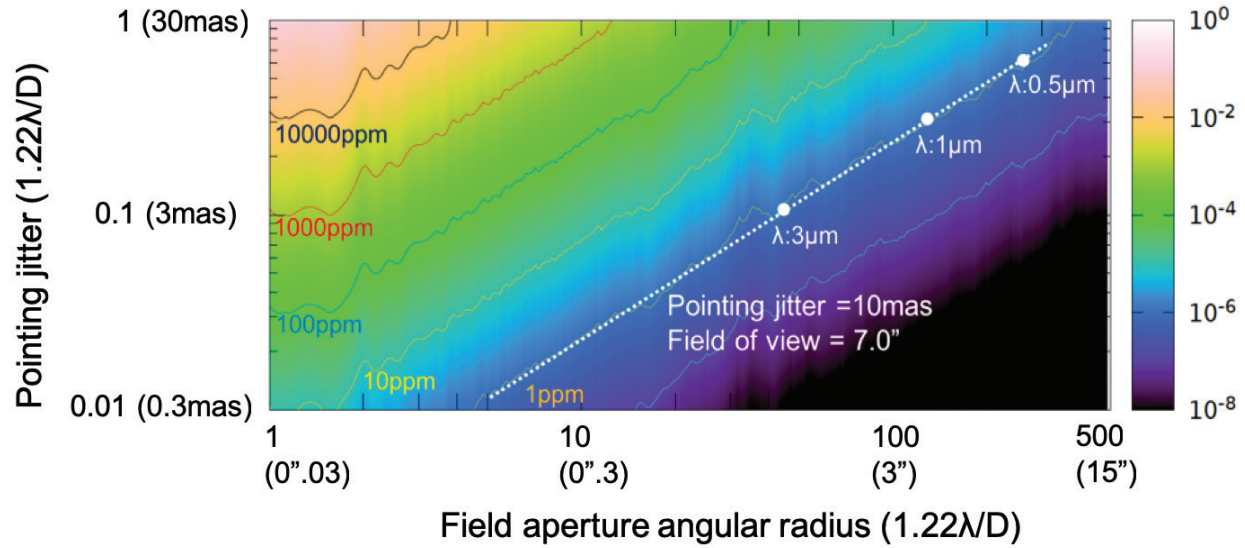


Figure I-14. Photometric variation due to the PSF motion loss induced by the telescope pointing jitter as a function of the radius of the field stop. The figures in parentheses represent arcseconds of jitter at $1\ \mu\text{m}$. Given that the pointing jitter of LUVOIR-B is 10 mas and the radius of the field stop is 3.5 arcseconds, the photometric variation is approximately 1 ppm. Note that this analysis is performed based on a diffraction-limited image of a circular aperture.

cutoff wavelength are applied for the short, middle, and long wavelength channels, respectively. The total throughput over the entire wavelength range is 0.3 to 0.4. **Figure I-16** shows the footprints of the densified pupil spectra formed on the three detector planes for the

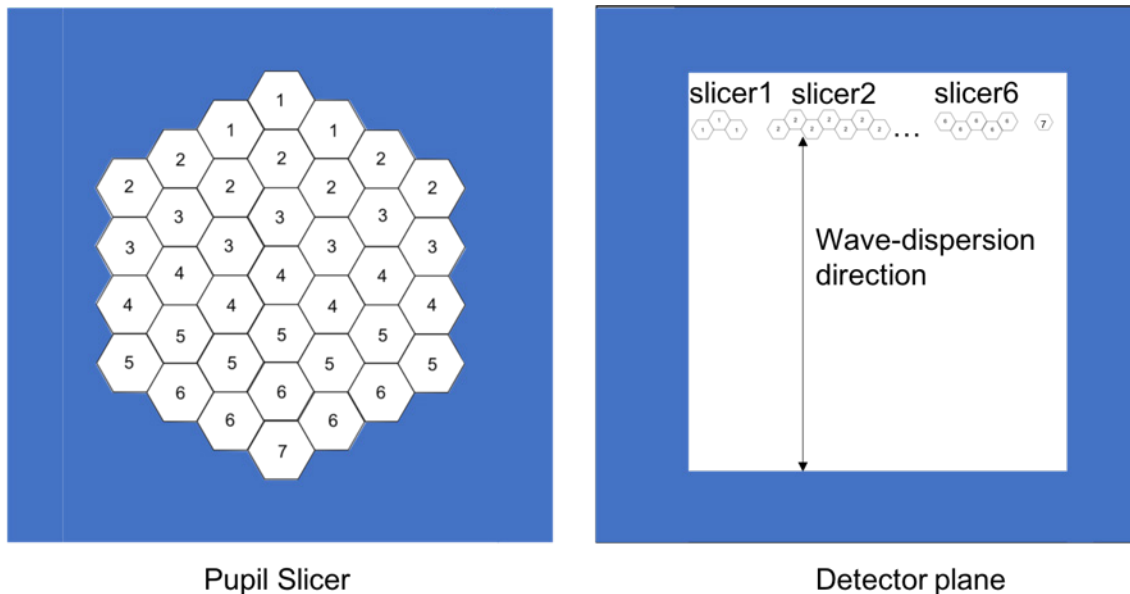


Figure I-15. (Left) Conceptual design of the pupil slicer for the extended wavelength option. The number printed on each segment mirror indicates which slicer it belongs to. The blue-colored region indicates a cold photon-shield mask. (Right) Science and reference pixels on detector plane. The blue-colored region is shielded by the pupil mask outside of the pupil slicer.

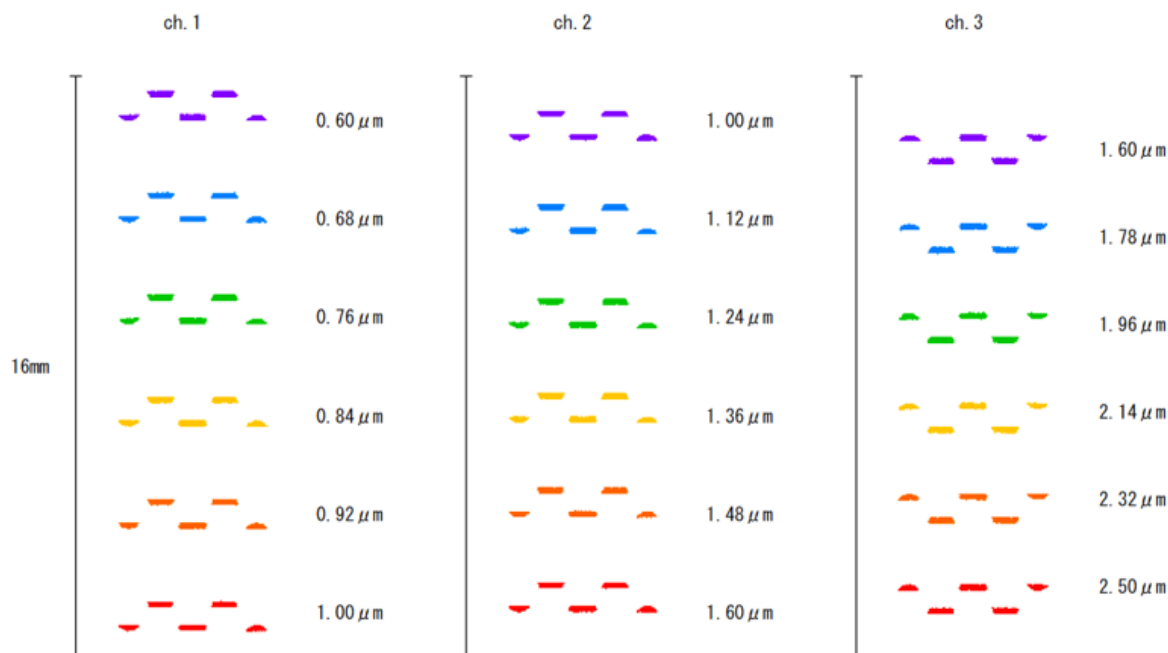


Figure I-16. Footprint of the densified pupil spectra on the three detector planes.

baseline specification. The length of each spectrum is less than 16 mm and fits the dimension of the 1k x 1k HgCdTe detector with a pixel size of 18 μm .

I.3.6 Thermal configuration

The overview of the thermal configuration for the LUVOIR transit spectrometer is shown in **Figure I-17**. The temperature of the LUVOIR transit spectrometer is set to 170 K, which meets the thermal requirements of the LUVOIR instruments. However, since HgCdTe detectors with long wavelength cutoffs of 2.5 μm are applied for both the baseline and extended designs, the detectors have to be cooled down to 120K to reduce the dark current to 1 e-/s.

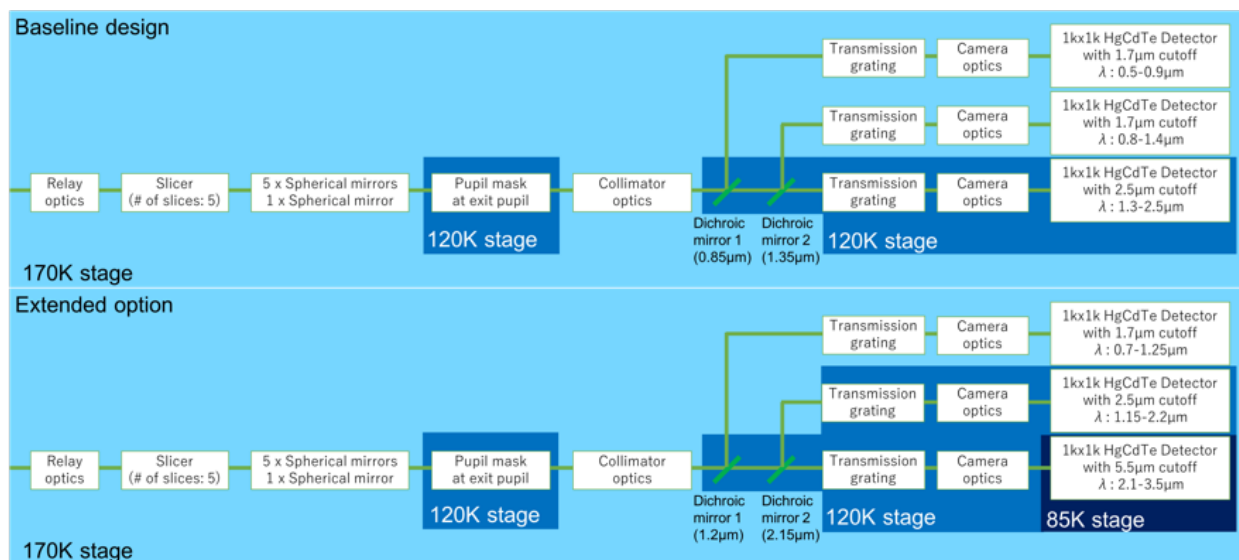


Figure I-17. Thermal configuration for the LUVOIR transit spectrometer.

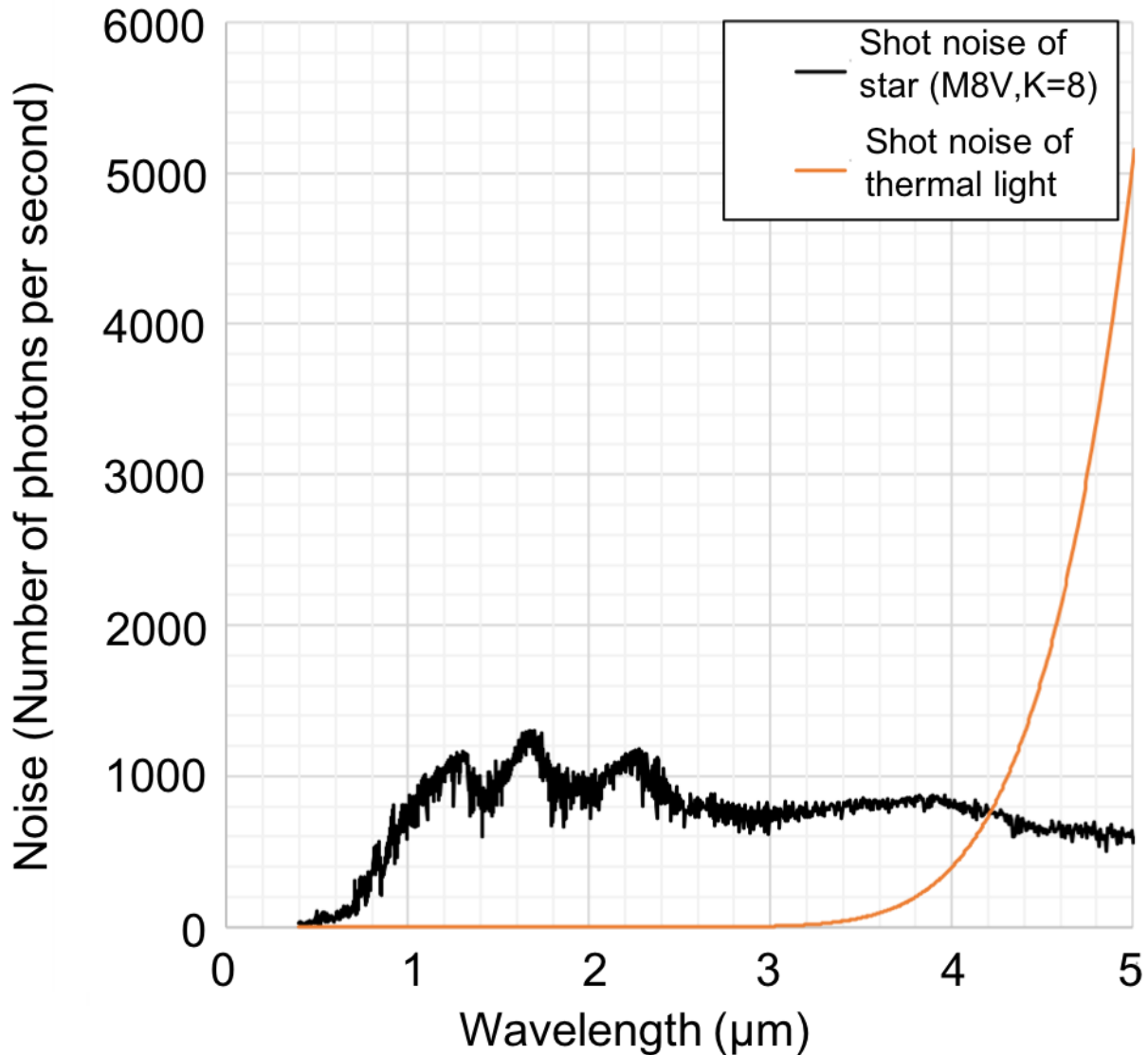


Figure I-18. Comparison of the shot noise of the thermal background light with that of the incident photons from a M8V star with $K=8$ mag. The number of the incident photons from the star was calculated based on a Phoenix stellar model. Given that the structure near the detector radiates with an emissivity of 1 and the temperature of the structure is 120 K, the number of the incident photons due to the thermal background was calculated.

In addition, a HgCdTe detector with a long wavelength cutoff of $5.5\ \mu\text{m}$ is applied only to the extended design and its temperature is set to 85 K. In order to reduce the thermal background from the instrument, the pupil mask, which is optically conjugated to the detector plane, the transmission grating, and the camera optics are cooled to the same temperature of the HgCdTe detector with the $2.5\ \mu\text{m}$ cutoff wavelength. **Figure I-18** shows a comparison of the shot noise of the thermal background from the instrument with that of the incident photons from a M8V star with $K=8$ mag. The shot noise of the thermal background is much smaller than the photon noise of the nearby bright star wavelengths less than $4\ \mu\text{m}$. Thus, the LUVOIR transit spectrometer provides spectra of host stars brighter than $K=10$ mag over the entire wavelength range if the temperature of the instrument can be cooled down to 120 K.

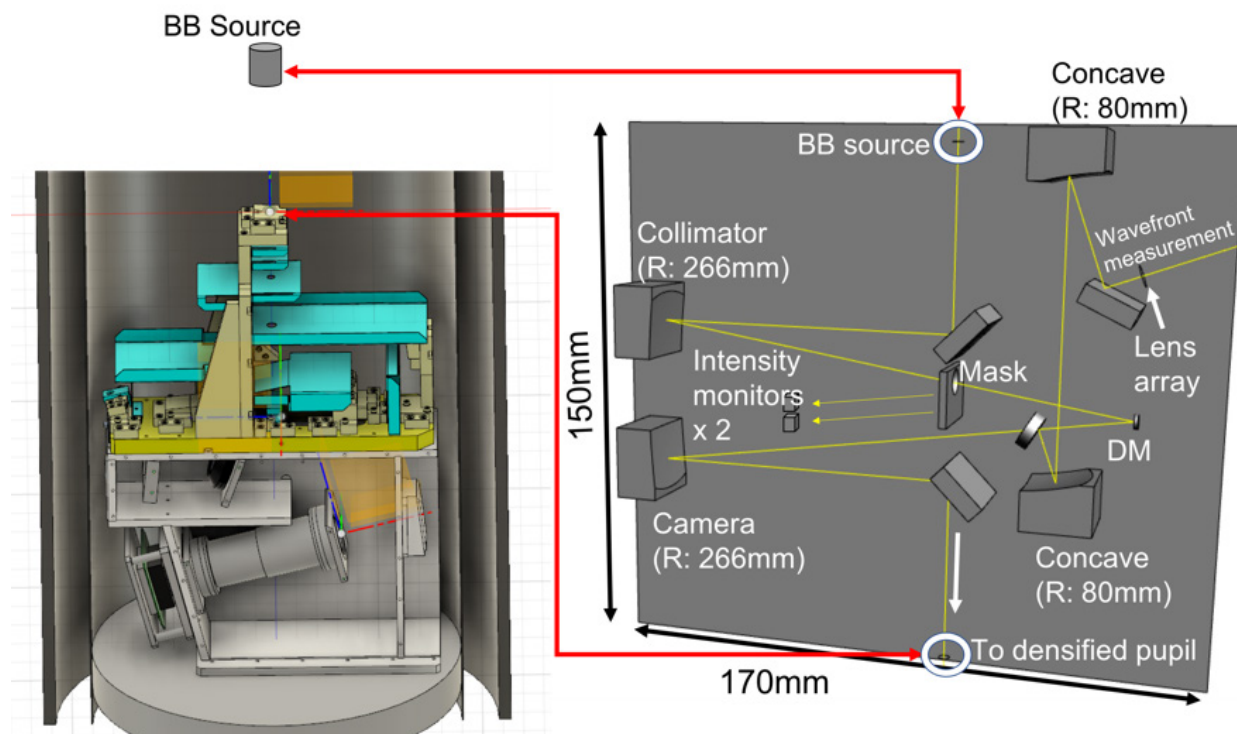


Figure I-19. Overview of the cryogenic testbed developed at NASA Ames Research Center. (Left) The model of the densified pupil spectrograph. The yellow part shows the pupil densification system and the blue components are baffles. The gray part between the pupil densification system and the 4 K cold surface corresponds to the spectrograph. (Right) The cryogenic telescope simulator that will be operated at 77 K. The simulator is composed of a deformable mirror (DM), an infrared Shack-Hartmann wavefront sensor, and infrared intensity monitors. The Hex-111 produced by the Boston Micromachines Corporation will be applied and its figure is similar to that of the LUV0IR-B concept.

I.3.7 Development plan

We are currently developing a new cryogenic testbed at NASA Ames Research Center for demonstration of the densified pupil spectrograph and will operate the testbed from the beginning of 2019. The goal of the testbed is to achieve 5 ppm over a timescale of a few hours.

Figure I-19 shows the overview of the testbed.

All of the components including the blackbody source as well as the transit spectrograph are installed in a large dewar and are thermally controlled to stabilize the blackbody source and thermal background. The optical elements and structure system of the testbed were built by cordierite ceramics, which have an extremely small linear expansion coefficient, to precisely maintain the optical alignment even under cryogenic conditions (see **Figure I-20**). We will build a cryogenic telescope simulator, composed of a segmented deformable mirror (HEX-111 produced by Boston Micromachines Corporation) and an infrared wavefront sensor, to introduce any low-order wavefront error to the densified pupil spectrograph.

We will evaluate the stability of the testbed, imitating the observing conditions of a segmented space telescope. Note that the shape of the segmented deformable mirror is very similar to the primary mirror of the LUV0IR-B concept. A Si:As IBC detector that had been developed for the James Webb Space Telescope (JWST) is used in the current testbed as a first step. In near future, a HgCdTe detector with 5.5 or 10.5 μm cutoff wavelength will be

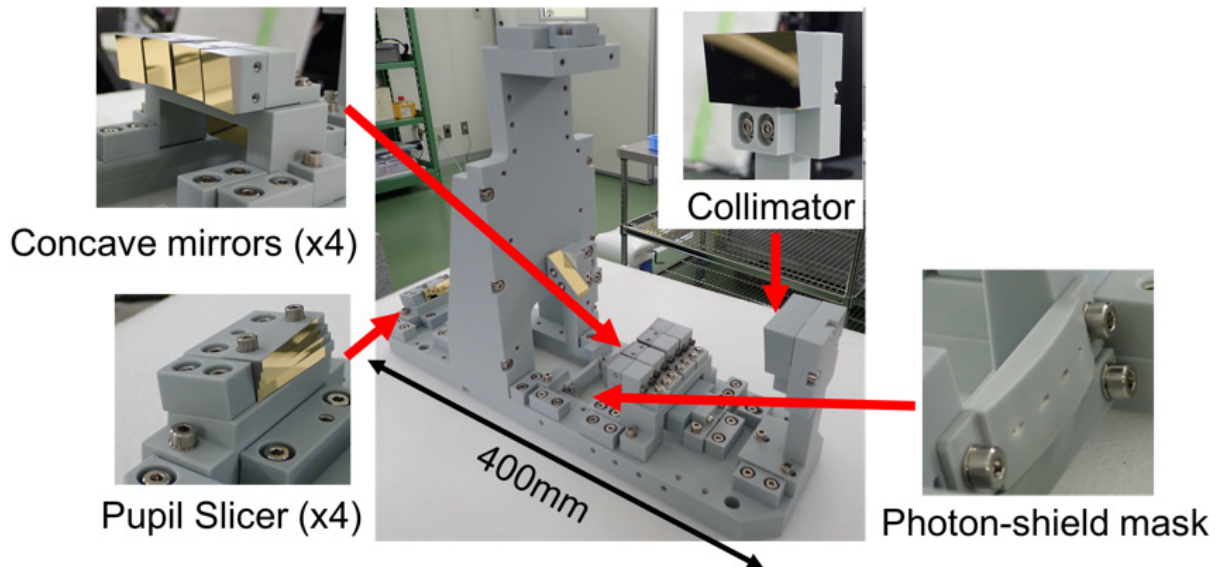


Figure I-20. Overview of the densified pupil system used for the testbed. All of the components are made of cordierite ceramic. The relative position accuracy among the optical components is better than $10\ \mu\text{m}$.

provided by Teledyne and used to upgrade the testbed. The specification of the upgraded testbed is almost same as that of the densified pupil spectrograph optimized for the LUVOIR concept. Thus, we will evaluate the stability of the testbed for the LUVOIR transit spectrometer, imitating the primary mirror of the LUVOIR-B concept, and hope to achieve TRL=4 by 2022.

APPENDIX J. ASTRO2020 PRE-DECADAL COST ESTIMATION OF LUVOIR

J.1 Introduction

Cost estimates are provided for the two LUVOIR concepts, LUVOIR-A and LUVOIR-B, as described in this report. The LUVOIR architecture encompasses a family of deployable segmented-aperture telescopes between 15-m (LUVOIR-A) and 8-m (LUVOIR-B) that will transform our understanding of our universe and our place in it. Together, the two LUVOIR concepts bound a trade space with defined science capability, estimated cost, and risk posture that can be explored to optimize science return on investment.

As part of the Astro2020 Decadal Survey, the National Academy of Sciences (NAS) will be performing Technical, Risk, and Cost Evaluation (TRACE) assessments of the large mission concepts, including LUVOIR. In addition, NASA HQ requested that each Mission Concept Study Team generate cost estimates using their assigned NASA Center's Cost Estimating Offices prior to the Astro2020 Decadal. The LUVOIR Study was assigned to NASA's Goddard Space Flight Center (GSFC), which has two independent cost estimation offices that are firewalled from each other. The two offices are Goddard's Cost Estimating, Modeling, and Analysis (CEMA) Office and NASA Goddard's Resource Analysis Office (RAO). Estimates for all LUVOIR configurations were prepared by each organization.

This appendix includes:

- J.1.1 Background on NASA's life cycle of space flight projects
- J.2 Cost input assumptions provided to both CEMA and RAO
- J.3 Estimating methodologies of both CEMA and RAO
- J.4 LUVOIR estimates of cost
- J.5 LUVOIR Work Breakdown Structure (WBS)
- J.6 Summary and conclusion

J.1.1 Background: NASA's life cycle for space flight projects

It is important to understand where this study falls in regards to the life cycle of a NASA flight project. The current design concepts and estimated costs presented in this study fall within Pre-Phase A, on the formulation side of a project. These early concepts and first estimates of cost are to aid the Agency in understanding the budget profiles that would be required to implement the mission so that funding can be planned in the appropriate out years.

Figure J-1 illustrates the lifecycle of a NASA Space Flight Project. As can be seen from the figure, the early concepts/estimates in this study are just the first step in evolving a mission to implementation. The following text from the Government Accounting Office (GAO) summarizes the NASA process:

“Project formulation consists of Phases A and B, during which the projects develop and define requirements, cost and schedule estimates, and the system's design for implementation. NASA Procedural Requirements 7120.5E, NASA Space Flight Program and Project Management Requirements specifies that during formulation, the project must complete a formulation agreement to establish the technical and acquisition work that needs to be conducted during this phase and define the schedule and funding requirements for that work.

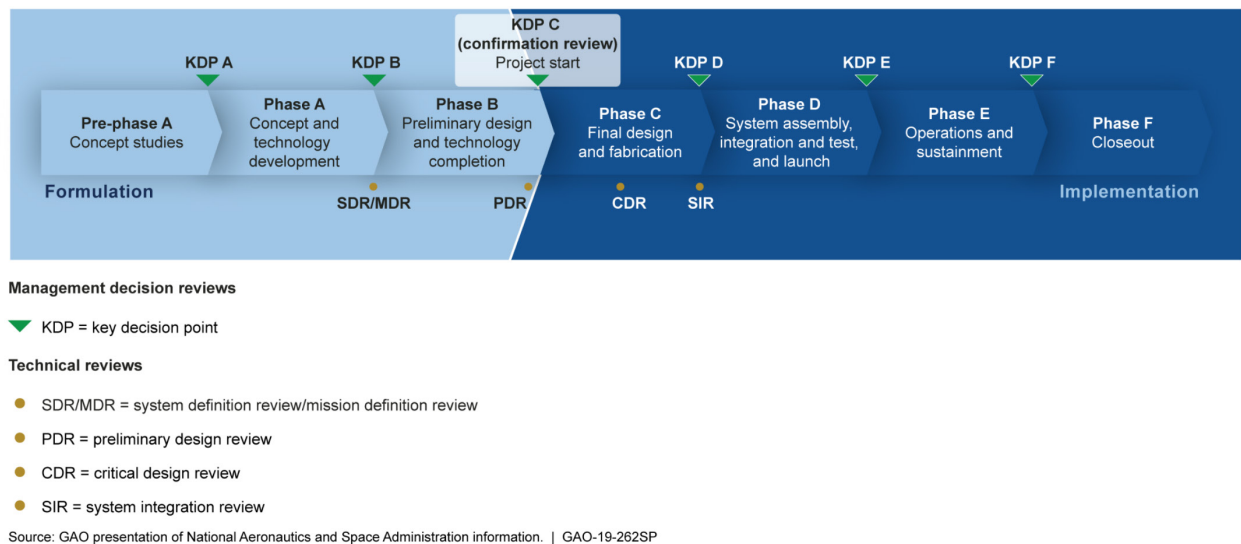


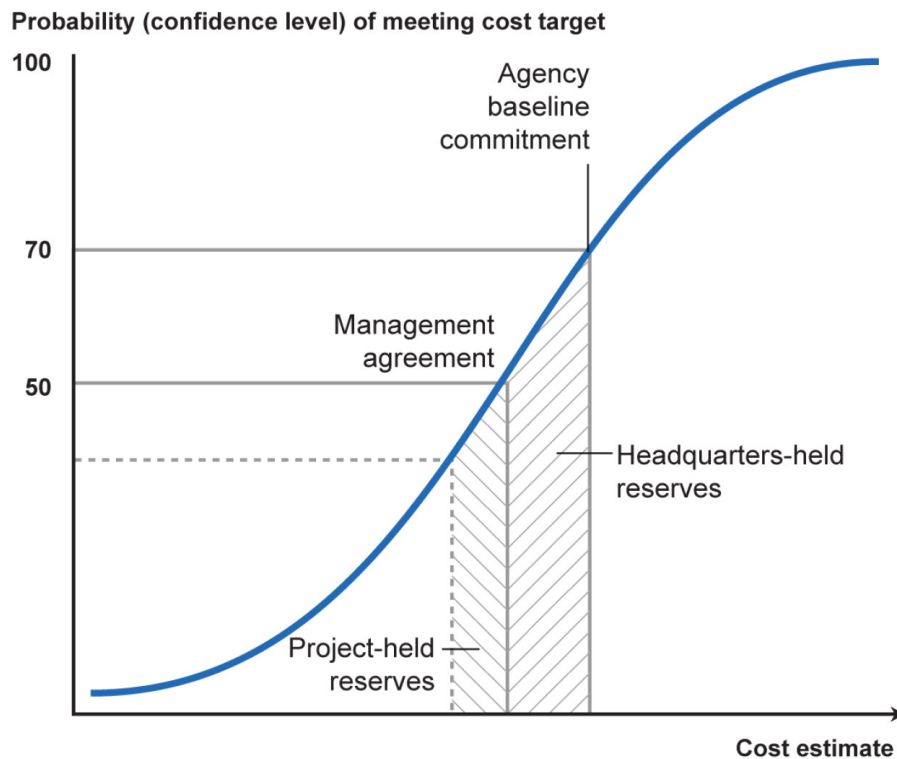
Figure J-1. NASA's life cycle for space flight projects

"The formulation agreement should identify new technologies and their planned development, the use of heritage technologies, risk mitigation plans, and testing plans to ensure that technologies will work as intended in a relevant environment. Prior to entering Phase B, projects develop a range of the project's expected cost and schedule which is used to inform the budget planning for that project. During Phase B, the project also develops programmatic measures and technical leading indicators, which track various project metrics such as requirement changes, staffing demands, and power utilization. Near the end of formulation, leading up to the preliminary design review, the project team completes technology development and its preliminary design. Formulation culminates in a review at Key Decision Point C (KDP-C), known as project confirmation, where cost and schedule baselines are established and documented in the decision memorandum.

"The decision memorandum outlines the management agreement and the agency baseline commitment. The management agreement can be viewed as a contract between the agency and the project manager. The project manager has the authority to manage the project within the parameters outlined in the agreement. The agency baseline commitment includes the cost and schedule baselines against which the agency's performance on a project may be measured.

"To inform the management agreement and the agency baseline commitment, each project with a life-cycle cost estimated to be greater than \$250 million must also develop a joint cost and schedule confidence level (JCL)¹. The JCL initiative, adopted in January 2009, produces a point-in-time estimate that includes, among other things, all cost and schedule elements in Phases A through D, incorporates and quantifies known risks, assesses the effects of cost and schedule to date on

¹ JCL Cost and Schedule Confidence Level (JCL) Requirements Update was issued as NID 7120.122 and appended to NPR 7120.5. This currently effective directive defines new JCL requirements for Single-Project Programs with a Life Cycle Cost (LCC) of \$1B or more. This JCL update now requires the first JCL estimate be required for Key Decision Point (KDP)-B.



Source: GAO analysis of National Aeronautics and Space Administration data. | GAO-19-262SP

Figure J-2. *Notional distribution of cost reserves for a project budgeted at the 70% confidence level*

the estimate, and addresses available annual resources. NASA policy requires that projects be baselined and budgeted at the 70 percent confidence level and funded at a level equivalent to at least the 50 percent confidence level.

“The management agreement and agency baseline commitment include cost and schedule reserves held at the project and NASA headquarters level, respectively. Cost reserves are for costs that are expected to be incurred—for instance, to address project risks—but are not yet allocated to a specific part of the project. Schedule reserves are extra time in project schedules that can be allocated to specific activities, elements, and major subsystems to mitigate delays or address unforeseen risks. Project-held cost and schedule reserves are within the project manager’s control.

“If the project requires additional time or money beyond management agreement—for example, if a project needs additional funds for an issue outside of the project’s control—NASA headquarters may allocate headquarters-held reserves (a.k.a. Unallocated Future Expense, or UFE). The total amount of cost and schedule reserves held at the project level varies based on where the project is in its life cycle. **Figure J-2** notionally depicts how NASA would distribute cost reserves for a project that was baselined in accordance with its JCL policy.

“After a project is confirmed, implementation begins, consisting of Phases C, D, E, and F. In this report, we refer to projects in Phases C and D as being in development. A critical design review is held during the latter half of Phase C to

determine if the design is mature enough to support proceeding with the final design and fabrication. After the critical design review and just prior to beginning Phase D, the project completes a system integration review to evaluate the readiness of the project and associated supporting infrastructure to begin system assembly, integration and test. In Phase D, the project performs system assembly, integration, test, and launch activities. Phases E and F consist of operations and sustainment and project closeout, which includes final delivery of all remaining project deliverables and safe decommissioning/disposal of space flight systems and other project assets.”

The LUVUOIR study does not address Phase F (decommissioning).

J.2 LUVUOIR cost input assumptions

NASA HQ directed all four large mission concept study teams to provide mission cost estimates in both constant year dollars (FY20\$) and Real Year dollars (RY\$). In order to facilitate comparison between missions, it is helpful to report mission costs in constant year dollars, and NASA HQ has selected constant year reporting in FY20 for this study.

Early formulation costs in real year dollars assist NASA HQ in understanding the required funding profile necessary to execute the proposed mission. Also, historical costs are typically captured in real year dollars within the NASA Cost Analysis Data Requirement (CADRe) hosted on the One NASA Cost Engineering (ONCE) database. A CADRe brochure is available from the NASA Office of the Chief Financial Officer, Strategic Investment Division website at:

https://www.nasa.gov/sites/default/files/files/CADRe_Brochure-021512_TAGGED.pdf

The same technical and schedule information for each LUVUOIR configuration was provided to both CEMA and RAO to inform their parametric estimates of cost. The methodologies of each organization are discussed in subsequent sections of this appendix.

LUVUOIR’s total cost estimates are subdivided as follows and discussed in more detail in **Sections J.2.1 and J.2.2:**

1) Pre-Phase A (Early Technology Development)

- a. Grassroots estimate of cost by Subject Matter Experts
- b. Includes cost reserve and funded schedule reserve
- c. Same estimate for LUVUOIR-A and LUVUOIR-B
- d. Matures technologies to Technology Readiness Level (TRL) 6 before start of Phase A
- e. Refines science objectives and goals
- f. Addresses early planning of integration, test and verification

2) Phases A-E (NASA Standard Lifecycle Estimate)

- a. Estimates for LUVOIR-A and LUVOIR-B generated by each estimating organization (CEMA and RAO)
- b. Estimates are compliant with all NASA policies relating to cost, including NASA Procedural Requirement 7120.5E, “NASA Space Flight Program and Project Management Requirements with Changes 1-16”.
- c. Conceptual servicing hardware and interface accommodations addressed in hardware designs and costing (see Master Equipment Lists, also known as MELs).

J.2.1 Pre-Phase A (Early Technology Development) cost input assumptions

This is a technology development program that will mature all technologies at the component, subsystem, and system level to TRL 6 before the start of Phase A, consistent with the plan described in **Chapters 11** and **12** of this report.

LUVOIR’s proposed technology plan involves substantial funding and schedule commitments to achieve success. Therefore, it is recommended that a Pre-Phase A Project Office be established to oversee the multiple parallel activities and tasks described in **Chapter 12** and **Section 12.2**. Work will be conducted in accordance with NASA Procedural Requirement 7120.8A, “NASA Research and Technology Program and Project Management Requirements.”

These major activities include:

- a. A community-led Science Steering Committee (SSC) will be funded to interpret the Astro2020 Decadal Committee’s findings and recommendations. This SSC will be responsible for coordinating inputs from the broader scientific community and using the Astro2020 recommendations to refine the mission science goals, objectives, and requirements. It will act as the steward of these mission science objectives, setting a formal process for how new science requirements are proposed and accepted or rejected.
Ultimately, this team will be responsible for freezing the mission science requirements in Phase A sufficiently early to allow mission concept definition to be completed. Changing science requirements and requirements creep are cited multiple times as causes of inflated mission cost and schedule (e.g., Martin 2012; Windhorst et al. 2013; Arenberg et al. 2014; Bitten et al. 2019; Hylan et al. 2019; Crooke et al. 2019; and **Chapters 11** and **12** of this final report). Defining the science requirements by the end of Phase A and minimizing changes in science requirements in later mission phases will restrain cost and schedule growth. More discussion of this can be found in **Chapter 12** of this report as well as the papers referenced above.
- b. An Architecture Development Team will mature the LUVOIR architecture prior to Phase A. The LUVOIR architecture will be informed by the technology development program. An Engineering Team will also explore concept designs defined by the architectures. The activities of these teams are discussed in more detail in **Chapter 12** of this report.

- c. Other activities, as discussed in **Chapter 12**, will include: pathfinder planning, verification and validation approach planning, integration and test (I&T) planning, partnership interface development, facility development, ground support equipment (GSE) planning, contamination control plans, and servicing approach planning.

The Pre-Phase A maturation activities were estimated by the LUVUOIR Team and vetted by external subject matter experts not associated with LUVUOIR (see **Chapters 11** and **12**). A 30% cost reserve was applied to the Pre-Phase A estimates of cost.

Funded schedule reserve (FSR) was applied at a rate of 15 weeks per year for completing the technology maturation activities to achieve the resultant schedule estimate. Assuming a funding profile consistent with the plan described in this report, a Pre-Phase A duration of ~5 years is expected to complete all of the above activities.

J.2.2 Phase A through E (Lifecycle) cost input assumptions

The estimated Phase A-E costs assume:

- a. Adequate total funding that is phased in accordance with the development schedule described in Chapter 12 (i.e., all of the funding is available when it is needed).
- b. Stable funding, i.e., no lapses in disbursement of funds.
- c. Adequate reserves. Reserves are disbursed when needed as accounted for in the presented costs.
- d. All technologies are at TRL 6 and subscale system demonstrations have been completed and successful before starting Phase A.
- e. A Launch Vehicle cost of \$500M in RY\$, per NASA HQ direction.

The LUVUOIR Team provided the above inputs for Phases A through E to both CEMA and RAO for their cost estimates.

J.3 NASA GSFC's LUVUOIR costing methodologies

As stated previously, LUVUOIR had estimates prepared by two independent (firewalled) costing offices at NASA's GSFC. The first subsection below presents the methodology used by CEMA (**J.3.1**), while the second subsection presents the methodology used by RAO (**J.3.2**).

J.3.1 NASA GSFC's Cost Estimating, Modeling, and Analysis (CEMA) office methodology

The LUVUOIR low and high range estimates are consistent with the latest versions of NASA's Cost Estimating Handbook and NASA Space Flight Program and Project Management Requirements (NPR 7120.5). LUVUOIR is one of four NASA large mission concept studies for the 2020 Astrophysics Decadal Mission that NASA HQ commissioned in 2016. As such, the LUVUOIR mission is designated as a Class A, Category 1 Project under NPR 7120.5.

This is reflected in the design of all hardware elements, as described in the Master Equipment Lists (MELs) and the parametric costing of those configurations. As per NASA Procedural Requirement 8705.4, "Risk Classification for NASA Payloads (Updated with Change 3)", Risk Class A reflects LUVUOIR as a high priority mission, with very high national significance, high complexity, critical launch constraints and a longer mission lifetime. Risk

Class A drives the safety and mission assurance design requirements and was extensively addressed in the early concept designs of the GSFC Integrated Design Center and the final designs of the LUVOIR Engineering Team.

Key design requirements from Appendix C of NPR 9705.4 were met as relating to:

- a) Single-point failures (by the IDC and LUVOIR Engineering Team)
- b) Engineering Model and Prototype Hardware
- c) Flight Hardware Redundancy
- d) Spare Hardware
- e) Qualification, Acceptance and Protoflight Test Program requirements
- f) EEE Parts Requirements

The LUVOIR hardware designs are captured in the MELs and are the primary inputs to the point-design estimates, along with the Integrated Master Schedules (IMS's).

NASA GSFC's CEMA Office developed the parametric point-design estimate models, and the inputs for these models were based upon technical descriptions of the mission requirements, mission flight element MELs, mission implementation schedules, and hardware heritage descriptions (TRLs) as captured in the MELs. The minimum TRL used for parametric models was TRL 6, as noted in the MELs. The LUVOIR Project has committed to raising all TRLs to 6 before the start of Phase A. The funding for these activities is covered in a separate technology development budget.

CEMA's estimate was based on first developing parametric point-design estimates of flight hardware elements: WBS 5 (Payload) and WBS 6 (Spacecraft). These estimates used the Current Best Estimate (CBE) values of mass and TRL taken from the MELs. LUVOIR team-selected wrap factors were then applied to the combined total of WBS 5 and WBS 6 to derive the point estimates for other WBS elements. These included the following WBS elements: WBS 1 (Management), 2 (Systems Engineering), 3 (Safety and Mission Assurance), 4 (Science), 7 (Mission Operations), 9 (Ground Systems) and 10 (Systems Integration and Test). The result is a mission-level point-design estimate for WBS 1 through 10.

The above mission-level estimate is considered a 'Point Estimate' because it represents a single estimate among a range of possibilities. Parameters are selected from tables or entered as discrete values in the parametric estimating tool. Clearly, the eventual parameters for the as-built product can vary from these early-phase selections or CBEs. Selection of different parameter values would result in different cost estimates. Tools used in this point-design estimating work included Parametric Review of Information for Costing and Evaluation Hardware (PRICE-H), a modeling tool available from Price Systems; SEER-H and SEER-SEM, used to model detector hardware and flight software, respectively, available from Galorath, Inc. These tools are described in the NASA HQ OCFO NASA Cost Estimating Handbook (Version 4.0, Appendix E: Models and Tools).

Cost Risk Analysis attempts to address the risk that the eventual outcome of the parameters may differ from the CBE selections entered into the parametric model. Cost Risk capabilities in the parametric tools allow a range of values to be entered for the input parameters to generate a range of cost outcomes. The parameter inputs are represented by range distributions (e.g., triangular distribution) with values set to Low Value, Most Likely, and High

Value. A cost risk simulation is performed using well-known sampling techniques (e.g., Monte Carlo simulations) of the parameter ranges, resulting in a Probability Distribution Function (PDF) of possible cost outcomes, also known as a Density Curve. This PDF can also be represented as a Cumulative Distribution Function (CDF), also known as an S-Curve. The S-Curve provides a graphical representation of the probabilities of various cost outcomes.

The LUVUOIR Team used the technical margin philosophy described in **Section 12.3.3**. After development of the LUVUOIR point-design estimates for WBS 5 and WBS 6, the CEMA Office ran Monte-Carlo simulation uncertainty analyses of WBS 5 and 6 hardware elements in the PRICE-H tool by specifying uncertainty distributions for mass and complexity inputs. The mass uncertainty distribution uses the CBE as the minimum mass, CBE + Contingency for Maximum Expected Value (MEV) (i.e., most likely), and MEV + Margin to determine the Maximum Possible Value (MPV).

There are multiple complexity parameters in any given model, and they are derived from the project heritage, namely the TRLs in the MEL. As with the mass inputs, for the complexity parameters in the model we also use a triangular input distribution to reflect low, most likely, and high values. We further assume there is a tendency towards increasing complexity, rather than decreasing complexity. This is reflected in the percentage variation we assign to the low and high value inputs.

A mission level cost risk analysis was performed with Automated Cost Estimating Integrated Tools (ACEIT) using key statistical information available from the PRICE-H risk analysis described above. ACEIT mean and standard deviation risk parameters were set using statistics obtained from the spacecraft bus and instrument payload. Percentages were calculated for the spacecraft bus mean and standard deviation relative to the spacecraft bus point estimate. These percentages were entered into ACEIT for the spacecraft bus WBS 6 risk parameters. For each instrument, percentages were calculated for the instrument payload mean and standard deviation relative to the instrument payload point estimate. These percentages were entered into ACEIT for the Payload(s) WBS 5 risk parameters. Other WBS risk parameters were set to a weighted mean and standard deviation (weighting based on the relative contribution of the spacecraft bus and instrument payload to the total of the spacecraft bus plus payload point estimate). This approach captures the inherent risk of the flight hardware, as modeled with PRICE-H, and applies it to the other WBS elements effectively tying overall mission risk to flight hardware risk. Note that WBS 4 Science/Technology and WBS 8 Launch Vehicle/Services are handled as throughput costs with respect to the Mission Level cost risk analysis—i.e., these WBS elements do not have cost risk analysis applied since they are considered to be minimally impacted by flight hardware risk.

- For WBS 4, the point-design estimate with 30% reserve was passed through.
- For WBS 8, launch vehicle and services cost was provided by NASA HQ and passed through without reserve applied (\$500M RY).
- For Phase A, the wrap-based estimate was passed through without reserve.

The Phase-A estimate was based on a team selected-wrap of the mission point-estimate without launch vehicle services. The LUVUOIR Team plans to perform all of their technology

development and maturation to TRL 6 in Pre-Phase A. In addition, the LUVOIR Team elected for a higher Phase A wrap factor (8% of the Phase B–D cost, as opposed to 5%) to allow for a greater emphasis on systems engineering, requirements development, concept development, and ETU and pathfinder planning and development during Phase A. These areas of emphasis directly respond to the management strategies outlined in **Chapter 12**. The distribution of Phase A funds across the WBS elements was per LUVOIR Project direction. In summary, in the ACEIT analysis, there was no risk applied to Science, Launch Vehicle/Services and Phase A.

The final estimates by WBS (for both the low and high cost cases) were spread using the LUVOIR mission implementation schedule and calculated using the appropriate inflation index to arrive at Real Year dollars (RY\$).

J.3.2 NASA GSFC's Resource Analysis Office (RAO) costing methodology

The Resource Analysis Office (RAO) was chartered in 1976 by GSFC Center Management to provide independent, non-advocate assessments of cost and schedule risk for space flight missions. RAO employs a top-down approach for mission cost estimates and RAO relies on a database comprised of historical cost, technical, and programmatic data collected and normalized internally. For each major WBS element, RAO uses its database to develop top-down statistical models to predict cost and schedule based on mission characteristics. These models are built on actual data and represent cost and schedule for factors both internal and external to project control.

Two cost and schedule scenarios are presented to differentiate the cost and schedule risk at the start of Phase A. Ideally, one of the below scenarios would be more appropriate than the other.

“Phase A Ready”—According to the NASA Astrophysics Management Plan for Large Mission Concept Studies², “The final study deliverable shall include: ...Roadmap for maturation to both TRL 5 by the start of Phase-A and TRL 6 by the mission PDR.” Thus, any project which has substantial recent heritage and a TRL 5 and higher for all hardware at the start of Phase-A would be afforded a baseline cost and schedule risk.

“New Engineering”—This scenario pertains to a project with existing critical technology (i.e., cannot be descoped) that can be re-engineered or used in a different way and has no new component technology.

To facilitate this independent process, the LUVOIR Team supplied technical information from the 3.5-year study, bringing the concept to a tailored Concept Maturity Level 4 (CML 4*; see Wessen 2013 and the NASA Astrophysics Management Plan for Large Mission Concept Studies²). LUVOIR study leadership met with RAO independent estimators to validate that the assumptions used for the estimate development were accurate. The LUVOIR study leadership ascertained that the independent estimators were using the most current technical information. Reconciliation of differences produced the final parametric estimate.

For each LUVOIR Architecture, RAO presents a range of different cost numbers, bracketing the two different cost confidence levels at 50% and 70% for the two different risk scenarios described above.

2 NASA Large Mission Concept Studies Management Plan: https://smd-prod.s3.amazonaws.com/science-red/s3fs-public/atoms/files/Decadal_Studies_Management_Plan_RevF_APD_02_11_2019.pdf

J.4 NASA's GSFC cost estimates for LUVUOIR-A and LUVUOIR-B

The LUVUOIR cost estimates presented in this section are broken into two categories with their associated assumptions. The two categories are the Pre-Phase A cost estimates and the Phase A through E cost estimates. The LUVUOIR Team developed the Pre-Phase A cost estimates from a grassroots method described in **Section J.4.1**. **Section J.4.2** provides the details of the Phases A through E cost estimates performed independently by the CEMA and RAO cost estimation offices.

J.4.1 Pre-Phase A cost estimates

The LUVUOIR Study Team's grassroots estimates of Pre-Phase A costs were vetted by individuals from outside the team, considered well-seasoned Subject Matter Experts (SMEs).

The Pre-Phase A activities estimate covers funding required over a ~5-year period and assumes bringing all technologies to TRL 6. In addition, LUVUOIR will mature the architecture, science requirements, and other items as described in this final report. Note however, there are several technology development efforts that have already begun, are funded outside of this request, and will continue to occur throughout the Astro2020 Decadal process, as seen in the detailed IMS (Appendix G). These activities are not included in the costs discussed in this section.

The Pre-Phase A costs in **Table 12-2** reflect the additional technology development funding needed spread over 5 years to complete the LUVUOIR Technology Development Plan as stated in the Final Report (See **Chapter 11** and **Section 12.2**).

- a. Pre-Phase A technology maturation assumes a ~5-year period with a total funding level of \$536M FY20 (\$572M RY) to bring all component and system-level technologies to TRL 6.

This includes:

Technology Funding: \$412M FY20 (\$440M RY)
 Cost reserve (30%): \$124M FY20 (\$132M RY)

- b. Pre-Phase A Project Office activities will be performed over the same ~5-year period in parallel with the technology maturation effort. This covers the labor (FTEs) required to perform the activities described in this report at a total funding level of \$133M FY20 (\$142M RY).

This includes:

Labor: \$102M FY20 (\$109M RY)
 Cost Reserve (30%): \$31M FY20 (\$33M RY)

- c. Grand Total Pre-Phase A Costs: \$669M FY20 (\$714M RY)
Including Reserves of: \$155M FY20 (\$165M RY)

Note that Pre-Phase A cost estimates are the same for LUVUOIR-A and LUVUOIR-B, since these estimates include technology maturation and a project office, i.e., the same activities regardless of the design that is eventually selected for implementation.

Table J-1. This table shows the LUVOIR-A Cost estimate ranges for Phases A through E in FY20\$s and RY\$s from CEMA and RAO, assuming a 2025 Phase A start date. The first two rows from CEMA and RAO are labeled “Phase A Ready” with the definitions explained in the far right column.

LUVOIR-A Cost Estimate Ranges Phase A start through Phase E end			
	FY20 (\$B) 50%-70% CL	RY (\$B) 50%-70% CL	Definitions
Phase A Ready			
CEMA Cost Model	15-16	20-24	All Technologies are at TRL \geq 6 by KDP-A (Phase A start)
RAO Cost Model	13-16	19-24	All technologies are at TRL \geq 5 by KDP-A and TRL \geq 6 by mission PDR (current NASA standard)
Later Technology Development			
RAO Cost Model	19-24	28-35	All Technologies are at TRL=3 to 5 by KDP-A and TRL \geq 6 by mission PDR
These numbers assume a mission-enhancing contribution from ESA in the form of the POLLUX instrument. Costs to integrate that instrument are included here.			

J.4.2 Lifecycle cost estimates (Phase A-E)

This section includes estimates by NASA GSFC’s CEMA and RAO Offices using the tools and methodologies described earlier in this **Appendix J**.

Table J-1 and **Table J-2** show the LUVOIR-A and -B mission costs for Phases A through E in FY20\$s and RY\$s, with a Phase A start date of 2025. The first two rows from CEMA and RAO are labeled “**Phase A Ready**” with the definitions explained in the far right column. CEMA and RAO made different assumptions of the meaning of “Phase A ready,” as stated in the table.

In addition, RAO also performed a Phase A through E cost estimate in FY20\$s and RY\$s assuming the LUVOIR concepts would have a Phase A start in 2025 with **LUVOIR’s current state of low TRL technologies**. The assumption in the “**Late Technology Development**” section **assumes there is no progress in technology development between now (August 2019) and 2025**.

To reach the Total LUVOIR Mission Costs (Pre-Phase A through Phase E), the LUVOIR Pre-Phase A costs (\$669M FY20, \$714M RY) need to be added to the mission Phase A through Phase E costs for LUVOIR-A and LUVOIR-B.

Table J-2. This table shows the LUVUOIR-B Cost estimate ranges for Phases A through E in FY20\$s and RY\$s from CEMA and RAO assuming a 2025 Phase A start date. The first two rows from CEMA and RAO are labeled “Phase A Ready” with the definitions explained in the far right column.

LUVUOIR-B Cost Estimate Ranges Phase A start through Phase E end			
	FY20 (\$B) 50%-70% CL	RY (\$B) 50%-70% CL	Definitions
Phase A Ready			
CEMA Cost Model	11-12	15-18	All Technologies are at TRL \geq 6 by KDP-A (Phase A start)
RAO Cost Model	8-10	12-15	All technologies are at TRL \geq 5 by KDP-A and TRL \geq 6 by mission PDR (current NASA standard)
Later Technology Development			
RAO Cost Model	12-14	17-21	All Technologies are at TRL=3 to 5 by KDP-A and TRL \geq 6 by mission PDR
No international contribution assumed in these cost estimates.			

J.5 LUVUOIR Work Breakdown Structure (WBS)

LUVUOIR followed the NASA Work Breakdown Structure (WBS) Handbook, NASA/SP-2016-3404/REV-1 (January 2018) policy, definitions, guidelines, and development process to develop the LUVUOIR WBS. The LUVUOIR WBS is the same for LUVUOIR-A and LUVUOIR-B minus the CNES-led European contributed instrument POLLUX which is an instrument that can only be accommodated on LUVUOIR-A as shown in **Table J-3**.

J.6 Summary and conclusion

There is significant merit in executing a strong Pre-Phase A program to mature all technologies to TRL 6 before starting Phase-A.

The RAO estimates for “later technology development” (shown in **Tables J-1** and **J-2**) show that costs will increase if TRL is lower at the start of Phase A. An early start and finish on technology development results in mature science requirements and an architectural concept which lowers overall cost, schedule and risk for the mission. The LUVUOIR Study Team argues that implementing a strong Pre-Phase A effort, with coordinated activities that inform one another, will help enable NASA to continue its tradition of developing state-of-the-art national-asset observatories, while also making significant progress in continuing to improve cost and schedule performance.

Table J-3. This table shows the LUVOIR-A and LUVOIR-B Work Breakdown Structure (WBS). The only difference in the WBS structure between LUVOIR-A and LUVOIR-B is that LUVOIR-B would not have the POLLUX Instrument subsystem, WBS number LUVOIR-05-05. For clarification of the column labeled “architecture level” in this table, please see **Figure 12-3** in **Chapter 12**.

LUVOIR WBS						
WBS					Architecture Level	Entity
LUVOIR	01				n/a	Project Management
LUVOIR	02	01			n/a	Systems Engineering - Avionics
LUVOIR	02	02			n/a	Systems Engineering - Communications
LUVOIR	02	03			n/a	Systems Engineering - Data Systems
LUVOIR	02	04			n/a	Systems Engineering - Detectors
LUVOIR	02	05			n/a	Systems Engineering - Electrical
LUVOIR	02	06			n/a	Systems Engineering - Ground Systems
LUVOIR	02	07			n/a	Systems Engineering - Integrated Modeling
LUVOIR	02	08			n/a	Systems Engineering - Materials
LUVOIR	02	09			n/a	Systems Engineering - Mechanical
LUVOIR	02	10			n/a	Systems Engineering - Mechanisms
LUVOIR	02	11			n/a	Systems Engineering - Optical
LUVOIR	02	12			n/a	Systems Engineering - Propulsion
LUVOIR	02	13			n/a	Systems Engineering - Servicing
LUVOIR	02	14			n/a	Systems Engineering - Software
LUVOIR	03	01			n/a	Safety & Mission Assurance
LUVOIR	04	01			n/a	Science & Technology - Science
LUVOIR	04	02			n/a	Science & Technology - Technology
LUVOIR					Segment	Observatory
LUVOIR	05				Element	Payload
LUVOIR	05	01			Sub-system	Optical Telescope Assembly [OTA]
LUVOIR	05	01	01		Assembly	Primary Mirror
LUVOIR	05	01	01	01	Sub-Assembly	Primary Mirror Segment Assemblies
LUVOIR	05	01	01	02	Sub-Assembly	+P2 PMBSS #2
LUVOIR	05	01	01	03	Sub-Assembly	+P2 PMBSS #1
LUVOIR	05	01	01	04	Sub-Assembly	Center PMBSS + BSF
LUVOIR	05	01	01	05	Sub-Assembly	-P2 PMBSS #1
LUVOIR	05	01	01	06	Sub-Assembly	-P2 PMBSS #2
LUVOIR	05	01	02		Assembly	Secondary Mirror
LUVOIR	05	01	02	01	Sub-Assembly	Secondary Mirror Support Structure [SMSS]
LUVOIR	05	01	02	02	Sub-Assembly	Secondary Mirror Assembly [SMA]
LUVOIR	05	01	03		Assembly	Aft Optics Subsystem
LUVOIR	05	01	03	01	Sub-Assembly	Fast Steering Mirror
LUVOIR	05	01	03	02	Sub-Assembly	Aperture Plate
LUVOIR	05	01	03	03	Sub-Assembly	Telescoping Tube
LUVOIR	05	01	03	04	Sub-Assembly	Tertiary Mirror
LUVOIR	05	01	04		Assembly	Thermal Management System
LUVOIR	05	01	05		Assembly	Electrical Subsystems
LUVOIR	05	02			Sub-system	Extreme Coronagraph for Living Planetary Systems [ECLIPS]
LUVOIR	05	03			Sub-system	High Definition Imager [HDI]
LUVOIR	05	04			Sub-system	LUVOIR Ultraviolet Multi-object Spectrometer [LUMOS]
LUVOIR	05	05			Sub-system	Pollux <LUVOIR-A Only>
LUVOIR	05	06			Sub-system	Payload Articulation System [PAS]
LUVOIR	05	06	01		Assembly	Vibration Isolation and Precision Pointing System [VIPPS]
LUVOIR	05	06	02		Assembly	2-axis Gimbal
LUVOIR	05	06	03		Assembly	Articulating / Telescoping Arm
LUVOIR	05	06	04		Assembly	1-Axis Gimbal
LUVOIR	06				Element	Spacecraft
LUVOIR	06	01			Sub-system	Sunshade
LUVOIR	06	01	01		Assembly	Deployable Boom System / Assemblies
LUVOIR	06	01	02		Assembly	Blanket Assemblies
LUVOIR	06	02			Sub-system	Bus
LUVOIR	06	02	01		Assembly	Structure
LUVOIR	06	02	02		Assembly	Thermal Management System [TMS]
LUVOIR	06	02	03		Assembly	Attitude Control System [ACS]
LUVOIR	06	02	04		Assembly	Propulsion System
LUVOIR	06	02	05		Assembly	Avionics / C & DH
LUVOIR	06	02	06		Assembly	Communications
LUVOIR	06	02	07		Assembly	Electrical Power System
LUVOIR	07				n/a	Mission Operations
LUVOIR	08				n/a	Launch Vehicle / Services
LUVOIR	09				n/a	Ground Systems
LUVOIR	10				n/a	Systems Integration & Test
LUVOIR	11				n/a	Education & Public Outreach

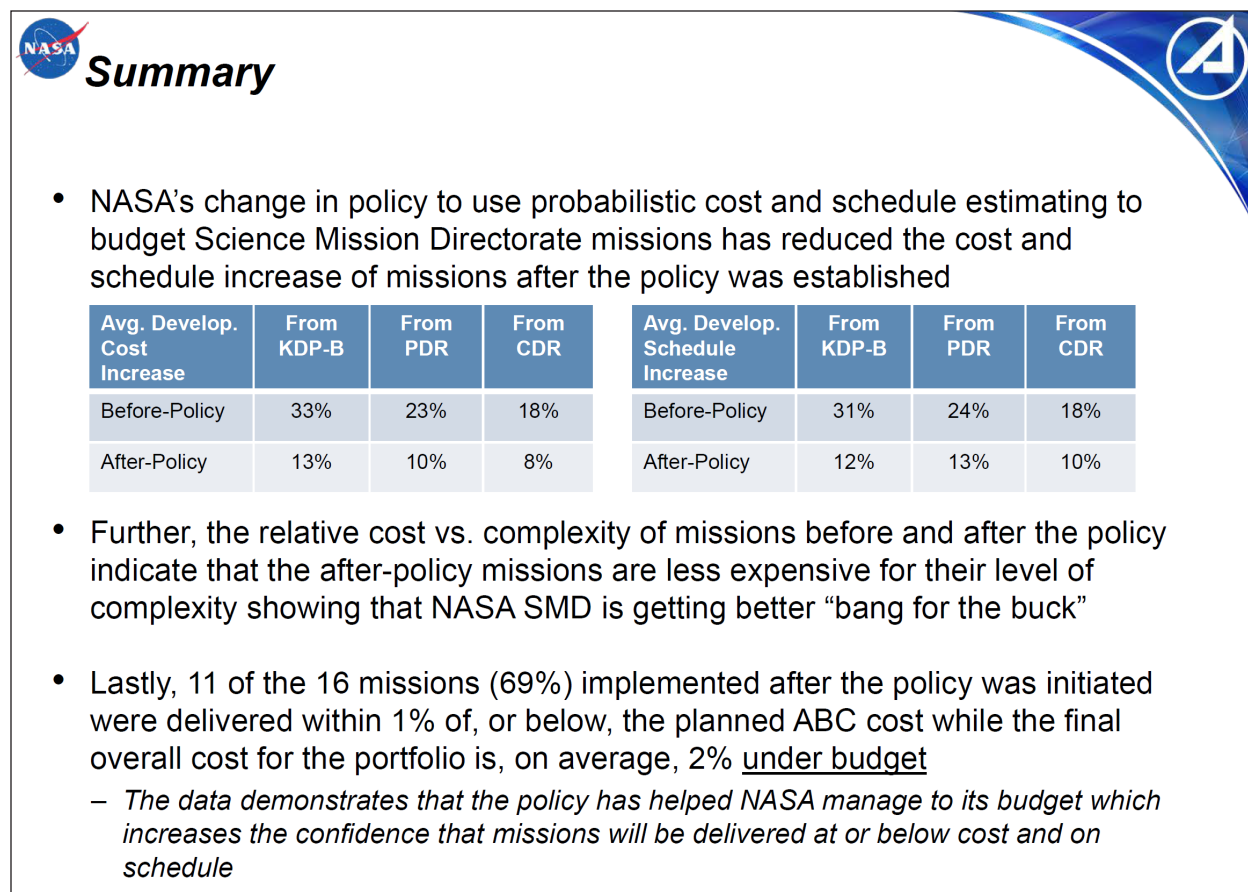


Figure J-3. The above slide is from a presentation on “The Effect of Policy Changes on NASA Science Mission Cost and Schedule Growth,” by B. Bitten, B. Kellogg, E. Mahr, S. Lang, D. Emmons and C. Hunt, which was shown at the NASA HQ sponsored 2018 NASA Cost and Schedule Symposium from 2019. This slide demonstrates the positive effects the JCL policy is having on Agency performance. Full presentation available at: https://www.nasa.gov/sites/default/files/atoms/files/06_aerospace_nasa_smd_mission_perf_policy_paper_ncss_08-06-18.pdf

As illustrated in **Figure J-1**, this concept study would be followed by the remaining mission formulation stages, allowing for continued optimization of the mission concept before confirmation and establishment of the Agency Baseline Commitment (ABC). The first JCL estimate (an integrated uncertainty analysis of cost and schedule), illustrating the probability that LUVUOIR’s cost will be equal to or less than the targeted cost and LUVUOIR’s schedule will be equal to or less than the targeted finish, will be available to inform decision makers at KDP-B. After refining the mission design during Phase B, the JCL will be updated for KDP-C. The KDP-C values for the ABC and Management Agreement (MA) will also be communicated to the Agency Program Management Council (APMC) for informational purposes. The JCL will not be updated for KDP-D, unless current development costs exceed the ABC cost or 5%.

Since it has been almost a decade since the JCL policy was instituted at NASA, it is appropriate for the Agency to evaluate its impact on mission success. At the NASA HQ sponsored 2018 NASA Cost and Schedule Symposium, the presentation, “The Effect of Policy Changes on NASA Science Mission Cost and Schedule Growth,” by B. Bitten, B. Kellogg, E. Mahr, S. Lang, D. Emmons and C. Hunt demonstrated the positive effects the JCL policy is

having on Agency performance. The summary slide of the presentation in **Figure J-3** illustrates this positive effect.

A JCL Overview Brochure (PDF) and the NASA Cost Estimating Handbook are available at the following URLs:

https://www.nasa.gov/sites/default/files/files/JCL_Overview_Brochure.pdf

<https://www.nasa.gov/offices/ocfo/nasa-cost-estimating-handbook-ceh>

REFERENCES

- Abe, Y., Abe-Ouchi, A., Sleep, N. H., & Zahnle, K. J. (2011). *Astrobiology*, 11, 443
- AcqNotes. (2010). Defense Acquisition Made Easy, Financial Management, Advanced Procurement Funding. <http://acqnotes.com/acqnote/careerfields/advance-procurement-funding>
- AcqNotes. (2010). Defense Acquisition Made Easy, Financial Management, Full Funding Policy. <http://acqnotes.com/acqnote/careerfields/full-funding>
- Adams, F. C. (2010). *ARA&A*, 48, 47
- Adams, B. W., Elagin, H. J., Frisch, R. O., et al. (2015). Nuclear Instruments and Methods in Physics Research Section A: Accelerators, Spectrometers, Detectors and Associated Equipment 795, 1
- Ádámkovics, M., Wong, M. H., Laver, C., & de Pater, I. (2007). *Science*, 318, 962
- Agol, E. & Blaes, O. (1996). *MNRAS*, 282, 965
- Agol, E., Steffan, J., Sari, R., Clarkson, W. (2005). *MNRAS*, 359, 567
- Airapetian, V. S., Gloer, A., Khazanov, G. V., et al. (2017). *ApJ*, 836, L1
- Alban, S. (2016). Mavenlink Blog. <https://blog.mavenlink.com/19-lessons-in-project-management-mistakes-from-nasa>
- Albornoz Vasquez, D., Rahmani, H., Noterdaeme, P., et al. (2014) *A&A*, 562, A88
- Alexander, R. D., & Pascucci, I. (2012). *MNRAS*, 422, L82
- Alexander, R., Pascucci, I., Andrews, S., et al. (2014). in *Protostars and Planets VI*, ed. H. Beuther et al. (Tucson, AZ: Univ. Arizona Press), 475
- ALMA Partnership, Brogan, C. L., Pérez, L. M., et al. (2015). *ApJ*, 808, L3
- Alvarez, M. A., Finlator, K., & Trenti, M. (2012). *ApJ*, 759, L38
- Andrews, S. M., Wilner, D. J., Zhu, Z., et al. (2016). *ApJ*, 820, L40
- Anglada-Escudé, G., Amado, P. J., Barnes, J., et al. (2016). *Nature*, 536, 437
- Antonucci, R., Kinney, A. L., & Hurt, T. (1993). *ApJ*, 414, 506
- Antonucci, R., Hurt, T., & Miller, J. (1994). *ApJ*, 430, 210
- Apai, D., Cowan, N., Kopparapu, R., et al. (2017). NASA ExoPAG SAG 15 Report, arXiv:1708.02821
- Arav, N. & Li, Z.-Y. (1994). *ApJ*, 427, 700
- Arav, N., Li, Z.-Y., & Begelman, M. C. (1994). *ApJ*, 432, 62
- Arenberg, J., Matthews, G., Atkinson, C., et al. (2014). SPIE, 9144, 91440Q
- Arney, G., Domagal-Goldman, S. D., Meadows, V. S., et al. (2016). *Astrobiology*, 16, 873
- Arney, G. N., Domagal-Goldman, S. D., & Meadows, V. S. (2018). *Astrobiology*, 18, 1
- Arney, G. N. (2019). *ApJ*, 873, L7
- Arnold, H., Liuzzo, L., & Simon, S. (2019). *Geophys. Res. Letters*, 46, 1149
- Arulanantham, N., France, K., Hoadley, K. (2018). AAS Meeting #231, 147.11
- Atek, H., Richard, J., Kneib, J.-P., & Schaerer, D. (2018). *MNRAS*, 479, 5184
- Balashev, S. A., Noterdaeme, P., Rahmani H., et al. (2017). *MNRAS*, 470, 2890
- Balasubramanian, K., Hennessy, J., Raouf, N., et al. (2017). SPIE, 10398, 103980X
- Bally, J., Yu, K. C., Rayner, J., & Zinnecker, H. (1998). *AJ*, 116, 1868
- Baraffe, I., Chabrier, G., Allard, F., & Hauschildt, P. (1998). *A&A*, 337, 403
- Barber, C., Starkenburg, E., Navarro, J. F., et al. (2014). *MNRAS*, 437, 959

- Barclay, T., Pepper, J., & Quintana, E. V. (2018). *ApJSS*, 239, 2
- Barr, A. C., Dobos, V., & Kiss, L. L. (2018). *A&A*, 613, 37
- Batalha, N. E., Mandell, A., Pontoppidan, K., et al. (2017). *PASP*, 129, 064501
- Batalha, N. E., & Line, M. R. (2017). *AJ*, 153, 151
- Batalha, N. E., Mandell, A., Pontoppidan, K., et al. (2017). *PASP*, 129, 64501
- Batalha, N. E., Lewis, N. K., Line, M. R., et al. (2018). *ApJ*, 856, L34
- Baur, J., Palanque-Delabrouille, N., Yéche, C., et al. (2017). *JCAP*, 12, 013
- Bauer, J. M., Buratti, B. J., Li, J., et al. (2010). *ApJ*, 723, L49
- Bean, J. L. & FINESSE Science Team (2017). AAS Meeting #229, 301.08
- Bean, J. L., Abbot, D. S., & Kempton, E. M. (2017). *ApJ*, 841, L24
- Beichman, C., Benneke, B., Knutson, H., et al. (2014). *PASP*, 126, 1134
- Belikov, R., Sirbu, D., Henze, C. E., et al. (2019). *SPIE*, 11117, 1111742
- Bell, E. A., Boehnke, P., Harrison, T. M., et al. (2015). *Proc. Natl. Acad. Sci.*, 112, 14518
- Berg, D. A., Skillman, E. D., Henry, R. B., C., et al. (2016). *ApJ*, 827, 2
- Berg, D. A., Erb, D. K., Henry, R. B., C., et al. (2019). *ApJ*, 874, 93
- Berg, T. A. M., Ellison, S. L., Tumlinson, J., et al. (2018). *MNRAS*, 478, 3890
- Bertone, S., Aguiere, A., & Schaye, J. (2013). *MNRAS*, 430, 3292
- Berzosa Molina, J., Rossi, L., & Stam, D. M. (2018). *A&A*, 618, 162
- Betremieux, Y. & Kaltenegger, L. (2014). *ApJ*, 791, 7
- Birkler, J., Schank, J., Chiesa, J., et al. (2002). Rand National Defense Research Institute Report. https://www.rand.org/content/dam/rand/pubs/monograph_reports/2005/MR1526.pdf
- Bitten, B., Kellogg, B., Hayhurst, M., et. al. (2014). NASA Cost Symposium. https://www.nasa.gov/sites/default/files/files/23_Reserves_on_STG_Briefing_FINAL_for_NCS_Approved_Tagged.pdf
- Bitten, R. E., Shinn, S. A., & Emmons, D. L. (2019). *IEEE*, 978-1-5386-6854-2, 19. <https://ntrs.nasa.gov/archive/nasa/casi.ntrs.nasa.gov/20190001455.pdf>
- Blandford, R. D. & Znajek, R. L. (1977). *MNRAS*, 179, 433
- Bland-Hawthorn, J., & Maloney, P. R. (1999). *ApJ*, 510, L33
- Bonfils, X., Astudillo-Defru, N., Díaz, R., et al. (2018). *A&A*, 613, A25
- Booth, M., Jordán, A., Casassus, S., et al. (2016). *MNRAS*, 460, L10
- Bordoloi, R., Tumlinson, J., Werk, J. K., et al. (2014). *ApJ*, 796, 136
- Bordoloi, R., Rigby, J. R., Tumlinson, J., et al. (2016). *MNRAS*, 458, 1891
- Borthakur, S., et al. (2016). *ApJ*, 833, 259
- Borucki, W. J., Koch, D., Basri, G., et al. (2010). *Science*, 327, 977
- Bourrier, V., Ehrenreich, D., Wheatley, P. J., et al. (2017). *A&A*, 599, L3
- Bouwens, R. J., Illingworth, G. D., Oesch, P. A., et al. (2015). *ApJ*, 811, 140
- Boylan-Kolchin, M., Weisz, D. R., Johnson, B.D., et al. (2015). *MNRAS*, 453, 1503
- Braithwaite, J. & Spruit, H. C. (2004). *Nature*, 431, 819
- Brammer, G. B., et al. (2011). *ApJ*, 739, 24
- Brandt, T. D., & Spiegel, D. S. (2014). *Proc. Natl. Acad. Sci.*, 111, 13278
- Bridge, J. S., Hayes, M., Melinder, J., et al. (2018). *ApJ*, 852, 9
- Brogi, M., Line, M., Bean, J., et al. (2016). *ApJ*, 839, L2
- Brown, R., Clark, R., Buratti, B., et al. (2006). *Science*, 311, 1425
- Brown, T. M., Postman, M., & Calzetti, D. (2010). arXiv:0902.2973

- Brown, T. M., et al. (2012). *ApJ*, 753, 21
- Buckley, M. R. & Peter, A. H. G. (2018). *Physics Reports*, 761, 1
- Buick, R. (2007). *Geobiology*, 5, 97
- Buie, M. W., Grundy, W. M., Young, E. F., et al. (2010). *AJ*, 139, 1128
- Bullock, J. S. & Boylan-Kolchin, M. (2017). *ARA&A*, 55, 343
- Buratti, B. J., Bauer, J. M., Hicks, M. D., et al. (2015). *Icarus*, 212, 835
- Burchett, J. N., Tripp, T. M., Bordoloi, R., et al. (2016). *ApJ*, 832, 124
- Byler, N., Dalcanton, J. J., Conroy, C., et al. (2018). *ApJ*, 863, 14
- Cady, E., Belikov, R., Dumont, P., et al. (2009). arXiv:0912.2938
- Cady, E., Balasubramanian, K., Carr, M., et al. (2010). SPIE, 7731, 77312F
- Cady, E., Mejia Prada, C., An, X., et al. (2015). *JATIS*, 2, 11004
- Caffau, E., Bonifacio, P., François, P., et al. (2011). *Nature*, 477, 67
- Cahoy, K. L., Marley, M. S., & Fortney, J. J. (2010). *ApJ*, 724, 189
- Cahoy, K., Clark, J., Allan, G., et al. (2019). Space-Based Laser Guide Star Mission to Enable Ground and Space Telescope Observations of Faint Objects, Astro2020 APC White Paper. http://surveygizmoresponseuploads.s3.amazonaws.com/fileuploads/623127/5043187/180-e360fd3ea5c785b14625422c2f5b0685_CahoyKerri.pdf
- Calzetti, D., Johnson, K. E., Adamo, A., et al. (2015). *ApJ*, 811, 75
- Cantalupo, S., Arrigoni-Battaia, F., Prochaska, J. X., et al. (2014). *Nature*, 506, 63
- Cappellari, M., McDermid, R. M., Alatalo, K., et al. (2012). *Nature*, 484, 485
- Carlson, R. W. (1999). *Science*, 286, 97
- Carr, M. H., Belton, M. J. S., Chapman, C. R., et al. (1998). *Nature*, 391, 363
- Carrera, D., Gorti, U., Johansen, A., & Davies, M. B. (2017). *ApJ*, 839, 16
- Catling, D. C., Krissansen-Totton, J., Kiang, N. Y., et al. (2018). *Astrobiology*, 18, 709
- Chandrasekhar, S. (1960). PNAS, 46, 253
- Chaplain, C., et al., May 2019, NASA Assessments of Major Projects, GAO Report to Congressional Committees., Rep. GAO-19-262SP. <https://www.gao.gov/products/GAO-19-262SP>
- Chaplain, C. (2018). GAO Report to Congressional Committees, GAO-18-273. <https://www.gao.gov/assets/700/690413.pdf>
- Charbonneau, D., Brown, T. M., Latham, D., & Mayor, M. (2000). *ApJ*, 529, 45
- Chaufray, J.-Y., Gladstone, G. R., Waite, J. H., et al. (2010). *J. Geophys. Res.*, 115, E05002
- Chisholm, J., Rigby, J. R., Bayliss, M., et al. (2019). arXiv :1905.04314
- Chyba, C. F. (2000). *Nature*, 403, 381
- Clarke, C. J., & Owen, J. E. (2015). *MNRAS*, 446, 2944
- Coc, A., Olive, K. A., Uzan, J.-P., et al. (2006). *Phys. Rev.*, 73, 083525
- Cockell, C. S., Bush, T., Bryce, C., et al. (2016). *Astrobiology*, 16, 89
- Cole, G. (2017). in Optical Design and Fabrication 2017, OSA Technical Digest (Optical Society of America), OW1B.4. <https://doi.org/10.1364/OFT.2017.OW1B.4>
- Conroy, C., & van Dokkum, P. G. (2012). *ApJ*, 760, 71
- Content, D. A., Armani, N. V., Baker, C. L., et al. (2013). SPIE, 8860, 88600F
- Cooke, R. J., Pettini, M., Jorgenson, R. A., et al. (2014). *ApJ*, 781, 31
- Cooke, R. J., Pettini, M., & Steidel, C. C. (2018). *ApJ*, 855, 102
- Corlies, L., & Schiminovich, D. (2016). *ApJ*, 827, 148

- Cowan, N. B., Agol, E., Meadows, V. S., et al. (2009). *ApJ*, 700, 915
- Cowan, N. B., Abbot, D. S., & Voigt, A. (2012). *ApJ*, 752, L1
- Cowan, N. B., Greene, T., Angerhausen, D., et al. (2015). *PASP*, 127, 311
- Cowan, R. (2015). EOS, 96, doi:10.1029 / 2015EO028625
- Cowen, R. (2015). Hubble Turns 25, EOS Earth & Space Science News. <https://eos.org/features/hubble-turns-25>
- Cox, D. P. (2005). *ARA&A*, 43, 337
- Coyle, L., Knight, S., Barto, A., et. al. (2019). Ultra-Stable Telescope Research and Analysis (ULTRA), Astro2020 APC White Paper. http://surveygizmoreponseuploads.s3.amazonaws.com/fileuploads/623127/5043187/117-dbbdb2ce3eb1a5650462436e-245ca81c_CoyleLauraE.pdf
- Coyle, L., Knight, S., Barto, A., et al. (2019). Ultra-Stable Telescope Research and Analysis (ULTRA) Program Phase 1 Report. NASA Contract 80NSSC18K0820. https://nspires.nasaprs.com/external/viewrepositorydocument/cmdocumentid=679697/solicitation-Id=%7BE879B8CD-FC43-BAB4-679E-39B4C90D567E%7D/viewSolicitationDocument=1/17SLSTD170003FRBall201904Public_2.pdf
- Crida, A., Morbidelli, A., & Masset, F. (2006). *Icarus*, 181, 587
- Cridland, A. J., Pudritz, R. E., Birnstiel, T., et al. (2017). *MNRAS*, 469, 3910
- Crill, B., Siegler, N., Bendek, E., et. al. (2019). Technology Challenges for the Study of Exoplanets and the Search for Habitable Worlds: Status and Path Forward, Astro2020 APC White Paper. http://surveygizmoreponseuploads.s3.amazonaws.com/fileuploads/623127/5043187/66-2bab1c0e6d10aeab3ec0637d616c2922_CrillBrendanP.pdf
- Crooke, J. A. & Hagopian, J. G. (1996). SPIE, 2814. <https://doi.org/10.1117/12.254152>
- Crooke, J. A., Gunderson, J. A., Hagopian, J. G., et al. (2006). SPIE 6271, 627108
- Crooke, J., Bolcar, M., & Hylan, J. (2019). Funding Strategy Impacts and Alternative Funding Approaches for NASA's Future Flagship Mission Developments, Astro2020 White Paper. http://surveygizmoreponseuploads.s3.amazonaws.com/fileuploads/623127/5043187/186-ccb4977b966d4d6f1414fb9c436e1271_CrookeJulieA.pdf
- Crossfield, I. J. M., Barman, T., & Hansen, B. M. S. (2011). *ApJ*, 736, 132
- Crouzier, A., Malbet, F., Henault, F., et al. (2016). *A&A*, 595, 108
- Crowther, P. A., Schnurr, O., Hirschi, R., et al. (2010). *MNRAS*, 408, 731
- Crowther, P. A., Caballero-Nieves, S. M., Bostroem, K. A., et al. (2016). *MNRAS*, 458, 624
- Cuntz, M., Saar, S. H., & Musielak, Z. E. (2000). *ApJ*, 533, L151
- Dalcanton, J. J., Williamn, B. F., Lang, D., et al. (2012). *ApJ*, 200, 18
- Dalcanton, J., Seager, S., Aigrain, S., et al., (2015). From Cosmic Birth to Living Earths, AURA Report. <http://www.hdstvision.org/report>
- Danforth, C. W., Keeney, B. A., Tilton, E. M., et al. (2016). *ApJ*, 817, 111
- Danieli, S., van Dokkum, P., Merritt, A., et al. (2017). *ApJ*, 837, 136
- Dean, B. H., Aronstein, D. L., Smith, J. S., et al. (2006). SPIE, 6265, 626511
- Debes, J. H., Jang-Condell, H., Weinberger, A. J., et al. (2013). *ApJ*, 771, 45
- Deharveng, J.-M., Faiesse, S., Milliard, B., & Le Brun, V. (1997). *A&A*, 325, 1259
- Delitsky, M. L., & Lane, A. L. (1998). *J Geophys Res*, 103, 31391
- Dent, W. R. F., Wyatt, M. C., Roberge, A., et al. (2014). *Science*, 343, 1490

- Des Marais, D. J., Harwit, M., Jucks, K., et al. (2001). NASA Jet Propulsion Laboratory Publication 01-008. <https://ntrs.nasa.gov/archive/nasa/casi.ntrs.nasa.gov/20020027887.pdf>
- Des Marais, D. J., Harwit, M. O., Jucks, K. W., et al. (2002). *Astrobiology*, 2, 153
- Dever, J. A., Pietromica, A. J., Stueber, T. J., et al. (2002). NASA / TM—2002-211337, <https://ntrs.nasa.gov/archive/nasa/casi.ntrs.nasa.gov/20020039136.pdf>
- Dewell, L., Nordt, A., Bell, R., et al. (2019). NASA Contract 80NSSC18K0817, System Level Segmented Telescope Design Final Report
- Dodge, M. (1984). *Applied Optics*, 23, 12
- Dittmann, J. A., Irwin, J. M., Charbonneau, D., et al. (2017), *Nature*, 544, 333
- Domagal-Goldman, S. D., Segura, A., Claire, M. W., et al. (2014). *ApJ*, 792, 90
- Domagal-Goldman, S., Arney, G., Lopez, E., et. al. (2019). Astrobiology as a NASA Grand Challenge, Astro2020 APC White Paper. http://surveygizmoreponseuploads.s3.amazonaws.com/fileuploads/623127/5043187/201-538b5710188b0a5fdbaba1f-05f5435ab_DomagalGoldmanShawnD.pdf
- Dong, R., & Fung, J. (2017). *ApJ*, 835, 146
- Dooley, G. A., Peter, A. H. G., Yang, T., et al. (2017). *MNRAS*, 471, 4894
- Douglas, E. S., Males, J. R., Clark, J., et al. (2019). *AJ*, 157, 36
- Dove, J. B., & Shull, J. M. (1994). *ApJ*, 430, 222
- Dove, J. B., Shull, J. M., & Ferrara, A. (2000). *ApJ*, 531, 846
- Dressing, C. D., & Charbonneau, D. (2013). *ApJ*, 767, 95
- Dressing, C. D. & Charbonneau, D. (2015). *ApJ*, 807, 1
- Dressing, C., Stark, C., Domagal-Goldman, S., et. al. (2019). The Landscape for Directly Characterizing Potentially Habitable & Inhabited Planets in the Late 2020s and Beyond, Astro2020 APC White Paper. http://surveygizmoreponseuploads.s3.amazonaws.com/fileuploads/623127/5043187/117-e96f42fb29dc0c3e-1963244c8342f307_DressingCourtneyD.pdf
- Driscoll, P. E. & Barnes, R. (2015). *Astrobiology*, 15, 739
- East, M., Wells, C. (2019). ULTRA Segment Stability for Space Telescope Coronagraphy, Astro2020 APC White Paper. http://surveygizmoreponseuploads.s3.amazonaws.com/fileuploads/623127/5043187/254-0f6b277cb8a7da16cfa9f4cce3342753_L3Harris_ULTRA_Segment_Stability_for_Space_Telescope_Coronagraphy_White_Paper.pdf
- Ehlmann, B. L., Mustard, J. F., Murchie, S. L., et al. (2011). *Nature*, 479, 53
- Ehrenreich, D., Bourrier, V., Wheatley, P. J., et al. (2015). *Nature*, 522, 459
- Eisenhower, M. J., Cohen, L. M., Feinberg, L. D., et al. (2015). SPIE, 9602, 96020A
- Eisenstein, D. J., & Hu, W. (1999). *ApJ*, 511, 5
- Ellis, R. S. (2014). arXiv:1411.3330
- Elmegreen, B. G., Bounaud, F., & Elmegreen, D. M. (2008). *ApJ*, 688, 67
- Elmegreen, B. G., Hurst, R., & Koenig, X. (2014). *ApJL*, 782, L1
- Elmegreen, D. M., Elmegreen, B. G., Ravindranath, S., et al. (2007). *ApJ*, 658, 763
- Emeriau-Viard, C. & Brun, A. S. (2017). *ApJ*, 846, 8
- Ercolano B., Rosotti G., (2015). *MNRAS*, 450, 3008
- Ercolano, B., & Pascucci, I. (2017). *RSOS*, 4, 170114
- Ertel, S., Defrère, D., Hinz, P., et al. (2018). *AJ*, 155, 194
- Esposito, L. W. & Travis, L. D. (1982). *Icarus*, 51, 374

- Etiope, G. & Sherwood Lollar, B. (2013). *Rev. of Geophysics*, 51, 276
- Fan, X., Carilli, C. L., & Keating, B. (2006). *ARA&A*, 44, 415
- Feaga, L. M., Protopapa, S., Schindhelm, E., et al. (2015). *A&A* 583, A27
- Feinberg, L., Arenberg, J., Yanatsis, D., et al. (2018). NASA Technical Reports Server, GSFC-E-DAA-TN57378. <https://ntrs.nasa.gov/archive/nasa/casi.ntrs.nasa.gov/20180003980.pdf>
- Feinberg, L., Hayden, B., Saif, B., et. al. (2019). Ultra-stable Technology for High Contrast Observatories, Astro2020 APC White Paper. http://surveygizmoresponseuploads.s3.amazonaws.com/fileuploads/623127/5043187/184-88217c9f817a16f20e4a7439c-5d5af67_Decadal_Whitepaper_Ultrastable_Feinberg.pdf
- Feldman, P. D., McGrath, M. A., Strobel, D. F., et al. (2000). *ApJ*, 535, 1085
- Feng, Y. K., Robinson, T. D., Fortney, J. J., et al. (2018). *AJ*, 155, 200
- Fernández-Perea, M., Larruquert, J. I., Aznárez, J. A., et al. (2006). *SPIE*, 6317, 63170L
- Ferrario, L., de Martino, D., & Gänsicke, B. T. (2015). *Space Sci. Rev.*, 191, 111
- Fettig, R., Lakew, B., Brasunas, J., et. al. (1998). *SPIE*, 3435. <https://doi.org/10.1117/12.323730>
- Figueroa, O., Michelson, P., Woods, D., et. al. (2017). NASA WFIRST Independent External Technical/Management/Cost Review (WIETR) Report. https://www.nasa.gov/sites/default/files/atoms/files/wieter_final_report_101917.pdf
- Finkelstein, S. L., Ryan, R. E., Papovich, C., et al. (2015). *ApJ*, 810, 71
- Finlator, K., Oh, S. P., Özel, F., et al. (2012). *MNRAS*, 427, 2464
- Fischer, D. A., Anglada-Escude, G., Arriagada, P., et al. (2016). *PASP*, 128, 066001
- Fischer, W. J., et al. (2019). Cosmic Origins Spectrograph Instrument Handbook, Version 11.0 (Baltimore : STScI)
- Fleming, B. T., McCandliss, S. R., Kaiser, M. E., et al. (2011). *SPIE*, 8145, 81450B
- Förster Schreiber, N. M., et al. (2011). *ApJ*, 739, 45
- Fortier, A., Beck, T., Benz, W., et al. (2014). *SPIE*, 9143, 91432J
- Fossati, L., Ingrassia, S., & Lanza, A. F. (2015a). *ApJ*, 812, L35
- Fossati, L., Castro, N., Schöller, M., et al. (2015b). *ApJ*, 582, 45
- Fox, G. K., Code, A. D., Anderson, C. M., et al. (1997a). *AJ*, 113, 1152
- Fox, G. K., Code, A. D., Anderson, C. M., et al. (1997b). *AJ*, 113, 1158
- Fox, G. K., Code, A. D., Anderson, C. M., et al. (1998). *MNRAS*, 298, 303
- Foust, J. (2016). Space News. <https://spacenews.com/report-warns-of-wfirst-cost-growth/>
- France, K., Schindhelm, E., Burgh, E. B., et al. (2011). *ApJ*, 734, 31
- France, K., Schindhelm, E., Herczeg, G. J., et al. (2012). *ApJ*, 756, 171
- France, K., Herczeg, G. J., McJunkin, M., & Penton, S. V. (2014). *ApJ*, 794, 160
- France, K., Fleming, B., Hoadley, K. (2016). *SPIE*, 9905, 990506
- France, K., Fleming, B., West, G., et al. (2017). *SPIE*, 10397, 1039713
- Frank, A., Ray, T. P., Cabrit, S., et al. (2014). in *Protostars and Planets VI*, ed. H. Beuther (Tucson, AZ: Univ. Arizona Press), 451
- Fujii, Y., Del Genio, A. D., & Amundsen, D. S. (2017). *ApJ*, 848, 100
- Fukugita, M., Hogan, C. J., & Peebles, P. J. E. (1998). *ApJ*, 503, 518
- Fulton, B. J., Petigura, E. A., Howard, A. W., et al. (2017). *AJ*, 154, 109

- Gady, Franz-Stefan. (2018). The Diplomat. <https://thediomat.com/2018/05/us-navys-13-billion-supercarrier-just-got-even-more-expensive/>
- Gaikwad, P., Khaire, V., Choudhury, T. R., et al. (2017). *MNRAS*, 466, 838
- Gao, P., Hu, R., Robinson, T. D., et al. (2015). *ApJ*, 806, 249
- García Muñoz, A. (2015). *International Journal of Astrobiology*, 14, 379
- García Muñoz, A. (2018). *MNRAS*, 473, 1801
- Garcia-Sage, K., Gloer, A., Drake, J. J., Gronoff, G., & Cohen, O. (2017). *ApJ*, 844, L13
- Garnett, D. R., Skillman, E. D., Dufour, R. J., et al. (1995a). *ApJ*, 443, 64
- Garnett, D. R., Dufour, R. J., Peimbert, M., et al. (1995b). *ApJ*, 449, L77
- Gates, D. M., Keegan, H. J., Schleter, J. C., et al. (1965). *Applied Optics*, 4, 11
- Gaudi, S., Domagal-Goldman, S., Fischer, D., et al. (2019). A Great Successor to the Hubble Space Telescope, Astro2020 APC White Paper. http://surveygizmoresponseuploads.s3.amazonaws.com/fileuploads/623127/5043187/119-3e5f7040ef241f36475c54065d46507b_GaudiBScott.pdf
- Geake, J. E. & Dolffus, A. (1986). *MNRAS*, 218, 75
- Geha, M. C., Brown, T. M., Tumlinson, J., et al. (2013). *ApJ*, 771, 29
- Geha, M. C. (2014). AAS Meeting #223, 314.03
- Geha, M. C., Wechsler, R. H., Mao, Y. Y., et al. (2017). *ApJ*, 847, 4
- Gillon, M., Triaud, A. H. M. J., Demory, B. O., et al. (2017). *Nature*, 542, 456
- Goda, S. & Matsuo, T. (2019). *AJ*, in press. arXiv:1810.09702
- Gómez de Castro A. I. & von Rekowski (2011). *MNRAS*, 411, 849
- Gómez de Castro, A. I., Gaensicke, B., Neiner, C., et al. (2016). *JATIS*, 2, 041215
- Gong, Q., McElwain, M., & Shiri, R. (2016). SPIE, 9904, 99043M
- González, V., Bouwens, R. J., Labbé, I., et al. (2012). *ApJ*, 755, 148
- Gorti, U., Liseau, R., Sándor, Z., & Clarke, C. (2016). *SSRv*, 205, 125
- Greene, T. P., Beichman, C., Eisenstein, D., et al. (2007). SPIE, 6993, 69930G
- Greene, T. P., Line, M. R., Montero, C., et al. (2016). *ApJ*, 817, 17
- Griffith, C. A., Owen, T., Miller, G. A., & Geballe, T. (1998). *Nature*, 395, 575
- Groff, T. D., Prada, C. M., Cady, E., et al. (2017). SPIE, 10400, 24
- Gry, C. & Jenkins, E. B. (2017). *A&A*, 598, A31
- Gunn, C. (2018). <http://sci.esa.int/jwst/60356-the-cargo-aircraft-that-transported-the-james-webb-space-telescope/>
- Gustin, J., Grodent, D., Radioti, A., et al. (2017). *Icarus*, 284, 264
- Gutro, R. (2017). NASA Web Feature. <https://www.nasa.gov/feature/goddard/2017/nasas-james-webb-space-telescope-completes-acoustic-and-vibration-tests>
- Guyon, O., Eisner, J. A., Angel, R., et al. (2013). *ApJ*, 767, 11
- Guzmán-Marmolejo, A., Segura, A., & Escobar-Briones, E. (2013). *Astrobiology*, 13, 550
- Haardt, F. & P. Madau (2012). *ApJ*, 746, 125
- Hagopian, J. G. (1996). SPIE, 2814. <https://doi.org/10.1117/12.254149>
- Hallinan, G., Littlefair, S. P., Cotter, G., et al. (2015). *Nature*, 523, 568
- Hamden, E. T., Linger, N., Kyne, G., et al. (2015). SPIE, 9601, 96010O

- Hammel, H., Grunsfeld, J., Sembach, K., et al. (2019). The Carl Sagan Observatory: A Visionary Space Telescope, Astro2020 APC White Paper. http://surveygizmoresponseuploads.s3.amazonaws.com/fileuploads/623127/5043187/136-c22da2822766b-4c566ed92924fc41855_HammelHeidiB.pdf
- Hansen, C. J., Esposito, L., Stewart, A. I. F., et al. (2006). *Science*, 311, 1422
- Hansen, C. J. & Paige, D. A. (1992). *Icarus*, 99, 273
- Harding, L., Demers, R., Hoenk, M., et al. (2016). *JATIS*, 2, 011007
- Harman, C. E., Schwieterman, E. W., Schottelkotte, J. C., et al. (2015). *ApJ*, 812, 137
- Harman, C. E., Felton, R., Hu, R., et al. (2018). *ApJ*, 56
- Harrison, T. M., Blichert-Toft, J., Müller, W., et al. (2005). *Science*, 310, 1947
- Haswell, et al. (2019). *Nature Astronomy*, submitted
- Heap, S. R., Lindler, D. J., Lanz, T. M., et al. (2000). *ApJ*, 539, 435
- Heath, M. J., Doyle, L. R., Joshi, M. M., et al. (1999). *Orig. Life Evol. Biosph.*, 29, 405
- Hedman, M. M., Gosmeyer, C. M., Nicholson, P. D., et al. (2013). *Nature*, 500, 182
- Hegde, S., Paulino-Lima, I. G., Kent, R., et al. (2015). *Proc. Natl. Acad. Sci.*, 112, 3886
- Heiles, C. (1997). *ApJ*, 481, 193
- Hendler, N. P., Pinilla, P., Pascucci, I. et al. (2018). *MNRAS*, 475L, 62
- Hendrix, A. R., Hurford, T. A., Barge, L. M., et al. (2019). *Astrobiology*, 19, 1
- Henry, A., Scarlata, C., Martin, C. L., et al. (2015). *ApJ*, 809, 19
- Henry, G. W., Marcy, G. W., Butler, R. P., et al. (2000). *ApJ*, 529, 41
- Herczeg, G. J., Linsky, J. L., Valenti, J. A., et al. (2002). *ApJ*, 572, 310
- Hertz, P. (2015). NASA. https://smd-prod.s3.amazonaws.com/science-pink/s3fs-public/atoms/files/Mission_Concept_Study_and_Definition_Team_Charter-V1_2015-12-28.pdf
- Hickey, G., Barbee, T., Ealey, M., & Redding, D. (2010). SPIE, 7731, 773120
- Hines, D. C., Schmidt, G. D., Gordon, K. D., et al. (2001). *ApJ*, 563, 512
- Hitchcock, D. R., & Lovelock, J. E. (1967). *Icarus*, 7, 149
- Hoadley, K., France, K., Kruczek, N., et al. (2016). SPIE, 9905, 99052V
- Hoang, T., Lazarian, A., & Martin, P. D. (2014). *ApJ*, 790, 7
- Homma, D., Chiba, M., Okamoto, S., et al. (2016). *ApJ*, 832, 21
- Hough, J. (2006) *Astronomy & Geophysics*, 47, 31
- Howell, S. B., Sobek, C., Haas, M., et al. (2014). *PASP*, 126, 398
- Hu, R., Seager, S., & Bains, W. (2012). *ApJ*, 761, 166
- Hu, R., Seager, S., & Bains, W. (2013). *ApJ*, 769, 6
- Hu, R., & Seager, S. (2014). *ApJ*, 784, 63
- Hurford, T. A., Helfenstein, P., Hoppa, G. V., et al. (2007). *Nature*, 447, 292
- Hylan, J., Croke, J. A., & Bolcar, M. (2019). Managing Flagship Missions to Reduce Cost and Schedule, Astro2020 White Paper. http://surveygizmoresponseuploads.s3.amazonaws.com/fileuploads/623127/5043187/66-353380de41bc-b86863845a4137b51ab1_HylanJasonE.pdf
- Ida, S., & Lin, D. N. C. (2008). *ApJ*, 685, 584
- Iliev, I. T., Mellema, G., Shapiro, P. R., & Pen, U. L. (2007). *MNRAS*, 376, 534
- Ingersoll, A. P., & Ewald, S. P. (2017). *Icarus*, 282, 260
- Ingleby, L., Calvet, N., Bergin, E., et al. (2011). *ApJ*, 743, 105
- Inoue, A. K., Shimizu, I., Iwata, I., et al. (2014). *MNRAS*, 442, 1805

- Inoue, K. T., Takahashi, R., Takahashi, T., et al. (2015). *MNRAS*, 448, 2704
- IPCC. (2007). Climate Change 2007: Synthesis Report, Contribution of Working Groups I, II, and III to the Fourth Assessment Report of the Intergovernmental Panel on Climate Change, ed. R. K. Pachauri & A. Reisinger (Geneva, Switzerland: IPCC)
- Irsic, V., Viel, M., Haehnelt, M.G., et al. (2017). *PhysRevD*, 96, 023522
- Itoh, S., Matsuo, T., Goda, S., et al. (2017). *AJ*, 154, 197
- Itoh, S., Matsuo, T., Shibai, H., & Sumi, T. (2019). *MNRAS*, in press. arXiv:1811.02762
- Jaacks, J., Thompson, R., & Nagamine, K. (2013), *ApJ*, 766, 94
- Jenkins, E. B. & Wallerstein, G. (1999). ASPC Conf. Series, 164, 118
- Jennings, D. E., Flasar, F., Nixon, C., et. al. (2017). *Applied Optics*, 58, 5274
- Jethwa, P., Erkal, D., & Belokurov, V. (2018). *MNRAS*, 473, 2060
- Jia, X., Kivelson, M. G., Khurana, K. K., et al. (2018). *Nature Astronomy*, 2, 459
- Johnson, S. D., et al. (2015). *MNRAS*, 449, 3263
- Johnstone, D., Hollenbach, D., & Bally, J. (1998). *ApJ*, 499, 758
- Kalousová, K., Sotin, C., Choblet, G., et al. (2018). *Icarus*, 299, 133
- Kaltenegger, L., Traub, W. A., & Jucks, K. W. (2007). *ApJ*, 658, 598
- Kaltenegger, L. & Traub, W. A. (2009). *ApJ*, 698, 519
- Kaltenegger, L., & Sasselov, D. (2010). *ApJ*, 708, 1162
- Kanzaki, Y., & Murakami, T. (2015). *Geochim Cosmochim Acta*, 159, 190
- Kasdin, J., Pogorelyuk, L., Zimmerman, N., et. al. (2019). Relaxing Stability Requirements on Future Exoplanet Coronagraphic Imaging Missions, Astro2020 APC White Paper. http://surveygizmoreponseuploads.s3.amazonaws.com/fileuploads/623127/5043187/137-e292909efc03bb7c92139e51641ced2f_KasdinNJeremy.pdf
- Keeling, C. D., Bacastow, R. B., Bainbridge, A. E., et al. (1976). *Tellus*, 28, 538
- Keller, G. R., Bianchi, L., & Maciel, W. J. (2014). *MNRAS*, 442, 1379
- Kenyon, S. J. & Bromley, B. C. (2004). *AJ*, 127, 513
- Keppler, M., Benisty, M., Mueller, A. et al. 2018, *A&A*, 617A, 44
- Kerber, F., Bristow, P., & Rosa, M. R. (2005a). STIS Calibration Enhancement (STIS-CE) : Dispersion Solutions Based on a Physical Instrument Model, 2005 HST Calibration Workshop. <http://adsabs.harvard.edu/full/2006hstc.conf..309K>
- Kerber, F., Bristow, P., Rosa, M., et al. (2005b). Characterization of Pt/Cr-Ne Hollow-Cathode Lamps for Wavelength Standards in Space *Astronomy*, 2005 HST Calibration Workshop. <https://pdfs.semanticscholar.org/56d6/4296868d1a5a7433af1c-c3eb410d166898f2.pdf>
- Kewley, L. & Ellison, S. (2008). *ApJ*, 681, 1183
- Kharecha, P., Kasting, J., & Siefert, J. (2005). *Geobiology*, 3, 53
- Khaire, V. & Srianand, R. (2015). *MNRAS*, 451, L30
- Khaire, V., Srianand, R., Choudhury, T. R., et al. (2016). *MNRAS*, 457, 4051
- Khan, A. (2017). Phys.org, <https://phys.org/news/2017-08-nasa-flagship-missions.html>
- Kiang, N. Y., Segura, A., Tinetti, G., et al. (2007a). *Astrobiology*, 7, 252
- Kiang, N. Y., Siefert, J., Govindjee, & Blankenship, R. E. (2007b). *Astrobiology*, 7, 222
- Kim, S. Y., Peter, A. H. G., & Hargis, J. R. (2017). arxiv:1711.06267

- Kimble, R., Davila, P., Diaz, C., et al. (2012). SPIE, 8442. <https://jwst.nasa.gov/resources/KimbleSPIE20128442-90.pptx>
- King J. A., Murphy M. T., Ubachs W., et al. (2011). *MNRAS*, 417, 3010
- King J. A., Webb J. K., Murphy M. T., et al. (2008) *Phys. Rev. Letters*, 101, 251304
- Kirk, H. & Myers, P. C. (2012). *ApJ*, 745, 131
- Kislyakova, K. G., Noack, L., Johnstone, C. P., et al. (2017). *Nature Astronomy*, 1, 878
- Kislyakova, K. G., Fossati, L., Johnstone, C. P., et al. (2018). *ApJ*, 858, 105
- Kivelson, M. G., Khurana, K. K., Russell, C. T., et al. (1996). *Nature*, 384, 537
- Klose, J. Z. & Bridges, J. M. (1987). *Applied Optics*, 26, 5202
- Köhler, K., Langer, N., de Koter, A., et al. (2015). *A&A*, 573, A71
- Kollmeier, J. A., Weinberg, D. H., Oppenheimer, B. D., et al. (2014). *ApJ*, 789, L32
- Kopparapu, R. K., Ramirez, R., Kasting, J. F., et al. (2013). *ApJ*, 765, 131
- Kopparapu, R. K., Wolf, E. T., Haqq-Misra, J., et al. (2016). *ApJ*, 819, 84
- Kopparapu, R. K., Wolf, E. T., Arney, G., et al. (2017). *ApJ*, 845, 5
- Kopparapu, R. K., Hébrard, E., Belikov, R., et al. (2018). *ApJ*, 856, 122
- Kornei, K. A., Shapley, A. E., Martin, C. L., et al. (2012). *ApJ*, 758, 135
- Kounkel, M., Hartmann, L., Mateo, M., et al. (2017). *ApJ*, 844, 138
- Kriek, M., et al. (2009). *ApJ*, 750, L71
- Krissansen-Totton, J., Bergsman, D. S., & Catling, D. C. (2016a). *Astrobiology*, 16, 39
- Krissansen-Totton, J., Schwieterman, E. W., Charnay, B., et al. (2016b). *ApJ*, 817, 31
- Krissansen-Totton, J., & Catling, D. C. (2017). *Nature Communications*, 8, 15423
- Krissansen-Totton, J., Olson, S., & Catling, D. C. (2018). *Science Advances*, 4, eaao5747
- Kryukova, E., Megeath, S. T., Gutermuth, R. A., et al. (2012). *AJ*, 144, 31
- Kutyrev, A. S., Collins, N., Chambers, J., et al. (2008). SPIE, 7010, 70103D
- Lada, C. J. & Lada, E. A. (2003). *ARA&A*, 41, 57
- Lagrange, A.-M., Bonnefoy, M., Chauvin, C., et al. (2010). *Science*, 329, 57
- Lagrange, A., Meunier, N., Desort, M., et al. (2011). *A&A*, 9, 4
- Lammer, H., Zerkle, A. L., Gebauer, S., et al. (2018). *A&ARv*, 26, 2
- Lamy, L., Prangé, R., Hansen, K. C., et al. (2017). *JGRA*, 122, 3997
- Landstreet, J. D., Bagnulo, S., Valyavin, G. G., et al. (2012). *A&A*, 545, A30
- Lanza, A. F. (2009). *A&A*, 505, 339
- Lanza, A. F. (2013). *A&A*, 557, A31
- Lanza, A. F. (2014). *A&A*, 572, L6
- Laor, A. & Netzer, H. (1989). *MNRAS*, 238, 897
- Larruquert, J. I., Rodríguez-de Marcos, L. V., Méndez, J. A., et al. (2013). *Optics Express*, 21, 27537
- Launius, R. & DeVorkin, D. (2014). In Hubble's legacy: reflections by those who dreamed it, built it, and observed the universe with it, ed. R. Launius & D. DeVorkin (Smithsonian Institution Scholarly Press)
- Lawrence, C., Redding, D., Steeves, J., et al., (2019). Active Telescopes for Future Space Astronomy Missions, Astro2020 APC White Paper. http://surveygizmoresponseuploads.s3.amazonaws.com/fileuploads/623127/5043187/254-fc89970f38203645ebae62ee-08ad4ab8_LawrenceCharlesR.pdf
- Lazarian, A. & Hoang, T. (2007). *MNRAS*, 378, 910

- Lebouteiller, V., Heap, S., Hubeny, I., et al. (2013). *A&A*, 553, A16
- Lee, D. A., Hogue, M. R., & Gallagher, M. A. (1994). Annual Department of Defense Cost Analysis Symposium, 94-05391. <https://apps.dtic.mil/dtic/tr/fulltext/u2/a275864.pdf>
- Leet, C., Fischer, D. A., & Valenti, J. A. (2019). *AJ*, 157, 187
- Le Gal, M., López, A. A., Pertenais, M., et al. (2018). Proceedings SF2A, 65. <http://adsabs.harvard.edu/abs/2018sf2a.conf...65L>
- Le Gal, M., Pertenais, M., López Ariste, A., et al. (2018). SPIE, 10706, 107061M
- Lehner, N., Savage, B. D., Wakker, B. P., et al. (2006). *ApJ*, 164, 1
- Lehner, N., Howk, J. C., Tripp, T. M., et al. (2013). *ApJ*, 770, 138
- Li, R., Frenk, C. S., Cole, S., et al. (2016). *MNRAS*, 460, 363
- Lincowski, A. P., Meadows, V. S., Crisp, D., et al. (2018). *ApJ*, 867, 76
- Lissauer, J. J. (2007). *ApJ*, 660, L149
- Livermore, R. C., Finkelstein, S. L., & Lotz, J. M. (2017). *ApJ*, 835, 113
- Lopez, E. D., Fortney, J. J., & Miller, N. (2012). *ApJ*, 761, 59
- Loyd, R. O. P., France, K., Youngblood, A., et al. (2016). *ApJ*, 824, 102,
- Luger, R., & Barnes, R. (2015). *Astrobiology*, 15, 119
- Lupu, R., Marley, M., Lewis, N., et al. (2016). *ApJ* 152, 217
- LUVOIR STDT. (2018). The LUVOIR Mission Concept Study Interim Report. arXiv:1809.09668
- Lyon, R. G., Herman, J., Abuhassan, N., et. al. (2004). SPIE, 5487. <https://doi.org/10.1117/12.552237>
- Lyon, R. G., Clampin, M., Melnick, G., et al. (2008). SPIE, 7010, 701045
- Lyons, T. W., Reinhard, C. T., & Planavsky, N. J. (2014). *Nature*, 506, 307
- Madau, P. & Dickinson, M., (2014). *ARA&A*, 52, 415
- Madau, P., & Haardt, F. (2015). *ApJ*, 813, L8
- Malec, A. L., Buning, R., Murphy, M. T., et al. (2010). *MNRAS*, 403, 1541
- Malhotra, R. (1993). *Nature*, 365, 819
- Mao, J., Ling, Z., & Zhang, S.-N. (2014). *ApJ*, 785, 23
- Marlowe, H., McEntaffer, R. L., Tutt, J. H., et al., (2016). *Applied Optics*, 55, 5548
- Marois, C., Zuckerman, B., Konopacky, Q. M., et al. (2010). *Nature*, 468, 1080
- Martin, C., (2005). *ApJ*, 621, 227
- Martin, D. C., et al. (2016). *ApJ*, 824, L5
- Martin, N. F., Ibata, R. A., Chapman, S. C., et al. (2007). *MNRAS*, 380, 281
- Martin, P. K. (2012). NASA Office of Inspector General Report, OIG Report No. IG-12-021. <https://oig.nasa.gov/docs/IG-12-021.pdf>
- Martin, R. G. & Livio, M. (2012). *MNRAS*, 425, L6
- Massari, D., Breddels, M. A., Helmi, A., et al. (2018). *Nature Astronomy*, 2, 156
- Matoba, S., Ishikawa, G., Moriya, S., et al. (2014). *Rev. of Sci. Inst.*, 85, 086105
- Matsubayashi, K., et al. (2012). *ApJ*, 761, 55
- Matsuo, T., Itoh, S., Shibai, H., et al. (2016). *ApJ*, 823, 139
- Matsuo, T., Greene, T., Roellig, T., et al. (2018). SPIE, 10698, 1069844
- Matthews, G., Barrett, D., Bolton, J., et al. (2003). SPIE, 5180, 169
- Mayor, M. & Queloz, D. (1995). *Nature*, 378, 355

- Mazoyer, J., Baudoz, P., Belikov, R., et al. (2019). High-Contrast Testbeds for Future Space-Based Direct Imaging Exoplanet Missions, Astro2020 APC White Paper. http://surveygizmoresponseuploads.s3.amazonaws.com/fileuploads/623127/5043187/161-676fa86289c700a4a14ecd4e041c1c30_Testbeds_for_space-based_Coronagraphs_APC_white_paper.pdf
- McCandliss, S. R. & J. M. O'Meara (2017). *ApJ*, 845, 111
- McCloskey, J. (2016). NASA. <https://ntrs.nasa.gov/archive/nasa/casi.ntrs.nasa.gov/20160005453.pdf>
- McCord, T. B., Hansen, G. B., Shirley, J. H., et al. (1999). *J. Geophys. Res.*, 104, 157
- McEntaffer, R., DeRoo, C., Schultz, T., et al. (2013). *Exp. Astron.*, 36, 389
- McGaugh, S. S. (2005). *ApJ*, 632, 859
- McGrath, M. A., Jia, X., Retherford, K., et al. (2013). *J. Geophys. Res. Space Phys.*, 118, 2043
- McKee, C. F. & Ostriker, J. P. (1977). *ApJ*, 218, 148
- McKee, C. F. & Ostriker, J. P. (2007). *ARAA*, 45, 565
- Meadows, V. S. (2008). in *Exoplanets: detection, formation, properties, habitability*, ed. J. Mason (Springer Science & Business)
- Meadows, V. S. (2017). *Astrobiology*, 17, 1022
- Meadows, V. S., Arney, G. N., Schwieterman, E. W., et al. (2018a). *Astrobiology*, 133
- Meadows, V. S., Reinhard, C. T., Arney, G. N., et al. (2018b). *Astrobiology*, 18, 630
- Menci, N., Grazian, A., Castellano, M., et al. (2016). *ApJ*, 825, L1
- Mesinger, A., & Dijkstra, M. (2008). *MNRAS*, 390, 1071
- Misra, A., Meadows, V., Claire, M., & Crisp, D. (2013). *Astrobiology*, 14, 67
- Misra, A., Meadows, V., & Crisp, C. (2014). *ApJ*, 792, 61
- Misra, A., Krissansen-Totton, J., Koehler, M. C., & Sholes, S. (2015). *Astrobiology*, 15, 462
- Mitchell, D. F. (2015). NASA Technical Reports Server, GSFC-E-DAA-TN23282, <https://ntrs.nasa.gov/archive/nasa/casi.ntrs.nasa.gov/20150009310.pdf>
- Montanes Rodriguez, P., Palle, E., Goode, P. R., & Martin-Torres, F. J. (2006). *AJ*, 651, 544
- Morbidelli, A., Chambers, J., Lunine, J. I., et al. (2000). *Meteorit. Planet. Sci.*, 35, 1309
- Morrissey, P., Harding, L., Bottom, M., et al. (2018). SPIE, 10709, 107090B
- Mortonson, M., & Hu, W. (2009). *Phys. Rev.*, 80, 7301
- Mulders, G. D., Pascucci, I., & Apai, D. (2015). *ApJ*, 798, 112
- Murray, N., Ménard, B., & Thompson, T. A. (2011). *ApJ*, 735, 66
- NASA. (2013). Enduring Quests – Daring Visions: NASA Astrophysics in the Next Three Decades, Astrophysics Roadmap Report. <https://arxiv.org/abs/1401.3741>
- NASA. (2016). NASA Systems Engineering Handbook, NASA/SP-2016-6105 Rev 2. <https://ntrs.nasa.gov/archive/nasa/casi.ntrs.nasa.gov/20170001761.pdf>
- NASA. (2018). Space Launch System (SLS) Mission Planner's Guide, Rev A, <https://ntrs.nasa.gov/archive/nasa/casi.ntrs.nasa.gov/20170005323.pdf>
- NASA. (2019). Astro2020 Decadal Survey Planning. <https://science.nasa.gov/astrophysics/2020-decadal-survey-planning>
- National Academies of Sciences, Engineering, and Medicine. (2017). Powering Science: NASA's Large Strategic Science Missions, (Washington, DC: The National Academies Press) <https://doi.org/10.17226/24857>

- National Academies of *Sciences, Engineering, and Medicine*. (2018). *Exoplanet Science Strategy Report*, (Washington, DC: The National Academies Press). <https://doi.org/10.17226/25187>
- National Academies of *Sciences, Engineering, and Medicine*. (2018). *An Astrobiology Strategy for the Search for Life in the Universe*, (Washington, DC: The National Academies Press). <https://doi.org/10.17226/25252>
- National Research Council. (2011). *Evaluation of U.S. Air Force Preacquisition Technology Development*, (Washington, DC: The National Academies Press). <https://doi.org/10.17226/13030>
- Natta, A., Testi, L., Alcalá, J. M., et al. (2014). *A&A*, 569, A5
- N'Diaye, M., Pueyo, L., & Soummer, R. (2015). *ApJ*, 799, 225
- Nemati, B. (2014). *SPIE*, 9143, 91430Q
- Nemati, B., Effinger, R., Demers, R., et al. (2016). *SPIE*, 9915, 99150M
- Nesvorný, D., Jenniskens, P., Levison, H. F., et al. (2010). *ApJ*, 713, 816
- Newton, O., Cautun, M., Jenkins, A., et al. (2018). *MNRAS*, 479, 2853
- Nikzad, S., Hoenk, M. E., Greer, F., et al. (2012). *Applied Optics*, 51, 365
- Nikzad, S., Hoenk, M., Jewell, A. D., et al. (2016). *MDPI Sensors*, 16, 927
- Nikzad, S., Jewell, A. D., Hoenk, M. E., et al. (2017). *JATIS*, 3, 036002
- Nimmo, F., Porco, C., & Mitchell, C. (2014). *AJ*, 148, 46
- Nordt, A., Dewell, L. (2019). Non-Contact Vibration Isolation and Precision Pointing for Large Optical Telescopes: Enabling breakthrough astronomy and astrophysics with ultra-stable optical systems, Astro2020 APC White Paper. http://surveygizmoresponseuploads.s3.amazonaws.com/fileuploads/623127/5043187/119-806ddbdf3b26fd17af-7803ce18b5cf5f_NordtAlisonA.pdf
- Noterdaeme, P., Petitjean, P., Srianand, R., et al. (2011). *A&A*, 526, L7
- Noterdaeme, P., López, S., Dumont, V., et al. (2012). *A&A*, 542, 33
- Noterdaeme, P., Krogager, J.-K., Balashev, S., et al. (2017). *A&A*, 597, 82
- Nutman, A. P., Bennett, V. C., Friend, C. R. L., et al. (2016). *Nature*, 537, 535
- Offner, S. S. R., Clark, P. C., Hennebelle, P., et al. (2014). in *Protostars and Planets VI*, ed. H. Beuther et al. (Tucson, AZ: Univ. Arizona Press), 53
- Okamoto, S., Arimoto, N., Yamada, Y., & Onodera, M. (2008). *A&A*, 487, 103
- Okrochkov, M., & Tumlinson, J. (2010). *ApJ*, 716, L41
- Olive, K. A., Petitjean, P., Vangioni, E., et al. (2012). *MNRAS*, 426, 1427
- Olson, S. L., Reinhard, C. T., & Lyons, T. W. (2016). *Proc Natl Acad Sci*, 113, 11447
- Olson, S. L., Schwieterman, E. W., Reinhard, C. T., et al. (2018). *ApJ*, 858, L14
- Ono, Y., Ouchi, M., Curtis-Lake, E., et al. (2013). *ApJ*, 777, 155
- Orlitová, I. et al. (2018). *A&A*, 616, 60
- O'Rourke, R. (2006). Congressional Research Service Report, RL32776. <https://fas.org/sgp/crs/weapons/RL32776.pdf>
- O'Rourke, R. (2007). Congressional Research Service Report, RL31404. https://www.everycrsreport.com/files/20070615_RL31404_399717ad5f8fab73080113e940e7c8b8bcf4d52c.pdf
- O'Rourke, R. (2019). Congressional Research Service Report for Congress. RS20643. <https://fas.org/sgp/crs/weapons/RS20643.pdf>

- O'Rourke, R. & Schwartz, M. (2019). Congressional Research Service Report for Congress, R41909. <https://fas.org/sgp/crs/natsec/R41909.pdf>
- Owen, J. & Wu, Y. (2013). *ApJ*, 775, 105
- Palle, E., Ford, E. B., Seager, S., Montanes-Rodriguez, P., & Vazquez, M. (2008). *ApJ*, 676, 1319
- Pang, X., Grebel, E. K., Allison, R. J., et al. (2013). *ApJ*, 764, 73
- Paquin, K. & Jenkins, A. (2008). NASA. https://www.nasa.gov/mission_pages/hubble/service-ing/series/instrument_repairs.html
- Park, S. C., Eisenhower, M. J., Bluth, M., et al. (2017). SPIE, 10398, 103980D
- Pascucci, I., & Sterzik, M. (2009). *ApJ*, 702, 724
- Pascucci, I., & Tachibana, S. (2010). in *Protoplanetary Dust: Astrophysical and Cosmochemical Perspectives*, ed. D. Apai & D. S. Lauretta (Cambridge: Cambridge Univ. Press), 263
- Pascucci, I., Proffitt, C., Ghavamian, P., et al. (2010). SPIE, 7731, 77313B
- Patterson, K., Seo, B.-J., Balasubramanian, K., et al. (2019). SPIE, 11117, 1111752
- Pavlov, A., Kasting, F., Brown, L. L., et al. (2000). *J Geophys Res*, 105, 11981
- Peeples, M. S., et al. (2014). *ApJ*, 786, 54
- Peeples, M. A., Corlies, L., Tumlinson, J., et al. (2019). *ApJ*, 873, 129
- Peña-Guerrero, M. A., et al. (2017). *ApJ*, 847, 107
- Pérez, L. M., Carpenter, J. M., Andrews, S. M., et al. (2016). *Science*, 353, 1519
- Perryman, M., Hartman, J., Bakos, G. A., & Lindegren, L. (2014). *ApJ*, 797, 14
- Pertenais, M., Neiner, C., Bernardi, P., et al. (2015). *Applied Optics*, 54, 7377
- Pertenais, M., Neiner, C., & Petit, P. (2016). SPIE, 9905, 99052Y
- Pertenais, M., Neiner, C., Bouillot, M., et al. (2017). SPIE, 10562, 105622A
- Petit, V., Keszthelyi, Z., MacInnis, R., et al. (2017). *MNRAS*, 466, 1052
- Planavsky, N. J., Reinhard, C. T., Wang, X., et al. (2014). *Science*, 346, 635
- Pogorelyuk, L. and Kasdin, N. J. (2019). in preparation. (see also Kasdin et al. 2019)
- Pohl A., Sissa, E., Langlois, M. et al., (2017). *A&A*, 605, A34
- Pohorille, A., & Pratt, L. R. (2012). *Orig Life Evol Biosph*, 42, 405
- Portegies Zwart, S. F., McMillan, S. L. W., & Gieles, M. (2010). *ARA&A*, 48, 431
- Puchwein, E., Bolton, J. S., Haehnelt, M. G., et al. (2015). *MNRAS*, 450, 4081
- Pueyo, L., Vanessa, B., Bolcar, M., et. al. (2019). Wavefront Sensing and Control technologies for Exo-Earth imaging, Astro2020 APC White Paper. http://surveygizmore-sponseuploads.s3.amazonaws.com/fileuploads/623127/5043187/183-acb3dd1f2f-85531b212888902e200b76_PueyoLaurentA.pdf
- Quanz, S. P., Crossfield, I., Meyer, M. R., et al. (2015). *Int. J. Astrobiol.*, 14, 279
- Quijada, M. A., Del Hoyo, J., & Rice, S. (2014). SPIE, 9144, 91444G
- Rahmani, H., Srianand, R., Gupta, N., et al. (2012). *MNRAS*, 425, 556
- Rahmani, H., Wendt, M., Srianand, R., et al. (2013). *MNRAS*, 435, 861
- Ramirez, R. M., & Kaltenegger, L. (2014). *ApJ*, 797, L25

- Ramos Almeida, C., Martínez González, M. J., Asensio Ramos, A., et al. (2016). *MNRAS*, 461, 1387
- Rappaport, S., Levine, A., Chiang, E., et al. (2012). *ApJ*, 752, 1
- Rauer, H., Catala, C., Aerts, C., et al. (2014). *Exp. Astronomy*, 38, 249
- Rauscher, B. J., Canavan, E. R., Moseley, S. H., et al. (2016). *JATIS*, 2, 41212
- Ray, T. P. (2007). in IAU Symp. 243: Star-Disk Interaction in Young Stars, ed. J. Bouvier & I. Appenzeller (Cambridge: Cambridge Univ. Press), 183
- Raymond, S. N., Quinn, T., & Lunine, J. I. (2006). *Icarus*, 183, 265
- Rein, H., Fujii, Y., & Spiegel, D. S. (2014). *Proc Natl Acad Sci*, 111, 6871
- Reinhard, C. T., Olson, S. L., Schwieterman, E. W., & Lyons, T. W. (2017). *Astrobiology*, 17, 287
- Ribas, A., Macias, E., Espaillat, C. C., et al. (2018). *ApJ*, 865, 77
- Ribas, I., Tuomi, M., Reiners, A., et al. (2018). *Nature*, 563, 365
- Richter, P. (2017). *ASSL*, 430, 15
- Ricker G. R., Winn, J. N., Vanderspek, R., et al. (2014). *SPIE*, 9143, 914320
- Ricotti, M., & Gnedin, N. Y., (2005). *ApJ*, 629, 259
- Rigby, J. R. (2017). *ApJ*, 843, 79
- Rivera-Thorsen, T. E., et al. (2017). *A&A*, 608, 4
- Roberge, A., Feldman, P. D., Lagrange, A. M., et al. (2000). *ApJ*, 538, 904
- Roberge, A., Lecavelier des Etangs, A., Grady, C. A., et al. (2001). *ApJ*, 551, L97
- Roberge, A., Rizzo, M. J., Lincowski, A. P., et al. (2017). *PASP*, 129, 124401
- Roberge, A., Fischer, D., Peterson, B., et. al. (2019). The Large UV/Optical/Infrared Surveyor (LUVOIR): Telling the Story of Life in the Universe, Astro2020 APC White Paper. http://surveygizmoreponseuploads.s3.amazonaws.com/fileuploads/623127/5043187/254-482488fe8621a9a6bd43e513c4e38a7f_RobergeAki.pdf
- Roberson, A. L., Roadt, J., Halevy, I., & Kasting, J. F. (2011). *Geobiology*, 9, 313
- Roberts, J. H., & Nimmo, F. (2008). *Icarus*, 194, 675
- Robinson, T. D., Meadows, V. S., & Crisp, D. (2010). *ApJ*, 721, L67
- Robinson, T. D., Meadows, V. S., Crisp, D., et al. (2011). *Astrobiology*, 11, 393
- Robinson, T. D., Stapelfeldt, K. R., & Marley, M. S. (2016). *PASP*, 128, 39
- Rogers, L. A. (2015). *ApJ*, 801, 41
- Rosing, M. T., Bird, D. K., Sleep, N. H., & Bjerrum, C. J. (2010). *Nature*, 464, 744
- Rossi, L. & Stam, D. M. (2018). *A&A*, 616, 117
- Roth, L., Saur, J., Retherford, K. D., et al. (2014). *Science*, 343, 171
- Ruane, G., Jewell, J., Mawet, D., et al. (2016). *SPIE*, 9912, 99122L
- Rugheimer, S., & Kaltenegger, L. (2017). *ApJ*, 854, 19
- Sabbi E., Lennon, D. J., Gieles, M., et al. (2012). *ApJ*, 754, L37
- Sacco, G. G., Flaccomio, E., Pascucci, I., et al. (2012). *ApJ*, 747, 142
- Sagan, C., Thompson, W. R., Carlson, R., et al. (1993). *Nature*, 365, 715
- Saif, B., Chaney, D., Greenfield, P., et al. (2017). *Applied Optics*, 56, 6457
- Saif, B., Greenfield, P., North-Morris, M., et al. (2019). *Applied Optics*, 58, 3156
- Sallum, S., Follette, K. B., Eisner, J. A. et al. (2015). *Nature*, 527, 342
- Samarkin, V. A., Madigan, M. T., Bowles, M. W., et al. (2010). *Nature Geosci*, 3, 341
- Saur, J., Duling, S., Roth, L., et al. (2015). *J Geophys Res Sp Ph*, 120, 1715

- Sayson, J. L., Ruane, G., Jovanovic, N., et al. (2019). *SPIE*, 11117, 1111754
- Scalo, J. & Elmegreen, B. G. (2004). *ARA&A*, 42, 275
- Scarrott, S. M., Draper, P.W., Stockdale, D. P., et al. (1993). *MNRAS*, 264, 7
- Schenker, M. (2015). PhD Thesis. California Institute of Technology, Publication Number: AAT 3636854, ISBN: 9781321187793, <https://thesis.library.caltech.edu/8626/>
- Schneider, A. (2015). *MNRAS*, 451, 3117
- Schwieterman, E. W., Cockell, C. S., & Meadows, V. S. (2015a). *Astrobiology*, 15, 341
- Schwieterman, E. W., Robinson, T. D., Meadows, V. S., et al. (2015b). *AJ*, 810, 57
- Schwieterman, E. W., Meadows, V. S., Domagal-Goldman, S. D., et al. (2016). *ApJ*, 819, L13
- Schwieterman, E., Reinhard, C., Olson, S., et al. (2018a). arXiv:1801.02744
- Schwieterman, E. W., Kiang, N. Y., Parenteau, M. N., et al. (2018b). *Astrobiology*, 18, 663
- Seager, S., Turner, E. L., Schafer, J., & Ford, E. B. (2005). *Astrobiology*, 5, 372
- Seager, S., Bains, W., & Hu, R. (2013). *ApJ*, 777, 95
- Segura, A., Krelove, K., Kasting, J. F., et al. (2003). *Astrobiology*, 3, 689
- Segura, A., Kasting, J. F., Meadows, V., et al. (2005). *Astrobiology*, 5, 706
- Segura, A., Walkowicz, L. M., Meadows, V., et al. (2010). *Astrobiology*, 10, 751
- Seo, B.-J., Cady, E., Gordon, B., et al. (2017). *SPIE*, 10400, 104000F
- Shaklan, S., Crill, B., Belikov, R., et al. (2019). Status of Space-based Segmented-Aperture Coronagraphs for Characterizing Exo-Earths Around Sun-Like Stars, Astro2020 White Paper. http://surveygizmoresponseuploads.s3.amazonaws.com/fileuploads/623127/5043187/136-f57702d78571272c5a01b9801f3d8f49_ShaklanStuartB.pdf
- Shapley, A. et al. (2003). *ApJ*, 588, 65
- Sheikh, D. (2019). Mirror Coating Technology and Infrastructure Plans for HabEx and LUVUOIR NASA Concept Missions, Astro2020 APC White Paper. http://surveygizmoresponseuploads.s3.amazonaws.com/fileuploads/623127/5043187/137-bd711b1d-10c86e9d716f09025e7e828f_SheikhDavidA.pdf
- Shi, F., An, X., Balasubramanian, K., et al. (2017). *SPIE*, 10400, 1040013
- Shi, F., Balasubramanian, K., Bartos, R. D., et al. (2015). *SPIE*, 9605, 960509
- Shi, F., Balasubramanian, K., Hein, R., et al. (2016). *JATIS*, 2, 11021
- Sholes, S. F., Krissansen-Totton, J., & Catling, D. C. (2019). *Astrobiology*, 19, 655
- Shu, F. H., Johnstone, D., & Hollenbach, D. (1993). *Icarus*, 106, 92
- Shull, J. M., Moloney, J., Danforth, C. W., et al. (2015). *ApJ*, 811, 3
- Siegel, E. (2019). Forbes.com. <https://www.forbes.com/sites/startswithabang/2019/03/22/one-of-these-four-missions-will-be-selected-as-nasas-next-flagship-for-astronomics/#18f391ce4b12>
- Simon, J. D., & Geha, M. (2007). *ApJ*, 670, 313
- Simon, J. D., Geha, M., Minor, Q. E., et al. (2011). *ApJ*, 733, 46
- Simon, M. N., Pascucci, I., Edwards, S., et al. (2016). *ApJ*, 831, 169
- Sing, F., Fortney, J., Nikolov, N., et al. (2016). *Nature*, 529, 59
- Skidmore, W., TMT International Science Development Teams, & TMT Science Advisory Committee (2015). *Res. in Astronomy and Astrophysics*, 15, 1945
- Slavin, J. D., Shull, J. M., & Begelman, M. C. (1993). *ApJ*, 407, 83
- Smith, D., Warwick, S., Glassman, T. M., et al. (2016). *SPIE*, 9904, 99043K

- Smith, L. J., Crowther, P. A., Calzetti, D., et al. (2016). *ApJ*, 823, 38
- Smith, R. J. (2014). *MNRAS*, 443, L69
- Smith, R. J., Lucey, J. R., & Conroy, C. (2015). *MNRAS*, 449, 3441
- Snellen, I. A. G., deKok, R. J., de Mooij, E. J. W., & Albrecht, S. (2010a). *Nature*, 465, 1049
- Snellen, I. A. G., de Mooij, E. J. W., Burrows, A. (2010b). *A&A*, 513, 76
- Snellen, I. A. G., de Kok, R. J., le Poole, R., et al. (2013). *ApJ*, 764, 182
- Snellen, I., de Kok, R., Birkby, J. L., et al. (2015). *A&A* 576, A59
- Snodgrass, C., Agarwal, J., Combi, M., et al. (2017). *A&ARv*, 25, 5
- Soderblom, L. A., Kieffer, S. W., Becker, T. L., et al. (1990). *Science*, 250, 410
- Somerville, R. S. & Davé, R. (2015). *ARA&A*, 53, 51
- Soummer, R., Laginja, I., Will, S. D., et al. (2019). *SPIE*, 11117, 1111756
- Sparks, W. B., Hand, K. P., McGrath, M. A., et al. (2016). *ApJ*, 829, 121
- Sparks, W. B., Schmidt, B. E., McGrath, M. A., et al. (2017). *ApJ*, 839, L18
- Spergel, D., Gehrels, N., Baltay, C., et al. (2015). arXiv:1503.03757
- Spiniello, C., Trager, S., Koopmans, L. V. E., et al. (2014). *MNRAS*, 438, 1483
- Spiniello, C., Trager, S. C., & Koopmans, L. V. E. (2015). *ApJ*, 803, 87
- Staab, D., Haswell, C. A., Smith, G. D., et al. (2017). *MNRAS*, 466, 738
- Stahl, P., Postman, M., Mosier, G., et al. (2014). *SPIE*, 9143. <https://doi.org/10.1117/12.2054766>
- Stahl, P. (2010). *SPIE*, 7796. <https://doi.org/10.1117/12.860264>
- Stanimirovi, S. & Zweibel, E. G. (2018). *ARA&A*, 56, 489
- Stanton, C. L., Reinhard, C. T., Kasting, J. F., et al. (2018). *Geobiology*, 16, 597
- Stark, C. C., Roberge, A., Mandell, A., et al. (2014). *ApJ*, 795, 122
- Stark, C. C., Roberge, A., Mandell, A., et al. (2015). *ApJ*, 808, 149
- Stark, C. C., Cady, E. J., Clampin, M., et al. (2016). *SPIE*, 9904, 99041U
- Stark, C. C., Belikov, R., Bolcar, M. R., et al. (2019). *JATIS*, 5, 024009
- Steidel, C. et al. (2010). *ApJ*, 717, 289
- Steigmann, G. A. (1978). *MNRAS*, 185, 877
- Stephan, K., Jaumann, R., Brown, R. H., et al. (2010). *Geophys Res Lett*, 37, L07104
- Stockman, H. S., Angel, J. R. P., & Miley, G. K. (1979). *ApJ*, 227, 55
- Stofan, E. R., Elachi, C., Lunine, J. I., et al. (2007). *Nature*, 445, 61
- Strigari, L. E., Bullock, J. S., & Kaplinghat, M. (2007). *ApJ*, 657, L1
- Strigari, L. E., Bullock, J. S., Kaplinghat, M., et al. (2008). *Nature*, 454, 1096
- Subedi, H., Groff, T. D., & Juanola-Parramon, R. (2019). *SPIE*, 11117, 1111757
- Sullivan, P. W., Winn, J. N., Berta-Thompson, Z. K., et al. (2015). *ApJ*, 809, 77
- Szulágyi, J. & Mordasini, C. 2017, *MNRAS*, 465L, 64
- Tamburello, V., et al. (2017). *MNRAS*, 468, 4792
- Tarter, J. C., Backus, P. R., Mancinelli, R. L., et al. (2007). *Astrobiology*, 7, 30
- Teolis, B. D., Perry, M. E., Hansen, C. J., et al. (2017). *Astrobiology*, 17, 926
- Thompson, T. A., Quataert, E., & Murray, N. (2005). *ApJ*, 630, 167
- Thomson, R. C., Robinson, D. R. T., Tanvir, N. R., et al. (1995). *MNRAS*, 275, 921
- Tian, F. (2015). *Earth Planet Sci Lett*, 432, 126
- Tonnesen, S., Smith, B. D., Kollmeier, J., et al. (2017). *ApJ*, 845, 47
- Toro Iniesta, J. C. & Collados, M. (2000). *Applied Optics*, 39, 1637

- Torrealba, G., Koposov S. E., Belokurov V., et al. (2016). *MNRAS*, 459, 2370
- Tout, C. A., Wickramasinghe, D. T., Leibert, J., et al. (2008). *MNRAS*, 387, 897
- Townsend, et al. (2010). *ApJ*, 714, 318
- Tremonti, C. A., Moustakas, J., & Diamond-Stanic, A. M., (2007). *ApJ*, 663, L77
- Tripp, T. M. (2013). arXiv:1303.0043
- Tumlinson, J., Thom, C., Werk, J. K., et al. (2013). *ApJ*, 777, 59
- Tumlinson, J., Peebles, M. S., & Werk, J. K., (2017). *ARA&A*, 55, 389
- Tumlinson, J., Arenberg, J., Mountain, M., et. al. (2019). The Next Great Observatories: How Can We Get There?, Astro2020 APC White Paper. http://surveygizmoresponseuploads.s3.amazonaws.com/fileuploads/623127/5043187/209-c872b1b64f09e326de-0c68106823549a_TumlinsonJason.pdf
- Turner, J. K., Beck, S. C., & Ho, P. T. P. (2000). *ApJ*, 532, 109
- Turtle, E. P., Genio, A. D. Del, Barbara, J. M., et al. (2011). *Geophys. Res. Letters*, 38, 1
- Tutt, J. H., McEntaffer, R. L., Marlowe, H., et al. (2016). *J. Astron. Instrument.*, 05, 1650009
- Ubachs, W., Bagdonaite, J., Salumbides, E. J., et al. (2016). *Rev. Mod. Phys.*, 88, 21003
- Ubachs, W. (2018). *SSRv*, 214, 3U
- ud-Doula, A., Owocki, S. P., & Townsend, R. H. D. (2008). *MNRAS*, 385, 97
- Ueno, Y., Yamada, K., Yoshida, N., et al. (2006). *Nature*, 440, 516
- van Dokkum, P. G., & Conroy, C. (2010). *Nature*, 468, 940
- van Dokkum, P., Conroy, C., Villaume, A., et al. (2017). *ApJ*, 841, 68
- van Weerdenburg F., Murphy M. T., Malec A. L., et al. (2011). *Phys. Rev. Lett.*, 106, 180802
- Verhamme, A. et al. (2018), *MNRAS*, 478, 60
- Viel, M., Becker, G. D., Bolton, J. R., et al. (2013). *PhysRevD*, 88, 043502
- Villard, E. (2018). <https://www.nasa.gov/feature/goddard/2018/follow-the-sttars-to-find-nasas-webb-telescope>
- Vink, J. S. & Harries, T. J. (2017). *A&A*, 603, 120
- Vogelsberger, M., Zavala, J., Cyr-Racine, F. Y., et al. (2016). *MNRAS*, 460, 1399
- von Rekowski, B., Brandengurg, A., Dobler, W., et al. (2003). *A&A*, 398, 825
- Wagner, A. Y., Bicknell, G. V., & Umemura, M. (2012). *ApJ*, 757, 136
- Wagner, K., Apai, D., Kasper, M., et al. (2015). *ApJ*, 813, L2
- Walker, J. C. G., Hays, P. B., & Kasting, J. F. (1981). *J Geophys Res Ocean*, 86, 9776
- Walsh, S. M., Willman, B., & Jerjen, H. (2009). *AJ*, 137, 450
- Wang, J., Mawet, D., Ruane, G., et al. (2017). *AJ*, 153, 183
- Weiner, B., et al. (2009). *ApJ*, 692, 187
- Weisz, D. R., et al. (2014). *ApJ*, 789, 147
- Wellman, J., Weaver, G., & Redding, D. (2012). AAS Meeting #219, 136.06. <https://ui.adsabs.harvard.edu/abs/2012AAS...21913606W/abstract>
- Werk, J. K., et al. (2014). *ApJ*, 792, 8
- Werner, M., Swain, M., Vasisht, G., et al. (2016). *JATIS*, 2, 041205
- Werneth, R. (2001). https://spacecraft.ssl.umd.edu/design_lib/ICES01-2204.HST_EVA_lessons.pdf

- Wessen, R., Borden, C. S., Ziemer, J. K., et al. (2013). AIAA Space 2013 Conference and Exposition, 5454. <https://www.tib.eu/en/search/id/BLCP%3ACN085455551/Space-Mission-Concept-Development-using-Concept/>
- Will, S. D. & Fienup, J. R. (2019). *SPIE*, 11117, 1111738
- Willman, B., et al. (2005). *ApJ*, 626, L85
- Williams, B., et al. (2014). *ApJ*, 215, 9
- Windhorst, R. & Smith, R. W. (2013). http://www.asu.edu/clas/hst/www/jwst/jwsttalks/jwst-lessons_aao13.pdf
- Winn, J. N. & Fabrycky, D. C. (2015). *ARA&A*, 53, 409
- Wiseman, J. (2015). IAU General Assembly, 29, 2258532
- Witt, E., Fleming, B., France, K., et al. (2018). *SPIE*, 10699, 1069904
- Woese, C. R., & Fox, G. E. (1977). *Proc Natl Acad Sci*, 74, 5088
- Wofford, A., Leitherer, C., Walborn, N.R., et al. (2012). arXiv:1209.3199
- Wofford, A., Leitherer, C., Chandar, R., & Bouret, J.-C. (2014). *ApJ*, 781, 122
- Wordsworth, R., & Pierrehumbert, R. (2014). *ApJ*, 785, L2
- Wordsworth, R. D., Schaefer, L. K., & Fischer, R. A. (2018). *ApJ*, 155, 195
- Wotta, C. B., et al. (2016). *ApJ*, 831, 95
- Wyse, R. F. G., Gilmore, G., Houdashelt, M. L., et al. (2002). *NewA*, 7, 395
- Yan, H. & Lazarian, A. (2006). *ApJ*, 653, 1292
- Yang, B., Hutsemékers, D., Shinnaka, Y., et al. (2018). *A&A* 609, L4
- Yang, J., Cowan, N. B., & Abbot, D. S. (2013). *ApJ*, 771, L45
- Young, S., Axon, D. J., Robinson, A., et al. (2007). *Nature*, 450, 74
- Youngblood, A., France, K., Loyd, R. O. P., et al. (2016). *ApJ*, 101
- Yusof, N., Hirschi, R., Meynet, G., et al. (2013). *MNRAS*, 433, 1114
- Zahnle, K. J., & Catling, D. C. 2017, *ApJ*, 843, 122
- Zerkle, A. L., Claire, M. W., Domagal-Goldman, S. D., et al. (2012). *Nature Geosci*, 5, 359
- Zhang, H., Yan, H., & Dong, L. (2015). *ApJ*, 804, 142
- Zhou, Y., Herczeg, G. J., Kraus, A. L., et al. (2014). *ApJ*, 783, L17
- Zhu, Z. (2015). *ApJ*, 799, 16
- Zimmerman, N. T., N'Diaye, M., St. Laurent, K. E., et al. (2016). *SPIE*, 9904, 99041Y